Une approche théorique à la photochimie moléculaire basées sur la densité pour l'étude de propriétés remarquables relatives aux états excités moléculaires

Federica Maschietto

▶ **To cite this version:**

Federica Maschietto. Une approche théorique à la photochimie moléculaire basées sur la densité pour l'étude de propriétés remarquables relatives aux états excités moléculaires. Autre. Université Paris sciences et lettres, 2019. Français. NNT : 2019PSLEC032 . tel-03203183

HAL Id: tel-03203183
https://pastel.hal.science/tel-03203183

Submitted on 20 Apr 2021

HAL is a multi-disciplinary open access archive for the deposit and dissemination of scientific research documents, whether they are published or not. The documents may come from teaching and research institutions in France or abroad, or from public or private research centers.

L'archive ouverte pluridisciplinaire **HAL**, est destinée au dépôt et à la diffusion de documents scientifiques de niveau recherche, publiés ou non, émanant des établissements d'enseignement et de recherche français ou étrangers, des laboratoires publics ou privés.

PSL UNIVERSITÉ PARIS

THÈSE DE DOCTORAT
DE L'UNIVERSITÉ PSL

Préparée à Chimie ParisTech

Density-based approaches to photo-induced properties and reactivity of molecular systems

Soutenue par
Federica Maschietto
Le 21 octobre 2019

Ecole doctorale n° 388
Chimie Physique et Chimie Analytique de Paris-Centre

Spécialité
Chimie physique

Composition du jury :

Esmail, ALIKHANI Professeur, Sorbonne Université	*Président*
Masahiro, EHARA Professor, Institute for Molecular Science	*Rapporteur*
Nadia, REGA Professor, Università degli Studi di Napoli	*Rapporteur*
Victor S., BATISTA John Randolph Huffman Professor of Chemistry, Yale University	*Examinateur*
Ilaria, CIOFINI Directrice de recherche, Chimie ParisTech	*Directrice de thèse*

Chimie Paris ParisTech | PSL

ACKNOWLEDGMENTS

I am thankful for so much in this three-year cycle, I (at least) owe a debt of gratitude to all those I had the privilege to work alongside. Each has contributed considerably to enrich this time and their thoughts and suggestions have been essential. I want to take the chance to you all here.

I first must express my gratitude to my phD advisor, Ilaria Ciofini, to whom I am deeply grateful for the constant scientific, but also human support she has offered me during these years. Having a mentor is a privilege, especially as you are to me a brilliant example of how a professional scientist should think and work. I will always be grateful to you for the many advises and constructive critics you have addressed to me.

If it is true, as I believe, that each is the fruit of the environment in which it grows I can only address my thanks to Carlo Adamo - director of the department I have been working in. Thank you for for sharing your knowledge and expertise, as well as your memorable stories, unavoidable side-dish of every day's lunch.

My gratitude goes also to Frederic Labat, who, besides sharing his office with me, always made his knowledge and expertise available.

Thanks are given also to those who have kindly accepted to be members of the jury: Esmail Alikhani, Victor Batista, Masahiro Ehara and Nadia Rega.

My sincere thanks go to my near-office-friend Alistar Ottochian who did not miss one single occasion to prove its kindness and will to help, always prompt to take up a challenge and propose one.

Special thanks are also due to Liam Wilbraham and Pierpaolo Poier, sharp minds and and good friends, with whom I had the pleasure to share - and I hope I will continue sharing - long discussions, both science related and not.

I have enormous gratitude for all my colleagues and friends for making Chimie ParisTech such an enjoyable environment, each with his/her peculiar character and mind. In pseudo-chronological order of appearance Chiara Ricca, Alexandra Szemjonov, Stefania Di Tommaso, Davide Presti, Anna Notaro, Franz Heinemann, Johannes Karges, Marta Alberto, Marco Campetella, Juan Sanz-Garcia, Indira Fabre, Luca Perego, Gloria Mazzone, Laura Le Bras, Eleonora Menicacci, Umberto Raucci, Francesco Muniz Miranda, Anna Perfetto, Carmen Morgillo, Davide Luise, Jun Su, Bernardino Tirri, Dario Vassetti, Gabrielly Miyazaki, Laure Thieulloy. I extend the thanks also to the excellent collaborators I have had the pleasure to discuss and work with throughout this thesis, Aurelie Perrier, Gilles Gasser, Gilles Lemercier, Eric Brémond and Peter Reinhardt.

Big thanks to all friends at ENS, who have welcomed me in their environment in multiple occasion, and without whom all unconventional (but pleasant) working hours would have not even been imaginable.

Thanks to all friends in Paris, brothers-in-phD, who have shared with me this wonderful experience. You have enriched the last three years with you presence and wonderful company.
A warm acknowledgement goes to my four lovely friends Valentina Santolini, Blanche Lacoste, Lia Bruna and Giulia Cosentino and to my sister Vittoria, for this occasion, all exceptional proofreaders. Although you are now living far, you never miss an occasion to offer your support. You couldn't be more effective and delightfully persistent, and I thank you for this.
A huge thanks goes to my parents, undefeatable optimists and most convinced supporters of my life challenges and career. An additional thank is due to my father for the "special edition" my PhD thesis. This manuscript is the third title of a trilogy, which encloses the final writings of my cursus studiorum, including bachelor, master and finally doctoral thesis. Even if completely out of the usual themes of the MaschiettoEditore publishing house, you have proudly included all volumes in your catalog. Grazie Papà.
Finally, I would like to dedicate a word to my life partner and true lifeblood Lorenzo, who in these three years, and with timeless conviction, has always been ready to offer me his support. Your unwavering trust and unconditional tenderness have strengthened me every day and enlightened each step of this three-year journey. You have given me hope and courage for the future, and for that I will always be grateful to you.

ABSTRACT

The recent developments in theoretical photochemistry have proven the capability of theoretical methods to provide solutions for an in-depth characterization of the photochemical properties and reactivity of organic and inorganic chromophores. In particular, time-dependent functional methods are nowadays considered amongst the most reliable and cost-effective computational tools to investigate excited state processes, and have contributed to confer theory a leading position in assisting new discoveries through rational photosynthetic design.

However, the results of these theoretical methodologies are often hard to interpret on a chemical basis, as an accurate description of the modeled system requires handling a large set of output mathematical objects such as density matrices and orbital coefficients.

This thesis focuses on devising, constructing, and applying cost-effective approaches to calculate the photophysical properties of molecular systems in the context of density functional theory. The objective of our work is to define a set of purposely-derived density descriptors that can be combined to provide a straightforward interpretation of the relevant photophysical pathways for the many processes taking place at the excited state. More specifically, we deliver a collection of TDDFT-based computational protocols, based on the knowledge of ground and excited state densities, to characterize the excited-state potential energy surfaces of molecular systems.

In the first part of this manuscript, which comprises Chapter 2 and 3, we provide a brief introduction of the theoretical background and state of the art that motivates our developments.

The second part is dedicated to a systematic assessment of the D_{CT} index [1], that is, an established metric that measures the extent of charge separation that results from the hole/particle generation of the excited state. This descriptor is the key component of our methodology and lays the foundations for our developments. In Chapter 4, we systematically analyze how the D_{CT} index is affected by the density relaxation involved in the post-linear response treatment of time-dependent density functional theory. For this purpose, we consider a family of push-pull dyes of increasing length, where the primary hole/particle charge-separation distance grows with the length of the molecular skeleton. First, we benchmark the influence of different density functional approximations on this descriptor, showing that it might yield considerably-different representations depending on the kernel used for generating the exciton. Then, starting from this evidence, we then investigate the effect of relaxed and unrelaxed densities, showing that they both yield a consistent qualitative assessment of the nature of the excited states. In Chapter 5, we further benchmark the D_{CT} index for retrieving the nature of excited states along a full reaction. Using a prototype excited-state proton transfer reaction as a test case, we show that the D_{CT} and other density-based descriptors can be safely used for a quantitative and qualitative assessment of excited states along the full photochemical process. More precisely, the D_{CT} provides a good description of the occurring electronic rearrangements both using density functional and multiconfigurational methods - here CASSCF-CASPT. We then discuss how the D_{CT} could be employed, as it is usually done with energy

gradients, to locate minima on potential surfaces. In Chapter 6, we complement out the investigation with a diagnostic analysis probing the accuracy of TDDFT methods. Here, we rationalize what the pitfalls of TDDFT are, what is the reason for their appearance and under what circumstances existing approximations work well or fail. The application of the M_{AC} diagnostic analysis on different organic chromophores allows us to identify ghost- and spurious-low-lying excitations that result from a chosen density functional approximation. Furthermore, in Chapter 7, we extend such analysis to probe singlet and triplet excitations in metal-containing complexes.

The third part is dedicated to the exploration of the excited state landscapes and relaxation pathways, based on the density arguments. In Chapter 8, we extend our computational setup to characterize excited-state pathways in the case of reactions involving a profound structural change. This investigation fits in the broader context of the computer-assisted design of new molecular architectures with peculiar photochemical traits, able for instance, to store energy through reversible conformational changes induced by electronic excitations. In particular, we extend the formulation of the index Π [2] to the characterization of potential energy surfaces of the lowest-lying excited states away from the Franck-Condon region, for instance, in regions involved in radiative and non-radiative decay patterns.

Finally, in Chapter 9 we introduce a novel methodology aimed at tracking the nature of electronic states along the nuclear trajectory. This approach is based on the definition of a state-specific *fingerprint* that leverages the full information contained in the transition vectors to give a unique characterization to any excited state of interest. We benchmark this method on three known photochemical reactions and show that it is able to precisely recover the nature of the excited state at each step of the reaction, for all systems.

Overall, the state-tracking algorithm and the density-descriptors outlined in this thesis collectively provide a reliable and cost-effective way of disclosing excited state pathways within the theoretical modeling of photophysical processes. The proposed approach can be computed "on the fly" to identify critical areas for TDDFT approaches while, contextually, providing a method for the qualitative identification - in conjunction with energy criteria - of possible reactions paths.

PUBLICATIONS

This manuscript comprises the research work I have carried during my graduate studies in the group of Chimie Théorique et Modélisation of École Nationale Superieure de Chimie Paris, under the supervision of prof. Ilaria Ciofini, and includes a number of published as well as original results.

A consistent part of my graduate research work has been dedicated to the development of computational protocols, rooted on time-dependent density functional theory (TDDFT), aimed at the description of excited state processes at a molecular level. In particular, this project focused on the design and benchmark of a computational setup that makes use of purposely-developed density indexes to efficiently explore and describe the evolution of excited states far from the Franck Condon region. Results from this line of work are reported in Chapters 4, 6, and 7.

In chapter 4, I report our work on charge-transfer (CT) states showing the dependence of their description on the quality of the density. Chapter 6 concerns the origins of the failure of currently used density functional approximations in the calculation of excited states possessing a long-range CT character, and introduces a new index to spot the presence of problematic excitations. Chapter 7 extends the diagnostics of erratic TDDFT behavior related to this class of excitations to metal complexes. Finally, Chapter 8 presents a combined application of our framework to the analysis of the relevant photophysical pathways of several concomitant processes that take place at the excited state, such as structural reorganization and radiative/non-radiative decay.

Chapters 4, 6, and 8 have been published as research papers [3–7], while Chapter 7 is a work in progress at the draft stage [8].

Finally Chapter 9 concerns a new methodology providing a simple and straightforward solution to track excited states along a reaction path, without the need for any parameter optimization, neither requiring the knowledge of the energy profiles. The results of this study will be published in a future paper, now at the draft stage [7].

While this thesis mostly covers results obtained on theoretical models, during these three years I have worked in close collaboration with experimental groups on multiple projects. Specifically, these collaborations focused on the application of our theoretical TDDFT-based framework to the design of new photoactive molecules with specific desired charge transfer properties.

In collaboration the team of Gilles Gasser, from the Inorganic Chemical Biology group at Chimie ParisTech, we focused on the rational design of one- and two- photon synthesizers for anti-cancer phototherapy (PDT). Part of the results are published in [9]. Two future papers are now at the draft stage [10, 11].

In collaboration with the team of Thierry Pauporté from the IRCP, Paris, we have designed new dendritic core carbazole-based hole transporting materials for efficient and stable hybrid perovskite solar cells. The result of such studies are published in [12].

Publications

[3] J. Sanz García, F. Maschietto, M. Campetella, and I. Ciofini. "Using Density-Based Indexes and Wave Function Methods for the Description of Excited States: Excited State Proton-Transfer Reactions as a Test Case.", 2017

[4] F. Maschietto, M. Campetella, M. J. Frisch, G. Scalmani, C. Adamo, and I. Ciofini. "How are the charge-transfer descriptors affected by the quality of the underpinning electronic density?." 2018

[5] M. Campetella, F. Maschietto, M. J. Frisch, G. Scalmani, I. Ciofini, and C. Adamo. "Charge-transfer excitations in TDDFT: A ghost-hunter index.", 2017

[6] F. Maschietto, J. Sanz García, M. Campetella, and I. Ciofini. "Using density based indexes to characterize excited states evolution.", 2019

[7] F. Maschietto, A. Perfetto, and I. Ciofini. "Following excited states in molecular systems using density-based indexes: a dual-emissive system as a test case.", 2019 (†: joint first authors)

In preparation

[8] F. Maschietto, J. Sanz-Garcia, C. Adamo, and I. Ciofini. "Charge-Transfer Metal Complexes using Time-Dependent Density Functional theory: how to spot ghost and spurious states?.", *In preparation*, 2019

[13] F. Maschietto, A. Ottochian, L. Posani, and I. Ciofini. "Mapping states along reaction coordinates: A state-specific fingerprint for efficient state tracking.", *In preparation*, 2019

Publications with experimental collaborators

[9] J. Karges, F. Heinemann, F. Maschietto, M. Patra, O. Blacque, I. Ciofini, B. Spingler, G. Gasser. "A Ru(II) polypyridyl complex bearing aldehyde functions as a versatile synthetic precursor for long-wavelength absorbing photodynamic therapy photosensitizers. " 2019

[12] T. Bui, M. Ulfa, F. Maschietto, A. Ottochian, M. Nghiêm, I. Ciofini, F. Goubard, and T. Pauporté. "Design of dendritic core carbazole-based hole transporting materials for efficient and stable hybrid perovskite solar cells.", 2018

In preparation

[10] F. Heinemann, M. Jakubaszek, J. Karges, C. Subecz, F. Maschietto, M. Dotou J. Seguin, N. Mignet, E. V. Zahínos, M. Tharaud, O. Blacque, P. Goldner, B. Goud, B. Spingler, I. Ciofini, and G. Gasser. "Towards DFT-Rationally Designed Long-Wavelength Absorbing Ru(II) Polypyridyl Complexes as Photosensitizers for Photodynamic Therapy.", *In preparation*, 2019

[11] J. Karges, M. Jakubaszek, F. Maschietto, J. Seguin, N. Mignet, M. Tharaud, O. Blacque, P. Goldner, B. Goud, B. Spingler and I. Ciofini, G. Gasser. "Evaluation of the Medicinal Potential of Ruthenium(II) Polypyridine based Complexes as One- and Two-Photon Photodynamic Therapy Photosensitizers.", *In preparation*, 2019

CONTENTS

1 INTRODUCTION AND THESIS FRAMEWORK 13
1.1 The art of building simple models to describe complex electronic excitations 13
1.2 Thesis framework 14

I GENERAL BACKGROUND AND OVERVIEW OF STATE OF THE ART DENSITY-BASED METHODS

2 THEORETICAL BACKGROUND AND METHODS 19
2.1 Context 19
2.2 Ground state density functional theory in a nutshell 20
2.2.1 The many body problem 20
2.2.2 The basic idea behind DFT 21
2.2.3 Constrained search 23
2.3 The Kohn-Sham equations 24
2.3.1 The non-interacting system 24
2.4 Enforcement of the Kohn-Sham approach 28
2.4.1 Spin-orbital approximation 28
2.4.2 Linear Combination of Atomic Orbitals (LCAO) 28
2.4.3 The Self-Consistent Field (SCF) method 30
2.4.4 The exchange-correlation approximation 30
2.4.5 Self-interaction and derivative discontinuities 36
2.5 Time-Dependent Density Functional Theory 38
2.5.1 Runge-Gross theorem 39
2.5.2 The van Leeuven theorem 40
2.5.3 Time-dependent Kohn-Sham framework 40
2.5.4 Spin-dependent formalism 44
2.5.5 Excitation energies in TDDFT 45
2.5.6 The adiabatic approximation in TDDFT 46
2.5.7 Reductions of the TDDFT scheme 47
2.5.8 Tamm-Dancoff approximation 47
2.6 Time-dependent DFT and charge-transfer states 48
2.6.1 Charge transfer states in the limit of a large separation 49
2.6.2 Improved description of charge-transfer states 50
2.6.3 Range-separated hybrid functionals 51
2.7 Solvation Models 51
2.7.1 The polarizable continuum model 51

3 METHODS FOR THE DESCRIPTION OF ELECTRONIC EXCITATIONS: AN OVERVIEW 53
3.1 Context 53
3.2 Introduction 54

3.3 Density matrices 56
3.3.1 One-particle transition density matrices 56
3.3.2 One-particle reduced density matrices 60
3.3.3 Difference density matrices 61
3.4 Density descriptors derived from the 1DDM 62
3.4.1 The D_{CT} index, a charge-transfer distance derived in real space 62
3.4.2 Excited state metrics based on attachment/detachment density matrices 64
3.4.3 Hilbert-space related attachment/detachment density matrices-based centroids of charge 69
3.5 Analysis of excited states from 1TDM 70
3.5.1 An orbital based descriptor: Δr 70
3.5.2 Exciton descriptors 72

II TDDFT ROOTED PROCEDURES FOR THE DESCRIPTION OF EXCITED STATES

4 EXCITED STATES FROM TDDFT: A MEASURE OF CHARGE-TRANSFER 79
4.1 Context 79
4.2 Introduction 79
4.3 Theoretical background and methods 81
4.3.1 Excited state properties and the Z-vector method 82
4.4 Computational Details 87
4.5 On the nature of the first excited state of push-pull molecules of various length 87
4.6 Conclusions 96

5 APPLICATION OF DENSITY-BASED INDEXES FOR THE DESCRIPTION OF EXCITED STATES 99
5.1 Context 99
5.2 Introduction 99
5.3 Computational details 101
5.4 Assessment of the model system: HT vs HBT 102
5.5 Description of the ESIPT in HT Using CASSCF-CASPT2 calculations and density based indexes. 106
5.6 Conclusions 108

6 THE PROBLEMATIC DESCRIPTION OF CHARGE-TRANSFER EXCITATIONS USING DFT 111
6.1 Context 111
6.2 Introduction 111
6.3 A ghost-hunter index for charge-transfer excitations 114
6.4 Performance of the M_{AC} index on inter- and intramolecular excitations 116
6.4.1 Proof of concept using a popular test case 116
6.4.2 Charge-transfer transitions in push-pull systems 118
6.5 M_{AC} diagnostics in real systems 121

6.5.1 First step to build an effective strategy for the characterization of photochemical processes 121
6.5.2 Excited state intramolecular proton transfer in CPDNO 124
6.5.3 Charge-transfer process in DMABN 125
6.5.4 Charge-transfer process in Phen-PENMe$_2$ 127
7 M_{AC} DIAGNOSTICS IN METAL COMPLEXES 131
7.1 Context 131
7.2 Introduction 133
7.3 Analysis of the absorption spectra of Ru(II) polypyridyl complexes 134
7.4 M$_{AC}$ diagnostics in metal complexes 135
7.4.1 Triplet states 144
7.5 Conclusions 144

III EXPLORATION OF THE EXCITED STATE LANDSCAPE ALONG A RELAXATION PATHWAY BASED ON THE REORGANIZATION OF THE DENSITY
8 FOLLOWING EXCITED STATES IN MOLECULAR SYSTEMS USING DENSITY-BASED INDEXES 149
8.1 Context 149
8.2 Introduction 150
8.3 Π descriptor for the study of excited state evolution and reactivity. 152
8.4 Insights on the mechanism of the excited state proton transfer in CPDNO 153
8.5 Uncovering the excited state pathway to dual emission 155
8.6 Multiple paths towards dual emission in DMABN 157
8.7 An excursion through the excited energy levels of Phen-PENMe$_2$ 159
8.7.1 Considerations on the energy profiles of the lowest excited states. 159
8.7.2 Simulation and interpretation of the observed absorption spectrum 162
8.7.3 Interpretation of the excited state pathway 163
8.7.4 Conclusions 167
9 A STATE-SPECIFIC FINGERPRINT FOR AN EFFICIENT EXCITED STATE TRACKING 169
9.1 Context 169
9.2 Introduction 170
9.3 Methods 171
9.3.1 State tracking procedure 171
9.3.2 Construction of the "true" matrix 174
9.4 Results 176
9.5 Overlap-based methods 177
9.5.1 Performance of the overlap method 180
9.6 Discussion and perspectives 181
10 CONCLUSION AND PERSPECTIVES 185
10.1 Outline 185
10.2 Methodology and future research 187

IV APPENDIX

11 SUPPLEMENTARY MATERIALS 191
11.1 Computational details 191
11.2 2D excited state S_1 PES and related D_{CT} surfaces computed for HBT and HT 193
11.3 Collection of computed data relative to the M_{AC} diagnostics in Chapter 6 195
11.3.1 Raw data relative to Section 6.4.2 195
11.3.2 Raw data relative to Section 6.5 196
11.4 Raw data relative to calculation of Π values in Section 8.7 206
11.5 Natural transition orbitals of CPDNO, DMABN and PHEN-PENMe$_2$ 208
11.6 Data for to the construction of the reference map of CPDNO and DMABN 215
11.6.1 DMABN 215
11.6.2 CPDNO 215
11.7 Computational details relative to the calculations of Ru(II) complexes in Section 7.4 216
11.8 Raw data relative to the calculations of Ru(II) complexes 216
11.9 Natural transition orbitals of the metal complexes 226

V RÉSUMÉ EN FRANÇAIS

12 RESUMÉ EN FRANÇAIS 241
12.1 Introduction 241
12.1.1 L'art de construire des modèles simples pour décrire des excitations électroniques complexes. 241
12.1.2 Contexte générale de la thèse 242
12.2 Contexte théorique et méthodes 245
12.3 Méthodes de description des excitations électroniques : une vue d'ensemble 246
12.4 Une mesure de transfert de charge dans les transictions électroniques 248
12.5 Application d'indices basés sur la densité pour la description des états excités 249
12.6 La description problématique des excitations de transfert de charges à l'aide de la DFT 250
12.7 Diagnostic M_{AC} dans les complexes métalliques 251
12.8 Suivi des états excités dans les systèmes moléculaires 253
12.9 Determiner la distribution rélative des états excités le long d'un chemin réactionnel 254

1

INTRODUCTION AND THESIS FRAMEWORK

1.1 THE ART OF BUILDING SIMPLE MODELS TO DESCRIBE COMPLEX ELECTRONIC EXCITATIONS

"Photoactive" molecules are those from which an observable response may be elicited by an interaction with light [14]. The perturbation of the electronic structure may be released through an induced chemical reaction, change in color or luminescence, an alteration of magnetic properties, or a combination of several of these. Molecules (and materials) with such properties find applications in a wide range of different fields, and devices may be fabricated which harness their intrinsic properties for a particular scope, from the biological and medical world [15, 16], to optoelectronics end energy storage [17, 18].

The constant research of new photoactive molecules of interest in such areas is driven by the need for greater efficiency, improved performance, and reduced cost. Innovation in this field cannot but be related to the accurate knowledge of the mechanisms underlying photo-driven phenomena, at a molecular level, and even more deeply at the electronic structure level. Light-induced processes can be understood in terms of electronic density reorganization, and the question of how does the electron density redistributes in response to a light-induced perturbation may be addressed. It is apparent that the ability to carefully modulate the magnitude of a light-induced perturbation is crucial for the rational design of such class of molecules.

Theoretical chemistry has now reached a level of specificity and diversification that makes it possible to characterize the extent of a deformation of the excited state reactivity of given chromophore by simply applying different strategies and computational tools, and it is possible to obtain a complete description of a reactive process - i.e., its evolution along a specific reaction coordinate - from the absorption of energy to the formation of photoproducts. With currently available hardware and recent developments in theoretical methods such as time-dependent density functional theory (TDDFT), theory has already demonstrated its ability to provide solutions for an in-depth characterization of such processes and is well-positioned to lead the discoveries through the rational pre-synthetic design. The many works published in the last few decades regarding excited states witness the relevance of this topic in the current research.

The possible approaches to the study of photochemical processes are manifold. In general, two main categories can be identified. The first is to study the temporal evolution of a wave packet through the resolution of the time-dependent Schrödinger equation. A second approach - the one we adopt in this thesis - is that of sequencing the course of a light-induced reaction through the characterization of minima on the potential energy surfaces along which the reaction develops, thus identifying relevant steps of the

photochemical path that connects the Franck-Condon region, where the system absorbs, to the return to the ground state, with the formation of photoproducts.

Aside from the energetics of the reaction, an essential quantity that can be looked at to understand and modulate the excited state properties of said molecular systems is the electron density. It is well known that photophysical properties of a given molecular system can be strongly influenced, and are generally predetermined by the presence of particular structural features, for instance, strong electron donating-accepting groups which direct the charge transfer in the excited state. In this context, in the last years, considerable resources have been dedicated to devising efficient strategies to qualitatively and quantitatively characterize this photoinduced charge transfer, and control over different excited state processes which can give rise to potentially useful photophysical traits.

This is the general framework of this thesis. Throughout this work, we will discuss how the joined information delivered by energy and density can provide a comprehensive view of photoinduced processes, in all their complexity, and with the desired accuracy. The energy makes it possible to characterize the local properties of potential surfaces, for instance, saddle points, maximum and minimum points, slopes and energy barriers, and intersections between states. The analysis of the electronic density distributions adds the desired shades to this somewhat discrete description.

1.2 THESIS FRAMEWORK

Nowadays we know that the electron density variation of a chromophore results from the photogeneration of an exciton, that is, the generation of an electron-hole pair. Many works can be found in literature dealing with the definition of systematic yet cost-effective and precise methodologies for the description of vertical excited states [19–21]. In the last decades, advancements in the field have proven the ability of TDDFT to provide an objective and comprehensive description of molecular architectures, from model to complex, chemically relevant systems [22–24]. TDDFT rooted approaches are widely used due to their favorable cost-accuracy ratio and their capability to integrate environmental effects, in a computationally inexpensive manner. Extensive benchmarks [25, 26] examining the performance of TDDFT compared to wave function and experimental methods have contributed to highlight the deficiencies of time-dependent density-based approaches, which can be primarily traced back to the use of approximated exchange-correlation functionals [27–31]. For instance, it is now well known that density functional approximations require unique treatments to correct for the erroneous description of electronic transitions possessing a relevant through space charge-transfer (CT) character [28, 29]. Though the limits of density functional approximations have been well identified, TDDFT remains one of the most used approaches in the context of our investigations, for the reasons above, which in turn make it an optimal choice on which to build a computational setup enabling an accurate and efficient exploration of excited states.

It is, therefore, essential to know how to deal with these limitations and find possible workarounds. Part of the work presented in this thesis is aimed to this purpose. As the transition from the ground state to the excited state implies the transfer of an electron from

one region to another - typically between a donor and an acceptor situated on two different fragments of the same molecule - the initiating step of a photochemical reaction process is unavoidably related to the phenomenon of charge transfer. Hence, our first concern is to introduce a measure to quantify the spatial extent of the charge transfer involved in the initiating step of a photochemical reaction. However, as we aim to track the changes in nature and character of excited states in different regions of the potential energy surfaces, we need to define an adapted metric for the excited state processes. In this context, we seek to develop and apply a relatively low-cost strategy to characterize excited state processes and to track the evolution of excited states along specific reaction coordinates. The strategy we propose is based on the development of new computational procedures rooted in TDDFT and on the use of purposely developed density descriptors. These last all rely on the same metric but, when combined, they make it possible to acquire a qualitative picture and yet a broad understanding of photophysical pathways for the many and concurrent processes taking place at the excited state (structural reorganization, non-radiative decay). These types of indexes, translate computational outcomes in simple chemical and physical concepts, thus delivering a qualitative interpretation of the experimentally observed phenomena.

We apply our protocol both to the description of model compounds and to the determination and prediction of new molecular systems. These novel compounds that allow for the light-induced formation of bonds, can be oriented to different type of applications especially in the field of energy transformation and information, ranging from dual emitters to photo-molecular devices. For their functioning, all systems rely, on substantial structural modifications at the excited state and in the possible crossing of excited states of different nature.

After a brief introduction of DFT and TDDFT methods in Chapter 2, in Chapter 3 we review of some of the existing tools, developed in the last decades for the characterization of the density reorganization which in turn defines the nature and character of an excited state. The following discussion is centered in particular on the density indexes developed within the last three years, which are at the heart of the investigations presented herein.

Chapters 4 and 5 concern the validation of TDDFT rooted procedures for the description of excited states and are devoted to investigating two main issues. The first deals with the impact of the quality of the density on the performance of density-based indexes. This analysis, which is the subject of Chapter 4, serves ultimately to understand where the deficiencies of TDDFT come from and what is their impact when it comes to the characterization of excited states. Secondly, in Chapter 5 we look at some applications of density-descriptors, no longer only in the context of density functional approaches but also of wave function methods. Chapters, 6 and 7 are dedicated to a diagnostic index for the detection of erratic TDDFT behavior both in organic molecular systems and in metal complexes respectively.

A step away from the methodological issues related to the characterization of the charge transfer induced by the chromophore's transition from the ground to the excited state, the subsequent part of this thesis concerns the portrayal of the excited states away from the Franck-Condon region, and the description of the reorganization of the electronic density

in the pathway leading to the photoproducts formation. In Chapter 8, we focus on excited-to-excited state transitions and investigate the pathway of radiative and non-radiative decays. Serving as an illustrative study into other issues related to the tracking of excited states along a reaction coordinate, in Chapter 9 we develop an algorithm for excited state recognition based on the definition of a state-specific fingerprint.

Part I

GENERAL BACKGROUND AND OVERVIEW OF STATE OF THE ART DENSITY-BASED METHODS

2

THEORETICAL BACKGROUND AND METHODS

2.1 CONTEXT

The present work is mainly concerned with the theoretical description of electronic excitation processes and the associated time evolution in molecules. *Ab initio* electronic structure methods respond to this task, providing a route to electronic properties through the solution of the - here non-relativistic - electronic Schrödinger equation, without the addition of any adjustable parameter. For a system consisting of electrons and nuclei, this means that firstly we want to determine quantities such as total ground-state energies, electronic density distributions, equilibrium geometries, bond lengths and angles, forces and elastic constants, dipole moments and static polarizabilities, magnetic moments. All tasks that lie in the domain of applicability of ground-state Density functional Theory (DFT) [32].

Among *ab initio* methodologies, DFT constitutes a formally exact approach to the many-body problem. Besides, DFT appoints the basic premises for another theoretical and computational framework, time-dependent density functional theory (TDDFT). TDDFT allows to describe the behavior of quantum systems out of their equilibrium and thus applies to the description of electronic excitation processes which are described by the (non-relativistic) *time-dependent* electronic Schrödinger equation. Although the concept of "out of equilibrium" can delineate a whole variety of different scenarios, the picture we are specifically interested in concerns systems that are initially in their ground state and are perturbed by an external stimulus, typically a light irradiation.

This phenomenon is closely related to various spectroscopic techniques. In general, the execution of a spectroscopic measurement means that the system in question is subjected to certain external stimulus - i.e., electromagnetic field - which induces a change in the sample, such as electronic transitions. The effects of this action are then measured and analyzed by a detector, revealing the associated spectral properties of the system under study. Many different spectroscopic techniques exist. In this work we will mostly deal with the description of absorption and emission processes, which are usually studied through UV-visible absorption and fluorescence spectroscopies. Both techniques belong to the class of linear spectroscopies, meaning that the change they measure is linearly proportional to the strength of the perturbation applied. However, it should be mentioned that, non-linear spectroscopies may also be studied by TDDFT [32].

In this chapter, we first review the basic of ground state DFT, and later explore its extension to excited states, withing the framework of TDDFT. Furthermore, we introduce a number of useful concepts and approximations related to the study of photochemical processes.

2.2 GROUND STATE DENSITY FUNCTIONAL THEORY IN A NUTSHELL

2.2.1 *The many body problem*

DFT can be considered -a least formally - an exact approach to the time independent many-body problem. Before reviewing the formal framework of DFT, in this section we introduce the many-body problem. This last consists in finding the solution of the time-independent Schrödinger equation for a system of N interacting particles,

$$\hat{H}\Psi(\mathbf{x}_1,\cdots,\mathbf{x}_N) = E\Psi(\mathbf{x}_1,\cdots,\mathbf{x}_N), \tag{1}$$

where $\hat{H}$ is the Hamiltonian operator, $\Psi(\mathbf{x}_1,\cdots,\mathbf{x}_N)$ is the many-body wave function, which contains all information on the quantum state of the system, and E is the total energy of the system. For a system of M nuclei and N electrons, the non-relativistic Hamiltonian is written as a sum of kinetic and potential energies:

$$\hat{H} = \hat{T}_e + \hat{T}_N + \hat{V}_{Ne} + \hat{V}_{ee} + \hat{V}_{NN}, \tag{2}$$

$$\hat{H} = -\sum_i^N \frac{\hbar}{2m_e}\nabla_i^2 - \sum_\alpha^M \frac{\hbar}{2m_\alpha}\nabla_\alpha^2 - \sum_\alpha^M\sum_i^N \frac{e^2 Z_\alpha}{4\pi\epsilon_0 r_{i\alpha}} + \sum_i^{N-1}\sum_{j>i}^N \frac{e^2}{4\pi\epsilon_0 r_{ij}} + \sum_\alpha^{M-1}\sum_{\beta>\alpha}^M \frac{e^2 Z_\alpha Z_\beta}{4\pi\epsilon_0 r_{\alpha\beta}}, \tag{3}$$

where indexes i and j (α and β) run over all electrons (nuclei); q and m_e (Z and m) are the charge and mass of an electron (nucleus); r is the inter-particle distance; $\hbar$ is the reduced Plank's constant and ∇^2 is the Laplacian. The wave function is then defined as a function of $3(N+M)$ coordinates. The two terms denoted by $\hat{T}$ are the kinetic energy operators for the electrons $\hat{T}_e$ and nuclei $\hat{T}_N$. Terms denoted by $\hat{V}$ are the electrostatic term, representing the attraction between electrons and nuclei ($\hat{V}_{Ne}$), the electron-electron repulsion ($\hat{V}_{ee}$) and inter-nucleus repulsion ($\hat{V}_{NN}$). All quantities are expressed in atomic units. Equation 1 is an eigenvalue equation, whose solutions give the many-body wave function Ψ and total energy of the system E_{tot}. By using atomic units ($m_e = 1, \hbar = 1, \frac{e^2}{4\pi\epsilon_0} = 1$), the Hamiltonian reduces to a more compact form,

$$\hat{H} = -\sum_i^N \frac{1}{2}\nabla_i^2 - \sum_\alpha^M \frac{1}{2m_\alpha}\nabla_\alpha^2 - \sum_\alpha^M\sum_i^N \frac{q_i Z_\alpha}{r_{i\alpha}} + \sum_i^{N-1}\sum_{j>i}^N \frac{q_i q_j}{r_{ij}} + \sum_\alpha^{M-1}\sum_{\beta>\alpha}^M \frac{Z_\alpha Z_\beta}{r_{\alpha\beta}}. \tag{4}$$

At this stage, it is useful to introduce a fundamental approximation in quantum chemistry, which allows the separation of electronic and nuclear degrees of freedom. The many-body Hamiltonian in Eq. 3 describes both the motion of the electrons and that of the nuclei. However, electrons and nuclei move on a very different timescale. Due to their difference in mass, nuclei move about three orders of magnitude slower. This is not very surprising if one considers that the mass of a given nucleus is always far greater than that of an electron. Therefore, electronic motion can be considered to take place at a fixed position

of the nuclei, and thus the nuclei are stationary with respect to the motion of the electrons. This is the basic thought behind the **Born-Oppenheimer approximation**(BOA) [33]. As a result, the movement of nuclei and electrons are decoupled and the electronic properties of the system can be calculated at a fixed nuclear geometry. Additionally the nuclear repulsion term becomes a parametric quantity and thus is simply added to the total energy. Under the constraint of BOA, the Hamiltonian in Eq. 3 can be recast into the sum of an electronic Hamiltonian and a constant term $\hat{V}_{NN}$:

$$\hat{H} = \hat{H}_{el} + \hat{V}_{NN} \tag{5}$$

$$= -\frac{1}{2}\sum_{i}\nabla_i^2 + \underbrace{\sum_{A=1}^{M}\sum_{i=1}^{N}\frac{Z_{iA}}{r_{iA}}}_{v_{(\mathbf{r})}} + \sum_{i=1}^{N-1}\sum_{j>i}^{N}\frac{1}{r_{ij}}. \tag{6}$$

$$\tag{7}$$

The electronic Schrödinger equation, is then

$$\hat{H}_{el}\Psi_{el} = E_{el}\Psi_{el}, \tag{8}$$

solving which returns the electronic wave function Ψ_{el} and the total electronic energy E_{el}. The total energy of the system is thus expressed as the sum of the electronic and the nuclear repulsion energy:

$$E_{tot} = E_{el} + E_{NN}, \tag{9}$$

It is convenient to rewrite this Hamiltonian as a sum of mono- and bi-electronic terms

$$\hat{H}_{el} = \sum_{i}^{N}\left(\hat{h}_1(i) + \sum_{j>i}^{N}\hat{h}_{12}(i,j)\right). \tag{10}$$

Because of the bi-electronic term represents the $e^- - e^-$ interaction, the Schrödinger equation cannot be solved analytically for systems with more complexity than hydrogenionic atoms. To study molecular systems of chemical relevance, it thus necessary to develop approximations which render the Schrödinger equation readily solvable.

2.2.2 *The basic idea behind DFT*

Rather than solving the Schrödinger equation for the N-electronic wave function, a complex mathematical object defined by $3N_{\text{electronic}}$ coordinates, Density Functional Theory (DFT) is based on relating the total energy of a system to a simple 3-dimensional observable: the electron density $\rho(r)$ [34]. The density is related to the wavefunction by,

$$\rho(\mathbf{r}) = \Psi^*(\mathbf{r})\Psi(\mathbf{r}) = |\,\Psi^2(\mathbf{r})\,|\,. \tag{11}$$

This approach is conceptually attractive in that it rules out the dependency on N electronic coordinates, significantly reducing the complexity of the electronic problem, still in

including electron-correlation. The density of the electronic ground state is related to the many-electron wave function by,

$$\rho_0(\mathbf{r}) = N \sum_{\sigma} \int d\mathbf{x}_2 \cdots \int d\mathbf{x}_N |\Psi_0(\mathbf{r}, \sigma, \mathbf{x}_2, \cdots, \mathbf{x}_N)|^2, \tag{12}$$

were the integration can be recast into the expression $\int \mathbf{x}_l = \sum_{\sigma l} \int_{\mathbb{R}^3} d\mathbf{r}_l$ to account explicitly for the summation over l spacial and l spin-coordinates. Integrating the ρ over full space returns the number of electrons.

$$\int_{\mathbb{R}^3} \rho(\mathbf{r}) d\mathbf{r} = N. \tag{13}$$

The rigorous formulation for such theory came from Hohenberg and Kohn in 1964 [35]. Their theorems provide the mathematical consistency which has contributed to confer DFT its position of prominence, as one of the most used approaches in theoretical chemistry.

The Hohenberg-Kohn Theorems

In their first theorem Hohenberg and Kohn [35] demonstrated that the electron density of an N-electron system, with a given electronic interaction, uniquely determines the Hamilton operator and thus all properties of the system. The content of the first theorem can be summarized as follows:

> FIRST HOHENBERG-KOHN THEOREM In a finite, interacting N-electron system the ground state density ρ_0 determines the potential $v_0(\mathbf{r})$ up to an additive constant, and consequently it determines also the ground-state wave function $\Psi_0 = \Psi[\rho_0]$, from which all the ground-state properties can be calculated. As a consequence, any observable can be written as a functional the electron density.

This first theorem therefore shows that we can develop a rigorous theory that uses the electron density a the fundamental variable. The total energy can thus be expressed as a *functional* of the density,

$$E_{v0}[\rho] = T[\rho] + V_{Ne}[\rho] + V_{ee}[\rho] = \int_{\mathbb{R}^3} d\mathbf{r} \rho(\mathbf{r}) v_0(\mathbf{r}) + F[\rho]. \tag{14}$$

The second term of this expression introduces the dependence of the total-energy functional on the external potential. The remaining two terms are respectively the kinetic energy functional $T[\rho]$ and the electron-electron repulsion potential $V_{ee}[\rho]$. These last are *universal* functionals, therefore they depend only on the electrons. Therefore, for any N-electron system these terms will be the same, independently of the external potential. In the right-hand side of Eq. 14, $F[\rho]$ is a universal functional of ρ

$$F[\rho] = T[\rho] + V_{ee}[\rho] = \langle \Psi | \hat{T} + \hat{V}_{ee} | \Psi \rangle \tag{15}$$

The second Hohenberg-Kohn theorem establishes a variational principle based on the electron density, thus providing a method for its calculation. Given an approximate density $\tilde{\rho}$, this last determines completely its own potential $\tilde{v}(\mathbf{r})$ and hence its own wavefunction $\tilde{\Psi}$. If $\Psi_0[\rho]$ is the unique ground-state wave function which produces the density ρ_0, then $E_{v0}[\tilde{\rho}]$, calculated using the standard variational procedure satisfies the following property,

SECOND HOHENBERG-KOHN THEOREM

$$\langle\Psi|\hat{H}|\Psi\rangle = \int_{\mathbb{R}^3} d\mathbf{r}\tilde{\rho}(\mathbf{r})v_0(\mathbf{r}) + F[\tilde{\rho}] = E_{v0}[\tilde{\rho}] \geq E_0. \tag{16}$$

meaning that the exact ground state energy is a lower bound to what can be obtained with DFT.

Of note, the Hamiltonian in Eq.16 is the exact Hamiltonian, and as such it involves the exact external potential $v_0(\mathbf{r})$. As a result the exact density ρ minimizes the exact energy expression. Therefore, to obtain the density $\tilde{\rho}$ such that it is the closest to the exact density ρ_0, one has to minimize the energy with respect to the density variation, under the usual constraint that the number of electrons remains unvaried, $\int_{\mathbb{R}^3} d\mathbf{r}\rho(\mathbf{r}) = N$.

As a result, the exact ground-state density $\rho_0(\mathbf{r})$ of an interacting N-electron system can then be found from the Euler equation,

$$\frac{\delta}{\delta\rho(\mathbf{r})}\left(E_{v0}[\rho] - \mu\left[\int_{\mathbb{R}^3} d\mathbf{r}\rho(\mathbf{r}) - N\right]\right) = 0. \tag{17}$$

$$\frac{\partial E_{v0}[\rho]}{\partial\rho(\mathbf{r})} - \mu = 0 \tag{18}$$

Here, μ is a Lagrange multiplier which ensures the correct total number of electrons, and it is identified as the chemical potential, $\mu = \frac{\partial E}{\partial N}$. Given that

$$E_{v0}[\rho] = \int_{\mathbb{R}^3} d(\mathbf{r})\rho(\mathbf{r})v_0(\mathbf{r}) + F[\rho], \tag{19}$$

and solving for μ, one gets,

$$\mu = v_0(\mathbf{r}) + \frac{\partial F[\rho]}{\partial\rho\mathbf{r})}. \tag{20}$$

Hohenberg-Kohn's theorems allow for a transfiguration of the electronic many-body problem: the ground state density ρ_0 replaces the wave function Ψ_0 as the fundamental quantity to be calculated. Yet, the form of the universal functional $F[\rho]$ is unknown.

2.2.3 *Constrained search*

The original Hohenberg–Kohn analysis involved a minimization over all v-representable densities (i.e., those associated with an antisymmetric ground state wavefunction of a

Hamiltonian of the form of Eq. 7. However the conditions for a v-representable density remain elusive to this day. The limits of the original definition have been somewhat overcome by looking at the problem from an alternative view, known as Levy's *constrained search formalism* [36]. The key idea of the constrained search starts from the definition that the ground-state energy E_0, corresponding to the Hamiltonian in Eq. 7 can be mathematically expressed as,

$$E[\rho] = \min_{\Psi} \langle \Psi | \hat{T} + \hat{V}_{ee} + \hat{V}_{Ne} | \Psi \rangle, \tag{21}$$

The result of this search is the wave function $\Psi[\rho]$ that yields the minimum energy. But one can reach an identical result by splitting the constrained search in two steps. Then, the first search is performed over all wavefunctions that return a given density, the second one over all densities, to select the one that returns the overall lowest energy, namely the ground state density $\rho_0(\mathbf{r})$.

$$E_{v0}[\rho] = \min_{\rho} \Big\{ \min_{\Psi \to \rho} \langle \Psi | \hat{T} + \hat{V}_{ee} + \hat{V}_{Ne} | \Psi \rangle \Big\}, \tag{22}$$

$$E_{v0}[\rho] = \min_{\Psi \to \rho} \langle \Psi | \hat{T} + \hat{V}_{ee} + \hat{V}_{Ne} | \Psi \rangle, \tag{23}$$

which provides a definition for the **universal functional** $F[\rho]$,

$$F[\rho] = \min_{\Psi \to \rho} \langle \Psi | \hat{T} + \hat{V}_{ee} | \Psi \rangle. \tag{24}$$

Fully consistent with the Hohenberg-Kohn derivation, the *constrained search* demonstrates that we only need to consider N-representable densities (i.e., those associated with an antisymmetric N-electron wavefunction Ψ).

2.3 THE KOHN-SHAM EQUATIONS

2.3.1 *The non-interacting system*

As shown in the previous section, the Euler equation can be solved to yield the exact density.

$$\mu = v_0(\mathbf{r}) + \frac{\partial F[\rho]}{\partial \rho(\mathbf{r})} \tag{25}$$

$$= v_0(\mathbf{r}) + \frac{\partial T[\rho]}{\partial \rho(\mathbf{r})} + \frac{\partial V_{ee}\rho]}{\partial \rho(\mathbf{r})}. \tag{26}$$

In practice, to apply Eq. 20, one still needs to find a rigorous functional form for the $e^- - e^-$ interaction $V_{ee}[\rho]$ and the kinetic energy $T[\rho]$ of the interacting system. From the Virial theorem we know that the kinetic term is very large[1]. As a result, even small errors in this

1 Twice the average total kinetic energy $\langle T \rangle$ equals N times the average total potential energy $\langle V_{\text{tot}} \rangle$. V_{tot} represents the total potential energy of the system, i.e., the sum of the potential energy over all pairs of particles in the system

term would make the theory useless. After several early attempts, a solution was given by Kohn and Sham in 1965 [37], who recognized that the kinetic energy for a non-interacting system with the same density distribution as the interacting one can be **exactly** computed. Under this assumption, they expressed the total energy of the interacting system as a functional of the non-interacting kinetic energy plus a residual term, which accounts for the differences between the two. The resulting practical scheme though requires to solve a system of N-equation, rather than a single Euler equation. The analysis runs as follows.

Let us start again from the electronic density as defined in Eq. 19, and the universal functional defined as

$$F[\rho] = T[\rho] + V_{ee}[\rho]. \tag{27}$$

If one could find a system of non-interacting particles, having the exact same density as the fully-interacting one. Then one could express the universal functional of this fictitious system as

$$F[\rho] = T_s[\rho] + J[\rho] + E_{\text{xc}}[\rho], \tag{28}$$

where the subscript s denotes that the system is a non-interacting system one. T_s represents a non-interacting kinetic energy, J is the classical repulsion of the density with itself, and the $E_{\text{xc}}[\rho]$ is the exchange-correlation energy. This last contains the energy contributions that account for the difference between the non-interacting and the interacting system. In simple words, it behaves like a "rest" gathering a share of kinetic energy and the non-classical part of the electron-electron interaction energy.

$$E_{\text{xc}}[\rho] = T[\rho] - T_s[\rho] + V_{ee}[\rho] - J[\rho] \tag{29}$$

Then, the electronic energy, reformulated in terms of the non interacting kinetic energy functional would be,

$$E_{v0}[\rho] = \int_{\mathbb{R}^3} d(\mathbf{r})\rho(\mathbf{r})v_0(\mathbf{r}) + T_s[\rho] + J[\rho] + E_{\text{xc}}[\rho]. \tag{30}$$

This is the quantity that one has to minimize, subject to the constraint of fixed N - following the variational procedure introduced by the second Hohenberg-Kohn theorem, and yielding the Euler equation.

$$\mu = v_s(\mathbf{r}) + \frac{\partial T_s[\rho]}{\partial \rho(\mathbf{r})}, \tag{31}$$

where the effective potential v_s is defined as,

$$v_s(\mathbf{r}) = v_0(\mathbf{r}) + \frac{\partial J[\rho]}{\partial \rho(\mathbf{r})} + \frac{\partial E_{\text{xc}}[\rho]}{\partial \rho(\mathbf{r})}. \tag{32}$$

At this stage we can actually make the key observation thus validating the initial assumption. The Euler equation for the non-interacting system (Eq.31) is actually the same as the conventional DFT Euler equation (in Eq. 25) if the latter is calculated for a system of non-interacting particles, moving in an external potential $v_s(\mathbf{r})$ - ($T = T_s$, and $V_{ee} = 0$). From this observation we land to the conclusion that, **the density of the real system**

is exactly the same as the density of a non interacting system with external potential $v_s(\mathbf{r})$. This ultimately legitimates the choice of a system of non-interacting particles. The Hamiltonian of such system, denoted as $\hat{H}_s$, reduces to,

$$\hat{H}_s = \hat{T}_s + \hat{V}_s = \sum_j^N \Big(-\frac{1}{2}\nabla_j^2 + v_s(\mathbf{r}_j) \Big). \tag{33}$$

This operator is now separable, and consists of the sum of N single particle operators. Moreover, the wavefunction of a non-interacting system is trivially represented by a Slater determinant,

$$\Psi(\mathbf{x}_1, \mathbf{x}_2, \ldots, \mathbf{x}_N) = \frac{1}{\sqrt{N!}} \begin{vmatrix} \varphi_1(\mathbf{x}_1) & \varphi_2(\mathbf{x}_1) & \cdots & \varphi_N(\mathbf{x}_1) \\ \varphi_1(\mathbf{x}_2) & \varphi_2(\mathbf{x}_2) & \cdots & \varphi_N(\mathbf{x}_2) \\ \vdots & \vdots & \ddots & \vdots \\ \varphi_1(\mathbf{x}_N) & \varphi_2(\mathbf{x}_N) & \cdots & \varphi_N(\mathbf{x}_N) \end{vmatrix},$$

where the single particle orbitals are a set of orthonormal orbitals, each of which is a solution of the Schrödinger equation,

$$\Big(-\frac{\nabla^2}{2} + v_s \Big) \varphi_j(\mathbf{r}) = \epsilon_j \varphi_j(\mathbf{r}), \tag{34}$$

$$\forall \{i,j\} \in [1,N]^2 \quad \Big\langle \varphi_i \Big| \, \varphi_j \Big\rangle = \delta_{ij} \tag{35}$$

where once more,

$$v_s(\mathbf{r}) = v_0(\mathbf{r}) + \int_{\mathbb{R}^3} d\mathbf{r'} \frac{\rho(\mathbf{r'})}{\mathbf{r} - \mathbf{r'}} + v_{\mathrm{xc}}(\mathbf{r}); \quad v_{\mathrm{xc}}(\mathbf{r}) = \frac{\partial E_{\mathrm{xc}}}{\partial \rho(\mathbf{r})}. \tag{36}$$

Then, the ground state density of the non-interacting system, which is identical to the density of the real system is simply given by the sum of the square of all the single-particle wavefunctions - the summation runs here over the N lowest occupied single-particle orbitals.

$$\rho_s(\mathbf{r}) = \sum_{j=1}^N | \, \varphi_j(\mathbf{r}) \, |^2, \tag{37}$$

and the kinetic energy of the non-interacting system, which is by definition different from the interacting one, is then,

$$T_s[\rho] = \sum_j^N \Big\langle \varphi_j \Big| -\frac{1}{2}\nabla^2 \Big| \varphi_j \Big\rangle. \tag{38}$$

Eqs. 34 to 37 are the so-called Kohn-Sham equations. We have thus demonstrated that the ground state electronic density can be calculated using the variational method, by reformulating the Hohenberg-Kohn variational principle using a fictitious non-interacting

system. Once the Konh-Sham equations of the non-interacting system are solved, the summation over all orbital energies yields,

$$\sum_{j}^{N} \epsilon_j = T_s[\rho_0] + \int_{\mathbb{R}^3} d\mathbf{r}\, \rho(\mathbf{r}) v_s(\mathbf{r}). \tag{39}$$

Rearranging and plugging Eq. 39 into Eq. 30 yields an alternative and convenient expression for the interacting system:

$$E_{v0}[\rho] = \underbrace{\sum_{j}^{N} \epsilon_j - \frac{1}{2}\int_{\mathbb{R}^3} d\mathbf{r} \int_{\mathbb{R}^3} d\mathbf{r'} \frac{\rho_0(\mathbf{r})\rho_0(\mathbf{r'})}{\mathbf{r}-\mathbf{r'}}}_{E_{\mathrm{KS}}[\rho]} - \int_{\mathbb{R}^3} d\mathbf{r}\, \rho_0(\mathbf{r}) v_{\mathrm{xc}}(\mathbf{r}) + E_{\mathrm{xc}}[\rho]. \tag{40}$$

where we have denoted the non-interacting energy as E_{KS}. At this point one only needs to define a proper expression for the E_{xc} functional, knowing that this term incorporates not only the exchange and correlation energy but also contains all other interactions - including electron exchange, static and dynamic correlation and changes to the kinetic energy brought by inter-electron interactions. However, no obvious formulation is known, capable of recovering universally its form and properties. This is in fact a fundamental issue in DFT: we do not know how to write down the exact $E_{\mathrm{xc}}[\rho]$ functional. A more in-depth discussion follows in section 2.4.4

We conclude this section with the observation, that the Kohn-Sham equations

$$E = \sum_{j}^{N} \left\langle \varphi_j \right| -\frac{1}{2}\nabla_j^2 \left| \varphi_j \right\rangle + \int_{\mathbb{R}^3} d\mathbf{r} \rho(\mathbf{r}) v(\mathbf{r}) + J[\rho] + E_{\mathrm{xc}}[\rho] \tag{41}$$

$$\left(-\frac{1}{2}\nabla_j^2 + v(\mathbf{r}) + \frac{\partial J[\rho]}{\partial \rho(\mathbf{r})} + \frac{\partial E_{\mathrm{xc}}[\rho]}{\partial \rho(\mathbf{r})} \right) \varphi_j(\mathbf{r}) = \epsilon_j \varphi_j(\mathbf{r}) \tag{42}$$

bear a striking resemblance to those of Hartree-Fock theory [38],

$$E = \sum_{j}^{N} \left\langle \varphi_j \right| -\frac{1}{2}\nabla_j^2 \left| \varphi_j \right\rangle + \int_{\mathbb{R}^3} d\mathbf{r} \rho(\mathbf{r}) v(\mathbf{r}) + J[\rho] + [\rho] \tag{43}$$

$$\left(-\frac{1}{2}\nabla_j^2 + v(\mathbf{r}) + \frac{\partial J[\rho]}{\partial \rho(\mathbf{r})} \right) \varphi_j(\mathbf{r}) - \int_{\mathbb{R}^3} d\mathbf{r'} \frac{\rho(\mathbf{r},\mathbf{r'})}{|\mathbf{r}-\mathbf{r'}|} \varphi_j(\mathbf{r}) = \epsilon_j \varphi_j(\mathbf{r}) \tag{44}$$

where E_{x} is the exact exchange energy,

$$E_{\mathrm{x}} = -\frac{1}{4}\int_{\mathbb{R}^3} d\mathbf{r} \int_{\mathbb{R}^3} d\mathbf{r'} \frac{\rho(\mathbf{r},\mathbf{r'})^2}{|\mathbf{r}-\mathbf{r'}|}, \tag{45}$$

and $\rho(\mathbf{r},\mathbf{r}')$ is the one-particle density matrix,

$$\rho(\mathbf{r},\mathbf{r}') = 2\sum_{j}^{N_{occ}} \varphi_j(\mathbf{r})\varphi_j^*(\mathbf{r}'). \tag{46}$$

Although we will not delve into the details of this method here, it is worth to mention that their similarity arises by virtue of the fact that both approaches are based on a Slater determinant, though there is one main difference which deserves to be clarified. By explicitly *approximating* the wavefunction of the interacting system as a single determinant, Hartree-Fock implicitly leaves out all correlation effects. On the other hand, DFT explicitly *represents* the wave function of the non-interacting system by a single determinant, yielding the exact density and kinetic energy T_s associated with this system. From the Kohn-Sham derivation, we know this density to be the same as the fully interacting one. Therefore, the ground state energy can be reassembled from Eq.40. This last would in principle yield the *exact* ground state energy if the true expression of the E_{xc} functional was known.

2.4 ENFORCEMENT OF THE KOHN-SHAM APPROACH

2.4.1 *Spin-orbital approximation*

The key insight of Kohn and Sham is that one may adopt an effective single-particle picture to transform DFT into the practical scheme that is implemented nowadays in most quantum chemistry programs. As a result, the N-electronic problem can be decomposed into N non-interacting entities, and the electronic Hamiltonian is written as a sum of mono-electronic operators:

$$\hat{h}_i\varphi_i(\mathbf{r}) = \epsilon_i\varphi_i(\mathbf{r}) \tag{47}$$

Each operator $\hat{h}_i$ does not include the spin explicitly. Taking into account the property of electron spin, we may define our orbitals as a product of space and spin functions, yielding the so-called spin-orbitals. As far as we are concerned the Hamiltonian we deal with does not account for relativistic effect, thus all coupling between spin and space functions are neglected. Such orbitals can then be written as a product of space φ_i and spin σ_i functions:

$$\varphi(\mathbf{r}_i) = \phi_i(\mathbf{r}_i)\sigma(\mathbf{s}_i). \tag{48}$$

The spin function describes the the intrinsic angular moment of an electron, which may take two values: $\pm\frac{1}{2}$, generally denoted by α and β.

2.4.2 *Linear Combination of Atomic Orbitals (LCAO)*

In order to solve the Kohn-Sham equations for molecules, it is necessary to define the space in which the molecular wavefunction extends. This is done by introducing a set of

variable functions [39], generally referred as basis set. The molecular orbitals, are thus expressed mono-electronic functions, which are defined using a linear combination of basis functions - or atomic orbitals χ_i - centered on each atom,

$$\varphi_i(\mathbf{r}) = \sum_{\mu}^{K} c_{\mu i}\phi_{\mu}(\mathbf{r}) \tag{49}$$

where $c_{\mu i}$ are the expansion coefficients - which may be optimized variationally to yield the ground state wavefunction. As a result, the electronic Schrödinger equation assumes a matrix representation, and can be solved by linear-algebraic matrix techniques. Generally, quantum chemical calculations are performed using either Slater-type orbitals (STO) or Gaussian-type orbitals (GTO). The former have an exponential form,

$$\chi^{\mathrm{STO}} = \frac{[2\zeta]^{n+1/2}}{[(2n)!]^{1/2}} r^{n-2} e^{-\zeta r} Y_l^m(\theta,\Pi), \tag{50}$$

with n, l and m as principal, angular and spin quantum numbers, $Y_l^m(\theta,\Pi)$ spherical harmonics as a function of radial coordinates and ζ as the exponent of the function which controls its overall spread out away from nuclear center. STOs have the advantage that they closely mimic the orbital shape of the hydrogen atom. In practice, however, the calculation of their integrals is cumbersome. Therefore, the common approach is to use a linear combination of GTOs - which, thanks to their Gaussian shape are far simpler to integrate, - to reproduce as close as possible the overall form of a given STO. The general form of a GTO is the following,

$$\chi^{\mathrm{GTO}} = \left(\frac{2\alpha}{\pi}\right)^{3/4} \left[\frac{(8\alpha)^{i+j+k} i!j!k!}{(2i)!(2j)!(2k)!}\right]^{1/2} x^i y^j z^k e^{-\alpha r^2} \tag{51}$$

Gaussian functions, however, are less similar to the $1s$ hydrogen functions, mainly for two reasons: they are not peaked at the nuclear center, and they decay more rapidly. To account for this limitation, *contracted* Gaussian functions (CGTO) are constructed as a linear combination of so-called *primitive* Gaussian functions according to the following expression

$$\chi^{\mathrm{CGTO}(\mathbf{r})} = \sum_{\mu} d_{\mu r} \chi_{\mu}^{\mathrm{GTO}}(\mathbf{r}). \tag{52}$$

where $d_{\mu r}$ are the *contraction* coefficients, allowing to control the overall shape of the CGTO. Each primitive function in the linear combination possesses the same overall character (i, j, k are identical) and differ in the exponent α. In addition, generally, for a given contraction, the standard procedure is to hold the coefficients constant and control the weight of each contraction by an external coefficient. By doing so, one minimizes the number of coefficients to be determined during the optimization of the overall wave function, reducing the cost of the calculation. It is with this type of basis functions that all work in this thesis was carried out.

2.4.3 *The Self-Consistent Field (SCF) method*

The fundamental theorems of DFT evidence the link between the electronic density of a given system and the associated wave function, though they do not deliver a solution to resolve the dependence of the orbitals on the density itself. As a result the Kohn-Sham equations have to be solved variationally, in an iterative manner. This Self Consistent Field (SCF) procedure is outlined in Figure 1. The first SCF cycle starts by generating an initial density matrix $\tilde{\mathbf{D}}$, calculating the external potential v_s (Eq. 34) to be inserted in the Kohn-Sham equations and diagonalizing the set of N eigenvalue equations (Eq. 36). Then, the energy eigenvalues and renewed basis function coefficients resulting from this first step are used to replicate the same procedure until the density matrix elements of the nth and $n-1$th cycles differ by less than a predefined threshold, δ_{tol}. From a physical point of view, *convergence* is reached when the mean-field produced by a given charge density is identical to the field produced from the same density.

2.4.4 *The exchange-correlation approximation*

At this point it is important to state that, in the formalism described above, DFT is formally exact. This means that, if we knew the **exact** form of the exchange correlation potential, DFT would yield the exact energy of the system in question. The inherent complexity of the exchange-correlation functional, however, means that its exact form is unknown, approximations are therefore unavoidable. As already mentioned before, the quest of an universal, accurate as possible yet sufficiently simple functional is still ongoing (and will most likely pursue in the near future). Now one could argue that DFT, compared to other ab-initio methods might be hard to improve in a rigorous way, as exchange-correlation many-body effects are included through the problematic E_{xc} functional, while individual contributions cannot be treated separately in a systematic manner. Though this view is less and less acceptable and accepted, as DFT is more and more accurate compared both to experimental results and sophisticated wave-function methods, with difference that it demands much less computational effort.

By contrast the studies and progresses in the field over the last fifty years, have proven DFT to be rather systematic: xc functionals can be constructed on a formal level by using many-body perturbation theory and proceeding order by order (however, at the price of increasing complexity). In practice, the most successful strategies for constructing approximate xc functionals focus on trying to reproduce some known exact properties. The following paragraph will be devoted to discuss some of these properties.

ORBITALS, EIGENVALUES, ASYMPTOTIC BEHAVIOR It is worth to mention that although the Kohn-Sham ground state slater determinant correctly reproduces the ground-state density, there is no such correspondence with the fully interacting wavefunction. This, in turn plays a role in the calculation of different observables which can hardly be expressed as functional of the density, but can be easily written in the terms of Kohn-Sham orbitals. In this respect, orbital energies deserve a bit of discussion. Let us consider the highest

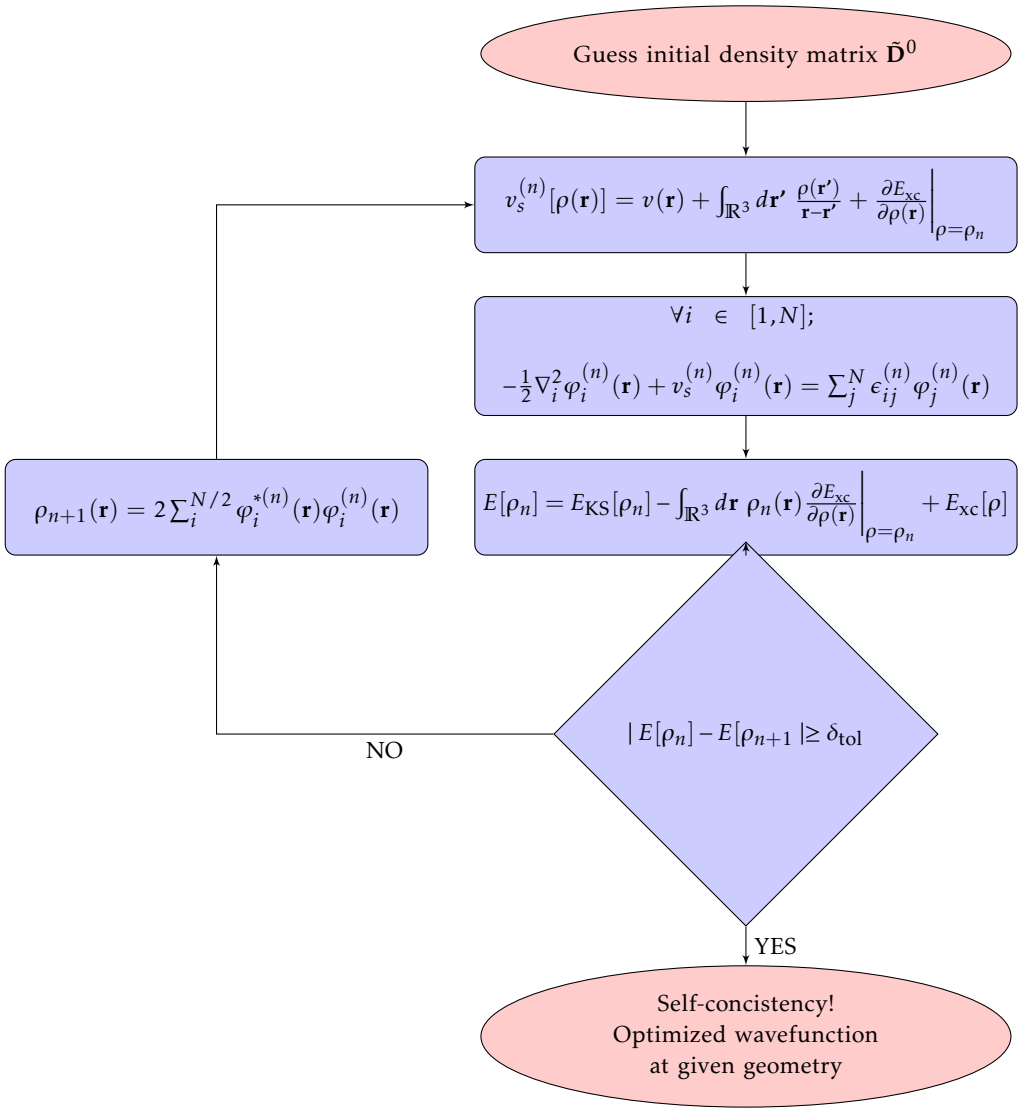

Figure 1: Flowchart of the SCF procedure within the DFT approach

occupied eigenvalue ϵ_N of an N-electron system. According to Koopmans' theorem [40, 41] ϵ_N equals the negative of the ionization potential (IP) of the system - i.e. the energy required to remove an electron from the system and place it at infinite distance. We may therefore write,

$$\epsilon_N(N) = E(N) - E(N-1) = -IP(N), \tag{53}$$

where $E(N)$ and $E(N-1)$ denote the energies of the N- and $N-1$-electron systems, respectively. Hence, ϵ_N has a rigorous physical meaning. The same does not hold true for all other energy eigenvalues ϵ_j. However, one can still relate the lowest unoccupied eigenvalue ϵ_{N+1} to the electron affinity (EA) - the energy gained as an electron - placed at infinite distance - is added to the system. Therefore,

$$\epsilon_{N+1}(N+1) = E(N+1) - E(N) = -EA(N), \tag{54}$$

Because the LUMO is not correctly reproduced (the reason for this will be better explained in the following), the Kohn-Sham excitation energy ($\epsilon_a - \epsilon_i$) differs from the exact excitation energy of a many-body system - a and i denote a virtual and an occupied orbital. Although one may use the former as a first approximation, the orbital difference will get closer to the exact value, the more accurately the unoccupied levels are described. This of course depends on the quality of the approximate xc functional used.

We shall spend a word on the asymptotic behavior of the of the overall potential of an N-electron system (with N positive charges). In the limit of $r \to \infty$ the external and Hartree potentials (in Figure 2) behave as,

$$v(\mathbf{r}) \to -\frac{N}{r}, \quad v_{\mathrm{H}}(\mathbf{r}) \to \frac{N}{r}. \tag{55}$$

When a hole is created, the electron which moves apart perceives the Coulomb potential generated by the remaining $N-1$. This interaction is taken into account by the exchange potential. To cancel the unphysical self-interaction in the Coulomb term, the exchange-correlation potential must therefore have a $-1/r$ dependence at large distances (the reason why correlation effects can be neglected here is that the correlation potential is much more short-ranged. Thus, it usually suffices to analyze only the exchange potential in the asymptotic region).

$$v_{\mathrm{xc}}(\mathbf{r}) \to -\frac{1}{r}. \tag{56}$$

The HF exchange functional exactly shows the correct $-1/r$ decay for large distances while most DFT approximate functionals fail. The corresponding potentials of most functionals used decrease exponentially rather than as $-1/r$. As a consequence, these approximate potentials are less attractive than the exact one at large r values.

Local Density Approximation

We shall discuss the formulation of various functionals, which are historically the most important, and constitute the milestones of the advancement in the field of DFT. All these

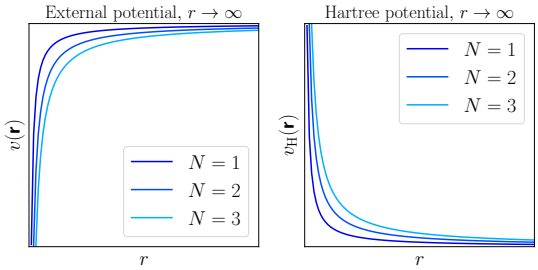

Figure 2: Schematic depiction of the asymptotic behavior of the external and Hartree potentials.

formulations differ by the functional dependence of E_{xc} on the electron density. This is expressed as the intergral of the product between the electron density and a so-called *energy density* ε_{xc} that depends explicitly on the electron density:

$$E_{\text{xc}}[\rho] = \int d\mathbf{r}\rho(\mathbf{r})\varepsilon_{\text{xc}}[\rho(\mathbf{r})]. \tag{57}$$

Here, the energy density is a sum of individual exchange and correlation contributions.

The Local Density Approximation, [37] takes into account the energy density at each position r, computed using the value of ρ at that same position - therefore the functional is local.

$$E_{\text{xc}}^{LDA}[\rho(r)] = \int d\mathbf{r}\rho(r)\varepsilon_{xc}[\bar{\rho}(r)]_{\rho=\bar{\rho}}. \tag{58}$$

In practice, the functionals of this class that are still applied are those that derive from the uniform electron gas [42]. For each given point the exchange-correlation energy is computed as the energy of a uniform electron gas of the same local density.

Generalized Gradient Approximation and Kinetic Energy Density

As the electron density is typically rather inhomogeneous, LDA suffers of severe limitations. An obvious way to get over these limitations - at least partially - is by constructing exchange correlation functionals which depend not only on the local value of the density but also on its gradient. Usually, gradient corrected functionals are obtained by adding a correction term to the LDA functional:

$$\varepsilon_{\text{xc}}^{\text{GGA}}[\rho(\mathbf{r})] = \varepsilon_{\text{xc}}^{\text{LDA}}[\rho(\mathbf{r})] + \Delta\varepsilon_{\text{xc}}\left[\frac{|\nabla\rho(\mathbf{r})|}{\rho^{4/3}(\mathbf{r})}\right], \tag{59}$$

where the correction depends on the dimensionless reduced gradient $\left(\frac{|\nabla\rho(\mathbf{r})|}{\rho^{4/3}(\mathbf{r})}\right)$. This class of functionals is generally referred to as the Generalized Gradient Approximation (GGA) [43].

If including the gradient of the density constitutes an improvement over LDA, a logical step forward - in the same vein as a Taylor expansion - is to use higher order derivatives

of the density. The so-called meta-GGA (mGGA) [44] functionals are constructed using the second order derivative. However, instead of including the Laplacian of the density - which often leads to numerical instabilities - they are formulated using the Kohn-Sham orbital kinetic energy densities τ that one can prove to be connected to the Laplacian,

$$\tau_\sigma(\mathbf{r}) = \sum_i^{occ} \frac{1}{2}|\nabla\varphi(r)|^2. \tag{60}$$

Adiabatic connection and hybrid functionals

According to Kohn-Sham scheme the E_{xc} functional is defined assuming a fully non-interacting reference system of particles. Instead one could imagine to follow up the extent of the electron-electron interaction with an extra parameter. This last is the idea which underlies the adiabatic connection formalism [45], which make it possible to establish the relationship between the real and the non-interacting system [34]. The adiabatic connection follows directly from the Hellmann–Feynman, which relates the derivative of the total energy with respect to a parameter, to the expectation value of the derivative of the Hamiltonian with respect to that same parameter. As a result, the exchange-correlation energy can be expressed as,

$$E_{\text{xc}}[\rho] = \int_0^1 \langle\Psi(\lambda)\big|\, V_{\text{xc}}[\rho](\lambda)\,\big|\Psi(\lambda)\rangle, \tag{61}$$

where the parameter λ controls the amount of electron-electron interaction, which varies between 0 and 1. Using the adiabatic connection formalism, one can express the exchange-correlation potential as a function of λ. This results in a polynomial function of degree $n-1$, and dependent on the parameter λ, which controls the mixing of both the exchange and correlation from DFT, and the HF exchange. In other words, n controls the speed with which the correction brought to DFT is canceled when λ tends towards the unit,

$$U_{\text{xc}}^{\lambda}[\rho] = E_{\text{xc},\lambda}^{\text{DFT}}[\rho] + (E_{\text{x}}^{\text{HF}} - E_{\text{x}}^{\text{DFT}}[\rho])(1-\lambda)^{n-1}. \tag{62}$$

Integration of this relation (67) over the interval $\lambda \in [0,1]$ then gives:

$$E_{\text{xc}}[\rho] = \int_0^1 d\lambda U_{\text{xc}}^{\lambda}[\rho] \tag{63}$$

$$= E_{\text{xc}}^{\text{DFT}}[\rho] + \frac{1}{n}(E_{\text{x}}^{\text{HF}} + E_{\text{x}}^{\text{DFT}}[\rho]) \tag{64}$$

The parameter λ allows one to go smoothly from the fully non-interacting to the interacting system - at a fixed density value (ρ_0). Thus, the exchange-correlation energy is nothing other than the average of the exchange-correlation hole, E_h,

$$E_{\text{xc}}[\rho] = \int_0^1 \langle\Psi(\lambda)\big|\, V_{ee}[\rho](\lambda)\,\big|\Psi(\lambda)\rangle - J[\rho] = E_h[\rho]. \tag{65}$$

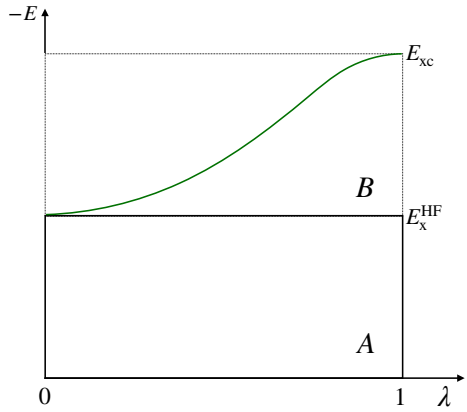

Figure 3: Pictorial representation describing the adiabatic connection method. Rectangle A represents the fully non-interacting system, for which we only have exchange interaction. The full exchange-correlation energy is represented by the sum of the area of rectangle A and that under the green curve in rectangle B

A graphical representation of this integral is particularly insightful. Figure 3 depicts the electron-electron interaction, partitioned into two portions -the lower rectangle, A, and the fraction of upper rectangle delimited by the green line, B. The bottom rectangle represents the fully non-interacting system - in which the only contribution to the electron-electron interaction is the non-classical exchange term E_h ($E_{\mathrm{x}}^{\mathrm{HF}}$ in Hartree-Fock). The upper rectangle, instead, depicts the contribution of the electronic interaction due to the exchange-correlation energy. At $\lambda = 1$ the total interaction energy relative to the lower portion is thus 1 times the exact exchange (HF) energy $E_{\mathrm{x}}^{\mathrm{HF}}$. The formal difference between E_h and $E_{\mathrm{x}}^{\mathrm{HF}}$ is that they are derived using Kohn-Sham orbitals and HF orbitals, respectively. The remaining interaction energy is represented by the area under the green curve in rectangle B, i.e. some fraction x of rectangle B. As we do not know x, nor the expectation value of the fully interacting exchange-correlation potential, we may only regard x as a parameter to optimize. Thus, one can approximate the fully interacting system (upper right corner of B) using some choice of DFT functional, weighted by an appropriate value of x. Using this strategy, the total area under the curve (A+xB) can be approximated as:

$$E_{\mathrm{xc}}[\rho] = E_{\mathrm{x}}^{\mathrm{HF}} + x(E_{\mathrm{xc}}^{DFT}[\rho] - E_{\mathrm{x}}^{\mathrm{HF}}) \tag{66}$$

It is convention to express E_{xc} in terms of an alternative parameter, a, defined as $1 - x$, yielding:

$$E_{\mathrm{xc}} = (1-a)E_{\mathrm{xc}}^{\mathrm{DFT}}[\rho] + aE_{\mathrm{x}}^{HF} \tag{67}$$

In practice, Eq. 67 draws the connection between the interacting and non-interacting systems by mixing a fraction of exact exchange, derived from HF theory [38] with a

standard LDA or GGA. This concept forms the basis for what are known as hybrid density functionals.

One such Hybrid Functional, widely known as PBE0 [46], is constructed using a value of a = 0.25 (i.e. 25% HF exchange):

$$E_{\mathrm{xc}}[\rho] = E_{\mathrm{xc}}^{\mathrm{PBE}}[\rho] + \frac{1}{4}(E_{\mathrm{x}}^{HF} + E_{\mathrm{x}}^{\mathrm{PBE}}[\rho]), \tag{68}$$

where the xc functional used to approximate the fully-interacting system is that of Perdew, Burke and Ernzerhoff - known as PBE [43].

2.4.5 *Self-interaction and derivative discontinuities*

DFT is in principle an exact theory. However, the construction of approximate exchange-correlation functionals leads to basic flaws. Hence, the resulting density functional approximations (DFA) are affected by different sources of error, where by DFA we mean any standard approximation to the exchange-correlation energy within DFT. Among the known errors, the self-interaction error (SIE) in DFAs appears from the fact that the residual self-interaction in the Coulomb part and that in the exchange part do not cancel each other exactly. This error is responsible for the unphysical orbital energies of DFT and the failure to reproduce the potential energy curves of several physical processes. As previously mentioned, the Kohn-Sham excitation energy differs from the exact excitation energy of a many-body (interacting) system. If we where to express the exact excitation energy E_{ex} in terms of the Kohn-Sam eigenvalues, we would write,

$$E_{\mathrm{ex}}(N) = \epsilon_{N+1}(N+1) - \epsilon_N(N). \tag{69}$$

By contrast in the non-interacting system the excitation energy $E_{\mathrm{ex,s}}$ is simply the difference between the highest occupied and lowest unoccupied single-particle orbital,

$$E_{\mathrm{ex,s}}(N) = \epsilon_{N+1}(N) - \epsilon_N(N). \tag{70}$$

Then, we may relate the two excitation energy values as,

$$E_{\mathrm{ex}}(N) = E_{\mathrm{ex,s}}(N) + \Delta_{\mathrm{xc}}. \tag{71}$$

In this expression, Δ_{xc} is the so-called derivative discontinuity, a known source of error in DFT. This term is related to the fact that Exact $v_{\mathrm{xc}}(\mathbf{r})$ jumps discontinuously by a constant amount Δ_{xc} - several eV - as N crosses the integer. This in turn has the consequence that an accurate continuous potential should not vanish asymptotically but rather decay as

$$\lim_{r\to\infty} v_{\mathrm{xc}}(\mathbf{r}) = -\frac{1}{r}. \tag{72}$$

This phenomenon reflects the chemical potential to exchange particles between two systems -i.e, it ensures that heteroatomic molecules dissociate to neutral fragments. Again the exchange part of HF models this behavior correctly, while none of the standard

approximate functionals, which are all characterized by a continuous potential with respect to variations in the number of electrons, is able to do this. Hybrid functionals, which incorporate a fraction of exact exchange do rectify these problem to some extent. In this respect, one could think that simply increasing the amount of HF exchange to 100% would solve the problem. In practice, turns out that this is just a sham solution, as it introduces the substantial error related to the lack of correlation-effects in HF.

In Table 1 we reported a selection of density functionals of different classes, in alphabetical order. These are the functionals selected for the benchmark study in Chapter 4. Despite the number of functionals included, the list is far from being complete, witnessing the extensive work that has been devoted to the development of density functionals with the desired properties.

Class[a]	Functional	X[b]	Reference(s)
GH-GGA	B1B95	28	[47]
GH-GGA	B1LYP	25	[45,48]
GH-GGA	B3LYP	20	[45,48]
GH-GGA	B3P86	20	[45,49]
GH-GGA	B3PW91	20	[45,50]
GH-GGA	B98	21.98	[51]
GGA+D	B97D	0	[52]
GH-GGA	BHandHLYP	50	[53]
mGGA	BMK	42	[54]
GGA	BLYP	0	[48,55]
GGA	BP86[c]	0	[49,55]
GGA	BPBE	0	[43,55]
GGA	BPW91	0	[50,55]
RSH-GGA	CAM-B3LYP	19-65	[56]
GGA	HCTH407	0	[57]
GGA	HCTH	0	[57]
GH-GGA	HFPW91	100	[39,50]
RSH-GGA	HSEH1PBE	25	[58]
GH-mGGA	M05	28	[59]
GH-mGGA	M06	27	[26]
GH-mGGA	M052X	56	[60]
GH-mGGA	M062X	54	[26]
GH-mGGA	M08HX	52.23	[61]
mGGA	M06L	0	[62]
GH-mGGA	M06HF	100	[63]
RSH-mGGA	M11	42.8-100	[64]
mGGA	M11L	0	[65]
NGA	MN12L	0	[66]
GGA	MPWLYP	0	[48,67]
GGA	MPWP86	0	[49,67]

GH-GGA	mPW1PW	25	[67]
GGA	MPWPW91	0	[68]
RSH-GGA	N12SX	25	[68]
GGA	OLYP	0	[48,69]
GH-GGA	O3LYP	11.61	[48,70]
GGA	PBE	0	[43]
GH-GGA	PBE0	25	[46]
GH-GGA	PBE0-DH[e]	25	[71]
GGA	PBEPW91	0	[43,50]
GGA	PW91	0	[50]
GGA	SOGGA11	0	[72]
GH-GGA	SOGGA11X	40.15	[73]
LSDA	SVWN	0	[35,37,74]
mGGA	tHCTH	0	[75]
mGGA	TPSS	0	[44]
GH-mGGA	TPSSh	10	[76]
GH-mGGA	tHCTHhyb	40.15	[75]
mGGA	VSXC	0	[77]
RSH-GGA	wB97	0-100	[78]
RSH-GGA	wB97X	15.77-100	[79]
RSH-GGA+D	wB97XD	22.2-100	[79]

Table 1: Assessment of common DFT functional of different classes.
[a] The acronyms in this column are: LSDA = local spin density approximation, GGA = generalized gradient approximations, +D = addition of molecular mechanic dispersion corrections, NGA = non-separable gradient approximation, WFT = wave function theory, GH = global hybrid, RSH = range-separated hybrid (which can be either long-range-corrected or screened-exchange), mGGA = meta-GGA.
[b] X denotes the percentage of HF exchange
[c] The B86 exchange functional can be also called $X\alpha\beta\gamma$.
[d] The PBE0 functional can be also called PBE1PBE and PBEh, although PBEh is a deprecated name since it is also used for another functional.
[e] PBE0-DH has not been used in this work. We include it here as it is the exponent of a relatively new class of functionals, the so-called double hybrids including a perturbation term into the correlation energy.
[f] Range Separated Hybrid functionals are later defined in section 2.6.3

2.5 TIME-DEPENDENT DENSITY FUNCTIONAL THEORY

By know we have revised the formal framework of ground state DFT. In the following we discuss how it can be extended to the calculation of excited state properties, according to the Time-Dependent Density Functional Theory (TDDFT) scheme [32]. In the following we introduce the basic formalism of TDDFT, from the proof of existence, to the practical

solution of the Kohn-Sham equation. We will discuss how TDDFT can be used to calculate excited-states of molecules, the sources of errors and limitations of this approach along with some approaches to overcome - at least partially - these limits.

Let us consider the usual system of N interacting (non-relativistic) electrons. The system evolves in a scalar potential, which, differently from the static case is a function both of time and space. The total Hamiltonian varies now in time, and the associated Schrödinger equation writes,

$$\hat{H}_{el}(\mathbf{r},t)\Psi_{el}(\mathbf{r},t) = i\frac{\partial}{\partial t}\Psi_{el}(\mathbf{r},t), \tag{73}$$

where:

$$\hat{H}_{el}(\mathbf{r},t) = \hat{T}_e(\mathbf{r}) + \hat{V}_{ee}(\mathbf{r},t) + v(\mathbf{r},t). \tag{74}$$

This expression retraces the time-independent one, with the difference that the time dependency is now explicitly included. Then, the first two terms are again the kinetic and electron-electron repulsion terms. The final term is an external potential, which also evolves in time, and has the form,

$$v(\mathbf{r},t) = v_0(\mathbf{r}) + \theta(t-t_0)v_1(\mathbf{r,t}), \tag{75}$$

where θ is the Heaviside function [80]. The time dependence is "switched-on" at times that are greater than t_0. It follows that for times $t \leq 0$, the external potential is constant and therefore reduces to what we find in the previous sections for the time-independent case. At times $t_0 \neq 0$ the density will start oscillating. Such formalism provides a convenient representation of the physical processes we are interested in - i.e., a molecule hit by a light pulse. Of particular interest are those potentials that can be treated as weak perturbations. As we will show in section 2.5.3, taking the first order response to those perturbations is enough to calculate the excitation energies of a system [32].

2.5.1 *Runge-Gross theorem*

The time-dependent potential $v(\mathbf{r},t)$ fully determines the evolution of the system, through the time-dependent Schrödinger equation. This means that the Schrödinger equation establishes a formal map by which any chosen external potential $V(t)$ produces a time dependent wave function $\Psi(t)$, which represents the time-evolution of given initial state Ψ_0. $\Psi(t)$ can then be used to map a time-dependent density $\rho(\mathbf{r},t)$,

$$v(t) \rightarrow \Psi(t) \rightarrow \rho(r,t) \tag{76}$$

In order to legitimate the time-dependent theory this map must be inverted. Just as for the time-independent case, we need to proof that there is a one-to-one correspondence between the time dependent densities and potential. By virtue of this correspondence the density, $\rho(\mathbf{r},t)$ can be used as an alternative variable to the potential to determine the time-evolution of the system. This correspondence was first demonstrated by Runge and

Gross in 1984, [81]. As a result, the many-body Hamiltonian $\hat{H}(t)$ and thus the many-body wave function $\Psi(t)$ are functionals of $\rho(\mathbf{r},t)$.

RUNGE-GROSS THEOREM

$$v(\mathbf{r},t) = v[\rho,\Psi_0](\mathbf{r},t) \implies \hat{H}(t) = \hat{H}[\rho,\Psi_0](t) \implies \Psi(t) = \Psi[\rho,\Psi_0](t). \quad (77)$$

2.5.2 *The van Leeuven theorem*

The Runge-Gross theorem does not yet offer a practical scheme - equivalent to the Kohn–Sham formalism for static DFT - to calculate time-dependent densities in a simpler manner than by solving the full many-body Schrödinger equation. The theorem of van Leeuven (1999) provides a solid foundation to the construction of such a scheme and states the following,

VAN LEEUVEN THEOREM Given a time-dependent density $\rho(\mathbf{r},t)$, associated with a many-body system, with a particle-particle interaction $\omega(|\mathbf{r}-\mathbf{r}'|)$, an external potential $v(\mathbf{r},t)$, and an initial state Ψ_0, there exists a different many-body system with interaction $\omega'(|\mathbf{r}-\mathbf{r}'|)$ and a distinct, unique external potential $v'(r,t)$ which reproduces the exact same time-dependent density - up to a time-dependent constant $c(t)$. The only requirement being that the initial state Ψ_0' in this system must be chosen such that it reproduces the initial density and its time derivative at $t = 0$.

It follows directly that under the constraint $\Psi_0 = \Psi_0'$, and by imposing that the interaction energy of a real system can be reproduced by a fictitious one ($\omega(|\mathbf{r}-\mathbf{r}'|) = \omega'(|\mathbf{r}-\mathbf{r}'|)$), there exists a unique potential $v(\mathbf{r},t)$ that reproduces the interacting density $\rho(\mathbf{r},t)$. This is precisely what is stated by Runge–Gross theorem, revealing this last to be a special case of the van Leeuwen theorem.

2.5.3 *Time-dependent Kohn-Sham framework*

In this section we shall introduce the formal framework of TDDFT, which can be used to calculate excited state properties. TDDFT is able to capture the dynamical nature of an excitation process. During a transition between the ground and a given excited state, periodic charge-density fluctuations are induced, accompanied by dynamical many-body effects and mixing of Kohn-Sham eigenstates. This in turn leads to a modification of the original spectrum, calculated using the Kohn-Sham eigenvalues, towards the real spectrum. These dynamical many-body effects are embedded in the so-called *exchange-correlation kernel* (f_{xc}), the key component of TDDFT, which plays the same role in TDDFT as the the exchange-correlation functional plays in Kohn-Sham DFT.

Up until now, we have spoken only in terms of the time-dependent Schrödinger equation. In practice, the generation of excited states can be looked as an ultrafast process, implying only small deviations from the ground state. Under this perspective, attempting to find the full solution to the time-dependent Schrödinger equation seems rather exaggerate, and unnecessary. Instead, one might attempt to calculate these deviations directly, this is precisely what is done through the response theory [32].

Response theory, and more specifically linear response theory, is a widely used method one can apply to study how a system responds to weak perturbations. In the context of optical spectroscopy techniques, the perturbation is generated by the light irradiations of the ground state. The linear response of the system as it interacts with the electric field contains all of the information about its optical spectrum.

The Runge-Gross and van Leeuwen theorems legitimate the use of a non-interacting system in TDDFT, just as the Hohenberg-Kohn theorems did in ground state DFT. In the time dependent case the density can be expressed as,

$$\rho(\mathbf{r},t) = \sum_{i}^{N} |\Psi_i(\mathbf{r},t)|^2. \tag{78}$$

These single particle orbitals satisfy the time-dependent Kohn-Sham equation,

$$\left[-\frac{1}{2}\nabla^2 + v_s(\mathbf{r},t) \right] \Psi_i = i\frac{\partial}{\partial t}\Psi_i(\mathbf{r},t), \tag{79}$$

where the effective potential has the form,

$$v_s(\mathbf{r},t) = v(\mathbf{r},t) + \int_{\mathbb{R}^3} d\mathbf{r}' \frac{\rho(\mathbf{r},t)}{|\mathbf{r}-\mathbf{r}'|} + v_{\mathrm{xc}}[\rho,\Psi_0,\Psi_{s0}](\mathbf{r},t). \tag{80}$$

The effective potential depends through v_{xc} both on the initial state of the interacting system (Ψ_0), and the initial state of the Kohn-Sham system (Ψ_{s0}). The external potential $v_s(\mathbf{r},t)$ is assumed to have the form shown in equation 75. If the system of interest is initially in the ground state, the time-dependent exchange-correlation potential $v_{\mathrm{xc}}[\rho](\mathbf{r},t)$ can be written as a functional of the density only [32], through the so called adiabatic approximation. In a similar vein to the approach discussed in Section 2.4.4 such approach can be used to construct the 'time evolved' potential from the ground state potential as,

$$v^A_{\mathrm{xc}}(\mathbf{r},t) = v^{\mathrm{gs}}_{\mathrm{xc}}[\rho_0](\mathbf{r})|_{\rho_0=\rho(\mathbf{r},t)}. \tag{81}$$

The adiabatic approximation guarantees that the same functionals as the one defined in Section 2.4.4 for ground state DFT can be used in TDDFT as well. These functionals have the exact same form but are evaluated at the instantaneous time-dependent density.

THE LINEAR RESPONSE FORMALISM We consider a time-dependent Kohn-Sham potential of the form of Eq. 75. This implies that the system is in its ground state for $t \leq t_0$ and $v_1(\mathbf{r},t)$ is a small time-dependent perturbation switched on at t_0. The initial many-body ground state is uniquely determined as stated by the Hohenberg-Kohn theorems of static DFT, and according to the Runge-Gross theorem, there exists a unique one-to one correspondence between $v_s(\mathbf{r},t)$ and $\rho(\mathbf{r},t)$. If the potential is time dependent, the density will be as well. Therefore we can write the time-dependent density as a functional of the external potential, without any dependence on the initial state.

$$\rho(\mathbf{r},t) = \rho[v](\mathbf{r},t) \tag{82}$$

If the perturbation is weak enough, the potential can be expanded in Taylor series as follows,

$$v(\mathbf{r},t) = v_0(\mathbf{r}) + v_1(\mathbf{r},t) + v_2(\mathbf{r},t) + \cdots \tag{83}$$

accordingly the density can be expressed as,

$$\rho_1(\mathbf{r},t) - \rho_0(\mathbf{r}) = \rho_1(\mathbf{r},t) + \rho_2(\mathbf{r},t) + \cdots \tag{84}$$

where ρ_0 is the ground state density, ρ_1 is the first order change in density. The first order term will dominate over the higher order terms in the case of a weak potential so the rest can be neglected. Hence, the first order term density response can be written as,

$$\rho_1(r,t) = \int_{-\infty}^{\infty} dt' \int_{\mathbb{R}} d\mathbf{r}' \chi(\mathbf{r},t,\mathbf{r}',t') v_1(r',t') \tag{85}$$

where χ is the density-density response function [32], defined as,

$$\chi(\mathbf{r},\mathbf{r},t-t') = -i\theta(t-t')\langle\Psi_0|[\hat{\rho}(\mathbf{r},t-t'),\hat{\rho}(\mathbf{r})]|\Psi_0\rangle \tag{86}$$

The frequency dependent response function is the Fourier transform of equation 85, that is

$$\rho_1(r,\omega) = \int_{\mathbb{R}} d\mathbf{r}' \chi(\mathbf{r},\mathbf{r}',\omega) v_1(r',\omega) \tag{87}$$

with

$$\chi_s(r,r',\omega) = \sum_{n=1}^{\infty} \frac{\langle\Psi_0|\hat{\rho}(\mathbf{r})|\Psi_n\rangle\langle\Psi_n|\hat{\rho}(\mathbf{r}')|\Psi_0\rangle}{\omega-\Omega_n+i\eta} - \frac{\langle\Psi_0|\hat{\rho}(\mathbf{r}')|\Psi_n\rangle\langle\Psi_n|\hat{\rho}(\mathbf{r})|\Psi_0\rangle}{\omega-\Omega_n+i\eta} \tag{88}$$

where the limit $\eta \to 0_+$ is known [82]. The nth excitation energy, Ω_n is given by $E_n - E_0$. The response function diverges when the frequency matches the excitation energy - each of these events translate into the appearance of a peak within a spectra.

This time-dependent density $\rho(\mathbf{r},t)$, corresponding to $v(\mathbf{r},t)$ can also be reproduced in a non-interacting time-dependent Kohn-Sham system, with an effective potential, $v_s(\mathbf{r},t)$. Then, for such non-interacting system we can write,

$$\rho_1(r,\omega) = \int_{\mathbb{R}} d\mathbf{r}' \chi_s(\mathbf{r},\mathbf{r}',\omega) v_{s1}(r',\omega) \tag{89}$$

This is the linear response equation in TDDFT, which is the density-density response function for a non-interacting Kohn-Sham particles and yields the same response as the fully interacting, many-body response equation. Similar to equation 80 the effective potential writes,

$$v_s[\rho](\mathbf{r},t) = v(\mathbf{r},t) + \int_{\mathbb{R}^3} d\mathbf{r}' \frac{\rho_1(\mathbf{r},t)}{|\mathbf{r}-\mathbf{r}'|} + v_{\mathrm{xc}}(\mathbf{r},t). \tag{90}$$

The perturbation acts at each t giving rise to a retarded density response at all $\mathbf{r}$, and all of these are then integrated over space. The density-density response function for non-interacting particles is expressed as,

$$\chi_s = \left.\frac{\delta\rho[v_s](\mathbf{r},t)}{\delta v_s(\mathbf{r}',t')}\right|_{v_s[\rho_0](r)}. \tag{91}$$

While the first two terms in Eq. 90 can actually be written down, the last term - the linearized exchange-correlation potential - can be written explicitly only via a functional Taylor expansion:

$$v_{\mathrm{xc}} = \int_{-\infty}^{\infty} dt' \int_{\mathbb{R}^3} d\mathbf{r}' \left.\frac{\delta v_{\mathrm{xc}}[\rho](\mathbf{r},t)}{\rho(\mathbf{r}',t')}\right|_{\rho_0(r)} \rho_1(\mathbf{r}',t'). \tag{92}$$

This expansion reveals the so-called time dependent exchange-correlation kernel:

$$f_{\mathrm{xc}}(\mathbf{r},t,\mathbf{r}',t') = \left.\frac{\delta v_{\mathrm{xc}}[\rho](\mathbf{r},t)}{\rho(\mathbf{r}',t')}\right|_{\rho_0(\mathbf{r})}, \tag{93}$$

which is a functional of the ground state density. As previously alluded to, the kernel is the key quantity of TDDFT in the linear response regime. Now that we have an expression for the linearized potential v_{xc} we can substitute it into the TDDFT linear response equation 85 and get:

$$\begin{aligned}\rho_1(\mathbf{r},t) = &\int_{-\infty}^{\infty} dt' \int_{\mathbb{R}^3} d\mathbf{r}' \chi_s(\mathbf{r},t,\mathbf{r}',t') \times \\ &\underbrace{\left[v_1(\mathbf{r}',t') + \int_{-\infty}^{\infty} dt'' \int_{\mathbb{R}^3} d\mathbf{r}'' \left\{ \frac{\delta(t'-t'')}{|\mathbf{r}'-\mathbf{r}''|} + f_{\mathrm{xc}}(\mathbf{r}',t',\mathbf{r}'',t'') \right\} \rho_1(\mathbf{r}'',t'') \right]}_{:= v_{s1}\,\text{linearized effectivee potential}}.\end{aligned} \tag{94}$$

where the doubly primed variables r'' and t'' are used to emphasize the different double integrals. This expression highlights the dependency of the linearized potential on $\rho_1(r,t)$, and thus demonstrates that the overall linear density response must be solved

self-consistently. The interacting and non-interacting response functions only depend on the time difference $t - t'$, therefore we can Fourier transform the Eq. 94 and obtain,

$$\begin{aligned}\rho_1(\mathbf{r},\omega) = \int_{\mathbb{R}^3} d\mathbf{r}' \chi_s(\mathbf{r},\mathbf{r}',\omega)\Bigg[v_1(\mathbf{r}',\omega) \\ + \int_{\mathbb{R}^3} d\mathbf{r}'' \left\{ \frac{1}{|\mathbf{r}'-\mathbf{r}''|} + f_{\mathrm{xc}}(\mathbf{r}',\mathbf{r}'',\omega) \right\} \rho_1(\mathbf{r}'',\omega) \Bigg].\end{aligned} \tag{95}$$

The frequency dependent, non-interacting Kohn-Sham response function is given by

$$\chi_s(r,r',\omega) = \sum_{j,k=1}^{\infty} (f_k - f_j) \frac{\varphi_j^0(\mathbf{r})\varphi_k^{*0}(\mathbf{r})\varphi_j^{*0}(\mathbf{r}')\varphi_k^0(\mathbf{r}')}{\omega - \omega_{jk} - i\eta} \tag{96}$$

where f_k and f_j are the occupation numbers on the ground state Kohn-Sham orbitals and $\omega_{jk} = \epsilon_j - \epsilon_k$ are the differences between the Kohn-Sham eigenvalues. The structure of the double summation in $\chi_s(r,r',\omega)$ is such that only those terms contribute where one summation index refers to an occupied orbital ($f = 1$) and the other refers to an unoccupied orbital ($f = 0$), all other terms cancel out. This means that the absolute values of the quantities ω_{jk} are the excitation energies of the Kohn–Sham system.The denominator is such that the non-interacting Kohn–Sham response function χ_s has poles at the excitation energies of the Kohn–Sham system. It is important to notice that the transition energies of the non-interacting system ($\omega_{jk} = \epsilon_j - \epsilon_k$) are different compared to Ω_n - excitation energies of the real system. This apparent inconsistency, however, is resolved during the self consistent solution of the density response which cancels out the wrong poles and leaves the correct ones [32].

2.5.4 *Spin-dependent formalism*

For brevity, in the discussion above, we have not included the spin explicitly. However, linear response TDDFT is more commonly applied in an explicitly spin-dependent formalism. Moreover, several reductions of the TDDFT scheme can be better understood if the spin dependent formalism is used. Therefore, it is useful to write down the generalization of the essential equations derived in the previous section [83]. The linear spin-density response is given by

$$\rho_{1\sigma}(r,\omega) = \sum_{\sigma'} \int_{\mathbb{R}} d\mathbf{r}' \chi_{s,\sigma\sigma'}(\mathbf{r},\mathbf{r}',\omega) v_{s1\sigma'}(r',\omega). \tag{97}$$

The spin-dependent linearized effective potential is,

$$v_{s1\sigma}(\mathbf{r},t) = v_{s1\sigma}(\mathbf{r},\omega) \sum_{\sigma'} \int_{\mathbb{R}^3} d\mathbf{r}' \left\{ \frac{1}{|\mathbf{r}-\mathbf{r}'|} + f_{\mathrm{xc},\sigma\sigma'}(\mathbf{r},\mathbf{r}',\omega) \right\} \rho_{1\sigma'}(\mathbf{r}',\omega).\Bigg] \tag{98}$$

The non-interacting Kohn-Sham response function is diagonal in the spin indices:

$$\chi_{s,\sigma\sigma'}(r,r',\omega) = \delta_{\sigma\sigma'} \sum_{j,k=1}^{\infty} (f_{k\sigma} - f_{j\sigma}) \frac{\varphi^0_{j\sigma}(\mathbf{r})\varphi^{*0}_{k\sigma}(\mathbf{r})\varphi^{*0}_{j\sigma}(\mathbf{r}')\varphi^0_{k\sigma}(\mathbf{r}')}{\omega - \omega_{jk\sigma} - i\eta} \tag{99}$$

where $f_{k\sigma}$ and $f_{j\sigma}$ are the occupation numbers of the Kohn-Sham orbitals and

$$\omega_{jk\sigma} = \epsilon_{j\sigma} - \epsilon_{k\sigma} \tag{100}$$

2.5.5 *Excitation energies in TDDFT*

At this point, we summarize that the exact excitation energies Ω_n are given by the poles of the density-density response function, and the density response diverges if the system is subjected to any perturbation at such a frequency. In practice, in a system of N-electrons, excitations can be considered as a dynamic transition between two eigenstates. In this picture the excitation energies correspond to a characteristic eigenmode of the interacting system [32]. An external perturbation is not even required: a system can sustain a finite response at its excitation frequencies without any external stimulation, as this finite response has in fact the desired character of eigenmode of the system. In order to calculate the eigenmodes and eigenfrequencies we start from the linear-response equation without an external perturbation v_1,

$$\rho_{1\sigma}(\mathbf{r},\Omega) = \sum_{\sigma'\sigma''} \int_{\mathbb{R}^3} d\mathbf{r}' \chi_{s,\sigma\sigma'}(\mathbf{r},\mathbf{r}',\Omega) \int_{\mathbb{R}^3} d\mathbf{r}'' f_{\mathrm{Hxc},\sigma'\sigma''}(\mathbf{r}',\mathbf{r}'',\Omega)\rho_{1\sigma''}(\mathbf{r}'',\Omega)\Big] \tag{101}$$

where,

$$f_{\mathrm{Hxc},\sigma\sigma'}(\mathbf{r}',\mathbf{r}'',\Omega) = \int_{\mathbb{R}^3} d\mathbf{r}' \left\{ \frac{1}{|\mathbf{r}-\mathbf{r}'|} + f_{\mathrm{xc},\sigma\sigma'}(\mathbf{r}',\mathbf{r}'',\Omega) \right\} \rho_1(\mathbf{r}',\Omega) \tag{102}$$

Equation 101 is an eigenvalue equation of a frequency-dependent integral operator acting on $\rho_1(\mathbf{r},\Omega)$, and the frequencies Ω which give the eigenvalue 1 are the excitation energies we are looking for. This eigenvalue equation can be written in the following compact matrix notation known as Casida equation [84], from which the eigenmodes can be calculated as,

$$\begin{pmatrix} \mathbb{A} & \mathbb{B} \\ \mathbb{B} & \mathbb{A} \end{pmatrix} \begin{pmatrix} \mathbf{X} \\ \mathbf{Y} \end{pmatrix} = \Omega \begin{pmatrix} -\mathbb{1} & \mathbf{0} \\ \mathbf{0} & \mathbb{1} \end{pmatrix} \begin{pmatrix} \mathbf{X} \\ \mathbf{Y} \end{pmatrix} \tag{103}$$

where matrix elements of $\mathbb{A}$ and $\mathbb{B}$ are:

$$\begin{aligned} A_{ia\sigma,i'a'\sigma'}(\Omega) &= \delta_{ii'}\delta_{aa'}\delta_{\sigma\sigma'}\omega_{i'a'\sigma'} \\ &\quad + \underbrace{\int_{\mathbb{R}^3} d\mathbf{r} \int_{\mathbb{R}^3} d\mathbf{r}' \varphi^{*0}_{i\sigma}(\mathbf{r})\varphi^0_{a\sigma}(\mathbf{r}) f_{\mathrm{Hxc}}(\mathbf{r}',\mathbf{r}'',\Omega)\varphi^0_{i'\sigma'}(\mathbf{r}')\varphi^{*0}_{a'\sigma'}(\mathbf{r}')}_{K_{ia\sigma,i'a'\sigma}}(\omega) \\ B_{ia\sigma,i'a'\sigma'}(\Omega) &= K_{ia\sigma,i'a'\sigma'}(\Omega) \end{aligned} \tag{104}$$

and

$$X_{ia\sigma}(\Omega) = -\left\{ \sum_{\sigma'} \sum_{jk} \frac{f_{j\sigma} - f_{k\sigma}}{\Omega - \omega_{jk\sigma'}} \int_{\mathbb{R}^3} d\mathbf{r} \int_{\mathbb{R}^3} d\mathbf{r}' \varphi^{0*}_{i\sigma}(\mathbf{r}) \varphi^{0}_{a\sigma}(\mathbf{r}) f_{\mathrm{Hxc}}(\mathbf{r}', \mathbf{r}'', \Omega) \varphi^{0}_{i'\sigma'}(\mathbf{r}') \varphi^{*0}_{a'\sigma'}(\mathbf{r}') \right\} \frac{1}{\Omega - \omega_{ia\sigma'}} \tag{105}$$

$$Y_{ia\sigma}(\Omega) = -X_{ia\sigma}(\Omega) \tag{106}$$

$\mathbb{A}$ and $\mathbb{B}$ are sometimes referred to as the orbital rotation Hessians [32]. Note that, the matrix pseudo-eigenvalue equation has infinite dimension, so in practice we only solve for a given number of excitation energies (i.e. a predefined number of eigenvalues). Generally, the accuracy of an eigenvalue associated with a given excitation energy increases with the number of higher-energy eigenvalues computed, meaning that one should usually consider a greater number of excited states than explicitly required. Moreover equation 103 is only defined where $f_j - f_k \neq 0$, therefore only transitions from unoccupied to occupied Kohn-Sham states (and vice-versa) will finally be considered. In general, the Casida equation returns the exact excitation energies of any many-body system. In order to obtain exact excitation energies however, certain conditions must be met.

- One should have knowledge of the exact Kohn-Sham ground state of the system, which implies that the exact density of the density functional should be known. On top of this one should solve the Casida equation for all possible occupied-virtual transitions, including the continuum states.
- This would of course require the knowledge of the exact, frequency-dependent exchange-correlation kernel, f_{xc}, using which one should solve the infinite eigenvalue problem.
- Not to mention that since the matrix elements of $\mathbb{A}$ and $\mathbb{B}$ explicitly depend on the frequency via the exchange-correlation kernel, all this must still be done in a self-consistent manner.

Needless to say that, in practice, none of these conditions can be fulfilled exactly. Therefore, approximations must be introduced. It is also important to note that setting the coupling matrix elements $K_{ia\sigma,i'a'\sigma'}$ to zero simply yields the Kohn-Sham excitation energies ω_{ij} as eigenvalues; these are single excitations. Therefore, no double or multiple excitations are accounted for in TDDFT. On the other hand, if we were to possess an exact, frequency-dependent kernel, we would obtain poles of the many-body response function Ω with multiple-excitation character. In the following we discuss some additional reasons why this is never true in real life.

2.5.6 *The adiabatic approximation in TDDFT*

As outlined above, the key quantity in TDDFT is the frequency dependent exchange-correlation kernel, which describes the frequency dependent exchange-correlation potential $v_{xc}[\rho](r, \omega)$. In analogy to ground-state DFT, application of TDDFT requires an approximation of this potential. The simplest approximation to make here would be to

transfer the exchange-correlation functionals used in ground-state DFT (e.g. GGA, Hybrid Functionals) to the excited state, where we substitute the frequency-dependent density for the ground state density, according to Equation 81. In TDDFT, this is known as the adiabatic approximation [32]. The term *adiabatic* indicates that $v_{xc}^{A}(r,\omega)$ becomes exact where a perturbation acting on the system is sufficiently slow. In reality, this condition is rarely realized, however the adiabatic approximation is used in almost all applications of TDDFT in chemistry. A consequence of this approximation is that in practice the xc kernel is not truly frequency dependent, and only singly-excited states may be accessed within the adiabatic approximation.

2.5.7 *Reductions of the TDDFT scheme*

The Casida equation [84] is often cast into the alternative form

$$\mathbf{CZ} = \Omega^2 \mathbf{Z}. \tag{107}$$

To arrive at this expression, one assumes that the Kohn-Sham orbitals are real and that f_{xc} is frequency-independent, so that the matrices $\mathbb{A}$ and $\mathbb{B}$ become real. Then $\mathbf{C}$ and $\mathbf{Z}$ can be defined as,

$$C = (A-B)^{1/2}(A+B)(A-B)^{1/2}, \tag{108}$$

$$Z = (A-B)^{1/2}(X-Y). \tag{109}$$

Using the explicit forms of the matrix elements of A and B one finds

$$\sum_{i'a'\sigma'} [\delta_{ii'}\delta_{aa'}\delta_{\sigma\sigma'}\omega^2_{a'i'\sigma'}] + \sqrt{\omega_{ai\sigma}\omega_{i'a'\sigma'}}K_{ia\sigma,i'a'\sigma'}]Z_{i'a'\sigma'} = \Omega^2 Z_{ia\sigma}. \tag{110}$$

This approximate version of the Casida equation is implemented in most TDDFT codes. The eigenvalues of the Casida equation in the form of Eq. 108 are the squares of the excitation energies; this means that for each excitation energy Ω_n the Casida equation also delivers the corresponding negative value, $-\Omega_n$. Physically, the pair (Ω_n, $-\Omega_n$) corresponds to the excitations and de-excitations of the system.

2.5.8 *Tamm-Dancoff approximation*

The Tam-Dancoff approximation (TDA) is the exact TDDFT linear response scheme in which all de-excitation processes are neglected. In practice, one simply neglects the off-diagonal matrices $\mathbb{B}$ in the Casida equations, keeping the matrix $\mathbb{A}$ unvaried. As a result, the eigenvalue problem reduces to

$$\mathbb{A}\mathbf{X} = \Omega\mathbf{X} \tag{111}$$

Further simplification of the original Casida equation can be achieved by neglecting all the off-diagonal terms, both in the matrices $\mathbb{A}$ and $\mathbb{B}$. Such approach follows from the the

evidence that the coupling matrix elements $K_{ia\sigma,i'a'\sigma}$ decay relatively rapidly away from the diagonal, because the overlap of increasingly different orbitals becomes smaller by cancellation of oscillations. This scheme is known as small-matrix approximation (SMA).

$$\Omega_{\pm}^2 = \omega_{ia\sigma}^2 + 2\omega_{ia\sigma}[K_{ia\sigma,ia\sigma}(\Omega) \pm K_{ia\sigma,ia\bar{\sigma}}(\Omega)] \tag{112}$$

The SMA can be simplified further by making the TDA, i.e., by including only the positive excitation energy, which leads to

$$\Omega_{\pm} = \omega_{ia\sigma} + [K_{ia\sigma,ia\sigma}(\Omega) \pm K_{ia\sigma,ia\bar{\sigma}}(\Omega)] \tag{113}$$

Neglecting the frequency-dependence of the xc Kernel yields the single-pole approximation (SPA),

$$\Omega_{\pm} = \omega_{ia\sigma} + [K_{ia\sigma,ia\sigma}(\omega_{ia\sigma}) \pm K_{ia\sigma,ia\bar{\sigma}}(\omega_{ia\bar{\sigma}})] \tag{114}$$

Under the assumption that the Kohn-Sham ground state is not spin-polarized, so that $\omega_{ia\uparrow} = \omega_{ia\downarrow} = \omega_{ia}$ the SPA has the following two solutions

$$\Omega_{+} = \omega_{ia} + 2\int_{\mathbb{R}} d\mathbf{r} \int_{\mathbb{R}} d\mathbf{r}' \phi_i^{0*}(\mathbf{r})\phi_a^0(\mathbf{r})\left[\frac{1}{\mathbf{r}-\mathbf{r}'} + f_{\mathrm{xc}}(\mathbf{r},\mathbf{r}',\omega_{ia})\right]\phi_i^{0*}(\mathbf{r}')\phi_a^0(\mathbf{r}') \tag{115}$$

$$\Omega_{-} = \omega_{ia} + 2\int_{\mathbb{R}} d\mathbf{r} \int_{\mathbb{R}} d\mathbf{r}' \phi_i^{0*}(\mathbf{r})\phi_a^0(\mathbf{r}) g_{\mathrm{xc}}(\mathbf{r},\mathbf{r}',\omega_{ia})\phi_i^{0*}(\mathbf{r}')\phi_a^0(\mathbf{r}') \tag{116}$$

where

$$f_{\mathrm{xc}}(\mathbf{r},\mathbf{r}',\omega) = \frac{1}{2}[f_{\mathrm{xc}}\uparrow\uparrow(\mathbf{r},\mathbf{r}',\omega) + f_{\mathrm{xc}}\uparrow\downarrow(\mathbf{r},\mathbf{r}',\omega)] \tag{117}$$

$$g_{\mathrm{xc}}(\mathbf{r},\mathbf{r}',\omega) = \frac{1}{2}[f_{\mathrm{xc}}\uparrow\uparrow(\mathbf{r},\mathbf{r}',\omega) - f_{\mathrm{xc}}\uparrow\downarrow(\mathbf{r},\mathbf{r}',\omega)] \tag{118}$$

where $f_{\mathrm{xc}}\uparrow\uparrow$ and $f_{\mathrm{xc}}\uparrow\downarrow$ are the spin-independent xc kernels defined in 2.5.5. In general, the TDA, and further simplified schemes yield excitation energies of comparable accuracy, as compared with TDDFT, with better convergence and lower memory requirements. However, the sum rules are not fulfilled. As a result, quantities such as the oscillator strength are poorly reproduced [85].

2.6 TIME-DEPENDENT DFT AND CHARGE-TRANSFER STATES

One of the drawbacks of TDDFT when using local density functionals such as LDA or GGA is its inability to routinely and accurately describe excitations of long-range spacial extent, therefore, a note of caution is appropriate when spatially extended Rydberg excitations and charge transfer (CT) states are concerned. Such excitations can occur in a wide range of systems, such as in molecular aggregates or intramolecularly, between two different functional groups. In general, this class of excitations occurs as a one electron displacement between two molecular subunits, that are identified as a donor (D) and an acceptor (A). In this section we elucidate why TDDFT fails when it comes to describing CT excitations and what can be done about it.

2.6.1 *Charge transfer states in the limit of a large separation*

It is instructive to start out our discussion considering a limiting case, where a donor and an acceptor are well separated, placed at distance R one from the other. The equation ruling charge transfer processes can be expressed as,

$$IP_D = D - e^- \tag{119}$$

$$EA_A = A + e^- \qquad\qquad IP - EA = D^+ - A^- \tag{120}$$

The minimum energy required to remove an electron from a molecule is its ionization potential. On the other hand, the energy associated with the acquisition of an electron is known as electron affinity. The subscripts D (and A) denote that an electron has been removed from (added to) the donor (acceptor) fragment, respectively. Once the electron displacement has occurred D and A resent an attractive electrostatic interaction $-1/R$ generated by the exciton pair (R being the charge-separation coordinate). Hence, the *lowest energy boundary* for a CT state, Ω_{CT} - as derived originally by Mulliken [86] - follows from elementary arguments, as

$$\Omega_{\mathrm{CT}} = IP_D - EA_A - \frac{1}{R} \tag{121}$$

It is instructive to compare this value with what we would obtain from TDDFT, in the limit of a single excitation transferring one electron from the HOMO to the LUMO. If the poles of the response function 100 are sufficiently spaced (i.e., HOMO and LUMO are well separated in energy from the neighboring orbitals) one can express the energy of a CT state using the SPA - the simplest form of the TDDFT in which de-excitations are discarded and spin-independent kernels are considered - as introduced in Section 2.5.8,

$$\Omega_{\mathrm{CT}}^{SPA} = \epsilon_L^a - \epsilon_H^d + 2\int_{\mathbb{R}^3} dr \int_{\mathbb{R}^3} dr' \varphi_L^a(\mathbf{r})\varphi_H^d(\mathbf{r}) f_{\mathrm{Hxc}}(\mathbf{r},\mathbf{r}',\omega)\varphi_L^a(\mathbf{r})\varphi_H^d(\mathbf{r}) \tag{122}$$

Here, the orbitals in question are the highest occupied $\varphi_d(\mathbf{r})$ and lowest unoccupied $\varphi_a(\mathbf{r})$ orbitals of the donor and acceptor moieties, respectively. Since $\varphi_d(\mathbf{r})$ and $\varphi_a(\mathbf{r})$have an exponentially vanishing overlap, at large distances the final term tends to zero. As a result, the excitation energy computed at TDDFT level collapses to the difference in the Kohn-Sham orbital eigenvalues:

$$\Omega_{\mathrm{CT}}^{\mathrm{SPA}} = \epsilon_L^a - \epsilon_H^d. \tag{123}$$

This result is insufficient in two different aspects. The first is the missing $-1/R$ term, the second is the absence of the derivative discontinuity. From Section 2.4.5 we know that in the limit of the exact exchange-correlation functional:

$$IP_d = -\epsilon_d^{\mathrm{DFT}}, \qquad EA_a = -\epsilon_a^{\mathrm{DFT}}, \tag{124}$$

however, we do not possess the exact exchange-correlation functional. Within standard approximations (i.e. GGA), DFT tends to provide excitation energies which are significantly underestimated - as the LUMO does not account for the missing derivative discontinuity, letting local and semilocal xc functionals decay faster than $1/R$. This, in turn, explains why TDDFT can often drastically fail when computing charge-transfer phenomena. Hybrid xc functionals, which contain a fraction of the exact HF exchange give some improvement over standard TDDFT approximations since they lead to larger band gaps as compared to "pure" DFT, thus yielding xc kernels for which the matrix element in the SPA does no vanish.

2.6.2 *Improved description of charge-transfer states*

Next, let us consider the same model, only this time we apply a time-dependent Hartree-Fock (TDHF) approach [20][2]. Then,

$$\Omega_{\mathrm{CT}}^{\mathrm{TDHF}} = \epsilon_a^{\mathrm{HF}} - \epsilon_d^{\mathrm{HF}} - \int_{\mathrm{R}^3} d\mathbf{r} \int_{\mathrm{R}^3} d\mathbf{r}' \, \frac{\varphi_a(\mathbf{r})\varphi_d(\mathbf{r})\phi_a(\mathbf{r}')\phi_d(\mathbf{r}')}{|\mathbf{r}-\mathbf{r}'|}, \tag{125}$$

which becomes, in the limit of large separation:

$$\omega_{\mathrm{CT}}^{\mathrm{TDHF}} = \epsilon_a^{\mathrm{HF}} - \epsilon_d^{\mathrm{HF}} - \frac{1}{R}. \tag{126}$$

This demonstrates that the exact-exchange integral is responsible for the $1/R$ behavior. Additionally, from Koopmans theorem [40], we know that the difference in orbital eigenvalues computed with Hartree-Fock can be approximated to be equal to the difference between the ionization potential of the donor and the electron affinity of the acceptor. As a result, charge-transfer excitation energies computed from TDHF should be at least qualitatively correct.

This ultimately proofs that the inclusion of exact exchange into the exchange-correlation functional (i.e. Hybrid functionals), results in an improved description of charge-transfer excitations. As previously alluded to, using the adiabatic approximation one can estimate the correct amount of Hartree-Fock exchange to include in the xc kernel - bearing an optimal balance of DFT- and HF-exchange - so to preserve the short-range qualities of a given functional as well as to include the long range correction. This apparent trade-off problem has been tackled by a class of functionals known as **range-separated hybrids**, which are discussed in the next section.

2 The basic idea of TDHF is that the many-body wave function is assumed to have the form of a Slater determinant

2.6.3 *Range-separated hybrid functionals*

A particular class of hybrid functionals are the so called range-separated hybrids (RSH). These are constructed based on a partition of the Coulomb interaction into a long-range (LR) and a short range part (SR),

$$\frac{1}{|\mathbf{r}-\mathbf{r}'|} = \frac{f(\mu|\mathbf{r}-\mathbf{r}'|)}{|\mathbf{r}-\mathbf{r}'|} + \frac{1-f|\mathbf{r}-\mathbf{r}'|}{|\mathbf{r}-\mathbf{r}'|}, \tag{127}$$

where f is typically a function such as our functional has the properties $f(mx) \to 0 = 1$ and $f(mx) \to \infty = 0$. The parameter μ is determined either empirically or using physical arguments. The resulting general formula for a range-separated hybrid (RSH) is then:

$$E_{\mathrm{xc}}^{RSH} = E_{\mathrm{x}}^{SR-DFA} + E_{\mathrm{x}}^{LR-HF} + E_{\mathrm{c}}^{DFA} \tag{128}$$

where DFA stands for 'density functional approximation', meaning any standard approximation to the exchange-correlation energy within DFT. Since the separation function forces the exact-exchange contribution to E_{xc} to be 100% at large distances, range-separated hybrids have the correct asymptotic behavior $(-1/R)$ while at short distances they make use of the full density functional approximation. In practice, RSH recover the correct asymptotic behavior of external potentials at long distances, allowing for an improved description of molecular properties such as polarizabilities of long-chain molecules and of charge-transfer excitations.

At several points throughout this thesis, we have employed this type of functionals for the study of charge-transfer processes in molecular systems. In Chapter 4 we analyze the impact that the use of different classes of functionals has on the quality of computed electronic densities.

2.7 SOLVATION MODELS

Whether analyzing the absorption properties or excited state lifetime of a molecular system, the majority of photophysical measurements take place in solution. Accurate modeling of the solvation environment, therefore, is crucial to reproduce experimental values correctly. Modeling of solvation effects in simulations can be done implicitly or explicitly. In brief, explicit models, include the solvent molecules, that are accounted for either classically or quantum mechanically. *Implicit* models treat the solvent as a continuum dielectric with the solute in a void cavity.The latter is by far the most commonly employed for modeling solute-solvent interactions and it is this method that we have employed throughout this work.

2.7.1 *The polarizable continuum model*

The polarizable continuum model (PCM) [87] represents the most frequently used implicit method. Two formalisms are available to compute transition energies within the PCM

framework: State-Specific (SS) and Linear-Response (LR) [88, 89]. We will not go into the details of these two approaches. It suffices to know that the former considers the solute-solvent interaction explicitly using the difference between the ground-state and excited state expectation values. As a consequence, it provides a more complete account of the solute-solvent polarization in the excited states as compared to the LR formalism, which describes the corresponding energy as the direct product of transition density. The latter, however, is computationally very efficient (i.e. comparable to a gas phase calculations) and transition properties are well defined. Hence, throughout this work we have used this formalism to account for solvation effects into TDDFT calculations.

3

METHODS FOR THE DESCRIPTION OF ELECTRONIC EXCITATIONS: AN OVERVIEW

3.1 CONTEXT

In Section 1 we have introduced the general framework of photochemical processes. In this chapter, we will try to give an overview of the existing tools that have been developed to analyze these processes from a theoretical standpoint. In particular, these methods are aimed at quantifying the redistribution of charge density involved in the excitation, and afford a concise description of the electronic transition.

As previously alluded to in Chapter 2, any excited state calculation requires the preliminary definition of a ground state reference form which the excited state can be constructed. If this ground-state reference is a Hartree-Fock (single-reference) type Slater determinant, the corresponding excited state methods that we will rely on are the configuration interaction singles (CIS) [20] and time-dependent Hartree-Fock (TDHF) [20]. Alternatively, one may start from a Kohn-Sham type single-reference Slater determinant. In that case, the associated excited state methods we will use are the Tamm-Dancoff approximation (TDA) [90] and time-dependent density functional theory (TDDFT) [32].

All these methods construct the excited-state wave function as a **linear combination of Slater determinants**, in which a virtual determinant replaces an occupied one. Throughout this work, we will mainly focus on single-reference derived excited states. However, it is important to mention that one can adapt this simple molecular orbital picture of electronic transitions to the general correlated wave function - as we will briefly recall in Chapter 5. The outcome of these methods can be processed to analyze any selected electronic transition that may be of interest for a given molecular system. In particular, the main quantity we will look at are the density distributions that are generated upon the transition [91].

A common strategy, when it comes to analyzing excited states, consists of visualizing the excited state filled/vacant orbitals in the **ground state (canonical) basis**. However, in some cases, this approach may be intractable and of difficult interpretation due to the multiple Slater determinants describing the excited state involved in the transition [31]. Besides, within this framework, the orbitals depend on the ground state of reference, which may not be necessarily the best choice for the description of excited states. A well-known methodology to avoid the ground state dependence is to introduce *reduced density matrices*, which allow for appropriate orbital transformations and result in a more convenient and ground state-independent representation of the excited-state picture. As we will discuss later in this chapter, well-known examples of the latter strategy are the use of natural transition orbitals (NTOs), attachment/detachment densities [91, 92].

Indeed, excited state studies based on distinct manipulation of density matrices are widely reported in the literature. Since we are mainly concerned with one-electron transitions, the density objects that are more suited for our purposes are **reduced density matrices**. Two major approaches exist, which differ by the definition of the density matrix used for the analysis of the excited state, namely the **one-particle transition density matrix** (1TDM) and the **one-particle difference density matrix** (1DDM) [93]. Not only these particular density matrices afford an elegant and condensed description of electronic transitions but, from these, one may derive a variety of useful descriptors for the characterization of the excited state phenomena [1, 91, 94, 95].

The purpose of this Chapter is to give an overview of the methodologies which have been devised in the past decades to investigate the locality of excited states, highlighting the qualities and novelty of each.

3.2 INTRODUCTION

Among the first detailed analysis of excited states are the contributions of Luzanov [93, 96–102], who first introduced "explicit concepts and definite criteria" involving estimation of excited state localization and charge transfer for interpreting electronic transitions. In particular, he first suggested discarding orbital analysis in favor of some non-invariant entities derived from the transition density matrices [96]. The essential quantities of this analysis, which he summarized later under the name of excited state structural analysis (ESSA) [102], are the excitation localization indexes for the quantitative evaluation of the total charge transfer between fragments. This charge-transfer metric is based on the projection of the exciton wave function into the atomic spin-orbital base and measures the probability of an electron to transfer from a molecular fragment to another. A position of relevance in our overview of density based indexes is due to the charge-transfer metric (D_{CT}) [1], which constitutes the theoretical foundation for the excited state analysis carried out in this work. The D_{CT} metric resides on the partition of the 1DDM and on the corresponding definition of positive and negative charge distributions associated with the electronic transition. Rooted on a similar apportionment of the 1DDM, Etienne [103–106] has derived several additional and insightful descriptors dedicated to the study of excited states topology based on centroids of charge obtained from the Attachment/Detachment density matrices (originally introduced for excited states analysis by Head-Gordon [91]). Although this approach also consists of a vectorial analysis of the difference density distribution induced by the transition, there are some substantial differences to the D_{CT} metric, which we will illustrate in greater detail later in the discussion. Additionally, the same author has substantially contributed to forming a consistent and general formalism for the topological analysis of electronic transitions from single-reference excited states calculations, **bridging** the **1DDM** and the **1TDM** approach [94].

The work of Plasser and Drew also deserves to be mentioned. Plasser [107–110] provides a general theory and comprehensive formalism for the correct evaluation of exciton properties both at a molecular level and in extended systems. This is done through the definition of an exciton wave-function out of a many-body wave function

obtained through quantum-chemical excited state calculations. This theory of **exciton analysis** relies on the assumption that the 1TDM can be interpreted as a **two-body exciton wave function** describing the motion of a correlated hole-electron entity. In the same vein to what mentioned above for the 1DDM, the exciton wave function can also be analyzed with the aid of a series of descriptors. While the original work proposed the analysis of this exciton wave function through a population analysis [95], later this model has been generalized [107,110–112]. The exciton analysis is carried out through the computation of the expectation value of any operator acting in the same orbital basis of the 1TDM. This strategy is then proven to be **independent** of atom-centered basis functions and **not to require partitioning** of the wave function into atom- or fragment-centered contributions [112].

Several other **alternative descriptors** exist, some of which proposed as a modification of formerly existing indexes, other being brand new definitions, aimed at further exploring the metric of excited electronic states in the framework of density functional theory. We cite here the Δr approach by Guido and Adamo [113], which relies on the calculation of the **charge centroids of natural transition orbital pairs** (relevant for a given transition). This index renders the concept of **average hole-electron distance** upon excitation. The authors also address differences and similarities towards another well-known index (Λ) by Tozer and Helgaker, which measures the spatial overlap in a given excitation. Although Λ may also provide an estimate of the spatial extent of an electronic transition, it is more a diagnostic tool for TDDFT methodological failures, and it was devised to establish the reliability of a general electronic transition. We will elaborate more on density indexes for diagnostics in Chapter 6.

Another strategy consists to quantitatively characterize the charge displacement occurring upon excitation by integrating the electronic density along a chosen axis (which coincides with the electron-transfer coordinate) [114]. Altogether, these studies have contributed to the evolution of the models employed for the study of excited states. Below we provide a more detailed description of some of the descriptors mentioned above. This summary aims at giving a comprehensive view of the methodologies that are available for examining electronic excitations and at providing a context for the work presented later on.

NOTATION REMINDER Throughout the chapter we denote orbital indexes with three type of subscripts,

- Atomic orbitals (AO) are denoted the letter ϕ with Greek subscripts: $\mu, \nu, \lambda, \sigma$

- Molecular orbitals are indicated by φ with corresponding indexes following the usual convention: $i, j, k, l, \ldots$ for occupied; $a, b, c, d, \ldots$ for virtual; $p, q, r, s, \ldots$ for generic orbitals. Density matrices expressed in a canonical orbital basis are indicated by the $\boldsymbol{\gamma}$. Density matrices expressed within the MO basis are marked with a tilde: $\tilde{\mathbf{D}}^0$. We use boldface characters to denote matrices and vectors and plain style to refer to their elements.

3.3 DENSITY MATRICES

3.3.1 *One-particle transition density matrices*

State density matrices and difference density matrices give rise to the most widely used concepts in quantum chemistry. Before discussing in more details the main methodologies for the analysis of excited states, we first recall some useful concepts related to transition density matrices, reduced density matrices and their properties [105].

We consider again an N-electron system , described by a Slater Determinant,Ψ, which is composed of L spin-orbitals φ, N of which are occupied and the remaining $L-N$ are virtual, constructed by a LCAO expansion of K basis function ϕ. Unless the basis has some linear dependencies, L and K are the same numbers. The ground state is given as the lower energy (0) eigenfunction,

$$\hat{H}\Psi^0(\mathbf{x}_1,\mathbf{x}_2,...,\mathbf{x}_N) = E^0\Psi^0(\mathbf{x}_1,\mathbf{x}_2,...,\mathbf{x}_N), \tag{129}$$

where x is a four-dimensional vector containing spatial $\mathbf{r}_i$ and spin σ coordinates of the nth electron (with $n = 1,...,N$), $x_n = \sum_{\sigma=\alpha,\beta} r_n\sigma_n$. One can formally construct and excited state as

$$\hat{H}\Psi^X(\mathbf{x}_1,\mathbf{x}_2,...,\mathbf{x}_N) = E^X\Psi^X(\mathbf{x}_1,\mathbf{x}_2,...,\mathbf{x}_N). \tag{130}$$

The two many-particle wave functions Ψ^0 and Ψ^X may differ by any orbital substitution. Since we now compare ground state and excited state wave functions in terms of orbitals it is instructive to express the latter in a spin-orbital basis: where the summation runs over L spin-orbitals.

$$\Psi^X = \left(\sum_{pq} c^X_{pq}\hat{p}^\dagger\hat{q} + \sum_{pqrs} c^X_{pqrs}\hat{r}^\dagger\hat{p}^\dagger\hat{q}\hat{s} + ...\right)\Psi^0. \tag{131}$$

Equivalently we could also express the same wave function in an atomic-orbital basis,

$$\Psi^X = \left(\sum_{\mu\nu} c^X_{\mu\nu}\hat{a}^\dagger_\mu\hat{a}_\nu + \sum_{\mu\nu\mu'\nu'} c^X_{\mu\nu\mu'\nu'}\hat{a}^\dagger_{\mu'}\hat{a}^\dagger_\mu\hat{a}_{\nu'}\hat{a}_\nu + ...\right)\Psi^0. \tag{132}$$

where the summation runs over the K basis functions. Here Ψ_0 is the ground state from which the excited state is generated by applying a series of annihilation and creation operators, which successively generate *hole* and *particles* in the reference wave function. Depending on the number of these operations the resulting state is singly, doubly excited, etc. Visualizing such excited wave function is not trivial. Indeed one can notice from expression 132 that the wave function, projected in an atomic orbital basis, depends on the chosen basis via the orbital coefficients $c^X_{\mu\nu}, c^X_{\mu\nu\mu'\nu'}$. Thus, the choice of basis determines the quality of the excited state representation and the coefficients can not be directly used for the analysis of excited states. However, a related concept exists, more suitable for this purpose, that is the reduced transition density matrix.

An element of the transition density matrix between the molecular orbital ϕ_p in the ground state Ψ^0 and the molecular orbital ϕ_q in the excited state Ψ^X writes,

$$\tilde{D}^{0X}_{pq} = \left\langle \Psi^0 \middle| \hat{p}^\dagger \hat{q} \middle| \Psi^X \right\rangle = \left\langle \Psi^X \middle| \hat{q}^\dagger \hat{p} \middle| \Psi^X \right\rangle = \tilde{D}^{X0}_{qp} \tag{133}$$

$$\tilde{D}^{X0}_{pq} = \left\langle \Psi^X \middle| \hat{p}^\dagger \hat{q} \middle| \Psi^0 \right\rangle = (\tilde{D}^{0X}_{pq})^T, \tag{134}$$

where $\hat{p}^\dagger$ and $\hat{q}$ are the creation and annihilation operators acting on ϕ_p and ϕ_q molecular orbitals. The transition density matrix $\tilde{\mathbf{D}}^{0X}$ as constructed such, is a $L \times L$ squared matrix. If the excited state can be described as a linear combination of single excitations as it is the case in CIS or TDDFT [20], the wave function writes,

$$\left|\Psi^X\right\rangle = \sum_{i=1}^{N} \sum_{a=N+1}^{L} N_x^{-1/2} \tilde{D}^{0X}_{ia} \left|\Psi^a_i\right\rangle; \quad \left|\Psi^a_i\right\rangle = \hat{a}^\dagger \hat{i} \left|\Psi^0\right\rangle. \tag{135}$$

Since a transition can never occur between two occupied or two virtual orbitals, the molecular orbital indexes i and a restrict to one only kind. Hence it is convenient to switch from the general p,q indexes the i,a pair. i denotes strictly occupied orbitals, while a denotes only virtual ones. $\hat{a}^\dagger$ and $\hat{i}$ are the associated creation and an annihilation operators and N_x is a normalization factor $N_x = tr(\tilde{\mathbf{D}}^{0X} \tilde{\mathbf{D}}^{0X\dagger})$. $\tilde{D}^{0X}_{ia}$ is a transition matrix element for the $0 \rightarrow X$ state transition.

In the case of CIS, the elements $\tilde{D}^{0X}_{pq}$ correspond to the weights of the electronic transitions between the respective molecular orbitals, $\tilde{D}^{0X}_{pq} = \delta_{pi}\delta_{qa} c^a_i = \tilde{D}^{0X}_{ia}$, where c^a_i is a CIS coefficient corresponding to a Ψ^a_i (that is a Slater determinant in which an electron is excited from the occupied orbital i to the virtual one, a). Thus, in CIS, the 1TDM elements directly give the expansion coefficients. This holds in TDDFT as well [20]. Note that the matrix elements $\tilde{D}^{0X}_{ia}$ differ from $\tilde{D}^{0X}_{pq}$, in that i,a indicate occupied and virtual spin-orbitals, while p,q are general indexes. Hence $\tilde{\mathbf{D}}^{0X}$ is an $(N_o \times N_v)$ matrix, where $N_o = N$ and $N_v = L - N$ denote the number of occupied and virtual MOs, respectively.

Three main types of analysis exist to analyze density matrix objects, namely plotting the density, performing a population analysis, and diagonalizing the density matrices [111, 115]. For visualization, it is convenient to express the 1TDM in coordinate space,

$$\gamma^{0X}(\mathbf{r}_1, \mathbf{r'}_1) = N \sum_{\sigma=\alpha,\beta} \int d\mathbf{x}_2 ... \int d\mathbf{x}_N \Psi^0(\mathbf{r}_1, \sigma, ..., \mathbf{x}_N), \Psi^{*X}(\mathbf{r}'_1, \sigma, ..., \mathbf{x}_N) \tag{136}$$

where the integration extends over all coordinates except for the first. Equivalently one can also extract the 1TDM elements from the exciton wave function:

$$\gamma^{0X}(\mathbf{r}_1, \mathbf{r'}_1) = N_x^{-1/2} \sum_{i=1}^{N} \sum_{a=1}^{L-N} \varphi_i(\mathbf{r}_1) \tilde{D}^{0X}_{ia} \varphi^*_a(\mathbf{r'}_1). \tag{137}$$

This relation is the foundation for the class of descriptors stemming from the 1TDM. Integrating the product of γ^{0X} with the corresponding spin-orbitals gives back the elements,

$$\tilde{D}_{ia}^{0X} = \int_{\mathbb{R}^3} d\mathbf{r}_1 \int_{\mathbb{R}^3} d\mathbf{r}_1' \varphi_i^*(\mathbf{r}_1)\gamma^{0X}(\mathbf{r}_1,\mathbf{r}_1')\varphi_a^*(\mathbf{r}_1') \tag{138}$$

$$. \tag{139}$$

Alternatively,

$$\tilde{D}_{ia}^{0X} = \left\langle \Psi^0 \middle| \hat{i}^\dagger \hat{a} \middle| \Psi^X \right\rangle = \sum_{j=1}^{N} \sum_{b=1}^{L-N} \tilde{D}_{jb}^{0X} \left\langle \Psi^0 \middle| \hat{i}^\dagger \hat{a} \middle| \Psi_j^b \right\rangle \tag{140}$$

$$= \sum_{j=1}^{N} \sum_{b=1}^{L-N} \tilde{D}_{jb}^{0X} \overbrace{\left\langle \Psi_i^a \middle| \Psi_j^b \right\rangle}^{\delta_{ij}\delta_{ab}} = \tilde{D}_{ia}^{0X}. \tag{141}$$

An alternative and compelling way to visualize density matrices is by diagonalizing them, so that the number of configurations representative of the transition drastically reduces. Due to the rectangular shape, a simple diagonalization of the 1TDM is not possible. However, it is instructive to perform a singular value decomposition SVD, which leads to the natural transition orbitals NTOs. This transformation is crucial for the analysis of electronic transitions.

Analysis of transition density matrices: Natural Transition Orbitals

The analysis of excited states is hugely simplified by constructing Natural Transition Orbitals (NTOs) for the excited states. The basic idea behind NTOs is rather old [96], (the term "natural transition orbitals" was coined in Ref [92] and consist transforming the 1TDM via singular value decomposition. We have introduced in Eq. 137 the 1TDM, $(\mathbf{D})_{ia}$, which consists of a one-particle density generated by exciting an electron from an occupied orbital i to a virtual one, a. Once again, the dimension of this matrix is $N_o \times N_v$, where N_o and N_v designate the number of occupied and virtual MOs, respectively. By applying the matrices $\mathbf{U}$ and $\mathbf{V}$ to the canonical orbitals, one obtains two rotated sets of orbitals, named natural transition orbitals (NTO) [92, 96, 116].

$$diag(\sqrt{\lambda_1}, \sqrt{\lambda_2}, ...) = \mathbf{U}^\dagger \mathbf{D} \mathbf{V} \tag{142}$$

where $diag(\sqrt{\lambda_1}, \sqrt{\lambda_2}, ...)$ contains the singular values of D at most N_o non-zero elements, sorted in decreasing order. The matrix $\mathbf{U}$ is a unitary transformation from the canonical occupied MOs to a set of NTOs that together represent the *hole* orbital generated upon

transition, while **V** rotates the canonical virtual MOs into a new set of NTOs representing the excited electron, conventionally named as *particle*,

$$\varphi_i^h(\mathbf{r}_h) = \sum_{j=1}^{N_o} \mathbf{U}_{ji}\varphi_j(\mathbf{r}), \tag{143}$$

$$\varphi_i^p(\mathbf{r}_p) = \sum_{j'=1}^{N_v} \mathbf{V}_{j'i}\varphi'_j(\mathbf{r}), \text{with } i = (1,...,N). \tag{144}$$

U is the matrix diagonalizing the *hole* $N_o \times N_o$ transition density matrix, expressed as $\mathbf{TT}^\dagger$ while **V** diagonalizes the *particle* $N_v \times N_v$ transition density matrix $\mathbf{T}^\dagger\mathbf{T}$. **U** and **V** matrices are determined according to the following eigenvalue equations,

$$\mathbf{TT}^\dagger u_i = \lambda_i^o u_i, i = 1,...,N_o \tag{145}$$

$$\mathbf{TT}^\dagger v_i = \lambda_i^v v_i, i = 1,...,N_v, \tag{146}$$

$$\mathbf{U} = \sum_{i=1}^{N_o} u_i;\ \mathbf{V} = \sum_{i=1}^{N_v} v_i. \tag{147}$$

The new orbitals have some useful properties:

(a) *Hole* and *particle* NTOs come in pairs and their relative importance in describing the excitation is determined by the diagonal elements of $diag(\sqrt{\lambda_1}, \sqrt{\lambda_2}, ...)$,

(b) $diag(\sqrt{\lambda_1}, \sqrt{\lambda_2}, ...)$ are the excitation amplitudes in the NTO basis

(c) $1 \geq \lambda_i^o \equiv \lambda_i^v \geq 0; i = 1,...,N_o$

(d) $\sum_{i=1}^{N_o} = 1$, in absence of de-excitation operator, as in CIS, TDA [20, 90]. We may equivalently express the eigenvalues λ_i in a square-diagonal matrix, and write:

$$\sum_{i=1}^{N_o} \lambda_{ii} \equiv \sum_{j=1}^{N_o} (\mathbf{TT}^\dagger)_{jj} \tag{148}$$

While in CIS the diagonal entries add up to 1, in TDDFT and RPA the sum of the λ_i elements deviates from the unit to the extent that the de-excitation operators are significant. The de-excitation terms are in most cases rather small, as witnessed by the proven ability of TDA to reproduce TDDFT values [20, 90].

(e) the eigenvectors $v_{N_o+1}, ..., v_{N_v}$ will have zero eigenvalues.

Trough the SV decomposition, any excited state may be represented using at most N_o excitation amplitudes and corresponding hole/particle NTO pairs, rather than $N_o N_v$, as it is the case for the canonical orbitals. Thus, with each hole in the occupied space, one can associate a single corresponding particle in the virtual space.

3.3.2 *One-particle reduced density matrices*

Similarly to 1TDM, one can also define state density matrices or one-particle reduced density matrices (1RDM), which are expressions of type,

For $\mathbf{r}_1 = \mathbf{r}_1'$ the state density matrix reduces to the electron density.

$$\gamma^0(\mathbf{r}_1\mathbf{r}_1) \equiv \rho^0(\mathbf{r}_1) = \sum_{p=1}^{L}\sum_{q=1}^{L} \varphi_p(\mathbf{r}_1)\tilde{D}^0_{pq}\varphi^*_q(\mathbf{r}_1) \tag{149}$$

$$\Rightarrow \int d\mathbf{r}_1\, \rho^0(\mathbf{r}_1) = N. \tag{150}$$

Just as for the 1TDM, integrating the product of γ^0 with the corresponding spin-orbitals gives back the elements,

$$\tilde{D}^0_{pq} = \int_{\mathbb{R}^3} d\mathbf{r}_1 \int_{\mathbb{R}^3} d\mathbf{r}_1' \varphi^*_p(\mathbf{r}_1)\boldsymbol{\gamma}^0(\mathbf{r}_1,\mathbf{r}_1')\varphi^*_q(\mathbf{r}_1'). \tag{151}$$

One can also represent density matrices in the atomic orbital basis. For this purpose, it is useful to introduce the density operator,

$$\hat{\gamma} = \sum_{p=1}^{N}\sum_{q=1}^{N} \left|\varphi_p(\mathbf{r}_1)\right\rangle \tilde{D}_{pq} \left\langle\varphi_q(\mathbf{r}_1')\right|, \tag{152}$$

where the $\tilde{D}_{pq}$ are the elements of the 1RDM, expressed in MO basis. By expanding the spin-orbitals as linear a combination of atomic orbitals we get,

$$\hat{\gamma} = \sum_{p=1}^{N}\sum_{q=1}^{N}\sum_{\mu=1}^{K}\sum_{\nu=1}^{K} \left|\phi_\mu(\mathbf{r}_1)\right\rangle \underbrace{C_{\mu p}\tilde{D}_{pq}C^*_{\nu q}}_{D_{\mu\nu}} \left\langle\phi_\nu(\mathbf{r}_1')\right|. \tag{153}$$

$(\mathbf{C})_{\mu p}$ and $(\mathbf{C})_{\nu q}$ are the $K \times L$ matrices containing the LCAO expansion coefficients. Note that the absence of the tilde indicates that the $D_{\mu\nu}$ elements are expressed in the atomic orbital basis. From the basis set expansion, we get,

$$\sum_{p=1}^{N}\sum_{q=1}^{N} C_{\mu p}\delta_{p\nu}(C^\dagger)_{\nu q} = \sum_{p=1}^{N} C_{\mu p}(C^\dagger)_{p\nu} \Rightarrow \hat{\gamma} = \sum_{\mu=1}^{K}\sum_{\nu=1}^{K} \left|\phi_\mu(\mathbf{r}_1)\right\rangle D_{\mu\nu} \left\langle\phi_\nu(\mathbf{r}_1')\right|. \tag{154}$$

The matrix elements corresponding to the density operator $\hat{\gamma}$, in an atomic orbital basis, write,

$$D_{\mu\nu} = \sum_{\zeta=1}^{K}\sum_{\lambda=1}^{K} \left\langle\phi_\mu(\mathbf{r}_1)\right| \phi_\zeta(\mathbf{r}_1)\left\rangle D_{\zeta\lambda} \left\langle\phi_\lambda(\mathbf{r}_1')\right| \phi_\nu(\mathbf{r}_1')\right\rangle = \sum_{\zeta=1}^{K}\sum_{\lambda=1}^{K} S_{\mu\zeta}D_{\zeta\lambda}S_{\lambda\nu}. \tag{155}$$

where $\mathbf{D}(K \times K)$ is the density matrix, and $\mathbf{S}(K \times K)$ is the overlap matrix expressed in atomic orbitals. Finally, we find back,

$$\gamma^0(\mathbf{r}_1, \mathbf{r}'_1) = \sum_{\mu=1}^{K} \sum_{\nu=1}^{K} D_{\mu\nu} \phi_\mu(\mathbf{r}_1) \phi_\nu(\mathbf{r}'_1). \tag{156}$$

The total electronic density is nothing but the diagonal part of the state density matrix. Setting $\mathbf{x} = \mathbf{x'}$ and integrating the density over all space returns the number of electrons, equivalently one can compute the trace of **DS**.

$$N = \sum_{\mu=1}^{K} \sum_{\nu=1}^{K} \int d\mathbf{x}_1 \; \phi_\mu(\mathbf{r}_1) D_{\mu\nu} \phi_\nu(\mathbf{r}_1) \tag{157}$$

$$= Tr(\mathbf{DS}). \tag{158}$$

3.3.3 *Difference density matrices*

In the previous section, we have introduced transition density matrices and state density matrices, discussing their importance in the analysis of excited states. We now introduce the one-particle difference density matrix (1DDM) [105].

> Defined as the difference between the densities of two states involved in a transition, the 1DDM also can be manipulated to obtain ah-hoc descriptors, for the analysis of excited states.
>
> $$\gamma^{0X}_{\Delta}(\mathbf{r}_1, \mathbf{r}'_1) = \gamma^X(\mathbf{r}_1, \mathbf{r}'_1) - \gamma^0(\mathbf{r}_1, \mathbf{r}'_1). \tag{159}$$

This density matrix can be projected into the Euclidean space in order to directly visualize the negative and positive contributions, for instance after the light-induced charge displacement.

$$\rho_\Delta(\mathbf{r}_1) = \sum_{p=1}^{L} \sum_{q=1}^{L} \varphi_p(\mathbf{r}_1) \tilde{D}^{\Delta}_{pq} \varphi^*_q(\mathbf{r}'_1) = \rho^X(\mathbf{r}_1) - \rho^0(\mathbf{r}_1). \tag{160}$$

As for the case of transition densities, plotting the difference density is not very instructive, as $\boldsymbol{\gamma}_\Delta$ is a complicated function [105].

$$\rho^{0X}_{\Delta}(\mathbf{r}_1) = \gamma^{0X}_{\Delta}(\mathbf{r}_1, \mathbf{r}_1) = \gamma^X(\mathbf{r}_1, \mathbf{r}_1) - \gamma^0(\mathbf{r}_1, \mathbf{r}_1) = \rho^X(\mathbf{r}_1) - \rho^0(\mathbf{r}_1). \tag{161}$$

Besides, just as for the transition density, the integral of the difference density over all space is zero, since no fraction of charge adds up or vanishes during the electronic transition:

$$\int d\mathbf{r}_1 \; \rho^{0X}_{\Delta}(\mathbf{r}_1) = 0. \tag{162}$$

Again, a more instructive way to analyze the difference density matrix is to partition it. Several methods exist, based on the diagonalization of the 1DDM or the construction of a positive and negative severance of this initial distribution.

3.4 DENSITY DESCRIPTORS DERIVED FROM THE 1DDM

In this section we provide an overview of the most important descriptors that appeared in the literature in the last years. For a recent review on the subject we refer to [115]. Among these an important class is the one of the descriptors that are derived from the 1DDM. These objects are aimed at obtaining meaningful quantities for the analysis of 1DDMs and allow an insightful interpretation of excited states.

3.4.1 *The D_{CT} index, a charge-transfer distance derived in real space*

Some years ago, a simple model was proposed to define a measure of the length of a CT excitation solely from the total electronic density in a real-space representation [1,117], computed for the ground and excited states. This idea is condensed in a descriptor, that we will refer to as D_{CT}. In the following, we present the mathematical derivation of the D_{CT}. In light of its simple formulation, it becomes clear that this method applies to any quantum chemical method supplying densities for the ground and excited states and provides in principle an effortless way to qualitatively compare the outcomes of post-Hartree-Fock (HF) and DFT-based approaches [3].

Let $\rho^0(\mathbf{r})$ and $\rho^X(\mathbf{r})$ be the electronic densities associated to the ground and excited state X, respectively. The density variation associated to the electronic transition $\rho_\Delta(\mathbf{r})$ is given by Eq. 159. From the density difference, one can define two functions $\rho_+(\mathbf{r})$ and $\rho_-(\mathbf{r})$, which collect the points in space where an increment or a depletion of charge has occurred due to the transition:

$$\rho_+(\mathbf{r}) = \begin{cases} \rho_\Delta(\mathbf{r}) & if\ \rho_\Delta(\mathbf{r}) > 0 \\ 0 & if \rho_\Delta(\mathbf{r}) < 0 \end{cases} \tag{163}$$

$$\rho_-(\mathbf{r}) = \begin{cases} \rho_\Delta(\mathbf{r}) & if\ \rho_\Delta(\mathbf{r}) < 0 \\ 0 \quad , & if \rho_\Delta(\mathbf{r}) < 0. \end{cases} \tag{164}$$

It is instructive to calculate the barycenters of charge relative to these two spatial distributions, for instance discretizing $\rho_+(\mathbf{r})$ and $\rho_-(\mathbf{r})$ on a three-dimensional (3D) grid around the molecule, as

$$R_+ = \varkappa^{-1} \int_{\mathbb{R}^3} d\mathbf{r}\ \mathbf{r}\rho_+(\mathbf{r}) = (x_+, y_+, z_+) \tag{165}$$

$$R_- = \varkappa^{-1} \int_{\mathbb{R}^3} d\mathbf{r}\ \mathbf{r}\rho_-(\mathbf{r}) = (x_-, y_-, z_-), \tag{166}$$

where $\varkappa$ is the total integrated positive/negative charge, defined as

$$\varkappa = \int_{\mathbb{R}^3} d\mathbf{r}\, \rho_\xi(\mathbf{r}). \tag{167}$$

with ξ «+» or «-». The D_{CT} measures the effective excitation length (hence it is calculated in Å (or Bohr)). It is expressed as the spatial distance between the two barycenters of the positive and negative density distributions:

$$D_{\mathrm{CT}} = | R_+ - R_- | . \tag{168}$$

Additionally, one can also quantify the amount of charge transferred along the transition q_{CT} by integrating $\rho_+(\mathbf{r})$ and $\rho_-(\mathbf{r})$ over all space. For one electron excitations, q_{CT} assumes values between 0 and 1 and is expressed in atomic units.

$$q_\xi = \int_{\mathbb{R}^3} d\mathbf{r}\, \rho_\xi(\mathbf{r}) \implies q_{\mathrm{CT}} = \frac{1}{2} \sum_{\xi=+,-} q_\xi . \tag{169}$$

The norm of the dipole moment associated to the transition writes,

$$\| \mu \| = \mu_\Lambda^{X0} = D_{\mathrm{CT}} \int d\mathbf{r}\, \rho_+ \mathbf{r} = -D_{\mathrm{CT}} \int d\mathbf{r}\, \rho_- \mathbf{r} = D_{\mathrm{CT}} \cdot q_{\mathrm{CT}}. \tag{170}$$

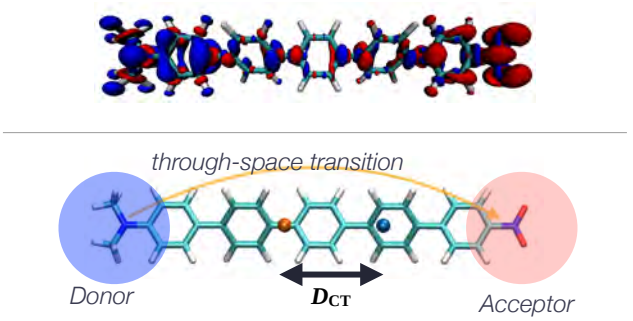

Figure 4: Pictorial representation of the density distributions of charge increase (red) and depletion (blue), obtained from the 1DDM (upper). Representation of the calculated barycenters of charges R_+ and R_- and their distance, D_{CT}.

Moreover, In Ref. [1] two additional descriptors are introduced, one measuring the spread of positive and negative densities along a selected axes (H), the other defined as the difference between the charge-transfer distance and the spread. Although they were specifically devised for the study of excitation in push-pull molecules we report them

here. Both take into account the root-mean-square deviation of the density distributions along the three axis (σ_{aj}; $j = x,y,z; a = +or-$),

$$\sigma_{a,j} = \sqrt{\frac{\sum_i \rho_a(\mathbf{r}_i)(j_i - j_a)^2}{\sum_i \rho_a(\mathbf{r}_i)}}, \tag{171}$$

from which H and t are computed as,

$$H = \frac{\sigma_{+x} + \sigma_{-x}}{2} \tag{172}$$

$$t = D_{\mathrm{CT}} - H. \tag{173}$$

H values larger than the D_{CT} imply diffuse charge distributions, which results in larger overlaps between the centroids of density corresponding to the density depletion and the density increment regions, along with this axis. This index, contrary to D_{CT}, does not necessarily vanish for symmetric systems, but it has no physical relationship with a charge-transfer distance, as D_{CT} has. t on the other side was suggested as a simple qualitative diagnostic index for unphysical through-space CT excitations, of interest at TDDFT level. The aim of the model outlined in Ref. [1] was to classify qualitatively different push-pull compounds in terms of length and magnitude of charge transferred. Since then it has been applied copiously. Since it relies only on the computed electronic density for ground and excited states, the D_{CT} can be computed at any level of theory. The ability of the D_{CT} to characterize electronic transition calculated with both density-based and wave function-based methods is witnessed in a recent publication [3] of ours, where TDDFT- and CASSCF-computed D_{CT} values delivered the same interpretation, for transitions belonging to different nature. An apparent drawback of the D_{CT} is that this index is exactly zero for any symmetric system. In such a case the index may be evaluated on the corresponding symmetry irreducible subunits, as suggested in recent work [118], where the authors examine a variant of the D_{CT} index, designed for symmetric systems.

3.4.2 *Excited state metrics based on attachment/detachment density matrices*

An insightful description of electronic transitions can be achieved by diagonalizing the 1DDM [91].

$$\mathbf{W}^{\dagger}\gamma_{\Delta}\mathbf{W} = diag(k_1, k_2, ...). \tag{174}$$

The eigenvalues $diag(k_1, k_2, ...)$ are the occupation numbers of the transition in canonical space. By considering only the negative eigenvalues, one obtains the so-called detachment matrix,

$$\mathbf{d} = \sum_{i=1}^{L} min(k_i, 0). \tag{175}$$

Analogously, one can collect only the positive eigenvalues and construct the attachment matrix,

$$\mathbf{a} = \sum_{i=1}^{L} max(k_i, 0). \tag{176}$$

d and **a** correspond respectively to charge **removal** and **accumulation**. Back-transforming to the initial orbital basis one obtains the attachment (ρ_a) /detachment ($\rho_d(\mathbf{r})$) densities. These can be interpreted as *hole* and *particle* densities associated to the transition.

$$\mathbf{WdW}^{\dagger} = \boldsymbol{\gamma}_d \xrightarrow{\mathbb{R}^3} \rho_d(\mathbf{r}) = \sum_{p=1}^{L}\sum_{q=1}^{L} \tilde{D}^d_{pq}\varphi_p(\mathbf{r}_1)\varphi^*_q(\mathbf{r}'_1), \tag{177}$$

$$\mathbf{WaW}^{\dagger} = \boldsymbol{\gamma}_a \xrightarrow{\mathbb{R}^3} \rho_d(\mathbf{r}) = \sum_{p=1}^{L}\sum_{q=1}^{L} \tilde{D}^a_{pq}\varphi_p(\mathbf{r}_1)\varphi^*_q(\mathbf{r}'_1), \tag{178}$$

Hence, the difference density matrix is connected to the attachment/detachment matrices as,

$$\boldsymbol{\gamma}^{\Delta} = \boldsymbol{\gamma}^a - \boldsymbol{\gamma}^d, \tag{179}$$

all matrices expressed in canonical space. The integrals over all space give the so-called *"promotion numbers"*,

$$\begin{cases} p_d &= Tr(\boldsymbol{\gamma}_d) = \sum_i d_i \\ p_a &= Tr(\boldsymbol{\gamma}_a) = \sum_i a_i \end{cases} \equiv \begin{cases} p_d &= \int_{\mathbb{R}^3} d\mathbf{r}\ \rho_d(\mathbf{r}) \\ p_a &= \int_{\mathbb{R}^3} d\mathbf{r}\ \rho_a(\mathbf{r}), \end{cases} \tag{180}$$

which are nothing but the number of attached and detached electrons, respectively. In the case of an excitation not involving any loss or gain of electrons it holds that $p_d \equiv p_a$ or more simply p. **Unrelaxed** CIS calculations give $p = 1$. However, when **relaxation effects** are taken into account, the number of **promoted electrons exceeds 1**. In general this is true when any correlated wavefunction model is used. The reasons that let p deviate from 1 are therefore twofold: on one side orbital relaxation effects, on the other double excitation character [91]. On the distinction between relaxed an unrelaxed densities we will come back later, in Chapter 4. It is interesting to note that ρ_a and ρ_d are different from ρ_+ and ρ_- (see Eq.164), which are derived by direct integration of the real-space representation of the difference density function. Conversely, attachment and detachment densities are derived in Hilbert space, and later projected into real space. By taking the difference between ground state and excited density the **shared terms** between the positive and negative **real-space density distributions cancel out**. This is not true for attachment and detachment densities which are derived directly from the 1DDM, rather than from the density projection in direct space. Attachment and detachment densities can be manipulated to construct several descriptors which may be applied for evaluating the **magnitude of the electronic reorganization** produced by a transition. Among these

quantities we cite here a dimensionless quantity, $\mathcal{S}_{ad}$, which is defined as the normalized overlap between the *hole* and *particle* densities [103]:

$$\mathcal{S}_{ad} = s_x^{1/2} \int_{\mathbb{R}^3} d\mathbf{r}\, \sqrt{\rho_d(\mathbf{r})\rho_a(\mathbf{r})}; \qquad N_x = \frac{1}{2} \sum_{q=a,d} \int_{\mathbb{R}^3} d\mathbf{r}\, \rho_q(\mathbf{r}). \tag{181}$$

N_x is a normalization factor, imposing that $\mathcal{S}_{ad}$ ranges between 0 and 1. Through-space transitions arise when the overlap between particle/hole is poor, in which case one finds low $\mathcal{S}_{ad}$ values. The opposite is true for local excitations. Of note, $\mathcal{S}_{ad}$ has also been applied for the diagnostics of problematic charge-transfer excitations within the TDDFT framework [103]. In a later publication, the same authors introduced the a new index $\mathscr{AS}$ [106], whose definition is a complex number, the real and imaginary part of which respectively define the normalized transferred charge $\mathscr{I}$ and the overlap $\mathcal{S}_{ad}$. Thus, $\mathscr{AS}$ bridges the real-space and Hilbert-space derived metrics; it writes:

$$\mathscr{I} = \frac{\varkappa^{-}1}{2} \sum_{\xi=+,-} \int_{\mathbb{R}^3} d\mathbf{r}\, \rho_\xi(\mathbf{r}).$$

$\mathscr{AS}$ is therefore a normalized quantity

$$\mathscr{AS} = \mathscr{I} + i\mathcal{S}_{ad}. \tag{182}$$

Equivalently, $\mathscr{AS}$ can be expressed as

$$\mathscr{AS} = 2\pi^{-1} \underbrace{\arctan\Big(\frac{\mathcal{S}_{ad}}{\mathscr{I}}\Big)}_{\theta_s} = \frac{2\theta_s}{\mathscr{I}}. \tag{183}$$

The $\mathscr{AS}$ metric can be interpreted as the normalized angle resulting from the projection of both $\mathscr{I}$ and $\mathcal{S}_{ad}$ in a complex plane. θ_s is then the angle between the latter projection and the real axis (a pictorial representation is provided in ref [106]). The $2\pi^{-1}$ factor ensures that θ_s is normalized.

Alternative derivation of $\mathcal{S}_{ad}$, $\mathscr{I}$, $\mathscr{AS}$ using the NTO formalism.

In subsection 3.3.1 we have introduced the SV decomposition of the transition density matrix, transforming the latter in a diagonal matrix $diag(\lambda_1, \lambda_2, ...)$ with at most N_o nonzero entries.

$$diag(\sqrt{\lambda_1}, \sqrt{\lambda_2}, ...) = \mathbf{U}^\dagger \mathbf{T} \mathbf{V} \tag{184}$$

Let us consider the LCAO coefficient matrix expansion, $\mathbf{C}$ of dimensions $(L \times L)$. One can express $\mathbf{C}$ as the composition of two matrices $\tilde{\mathbf{U}}(K \times N)$ and $\tilde{\mathbf{V}}(K \times [L-N])$, containing occupied and virtual orbital coefficients, respectively. The product of $\tilde{\mathbf{U}}$ and $\tilde{\mathbf{V}}$ with the $\mathbf{U}$

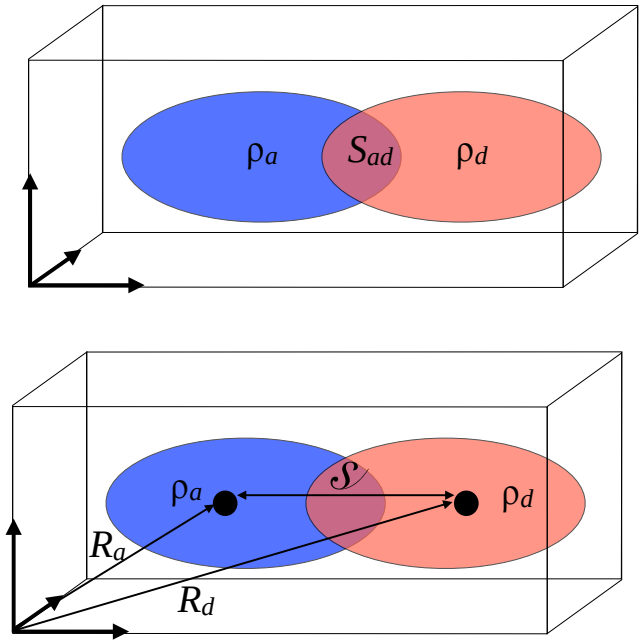

Figure 5: Graphical depiction of the S_{ad} descriptor as the overlap between detachment and attachment densities (top). Detachment/attachment densities centroids (bottom). Picture adapted from reference [104].

and $\mathbf{V}$ defined in Eq.147 build the LCAO expansion coefficient matrices for the occupied and virtual NTOs [119]:

$$\mathbf{C}^o = \tilde{\mathbf{U}}\mathbf{U} \quad (K \times N) \quad \text{and} \tag{185}$$
$$\mathbf{C}^v = \tilde{\mathbf{V}}\mathbf{V} \quad (K \times [L-N]). \tag{186}$$

The expression of the occupied and virtual density matrices in the LCAO-NTOs basis is then,

$$(\mathbf{D}^o)_{ij} = \sum_{l=1}^{N} \lambda_{ll} (\mathbf{C}^o)_{il} (\mathbf{C}^o)_{jl} \quad \text{and} \tag{187}$$
$$(\mathbf{D}^v)_{ij} = \sum_{l=1}^{N} \lambda_{ll} (\mathbf{C}^v)_{il} (\mathbf{C}^v)_{jl}; \tag{188}$$

and the following relations hold:

$$\sum_{i=1}^{K}(\mathbf{D}^{o}\mathbf{S})_{ii}=\sum_{i=1}^{N}\lambda_{ii}=\sum_{i=1}^{K}(\mathbf{D}^{v}\mathbf{S})_{ii}, \tag{189}$$

from which we can construct,

$$\rho^{X}(\mathbf{r})=\rho^{0}(\mathbf{r})-\underbrace{\sum_{k=1}^{N}\lambda_{kk}|\varphi_{k}^{h}(\mathbf{r}_{h})|^{2}}_{\rho^{o}(\mathbf{r})}+\underbrace{\sum_{k=1}^{N}\lambda_{kk}|\varphi_{k}^{p}(\mathbf{r}_{p})|^{2}}_{\rho^{v}(\mathbf{r})}. \tag{190}$$

Hence we can conclude that

$$\rho^{X}(\mathbf{r})-\rho^{0}(\mathbf{r})=\rho^{v}(\mathbf{r})-\rho^{o}(\mathbf{r})\Leftrightarrow\mathbf{D}^{X}-\mathbf{D}^{0}=\mathbf{D}^{v}-\mathbf{D}^{o}. \tag{191}$$

Equation 191 only holds if $\mathbf{D}^{X}$ is the unrelaxed density matrix for the Xth excited state. In such a case the difference density matrix is a composition of occupied/occupied and virtual/virtual terms, and the mixed occupied/virtual blocks are 0. $\mathbf{D}^{v}$ and $\mathbf{D}^{o}$ in Eq. 191 are the density matrices associated to the electron depletion and increase generated upon transition. By comparison with Eq. 179, we may notice that the difference between $\mathbf{D}^{v}$ and $\mathbf{D}^{o}$ analogously to the difference between $\mathbf{D}^{a}$ and $\mathbf{D}^{d}$ gives the 1DDM. Hence, one may use without distinction the NTO approach as well as the attachment/detachment one to derive the aforementioned descriptors [94].

Connection between detachment/attachment and NTO formalism.

Ref. [94] provides a rigorous demonstration that, for single reference excited state calculation methods, expressing the electronically excited state as a linear combination of singly excited Slater determinants, the detachment/attachment and NTO paradigms are directly connected. Not only the author shows that the metrics associated to one or the other method can be derived equivalently from both approaches, but it also points out **that attachment/detachment densities can be computed directly from SVD of the 1TDM, without requiring any matrix diagonalization**. This transformation is proven by using the structure of the difference density matrix. A theorem is also assumed as part of this derivation, stating that NTOs are the eigenvectors of the detachment/attachment density matrices. We summarize in the present paragraph the crucial points of this derivation. The 1DDM, expressed in a canonical base can be shown to be built from the direct sum of two matrices $-\mathbf{T}\mathbf{T}^{\dagger}$ and $\mathbf{T}^{\dagger}\mathbf{T}$:

$$\boldsymbol{\gamma}_{\Delta}=-\mathbf{T}\mathbf{T}^{\dagger}\oplus\mathbf{T}^{\dagger}\mathbf{T}=\begin{pmatrix}0_{o} & 0_{o\times v}\\ 0_{v\times o} & \mathbf{T}^{\dagger}\mathbf{T}\end{pmatrix}-\begin{pmatrix}\mathbf{T}\mathbf{T}^{\dagger} & 0_{o\times v}\\ 0_{v\times o} & 0_{v}\end{pmatrix} \tag{192}$$

where 0 denote zero matrices the dimensions of which are specified by the corresponding subscripts. We know from previous discussion that the diagonalization of $\boldsymbol{\gamma}_{\Delta}$ writes,

$$\mathbf{W}^{\dagger}\boldsymbol{\gamma}_{\Delta}\mathbf{W}=diag(k_{1},k_{2},...). \tag{193}$$

By construction, $-\mathbf{T}\mathbf{T}^\dagger$ and $\mathbf{T}^\dagger\mathbf{T}$ are positive definite [94, 103], therefore all negative eigenvalues of γ_Δ belong to the occupied × occupied block, while the positive ones stem from the virtual × virtual block. Therefore, the following relation hold,

$$\mathbf{T}\mathbf{T}^\dagger \oplus 0_v = \boldsymbol{\gamma}^d_\Delta \quad ; \quad 0_o \oplus \mathbf{T}^\dagger\mathbf{T} = \boldsymbol{\gamma}^a_\Delta. \tag{194}$$

Besides, according to Eq.147, we know that

$$diag(k_1, k_2, ...) = -\boldsymbol{\lambda}^o \oplus \boldsymbol{\lambda}^v, \tag{195}$$

and that the matrix W diagonalizing the 1DDM is given by:

$$\mathbf{W} = \mathbf{U} \oplus \mathbf{V}. \tag{196}$$

From Eq.194 one deduces that the eigenvectors of the detachment/attachment matrices are the occupied/virtual transition orbitals. The matrices $\mathbf{Z}^a, \mathbf{Z}^d$ diagonalizing $\boldsymbol{\gamma}_\Delta$ write,

$$\mathbf{Z}^a = \mathbf{0}_o \oplus \mathbf{O} \implies \mathbf{Z}^{a\dagger}\boldsymbol{\gamma}^a\mathbf{Z}^a = \mathbf{0}_o \oplus \lambda_v \quad ; \quad Z^d = \mathbf{O} \oplus \mathbf{0}_v \implies \mathbf{Z}^{d\dagger}\boldsymbol{\gamma}^d\mathbf{Z}^d = \lambda_v \oplus \mathbf{0}_v \tag{197}$$

Based on these relation Ref. [94] delineates a scheme for the joint computation of detachment/attachment densities from the eigenvectors and singular values of the 1TDM.

- $\mathbf{U}^\dagger\mathbf{T}\mathbf{V} = diag(\sqrt{\lambda_1}, \sqrt{\lambda_2}, ...) \rightarrow \{\boldsymbol{\lambda}^o; \boldsymbol{\lambda}^v\} \rightarrow \boldsymbol{\gamma}_\Delta = -\mathbf{U}\boldsymbol{\lambda}^o\mathbf{U}^\dagger \oplus \mathbf{V}\boldsymbol{\lambda}^v\mathbf{V}^\dagger$
- according to the structure of $diag(k_1, k_2, ...)$ one can express the attachment/detachment eigenvalues, $\mathbf{a}$ and $\mathbf{d}$ as $diag(k_1, k_2, ...) = -\boldsymbol{\lambda}^o \oplus \boldsymbol{\lambda}^v \Rightarrow \mathbf{a} = 0_o \oplus \boldsymbol{\lambda}^v; \quad \mathbf{d} = 0_v \oplus \boldsymbol{\lambda}^o$.
- which leads to

$$\boxed{(\boldsymbol{U} \oplus \boldsymbol{V})\mathbf{a}(\boldsymbol{U}^\dagger \oplus \boldsymbol{V}^\dagger) = \boldsymbol{\gamma}^a} \quad \text{and} \quad \boxed{(\boldsymbol{U} \oplus \boldsymbol{V})\mathbf{d}(\boldsymbol{U}^\dagger \oplus \boldsymbol{V}^\dagger) = \boldsymbol{\gamma}^d} \tag{198}$$

- from which all the desired metrics can be obtained, $\{\boldsymbol{\gamma}^a, \boldsymbol{\gamma}^d\} \rightarrow \{\mathcal{S}_{ad}, \mathcal{J}, \mathcal{K}\}$

3.4.3 *Hilbert-space related attachment/detachment density matrices-based centroids of charge*

Attachment and detachment densities can be used to measure the charge displacement length, by computing the difference between the charge centroids associated to these two distributions. For a detailed discussion on Hilbert-space related attachment/detachment density matrices-based centroids of charge we refer to references [103, 104, 106]. Just as for the D_{CT} which we have introduced in Section 3.4.1, one computes the centroids ($\mathcal{R}_a$, $\mathcal{R}_d$) of the attachment and detachment densities as,

$$R_d = \varkappa^{-1} \int_{\mathbb{R}^3} d\mathbf{r}\, \mathbf{r}\rho_d(\mathbf{r}), = (x_d, y_d, z_d) \tag{199}$$

$$R_a = \varkappa^{-1} \int_{\mathbb{R}^3} d\mathbf{r}\, \mathbf{r}\rho_a(\mathbf{r}), = (x_a, y_a, z_a) \tag{200}$$

where $\varkappa$ is the total integrated attached/detached charge, defined as

$$\varkappa = \int_{\mathbb{R}^3} d\mathbf{r}\, \rho_\xi(\mathbf{r}). \tag{201}$$

where ξ takes values of a or d. The distance between the two centroids writes,

$$\eth_{\mathrm{CT}} = \mid \mathcal{R}_d - \mathcal{R}_a \mid . \tag{202}$$

Similarly the transferred charge is given by the norm,

$$w_\tau = \int_{\mathbb{R}^3} d\mathbf{r}\, \rho_\tau(\mathbf{r}) \implies w_{\mathrm{CT}} = \frac{1}{2} \sum_{\tau=a,d} w_\tau. \tag{203}$$

Again, it is interesting to ponder on the difference between the ρ_d and ρ_a densities and the ρ_+ and ρ_- pair. The same holds for w_τ and q_{CT}. One may notice that alternative derivations of the same quantities are possible, by employing the methodologies illustrated above. For instance, one can extract the positive and negative density distributions respectively from the attached and detached densities. If we denote the charge-transfer distance and the charge displaced, calculated with this third strategy as $\tilde{D}_{\mathrm{CT}}$ and $\tilde{q}_{\mathrm{CT}}$, the following relations hold:

$$q_{\mathrm{CT}} \equiv \tilde{q}_{\mathrm{CT}} \leq w_{\mathrm{CT}} \tag{204}$$

$$D_{\mathrm{CT}} \equiv \tilde{D}_{\mathrm{CT}} \geq \eth_{\mathrm{CT}}, \tag{205}$$

$$\tag{206}$$

where the inequality stems from the fact that w_{CT} incorporates a portion of overlapping density that cancels out in q_{CT}, which is computed form real-space difference density. This discrepancy extends to the barycenters as well. Furthermore, we have seen in the previous section that the three descriptors $\mathcal{I}$and $\mathcal{AS}$ and $\mathcal{S}_{ad}$ can be equivalently derived both using the 1DDM and the 1TDM approach. The analogous correspondence applies to $\tilde{q}_{\mathrm{CT}}$ and $\tilde{D}_{\mathrm{CT}}$. As a result, the following equivalences also hold:

$$\boldsymbol{\gamma}_a^{\mathrm{NTO}} - \boldsymbol{\gamma}_d^{\mathrm{NTO}} = \boldsymbol{\gamma}_a - \boldsymbol{\gamma}_d \Rightarrow \tilde{q}_{\mathrm{CT}} = \tilde{q}_{\mathrm{CT}}^{\mathrm{NTO}};\ \tilde{D}_{\mathrm{CT}} = \tilde{D}_{\mathrm{CT}}^{\mathrm{NTO}}, \tag{207}$$

where the superscript NTO indicates that the descriptors are obtained from SVD of the 1TDM.

3.5 ANALYSIS OF EXCITED STATES FROM 1TDM

3.5.1 *An orbital based descriptor: Δr*

In the previous part, we have given an overview of the latest advances regarding excited states descriptors derived from the 1DDM. As anticipated before, a second approach exists, based on the 1TDM. The two methods are formally connected. Specifically, for the case of electronically excited states expressed as a linear combination of singly excited

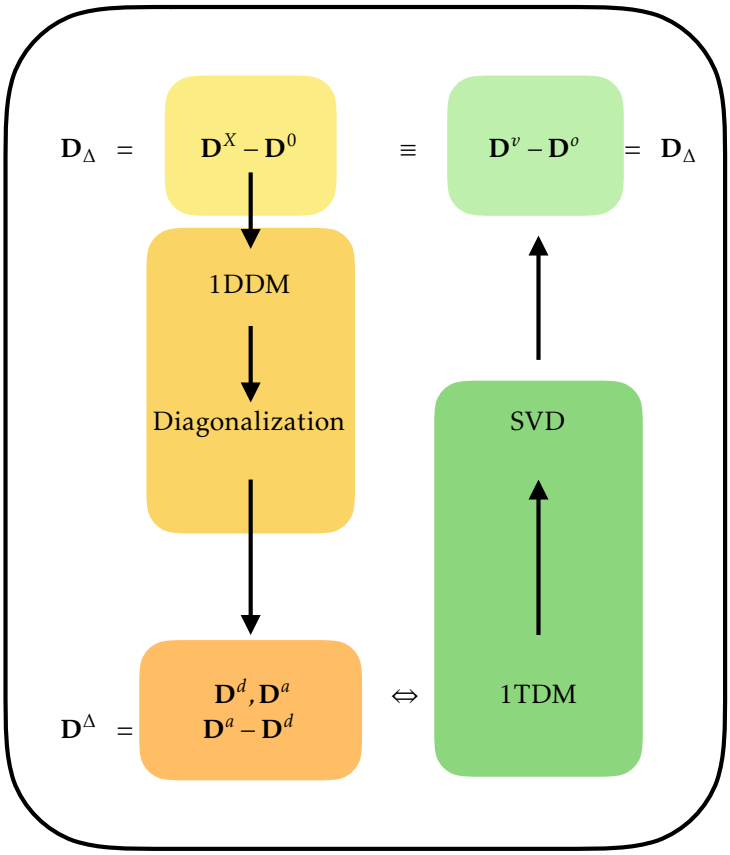

Figure 6: Connection between 1DDM and 1TDM

Slater determinant generated from single reference wave functions, 1DDM and 1TDM give analogous results. Metrics other than the D_{CT} and the attachment/detachment density based ones exist for the qualitative and quantitative analysis of excited states. Notably, Guido et al. [113, 120] have proposed an index Δr providing an alternative measure of the effective $hole - particle$ length of a transition. The definition is based on the weighted sum of orbital centroids differences. If the orbital considered are the $\varphi_i^h(\mathbf{r}_h)$ and $\varphi_i^p(\mathbf{r}_p)$, which result rotating the canonical orbitals according to a rotation matrix obtained via

SVD of the 1TDM (see Eq. 144), then the maximal correspondence between excited *hole* and *particle* is obtained. The Δr index writes,

$$\Delta r = \frac{\sum_i^{N_o} \lambda_{ii} \left| \left\langle \varphi_i^p(\mathbf{r}_p) \middle| \mathbf{r} \middle| \varphi_i^p(\mathbf{r}_p) \right\rangle - \left\langle \varphi_i^h(\mathbf{r}_h) \middle| \mathbf{r} \middle| \varphi_i^h(\mathbf{r}_h) \right\rangle \right|}{\sum_i^{N_o} \lambda_{ii}}, \tag{208}$$

where the $\left\langle \varphi_i^{p(h)}(\mathbf{r}_{p(h)}) \middle| \mathbf{r} \middle| \varphi_i^{p(h)}(\mathbf{r}_{p(h)}) \right\rangle$ are defined as the norm of the orbital centroids and the λ_{ii} are the singular values of the 1TDM (i.e., the eigenvalues associated to the ith *hole-particle* transition). Moreover to best characterize an electronic transition one wants to give an estimate of the delocalization of the electrons around the orbital centroids. Based on this observation, the authors modified the original Δr definition by coupling it to a measure of the particle spread around the charge centroids are given by,

$$\sigma_p = \sqrt{\left\langle \varphi_i^p(\mathbf{r}_p) \middle| \mathbf{r}^2 \middle| \varphi_i^p(\mathbf{r}_p) \right\rangle - \left\langle \varphi_i^p(\mathbf{r}_p) \middle| \mathbf{r} \middle| \varphi_i^p(\mathbf{r}_p) \right\rangle^2}. \tag{209}$$

The two can be combined into a new metric Γ,

$$\Gamma = \Delta r + \Delta\sigma = \frac{\left\langle \varphi_i^p(\mathbf{r}_p) \middle| \mathbf{r} \middle| \varphi_i^p(\mathbf{r}_p) \right\rangle - \left\langle \varphi_i^h(\mathbf{r}_h) \middle| \mathbf{r} \middle| \varphi_i^h(\mathbf{r}_h) \right\rangle |}{\sum_i^{N_o} \lambda_{ii}} + \frac{\sum_i^{N_o} \lambda_{ii} \left| \sigma_p - \sigma_h \right|}{\sum_i^{N_o} \lambda_{ii}}. \tag{210}$$

In the context of TDDFT, Γ may also be used to discriminate between short and long-range excitations. Given its formulation, which provides both a measure of the charge-transfer distance and of the spread of the electrons around the centroids, Γ can individuate any transition, from valence to charge-transfer and Rydberg states. Finally, not only Γ provides a measure of the effective $hole-particle$ distance covered during the excitations, but its interest also resides in the ability to render a reliable diagnostic of the performance of TDDFT, even in those cases where other diagnostic indexes fail [121].

3.5.2 *Exciton descriptors*

The present discussion, although legitimate for our purposes, is certainly limited in terms of the topics covered and compared to the abundance of papers devoted to excited states analysis. In particular, one major question we have not addressed until now, is the possibility of including static and dynamic electronic correlation effects. These can be important, as there are properties that derive directly from it, for instance, electron-hole binding and exciton sizes. These, are naturally more of concern in the context of solid-state physics, which deviates quite from our focus. However, for large molecular systems, it has been shown that exciton-effects may be crucial for a correct interpretation of the electronic excitation [31, 122–125].

Furthermore, there it has been pointed out that hole/electron pairs, generated in electronic excitations suffer the same limits at the TDDFT level as charge-transfer states do [124]. In this context it is interesting to mention the work carried out by Plasser et

al. [108, 112], which offers an additional interpretation of the 1TDM which we have not yet discussed. The one-one particle difference density matrix can be interpreted as the effective two-body exciton wave function, describing the correlated hole-particle motion. This identification is justified in Ref. [112] in term of many-body Greens-function theory. Based on this assumption, the authors propose a set of descriptors yielding a quantitative analysis of excited states [107, 110, 112]. The central quantity of this analysis is again the 1TDM, defined in Eq. 137. The latter, is expressed in coordinate space as,

$$\chi^X(\mathbf{r}_h, \mathbf{r}_p) = \sum_p^L \sum_q^L \varphi_p*(\mathbf{r}_h) \left\langle \Psi^0 \right| \hat{a}_p^\dagger \hat{a}_q \left| \Psi^X \right\rangle \varphi_q(\mathbf{r}_p) \tag{211}$$

$$= \boldsymbol{\gamma}^{0X}(\mathbf{r}_p, \mathbf{r}_h), \tag{212}$$

where $\mathbf{r}_p, \mathbf{r}_h$ denote *hole* and *particle* coordinates, and $\hat{a}_p^\dagger, \hat{a}_q$ annihilate the electron in φ_p and create a hole in orbital φ_q, respectively. The exciton wave function may be expressed in an even more compactly by using the NTOs.

$$\chi_{\text{exc}}(\mathbf{r}_h, \mathbf{r}_p) = \sum_{i=1}^N \sqrt{\lambda_i} \varphi_i^h(\mathbf{r}) \varphi_i^p(\mathbf{r}). \tag{213}$$

Here $\varphi_i^h(\mathbf{r})\varphi_i^p(\mathbf{r})$ are the *hole* and *particle* wave functions and the label i indexes the orbital pair corresponding to the singular values $\sqrt{\lambda_i}$. This representation of the electronic transition avoids the bias associated with a specific orbital choice, leading to a compact and more realistic representation of the exciton.

In summary, the theory of exciton analysis is independent of the wave function model and provides an exact picture of the electronic excitation. Moreover, it may be applied to calculate a variety of wave function properties, while being invariant from orbital rotation nor dependent on a partitioning of the wave function into atomic contributions [94, 112]. This representation of the electronic transition avoids the arbitrariness associated with a specific molecular orbital choice [112] leading to a sound and more rigorous description of the exciton [107, 111]. The non zero singular values of the 1TDM inherently deliver the information of the number of relevant contributions that are needed to describe the excitation. This concept may be quantified as the participation ratio [107],

$$PR_{NTO} = \frac{\sum_i (\lambda_i)^2}{\sum_i \lambda_i^2} = \frac{\Omega}{\sum_i \lambda_i^2} \tag{214}$$

where Ω is the squared norm of the exciton wave function

$$\Omega = \langle \chi_{\text{exc}} | \, \chi_{\text{exc}} \rangle = \boldsymbol{\gamma}^{\mathbf{0X}}(\mathbf{r}_h, \mathbf{r}_p)^2 = \| \, \boldsymbol{\gamma}^{0X} \, \|^2 \, . \tag{215}$$

The PR_{NTO} expresses the number of independent configuration needed to describe an excitation. For wave functions other than in an unrelaxed CIS/TDA calculation, in which case $PR_{NTO} = 1$, the latter can be considered as a estimation of the amount of single excitation character. A $PR_{NTO} > 1$ implies that several configurations contribute to a

state. Differently stated it gives a measure of the static correlation. All information carried within the exciton wave function is released by calculating the expectation value of the latter with respect to an operator of interest,

$$\langle \hat{O} \rangle = \frac{\langle \chi_{\text{exc}} | \hat{O} | \chi_{\text{exc}} \rangle}{\langle \chi_{\text{exc}} | \chi_{\text{exc}} \rangle} \tag{216}$$

An approach to characterize exciton wave functions is to compute its spacial and statistical properties, which provide a measure of its broadness and delocalization in space. The derivation of the latter relies on Eq.216 [112]. As stated by Eq. 215 the denominator is the squared norm of the transition density matrix. Written in atomic orbital space the latter reads,

$$\Omega = Tr(\mathbf{D}^{0X^\dagger} \mathbf{S} \mathbf{D}^{0X} \mathbf{S}) \tag{217}$$

where $\mathbf{S}$, has elements $S_{\mu\nu}$, that are the atomic orbital overlaps of $\chi_\mu(\mathbf{r}), \chi_\nu(\mathbf{r})$. The numerator can be simplified by expressing the operator as product of one particle operators,

$$\hat{O} = \hat{h}(\mathbf{r}_h)\hat{p}(\mathbf{r}_p). \tag{218}$$

Writing the expectation value in orbital representation leads to

$$\hat{h}(\mathbf{r}_h)\hat{p}(\mathbf{r}_p) = \frac{1}{\Omega} \sum_{\mu}^{K} \sum_{\nu}^{K} \sum_{\zeta}^{K} \sum_{\xi}^{K} D_{\mu\nu} D_{\zeta\xi} \times \tag{219}$$

$$\int_{\mathbb{R}^3} d\mathbf{r}_h \; \chi_\mu(\mathbf{r}_h) \hat{h}(\mathbf{r}_h) \chi_\xi(\mathbf{r}_h) \times \int_{\mathbb{R}^3} d\mathbf{r}_p \; \chi_{nu}(\mathbf{r}_p) \hat{h}_p(\mathbf{r}_p) \chi_\zeta(\mathbf{r}_h) \tag{220}$$

$$= \frac{1}{\Omega} \sum_{\mu}^{K} \sum_{\nu}^{K} \sum_{\zeta}^{K} \sum_{\xi}^{K} h_{\mu\nu} p_{\zeta\xi} \tag{221}$$

$$= \frac{1}{\Omega} Tr(\mathbf{D}^{0X\dagger} \mathbf{h} \mathbf{D}^{0X} \mathbf{p}) \tag{222}$$

Moreover of the operators are functions of $\mathbf{r}_h$ and $\mathbf{r}_p$, but do not act explicitly on hole and particle coordinates, i.e., $\hat{h}(\mathbf{r}_h)\hat{p}(\mathbf{r}_p) = \langle f(\mathbf{r}_h, \mathbf{r}_p) \rangle$, then the expectation value reduces to the integration of the product of a $\langle f(\mathbf{r}_h, \mathbf{r}_p) \rangle$ and the squared norm of the 1TDM. If $\langle f(\mathbf{r}_h, \mathbf{r}_p) \rangle$ is a multipole matrix one can derive several relations to compute the locality of an exciton.
The size of the exciton is given by,

$$d_{\text{exc}} = \sqrt{\langle | \mathbf{r}_h - \mathbf{r}_p |^2 \rangle}. \tag{223}$$

Expanding, gives

$$d^2_{\text{exc}} = \sum_{r=x,y,z} \langle (r_h - r_p) \cdot (r_h - r_p) \rangle_{\text{exc}} \tag{224}$$

$$= \sum_{r=x,y,z} \langle (r_h \cdot r_h) \rangle_{\text{exc}} - \langle 2(r_h \cdot r_p) \rangle_{\text{exc}} + \langle (r_p \cdot r_p) \rangle_{\text{exc}} \tag{225}$$

$$= \sum_{r=x,y,z} \langle r_h^2 \rangle_{\text{exc}} - \langle 2 r_h \cdot r_p \rangle_{\text{exc}} + \langle r_p^2 \rangle_{\text{exc}}. \tag{226}$$

The nine terms of Eq. 226 are the expectation values of the one-electron multipole operators. Considering Eq. 222, these write,

$$\langle x_h^k x_h^k \rangle_{\text{exc}} = \frac{1}{\Omega} Tr(\mathbf{D}^{X0} \mathbf{M}_x^{(l)} \mathbf{D}^{0X} \mathbf{M}_x^{(l)}). \tag{227}$$

The elements of $\mathbf{M}_x^{(l)}$ are the k-order multipole moments for component x, given as,

$$M_k^{(l)}, \mu\nu = \int_{\mathbb{R}^3} \chi_\mu(\mathbf{r}) x^k \chi_\nu(\mathbf{r}) \tag{228}$$

The calculation of d_{exc} reduces then to a series of matrix multiplications. The practical equation that can be used to calculate the exciton size is:

$$d^2_{\text{exc}} = \frac{1}{\Omega} \sum_{r=x,y,z} (Tr(\mathbf{D}^{X0} \mathbf{M}_r^{(2)} \mathbf{D}^{0X} \mathbf{S}) - 2Tr(\mathbf{D}^{X0} \mathbf{M}_r^{(1)} \mathbf{D}^{0X} \mathbf{M}_r^{(1)}) + Tr(\mathbf{D}^{X0} \mathbf{S} \mathbf{D}^{0X} \mathbf{M}_r^{(2)})). \tag{229}$$

the second order terms contain the quadrupole moments of *hole* density ($\mathbf{D}^{0X} \mathbf{S} \mathbf{D}^{X0}$) and of the particle density ($\mathbf{D}^{X0} \mathbf{S} \mathbf{D}^{0X}$), respectively, while the first order term expresses the mixed dipole contributions deriving from the correlated motion of the *hole* and *particle* [112]. A complementary quantity to the exciton size is the vectorial distance between the centroids of the hole and particle distributions:

$$\vec{d}_{h \to e} = \langle \mathbf{r}_h - \mathbf{r}_p \rangle_{\text{exc}}. \tag{230}$$

While $\vec{d}$ is a measure of the linear charge transfer, d_{exc} also incorporates the exciton charge resonance effects. Analogously to the exciton size, one can also compute hole and particle sizes separately, as,

$$\sigma_h = (\langle \mathbf{r}_h^2 \rangle_{\text{exc}} - \langle \mathbf{r}_h \rangle_{\text{exc}}^2)^{1/2} \tag{231}$$

$$\sigma_e = (\langle \mathbf{r}_p^2 \rangle_{\text{exc}} - \langle \mathbf{r}_p \rangle_{\text{exc}}^2)^{1/2} \tag{232}$$

These can be related to the mean average positions $\langle r_h \rangle_{\text{exc}}$,$\langle r_p \rangle_{\text{exc}}$ to give an estimate of the spread of hole and particle with respect to the charge centroids. Along with the geometrical descriptors discussed above, a statistical interpretation of the exciton has also

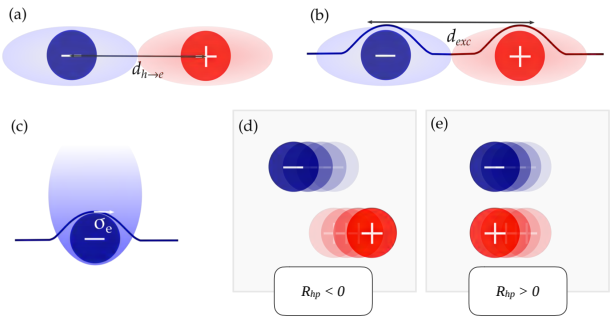

Figure 7: (a) Vectorial electron-hole distance $d_{h\to p}$, (b) exciton size d_{exc} rmsd electron-hole distance, (c) electron size σ_h,σ_p rms deviation from the centroid of the electron density, (d) negative electron-hole correlation $R_{hp} < 0$ i.e., dynamical charge avoidance, and (e) positive electron-hole correlation $R_{hp} > 0$, i.e., joint electron-hole motion as bound exciton. Picture adapted from reference [110]

been proposed [110], quantifying the linear correlation between particle and hole. The two descriptors proposed are,the covariance and the correlation,

$$\text{COV}(\mathbf{r}_h\mathbf{r}_p) = \langle \mathbf{r}_h \cdot \mathbf{r}_p \rangle_{\text{exc}} - \langle \mathbf{r}_h \rangle_{\text{exc}} - \langle \mathbf{r}_p \rangle_{\text{exc}}; \qquad \text{COR}_{hp} = \frac{COV(\mathbf{r}_h\mathbf{r}_p)}{\sigma_h, \sigma_p}. \tag{233}$$

The correlation coefficient may be positive or negative, depending on the sign of the numerator. The covariance is a measure of the joint variability hole and particle. If the a shift in the position of the *hole* induces a change in the same direction in the particle, (i.e., hole and particle tend to show similar behavior), the covariance is positive. Conversely, when the particle moves in opposite direction with respect to the hole, (i.e., the variables tend to show opposite behavior), the covariance is negative.The sign of the covariance therefore shows the tendency in the linear relationship between the hole and the particle. While the first case delineates correlated hole/particle motion, the latter denotes an anti-correlated behavior. Zero correlation implies that hole and particle behave independently. The descriptors discussed in the present subsection follow directly from the definition of the exciton wave-function. Eq.213 formally connects the exciton paradigm with the NTO representation of the electronic excitation. Thus, all equations can be equivalently reformulated in the NTO basis [108].

Part II

TDDFT ROOTED PROCEDURES FOR THE DESCRIPTION OF EXCITED STATES

4

EXCITED STATES FROM TDDFT: A MEASURE OF CHARGE-TRANSFER

4.1 CONTEXT

The time-dependent response theory approach outlined in Chapter 3 provides a route to excitation energies and transition moments. Excited state (ES) total energies are then accessed by adding the excitation energy to the corresponding ground state (GS) energy. This methodology gives access to useful objects, such as the 1DDM, which enclose the information related to the polarization of the electronic cloud occurring within the excitation. Within the Time-Dependent Functional Theory (TDDFT), additionally, to improve the description of the density matrices, one may perform a **post-linear response treatment** of the excited state calculation, by computing the so-called Z-vector [126]. In the TDDFT scheme, this computation results in the addition of a matrix (occupied-virtual terms) to the 1DDM to account for the **density relaxation** following the hole/particle generation. The resulting redistributed excited state density is the so-called *relaxed* difference density matrix.

This procedure opens the question of how the quality of the computed densities affects the descriptors that are directly derived from it. This question is the focus of a recent publication of ours: "How are the charge-transfer descriptors affected by the quality of the underpinning electronic density?", by myself, Marco Campetella, Michael J. Frisch, Giovanni Scalmani, Carlo Adamo, and Ilaria Ciofini, published in the Journal of Computational Chemistry. The present chapter constitutes an adaptation of the latter publication.

4.2 INTRODUCTION

In the recent decades, we have witnessed an intensive and increasing use of theoretical approaches to describe and predict excited state phenomena and properties of molecular compounds [20, 127, 128]. Among different methods, TDDFT has emerged as one of the most applied, mainly due to its low cost to accuracy ratio and its simple formalism, making it widely available to both theoretical and experimental chemists' community [19]. Nonetheless, besides its numerous successes, it is nowadays well established that TDDFT approaches have severe drawbacks that can be in large part ascribed to the **quality** of the **underlying density functional** approximation used to describe the exchange-correlation energy [127]. Indeed, several works pointed out that TDDFT approaches yield significant errors when applied to the description of **CT excitations**, especially when local exchange-correlation functionals (such as Generalized Gradient Approximation, GGA or Local Density Approximation, LDA) are used [129]. More specifically, these type of functionals

do not correctly recover the *1/R asymptotic behavior* relevant for the description of CT states and global or range-separated hybrid functionals, including in different ways exact Hartree–Fock exchange have been often proposed as a suitable alternative to improve TDDFT performances in the description of this type of excited states [30,121,130].

However, if a *correct description* of CT phenomena is still tricky to achieve [121,131,132] the design of molecules able to give rise to CT or charge separation (CS) at the excited state is a flourishing experimental field due to their relevance in many fields of application ranging from artificial photosynthesis to hybrid solar cells. The so-called **push-pull systems** represent one of the most common molecular topologies, experimentally used to generate these type of excited states. These molecular structures that are made up of an electron-donating group (D) and acceptor group (A) covalently bound often in a rigid and rod-like fashion by a spacer, whose length and conjugation degree can be eventually changed to tune their properties (e.g., the absorption energy) [117,133,134].

These systems display at least one low lying intensively absorbing excited state with relevant CT character and schematically corresponding to the transfer of an electron from the D to the A, which leads to the formation of a formal [D-A] excited state. However, in most cases, both the excited state hole and electron are far from being strictly localized on the donor/acceptor fragments. Depending on their chemical nature, as well as on the bridge length, the spatial extent and the magnitude of the electron transfer can be significantly different. As introduced in Chapter 3, many indexes have been devised in the last years to define the nature—and eventually measure—the extent of CT excitation as well as to diagnostic the reliability of TDDFT approaches in calculating the energy and intensity of the electronic transition [117,127,134–136].

Among others, and for this purpose, an index, the (D_{CT}), has been recently developed by some of us, allowing to define the **spatial extent** associated with a given transition, using only the density distributions of the associated ground and excited electronic states [1]. More recently we have also proposed a new index (the $\mathrm{M_{AC}}$index) enabling to assess the degree of reliability of CT excitations has been more recently further derived from the D_{CT} by us [5]. Both these indexes are based on the evaluation of ground and excited state densities. According to the Z-vector method [126], the TDDFT total ES density can be refined by applying a post-linear-response correction, which accounts for relaxation effects [137], associated with electronic transitions, when the excited states are calculated either in the diabatic framework or vertically. Since then, several works have been published on the importance of the inclusion of density relaxation effects in the adiabatic framework and beyond [138–141]. As reported in the latter works, the density variation within the adiabatic picture - referred to as *unrelaxed* - differs from the diabatic - *relaxed* - picture by the inclusion of the effect of the charge rearrangement and the change in bond order due to the electronic excitation. Accordingly, in this contribution, we apply the same terminology.

In this work, we used a prototype push-pull system (namely the family of the α,ω-dimethylamino-nitropolyphenylene,8) to evaluate the impact of ES density relaxation on the computed density-based descriptor (i.e., the D_{CT} index). As the CT parameters strongly depend on the exchange-correlation functional used, we investigate such effect

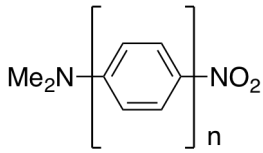

Figure 8: The family of molecules considered and associated labeling scheme (n = 1 to 10).

for a variety of density functional approximations (52 functionals) ranging from LDA to range-separated hybrids. We compute the energies and the density index associated with the CT excitation for each functional, using either of the ES densities, i.e., the *relaxed* and *unrelaxed* one. By doing so, we quantitatively evaluate the effect of employing either of the two electronic density definitions in the calculation of the D_{CT}. As we want to evaluate the impact of the quality of the density as a function of the CT distance, we consider push-pull chains of growing length, by increasing the number of spacers from 1 to 10 (refer to Scheme 8).

The outline of this chapter is the following: first, we recall the methods in Section 4.3.1 and the computational details in Section 4.4. Section 4.3.1 is substantially revised compared to the original paper, including a detailed description of the Z-vector method. Next, in Section 4.5, we discuss the computed excitation energies, and density indexes for the different classes of functionals, with a focus on a few selected instructive examples. Finally, we draw some general conclusions.

4.3 THEORETICAL BACKGROUND AND METHODS

We have introduced earlier in Section 3.4.1 the procedure allowing to define the D_{CT} [1] from the GS and ES densities. Here, for the sake of clarity and for a better readability we recapitulate the original procedure and extend it to the context of *relaxed* and *unrelaxed* densities. The computed difference density (1DDM) between any excited state S_X and ground state, S_0 is given by

$$\rho_{\Delta}(\mathbf{r}) = \rho^{X}(\mathbf{r}) - \rho^{0}(\mathbf{r}), \tag{234}$$

from which one can define two quantities (ρ^{+} and, analogously, ρ^{-}), accounting for the increase or decrease of density resulting from an electronic transition

$$\rho^{+} = \begin{cases} \Delta\rho(\mathbf{r}) & \textit{if } \Delta\rho(\mathbf{r}) > 0 \\ 0 & \textit{if } \Delta\rho(\mathbf{r}) < 0, \end{cases} \tag{235}$$

together with the associated barycenters of density $R+$ and $R-$,

$$R^{+} = (x^{+}, y^{+}, z^{+}) = \frac{\int \mathbf{r}\rho^{+}(\mathbf{r})\mathrm{d}(\mathbf{r})}{\int \rho^{+}(\mathbf{r})\mathrm{d}(\mathbf{r})}. \tag{236}$$

The spacial distance between the two barycenters of density distributions is then used to quantify the length of the CT excitation:

$$D_{CT} = \mid R^{+} - R^{-} \mid . \tag{237}$$

Clearly, all these quantities depend on the quality of ground and excited state densities. Recent publications have highlighted the importance of density relaxation [140, 142, 143] in the context of the analysis of electronic transitions arising from a TDDFT calculation. The question on how are the charge-transfer descriptors affected by the quality of the associated electronic density is, therefore, strictly related to the *re-distribution* of the electronic density due to the excitation process. In particular, the concept of the magnitude of such relaxation can be better quantified by the inclusion of the Z-vector in the difference density matrix definition.

4.3.1 *Excited state properties and the Z-vector method*

The Z-vector equation can be conveniently derived using a Lagrangian formalism in the linear response framework. This method, proposed initially by Handy and Shäfer [126] has been later applied to derive excited state gradients for CIS [144] and implemented in the Gaussian package [145]. In a later publication by Furche and Alrichs this the Z-vector method has been derived explicitly for TDDFT. In the following, we review the critical steps of the derivation. More details can be found in the Reference [138]. The following derivations follow the spin-orbital formulation, where all spin orbitals are considered to be real.

Time-dependent response theory, which we have introduced in Section 2.5.3, provides a root to excited states. As mentioned previously in Section 2.5.5, within the TDDFT linear response formulation, excitation energies are obtained as the solutions of Casida equations (Eq. 103). It is, however, convenient to introduce an equivalent, variational formulation, as follows. Excited states are the stationary points of the functional

$$G[\mathbf{X},\mathbf{Y},\Omega] = \langle \mathbf{X},\mathbf{Y}|\,\Lambda\,|\mathbf{X},\mathbf{Y}\rangle - \Omega(\langle \mathbf{X},\mathbf{Y}|\,\Delta\,|\mathbf{X},\mathbf{Y}\rangle - 1), \tag{238}$$

where Ω is a real Lagrange multiplier, and the vectors

$$\langle \mathbf{X},\mathbf{Y}| = \begin{pmatrix}\mathbf{X}\\ \mathbf{Y}\end{pmatrix}, \tag{239}$$

are defined in the Hilbert space of occupied and virtual molecular orbitals. The molecular orbitals(MOs) $\varphi_{p\sigma}(\mathbf{r})$ are solutions of the ground state spin unrestricted Kohn-Sham (KS) equations with orbital eigenvalues $\epsilon_{p\sigma}$. As usual the indexes $i,j,\cdots$, denote occupied, $a,b,\cdots$, virtual and $p,q,\cdots$ generic orbitals. The MOs are expanded in the basis of atom centered contracted Gaussians $\chi_{\mu}(\mathbf{r})$, the expansion coefficients C_{pq} being stored in the coefficient matrix $\mathbf{C}$. X and Y above are the expansion coefficients of the transition, that is the first order linear response density in terms of the ground state KS-orbitals

$$\rho^{(1)}(\mathbf{r},\mathbf{r'}) = \frac{1}{2}\sum_{ia\sigma}(X_{ia\sigma}\varphi_{a\sigma}(\mathbf{r})\varphi_{i\sigma}(\mathbf{r'}) + Y_{ia\sigma}\varphi_{i\sigma}(\mathbf{r})\varphi_{a\sigma}(\mathbf{r'})). \tag{240}$$

Λ and Δ are the so called "superoperators",

$$\Lambda = \begin{pmatrix} \mathbf{A} & \mathbf{B} \\ \mathbf{B} & \mathbf{A} \end{pmatrix}, \quad \Delta = \begin{pmatrix} \mathbf{1} & \mathbf{0} \\ \mathbf{0} & \mathbf{-1} \end{pmatrix}. \tag{241}$$

A and **B** are defined from the matrix elements of the time-independent KS Hamiltonian

$$A_{ia,jb} = (\epsilon_a - \epsilon_i)\delta_{ij}\delta_{ab} + (ia|jb) + (ia|f_{\mathrm{xc}}|jb) \tag{242}$$

$$B_{ia,jb} = (ia|jb) + (ia|f_{\mathrm{xc}}|jb) \tag{243}$$

where the integrals are expressed in Mulliken notation. **A** and **B** are generally referred to as the orbital rotation Hessians. Their matrix representation writes,

$$(A+B)_{ia\sigma jb\sigma'} = (\epsilon_{a\sigma} - \epsilon_{i\sigma})\delta_{ij}\delta_{ab}\delta_{\sigma\sigma'} + 2(ia\sigma|jb\sigma') + 2f^{\mathrm{xc}}_{ia\sigma jb\sigma'} - c_{\mathrm{x}}\delta_{\sigma\sigma'}[(ja\sigma|ib\sigma) + (ab\sigma|ij\sigma)], \tag{244}$$

$$(A-B)_{ia\sigma jb\sigma'} = (\epsilon_{a\sigma} - \epsilon_{i\sigma})\delta_{ij}\delta_{ab}\delta_{\sigma\sigma'} + c_{\mathrm{x}}\delta_{\sigma\sigma'}[(ja\sigma|ib\sigma) - (ab\sigma|ij\sigma)] \tag{245}$$

where $f^{\mathrm{xc}}_{pq\sigma rs\sigma'}$ is the exchange-correlation kernel in the adiabatic approximation.

$$f^{\mathrm{xc}}_{\sigma\sigma'}(\mathbf{r},\mathbf{r'}) = \frac{\delta^2 E^{\mathrm{xc}}}{\delta\rho_\sigma(\mathbf{r})\delta\rho_{\sigma'}(\mathbf{r'})} \tag{246}$$

E^{xc} denotes the exchange-correlation energy functional, that is evaluated at the ground state energy. Then, the Lagrangian G may be expressed in the form,

$$G[\mathbf{X},\mathbf{Y},\Omega] = \frac{1}{2}\Big[(\mathbf{X}+\mathbf{Y})^{\dagger}(\mathbf{A}+\mathbf{B})(\mathbf{X}+\mathbf{Y})(\mathbf{X}-\mathbf{Y})^{\dagger}(\mathbf{A}-\mathbf{B})(\mathbf{X}-\mathbf{Y})\Big] + \frac{\Omega}{2}\Big[(\mathbf{X}+\mathbf{Y})^{\dagger}(\mathbf{X}-\mathbf{Y}) + (\mathbf{X}-\mathbf{Y})^{\dagger}(\mathbf{X}+\mathbf{Y}) - 2\Big]. \tag{247}$$

By applying the variational principle one obtains the stationarity conditions for G,

$$\frac{\partial G}{\partial (X+Y)_{ia\sigma}} = \sum_{jb\sigma'}(A+B)_{ia\sigma jb\sigma'}(X+Y)_{jb\sigma'} - \Omega(X-Y)_{ia\sigma} = 0, \tag{248}$$

$$\frac{\partial G}{\partial (X-Y)_{ia\sigma}} = \sum_{jb\sigma'}(A-B)_{ia\sigma jb\sigma'}(X-Y)_{jb\sigma'} - \Omega(X+Y)_{ia\sigma} = 0, \tag{249}$$

$$\frac{\partial G}{\partial \Omega} = \sum_{ia\sigma}(X+Y)_{ia\sigma}(X-Y)ia\sigma = 0. \tag{250}$$

These conditions yield the original linear response equation and the normalization conditions for the coefficients X,Y.

Eq. 248,249,250 are evaluated at a chosen stationary point $(\mathbf{X},\mathbf{Y}),\Omega$. As a result one obtains a specific excitation energy Ω and transition densities $(\mathbf{X}+\mathbf{Y})$ and $(\mathbf{X}-\mathbf{Y})$.

Once excitation energies are computed, one may compute excited state properties by the first-order derivation of the energy with respect to an external perturbation. The total electronic energy is the sum of the ground state and the excitation energy. By analogy, the excited state properties are a sum of the corresponding ground state and excitation parts, where the latter is simply the derivative of the excitation energies. These observations are a direct consequence of the Hellman-Feynman theorem (which specifies how to compute the derivative of the energy of a bound state with respect to a parameter in the Hamiltonian in terms of the expectation values of the operator) and more generally of the Wigner $2n+1$ rule. The latter states that that the $(2n+1)th$ order properties can be evaluated from a knowledge of the wavefunction through nth order. If one denotes an external perturbation as ξ, one may write

$$\Omega^{\xi} = G^{\xi}[\mathbf{X},\mathbf{Y},\Omega] = \langle \mathbf{X},\mathbf{Y}|\Lambda^{\xi}|\mathbf{X},\mathbf{Y}\rangle. \tag{251}$$

It is interesting to note that due to the variational principle, first-order properties do not require the computation of the derivatives of the excitation vectors, (which are zero by definition, as they are stationary points of G). However calculating Λ^{ξ} still involves the derivatives of the MO coefficients, expressed as linear combination of atom centered functions,

$$\varphi_{p\sigma}(\mathbf{r}) = \sum_{\mu} C_{p\sigma\mu}\chi_{\mu}(\mathbf{r}). \tag{252}$$

If we denote as ε the number of nuclear degrees of freedom in a single molecule, then computing the derivatives of the MOs would involve ε perturbations, and would be therefore ε time more demanding than computing unperturbed MOs. Luckily, it as pointed out before [138], [139], [32, chapter 16], it is possible to avoid the computation of the derivatives of C^{ξ}. This is possible by introducing the so-called "relaxed" densities, which in turn allow computing excited state properties at a computational cost that is independent of ε. The Lagrangian of the excitation energy can be expressed [138] as,

$$L[\mathbf{X},\mathbf{Y},\Omega,\mathbf{C},\mathbf{Z},\mathbf{W}] = \langle \mathbf{X},\mathbf{Y}|\Lambda|\mathbf{X},\mathbf{Y}\rangle - \Omega(\langle \mathbf{X},\mathbf{Y}|\Delta|\mathbf{X},\mathbf{Y}\rangle - 1) + \sum_{ia\sigma} F_{ia\sigma} - \sum_{pq\sigma} W_{pq\sigma}(S_{pq\sigma} - \delta_{pq}). \tag{253}$$

$S_{pq\sigma}$ are the overlap integrals of the KS orbitals. The matrix elements $F_{ia\sigma}$ are obtained by replacing the diagonal part of $(A+B)$ and $(A-B)$ in equations 244 and 245 by $F_{ab\sigma}\delta_{ij} - F_{ij\sigma}\delta_{ab}\delta_{\sigma\sigma'}$. The effective KS one particle Fock operator comprises the usual terms, that are the core Hamiltonian h, a Coulomb and exchange part, and the exchange-correlation potential respectively,

$$F_{pq\sigma} = h_{pq\sigma} + \sum_{i\sigma'}[(pq\sigma|ii\sigma') - c_{\mathrm{x}}\delta_{\sigma\sigma'}(pi\sigma|iq\sigma) + V^{\mathrm{xc}}_{pq\sigma}] \tag{254}$$

$$V^{\mathrm{xc}}_{\sigma} = \frac{\delta E^{\mathrm{xc}}}{\delta\rho_{\sigma}(\mathbf{r})} \tag{255}$$

The introduction of F is particularly appropriate: by construction F is diagonal, with eigenvalues $\epsilon_{p\sigma}$ on the diagonal. This substitution renders the excited state formalism invariant under any unitary transformation of occupied and virtual orbitals since all physical properties are invariant under the same transformations. These conditions is reinforced by requiring the Lagrangian L to be stationary with respect to all its parameters, $\mathbf{X},\mathbf{Y},\Omega,\mathbf{C}$ and $\mathbf{W}$. Hence the summation of the GS Lagrangian and L provides a *fully variational root* to excited state energies.

The variation of L with respect to $|\mathbf{X},\mathbf{Y}\rangle$ and Ω lead back to Eqs. 248,249 and 250, while the Lagrange multipliers $Z_{ia\sigma}$ and $W_{pq\sigma}$ introduce N^2 constraints in the variation of G. As a result, the KS MOs are constrained to satisfy the KS equations and to remain orthonormal [138], for $\xi \neq 0$. Thus, the MO coefficients are fixed and Z and W can be determined using the stationarity of L with respect to the expansion coefficients $C_{\mu p\sigma}$,

$$\frac{\partial L}{\partial C_{\mu p\sigma}} = 0. \tag{256}$$

The expression for $Z_{ia\sigma}$, known as Z-vector equation, writes,

$$\sum_{jb\sigma'} (\mathbf{A}+\mathbf{B})_{ia\sigma jb\sigma'} Z_{jb\sigma'} = -R_{ia\sigma}. \tag{257}$$

The right hand side of Eq. 257 takes the form,

$$\begin{aligned} R_{ia\sigma} = \sum_b \Big\{ &[(X+Y)_{ib\sigma} H^+_{ab\sigma}[\mathbf{X}+\mathbf{Y}] - (X-Y)_{ib\sigma} H^-_{ab\sigma}[\mathbf{X}-\mathbf{Y}]\Big\} \\ &- \sum_j \Big\{ (X+Y)_{ja\sigma} H^+_{ji\sigma}[\mathbf{X}+\mathbf{Y}] - (X-Y)_{ja\sigma} H^-_{hi\sigma}[\mathbf{X}-\mathbf{Y}]\Big\} \\ &+ H^+_{ia\sigma}[P^U_\Delta] + 2 \sum_{jb\sigma' kc\sigma''} g_{ia\sigma jb\sigma' kc\sigma''} (X+Y)_{jb\sigma'} (X+Y)_{kc\sigma''}, \end{aligned} \tag{258}$$

where $g^{\mathrm{xc}}_{pq\sigma rs\sigma' tu\sigma''}$ is third order functional derivative matrix element,

$$g^{\mathrm{xc}}_{\sigma'\sigma'\sigma''}(\mathbf{r},\mathbf{r'},\mathbf{r''}) = \frac{\delta^3 E^{\mathrm{xc}}}{\delta\rho_\sigma(\mathbf{r})\delta\rho_{\sigma'}(\mathbf{r'})\delta\rho_{\sigma''}(\mathbf{r''})}. \tag{259}$$

The operators H^+ and H^- are linear rotation operators which transform the difference density, determining the relaxation. The results of these operators acting on a arbitrary vectors - $V_{pq\sigma}$ are,

$$H^+_{pq\sigma}[V] = \sum_{rs\sigma'} \Big\{ 2(pq\sigma|rs\sigma') + 2f^{\mathrm{xc}}_{pq\sigma rs\sigma'} - c_{\mathrm{x}}\delta_{\sigma\sigma'}\Big[(ps\sigma|rq\sigma)_(pr\sigma|sq\sigma)\Big]\Big\} V_{rs\sigma} \tag{260}$$

$$H^-_{pq\sigma}[V] = \sum_{rs\sigma'} c_{\mathrm{x}}\delta_{\sigma\sigma'}\Big[(ps\sigma|rq\sigma) - (pr\sigma|sq\sigma)\Big] V_{rs\sigma}. \tag{261}$$

The unrelaxed difference density matrix P_Δ^U containing the products of the excitation vectors is defined as:

$$P_{ab\sigma} = \frac{1}{2}\sum_i \{(X+Y)_{ia\sigma}(X+Y)_{ib\sigma} + (X-Y)_{ia\sigma}(X-Y)_{ib\sigma}\}, \tag{262}$$

$$P_{ij\sigma} = -\frac{1}{2}\sum_a \{(X+Y)_{ia\sigma}(X+Y)_{ja\sigma} + (X-Y)_{ia\sigma}(X-Y)_{ja\sigma}\}, \tag{263}$$

$$P_{ai\sigma} = P_{ia\sigma}. \tag{264}$$

In the MO basis, P_Δ^U is a symmetric matrix with both occupied-occupied (OO) and virtual-virtual (VV) contributions only, all occupied-virtual (OV) elements being zero. Once the Z-vector equation (Eq. 257) is solved, the *relaxed* one-particle difference density matrix P_Δ^R is obtained by adding the matrix Z to the *unrelaxed* difference density matrix P_Δ^U. P_Δ^R will have exactly the same OO and VV contributions as P_Δ^U, but the OV terms are not all zero. The appearance of these off-diagonal block elements in the excited-state density matrix can be interpreted as orbital relaxation following the initial gross charge rearrangement due to excitation.

$$P_\Delta^R = P_\Delta^U + Z. \tag{265}$$

The information contained in P_Δ^R integrates that provided by the transition vector. While the latter is related to the matrix elements between the ground state and the excited states, P_Δ^R accounts for the *difference of expectation value* between excited and ground states. For example, $\mathrm{tr}(P_\Delta^R \xi)$ is the change of an electron-dependent property upon excitation from the ground state. The summation of the ground state density matrix and P_Δ^R returns the excited state properties. Population analysis of P allows for an intuitive illustration of the charge redistribution induced by an electronic excitation. *Relaxed* and *unrelaxed* densities, as defined above, can be used to evaluate the D_{CT} and yield the corresponding indexes ${}^R D_{\mathrm{CT}}$ and ${}^U D_{\mathrm{CT}}$. The former reflects the spatial extent associated to a given transition, where the electronic density is allowed to gradually change and adapt to the final configuration, while the latter reproduces the CT distance, measured directly upon vertical excitation. In other words, the *relaxed* (${}^R D_{\mathrm{CT}}$), unlike its *unrelaxed* (${}^U D_{\mathrm{CT}}$) counterpart accounts for the redistribution of the electronic charge due to the excitation.

It is worth to add a couple of remarks as a conclusion to the derivation reported above. The Lagrangian in Eq. 253 is an explicit functional of any external perturbation. This expedient substantially simplifies the task of calculating excited state properties, and with it, the obtainment of *relaxed* and *unrelaxed* densities. Once the $\mathbf{X},\mathbf{Y},\Omega,\mathbf{C},\mathbf{Z},\mathbf{W}$ have been determined from stationarity conditions, derivatives of the excitation energy follow as,

$$\Omega^\xi = L^\xi[\mathbf{X},\mathbf{Y},\Omega,\mathbf{C},\mathbf{Z},\mathbf{W}] \tag{266}$$

$$= G^{(\xi)}[\mathbf{X},\mathbf{Y},\Omega] + \sum_{ia\sigma} Z_{ia\sigma} F_{ia\sigma}^{(\xi)} - \sum_{pq\sigma, p\leqq} W_{pq\sigma} S_{pq\sigma}^{(\xi)}. \tag{267}$$

A complete mathematical treatment of the set of equations leading to excited state properties falls beyond our scopes, here. However, the equations to determine the matrix $\mathbf{W}$ are

given explicitly in Ref. [139]). The reduced complexity of equation 267 (compared to eq. 251) lies in the fact that the derivatives can be computed easily, without need to recompute MO coefficients that are kept at their zero values, as indicated by the superscripts (ξ).

4.4 COMPUTATIONAL DETAILS

In this study, we have tested the 52 different functionals to evaluate the D_{CT} parameters (relaxed and unrelaxed), for push-pull dyes of increasing length. We calculated a series of α,ω-NMe_2,NO_2-push-pull systems, varying the number of phenyl rings in the chain from one to ten. The geometries were built such that the phenyl rings are 45° oriented one towards the other. All calculations were performed using the development version of the Gaussian suite of programs [145]. Optimized in vacuum GS structural parameters were determined for each functional, where an SCF energy convergence criterion of 10^{-8} a.u. was applied; the maximum SCF cycle number was set to 500, and the QC option was specified to prevent convergence failure problems. Frequency calculations indicated that all optimized structures correspond to minima. The optimized structures were proven to retain a linear shape. Gas-phase vertical excitation energies were computed by TDDFT calculations, on top of each optimized geometry. The 6-311G(d,p) atomic basis set was used both for the ground- and excited-sate calculations. Besides, we performed CIS reference calculations at the same level of theory.

The benchmark includes a broad variety of functionals taken from different classes, (the complete list is reported in Table 2). As for the **local density functionals** we tested the performance of the SVWN [35, 37, 74]. Furthermore, the performance of a number of GGA and mGGA functionals, namely BLYP [48, 55], BPBE [43, 55], BP86 [49, 55], BPW91 [50,55], B97D [52], OLYP [48,69], MPWP86 [49,67], MPWPW91 [50,67], MPWLYP [48, 67], HCTH [57], HCTH407 [57], PBE [43], PBEPW91 [43, 50], PW91PW91 [50], SOGGA11 [72], BMK [54], M06L [62], M11L [65], TPSSTPSS [44], VSXC [77], tHCTH [75] was tested. Along with the former we report the performance of a number of **global hybrid**-GGA and -mGGA functionals, B1LYP [45, 48], B1B95 [47], B3LYP [45, 48], B3PW91 [45,50], B3P86 [45,49], B98 [51], BHandHLYP [53], HFPW91 [50], O3LYP [48,70], mPW1PW [67], PBE0 [46], SOGGA11X [73], M05 [59], M06 [26], M052X [60], M062X [26], M06HF [63], M08HX [61], TPSSh [76], tHCTHhyb [75], for improved charge transfer description. Finally we included the **Range Separated Hybrids** (RSH) CAM-B3LYP [56], HSEH1PBE [146], N12SX [68], wB97 [78], wB97X [78], wB97XD [79]and M11 [64], the **long range corrected** LC-PBE [58] and the **Non separable Gradient Approximation** (NGA) functionals MN12L [68], N12 [68].

4.5 ON THE NATURE OF THE FIRST EXCITED STATE OF PUSH-PULL MOLECULES OF VARIOUS LENGTH

α,ω-Amino,nitro-polyphenylene molecules (Scheme 8 are a prototype family of push-pull systems for which the energy and nature of the first excited strongly depends on the length of the spacer that connects the electron donor (D, here an amino group NH_2) and

Table 2: Listed functionals included in the benchmark and relative exact exchange-correlation percentages (c_{HF}, (for range separated hybrids, the long range contribution is indicated).

Functional	% c_{HF}	**Functional**	% c_{HF}	**Functional**	% c_{HF}	**Functional**	% c_{HF}
B97D	0	N12	0	B3LYP	20	BMK	42
BLYP	0	OLYP	0	B3P86	20	BHandHLYP	50
BP86	0	PBE	0	B3PW91	20	M08HX	52.23
BPBE	0	PBEPW91	0	B98	21.98	M062X	54
BPW91	0	PW91PW91	0	N12SX	25	M052X	56
HCTH	0	SOGGA11	0	B1LYP	25	CAM-B3LYP	65
HCTH407	0	SVWN	0	mPW1PW	25	LC-PBE	100
M06L	0	tHCTH	0	PBE0	25	wB97	100
M11L	0	TPSSTPSS	0	HSEH1PBE	25	wB97X	100
MN12L	0	VSXC	0	M06	27	wB97XD	100
MPWLYP	0	TPSSh	10	M05	28	M11	100
MPWP86	0	O3LYP	11.61	B1B95	28	HFPW91	100
MPWPW91	0	tHCTHhyb	15	SOGGA11X	40.15	M06HF	100

the acceptor (A, here a nitro group, NO_2). We aim to assess the impact of the use of *relaxed* or *unrelaxed* excited state densities on the computed properties. To do so, we analyze the *relaxed* and *unrelaxed* CT indexes relative to the first electronic transition.

Of note and as clearly already pointed out in previous literature works [19,117,133,134], depending on the nature of the spacer and on the functional used we expect that the CT character associated with the first electronic transition to be substantially different. Structurally no significant differences are observed at the ground state both for bond lengths and for the interanular dihedral angles when varying the exchange-correlation functional.

Figure 9 shows the computed transition energy associated with the first excited state and the corresponding ${}^{U}D_{\mathrm{CT}}$ and ${}^{R}D_{\mathrm{CT}}$ for all the 52 functionals analyzed. Corresponding raw data are given as Supporting Information together with a separate plot of ${}^{U}D_{\mathrm{CT}}$ and ${}^{R}D_{\mathrm{CT}}$ values as a function of the spacer length. The following labeling scheme has been applied: four different symbols are used to group functionals as a function of their exact exchange contribution. In particular, filled dots represent local functionals ($c_{\mathrm{HF}} = 0\%$), triangles are used with low percentage of exact exchange ($1\% \leq c_{\mathrm{HF}} \leq 40\%$), while diamonds and twisted squares designate functionals with high percentage exact exchange ($40.15\% \leq c_{\mathrm{HF}} \leq 65\%$) or 100% of exact exchange. For range-separated hybrids, the long-range contribution is considered.

Figure 9 clearly shows that the evolution of the computed transition energy as a function of the number of spacers is extremely functional dependent. In this context, it is worth to recall that, experimentally, no significant variation of the excitation energy is observed when varying the spacer from 1 to 4 phenyl units. However, and as expected from previous literature works [1,117,134], a sharp decrease in the computed transition energy is observed as a function of the spacer length for practically all local functionals (labeled

with dots in Figure 9) such as LDA and GGAs: namely SVWN, B97D, BLYP, BP86, BPBE, BPW91, HCTH407, HCTH, MPWLYP, MPWP86, MPWPW91, OLYP, PBE, PBEPW91, PW91, SOGGA11. These functionals all converge to shallow transition energy (of the order of 978–1120 nm) for the most extended bridge unit. Qualitatively the same behavior is observed for functionals containing low percentage (i.e., below 40%) of exact exchange labeled with triangles in Figure 9 (namely B1B95, B1LYP, B3LYP, B3P86, B3PW91, B98, mPW1PW, O3LYP, PBE0, M05, M06, tHCTHhyb, TPSSh, HSEH1PBE, and N12SX) through the predicted transition energy for the longest -10 units- bridge is slightly higher, ranging from 412 nm for the M05 functional to 658 nm for the tHCTHhyb functional.

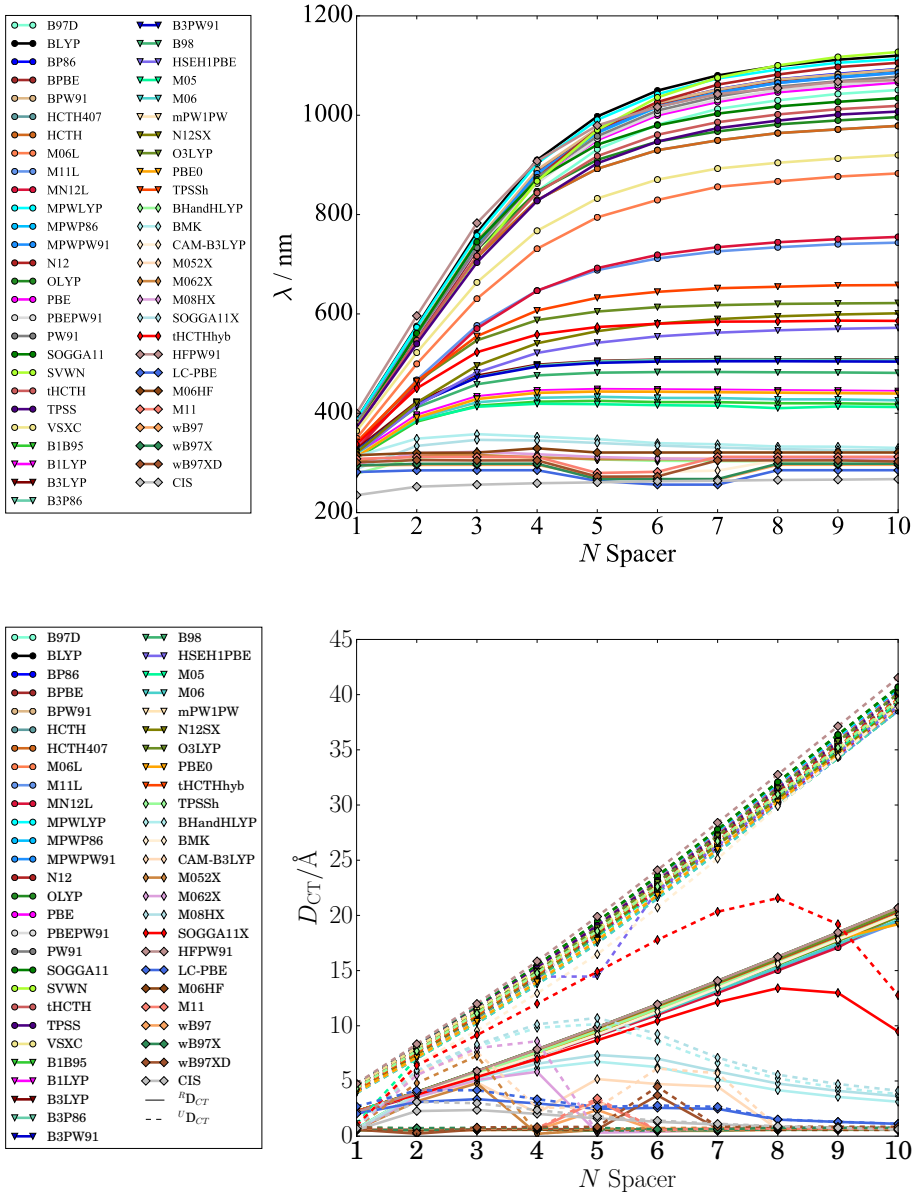

Figure 9: Computed transition energy (upper) and $^{U}D_{\mathrm{CT}}$ and $^{R}D_{\mathrm{CT}}$ values (in Å) (lower) associated with the first excited state. Different markers indicate distinct percentages of exact exchange (c_{HF}) associated with the functionals: respectively filled dots for standard local and semilocal xc functionals ($c_{\mathrm{HF}} \leq 50\%$), triangles for low percentage hybrids ($1 \leq c_{\mathrm{HF}} \leq 40$), diamonds for high percentage hybrids ($40.15 \leq c_{\mathrm{HF}} \leq 65$ 50%), and twisted squares for full hybrid functionals ($c_{\mathrm{HF}} = 100\%$).

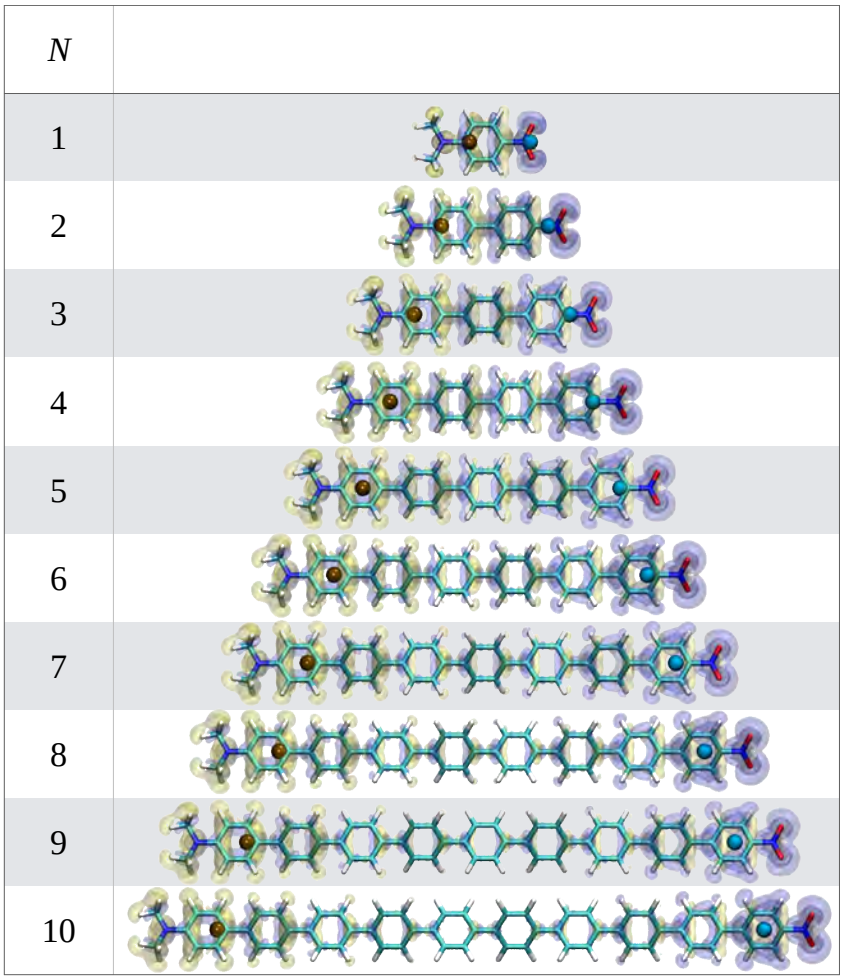

Figure 10: Computed (PBE0/6-31+G(d)) difference in total density computed for the ground and excited states, isocontour value 0.001 au.

Table 3: Computed $^{U}D_{CT}$ and $^{R}D_{CT}$ in Å and excitation wavelength λ in nm for O_N systems (N varying from 1 to 10), for the first electronic transition at different level of theory. Oscillator strength values relative to each transition are in brackets. Experimental values are taken from Ref. [147]

N	PBE			PBE0			LC-PBE			CIS			exp.
	λ	$^{U}D_{CT}$	$^{R}D_{CT}$	λ	$^{U}D_{CT}$	$^{R}D_{CT}$	λ	$^{U}D_{CT}$	$^{R}D_{CT}$	λ	$^{U}D_{CT}$	$^{R}D_{CT}$	λ
1	379.0(0.29)	2.2	4.6	312.1(0.41)	2.3	4.0	281.7(0.00)	0.7	0.5	235.1(0.00)	0.6	0.7	372
2	557.1(0.27)	3.9	8.1	391.1(0.44)	3.9	7.1	285.1(0.00)	0.7	0.5	252.2(0.95)	2.3	3.0	377
3	731.2(0.17)	5.8	11.6	428.6(0.35)	5.7	10.4	285.3(0.00)	0.7	0.6	256.3(1.42)	2.4	3.0	358
4	868.7(0.08)	7.8	15.3	441.0(0.22)	7.6	14.0	285.3(0.00)	0.7	0.6	259.1(1.95)	2.0	2.4	340
5	949.7(0.04)	9.8	19.1	443.7(0.13)	9.5	17.7	263.9(2.66)	2.6	2.5	260.9(2.50)	1.6	1.8	-
6	999.7(0.02)	11.9	23.2	443.3(0.06)	11.5	21.8	256.3(0.00)	0.6	0.5	263.2(3.07)	1.3	1.4	-
7	1026.7(0.01)	14.0	27.3	442.3(0.03)	13.6	26.0	256.3(0.00)	0.6	0.5	264.2(3.62)	1.0	1.1	-
8	1046.1(0.00)	16.1	31.6	441.4(0.01)	15.7	30.3	285.4(0.00)	0.7	0.6	265.7(4.18)	0.9	0.9	-
9	1056.4(0.00)	18.3	35.8	440.5(0.00)	17.9	34.5	285.4(0.00)	0.7	0.6	266.4(4.73)	0.7	0.7	-
10	1065.8(0.00)	20.6	40.2	439.7(0.00	19.2	38.8	285.4(0.00)	0.7	0.6	267.4(5.28)	0.6	0.6	-

This qualitatively and quantitatively wrong prediction is related to the *erratic asymptotic behavior* of the exchange-correlation functional used, as already pointed out in several previous works [5,20,148], giving rise to a low lying (**dark**) state of CT nature. Indeed, the analysis of the corresponding ${}^{U}D_{\mathrm{CT}}$ indexes, computed for all local functionals, (in Figure 9), suggests that all these approaches predict a transition of CT character as the lowest excitation. Specifically, the electron displacement occurs from the HOMO (localized on the donor group) to the LUMO (centered on the acceptor unit), with an associated charge-transfer distance ranging from 5 Å to 40 Å as a function of the number of spacer units. In this case, the predicted CT distances are not very different from the geometrical distance between the D and the A groups and increase practically linearly with the bridge length. Indeed, the distance between the nitrogen atoms of the amino and nitro groups ranges from 5.5 Å (for N=1) to 44.1 Å (for N=10). The difference observed between the geometrical D–A distance and the computed ${}^{U}D_{\mathrm{CT}}$ index is related to the conjugation of both the donor and the acceptor to the bridge units implying a partial delocalization of both HOMO and LUMO on the bridge. The D_{CT} is directly measured from the positive and negative barycenters of charge, which, in the case of HOMO–LUMO excitations are always placed along the π-bridge rather than on the D/A moieties at edges of the molecule. For the sake of clarity in Figure 10 we reported a graphical representation of the positive and negative barycenters of charge, together with the difference density plot for each compound, computed at the PBE0 level.

Not surprisingly, the relaxation of the excited state density strongly impacts the computed CT distance, especially in the case of large hole-electron separation. Indeed, the largest ${}^{R}D_{\mathrm{CT}}$ values (around 20 Å) are practically half of the corresponding ${}^{U}D_{\mathrm{CT}}$ ones (around 40 Å). Of note, the effect of relaxation increases as a function of the effective CT distance so that, overall, a linear increase in the computed ${}^{R}D_{\mathrm{CT}}$ as a function of the spacer is still found, though with a smaller increase per spacer unit (18.3 Å for the ${}^{R}D_{\mathrm{CT}}$ compared to 34.6 Å for the ${}^{U}D_{\mathrm{CT}}$ at the PBE level). These general observations both on the nature of the electronic transitions and on the effect of relaxation on the computed CT distance also holds for functionals possessing low (below 40%) exact like exchange (all represented as triangles in Figure 9).

In this case, although the predicted energies are not as strongly affected as for local functionals by the bridge length, a strong CT character is computed for all molecules with associated CT distances not very different from those computed for the corresponding GGA functionals. This behavior can be easily spotted by comparing the transition energies, ${}^{U}D_{\mathrm{CT}}$ and ${}^{R}D_{\mathrm{CT}}$ computed at PBE and PBE0 (25% of exact-like exchange) as reported in Table 3. Also, in this case, the relaxation of the excited state density determines an extreme variation of the associated D_{CT} value, with a ${}^{R}D_{\mathrm{CT}}$ value significantly smaller than the ${}^{U}D_{\mathrm{CT}}$ values and their difference linearly increasing with the CT length. Overall, we can thus conclude that as soon as the CT distance is more extensive than 5 Å, one observes substantial differences between the computed ${}^{U}D_{\mathrm{CT}}$ and ${}^{R}D_{\mathrm{CT}}$ so that estimation of quantities from the ${}^{U}D_{\mathrm{CT}}$ values could be affected by substantial errors.

When using hybrid functionals, with exchange contribution greater than 40% the situation becomes more involved. Here, we focus on the behavior of three global hybrids of

different nature, possessing from 40% to 56% of exact like-exchange, namely, SOGGA11X, BHandHLYP, and M08HX. For such functionals, the nature of the first computed transition varies as a function of the spacer length. The computed ${}^{U}D_{\mathrm{CT}}$ and ${}^{R}D_{\mathrm{CT}}$ values reflect this behavior. CT character and D_{CT} values increase with the bridge length, due to a partial contribution to the HOMO and the LUMO of the D and A units. This trend holds up to a given bridge length of 35.4 Å for SOGGA11X, 22.9 Å for BHandHLYP, and 23.0 Å for M08HX) starting from which the bridge contribution to the HOMO and LUMO becomes predominant, and the CT character decreases. ${}^{U}D_{\mathrm{CT}}$ and ${}^{R}D_{\mathrm{CT}}$ overall show a bell-shaped behavior with a maximum value that is indeed smaller than those computed for their corresponding local counterpart. For instance, a maximal ${}^{U}D_{\mathrm{CT}}$ of 10.1 Å is computed for BHandHLYP for five bridge units while, for the same bridge length, a value of 19.4 Å and 18.3 Å are computed at the BLYP and B3LYP level, respectively.

As already observed for local or low HF-exchange percentage functionals (dots and triangles in Figure 9) excited state density relaxation has a stronger impact on the computed D_{CT} for more considerable CT distances. Nonetheless, the relative relaxation (i.e., the difference between ${}^{U}D_{\mathrm{CT}}$ and ${}^{R}D_{\mathrm{CT}}$) for a given ${}^{U}D_{\mathrm{CT}}$ value seems rather insensitive to the chosen functional. As soon as the electronic excitation becomes of negligible CT nature (such as in the case of transitions with dominant bridge contribution to both the HOMO and the LUMO) the computed ${}^{U}D_{\mathrm{CT}}$ and ${}^{R}D_{\mathrm{CT}}$ converge to the same value. This behavior holds for the three analyzed functionals, for the most extended bridge lengths.

The behavior of hybrid functionals containing a high percentage of exact-like exchange, around 55%, (such as the M052X-$N \geq 3$ and M062X-$N \geq 5$ for instance) is somewhat different. In this case, the HOMO and LUMO are both delocalized on the bridge, and thus no CT character associated with the first electronic transition is computed, independently on the bridge length. This course gives rise to flat ${}^{U}D_{\mathrm{CT}}$ and ${}^{R}D_{\mathrm{CT}}$ profiles, with negligible difference between the two indexes. Besides, this behavior becomes more and more pronounced as the amount of exact exchange included reaches the highest percentage (i.e., M06HF, M11, and wB97 series) but interestingly it is not what is computed at CIS level for which a partial CT character is indeed computed (refer to Table 3) also for longer bridge reaching its maximum value for n=3. This behavior recalls the one observed for high percentage exact exchange functionals such as LC-PBE (see Table 3 and Figure 9). However, low lying CT states can intercalate to local bridge centered transition for specific bridge lengths giving rise to a non-continuous evolution of both ${}^{U}D_{\mathrm{CT}}$ and ${}^{R}D_{\mathrm{CT}}$ as a function of the bridge length as in the case of CAM-B3LYP. The same is also true for functionals such as M08HX, M11, or wB97 where CT and bridge centered states get close in energy for intermediate spacer lengths (5–6 units) eventually switching in energy thus giving rise to the bell-shaped D_{CT} curves.

Among the 100% exact exchange functionals, the only exception to this behavior is found in HFPW91 (PW91 correlation with 100% Hartree-Fock exchange), which displays a more local-like behavior. Figure 11 summarizes the dependence of the D_{CT} behavior on different DFAs using a subsample of functionals, which incorporate increasing HF exact exchange. Here, we show a selection of ΔD_{CT} values (expressed as the difference between ${}^{U}D_{\mathrm{CT}}$ and ${}^{R}D_{\mathrm{CT}}$ values) as a function of the number of spacers. Local functionals tend to

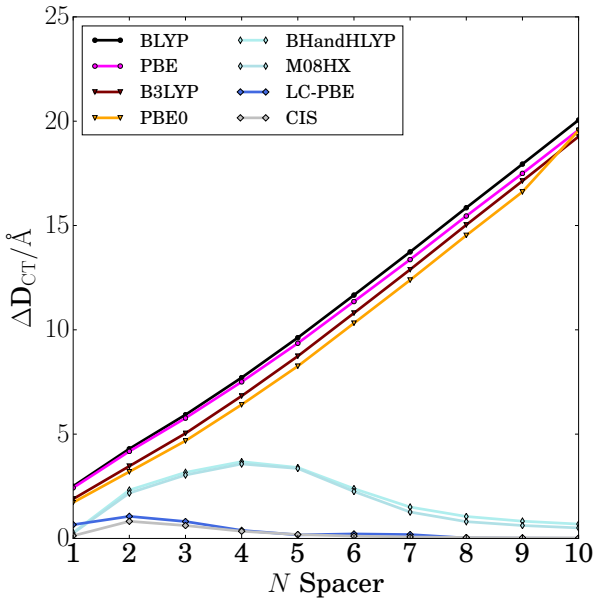

Figure 11: Difference between ${}^{U}D_{\mathrm{CT}}$ and ${}^{R}D_{\mathrm{CT}}$ values (ΔD_{CT} in Å) for selected functionals, as a function of the spacer length (N). The D_{CT} values are associated with the first excited state. Consistently with the previous figures, different markers indicate distinct percentages of exact-like exchange (c_{HF}). Filled dots for standard local and semilocal xc functionals functionals ($c_{\mathrm{HF}} \leq 50\%$), triangles for low percentage hybrids ($1 \leq c_{\mathrm{HF}} \leq 40$), diamonds for high percentage hybrids ($40.15 \leq c_{\mathrm{HF}} \leq 65$ 50%), and twisted squares 100% of exact like exchange.

display a strictly monotonically increasing ΔD_{CT}. As soon as 40% of HF exact exchange is included, one recovers the desired bell-shaped D_{CT} profile: the ΔD_{CT} function increases as the CT character becomes more pronounced, and decreases for longer chains. Finally, functionals with 100% HF exact exchange tend to localize the transition on the bridge, thus minimizing the *unrelaxed-relaxed* difference, which results in a flattened ΔD_{CT} profile. Functionals with greater c_{HF} accurately describe electronic delocalization at increasing chain lengths and allow one to acquire a consistent picture of the electron/hole recombination due to the transition. The character of the first electronic transition inevitably changes depending on the functional considered. While more local functionals strictly predict the first transition as to have CT character, the inclusion of a larger percentage of HF exact exchange shifts the through-space transition higher in energy, leaving a $\pi\pi*$ transitions of local character to be the lowest in energy. Figure 12 provides an evidence for the latter observation. As a result, the corresponding D_{CT} profiles in

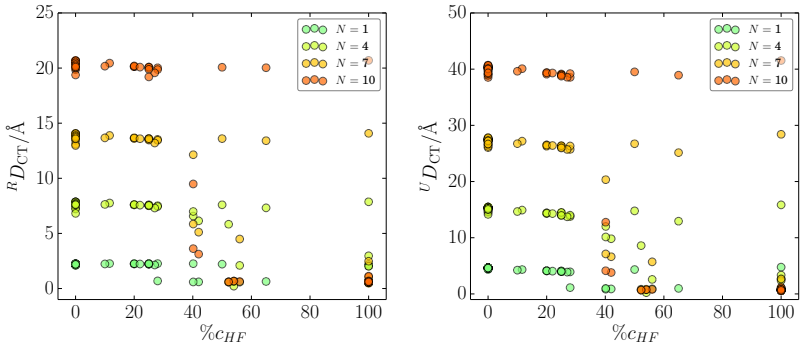

Figure 12: $^{U}D_{CT}$ and $^{R}D_{CT}$ for the first electronic transition against c_{HF} percentage, for selected spacer lengths ($N = 1, 4, 7, 10$). All 53 functionals are included. Three different regimes appear clearly. Functionals including a low percentage of HF exact exchange display a constant behavior, independently from the spacer length. An opposite behavior is found for full hybrid functionals ($c_{HF} = 100\%$). Long chains mostly display very small D_{CT} character, while only short chains have a first transition of charge-transfer character. High percentage hybrids ($40.15 \leq c_{HF}$, as well tend to display the same behavior.

Figure 13 representing the evolution of the lowest CT state display the desired bell-shaped profile. Therefore, the combined uses of $^{U}D_{CT}$ and $^{R}D_{CT}$ can be used a first indicator of CT pathologic cases for DFT. In particular, from Figure 11 and 13 we may deduce that monotonically increasing ΔD_{CT} curves are evidence of an unphysical and erratic CT state associated with local exchange-correlation functionals. By contrast, for asymptotically corrected functionals the difference between the two indexes diminishes as the transition changes its nature from a HOMO-LUMO to a $\pi\pi*$ state.

4.6 CONCLUSIONS

The impact of the use of relaxed or unrelaxed excited state density for the estimation of the nature and characteristic of electronically excited states with a recently developed density-based index (D_{CT}) has been assessed using a family of prototype push-pull molecules as test case, and employing 52 different exchange-correlation density functionals belonging to different density functional classes. The following general conclusions can be drawn:

- For a qualitative description $^{U}D_{CT}$ and $^{R}D_{CT}$ provide the same description regardless of the nature (CT or not) of the transition analyzed. Thus, to characterize the nature of electronic transitions, the associated $^{U}D_{CT}$ (which can be computed on-the-fly, without any additional computational cost) can be safely used.

- For a quantitative description, $^{U}D_{CT}$ and $^{R}D_{CT}$ provide similar values only in the case of transitions with moderate CT length (corresponding to distances around 4–5 Å). For transition with higher CT values, the use of $^{R}D_{CT}$ is warmly recommended.

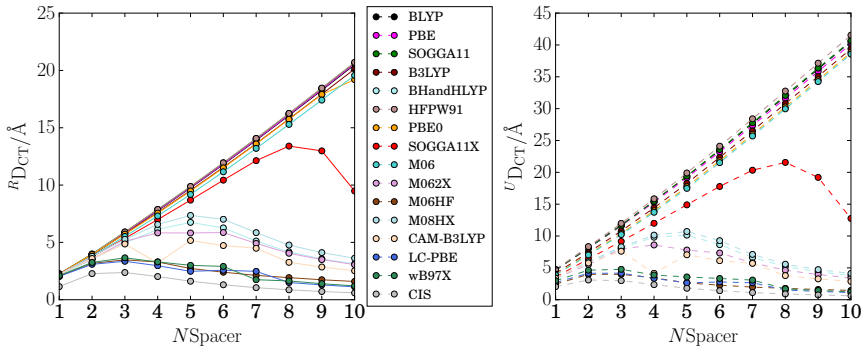

Figure 13: Computed $^{U}D_{CT}$ and $^{R}D_{CT}$ values (in Å) associated with the first **bright** excited state ($f_{osc} \geq 0.1$) as a function of the spacer length (N). Different markers indicate distinct percentages of exact-like exchange (c_{HF}). Filled dots for standard local and semilocal xc functionals ($c_{HF} \leq 50\%$), triangles for low percentage hybrids ($1 \leq c_{HF} \leq 40$), diamonds for high percentage hybrids ($40.15 \leq c_{HF} \leq 65$ 50%), and twisted squares 100% of exact like exchange.

This behavior is independent of the nature of the exchange-correlation functional used. Furthermore, the effect of relaxation (i.e., the difference between $^{U}D_{CT}$ and $^{R}D_{CT}$) seems rather insensitive to the functional used but only related to the CT distance, as calculated using the $^{R}D_{CT}$ value. Therefore, when aiming at quantitatively comparing CT distances (for instance to define the most effective bridge in push-pull systems) the use of $^{R}D_{CT}$ should be preferred.

5

APPLICATION OF DENSITY-BASED INDEXES FOR THE DESCRIPTION OF EXCITED STATES

5.1 CONTEXT

In the present chapter, we discuss how the D_{CT} can be used to measure the spatial extent of a photoinduced charge-transfer, to interpret photochemical reactions and, more generally, any charge-transfer process. We compute the D_{CT} using densities calculated both from density functional and post-HF methods. Both approaches have been extensively applied to characterize the absorption/emission properties of systems or to study the excited state potential energy surface (PES) and to get insights on their reactivity [14, 19, 115, 149–152]. However, very few comparative works are available in the literature reporting the use of density-based indexes coupled both with DFT and wavefunction methods [153]. In the previous chapters, indeed, we have only discussed density-based indexes in the context of time-dependent density functional theory methods [1, 4, 94, 95, 112]. However, as we show in the following, the compact representation of the excited state process delivered by density descriptors may be beneficial also in the case of multiconfigurational calculations.

In the following, we consider the case of a simple intramolecular excited state proton-transfer reaction. We apply both wave function (CASSCF-CASPT2) and density functional methods in conjunction with the D_{CT} analysis. The results confirm that, also in the case of multiconfigurational methods, the D_{CT} provides useful information concerning both the charge and the structural reorganization of a molecule in the excited state. This topic is the subject of a recent publication of ours: "Using Density-Based Indexes and Wave Function Methods for the Description of Excited States: Excited State Proton-Transfer Reactions as a Test Case", published by myself, Juan Sanz Garcia, Marco Campetella, and Ilaria Ciofini in the Journal of Physical Chemistry A. The present chapter constitutes an adaptation of the latter publication.

5.2 INTRODUCTION

Photoactive molecules capable of undergoing light-driven nuclear rearrangements attract an ever-growing interest among the scientific community. This interest arises from the wide scope of technological applications ranging from high optical-capacity storage devices to miniaturized photo-mechanical gadgets [154–157]. Phototriggered intramolecular proton-coupled electron transfer (PCET) is a very representative example of this phenomenon. Generally, this photoinduced-nuclear rearrangement results from excited state intramolecular proton transfer (ESIPT) between a proton donor and a proton acceptor group which are nearby. Upon photoabsorption, the redistribution of the electronic density across the molecule increases the acidity/basicity of the donor/acceptor groups

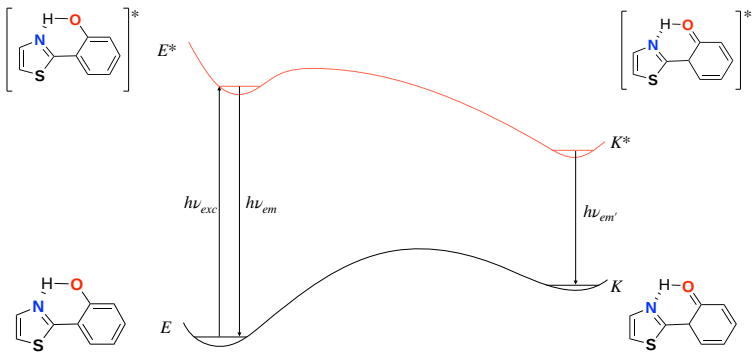

Figure 14: Schematic representation of the ESIPT reaction.

involved resulting in a fast proton transfer in the excited state. The photoinduced enol-keto tautomerization of the 2-(2'-hydroxyphenyl)benzothiazole (HBT) (Figure 14.) is a very well-known example of this kind of intramolecular PCET [158]. Excited state proton-transfer reactions (ESPT) and, more particularly, intramolecular ESPT and ESIPT have been often considered to benchmark and assess the quality of the underlying theoretical methods in the description of excited state profiles, as they feature a well-defined reaction coordinate [2, 159, 160], however with an extremely flat potential energy surface, with all the difficulties that it implies. Indeed, these types of systems are characterized by a proton transfer which occurs at the excited state between neighboring donor-acceptor atoms (such as oxygen or nitrogen) [161–163].

Typically, organic systems involved in an ESIPT and showing oxygen and nitrogen as heteroatoms present an energetically favorable enol form in the ground state (Figure 14). This tautomer may exhibit a strong intramolecular hydrogen bond with the acceptor atom (a nitrogen atom in the case depicted in Figure 14). As a photon is absorbed, the acidity of the enol group increases so that the keto conformer (K* in Figure 14) becomes the most stable form at the excited state. Hence, a light-induced tautomeric reaction occurs, giving rise to the four-level diagram depicted in Figure 14. If the E* and the K* species are stable enough, they can both radiatively decay into the corresponding ground state forms, and the molecule may display two distinct emission bands in the corresponding electronic spectra. This dual-emission phenomenon has been extensively used in designing novel chemosensors in various target applications [128, 161, 164–166]. Two of the most experimentally studied ESIPT dyes are the 2-(2- hydroxyphenyl)benzothiazole (HBT) and 2-(2- hydroxyphenyl)benzoxazole (HBO) molecules [158, 167], schematically depicted in Figure 15. Here we use the HBT molecule and a simplified model of it (2-(2-hydroxyphenyl)thiazole HT, in Figure 15) as prototype systems to analyze the effect of the use of wave function methods/density rooted approaches in the description of the ES involved in the proton transfer. Initially, we assess, at the TDDFT level, the relevance of the reduced model (HT) for representing the ground and excited state properties of the

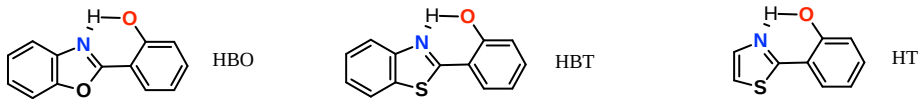

Figure 15: Prototype molecules which can undergo ESIPT.

full HBT molecule, both in terms of energetic and of the charge-transfer (CT) character - evaluated through the D_{CT} index [1,4]. Next, we analyze the excited state potential energy surface and the electronic properties of the HT molecule both at TDDFT and CASSCF-CASPT2 levels. Such calculations become possible thanks to the reduced dimension of the HT molecule which allows the use of reduced active space of 14 electrons in 12 orbitals, rather than 18 electrons in 16 orbitals (18e,16o) for the HBT molecule.

Here we examine the energetics and the CT profile of the reaction as calculated using both approaches. Our purpose is thus to assess if the relationship between the energetic features of the reaction and the D_{CT} profiles - previously defined in the context of TDDFT - still holds when multiconfigurational methods are employed. The discussion is structured as follows: after a brief presentation of the computational details, we discuss the results obtained at the TDDFT level for the HBT molecule and the HT model. Next, we compare the energetics (ES-PES) and the CT profiles (D_{CT} index) computed for the HT model both at the TDDFT and post-HF level, by scanning the PES along the two relevant, reaction coordinates. Finally, we draw some general conclusions.

5.3 COMPUTATIONAL DETAILS

The ground-state potential energy surfaces (PES) of HBT and HT have been evaluated performing a two-dimensional (2D) relaxed scan. We have constructed a 2D grid by optimizing one hundred homogeneously distributed structures, obtained by varying independently two constrained degrees of freedom: the N-O and O-H distances. In particular, we generated the structures varying the N-O distance from 2.54 to 2.72 Å in increments of 0.02 Å, and the O-H distance from 0.99 to 1.89 Å in increments of 0.10 Å to encompass the formulation of both the enol- and the keto-optimized forms. On the same grid, we computed the D_{CT} index. With the idea of comparing densities and energetics obtained by different methodologies, we calculated the GS relaxed scan at Hartree-Fock, density functional theory (DFT), and complete active space self-consistent field (CASSCF) [168] levels. On top of these, we computed excited state properties vertically using configuration interaction singles (CIS) [144], TDDFT [32], and complete active space with second-order perturbation theory (CASPT2) [169] calculations. A for the DFT and TDDFT calculations we used two different functionals: (i) the global hybrid functional PBE0 [46] and (ii) the range separated asymptotically corrected LC-PBE [41,43]). Furthermore, we employed the same computational protocol to perform a relaxed scan of

the ES at CIS and TDDFT level. The wave function (WF) used in the CASPT2 calculations was computed using the state-average-CASSCF (SA-CASSCF) technique with four equally weighted roots (the ground state and three more excited states) and an active space consisting on 14 electrons in 12 π orbitals delocalized in the whole planar HT molecule. Although CASSCF calculations are not able to recover dynamic correlation unless a prohibitively large active space is chosen, optimizations performed at the CASSCF level were the only feasible alternative to compute the optimized geometry grid. The evaluation of all optimized geometry energies at the GS (and ES) as well as vertical excitation energies in the Franck-Condon (FC) region was performed at the SA-CASSCF(14,12)/CASPT2 level of theory. We employed the imaginary shift technique (0.2 a.u.) to avoid the possible presence of intruder states [170], as previously reported in the literature for a similar organic chromophore as described in Ref. [163].

All calculations were carried out using the same diffuse-augmented polarization valence-double-ζ basis set (6-31+G-(d)) [171] with one set of d polarization functions [172, 173] and a set of s and p diffuse functions [174, 175] for all atoms but hydrogens. All calculations, but the post-HF-based ones, were performed with the Gaussian 16 quantum package [145]. CASSCF, as well as CASPT2 calculations, were performed using the MOLCAS 8.0 quantum package [176]. No solvents effects were included.

As previously discussed in 4, the D_{CT} density-based index allows to quantify the spatial extent of a charge-transfer excitation simply and intuitively. Using the electronic densities of the ground and excited state of interest (here the first singlet), $\rho_{\mathrm{GS}}(r)$ and $\rho_{\mathrm{EX}}(r)$, respectively, the D_{CT} has been mapped on the optimized GS and ES grid. For TDDFT calculations, the D_{CT} index was directly computed using the Gaussian 16 program [145], using both relaxed and unrelaxed densities. For the CASPT2 calculations, on the other hand, we computed the D_{CT} from the real space ground and excited state densities, using a freely distributed software of ours [177].

5.4 ASSESSMENT OF THE MODEL SYSTEM: HT VS HBT

To validate the use of the HT system (Figure 14) as a reasonable model to describe the ESIPT reaction of HBT, we performed TDDFT calculations using different functionals for both systems. Energy and D_{CT} maps were computed for both systems, as described in the previous section. In particular, ground state PESs were constructed, for both HT and HBT, performing a relaxed scan over the N-O and O-H coordinates, computed at the PBE0 level of theory, followed by single-point TDDFT calculations performed using the PBE0 and LC-PBE functional as well as at CIS level. Excited state parameters were obtained vertically from the optimized ground state geometries, using the same approach.

All systems obtained show a planar structure. Table 5 collects the energetic parameters most relevant to describe the enol to keto tautomerization, as extracted from the computed 2D maps. At the GS, the enol tautomer is the most stable in the PES (all values relative to HBT are in parentheses in the following), while the keto form appears at higher energy values, both for the HT and HBT molecule, independently of the method considered. Although the keto-enol energy difference is dependent on the method used, for a given

	HT (HBT)	HT (HBT)	HT (HBT)	HT
	PBE0	LC-PBE	HF/CIS	CASPT2
Δ(keto-enol)$_{GS}$	47.7 (43.1)	54.2 (52.2)	57.8 (52.8)	60.9
Δ(TS-enol)$_{GS}$	52.2 (50.5)	58.2 (55.4)	91.0 (88.7)	60.9[b]
Δ(keto-enol)$_{ES}$	-24.8 (-24.2)	-33.0 (-35.0)	-25.1 (-26.7)	[c]
Δ(TS-enol)$_{ES}$	1.6 (4.2)	3.5 (4.2)	38.9 (44.4)	[c]

Table 4: Estimated Relative Stability and Reaction Barrier for the keto-enol Tautomerization of HT and HBT, (in kJ/mol)[a] calculated at the TDDFT and CASPT2 level of theory.
[a]All values are calculated with respect to the enol form on a 2D grid of structure optimized at the GS at PBE0 level. [b]No transition state found in the ground state PES. [c]No E* minimum found in the excited state S_1 PES.

		HT (HBT)	HT (HBT)	HT (HBT)	HT
		PBE0	LC-PBE	CIS	CASPT2
enol	D_{CT}	1.44 (1.40)	0.82 (0.78)	0.39 (0.30)	1.01
keto	D_{CT}	0.98 (1.14)	0.34 (0.25)	0.44 (0.44)	0.18

Table 5: Computed D_{CT} values (Å) corresponding to the enol and keto form of the HT[a].
[a]Values correspond to the minima computed on a 2D grid of structures optimized at the GS at PBE0 level (see text for details).

approach, the difference in the relative stability of the two forms is practically equivalent when considering the HT or the HBT form. In particular, at the PBE0 level the keto tautomer is computed to be 47.7 kJ/mol (43.1 kJ/mol HBT) higher in energy than the enol one, while the energy gap predicted at LC- PBE0 level is 54.2 kJ/mol (52.2 kJ/mol HBT), and at the HF level is 57.8 kJ/mol (52.8 kJ/mol HBT). Therefore, for GS minima, HT seems to be a good model for HBT.

The same holds when considering the PT reaction barrier computed at the GS. Indeed, at the PBE0 level, the estimated GS activation energy (Table 4) for enol-keto tautomerization of HT is about 52.2 and 50.1 kJ/mol for HBT. The reverse reaction shows a barrier of ca. 4.5 kJ/mol for HT and of 7.0 kJ/mol HBT. All these considerations thus validate the use of the HT model. Analogous conclusions can be drawn examining the results obtained at the LC-PBE level and CIS, even though these two methods overestimate the energy barrier of the ESIPT. At LC-PBE, for instance, the computed barriers are significantly higher than those computed at the PBE0 level, 58.2 and 4.0 kJ/mol for the forward and reverse tautomerization for HT, and 55.4 and 3.2 kJ/mol for HBT. We deduce that for the ground state energetics the HT molecule shows to quantitatively reproduce the features of HBT, independently of the DFT method chosen and with discrepancies on the relative stability of the minima and barriers always lower than 4 kJ/mol.

The analysis of the S_1 potential energy surfaces computed using different DFAs points out to similar conclusions. Indeed, though in this case all methods predict a more stable keto form and much lower reaction barrier (in agreement with the experimentally observed ESIPT phenomena), HT and HBT results are quantitatively comparable thus

further confirming the suitability of HT as a model for the energetic profile of the PT both at the ground and the excited state. In Figure 16 (top and bottom), we compare the energy and D_{CT} S_1 surfaces of HT and HBT - computed using both the ground and excited state geometries. To validate the use of the HT system (Figure 14) as a reasonable model to describe the ESIPT reaction of HBT, we performed TDDFT calculations using different functionals for both systems. Energy and D_{CT} maps were computed for both systems, as described in the previous section. In particular, ground state PESs were constructed, for both HT and HBT, performing a relaxed scan over the N-O and O-H coordinates, computed at the PBE0 level of theory, followed by single-point TDDFT calculations performed using the PBE0 and LC-PBE functional as well as at CIS level. Excited state parameters were obtained vertically from the optimized ground state geometries, using the same approach.

Overall the computed profiles confirm the equivalence of the two representations. Indeed both in the case of HT and HBT, the PT occurs through synchronous contraction of the N-O distance and elongation of the O-H bond, in agreement with previous results [158]. The inspection of the minimum energy pathway along the S_1 PESs of HT and HBT allows us to identify three consecutive phases: first the distance N-O decreases (around 2.54 Å); next, the TS is reached (corresponding to a minimal N-O distance), and finally the proton is transferred. At the transition state the N-H bond measures about 1.20 Å (for both HT and HBT), while the O-H bond is stretched by ca. 0.60 Å as compared to the original enol structure. The D_{CT} maps, well represent the electronic rearrangement occurring upon excitation. As for the energy, we computed the ${}^{R}D_{CT}$ and ${}^{U}D_{CT}$ for each point on the grid. In agreement with previous studies of ESIPT reactions [128], independently of the method used, and for both HT and HBT, as the proton moved towards the nitrogen atom, both ${}^{R}D_{CT}$ and ${}^{U}D_{CT}$ values increase up to a maximum before decaying into a lower value, once the ketone form is accessed. The transition state lies at the point of the reaction path where the effective charge-transfer distance (i.e., the D_{CT}) is the largest. The final decrease of the D_{CT} is conditional to the post-PT geometrical rearrangements. In the present case, the keto form does not relax significantly and, accordingly, we observe no significant changes in the D_{CT} value.

The D_{CT} values for the keto and enol forms both at the ground and excited state, computed at different levels of theory are reported in Table 5. At this stage, it is interesting to comment on the differences between the ${}^{R}D_{CT}$ and ${}^{U}D_{CT}$ profiles. The overall shape of the two is reasonably close, although the ${}^{U}D_{CT}$ profiles shift by ≈ 0.2 Å. Thus, from a qualitative point of view, both ${}^{R}D_{CT}$and ${}^{U}D_{CT}$ can be used to investigate the reaction mechanism.

Overall, D_{CT} analysis confirms that the CT character and the nature of the electronic transition are the same for both systems. By consequence, the computed energy and D_{CT} profiles of HT and HBT are extremely similar. The 2D D_{CT} maps described herein deliver a convenient representation of ESIPT reactions, by depicting how the charge redistributes in the molecule all through the reaction. One can notice an evident analogy in the overall shape of the S_1 energy and D_{CT} surfaces. Independently of the method used all 2D-maps show a minimum in the enol region, a maximum in the central region - at intermediate

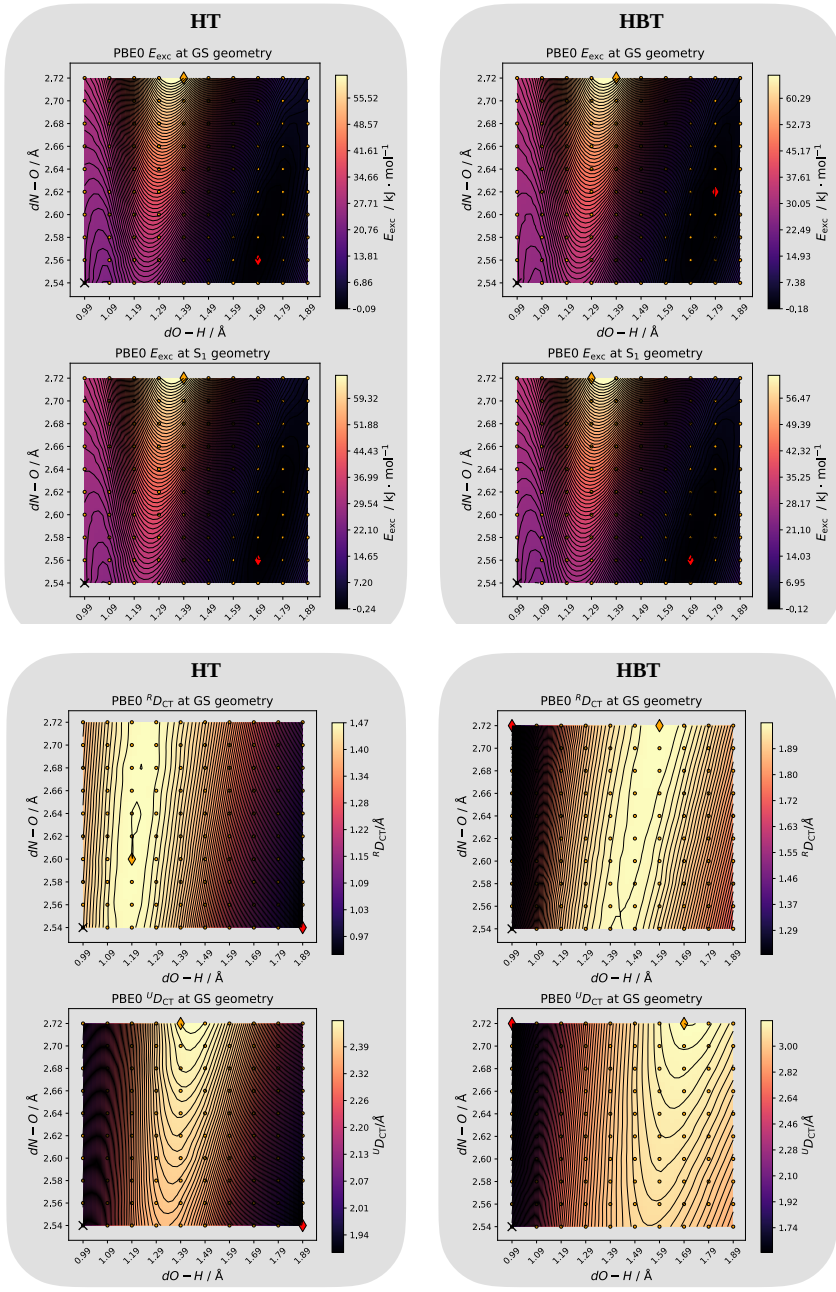

Figure 16: (a) upper panel - comparison of the energy profiles of HT and HBT computed at the PBE0/6-31+G* level of theory: all surfaces are substantially equivalent both computed using the ground state and S_1 optimized grid. (b) lower panel: ${}^{R}D_{CT}$ and ${}^{U}D_{CT}$ surfaces computed at the PBE0/6-31+G* level of theory, using the ground state grid optimized at the same level of theory. Both in HT and HBT ${}^{R}D_{CT}$ value locate the region of charge transfer at shorter O-H bond length as compared to the corresponding ${}^{U}D_{CT}$. The corresponding D_{CT} surfaces computed at the S_1 optimized geometry are given in Appendix in Figure 49.

N-O and O-H distances, and fall into a minimum as the proton moves toward the nitrogen. This evidence suggests that the D_{CT} could be used just as the energy to locating minima, and transition states on the excited state potential energy surfaces.

Finally, we computed all ground-state optimized geometries at the PBE0 level. Accordingly, we computed excited states vertically on top of this geometries - using LC-PBE and CIS. For the sake of completeness and to check that no artifact was introduced in such a way, we optimized the ground states and computed the corresponding vertical excited state surfaces, at each level of theory. All different methods result in nearly identical geometries, and no significant change was found in the two-dimensional contour maps (see Appendix 49). Hence, independently of the level of theory used, HT and HBT result nearly identical. These pieces of evidence ultimately validate the use of HT as a model system to elucidate quantitatively ESPT phenomena occurring in the HBT molecule. Thus, in the following, we limit the discussion to HT only.

5.5 DESCRIPTION OF THE ESIPT IN HT USING CASSCF-CASPT2 CALCULATIONS AND DENSITY BASED INDEXES.

At this point, we remind that neither the ground and first excited state PESs nor the first and second excited state surfaces of HT cross each other when the molecule is kept planar (as in the present case). This observation holds both in TDDFT and CASPT2. Accordingly, within the PES region studied, where the molecule is strictly planar, the electronic nature of the first singlet excited state remains unvaried ($\pi\pi*$ state). We therefore limit the discussion to the first excited state. We proceed to examine the same reaction using the density computed from multireference post-HF methods. For this purpose, we computed the ESIPT in HT at CASSCF-CASPT2 level and analyzed the energy and D_{CT} profiles on the same grid as previously done for TDDFT computed surfaces.

Let us first illustrate the topology of the ES PES and the corresponding D_{CT} map computed at the CASPT2 level, focusing on the Franck- Condon region. Based on CASPT2 calculations and in agreement with DFT results, at the ground state, the HT molecule exclusively exists in the enol tautomer form as confirmed by the higher energy stability of the enol relative to the keto form (60.9 kJ/ mol, Table 4). The redistribution of the electronic density across the molecule results that occurs upon absorption results in the increased acidity of the oxygen and basicity of the nitrogen, leading to the excited state tautomerization. The aromatic rings contribute to stabilize and promote the CT process, as confirmed by the difference between the sums of CASPT2 Mulliken charges. The phenol moiety, which has a total charge of (0.31 |e-|) in the ground state increases its charge at the excited state (0.44 |e-|). Correspondingly the overall charge in the thiazole fragment decreases from (-0.31 |e-|) to-0.44 |e-|).

Nonetheless, due to the arbitrary nature of the partition scheme used to compute atomic charges, it is hard to assess quantitatively the magnitude of the CT based on the sole analysis of atomic charges. Such imprecision can be avoided applying a D_{CT} based analysis which provides a neat solution to this ambiguity. This index allows both to quantify the spatial extent of the CT excitation and contextually to define the donor/acceptor molecular

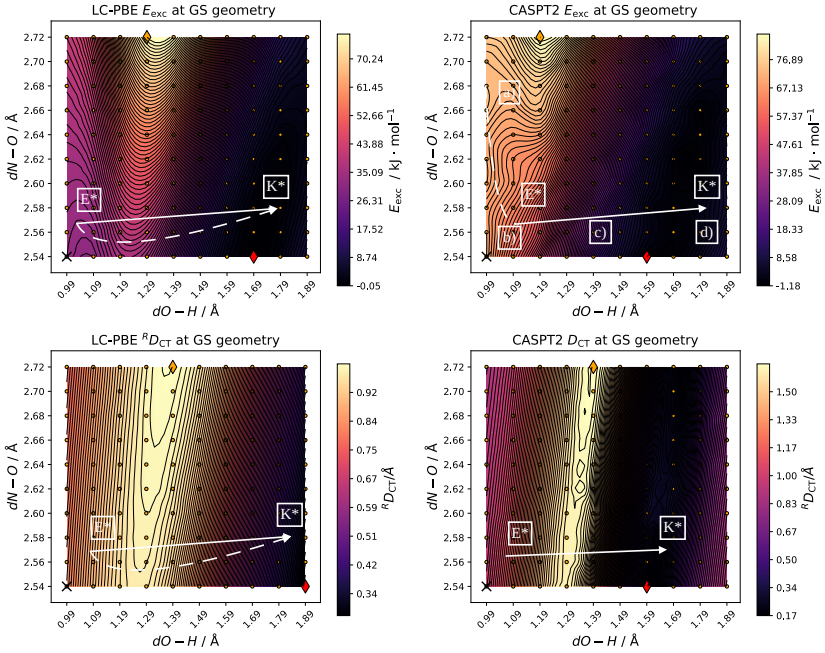

Figure 17: In top left and bottom left, respectively, the Vertical S_1 LC-PBE PES D_{CT} surface. In top right and bottom right the vertical S_1 CASSCF-CASPT2 PES, and the D_{CT} surface. All geometries have been computed at the ground state PBE0/6-31+G* level of theory. White arrow: ESIPT straight line pathway; dashed arrow: ESIPT minimum energy pathway; dashed line line: steepest decent pathway from Franck-Condon region to the minimum enol* tautomer.

regions unequivocally. This information is indeed inherently provided by the position of the positive and negative barycenters of charges. As a result, one obtains a full description of the charge transfer phenomenon.

At the ground state enol minimum, the initial photoinduced electronic rearrangement can be described as a "partial" intramolecular CT as evidenced by the small computed D_{CT} value (1.04 Å). Such charge displacement corresponds to a transition from the phenol ring to the C1-C2 bond. Of note, this value is smaller than what was computed at the TDDFT level. As the reaction progresses through the vertical S_1 PES from point (a) to point (b) (Figure 17), the molecule experiences a skeletal contraction: the N-O distance reduces by 0.1 Å - and the opposite way round the O-H bond distance elongates by 0.1 Å. Simultaneously the D_{CT} rises by 0.21 Å. From point (b) to point (c) the elongation of the O-H bond distance of 0.2 Å results in twice the increment of the D_{CT}. In the last step (from point (c) to point (d)) the K* tautomer is formed and the D_{CT} decreases to its lowest

value - the O-H bond distance increases by an additional 0.4 Å. The direct comparison of the topological features between S_1 PES and D_{CT} surface reveals remarkable common patterns independently of the method used. For instance, in the case of LC-PBE (see the top of Figure 17) both surfaces present a flat E* minimum, while a steep well-defined minimum appears in the K* region. In both surfaces (S_1 and D_{CT}) a hill separates the enol and keto region. Similar features also appear in the CIS profiles, though unlike in the DFT surfaces, the E* minimum is much steeper both in the S_1 PES and in the D_{CT} surfaces - all additional figures not shown in the main text can be found in Appendix, in Section 11.2.

Thus, the parallelism between energy and D_{CT} index remains valid also in this case: D_{CT} and energy surface have matching behavior. By contrast, unlike the PBE0, LC-PBE, and CIS vertical S_1 PESs, the CASPT2 surface does not show any E* minima but only a steep downhill slope at the Franck-Condon region which points toward the global K* minimum, with no other local minima along the steepest descent trajectory. This barrierless adiabatic S_1 pathway though is in agreement with previous findings [128] on ESIPT reactions studied at CASSCF-CASPT2 level.

As previously alluded to, optimizing the GS geometries at different levels of theory affords nearly identical structures. This results in the S_1 PES and D_{CT} surfaces being qualitatively the same with no remarkable differences to those computed using the PBE0 ground state optimized grid. By contrast, the relaxed (optimized) S1 surfaces are visibly different as computed with each method. The only meaningful S_1 relaxed surfaces are the one computed using the relaxed S_1 PBE0 geometries (in Figure 49). Regarding the grid values computed using the optimized S_1 structures, we observe, as a general trend that the minima in the excited state PES become steeper and more localized as compared to those observed in the vertical 2D grids, obtained using the GS geometries. This behavior is even more pronounced in the D_{CT} surfaces (see Appendix 49).

5.6 CONCLUSIONS

Using a prototype excited state proton-transfer reaction as a test case we have shown that density-based descriptors (such as the D_{CT} index) can be safely used to analyze excited states qualitatively and quantitatively, both at the TDDFT and post-HF level of theory (here CASSCF- CASPT2). Our study shows that the D_{CT} provides a good description of the electronic rearrangements during a photochemical reaction and delivers relevant information about the structure of the molecule, suggesting that the D_{CT} could be used to locate minima on a PES. This particular feature makes the D_{CT} a perfect candidate for optimization of stationary structures in excited states. Besides, the D_{CT} can be of particular relevance to quantify CT in complex systems avoiding arbitrary evaluation based on charge partitioning.

For the first time, we have examined a reaction using a multiconfigurational wavefunction method coupled with the D_{CT}. Our investigation confirms that any electronic structure method can be coupled to density-based indexed, as long as it provides accurate electronic densities for the ground and excited states, having a physical meaning in any region of a PES. Of course, all limitations concerning the D_{CT} itself (for instance its

null value by construction in the case of systems with quadrupole-like symmetry) hold independently of the underlying electronic method used to access to ground and excited state densities. In such cases, one may partition the molecule in asymmetric units and compute the D_{CT} separately on each fragment, as suggested in reference [118].

6

THE PROBLEMATIC DESCRIPTION OF CHARGE-TRANSFER EXCITATIONS USING DFT

6.1 CONTEXT

When TDDFT is used, through-space charge-transfer (CT) states happen to correspond to excited states in which photoexcited hole and electron charge distributions poorly overlap. This outcome, however, is typically an artifact of the method resulting from the use of approximate xc-potentials, which have incorrect functional asymptotics and are erroneously continuous. As discussed in Section 2.4.5, the exact exchange-correlation potential of a charge-transfer state jumps discontinuously by an amount Δ_{xc} as the number of electrons crosses the integer. As a consequence, the excitation energies for such states are usually significantly underestimated to the point that they can appear below the optical states. In the present chapter we discuss a methodology to spot these spurious unphysical states, through a new and computationally inexpensive index - M_{AC}.

The formulation of the M_{AC} index is derived as a modification of the Mulliken estimation of transition energy for CT excitations. It relies on two basic ingredients: an effective CT distance, computed using our density-based index (D_{CT}), and an orbital weighted estimation of the ionization potential and electron affinity. To verify the robustness of our approach we have tested our index on some model systems, representative of both intermolecular and intramolecular CT excitations by utilizing functionals belonging to different classes (generalized gradient approximation, global hybrids and range separated hybrids). These preliminary results confirm that ghost states are correctly spotted, also in the delicate case of intramolecular excitations displaying substantial donor-bridge-acceptor delocalization, regime in which the standard Mulliken formulation attends its limits. This first part of the chapter is adapted from a previous publication of myself, Marco Campetella, Mike J. Frisch, Giovanni Scalmani, Ilaria Ciofini and Carlo Adamo [5].

Furthermore, we have applied the M_{AC} index to the several organic dyes. Such analysis fits within the broader context of the construction of a comprehensive strategy for the description of photochemical processes, based on density-based indexes. Here we examine the charge-transfer excitations of different molecules evolving along a reaction coordinate, so to verify the correctness and reliability of the potential energy curves that we later examine with the aim to monitor the evolution of the excited states along the same coordinate - as discussed in the Chapter 8.

6.2 INTRODUCTION

TDDFT represents a sophisticated, yet moderately expensive tool to calculate excited states properties for a large variety of molecules in the gas-phase, in solution or even in more

anisotropic environments (see for instance Refs. [19,130]). As already mentioned in section 2.4.5, TDDFT yields substantial errors for charge-transfer excited states [20,30,131]. If short-range CT transitions, such as those occurring in some transition metal complexes [178] are reproduced with an acceptable error (< 0.2 eV in the UV-vis range), the long-range CT distances suffer from large deviations w.r.t. the experimental data. The failure of TDDFT in the calculation of long-range CT excited states can be understood by analyzing the central equation of TDDFT, expressing the orbital rotation Hessian matrices (defined in Section 2.5.5). If a general hybrid functional is applied, the elements of the matrices $\mathbb{A}$ and $\mathbb{B}$ can be formally written as,

$$A_{ia,i'a'} = \delta_{ii'}\delta_{aa'}(\epsilon_a - \epsilon_i) + (ia|i'a') - c_{\mathrm{HF}}(ii'|aa') + (1 - c_{\mathrm{HF}})(ia|f_{\mathrm{xc}}|i'a') \tag{268}$$

$$B_{ia,i'a'} = (ia|i'a') - c_{\mathrm{HF}}(ia'|ai') + (1 - c_{\mathrm{HF}})(ia|f_{\mathrm{xc}}|a'i') \tag{269}$$

where i, i' and a, a' are the occupied and virtual ground-state orbitals, ϵ refers to the ground-state orbital energies, and c_{HF} is the coefficient of the Hartree-Fock (HF) exchange in the hybrid functional. Let us consider the case of a long-range charge-transfer state where an electron is transferred from an occupied orbital i on a molecule, to a virtual orbital a of different one. For clarity, a representation of such scenario is given in Figure 18. If the molecules are sufficiently distant in space, the overlap between the orbitals on the two molecules is negligible. In such case, all terms of Eq. 268, containing products of the occupied and virtual orbitals, vanish [20]. The only remaining terms which contribute to the matrix $\mathbb{A}$ are the orbital difference and the nonlocal HF exchange part of the Kohn-Sham operator.

This last is not canceled as the both orbitals i and i' are on one molecule and a, a' on the other. This term is in fact Coulomb-like and represents the interaction between the (positive) hole and (negative) particle created upon the transition, reflecting the electrostatic attraction within the CT state. Therefore, this term is essential to retrieve the correct $1/R$ dependence of the potential energy curves of CT states along the intermolecular separation coordinate. Similar arguments apply to the elements of the matrix $\mathbb{B}$, all terms of which in fact cancel out.

If a local functional is used ($c_{\mathrm{HF}} = 0$), the excitation energy of the charge-transfer state reduces to the donor-acceptor (D/A) orbital difference. In Hartree-Fock this difference defines directly the charge-transfer energy, as from Koopmans' theorem, ϵ_i and ϵ_a can be directly related to the ionization potential IP_{D} electron affinity EA_{A}. In DFT, however, while the IP_{D} can still be related to ϵ_i, EA_{A} does not really correspond to ϵ_a, as - in DFT - the virtual orbital are calculated in the field of N electrons rather than in the field of $N+1$ electrons. It has been shown that for a local functional, the TDDFT intermolecular CT excitation energy for infinitely separated systems ($\epsilon_a - \epsilon_i$) approximately underestimates the exact value by the average of the integer discontinuities of the donor and acceptor molecules [30]. As a consequence, the accepting orbitals are usually more strongly bound (more negative) in DFT than they are in Hartree-Fock, and $-\epsilon_a$ is systematically larger than the true EA_A, resulting in a drastic underestimation of the excitation energy.

Moreover, the neglect of the non-local $c_{\mathrm{HF}}(ii'|aa')$ term affects the shape of the potential-energy curves of these states, which in turn do not exhibit the correct $1/R$ asymptotic

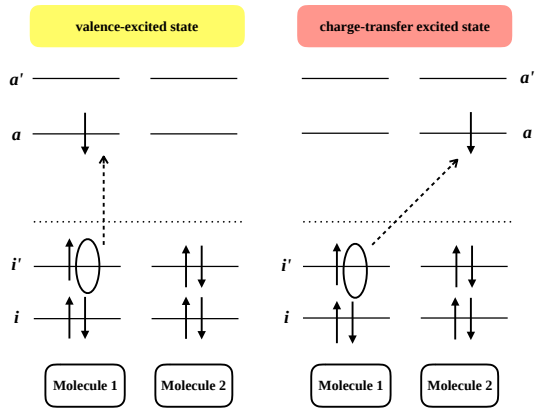

Figure 18: Schematic sketch of a typical valence excited state (left) and a charge-transfer excited state (right). In the first, the transition occurs on one molecule only, hence, the orbitals i,i' and a,a' are located on the same molecule. By contrast, in a CT excited state an electron is transferred from an occupied orbital i of molecule 1 into a virtual orbital a of another molecule 2. When the two molecules are spatially separated from each other the orbitals i and i' do not overlap with a and a'. (Reproduced from Ref. [135].)

behavior. The correct long-range behavior can only be recovered by the inclusion of some fraction of HF exact exchange.

The $1/R$ failure of TDDFT employing standard local and semilocal xc functionals can also be explained in terms of self-interaction error [20]. Let us consider the opposite extreme, where we set $c_{\mathrm{HF}} = 1$, this correspond to the inclusion 100% of exact Hartree-Fock exchange, and the excitation energy is dominated by the orbital difference $(\epsilon_a - \epsilon_i)$. ϵ_a contains the Coulomb repulsion of orbital a with all occupied orbitals of the ground state including the orbital i, which is no longer occupied in the CT state. In other words, the electrostatic repulsion between orbitals a and i, the integral $(ii|aa)$, is contained in the orbital energy difference although orbital i is empty in the CT state. This self-interaction artifact is canceled whenever a Hatree-Fock based correction is used, in which case the third term in Eq. 268 is $(ii|aa)$, giving rise to the hole-particle attraction. When density functional approximations (DFAs) are used, employing approximate xc functionals, this unphysical term remains, leading to the incorrect long-range behavior of the corresponding potential energy curves.

To summarize, the error associated to CT is related to the incorrect $1/R$ asymptotic behavior [123, 179], R being the hole-electron distance, and to the missing derivative discontinuity [30] of the chosen exchange-correlation functional. This error can be particularly relevant for functionals resting on the generalized gradient approximation (GGA) [21]. These drawbacks are mitigated using global and range-separated hybrid (GH

and RSH) functionals, which introduce, in a different way, a fraction of Hartree-Fock (HF)-like exchange [58]. Even better results can be obtained by less-standard and more computationally demanding methods, for instance, by tuning the RSH functional on the system under investigation [29]. Unfortunately, the excitation energies provided are often overestimated by RSH and not always of sufficient quality to allow for a quantitative agreement with the experimental spectra [180], so that most calculations still resort on the use of GH which are those still potentially affected by error in the estimation of CT transitions.

6.3 A GHOST-HUNTER INDEX FOR CHARGE-TRANSFER EXCITATIONS

We have now recalled what is the charge-transfer problem and what does it originate. Charge-transfer excitations, play a key role in many systems of relevance for biological and/or technological application, such as, for instance, light-harvesting complexes in plants and bacteria or as semi-conductor polymers [181, 182]. Hence, the issue of CT excitations in TDDFT has been largely debated in literature [129, 132, 183]), and several solutions have been suggested to diagnostic [184] and correct this failure [20, 131]. Besides an erroneous evaluation of electronic energies, which can be monitored by dedicated diagnostic indexes [19, 103, 120, 121, 180], the energy underestimation of the charge-transfer virtual orbitals causes TDDFT to be affected by another major drawback: the appearance of low-lying CT **ghost states** energetically well below the bright (real) state of a given system for both intermolecular and intramolecular excitations [131]. This spurious effect can be very important for the interpretation and prediction of the spectroscopic properties of a given molecular system as it would suggest, for instance, that an energetically higher bright state could decay non-radiatively into the lower CT states, leading to an electron-transfer quenching of the excited state fluorescence. In other words, the limitations of the TDDFT model used have an impact that is much larger than its numerical performances, (i.e., the error in computed transition energies w.r.t. a given reference) leading to a wrong interpretation of the photophysical behavior of the system under investigation. The undesirable consequences for chemical applications of these computational models are evident.

The existence of these low-lying CT states, referred to as "ghost" states, was discussed in the seminal works of Dreuw and Head-Gordon [131, 148]. In the case of a donor (D) – acceptor (A) system and assuming that the separated charges in the CT states could be treated as point charges, these authors showed that the distance-dependent excitation energy of the energetically lowest CT state $\omega_{\mathrm{CT}}(R)$ can simply be estimated via

$$\omega_{\mathrm{CT}} \geq IP_{\mathrm{D}} - EA_{\mathrm{A}} - \frac{1}{R}. \tag{270}$$

where R is the distance between the two subsystems and IP_{D} is the ionization potential of the donor, EA_{A} is the electron affinity of the acceptor, and $1/R$ is the electrostatic attraction between them. In this equation, the cation and anion are treated as point charges and the shortest possible distance R is assumed, which of course leads to an

overestimation of the electrostatic attraction. Previously, this simple and intuitive relation, has been used to verify the nature of TDDFT excitations in model systems [58, 131, 148], considering R as the geometrical distance between the donor and acceptor units and evaluating IP and EA from the Koopmans' theorem (i.e., from HOMO and LUMO orbital energies).

In this context, with the aim of providing a simple and robust reliable tool for the detection of ghost CT states in TDDFT, we have conceived a new descriptor, $\mathrm{M_{AC}}$, based on a modification of - Eq. 270. $\mathrm{M_{AC}}$ is the acronym for Mulliken averaged configuration as the definition, retraces the discussion on charge-transfer excitations originally proposed by Mulliken [86].

Eq. 270 can be considered as a lower energetic bound for a true CT transition. However, it is evident that this guesstimate remains rather inaccurate, when DFAs are used, as none of the terms is actually close to being exact. With little effort though, one can refine each term of Eq. 270, so to obtain a more reliable estimate of the minimal energy for a charge-transfer excitation. This is the basic idea behind the $\mathrm{M_{AC}}$ index, which is thus defined as

$$M_{\mathrm{AC}} = \sum_{ia} \frac{c_{ia}^2 (|\epsilon_a| - \epsilon_i)}{\sum_{ia} c_{ia}^2} - \frac{1}{D_{\mathrm{CT}}}. \tag{271}$$

Here the D_{CT} - in the place of R in Eq. 270 - provides a refined measure of the hole-electron distance. As we mentioned previously in Chapter 4, the D_{CT} is computed as the distance between the two barycenters of the spatial regions corresponding to an increase and to a decrease of the electron density upon excitation [1]. Therefore, it represents, in a very realistic and intuitive fashion, the effective (average) charge/hole distance associated to an electronic excitation. As for the remaining terms, Eq. 270 is obviously constrained to estimate the energy of the first and lowest CT transition, as it is defined from IP and EA, which, from Koopmans' theorem we may approximate as the negative of the frontier orbitals energy. One can virtually establish the minimal energetic bound of any given charge-transfer transition by substituting the HOMO and LUMO with the orbitals pairs (ϵ_i, ϵ_a) actually involved in the transition. As any electronic transition in TDDFT is more generally defined as a combination of different one-electron excitations, we replace IP_{D} and EA_{A} in Eq. 270 using a weighted average of the starting (ϵ_i) and final (ϵ_a) Kohn–Sham orbital energies. The absolute value ensures that IP and EA - derived from TDDFT - remain in the same relation as they appear in the original equation by Mulliken, and retain their chemical meaning. The weights for IP_{D} and EA_{A}, c_{ia} are the CI coefficients obtained as solution of TDDFT equations [21].

The $\mathrm{M_{AC}}$ index, defined in Eq. 271 defines the lowest threshold for a given transition, and can be used to diagnostic the presence of unphysical low-lying transitions. A given TDDFT transition will be, therefore, identified as ghost (and discharged) if its energy is lower than the corresponding $\mathrm{M_{AC}}$ index, while proper CT excitations will have an energy greater than $\mathrm{M_{AC}}$. Thus, for each electronic transition

$$E_{\mathrm{TDDFT}} < M_{\mathrm{AC}} \implies \textsc{ghost ct state} \tag{272}$$

$$E_{\mathrm{TDDFT}} > M_{\mathrm{AC}} \implies \textsc{real ct state}. \tag{273}$$

If follows from Eq. 271 that the M_{AC} index will assume meaningful values only in case of transitions possessing a charge-transfer character, for which, the D_{CT} takes values significantly greater than zero. Accordingly, in the following we will mainly focus the discussion on transitions of such kind, due to relevance of the Mulliken formula for this specific case.

6.4 PERFORMANCE OF THE M_{AC} INDEX ON INTER- AND INTRAMOLECULAR EXCITATIONS

In the following we discuss the validity and robustness of our descriptor. As a start, we tested our index using the same model systems employed in preceding relevant literature on this matter [131, 134, 148]. Computational details for the calculations - where not directly specified - are reported in Section 11.1, in Appendix.

6.4.1 *Proof of concept using a popular test case*

To test the reliability of the M_{AC} index, we analyzed the ten lowest transitions of the zincbacteriochlorin-bacteriochlorin (ZnBC-BC) complex. This last is considered an archetypal system for the study of intermolecular long-range CT transitions ever since it was used to demonstrate the failure of TDDFT for CT states [58, 131, 148].

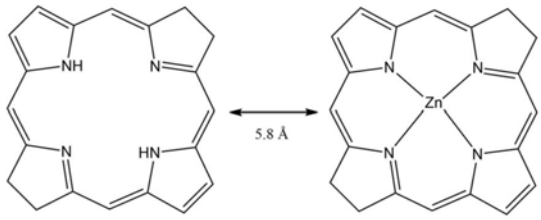

Figure 19: Molecular structure of the zincbacteriochlorin-bacteriochlorin model complex.

The complex is represented in Figure 19. Here, the donor (ZnBC) and the acceptor (BC) are coplanar and placed at a distance of 5.8 Å. As the two moieties in the complex are electronically not coupled, the orbitals involved in the lowest electronic transitions are clearly localized on only one of the two (D or A) parts [148]. The calculations were carried out using the PBE0 functional [46] as the behavior of different DF approximations, ranging from GGA to RSH, has been already well described in the literature [185]. All results are reported in Table 6. The general picture emerging from the PBE0 results is coherent with previous theoretical analysis, with alternating CT and valence excitations ($\pi\pi^*$). The M_{AC} index computed at PBEO level reveals the presence one low-lying CT state. The comparison of the corresponding M_{AC} index value (4.56 eV) and the calculated transition energy (1.96 eV) allows to class it as ghost CT state, following Eq. 272. Reference calculations, using range separated hybrid functionals, [185], symmetry adapted cluster

configuration interaction method [186] as well as the experiments [187] all agree in pointing out this TDDFT predicted CT state is indeed a ghost, in agreement with the M_{AC} based diagnostic.

State	E (eV)	M_{AC} (eV)	D_{CT} (Å)	Assignment
1	1.97 (1.94)	4.56 (5.03)	6.62 (6.64)	Ghost
2	2.06 (2.00)	-	0.37 (0.29)	$\pi\pi*$
3	2.11 (2.06)	-	0.17 (0.56)	$\pi\pi*$
4	2.13 (2.10)	4.69	6.64 (6.67)	Ghost
5	2.54	-	0.69	$\pi\pi*$
6	2.58	-	1.28	$\pi\pi*$
7	2.72	5.24	6.52	Ghost
8	2.81	5.37	6.53	Ghost
9	3.32	3.17	6.52	CT
10	3.42	-	1.34	$\pi\pi*$

Table 6: Excitation energies (E, in eV), Mulliken averaged configurations index (M_{AC} in eV), charge-transfer index (D_{CT} in Å) and assignment, for the first 10 electronic transitions of the zincbacteriochlorin-bacteriochlorin complex. The values have been computed at the PBE0/6–31G(d) level of theory, while the values in parentheses have been obtained with the -larger 6- 311G(d,p) basis set, to check for basis set dependence.

The second and third transitions are valence excitations $\pi\pi*$, localized either on the ZnBC or on BC moieties, corresponding to the so-called Q_x band. Accordingly, these states have very small D_{CT} values. The Q_y band appears at slight high energy, but is preceded by another ghost state. Analogously, the sixth and seventh excited states are classed as ghosts, the first real CT state occurring higher in energy, at 3.32 eV. In short, these preliminary calculations on a model system show that the M_{AC} index identifies the ghost states at D–A distance for which the Mulliken's relation - Eq. 270 - is valid. This is the far-nucleus asymptotic regime defined by Hirao and coworkers [58], which in the present case corresponds to D_{CT} values > 5 Å. One may argue that the the ZnBC-BC model complex is an "easy case", as the hole-electron distance is comparable to the geometrical distance between the D and A moieties [131]. Indeed, the edge-to-edge distance (5.8 Å) is not too far from the D_{CT} values computed for any of the CT transitions (6.5–6.6 Å).

Real chemical systems are, however, a more difficult playground, as holes and electrons are often not clearly localized, due to electronic conjugation/delocalization effects. The effective CT distance is therefore more difficult to be evaluated in terms of geometrical parameters only.

6.4.2 *Charge-transfer transitions in push-pull systems*

Push-pull systems, such as the one reported in Figure 20, can be considered as prototypes of donor–acceptor molecular dyads where D and A moieties are partially coupled via a –phenyl- bridge, allowing for a substantial delocalization of the electronic charge. In this

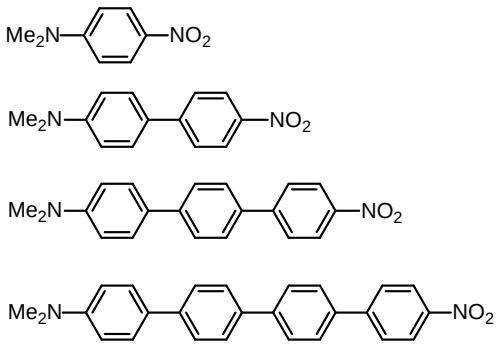

Figure 20

case, the CT character associated to the lowest excitation is modulated by the number of spacers present in the molecule. Indeed, up to two phenyl spacers the first transition has a CT character while for a greater number of spacers the bright transition shows a more localized $\pi\pi*$ character [134].

For this class of molecules, we performed TDDFT calculations using different functionals, so to investigate the relative distributions of CT or local excited states, and the eventual presence of ghost states, in dependence of the hybrid character of the functional. We used the PBE [43] (GGA) functional and its GH (PBE0) [46] and RSH (LC-PBE) [58] counterparts, coupled with the 6-31G(d,p) basis set. As a reference, we calculated the same system using the configuration interaction method CIS. In contrast to DFAs, CIS yields the correct $1/R$ behavior of the potential energy curves of CT states - with regard to the charge separation coordinate, because of the full inclusion non-local electrostatic attraction between the charge-separated species ($c_{\mathrm{HF}} = 1$). The calculated excitation energies are usually larger in CIS than in TDDFT, which can be attributed to the larger gaps between occupied and virtual orbitals in HF. Therefore, although CIS yields the correct asymptote for CT states, it only gives poor values for the excitation energies of both CT and valence-excited states. Hence, the CIS reference is not to be considered as an improvement over TDDFT - which yields accurate results at least for valence-excited. Here the purpose of the CIS is to verify that the $\mathrm{M_{AC}}$ index behaves correctly also in the case of methods showing the correct $1/R$ limiting behavior [58], i.e. when Eq. 270 is respected. No ghost states are, therefore, expected using such approach.

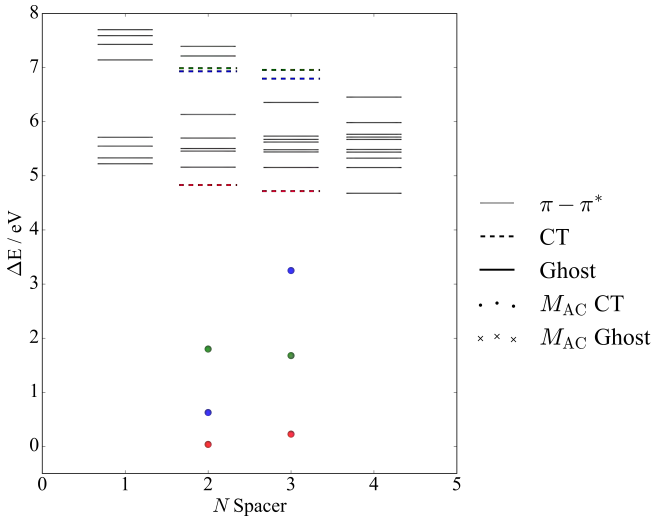

Figure 21: Excitation energies (straight lines) and M_{AC} parameters (dots and stars) computed for the CT transitions and evaluated at the CIS level for the push-pull family of molecules. M_{AC} values and TDDFT energies associated to the same electronic transition are depicted with the same color. The values are reported as a function of the number of phenyl bridges (N).

The CIS results are plotted in Figure 21. The smallest push-pull molecule (N=1) shows no low-lying CT excitations, all transitions having a $\pi\pi*$ character and a low D_{CT} value, due to the strong electronic coupling between D, A, and the π aromatic system of the phenyl spacer. CT states appear instead for molecules containing two and three phenyls (N=2 and N=3). All these CT states are compliant with the condition given in Eq. 272, that is their CIS computed energy is higher than the corresponding M_{AC} value. For the largest system (N=4), the nature of the excitations drastically change, all having a clear $\pi\pi*$ character as demonstrated by the computed D_{CT} value, and in accordance with what discussed in Chapter 4 [4].

The excitation energies and corresponding M_{AC} values computed using the PBE, PBE0 and LC-PBE functionals for the same push-pull family of molecules are reported in Figure 22 - the corresponding values are provided in Table 11. The three functionals provide a similar picture of the absorption spectrum of the smallest system (N=1), with an alternation of $\pi\pi*$ and CT transitions (see Table 11). More importantly, no ghost transitions are present in this case and the overall picture is in agreement with the CIS results. When two phenyl spacers are present (N=2) ghost states start to appear at low energies for PBE (3 states). Their number increases for N=3 (7 states) and N=4 (8 states), in parallel with the corresponding D_{CT} values. These states, whose energy is always lower than the corresponding M_{AC} (Eq. 272), are often grouped within few tenths of eV (as shown in Appendix, Table 11). When using PBE0, the presence of a fraction of HF exchange mitigates this effect, partially reducing the number of ghost states: 1 for N=2,

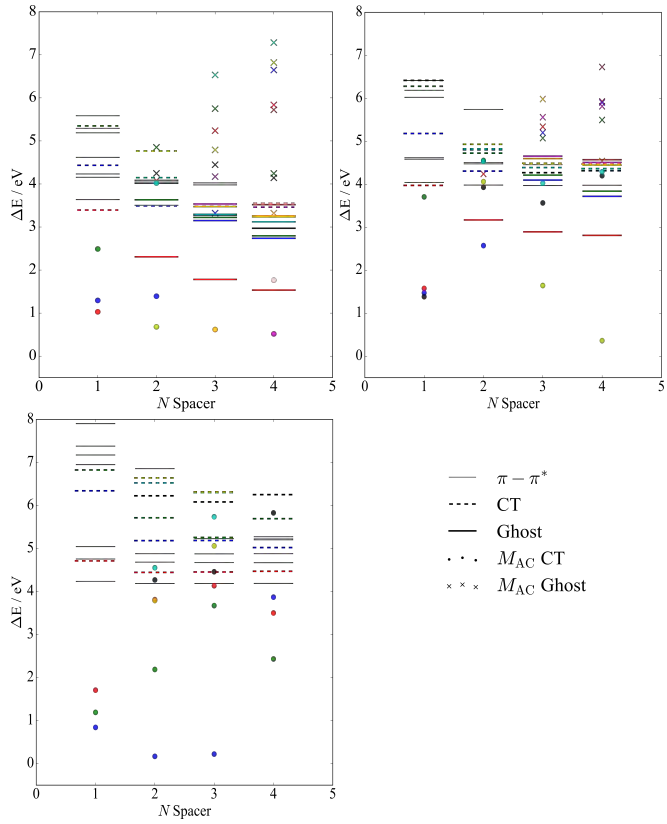

Figure 22: Excitation energies (straight lines) and MAC parameters (dots and stars) computed for CT transitions and evaluated at TDDFT level using different functionals, for the push-pull family of molecules considered. M_{AC} values and TDDFT energies associated to the same electronic transition are depicted with the same color. The values are reported a function of the number of phenyl bridges (N).

to 5 for N=3, and 6 to for N=4 (see Figure 22). Finally, the LC-PBE approach, which recovers the correct $1/R$ behavior, presents, as expected, no ghost states in the case of all push-pull molecules considered. The results confirm the robustness of the M_{AC} index for intramolecular CT excitations, even for D_{CT} values lower than the far-nucleus asymptotic regime threshold.

Note that while R, the distance between the donor and acceptor (here represented by the geometrical distance between the amino and nitro nitrogen atoms), ranges from 5.6 Å (for n=1) to 18.5 Å (N=4), the corresponding CT distances (D_{CT}) used to compute the M_{AC} are significantly shorter, due to the significant electronic coupling between donor, acceptor, and spacer(s). Indeed, in the smallest push-pull system (N=1) the

largest computed D_{CT} value is 2.0 Å (for the first CT transition), while the highest value is computed for the tenth transition in the largest molecules (N=4, D_{CT} 6.6 Å). Thus, both values remain considerably small compared to geometrical distance between the donor and acceptor fragments. It follows that the correct evaluation of the effective CT distance (using the D_{CT}) over the use of a simple geometrical distance is of crucial importance, especially in the case of systems possessing intramolecular CT excitations, where electron delocalization/conjugation can play a relevant role. Finally, it is worth stressing that especially higher energy excitations can possess a non-negligible multi-determinant character so that the weighted average, performed when computing the M_{AC} index, is relevant for a correct estimation of IP and EA.

In summary, the discussion above substantiates the effectiveness of M_{AC} index in detecting ghost CT states, a major problem in TDDFT calculations. The systems investigated here are representative of both intermolecular and intramolecular CT excitations. Besides, they comprise both charge-transfer states which fall within and beyond the far-nucleus asymptotic regime defined by Hirao, i.e., where donor and acceptor have a non-negligible overlap. Overall, the the M_{AC} index allows detecting the presence of ghost states, also in the case where the electronic features of the molecules (i.e., electronic delocalization) do not allow for an a-priori geometrical evaluation of the donor–acceptor distance. The widespread use of GGA and GH functionals, many of them providing accurate electronic absorption energies for valence excitations, can be made "safer" by the use of this descriptor. Of note, the evaluation of this index is rather computationally inexpensive. Although the discussion above is based on the results obtained strictly using *relaxed* densities [138] - as previously discussed in Chapter 4, we may in principle attempt to perform a similar analysis using *unrelaxed* densities as well. This last approach can be particularly convenient, just think of the advantage of computing the M_{AC} diagnostics on all vertical states at once, rather than compute the relaxed density of each. The effect of using relaxed/unrelaxed density is discussed more in depth in the following sections.

6.5 M_{AC} DIAGNOSTICS IN REAL SYSTEMS

6.5.1 *First step to build an effective strategy for the characterization of photochemical processes*

In the context of designing density-based strategies to draw a detailed understanding of excited state processes, the the M_{AC} index is particularly convenient.

Any method giving access to the energy and the electronic density can be used for the evaluation of density-based descriptors, the only critical point concerning its reliability. If the method used to determine the density is inaccurate, the ensuing observables will be clearly biased. In this respect, the M_{AC} diagnostics can be used to perform a preliminary analysis to ensure the correctness of the potential energy curves of the excited states of interest. Once this verification is completed, the quest of finding a strategy to describe photochemical processes can be pursued: one can apply other topological descriptors to characterize the nature of the calculated excited states and, for instance, investigate different regions of the potential energy surfaces of interest.

We have mentioned in the previous section that the presence of ghost states may result in the qualitatively incorrect interpretation of the electronic structures and spectra. We will now look at some practical cases, well known photochemical reactions that have

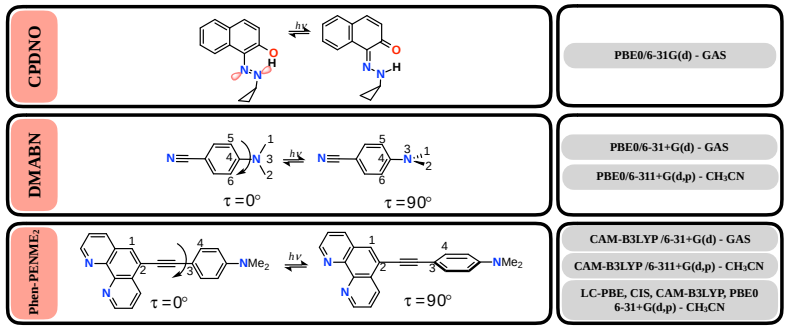

Figure 23: Reactions computed at the levels indicated, and tested using the M_{AC} diagnostics.

described up to now resort on "model" systems, which have the advantage of being easy to rationalize, with the downside of giving a somewhat simplistic picture.

In the present section we examine three different well known molecular systems in Figure 23. The purpose of this analysis is precisely to assess how the use of different methodologies - reported in previous literature, can impact on the quality of the result, and provide a strategy how to validate a TDDFT methodology. We focus on the states of charge-transfer character, and attempt to disclose the presence of unphysical states, in dependence of the choice of the functional and basis set used. Moreover we discuss, also in this context, the implications of the use of *relaxed* and *unrelaxed* densities.

In this analysis, we make an additional distinction concerning the characterization of the unphysical states, which we label either as ghost (G) or spurious states (S). The differentiation is based on the oscillator strength value, where the spurious states, unlike the ghosts have a non negligible oscillator strength. Such classification is required when studying system of increasing complexity. We have elucidated before how CT states in TDDFT correspond - when local xc functionals are used - to ES in which photoexcited hole and electron poorly overlap, due to the incorrect functional asymptotic and to the missing functional discontinuity of the approximate xc-potential with respect to the particle number.

With common local and semi-local functionals many bound excitons are not described at all. This because the xc-kernel is local and the overlap is negligible. In turn, the zwitterionic form where hole and particle are spatially well separated dominates over the neutral one. This determines the loss of the multideterminantal character of the CT state. Thus, the energy of the CT states which is then given by the constant difference of the energies of the electron donating and electron-accepting orbitals, diminishes so

significantly that these states become the lowest in the calculated electronic spectra. If adding exact exchange improves the results, the partial addition of some fraction of exact exchange, may only mitigate these deficiencies, resulting in an only partial correction. As a result, in real systems, the spectrum of unphysical-low-lying states counts of states whose degree of error can be of different significance, depending on the particle/hole overlap [24, 121]. Hence, there might be excited states of CT character which have non vanishing oscillator strength, but still appear too low in energy. These are the ones we refer to as "spurious". As we discuss in the following, deciding whether a state shall be discarded or not can be a hard task, as these intermediate cases may be difficult to judge.

There is an additional refinement that we can consider, to recover the correct energy placement of the vertical states, and precisely to get a better estimate of the virtual orbital energy values, ϵ_a. As previously mentioned, ϵ_a values are fairly wrong when DFAs are used, due to the fact that virtual KS orbitals are one-electron states, which resent the exact same local potential as the occupied orbitals. In Hartree-Fock instead, the potential for the virtual orbitals is devoid of the stabilizing hole potential. As a result, the ϵ_a orbitals "see" one electron more than the corresponding occupied ones - this is indeed the reason why Hartree-Fock virtual orbitals are more dimly bound, and therefore appear to be more diffuse.

A simple scheme to rectify the underestimation of the eigenvalues of the TDDFT-virtual orbitals is to compute the Hartree-Fock energies, for each given TDDFT density distribution. The procedure is easy and fast, as it requires simply to perform a single self-consistent field cycle on top of the converged Kohn-Sham orbitals. The newly obtained orbital energies are now corrected, and the virtual orbitals are shifted higher in energy, compared to the original KS orbitals. As only one SCF cycle is performed, the overall shape of the orbitals remains unchanged. Hence, based on these observations we reformulate Eq. 271 as,

$$M_{\mathrm{AC}} = \sum_{ia} \frac{c_{ia}^2 (\epsilon_a^{\mathrm{DFA-HF}} - \epsilon_i^{\mathrm{DFA-HF}})}{\sum_{ia} c_{ia}^2} - \frac{1}{D_{\mathrm{CT}}}. \tag{274}$$

As the correction basically affects only the unoccupied orbitals, equations 271 and 274 only differ by the amount in which virtual orbitals are lower in DFT than in Hartree-Fock. As a result, Hartree-Fock-corrected $\mathrm{M_{AC}}$ values are by definition greater or equal to the original value.

As the subject of our investigations, and particularly of this chapter is rather methodological than focused on mechanistic details, we will overlook - for now - describing the characteristics of the photo-induced processes which occur on the molecules on which we apply the $\mathrm{M_{AC}}$ diagnostics. We will here limit the discussion to few details necessary for our purposes, and refer to the next chapters - and dedicated references - for a more comprehensive discussion of reactions themselves.

6.5.2 *Excited state intramolecular proton transfer in CPDNO*

The cyclopropyldiazo-2-naphthol (CPDNO) molecule is a hydrogen-bonded azo-aromatic system, which undergoes an intramolecular proton-transfer reaction at the excited state [188]. The reaction connects, at the excited state, the ES-enol* to the ketone* form (Scheme 23). We consider the lowest excited levels and verify the correctness of the energy and nature of the excited states along the reaction coordinate, through the M_{AC} diagnostic. A convenient way to do so is to construct different structures - eight in the present - reasonably close one another, in which the H atom progressively shifts away from the enol-oxygen towards the nitrogen in steps of 0.1 Å.

On these structures we calculate the ten lowest vertical excited states using a global hybrid coupled with the 6-31G(d) basis-set - corresponding data are available in Appendix, in Table 12. Despite the rather small basis set, and the "standard" choice of functional, such methodology well reproduces the potential-energy curves of the lowest singlet states, in particular, S_0, S_1, and S_2). All values in Appendix, Table 12 are equivalent to those calculated using B3LYP functional coupled with a larger basis-set [163]. The computed surfaces and spectra are also in close agreement with those computed at the CASSCF/CASPT2 [3, 163] level, and are consistent with the experimentally observed photoproducts. Thus, we expect the computed M_{AC} index to reveal few or no ghost, at least when relaxed densities are taken into account.

Each panel in Figure 24 represents the computed relaxed and unrelaxed D_{CT} values, for the ten lowest excited states, at different structures (S001 to S008). The vertical states are labeled according to the computed M_{AC} value and character. Excited states possessing an energy value greater than their associated M_{AC} are classified as charge-transfer or locally excited states, based on their D_{CT} value. D_{CT} values below 2.0 Å are connotative of a spatially localized excited state "L", while D_{CT} values greater or equal to 2.0 Å are considered as "CT" transitions. Besides, excited states appearing at energy values lower than the corresponding M_{AC} are classified either as ghost "G" states if their oscillator strength value is below 0.001 or as spurious "S" otherwise.

Figure 24 reveals the presence of few spurious states - light blue scatters, $3rd$ and $9th$ vertical excited at reaction steps S001 and S002 and the first and $7th$ vertical positions at S005 and S006, to name a few. Additionally a number of ghost states (in orange) appear. All these states have large ${}^{U}D_{CT}$ value, ranging between 2.985 and 3.945 Å (raw data are available in Table 12 in Appendix). As such, the charge-transfer character of such states, as calculated with the PBE0/6-31G(d) method is clearly overestimated. The totality of these spurious states - only exception the S_9/S_8 excited state - turn into L states when the density relaxation is taken into account. Accordingly, the D_{CT} shrinks by half of the value.

The presence of such states, is ascribed to the combination PBE0/6-31G(d) which can only describe non-local effects limitedly. As a result, the effect of the relaxation is significant, and one should be careful in judging the G or S nature of the excited states using unrelaxed densities. The PBE0/6-31G(d) method remains a valid choice to

investigate the proton-transfer reaction, as the excited states which are crucially involved in the proton transfer are only the lowest two.

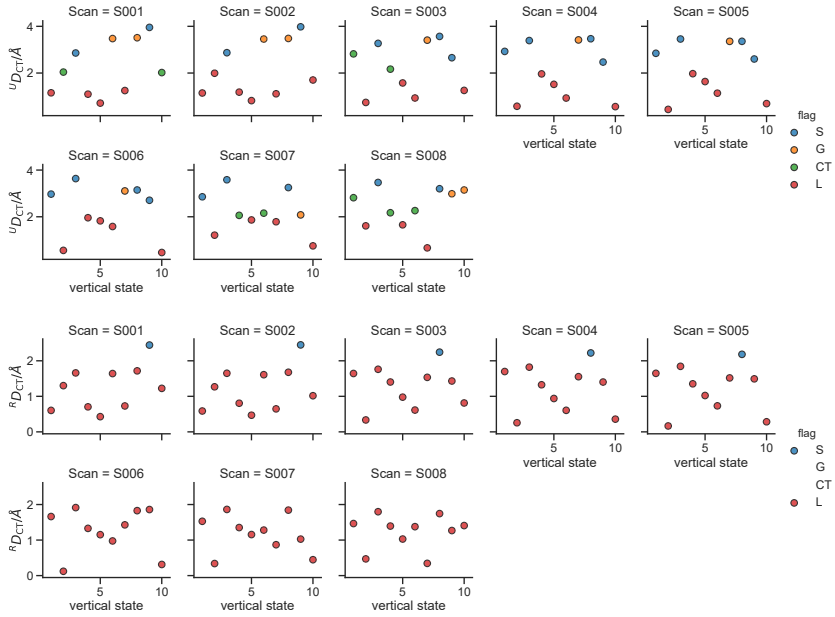

Figure 24: M_{AC} **diagnostics computed along the proton-transfer reaction coordinate in CPDNO**: $^{U}D_{CT}$ (upper) and $^{R}D_{CT}$ (lower) values for the first ten vertical states. The labels correspond to the following: G for ghost states, S for spurious states, CT for charge-transfer states - D_{CT}values $\geq$ 2.0 Å, L for local excitations.

6.5.3 *Charge-transfer process in DMABN*

DMABN is the archetypal representative of aromatic compounds bearing both an electron donating and an electron accepting group, and exhibiting a dual emission [189, 190]. Due to this particular feature, DMABN has attracted the interest of many, and has been extensively studied both from the experimental and theoretical [191, 192] point of view.

Despite its reduced size, DMABN is extremely complex to model. The reason for such complexity is that the charge-transfer process does not occur along a single reaction coordinate. The main coordinates which drive the process are the twisting and the out of plane wagging of the dimethylamino group, which determine the formation of two main

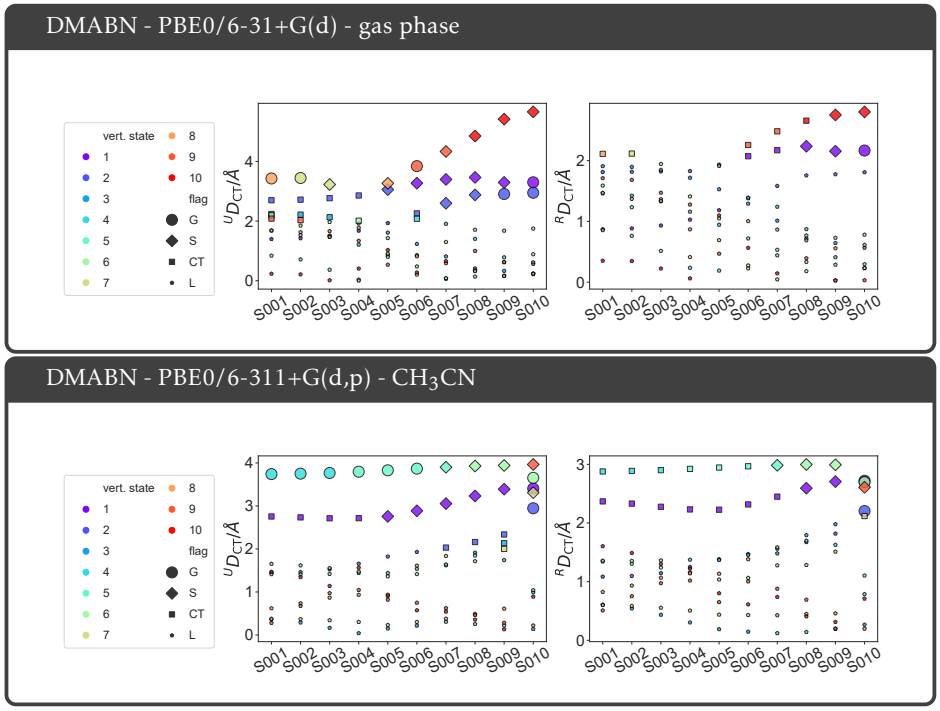

Figure 25: M_{AC} **diagnostics along the intramolecular charge-transfer coordinate in DMABN using different levels of theory**: $^{U}D_{CT}$ and $^{R}D_{CT}$ values for the first ten vertical states, along the intramolecular charge-transfer coordinate. The labels correspond to the following: G for ghost states, S for spurious states, CT for charge-transfer states - D_{CT}values ≥ 2.0 Å, L for local excitations.

species that differ by the orientation of the dimethylamino and phenyl groups, as shown in Figure 23 - we will come back on the mechanism which underlies the dual emission in DMABN later, in Chapter 8.

The intrinsic complexity of the charge-transfer process immediately translates in the difficulty to individuate the relevant excited potential energy surfaces which are to be examined. As in the present section we are only interested in testing the M_{AC} diagnostics on the potential energy curves calculated using different methodologies, we may reduce the complexity of the problem and inspect the lowest excited states along a single coordinate that is the twisting of the dimethylamino fragment. We are left with ten structures with increasing dihedral angle (C1C2C4C3) ranging from 0° to 90° in increments of 10°.

Figure 25 reports the $^{U}D_{CT}$ and $^{R}D_{CT}$ calculated at different levels of theory. Let us first consider the $^{R}D_{CT}$ profiles, computed in gas-phase (top right panel). Very little ghost and spurious states are found. All excitations are satisfactorily described using PBE0 in

combination with the double-ζ basis set, with the exception of the first vertical state as the molecule approaches the orthogonal conformation. For this last, the vanishing overlap of the hole and particle orbitals causes the artificial annihilation of oscillator strength, and subsequent appearance of a ghost state. As a result, we may conclude that the potential energy of the first state - as the torsion exceeds 60° - is severely underestimated in energy and displays the wrong oscillator strength.

It must be noticed though that the first two vertical states are energetically well separated from the third - which according to the M_{AC} diagnostics is correctly represented. This prevents the mixing of the two lowest excited states with the higher ones - corresponding data are collected in Table 13 and 14 in Appendix. Hence, the distribution of the lowest vertical states in PBE0 is likely to be correct, despite the energy underestimation. Based on the profiles calculated we would correctly guess which states are populated and in which order, though with the limit of little agreement between the experimental and the calculated spectra.

The M_{AC} diagnostics warns us about the limits of the methodology of our choice and which are the errors we might incur in. We might still decide to employ a GH-GGA functional as PBE0, though due caution is advised. Now let us asses impact of the use of relaxed and unrelaxed densities on the M_{AC} diagnostic, by looking at the curves in the upper panel of Figure 25. The ${}^{R}D_{CT}$ and ${}^{U}D_{CT}$ profiles point out in the same direction; unrelaxed densities though result in larger D_{CT} values. This in turn can lead to an overestimation of the presence of ghost states when unrelaxed densities are used. In this respect, the use of a large basis-set is convenient - see the ${}^{R}D_{CT}$ and ${}^{U}D_{CT}$ profiles in the bottom panel of Figure 25. These last are calculated using a triple-ζ basis-set and with added diffuse and polarization functions, and appear to be less subject to variations as compared with the curves in the upper panel, which are calculated using a double-ζ basis-set (6-31G(d)). Hence, to parity of functional used, larger basis-set render a more uniform distribution of the D_{CT} curves so that unrelaxed densities can be used instead of relaxed ones. Besides, this improved description is also assisted by the addition of solvent effects. The solvent of choice, acetonitrile, is a polar aprotic one, with reduced ability to form hydrogen bonds. Hence, the acetonitrile environment maintains the free torsion around the triple bond axis and allows the formation of both emissive species.

We conclude that the use of the large base set, together with the solvent effects, is beneficial, as it allows the use of non-relaxed densities instead of the relaxed ones, with the advantage that goes with it. The improvement, though is not such to eliminate the CT problem. As discussed above, the incorrect description of CT states has a well-defined origin, that is the incorrect shape of the potential energy curve computed using DFT. The use of diffuse functions does not compensate the missing overlap of the hole and particle orbitals, not even in a system of such reduced size.

6.5.4 *Charge-transfer process in Phen-PENMe$_2$*

Finally we examine the charge-transfer process in 5-(4-dimethylaminophenylenylethylyn)-1,10-phenanthroline, Phen-PENMe$_2$ in abbreviated form. We discuss in detail the photo-

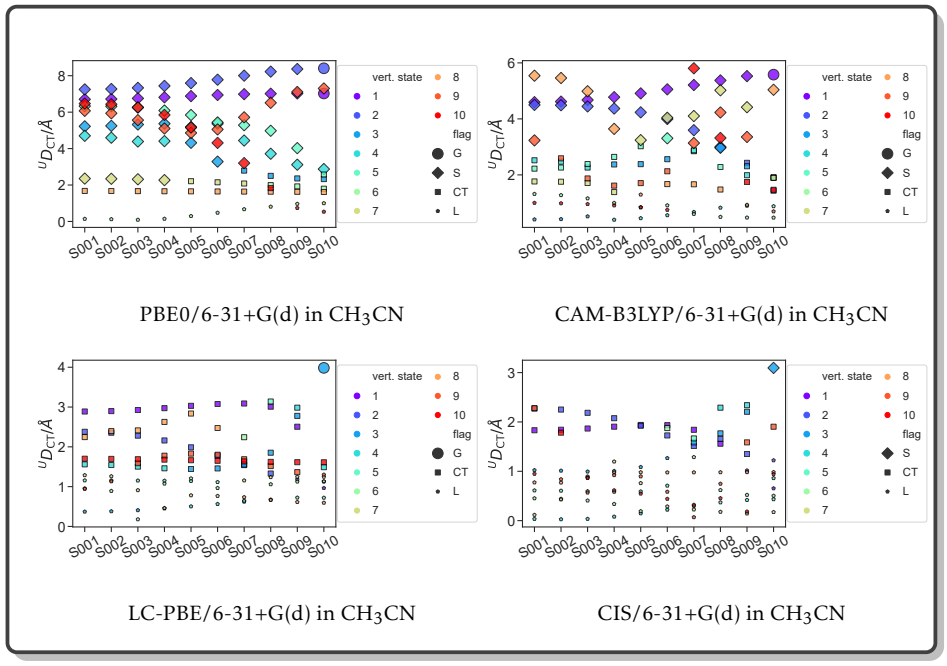

Figure 26: M_{AC} **diagnostics computed along the intramolecular charge-transfer coordinate in Phen-PENMe$_2$ using different functionals**: ${}^{U}D_{CT}$ values for the first ten vertical states, along the intramolecular charge-transfer coordinate. The labels correspond to the following: G for ghost states, S for spurious states, CT for charge-transfer states, L for local excitations. Each kind of excitation is represented with a circle of different dimensions.

chemistry of such system later, in Chapter 8. So far, we just recall that this system has been recently been reported as to be dual emissive [193]. The charge-transfer process which gives rise to this peculiar behavior has evident analogies with the charge-transfer process in DMABN discussed in the previous paragraph. The two main conformations which take an active part in the photo-induced charge-transfer process in Phen-PENMe$_2$ differ by the orientation of the phenyl and phenanthroline rings - shown in Figure 23. The reaction coordinate connecting these two (in Figure 23) is the dihedral angle C1C2C3C4. Once again, we analyze the M_{AC} profile on ten different structures constructed by varying the dihedral angle from 0° to 90° in increments of 10°. The resulting geometries encompass the full transformation from the planar to the twisted (perpendicular) structure.

We are interested to individuate the presence of ghost and spurious state in dependence of the use of different functionals. Figure 26 shows the ${}^{U}D_{CT}$ profiles of the lowest ten vertical states, all along the reaction coordinate, computed using the 6-31+G(d) double-ζ basis set in combination with four different functionals and implicit solvation in acetonitrile. Each functional incorporates a different amount of HF exchange, ranging

from 25 % in PBE0 to 100% in CIS. We recall that the M_{AC} is calculated using the HF corrected EA.

The comparison of the curves in Figure 26 is instructive. Evidently, the quality of the results changes significantly according to the functional used and with it the number of unphysical states. As the CIS has full HF exchange the potential energy curves display the correct asymptotic behavior. As such, no ghost states are found. However, as the full addition of HF exchange introduces the bias associated with the missing correlation effects, the energies are shifted too high in energy. The CIS curves are, once more, to be considered as a reference more than an improvement over the TDDFT results, as they entail wrong energy curves, but the correct $1/R$ asymptotic behavior and D_{CT}/M_{AC} profiles. Compared to these last, the LC-PBE curves have very similar profiles, which in turn signifies that LC-PBE recovers the correct charge-transfer character, though at the price of of a significant energy blue-shift compared do the experimental spectrum. Only one ghost state is found, corresponding to the third excited state. CAM-B3LYP is close to reaching the same quality in terms of charge-transfer distance profile. The ${}^{U}D_{CT}$ profiles very similarly distributed, with the exception of the S_7 and S_8 where the charge-transfer character is overestimated. Slight differences appear also for S_2, whose ${}^{U}D_{CT}$ profile has the correct shape, although shifted by ≈ 2 Å, compared to the corresponding LC-PBE curve.

The only state that is manifestly different is S_1, with an increasing CT character in CAM-B3LYP along the torsional coordinate, and opposite behavior in LC-PBE. In CAM-B3LYP, S_1 has vanishing oscillator strength in the twisted conformation. According to the M_{AC} diagnostics, S_1 lies erroneously very low in energy. This improper behavior is all the more marked as much the twist is important. Hence, the vanishing oscillator strength shall be considered as an artifact of the method, which is caused by the missing overlap of the HOMO and LUMO orbitals, lying in two separate regions in space - see Appendix, Section 11.5. However, the overall picture of the photochemical process delivered by the LC-PBE calculations is also likely to be biased, as the energies are significantly overestimated with respect to the experimental values. On the other hand, the oscillator strengths computed in CAM-B3LYP and PBE0 reproduce much closer the experimental spectrum - in Figure 27. PBE0, though, predicts wrong D_{CT} profiles of most excited states. We conclude that although CAM-B3LYP renders an inaccurate description of the lowest excited states, it still guarantees a better overall description, as compared to other long-range corrected functional, as LC-PBE, and to GGA functionals. As for S_1 in CAM-B3LYP, this state should lie slightly higher in energy and should display low - but non-vanishing oscillator strength. A final remark on the effect of the basis-set: the same arguments discussed in Section 6.5.3 for the DMABN are valid once again. At a given functional, the use of a larger basis is convenient as it has the effect to minimize the differences between relaxed and unrelaxed densities - see Appendix, Figure 51. Smaller basis sets results in large differences, with the appearance of additional low lying ghost states, which impose the necessary use of relaxed densities.

In summary, in this last section we have used the M_{AC} diagnostics to verify the reliability of the potential energy surfaces of the lowest excited states computed for different

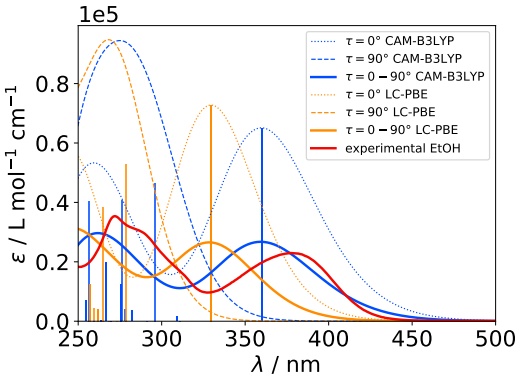

Figure 27: Comparison of the calculated absorption spectra of Phen-PENMe$_2$ - both in CAM-B3LYP and LC-PBE in CH_3CN and experimentally.

molecular systems, such as CPDNO, DMABN and Phen-PENMe$_2$. Here, we have ulteriorly refined the formulation of our index by introducing a mixed DFT-HF correction, yielding a better estimate for the energies of the virtual orbitals, which are typically underestimated using density functional approximations. Using our index we were able to identify the presence of ghost and spurious states, and to characterize all other excitations as having local or charge-transfer character. We have shown how the presence of ghost states can affect the interpretation of the excited state process and how our diagnostic analysis can be used for this purpose. Spurious states are not as critical as ghost states as they correspond to excited levels that are only partially mistaken by the method of choice. Relaxed densities in general provide better description of excited states possessing CT character. However, for the same density functional approximation the use of a larger basis set can be beneficial as it has the effect to mitigate the differences between the pictures obtained by using *relaxed* or *unrelaxed* densities. This observation supports the use of unrelaxed densities, instead of the more onerous relaxed ones.

7

M_{AC} DIAGNOSTICS IN METAL COMPLEXES

7.1 CONTEXT

The many controversies regarding the use of TDDFT for long-range charge-transfer excited states extend to metal-complexes as well. The prediction of the nature and properties of excited states of transition metal complexes is a fertile research area [194–196]. Due to their rather peculiar photochemical and photophysical properties, organometallic complexes of several metals are nowadays exploited in different fields and applications [197]. In particular, ruthenium complexes have been the basic components of dye-sensitized-solar cells from the very beginning of such technology and are still today among the most efficient dyes [23].

In a totally different field, ruthenium complexes have been largely applied as DNA probes, since they have a demonstrated ability to establish strong interaction with such macromolecule [198]. In fact, it has been shown that the photophysical properties of the complexes change radically upon interaction with DNA and the fluorescence can be tuned by the environment in which the complexes are immersed [199, 200]. In some cases, the fluorescence present in aqueous media, is quenched by DNA interaction [201], while in other cases dark solvated compounds show an intense fluorescence upon the addition of DNA. The high DNA binding affinity and unique light-switch effect of Ru complexes make them attractive compounds not only to investigate metal-to-biomolecules interactions, but also for related research areas such as sensitive diagnostics, chemotherapeutics, and photo-therapy [195]. Indeed, ruthenium complexes have known potential as antitumoral drugs, as they cause irreversible DNA damage through intercalation and subsequent excited state mediated charge-transfer process. In the field of biochemistry, the luminescence of Ru(II) complexes has also been observed in non-polar environment, such as hydrophobic cavities in proteins. These are only few of the many existing applications [202].

Processes of such intrinsically complex nature, are extremely interesting to study, yet difficult to understand based on sole experimental investigations. Indeed a good understanding of the photophysical processes involved in such phenomena is critical to recognize and improve the therapeutic properties of such systems. This is also the reason why such compounds, and especially Ru complexes, are the object of numerous of studies based on theoretical computations and spectroscopic techniques. Actually, the use of theoretical methods is crucial to correctly model the behavior of such complexes upon irradiation, and to acquire a realistic description of their excited state manifold [24].
Transition metal complexes cumulate most of the complexities inherent to theoretical studies: size, electronic delocalization, high density of electronic states of various characters, multi-reference nearly degenerate states, long-range charge-transfer states and

vibronic couplings. Moreover as the d and f shells become populated, relativistic effects, spin–orbit coupling, dissociative states, and states mixing become important.

With the aim of setting up computational protocols enabling to accurately predict and describe the nature and energetics of the excited states, specific quantum methods have been explicitly devised and benchmarked on metal containing complexes. Among these, the most popular methodologies used to treat these systems are density based methods but also the variational approaches based on the self-consistent- field (SCF) formalism and its multi-configuration extension complete-active-space SCF (CASSCF) [168] or the variants restricted- active-space SCF (RASSCF) [203]. These last have be ulteriorly improved by adding perturbative correction (CASPT2) [169], which allow including of non-dynamical electronic correlation effects. If the latter approaches have been proved to yield a high accuracy in describing both vertical absorption and photochemical behavior of metal complexes, these however impose a heavy computational burden which limits their domain of applicability to rather small compounds. Moreover, they require the selection of a relevant system-specific active space, which makes them unpractical and of difficult usage for routine applications.

Hybrid methods have also emerged [204], which combine DFT at short-range, and wave function or perturbative approaches at long-range. These last, however also suffer from the same drawbacks.

TDDFT approaches, on the contrary have the advantage of a favorable scaling, which has determined their widespread diffusion in the treatment of metal based complexes. In addition, density rooted approaches limit the user dependency to the choice of the exchange correlation functional to be used, which in practice renders these methods uncomplicated, though impressively accurate in the description of structural and spectroscopic properties of transition metal complexes, at least for what concerns the electronic ground state and the lowest excited states. Not surprisingly, TDDFT calculations and simulated spectra obtained from them are increasingly used to support experimental findings, where the actual characterization of the nature of the observed transition by electronic structure calculations can provide an extremely valuable addition and reinforcement to the experimental studies [24, 205, 206].

For these comparative studies, usually the choice of the exchange correlation functional is based on previous works dealing with similar compounds, showing a good agreement with the experimental results. However, matching experimental/theoretical spectra may just arise because of a lucky compensation of errors. Indeed, the limitation of DFT and TDDFT, apply to metal containing complexes too. The wrong asymptotics typical of local exchange functionals has severe consequence on the computed excitation energies of such class of compounds, which in turn, may strongly affect the predicted photophysical and photochemical properties, and with it the interpretation of the mechanism of the related excited state processes. Therefore, a note of caution is needed. In particular, transition metal complexes are often designed with the precise purpose of enhancing the CT character in the electronic ground stater, or in the lowest excited state, to obtain compounds possessing a low absorption wavelength and a high molar extinction coefficient simultaneously. For instance, compounds with such properties are extensively researched in the

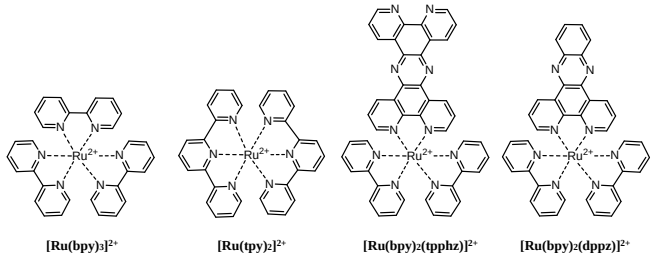

Figure 28: Chemical structures of the complexes studied.

context of photodynamic therapy (PDT) [11, 207], light-harvesting complexes in plants and bacteria [22], as well as for dye sensitized solar cells applications [205]. CT states are then generated by functionalizing the metal complexes skeletons with appropriate donor/accepting groups.

Naturally, the description of such though-space transitions strongly depends upon the selected density functional approximation. Transition metal complexes with such characteristics are in principle susceptible of the appearance of ghost and ligand-to-ligand charge-transfer states, particularly in the case of systems with extended ligands. It follows that to characterize such compounds with the desired accuracy it is necessary to use the appropriate methodology and to adopt a suitable strategy to diagnostic the reliability of the chosen TDDFT approach. In this respect, the M_{AC} index can provide relevant insights to detect unphysical CT states, that are computed with insufficient accuracy, and thus appear too low in the spectrum.

7.2 INTRODUCTION

In the following we analyze the excited state profiles of four metal complexes containing an octaedrally coordinated Ruthenium(II) center, namely $[Ru(bpy)_3]^{2+}$, $[Ru(tpy)_2]^{2+}$, $[Ru(bpy)_2(dppz)]^{2+}$, and $[Ru(bpy)_2(tpphz)]^{2+}$, whose structures are given in Figure 28. All compounds have been previously characterized experimentally, which makes them ideal candidates to perform a systematic analysis to the electronic transitions. Hence, we apply the M_{AC} index to inspect the character of the lowest 30 states, as computed with four different functionals, including varying amount of HF exact exchange. The diagnostic analysis provides relevant insights to detect ghost and spurious CT states when using TDDFT in conjunction with global hybrid and range separated functionals such as B3LYP, PBE0 and CAM-B3LYP. Aside to these we report the CIS values as a reference. As previously alluded to, the CIS potential energy curves display the correct asymptotic behavior, thus, by definition, CIS M_{AC} profiles are devoid of all artificially low-lying excitation. By contrast, the curves are systematically shifted too high in energy. Hence, we include these value as a ghost-free reference, though, without discussing the orbitals and spectra calculated from it.

The character of an electronically excited state is one of the most important descriptors employed to discuss the photophysics and photochemistry of all kinds of molecules, included transition metal complexes. In transition metal complexes, the interaction between the metal and the different ligands gives rise to a rich variety of excited states, including metal-centered (MC), ligand-centered (LC), metal-to-ligand-charge transfer (MLCT), ligand-to-metal-charge-transfer (LMCT), intra-ligand-charge-transfer (ILCT), and ligand-to-ligand-charge-transfer (LLCT) states. Most often, these excited states are identified by considering the most important wave function excitation coefficients and inspecting visually the involved orbitals. It is therefore clear that, discerning the unphysical spurious transition is of primary importance.

When π-accepting ligands, such as polypyridyl ligands, are coordinated to Ru(II), the complex, already in its ground state may exhibit intense singlet-singlet MLCT transitions in the visible region [208]. This behavior is common for both tris-bidentate and bis-tridentate complexes, although a red-shift of the absorption maximum wavelength is often observed for the bis-tridentate ones. The molar absorption coefficients for the ^{1}MLCT transitions depend on the ability of the ligand to delocalize the excited electron far from the metal center. Thus, complexes with higher electron accepting capabilities have higher molar absorption coefficients. Metal-centered and ligand-centered transitions can also be identified, in the electronic spectrum.

7.3 ANALYSIS OF THE ABSORPTION SPECTRA OF RU(II) POLYPYRIDYL COMPLEXES

Let as first comment on the absorption profiles of the four selected Ru(II) compounds, in acetonitrile. The normalized experimental absorption spectra - black dotted curve - as well as the simulated spectra, computed using four different functionals are shown in Figure 29. The measured and calculated absorption spectra of $[Ru(bpy)_3]^{2+}$ - tB in the following - are qualitatively similar. The broad band around 400-500 nm corresponds to multiple MLCT transitions from the Boltzmann-populated lowest-lying $d\pi^6$(Ru) to $\pi*$(tpy) [209]. The inspection of the NTOs - reported in Appendix, Figure 57 - and the computed energy values and oscillator strength - in Appendix, Table 11.7 - allows us to perform a similar assignment of the calculated bands. The most intense peaks in the visible region correspond to MLCT $d\pi*$ transitions around 430 nm - excited states 7, 8 in B3LYP and PBE0 and slightly higher in energy at $\approx$ 360 nm - excited states 5,6 - in CAM-B3LYP. As expected, the electronic transitions calculated using GH functionals - PBE0 and B3LYP - better reproduce the measured ones, while range separated functional such as CAM-B3LYP result in a significant blue shift. The CIS spectrum is not even close to reproducing any of the features of the experimental spectrum and is irrecoverably blue-shifted. These general trends apply analogously to $[Ru(tpy)_2]^{2+}$ - referred to as bT later on. Analogously, the lowest bright transitions correspond to MLCT $d\pi*$ transitions, which appear at around 450 nm in PBE0 and B3LYP and slightly higher in energy, at $\approx$ 390 nm in CAM-B3LYP.

The experimental absorption spectra of the substituted cyclometalated complexes $Ru[(bpy)_2(dppz))]^2+$ and $Ru[(bpy)_2(tpphz))]^2$ - D and T in the following - are character-

ized by an intense band centered at 290 nm corresponding to a strong absorption of the ligand-centered (LC) excited states and a weak absorption around 370 nm, which can be assigned to the metal centered (MC) transitions [210]. This shoulder is more intense in the dppz-substituted complex than in the $[Ru(bpy)_2(tpphz)]^{2+}$substituted one, as in this last the LC transitions propagate at lower energy and rise above the week metal centered bands. In contrast with the homoleptic complexes discussed above, *D* and *T* do not exhibit the tail of the visible band - extending towards 600 nm in *tB* and *bT*, and typical of the cyclometalated complexes that absorb between 400 nm and 550 nm in the low-lying metal-to-ligand-charge-transfer (MLCT) excited states.

In the B3LYP and PBE0 computed absorption profiles of *D* and *T* the LC band is slightly red-shifted compared to the measured spectra and broader as it incorporates also the higher energy intense LC(dppz) and ILCT(dppz) (and LC(tpphz) and ILCT(tpphz) transitions - visible as a shoulder at 260 nm in the experimental spectra.

The spectra of complexes *D* and *T* show a large blending of MLCT(dppz -tpphz) / MLCT(bpy) transitions in the visible energy domain with three intense absorptions at 456 nm, 423 nm and 415 nm - in the B3LYP spectrum of *D* - contributing to the large band between 500 nm and 400 nm. The same bands appear in the spectrum of *T* at 450 nm 423 nm and 414 nm, respectively. The comparison between experimental and computed spectra allows us to characterize the different spectral regions, and to assign the main bands to different kind of excitations, in agreement with previous literature [208,211–213]. We can summarize such analysis as follows: as all compounds contain an octaedrally coordinated Ru center, the absorption spectra display more or less the same features. The lowest energy region is dominated by the MLCT transitions. At higher energy one finds the LC transitions, i.e. transitions in which an electron is excited in on a ligand and transferred to a different one. The less intense MC bands lie in between.

7.4 m_{AC} DIAGNOSTICS IN METAL COMPLEXES

A crucial aspect of the excited states of *D* and *T* complexes is their localization on the dppz and tpphz ligands. In particular, it has been shown that their photochemical properties are tightly bound to the presence of different type of states which localize on distinct regions of the substituents: some states involve the part of dppz close to the metal atom (normally referred to as "proximal" subunit [215]), other involve the other part ("distal" [215]). The analysis of absorption profiles is somewhat the standard approach and first step in the investigation of the photochemical properties of metal complexes, as it tells which are the lowest dipole allowed transitions. Then, one can perform a full optimization of the lowest absorbing excited states to determine which excited state contribute to establish the charge delocalization pathway eventually leading to the emission. This is the main reason why it is important as a first step to determine which electronic excitations are well modeled by a given method, especially those that are significantly delocalized on the substituents. For instance, MLCT transitions are generally said to be well described by most of the commonly used DFAs, because of the large degree of overlap between the metal d orbitals and the accepting orbital on the ligand [24]. By contrast, through-space transitions are

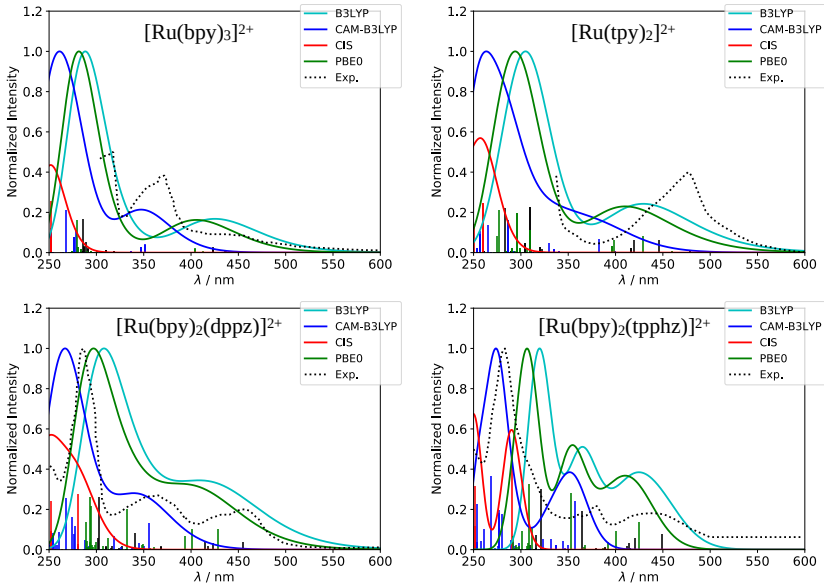

Figure 29: Computed absorption spectrum of $[Ru(bpy)_3]^{2+}$ [209], $[Ru(tpy)_2]^{2+}$ [214], $[Ru(bpy)_2(dppz)]^{2+}$ [212] and $[Ru(bpy)_2(tpphz)]^{2+}$ [213] computed using different functionals, along with the corresponding experimental spectra, retrieved from the indicated references. The simulated spectra were computed using a fwhm of 0.4 eV for all compounds, except for $[Ru(bpy)_2(tpphz)]^{2+}$, for which the best fit with the experimental values was achieved using a fwhm of 0.2 eV

susceptible to be wrongly characterized when using standard GH functionals, due to the missing hole-particle overlap. It is therefore important to assess if and which excited state levels are wrongly described and why. In this respect the M_{AC} diagnostics can be useful to determine the reliability of a given methodology. The analysis of the lowest 30 states of the four metal complexes is reported in Figures 30 and 31, where we report the energy levels and D_{CT} values calculated at four different level of theory. It is important specify that the D_{CT} values relative to the charge-transfer transition of homoleptic complexes are not null. This observation, in apparent contradiction with the definition of the D_{CT} introduced in Chapter 3, is however easy to explain. In fact, the CT transitions in tB and bT typically involve the displacement of an electron from the metal center to one of the bipyridine/terpyridine ligands. The charge distributions of these kind of transitions are not centrosymmetric, therefore yielding non-zero D_{CT} values. Since all ligands in the coordination sphere are identical any CT occurring on one ligand has the same probability to appear on the other ligands. Therefore each CT state is expected to be degenerate at least as many times as the number of identical subunits in the complex.

Let us start by commenting the results relative to the tB and bT complexes. These are homoleptic structures, where the Ru is either coordinated with two tridentate ligand (terpyridine) or with three bidentate ligands (bipyridine). The absence of an asymmetric charge withdrawing group, results in a reduced variability in the character of the excited states, at least for what concerns the lowest 30 singlet excited states. Accordingly, the NTOs - given in Appendix in Figure 56 to 56 - and 57 to 57 are largely dominated by MLCT states, intercalated by a reduced number of LC states. At higher energy an increasing number of MLCT states has mixed MLCT/LLCT character. The apparent absence of MC states can be traced back to the artificial delocalization of the virtual orbital in DFT, which in turn makes it difficult to distinguish the MC states from MLCT ones. There is no major difference given by the use of B3LYP, PBE0 or CAM-B3LYP, hence the excited state profiles of all three functionals are rather close, in both complexes.

As previously alluded to, the MLCT state are usually well described because the degree of overlap between the metal d orbitals and the π accepting orbitals of the ligand is large enough. As the excited state manifold of tB and bT is mostly composed by MLCT transitions - at least up to the $30th$ transition, we expect the M_{AC} profile to display no spurious and ghost states. The M_{AC} profiles in Figure behave as foreseen, as indeed, no artificially low-lying states are found - at least when relaxed densities are used - independent of the functional chosen. Figure 30 shows the energy levels, ${}^{U}D_{CT}$ and ${}^{R}D_{CT}$ values of the lowest 30 singlet states of tB and bT, calculated using the four different functionals.

Each state in Figure 30 is assigned a label according to its M_{AC} value, and represented using markers of different size (or length). As previously discussed in Section 6.5, transitions possessing D_{CT} values below 2.0 Å are denoted as local (L), while those having D_{CT} values CT greater or equal to to 2.0 Å are supposed to have a charge-transfer (CT) character. Besides, transitions with excitation energy values lower than the corresponding M_{AC} are classified either as ghost (G) states if their oscillator strength value is below 0.001

or as spurious (S) otherwise. The size of the corresponding marker in the plot increases according to the following ordering: L, CT, S, G.

As the bpy and tpy ligands are symmetrically distributed in the coordination sphere, they do not immediately cause the appearance of through space charger-transfer states. Therefore, the excited states of tB and bT shall not be concerned by the problems related to the description of charge-transfer states. Spurious and ghost states in the ${}^{U}D_{\mathrm{CT}}$ profiles of both tB and bT can be considered as artifacts related to the use of unrelaxed densities. Accordingly, the correct D_{CT} values are restored as soon as relaxed densities are used. Besides, the overestimation of the charge-transfer distance only affects higher excited states - $S_1 0$ or greater, with the only exception of the third excited state of tB. It is important to notice that unrelaxed densities deliver almost the same overall picture as relaxed densities, which in the context of transition metal complexes translates in significant savings in time and resources.

To fully appreciate the benefits of the diagnostic analysis it is appropriate to apply the M_{AC} index to investigate the electronic transitions of heteroleptic complexes, in which a ligand is responsible for the delocalization and stabilization of the perturbed charge distribution that is established upon excitation. D and T complexes are exemplary in this regard. The Ruthenium atom remains coordinated with three ligands, among which, the primary ligand, here dppz or tpphz, is responsible for the formation of numerous charge-transfer states. The variety of the transitions increases considerably. Among the MLCTs, some involve the transfer of an electron from the metal center to the ancillary ligands, in the present case the bipyridines. Other MLCT transitions, the more represented, occur between the Ru atom and the main ligand (dppz or tpphz). Among these, further diversification can be made as the transferred charge can be accumulated in different specific regions of the ligand - a list of structure and abbreviations is provided in Appendix, Figure 55. Of course, the transition landscape is not limited to MLCTs. The same variety extends to localized transitions too. MC transitions appear as well. The M_{AC} allows the systematic cataloging of transitions and identifying of the anomalies related to the use of an inappropriate functional.

Unlike what occurred for bT and tB, the number of spurious or ghost states - in Figure 31 - is consistent. In the following, we try to rationalize the different types of "spurious" states and identify the most problematic ones.

Let us focus on the ghost and spurious states of the D complex. The full list of the calculated states with excitation energies, oscillator strength and computed M_{AC} values is reported in Appendix, Table 21.

Spurious and ghost states fall into a very specific range of D_{CT} values. This is not surprising given that these states are associated with an incorrect estimate of the spatial extent of the transition. The D_{CT} values of such states range from 2.2 and 4.2 Å, with the sole exception of S_{28} with a D_{CT} value exceeding 5.5 Å. This last, though is not very significant, as it lies very high in energy.

The difference between the two panels in Figure 31 is very little, regardless of the functional used. Therefore the gain in using relaxed densities is negligible, and an unrelaxed density calculation is fully admitted to discern the presence of any spurious/ghost

state. This observation is in line with what discussed previously in Chapter 6 for small organic systems, where we have observed that the oscillation between the values of ${}^{U}D_{\mathrm{CT}}$ and ${}^{R}D_{\mathrm{CT}}$ is only significant when the basis set used is very small, independently of the functional.

Most of the states labeled with S or G appear exclusively when functionals containing a low percentage of HF exchange, such as B3LYP and PBE0, are used. The use of CAM-B3LYP drastically reduces their presence. In particular, the analysis reveals a single ghost state - corresponding to the first excited state, calculated in PBE0 or B3LYP. The density difference of this last - in Figure 32 - shows that this state is an MLCT in which the orbital acceptor is highly delocalized over the entire ligand. Thus, based on the M_{AC} analysis, we deduce that the delocalization is an artifact of the method and this state erroneously appears too low in energy.

The same state calculated in CAM-B3LYP is in fact resized and localized on the phenanthroline near the metal center alone - as shown in the NTO analysis in Appendix, in Figure 58. Besides, for the same state, the oscillator strength increases from 0.0001 in PBE0 to 0.002 in CAM-B3LYP. This small value, though, suggests that S_1 remains of little relevance in absorption, and therefore, does not contribute significantly to the formation of the CT states that populate the emissive state.

The first state that is optically active is the fourth - regardless of the functional used. The diagnostic analysis classifies this state as spurious - when PBE0 or B3LYP are used - as it appears below the limit defined by equation 274. Once again, the difference density plots reveal that such state is mistakenly delocalized over the whole dppz ligand. The same state, calculated in CAM-B3LYP, is again less widespread, although to a lesser extent than in S_1. By contrast, the absorption spectrum calculated in CAM-B3LYP is significantly blue-shifted compared the calculated spectrum in B3LYP, and differs significantly from the experimental one. S_4 is responsible for the lowest energy band in the absorption spectrum. The label S, assigned according to the M_{AC} value suggest that S_4 is slightly overestimated, and should be therefore treated with caution. The orbital shapes calculated with CAM-B3LYP give an idea what the distribution of S_4 should resemble to, though the correction provided by the range-separated hybrid is too drastic.

In the same vein of the discussion above, one can analyze the spurious excited states at higher energy. The difference density representation of a selection of states marked as spurious after applying the M_{AC} diagnostic analysis are shown in Figure 32. The density distributions of such states changes as one moves to higher energy. At lower energy the spurious states have MLCT character. Gradually the character changes, and the contributions of the ancillary ligands become more pronounced. Finally the higher spurious states have ILCT character.

We conclude that the electronic transitions calculated using B3LYP and PBE0 are correctly distributed, but slightly underestimated in energy as compared to the experimental data. It is evident that the classification of a state as spurious is not as problematic as that of ghost states. The general image that we derive is that the states classified as spurious are only partially affected by error and the resulting interpretation is not compromised.

These observations hold with no exception for complex T. The extended tpphz ligand determines an increase in the observed number of ghost/spurious states, independently of the functional. The patterns observed for dppz, though, remain unvaried. The lowest excited state is classified as a ghost. As in complex D this state has MLCT character, with very little overlap between hole and particle orbitals. The inaccuracy of the method in describing this state has no impact on the study of the photochemical pathway of this complex, as this state does not contribute to the absorption and the luminescence is attributed to a state of triplet multiplicity which is accessed upon ISC from the initially absorbing singlet state [194, 208]. Once again the equivalence in the use of U and R densities is verified, as the computed ${}^{U}D_{\mathrm{CT}}$ values are only limitedly higher compared to the relaxed counterparts.

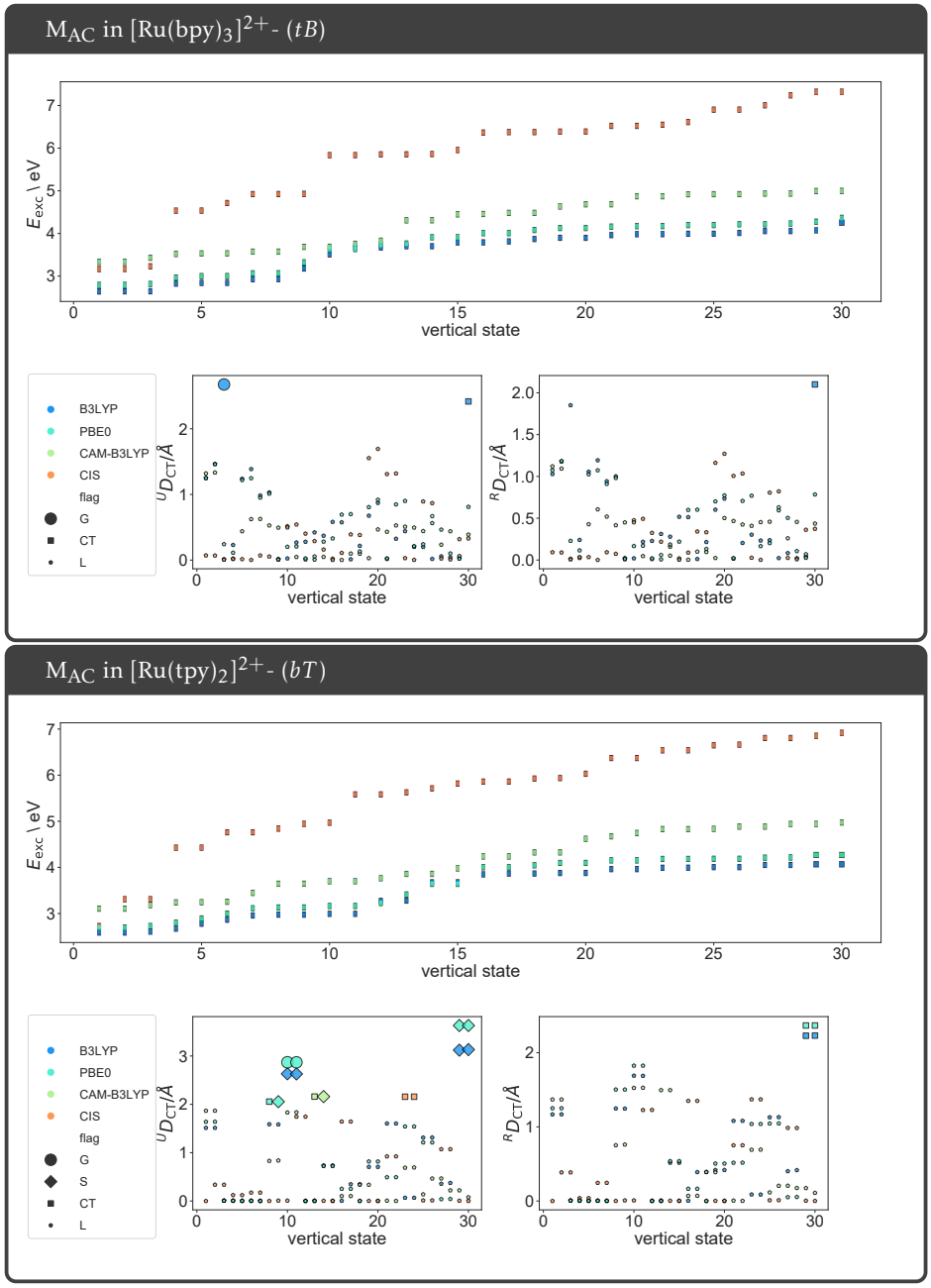

Figure 30: Energy levels, ${}^{U}D_{\mathrm{CT}}$ and ${}^{R}D_{\mathrm{CT}}$ values for the first 30 vertical states. The labels correspond to the following: G for ghost states, S for spurious states, CT for charge-transfer states, L for local excitations. Each type of state is denoted by scatters of different sizes and shapes, in descending order, G, S, CT, L. The length of the bar of each vertical transition is scaled in accordance with the size of the dot in the ${}^{R}D_{\mathrm{CT}}$ profile.

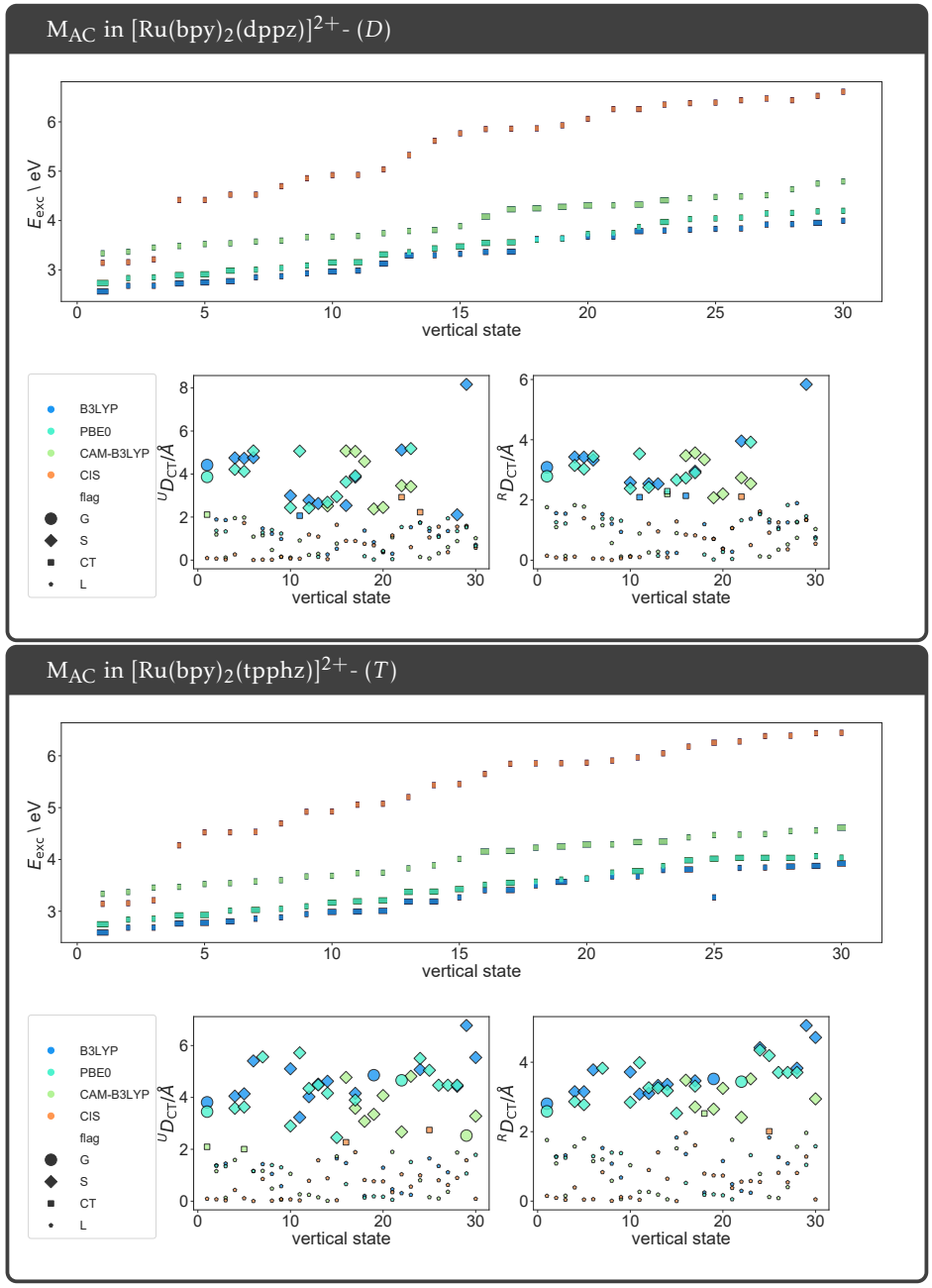

Figure 31: Energy levels, ${}^{U}D_{\mathrm{CT}}$ and ${}^{R}D_{\mathrm{CT}}$ values for the first 30 vertical states. The labels correspond to the following: G for ghost states, S for spurious states, CT for charge-transfer states, L for local excitations. Each type of state is denoted by scatters of different sizes and shapes, in descending order, G, S, CT, L. The length of the bar of each vertical transition is scaled in accordance with the size of the dot in the ${}^{R}D_{\mathrm{CT}}$ profile.

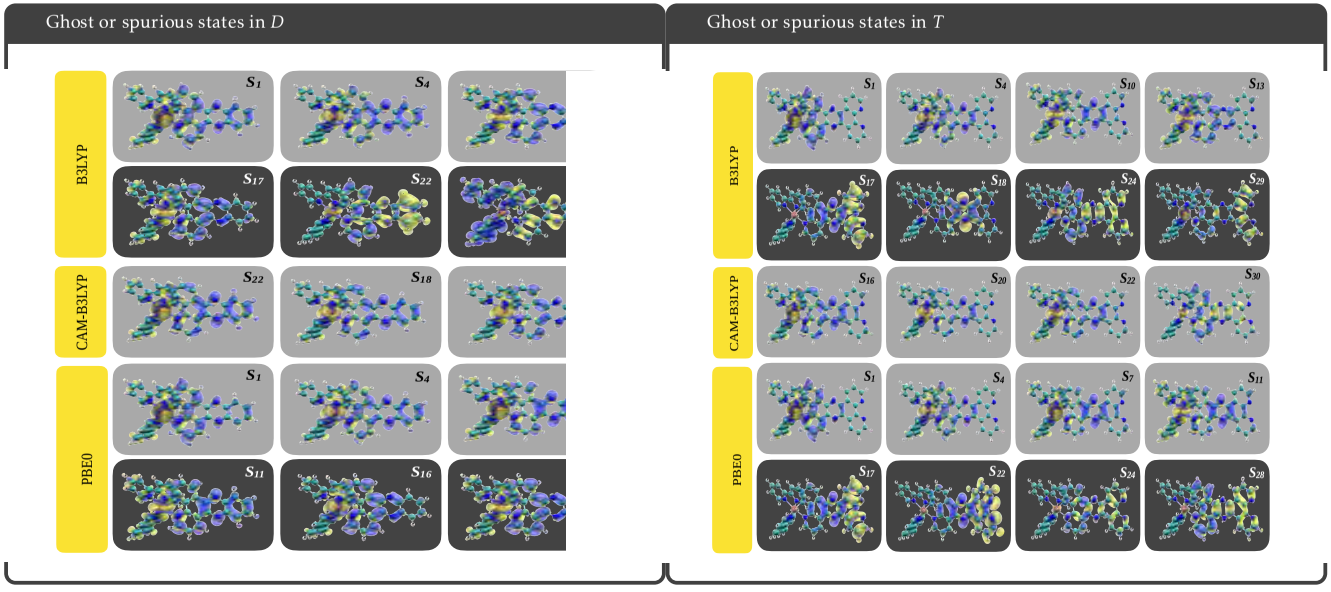

Figure 32: Difference density plots of a selection of ghost and spurious among the first 30 vertical states, computed in B3LYP, CAM-B3LYP and PBE0. Yellow and blue regions correspond respectively to the regions where the charge is depleted and accumulated upon transition. Spurious and Ghost states of MLCT character are represented with a light gray background, while spurious with ILCT character are represented with a dark gray background. The corresponding transition number is reported in the top right corner of each rectangle.

7.4.1 *Triplet states*

Although by now we have only mentioned singlet excitations, triplet excited states deserve a mention. The role of triplet states in *D* and *T* polypyridyl complexes is crucial. Previously, it has been shown that the relative energies of the low-lying triplet states of different nature—IL(dppz,tpphz), MLCT(bpy), MLCT(Tat), and MLCT(taT) govern the luminescence properties of such class of complexes - see Appendix, Figure 55 for a the nomenclature of the fragments. This observation is due to the different sensitivity of excited states of different character to the substituents, and to the environment in which they are created.

Once again, we have used the M_{AC} diagnostic to assess the quality of the triplet states in complexes *D* and *T*, and to determine their character and relative abundance. Figure 33 shows the excitation energies, relaxed and unrelaxed D_{CT} values of the lowest thirty vertical triplet states of the two complexed, calculated using B3LY. As for the singlet excitations the excited state manifold comprises excitations of various characters. However, for both complexes, the low-energy states are no longer dominated by MLCT states. Among the lowest states, at $\approx$ 2.4 eV and 2.6 eV - respectively in *D* and *T* - several ILCT transitions appear, involving both the dppz/tpphz and the bpy ligands - see Appendix, Figures 58 and 59. The M_{AC} diagnostics allows to classify several of the triplet states as ghosts, for instance T_2 in *D* and T_1, T_5 in *T*. It is important to notice that in the case of triplet states no distinction between spurious and ghost states can be made, as all vertical triplet states are dipole forbidden. This observation, however, does not mean that these states are of no interest. As already mentioned, low lying triplet states have been shown to be crucial in the photochemistry of such complexes [208], as they are rapidly accessed through intersystem crossing from the lowest absorbing singlet states. The presence of ghost states among the lowest triplet states suggests that one should proceed with all due caution, to select the correct state to optimize.

7.5 CONCLUSIONS

In this last analysis we showed how the M_{AC} diagnostics can be applied to provide a detailed analysis of the excited state manifold of metal complexes. The variety of types of electronic transitions present in organometallic compounds makes it difficult to characterize them in a systematic and unambiguous manner, especially since in TDDFT the choice of a functional can have a tremendous impact on the accuracy of the results when CT states are involved. Complex photochemical processes are closely linked to this class of transitions and mainly develops through these.

We have characterized the transitions of four metal complexes. The first two, homoleptic complexes, are substantially free of through-space charge-transfer states, while in the remaining two, heteroleptic complexes, the presence of a strongly conjugated polyaromatic ligand allows the the formation of though-space transitions. As these transitions can be delocalized across the entire length of the substituents, they are susceptible of being incorrectly modeled, using the most common density functional approximation.

As announced, the transitions in complexes such as $[Ru(tpy)_2]^{2+}$ and $[Ru(bpy)_3]^{2+}$ are free of errors related to the presence of charge-transfer transitions. The choice of the functional to be used can easily be done on the basis of the maximum similarity with the experimental spectrum. For complexes such as $[Ru(bpy)_2(dppz)]^{2+}$ and $[Ru(bpy)_2(tpphz)]^{2+}$ it is necessary to verify that no ghost states appear, which could compromise the interpretation of the photochemical behavior of the system. The diagnostic analysis revealed the almost total absence of ghost states among the singlet states, even when using hybrid functionals such as PBE0 and B3LYP. These functional also guarantee the best agreement with the experimental data. Their use is therefore to be preferred over range separated functionals. Triplet states should be treated carefully, as one cannot distinguish between spurious states and ghost states. By construction, triplet states have zero oscillator strength, therefore making it difficult to assess the margin of error associated with the calculation.

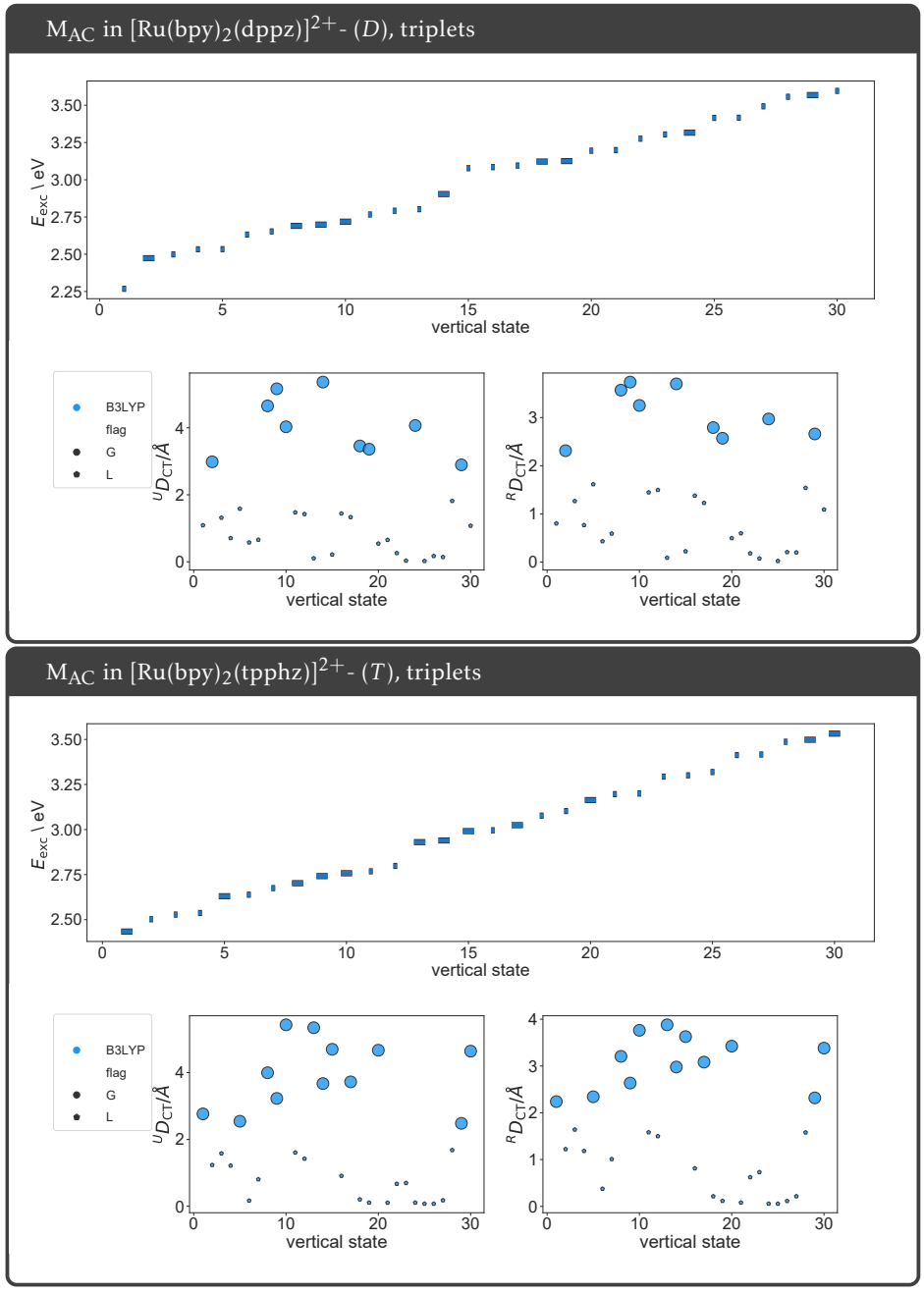

Figure 33: Energy levels, ${}^{U}D_{\mathrm{CT}}$ and ${}^{R}D_{\mathrm{CT}}$ values for the first 30 vertical *triplet* states. The labels correspond to the following: G for ghost states, S for spurious states, CT for charge-transfer states, L for local excitations. Each type of state is denoted by scatters of different sizes and shapes, in descending order, G, S, CT, L. The length of the bar of each vertical transition is scaled in accordance with the size of the dot in the ${}^{R}D_{\mathrm{CT}}$ profile.

Part III

EXPLORATION OF THE EXCITED STATE LANDSCAPE ALONG A RELAXATION PATHWAY BASED ON THE REORGANIZATION OF THE DENSITY

8

FOLLOWING EXCITED STATES IN MOLECULAR SYSTEMS USING DENSITY-BASED INDEXES

8.1 CONTEXT

In the previous chapters we have extensively discussed the concept of charge-transfer, how to measure the spacial extent of a given transition, what are the challenges in such measure, and how to handle them. By now, we have applied these concepts in the context of vertical transitions, occurring between the ground state and any excited state of interest. The logical step forward is to investigate the subsequent charge-reorganization process, leading to the population of the emissive state. This observation is consistent with the intuitive picture that, after a vertical excitation, a system will tend to structurally relax in order to minimize the produced excited state charge separation and reorganization. Here we extend the concepts introduced previously to account for excited-to-excited state transitions. In this context, the D_{CT} is no longer strictly related to the spatial amplitude of the charge separation produced by ground state to excited states electronic excitation, but to the distance between two excited states.

The present chapter is inscribed in this general context. The approach that we outline here combines together several density descriptors, originally devised for the qualitative interpretation of experimentally observed phenomena, and is aimed to provide a simple physical picture of the mechanism of excited state processes. Our strategy is intended to afford a computationally inexpensive characterization of excited state potential energy surfaces, which can be computed –on the fly- to allow both the identification of critical areas for TDDFT approaches and the qualitative recognition –in conjunction with energy criteria- of possible reactions paths.

We introduce, in the following, a new density based index, Π, which can be used to obtain a qualitative measure of the work necessary to redistribute the electron density going from one excited state to another at a given electronic configuration. Previously applied to disclose non-radiative decay channels from the first excited state to the ground state [2], this descriptor is simple, inexpensive, and can be coupled to any quantum method able to provide a description of electronic excited states. Indeed, it relies only on the knowledge of energetics and electron densities of the different electronic states involved in a decay. To exemplify the insights that this indexes may bring to the description excited state processes, we examine two distinct type of reactions. The first is an intramolecular proton transfer in occurring in CPDNO (1-(cyclopropyl)diazo-2-naphthol), an aromatic-azo compound, followed by the photo-induced charge-transfer processes in DMABN (N,N-dimethylaminobenzonitrile) and Phen-PENMe$_2$ (5-(4-dimethylaminophenylenylethylyn)-1,10-phenanthroline). All these molecules have been previously introduced in Chapter 6, where we have checked the reliability of the TDDFT methodology applied to compute

their potential energy curves along specific reaction coordinates. Besides, these systems have been extensively investigated and numerous studies exist in the literature, both theoretical [163, 216, 217] and experimental [188, 193, 218] level. The agreement with these earlier studies substantiates our results.

This chapter constitutes an adaptation of two previous works of myself, the first published in Journal of Computational Chemistry, in collaboration with Juan Sanz-Garcia, Marco Campetella and Ilaria Ciofini [6], the second, featured together with Anna Perfetto and Ilaria Ciofini and published in the Journal of Photochemistry and Photobiology A.

8.2 INTRODUCTION

Phototriggered charge-transfer reactions typically occur through the redistribution of the electronic charge induced by the interaction with light. The principal actors such processes, and in particular the ones we are about to describe are electrons and protons, which are transferred intramolecularly between different regions of a molecule. The reactions we examine belong to the category of excited state intramolecular proton transfer (ESIPT) and photoinduced electron transfer reactions.

The study of excited state (ES) reaction pathways, beyond the simple analysis of vertical excitations, far from the Franck–Condon region, is a flourishing research area [14, 19, 107, 127, 128, 150, 152, 219–221]. Indeed, localizing the most stable reaction intermediates, as well as shading light on the reaction pathways associated to photochemical processes, is still a challenge for quantum methods nowadays available.

To gain some knowledge from theory and computational approaches on photophysical and photochemical properties of photoactive molecules or materials is essential. As previously alluded to, these are used in a wide range of applications, from optoelectronic devices [222] to biological themes. The investigation of the mechanistic pathways that govern their photochemical properties is therefore essential not only for the understanding of their basic working principles but also for their design.

In this respect, it is our interest to develop simple tools to characterize the evolution of excited state of interest along a potential energy surface (PES). However, the concept of PESs implies that the Born–Oppenheimer approximation (BOA) holds, [27] which is generally true for reactions occurring at the ground state but may break down at the ES [223, 224]. In particular, in the case of many photoinduced processes occurring even in simple molecular systems, for specific nuclear coordinates two or more electronic ESs can get close enough so that their coupling cannot anymore be neglected, determining the breakdown of the BOA [19, 27, 95]. These nuclear conformations for which the PESs of different states are very close or even cross are commonly defined as “funnel” regions, and are indeed extremely important do disclose the photochemical and photophysical pathways of such systems. In particular, these last play a key role in defining their non-radiative decay pathways as well as their reactivity at the ES.

Simple approaches to identify these regions are therefore of great interest and simplify the description of phenomena occurring at the ES tremendously. There are at least two criteria that a method shall fulfill in order to deliver a good understanding of photochem-

ical processes. Firstly, it should reproduce correctly the potential energy surfaces (PES) of the excited states of interest, within and far from the Franck Condon (vertical excitation) region. Next, it should deliver a coherent picture of the photochemical process from the absorption to the emission.

Ab-initio excited state dynamic approaches [225–228] can provide these information but are often expensive for a routine analysis. By contrast, a static study of the PES as the one we adopt in the present chapter may provide a simplified picture of the possible decay channels in play, delivering a realistic, yet qualitative understanding of the whole process at an affordable computational cost.

Such research line is not unfrequented, and numerous theoretical studies [158, 192, 229–233], including the ones previously published in my own environment, [3, 128, 159, 164, 166, 216, 234] deserve a mention. As we saw in earlier chapters, the combination of robust and reliable density functional approaches and simple descriptors based on the electron density, provides a fair description of the PES at the excited state both from a quantitative (energy landscape) and a qualitative (hole–electron distance and charge transfer (CT) character) point of view. [1, 3, 4]

In the preceding chapters, this type of indexes were primarily aiming at the diagnostic of TDDFT based methodologies and description of excited states with a charge-transfer character, with the use of the so-called D_{CT} and M_{AC} indexes [5]. The present discussion, instead, primarily concerns the use of density-based indexes to follow the course of the reaction induced by light, by locating and characterizing the photochemical pathways - not necessarily in terms of minimum energy paths - pursued by the molecular system along the potential energy surfaces (PES) of the photochemically relevant states, from the Franck-Condon (FC) point on the spectroscopic state to the decay to the ground state with the formation of photoproducts. We do this based on the variation of the electron density distribution of the different excited states, through a recently defined index [2, 6] - so called Π - aimed at the identification of excited state potential energy regions where decay channels (both radiative or non-radiative) are highly expected. Unlike previous density descriptors, the Π index provides an estimate of the probability of different electronic states to interconvert, thus allowing to map the evolution of an excited state along a reaction coordinate. The Π index can also be rationalized in terms of classical electromagnetism, since this density-based index can be correlated to the inverse of the work (W_{CT}) necessary to reorganize the densities associated with two electronic ESs of interest.

The present chapter is thus the enforcement of the density-based approach outlined in the beginning of this thesis, motivated by the idea of proposing a strategy to follow the evolution of excited states along a given reaction coordinate. Here, we unveil the mechanistic details at work in different photochemical processes, through the Π index. We start our investigation by examining the excited state proton transfer occurring in CPDNO. Next, we analyze the ES-PESs of two dual-emissive molecules, namely DMABN and Phen-PENMe$_2$. Their chemical structures are given in Figure 34.

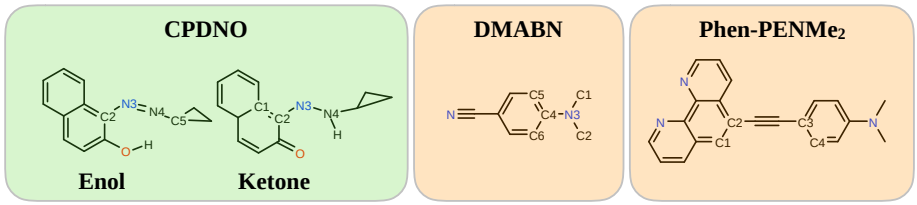

Figure 34: Schematic structure of the molecules which are discussed in the following. The colored boxes are used to highlight the different nature of the associated chemical processes, ESIPT in green and dual emission in orange.

8.3 Π descriptor for the study of excited state evolution and reactivity.

To characterize the nature and the evolution of the excited states, we computed both the D_{CT} and the Π indexes along selected reaction coordinate. A detailed description of the indexes mentioned above is provided in the literature [1,2,6]. As previously said, the D_{CT} quantifies the length of the hole-electron separation associated with a given electronic transition and therefore provides an estimate of the spatial extent of a given electronic transition, allowing to monitor the changes in the character of the excited states (for instance Locally Excited - LE versus CT). This index is calculated as the module of the distance between the barycenters of the charge density corresponding to the hole and particle. Positive and negative barycenters are obtained by integration of the associated electron densities, ρ^+ and ρ^-. These last are derived from the difference in total density of the two states S_p, S_q involved in a electronic transition.

The Π index broadens the information provided by the D_{CT}, by coupling this last both with a charge displacement and an energetic term. The definition of such index is disarmingly simple: let us consider two classical point charges q^+ and q^-, with a displacement vector ($\mathbf{r}$) pointing from the negative charge to the positive charge. The electric dipole moment which is established between them is given by

$$\Delta\mu_{pq} = |\mu_q - \mu_p| \tag{275}$$

One can expand $\Delta\mu_{pq}$ as a function of the actual hole-particle transferred charge, q_{CT}, and the charge-separation length associated with the given electronic transition, D_{CT}. Combining this product with the energy gap ΔE, the Π index is readily obtained as,

$$\Pi = \frac{1}{\Delta E \cdot D_{CT} \cdot q_{CT}}. \tag{276}$$

This descriptor qualitatively satisfies also some conditions that can be drawn based on chemical intuition. Indeed, one may expect that the closest the energy between any two states, the higher the probability for the system to undergo a non-radiative relaxation. Besides, if the total electronic density is similarly distributed in the two states involved, the probability of interconversion will be maximal. The first criterion translates in an

inverse dependence of the probability of state crossing on the two states energy gap. Hence, Π will diverge in the case that two states are degenerate. Conversely, the $D_{CT}{\cdot}q_{CT}$ term accounts for a complementary and intuitive interpretation, namely the fact that the interconversion will occur more easily if the electronic density redistribution associated with the transition is least. In other words, although the energy gap between the two states will be the leading term for many photochemical reactions implying a crossing of states, for a given energy gap a decay will actually be more efficient the more similar the electronic densities of the starting and final states. Since, quantitatively the D_{CT} value calculated between two states with equivalent charge distributions equals zero, the product $D_{CT}{\cdot}q_{CT}$ may be the leading term to identify radiationless pathway, that may be responsible for a peculiar photoreactivity.

Π can be also discussed according to the classical electromagnetism formalism. Here, the work (W_{CT}) necessary to redistribute an ensemble of charges in an electromagnetic field is defined as the integral over the space of the product between the transferred charge, the field, and the infinitesimal displacement. In this case, for each nuclear configuration undergoing a S_p to S_q interconversion, the electric work W_{CT} is a function of q_{CT}, which represents for the electronic charge rearranged when going from one electronic state to the other, of the transition length -D_{CT}, and, finally, of the transition energy ΔE, which magnitude is proportional to the field in which such rearrangement takes place. Hence,

$$\Pi \propto \frac{1}{W_{CT}}. \tag{277}$$

It should here be noted that in the limit of an infinite ΔE, W_{CT} diverges, as it should be expected for the work necessary to move a charge in an infinite field, which will let Π tend to zero. Conversely, if ΔE approaches to zero, W_{CT} will drop to zero, letting Π diverge to infinite. These observations all suggest that decay channels should appear in those regions of PESs where the work needed to interconvert two different ESs is the lowest, that is, where Π is the greatest.

8.4 INSIGHTS ON THE MECHANISM OF THE EXCITED STATE PROTON TRANSFER IN CPDNO

CPDNO is known to undergo an intramolecular proton transfer at the excited state. This photoinduced proton transfer involves crossing between a $\pi\pi*$ and a $n\pi*$ state. At the planar geometry, in the FC region, the reaction evolves almost barrierless along the PES of the bright $\pi\pi*$ state, connecting the ES enol* and the keto* form (in Figure 34). To examine the reaction, we scanned the $dN-H$ distance in the 1.8 – 1.1 Å range, while relaxing all other degrees of freedom. Details on the computational protocol are reported in Appendix, in Section 11.1.

At the planar configuration, that is, along the minimum $\pi\pi*$ profile the structures having $dN-H$ values between 1.8 and 1.4 Å are in the enol form, while around a distance of 1.3 Å one can consider the ketone to be formed. It is known that these two conformers are involved in two different independent pathways leading back to the GS [163, 188].

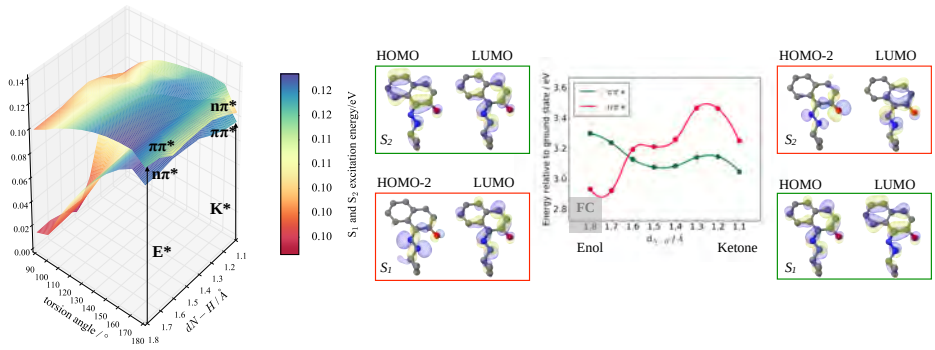

Figure 35: On the left, the TDDFT PES computed for the S_1 and S_2, as a function of the two twisting angles and $dN-H$ bond distance. On the right, selected orbital pairs in the enol and in the ketone regions respectively.

Hence we perturbed each the structure along the $\pi\pi*$ minimum profile by twisting specific coordinates, in order to get a full picture of the excited states PES, including the regions where the ketone and the enol tautomers relax to GS state. In practice, we generated nine additional structures at each step of the proton transfer reaction coordinate by varying a specific dihedral from 180° to 90°. For the enol forms the selected dihedral is the C2C3N4N5, involving the out-of-plane torsion of the cyclopropylic group. For the ketone structures, instead, the torsion (C1C2N3N4) involves the twisting of the cyclopropanamine group. A sketch of the ketone and enol structures is provided in Figure 34.

At the Franck-Condon geometry (FC), the $n\pi*$ state is lower in energy with respect to the $\pi\pi*$ state by ≈ 10 kcal/mol. As the proton moves towards the nitrogen, the $\pi\pi*$ state decreases in energy. For a N-H distance around 1.6 Å the two states become very close in energy and at shorter N-H distances, the $\pi\pi*$ state becomes the lowest in energy, as represented in Figure 35. Close to the Franck-Condon region, the dark $n\pi*$ state has local character and is mainly related to an HOMO-2 (n) to LUMO ($\pi*$) excitation. Both these orbitals are mainly localized on the diazenylphenol moiety, reflecting the localized nature of the transition. The $\pi\pi*$ bright excited state is predominantly stemming from a HOMO-LUMO excitation and is accompanied by a significant charge-transfer from the naphthalene fragment to the diazenyl part. After the crossing the picture is reversed.

The analysis of the Π index at different torsion-$dN-H$ pairs, in addition helps to clarify the preferential pathway of the tautomerization. The calculated Π function along the $n\pi*$ to $\pi\pi*$ interconversion trajectory displays one distinct peak corresponding to the $n\pi*/\pi\pi*$ crossing region. As soon as enough energy is provided for the proton to move towards the nitrogen, at about 1.6 Å, the $\pi\pi*$ state is accessed, and the enol-to-keto transformation occurs without any barrier. The Π index profile in Figure 35 points out the trajectory through which the reaction takes place, and nicely highlights the dihedral-distance pairs

along which the reaction evolves, preferentially. Although the proton transfer occurs mainly in the planar configuration, this is not the only lay in which the tautomerization takes place. Figure 36 well illustrates this.

The torsion of the diazenyl fragment shifts the $\pi\pi*$ state lower in energy, thus flattening the excited state surface. As a consequence the crossing does not necessarily occur at $dN-H$ 1.6 but may occur at shorter distances. While at $dN-H$=1.6 Å the leading term is the energy, at $dN-H$=1.3 $D_{CT}{\cdot}q_{CT}$ prevails. Through the Π index, we have identified an additional region of the PES where the S_1/S_2 is efficient, which appears at short $N-H$ distances. Although the energy gap in this region is large, the electronic densities of the two states are similarly distributed. In turn, in such region, the reorganization energy required to interconvert the S_2 $\pi\pi*$ and the $n\pi*$ attains a minimum, and the S_1/S_2 transition occurs smoothly.

Identifying the existing excited state decay pathways can be of great importance, especially if one wants to control a photochemical process, for example avoiding the system to evolve to a particular state, or enhancing the fluorescence from a single channel. Here, we have demonstrated how with a static approach we can identify possible non-radiative channels - not immediately evident only on the basis of energetic arguments - based on the similarity of the electronic density distributions of the two states. In the following we apply the Π index to identify the decay pathways at play in two excited state charge-transfer reactions. We aim to uncover the decay channels that contribute to populate the emitting levels.

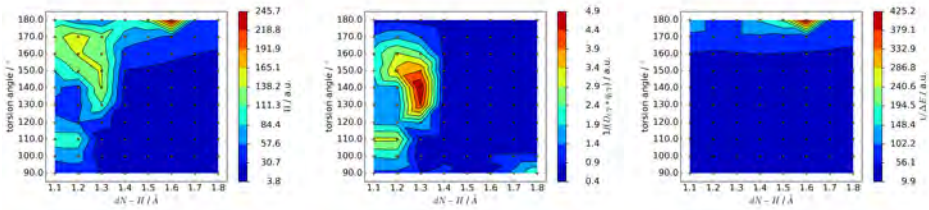

Figure 36: Left to right: 2D map of the Π index, $D_{CT}{\cdot}q_{CT}$ map and $1/\Delta E$ map, all in a.u., calculated along the two reaction coordinates. All quantities are computed at the PBE0/6-31G(d) level of theory.

8.5 UNCOVERING THE EXCITED STATE PATHWAY TO DUAL EMISSION

Dual emission in molecular systems is a phenomenon increasingly reported in the literature and attracting ever-growing interest [235–239]. Depending on the mechanism at the origin of dual emission, various classes of compounds may be identified. Indeed, widely documented is dual fluorescence occurring in small organic dyes undergoing excited state intramolecular proton-transfer (ESIPT) reactions [83, 158, 240–243] or excited state intramolecular charge-transfer processes. [128, 193, 216, 230, 237, 243–246]. Such dual-emission phenomena have been exploited in the synthesis of various novel

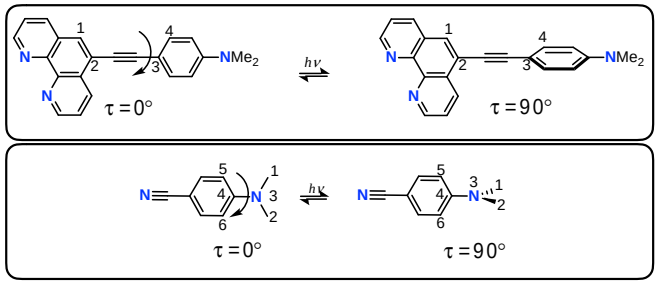

Figure 37: Schematic structure of the Phen-PENMe$_2$ (top) and DMABN molecules in the planar (τ=0°) and twisted conformations (τ=90°).

chemosensors with different target applications [149, 241, 247]. Dual emission through Thermally Activated Delayed Fluorescence (TADF) deserves of being explicitly mentioned [229, 235, 236, 248–250]. These systems are indeed regarded as promising next-generation organic electro-luminescent materials due to their potentially high internal quantum efficiency.

Besides their applications, molecules displaying dual emission provide a perfect playground to test and validate theoretical approaches aiming to investigate the structural and electronic features of excited states which are involved both in radiative [3, 225] and non-radiative [2, 164, 216, 228, 240] decay pathways. Indeed, besides molecular systems where dual emission is associated to a change in the chemical nature of the emitting species (ex. protonation state) [149, 240–242, 251], native dual emission is usually associated to the presence of two emissive -bright- excited states of different character that can be both populated and that are stabilized by a differential structural reorganization.Hence, theoretical approaches aiming at describing this kind of phenomena are of great interest.

In this respect, we consider two dual-emissive systems, namely the DMABN and Phen-PENMe$_2$ - in Scheme 34. Although the structural features which underlie the peculiar photochemical behavior are similar in both systems, the full mechanism ruling the interconversion leading to the dual emission is unique in each molecule. Since the discovery of dual emission by Lippert et al. [252], the DMABN has been the object of the investigation in an uncountable number of papers, as it is among the smallest molecular systems displaying such characteristic property. To retrace the findings of these studies through our index, seemed necessary.
By contrast the mechanism of the dual emission in Phen-PENMe$_2$ is still debated. Here, we explored the excited state landscape of these two systems by means of the Π index. We seek into different possible decay pathways thereby providing a deeper understanding of the electronic origins of the observed dual emission.

8.6 MULTIPLE PATHS TOWARDS DUAL EMISSION IN DMABN

In the last two decades, DMABN molecule has been the object of numerous experimental and [189, 191, 192, 231, 232, 252–264] studies, devoted to uncovering the origin of its dual-emissive properties [189, 252] - the references chosen are an essential but relevant collection. Several models have been proposed [189, 191, 217, 218, 221, 265–267] in the literature, which reveal the presence of different states accounting for the peculiar photophysical properties, depending on specific reaction coordinates. Among all the proposals, the one allowing better fitting with the experimental evidences is the so-called twisted-charge-transfer (TICT) model proposed by Grabowski and co-workers in 1973 [217]. According to the TICT model, the initially promoted planar and LE state interconvert rationalness to a CT state-from the amino-donor to the benzonitrile acceptor—upon rotation of 90°of the dialkylamino group with respect to the benzonitrile plane, yielding a conformation where the donor and acceptor groups of the molecule are perpendicular. The TICT model takes the twisting coordinate [189, 265] as the origin of the dual-emissive properties of the DMABN. Roughly 20 years later (in 1993), a different model was proposed by Zachariasse, the so-called planar - CT (PICT) [257, 268, 269]. This model predicts the formation of a quinoidal intramolecular CT (ICT) state promoted by the pyramidalization of the natively planar $-NMe_2$ group. This model implies that the coordinate for the LE to ICT interconversion is the aminomethyl out-of-plane wagging motion together with a quinoidal ring deformation TICT [191, 218, 231, 232, 254, 263, 270] and PICT [257–259, 271] models have been object of a large debate and a considerable number of works have been devised to relate the experimental photochemical properties to the electronic and geometric structures of the computed ICT states. In the following, we explore the potential energy surfaces described by these two coordinates through the Π index, to investigate the ICT to LE interconversion.

Starting from the planar ground state optimized geometry, we performed a relaxed scan, individually changing a linear combination of the two dihedral angles (D1 and D2), namely, the D1(C1N2C4C5) and the D2(C3N2C4C6). Refer to Scheme 37 for labeling. Indeed, in analogy with previous studies [191, 253], we followed independently a wagging (δ) or a twisting (τ) motion, depending on the angle θ defined as $\frac{1}{2}(D_1 + D_2)$. In order to construct the wagging motion of the dimethylamino moiety both dihedral angles were changed about the same amount, but opposite sign. In this case symmetry is C_s (for a 0° or 90° twisting angle). On the contrary, an equal change in the two dihedral angles leads to the twist of the amino group with respect to the planar benzonitrile ring. Along this coordinate, a C_2 symmetry is maintained. We constructed ten structures, corresponding to the twisting of the dimethylamino group from 0° to 90°. For each structure, we varied the wagging angle, up to 25° in steps of 5°.

Figure 38 shows the potential energy profile of the first two excited states as a function of twisting and wagging coordinates. Clearly, a crossing between the S_1 and S_2 surfaces takes place at a twisting angle of roughly 40°. At 0° the S_1 can be described as a combination of a HOMO-1→LUMO and a HOMO→LUMO+1 excitation, respectively, contributing by 9% and 91%. This state has a LE character, as confirmed by its low $D_{CT}[^{S_1}_{S_0}]$ value

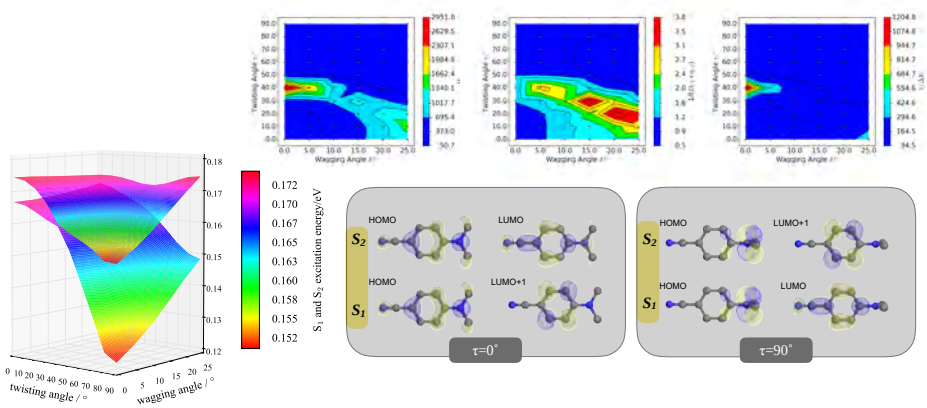

Figure 38: On the left:TDDFT PES computed for the S_1 and S_2, as a function of twisting and wagging angles. Top right: 2D map of the Π index, $D_{CT}{\cdot}q_{CT}$map and $1/\Delta E$ map, all in a.u., calculated along the two reaction coordinates. All quantities are computed at the PBE0/6-31G(d) level of theory. Bottom right:selected orbital pairs in the planar and twisted conformations, respectively

of 0.87 Å. Conversely, for the same geometrical structure, S_2 results essentially from a HOMO→LUMO excitation (96%) with a small percentage of a HOMO-1→LUMO+1 excitation (4%). In this case, a large $D_{CT}[^{S_2}_{S_0}]$ value is computed (1.81 Å) and a dipole S_0 moment by 7.5 Debye greater than the S_1 dipole (4.0 Debye), both connotative of CT character. As the dimethylamino group approaches the 90° twist the picture is indeed reversed, the HOMO→LUMO character changing from $\pi\pi*$ to $n\pi*$ (see Figure 38). Thus, for larger twisting angles, the S_1 progressively changes its nature to be the CT state observed at planar geometry, with large CT, large polarity, and small oscillator strength, due to the poor overlap between the nitrogen lone pair orbital and the π ring.

Figure 38-(a) shows a 2D map of the Π index calculated in the space of twisting and wagging angles. A clear peak appears in correspondence of 40° twist and 0° wagging angles. This spike, by far larger than what observed for any other pair of dihedral angles, clearly indicates that the electronic distributions are most akin is at this point, providing us with an unequivocal interpretation of the crossing occurring at the same spot in the PES. Once again, the decomposition of the Π index map endorses a step forward in the interpretation, yielding a clear and intuitive picture of the crossing at different twisted/wagged geometries. Figure 38 shows the distribution of the $1/\Delta E$ function along the two reaction coordinates. Close to the region of δ=0° and θ=40°, the inverse of the energy has the same behavior as the Π function, scaled by a factor of roughly a third. The $D_{CT}{\cdot}q_{CT}$displays a minimum in the same region. Unlike in the $1/\Delta E$ surface, this shallow region propagates in the same range of twisting values over the whole range of wagging angles, revealing a decay pathway connecting the 0° δ - 40° τ region and the 25° δ -10° θ region.

We have mentioned earlier that the Π index is inversely proportional to the work that needs to be accomplished to rearrange two charge distributions. Hence, the maximum region in the Π function points out the portion of the reaction space where the work needed to reorganize the S_2 into S_1 (and vice-versa) is the least, and the LE to CT transition is more likely to occur. Indeed, a large wagging motion of 25° strongly increases the possibility of the decay to occur at small twisting angles, around 10°. However, as soon as the twist becomes larger, the wagging motion reduces the probability of a non-radiative relaxation and with it the likelihood of the CT state to be populated.

In agreement with previous theoretical and experimental findings, we can assert that, while the twisting coordinate remains predominant, the wagging motion contributes to convey the system toward in the ICT state (where the emission occurs). In summary, the Π index individuates the S_1/S_2 crossing at the correct position, and more importantly it helps to identify other non-radiative decay channels, highlighting the role of the inversion mode on the ICT process in a simple and unequivocal manner.

8.7 AN EXCURSION THROUGH THE EXCITED ENERGY LEVELS OF PHEN-PENME$_2$

Phen-PENMe$_2$ can be considered as a typical push-pull system thus similar to many dual-emissive molecules relying on a Donor-π bridge-Acceptor structure (D-π-A). It is composed of a 1,10-phenanthroline core functionalized with a dimethylaminophenyl group acting as an electron donor, as shown in Figure 37. Recent combined experimental and theoretical studies performed by some of us [193,216] clarified that the observed dual emission is associated with the existence of two different emissive states: a planar Intra-Molecular Charge Transfer (ICT) state corresponding to an electronic transition from the donor moiety to the phenanthroline core, and a Locally Excited (LE) - state centered on the 1,10-phenanthroline, in which the donor and acceptor are orthogonally oriented. These earlier experimental and theoretical studies also investigated the solvent dependence of the dual-emission phenomenon and highlighted the importance of the use of polar-aprotic solution to allow for the formation of both conformations, thus yielding the dual emission. If the nature of the emissive states has been disclosed, [216] the pathways connecting the excited states initially populated in absorption to the ones that actually emit has not yet been thoroughly analyzed. This is the question we aim to answer in this work, using density-based descriptors.

8.7.1 *Considerations on the energy profiles of the lowest excited states.*

To investigate the photophysical behavior of the Phen-PENMe$_2$ molecule we analyze the evolution of the ground state and of the first six excited states, along the coordinate of interest (in Scheme 37). This last involves the formation of a planar and an orthogonal conformer, which differ in the orientation of phenyl and phenanthroline rings. Ground state DFT calculations computed at each reaction step revealed a rather flat ground state potential curve. The planar structure (τ=0°) is the minimum, though only by 0.04 eV

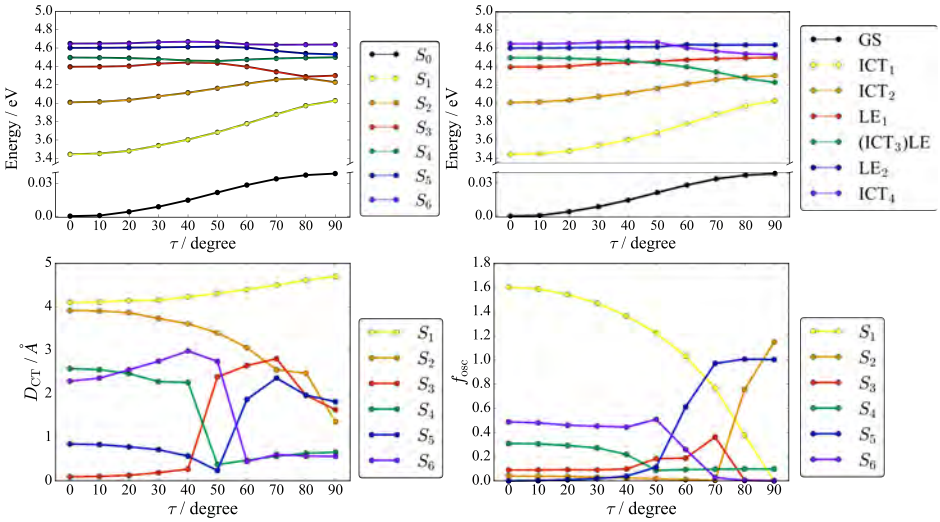

Figure 39: Ground (S_0) and first excited states (S_1-S_6) computed energy profiles (in eV) along the τ torsional degree of freedom. Upper-left panel: the excited state labels follow the energy indexing at τ°; upper-right panel: the excited state labels are assigned according to their nature at τ=0°. Lower panels: computed D_{CT} (in Å) and oscillator strength (f_{osc}, in a.u.) associated to each excited state, labeled according to the energy.

(1.45 kcal/mol) lower in energy compared to the orthogonal conformation (τ=90°), the maximum of the ground state curve.

Excitation in the 3.5-4.0 eV (354-310 nm) energy regime, populates the first excited state (S_1). All along the reaction coordinate, the potential energy curve of S_1 (in yellow in the upper panels of Figure 39) increases monotonically, without any crossing over other excited states curves. The absorption is most efficient in the Franck-Condon region - where the oscillator strength is maximal (1.60 a.u.) - and decreases ceaselessly, down to a value of 0.0 a.u. for the twisted conformation (τ=90°).

Figure 40, showing the normalized Boltzmann distributions of each state, points out to similar conclusions. Indeed, the ground state appears to be equally populated at all reaction steps, while the first excited state S_1 is only accessible in the $0° < \tau < 20°$ region. As a remark, conventional DFT functionals tend to overestimate the strength of π - conjugation, with a consequential flattening of the ground state profile [272], and deprecation of the GS Boltzmann population, though by using a range separated hybrid we mitigate this effect. To identify the local or non-local character of each state, we rely on the computed D_{CT} values [1]. S_1 possesses a charge-transfer character, denoted by the large D_{CT} values all along the reaction coordinate - ranging from 4.096 Å (τ = 0°) to 4.699 Å (τ = 90°). Accordingly, the two main-contributing natural transition orbitals (NTOs) in Appendix, Section 11.5 for such transition occupy two spatially different regions: the hole-orbital localizes on the dimethylaminophenyl donor fragment, while the particle sits

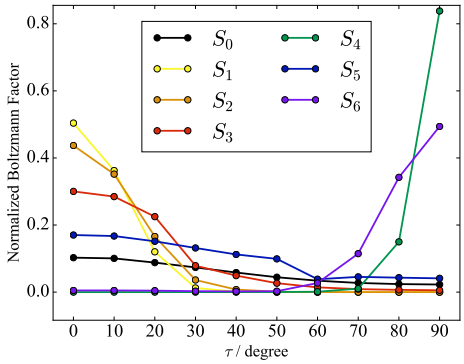

Figure 40: Computed normalized Boltzmann factors for the ground state and first six excited states (labeled as a function of their nature according to Figure 39 upper-right panel) as a function of τ dihedral angle. Each curve is normalized w.r.t. its maximum value.

on the phenanthroline as expected for a donor to acceptor transition. The marked CT character may also be inferred by the significant dipole moment variation computed for the S_1-S_0 transition (≈12 Debye at τ = 0°). Consistently, the D_{CT} is related to the norm of the difference in dipole moment $\Delta\mu_{ES-GS}$.

Irradiation at 4.0-4.2 eV (309-293 nm) allows the second excited state to be accessed (orange curve in upper-left image in Figure 39). The energy profile of S_2 increases in energy until it reaches its maximum and approaches the third excited state at about τ = 80°. At this point, we have the choice to analyze the energy profiles either according to their placement relative to the ground state curve or according to the nature of each excited state. This duple representation (shown in the upper left and right panels of Figure 39), turns out to be a handful approach, precisely to follow the evolution of the excited states, condensing the information provided by different observables - energy D_{CT}, and oscillator strength (f_{osc}) - in a unique picture. The Boltzmann population curves - in Figure 40 - are also labeled according to the nature of the states.

The D_{CT} profile computed for S_2 ranges from 3.913 Å at τ = 0° to 1.355 at τ = 90°, denoting a change in nature from a charge-transfer state to a locally excited one. Accordingly, the $\Delta\mu_{ES-GS}$ decreases by one order of magnitude, converging towards the ground state value (10 Debye at τ = 90°). Besides, S_4 changes from a dark state at τ = 0° (f_{osc} = 0.039) to a bright state at τ = 90° (f_{osc} = 1.148). S_3 (red curve in the upper-right panel of Figure 39) is only accessed irradiating at energies higher than 4.4 eV (289 nm). Also, this excited state approaches both S_4 and S_2 at $\tau \approx 30°$ and $\tau \approx 80°$ respectively. According to Figure 40, the population of S_3 (LE_1), decreases considerably, going from 0° to 90°, while the opposite occurs for S_4. As a result, one may infer that a crossing involving S_4 and S_3 occurs around τ = 30°- 40°. This inversion also appears in the D_{CT} profiles, where the S_4 and S_3 curves cross, pointing out a change in nature of the two states. In the τ = 0° to τ = 40° window, S_2 has a marked CT character, which translates in D_{CT} values ranging

from 2.581 to 2.262 Å. S_3, on the other hand, exhibits small D_{CT} values, synonymous of a localized transition (0.1-0.2 Å). At $\tau \approx 50°$, the picture is inverted. Here, the fourth excited state localizes on the dimethylaminophenyl fragment - the D_{CT} value drops to 0.374 Å while S_3 takes over the CT character (2.388 Å). At this stage, S_4 remains unvaried till the completion of the twist, while S_3 approaches S_2 close to $\tau \approx 80°$. The CT length decreases for both S_2 and S_3 states to ≈ 1.5 Å for the fully twisted conformation. As we will discuss later on, the S_4-S_3 inversion is the critical step to access the dual emission.

The photochemical pathway outlined results in the population of the S_4 state. In summary, S_3 acts as a bridge between S_4 - bright CT state in the FC region - and S_2, LE state - initially dark, and turning into a bright state around 80°. The NTOs in Appendix, Section 11.5, render an orbital picture of the changes in nature of the corresponding electronic transitions. Finally, the higher excited states, S_5 and S_6, require respectively excitation energies of 4.60 eV (269 nm) and 4.65 eV (267 nm) to be accessed. The corresponding D_{CT} curves cross around $\tau = 55°$, suggesting an inversion in their character. S_5 approaches then the trajectory of S_4 at $\tau \approx 90°$. The latter, though, lies ≈ 0.2 eV above S_3, limiting the mixing with the lower lying states. S_6 (ICT_4), however, appears to be populated between 50° and 90°, suggesting that it may contribute to feeding a non-radiative channel transferring its population to the lower states. It is worth recalling that, due to the very low energetic barrier, at the GS the molecule is able to freely rotate, hence all conformations are accessed. Irradiating the molecule at low energies limits the access to the excited state levels to the sole S_1. This, in turn, prevents the twisting and with it the formation of the LE state, thereby leading to a single emission from the planar ICT_1 (S_1). By contrast, exciting with sufficient energy, all excited states may be reached, leading to a multitude of decay pathways.

8.7.2 *Simulation and interpretation of the observed absorption spectrum*

Before analyzing in details the decay pathways it is useful to comment on the absorption properties of Phen-$PENMe_2$, as such analysis will later be helpful to disclose the mechanism leading to the dual emission. The simulated absorption spectrum at each reaction step (in Figure 41) reflects the vanishing of the ICT_1 state and rising of the LE state as the molecule twists. In the planar conformation ($\tau = 0°$), the absorption is dominated by a single transition at 355 nm. The resulting broad absorption band is ascribed to the lowest excited state, S_1 (Phen-$PENMe_2$), of CT character. The band at 270 nm arises from two higher ICT states - S_4 and S_6 - and, to a smaller extent, from an LE state of $n\pi*$ character (S_3). Despite the low oscillator strength of the states involved - they are not exceeding 0.5 a.u. at 0° - the band appears intense, as the three states involved (S_3, S_4, and S_6) are relatively close in energy.

At ($\tau = 90°$), the absorption spectrum consists of a single band at 296 nm - with a shoulder at higher energy (276 nm). This band is ascribed to vertical transitions stemming from two states: a LE state (S_2) of $\pi\pi*$ character centered on the 1,10-phenanthroline fragment and an ICT state (S_5). The absorption spectra computed at intermediate values of τ smoothly connect these two limiting pictures. The lowest energy band blue-shifts

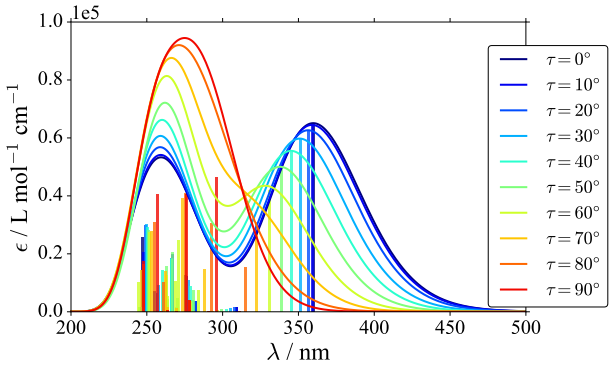

Figure 41: Absorption spectrum of Phen-PENMe$_2$ simulated by Gaussian convolution of the vertical transitions using a fmwh of 0.2 eV, computed at fixed dihedral angles, ranging from 0° to 90°. The color-coding highlights the raising and vanishing of the LE and ICT$_1$, respectively.

as the molecule twists and disappears entirely at $\tau \approx 90°$. At the same time, the highest energy band rises, while increasingly red-shifting.

The effect of the solvent in Phen-PENMe$_2$ was investigated previously [193, 216]. These studies illustrate that LE emission can be enhanced or suppressed by tuning the polarity of the solvent. Polar protic solvents stabilize the emission from the twisted species by intermolecular H-bonding, while in non-polar solvents a single ICT emission is observed. Therefore, solvation effects were here accounted for using acetonitrile, a polar solvent with reduced ability to form hydrogen bonds, which enables to access both emission bands.

As Phen-PENMe$_2$ freely twists in acetonitrile, each conformation contributes to the absorption. Therefore, it is convenient to estimate an average absorption by pondering each of the spectra – calculated at different values of τ - using their corresponding GS Boltzmann weights. The outcome is shown in Figure 42. The band around 350 nm is the result of the ICT$_1$ (S_0 to S_1) transition. The highest energy band at 265-295 nm arises from the convolution of mainly two different states, whose contribution is highlighted with a blue background in the simplified Jablonski diagram reported on the right hand of Figure 42. The transitions lying between 280 and 295 nm correspond to the evolution of the ICT$_3$ state, stemming from the S_0-S_4 transition in the $0° < \tau < 40°$ window. The same state is then populated by S_0-S_3 transition at dihedral values between 40° and 70°, and by S_0-S_2 transition at $70° < \tau < 90°$. Slightly higher in energy, at 280-270 nm the S_0-S_4 ($0° < \tau < 60°$) and S_0-S_5 transition ($60° < \tau < 90°$) sum up with the other closely lying transitions to form the second band.

8.7.3 *Interpretation of the excited state pathway*

Up to now, we have used a combination of several observables, each bearing a different physical meaning, to sketch a map of the excited state pathways from the absorption region

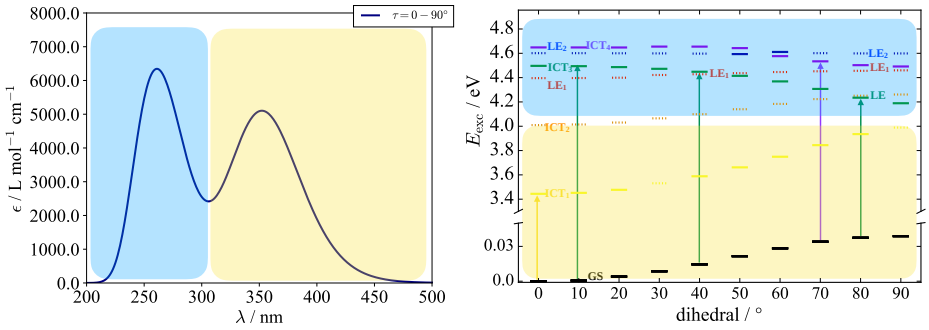

Figure 42: Left: Boltzmann weighted simulated absorption spectra of Phen-PENMe$_2$. Right: Jablonski diagram describing the absorption phenomena occurring in the Phen-PENMe$_2$ molecule.

to the emitting one. Also, we have postulated the existence of several decay channels. However, to reach the correct interpretation, it is essential to assess the relative importance of each. The Π index, precisely addresses this question. It is important to mention though that the methodology we are about to discuss is based on static considerations. Therefore, it does not give any indication on the time-scale of the photochemical process. As a result, any consideration on the kinetics of the electronic process remains out of our scope.

As previously mentioned, the Π index combines energetic arguments - ΔE - and a measure for charge rearrangement - $D_{\mathrm{CT}} \cdot q_{\mathrm{CT}}$ - and can be used as criteria to detect the presence of non-radiative decay channels. It is useful to compare the relative value of the Π between electronic transitions that involve a common electronic state. This approach provides a reasonable estimate of the relative likelihood of a decay channel, connecting more efficiently an electronic state with one or another state, lower in energy. Intuitively, this information shall be coupled with the vertical absorption spectra, in order to map the excited states all through the pathway that brings to the emission. As for this aspect, a radiative relaxation yielding an emission from any excited state S_q necessarily implies that this particular state of interest is populated either directly, by irradiation, or by decay from an energetically higher excited state. The Π index, combined with the absorption data, allows to estimate the relative efficiency of the relaxation pathways connecting any two states all along a reaction coordinate. The result is a qualitative strategy, which delivers a consonant interpretation of a photochemical process, in an uncomplicated manner. Besides, the Π index is also computationally inexpensive, which is often not the case when one uses alternative approaches to deal with such questions. Undoubtedly, the global understanding of the physical phenomena will strongly depend on the quality of the ground, and excited states computed PES and thus will be affected by the level of theory (method and basis set) used to calculate densities and energies. This said, the level of theory which we have used to perform our calculations was proven to be well accurate - as discussed in Chapter 6. Besides, the results of a previous benchmark [128] attest a good

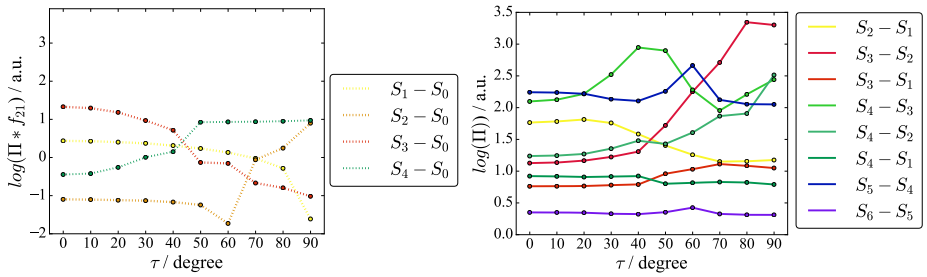

Figure 43: (Right) Evolution of Π index (in logarithm scale) along the reaction coordinated (the dihedral angle τ). (Left) The evolution of Π weighted by the oscillator strength (in logarithm scale

agreement with the experimental data, both for absorption and emission. More details are provided in Appendix, Table 10.

The Π index curves - in logarithmic scale - are reported in Figure 43. We recall that high values of the Π index correlate with a high probability of interconversion from a state to another. Two regions of decay result unequivocally. The first is the S_4 to S_3 decay, appearing around $\tau = 40°$ in the solid olive-green curve. The second connects S_3 and to and is indicated by the marked increment of the Π index associated with the S_3-to-S_2 transition between $\tau = 60°$ and $\tau = 90°$. These two curves allow identifying a leading non-radiative decay channel connecting S_4 to to via S_3. This decay pathway is essentially energy-driven, i.e., it is promoted by the energy nearness of the three states, at specific reaction coordinates. This channel corresponds to the S_4-to-S_2 decay pathway that we had anticipated earlier through the energetic analysis (refer to Figure 39 and related discussion).

The case of those decay channels that are governed by the product $D_{CT}{\cdot}q_{CT}$ is subtler. The analysis of Figure 43 suggests the existence of two further decay and emission channels at $\tau = 0°$ and $\tau = 90°$. In the left panel of Figure 43, we collected the Π curves relative to the excited levels to-S_0 transitions, weighted by their corresponding oscillator strength. As the oscillator strength is directly proportional to the transition probability, weighted-Π values provide a better estimate of the existing emission channels.

The largest weighted-Π value appears at $\tau = 0°$ and is associated with the S_3-S_0 transition (see left side of Figure 43), followed, in the same region by the S_1-S_0 transition. The observed shapes of the S_3-S_0 and S_1-S_0 curves suggest that the LE ($\pi\pi*$) state - corresponding to S_3- together with the ICT_1 state (S_1) are likely to be primarily responsible for the emission in the Franck-Condon region. Additionally, the computed Π profiles point out an efficient interconversion between S_2-S_1 (solid orange curve) and a non-negligible interconversion between S_3-S_2 (solid red curve) that transfer the electronic population to the lowest excited state. We conclude that the ICT_1 emission is compliant with Kasha's rule [273]. Although both S_3 and S_1 may be populated upon absorption, only the S_1 emits, and the S_3-S_2 and S_2-S_1 non-radiative decays enhance this emission channel. These out-

comes agree with the experimental data substantiating the existence of an efficient ICT_1 radiative channel [193, 216]. The vertical deactivation pathway transferring the electronic population from S_4 to S_1 (through the S_3-S_2-S_1 decay channels) and leading to the ICT_1 emission, is poorly efficient compared to the relaxation pathway activated by the torsion. As anticipated earlier in the discussion, if the molecule is irradiated with sufficiently high energy one activates the structural relaxation, which leads to the formation of the S_2 (LE) state at 90°. The pathway involves the conversion between state S_4 to state S_3 (at around 50°) followed by the conversion of S_3 to S_2 at $\approx$ 80°.

Furthermore, as the twist approaches 90°, two channels establish, which transfer the electronic population from S_4 to S_2. By contrast, the oscillator strength of S_4 (0.09 a.u. in the twisted region) is connotative of a poor absorption, suggesting that the existence of an emissive path from S_4 is conditioned to the presence of a higher excited state, transferring its population to S_4 through a non-radiative channel. The steep increase of the Π index associated with the S_5 to S_4 decay at $\tau = 90°$ validates this hypothesis. Similar reasoning holds for S_5, whose population is maintained by S_6, which absorbs at 0° and approaches S_5 at 60°.

Close to $\tau = 90°$, all Π curves, except that computed for the S_3-S_1, S_2-S_1, and the S_1-S_0 interconversion visibly rise. This pattern suggests the existence of several interconnected decay-channels (S_4-S_3, S_4-S_2, S_3-S_2), which transfer the population from S_4 to S_2. Once more, these sub-channels are not necessarily driven by the energy gap, which ranges between 0.01 a.u. for S_4-S_2 and 0.003 a.u. for S_3-S_2. As such, the formation of these channels is supported by the similar distributions of the electronic densities of the states involved, as witnessed by the small $D_{CT}{\cdot}q_{CT}$ values - computed Π values are reported in Table 17. Remarkably, the drop in the S_1-S_0 weighted-Π curve suggests the absence of the emission from S_1 (ICT_1) at 90°. Indeed, the orthogonality of the donor (dimethylaminophenyl) and acceptor (1,10-phenanthroline) hinders the formation of the ICT_1 state. As a consequence, the lowest emitting state at $\tau = 90°$ is S_2 (LE).

In light of the discussion above, the dual emission mechanism observed in Phen-PENMe$_2$ can be summarized by the Jablonski diagram shown in Figure 44. The population of the S_1 - ICT_1 planar state in the FC region - leads to the ICT_1 emission, calculated at 560 nm. Moreover, irradiation at a higher excitation wavelength allows reaching S_4. From S_4 a decay channel can open, leading to the population of to S_2, a $\pi\pi*$ state of local character (LE). The relaxation through the vibrational sub-levels of S_2 causes the observed fluorescence band (at 421 nm).

The S_4-S_0 curve suggests the existence of a further radiative decay at $\tau = 90$ °. This channel is connected to S_6 - in the planar conformation. However, further internal deactivation channels between S_4-S_3 and S_3-S_2 can intervene, reducing the decay from S_4 and resulting in an enhanced S_2-S_0 emission. Similarly, S_3-S_1 and S_3-S_2 curves hint to the existence of two non-radiative channels which, in the planar conformation, contribute to impoverish the S_3-S_0 channel. These evidences, altogether, suggest that the emission from the LE state violates Kasha's rule. To explain this unusual behavior, it is instructive to examine the energy, and $D_{CT}{\cdot}q_{CT}$ values of the S_2-S_1 transition, at $\tau = 0$ ° and $\tau = 90$ °. At $\tau = 0°$ ΔE equals 0.021 a.u.. The $D_{CT}{\cdot}q_{CT}$ product is small (0.83 a.u.), which reflects

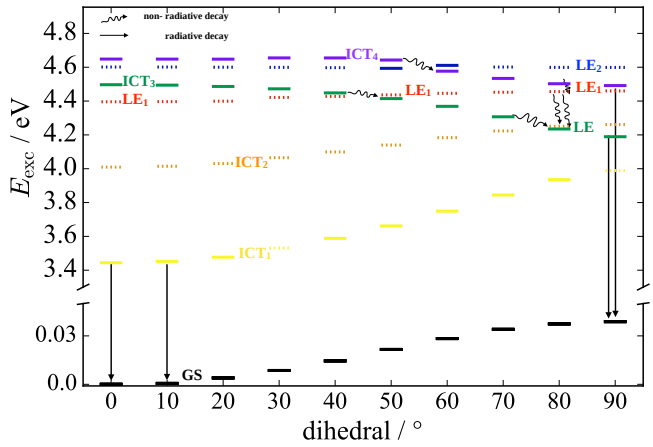

Figure 44: Jablonski Diagram describing the anti-Kasha dual emission of Phen-PENMe$_2$ molecule

a high similarity in the character of the two states. On the other hand, at 90°, while the energy gap shrinks to 0.007 a.u., $D_{CT}{\cdot}q_{CT}$ increases by one order of magnitude (9.07 a.u). Although S_1 and S_2 are closer in energy at 90° than at 0°, the computed Π index is higher at 0°, reinforcing the hypothesis that a decay channel transfers the population from to to S_1 at 0°, but not at 90°, allowing S_2 to emit radiatively.

8.7.4 *Conclusions*

In summary, we have applied the index Π to investigate the excited state landscape of the Phen-PENMe$_2$ molecule. We have postulated the existence of different radiative and non-radiative decay pathways - related to the structural reorganization occurring at the excited state and resulting in the observed dual emission.

Two factors are crucial when the interconversion between states is concerned. The closer in energy are the two states, the higher the likelihood that the interconversion occurs. On the other hand, the more similar the electronic densities of the two states, the higher the possibility of decay. The Π index includes both criteria in a single definition. The energy proximity of the two states is evaluated as the energy difference between two states, while the similarity between their electron densities is recovered through the product $D_{CT}{\cdot}q_{CT}$ - equivalent to the norm of the difference between their dipole moments. Using the index Π, we could estimate the relative probabilities of different radiative and non-radiative channels, and infer a coherent picture of the decay pathways of the states involved in this photochemical process.

In particular, we have individuated two main radiative channels, which lead to the formation of two structurally different emissive species, a planar and a 90° twisted one. These findings also agree with the outcomes of previous work [193, 216]. Remarkably,

our analysis points out the anti-Kasha mechanism of the LE emission. Besides, we have identified several sub-channels that play an essential role, enhancing either of the two emissions. To conclude, the analysis that we have carried out shows the capability of the Π index to draw a qualitative map of a photochemical reaction.

9

A STATE-SPECIFIC FINGERPRINT FOR AN EFFICIENT EXCITED STATE TRACKING

9.1 CONTEXT

Tracking each excited state along a reaction coordinate is a crucial problem in photochemistry. While calculating the optical properties is certainly a start, absorption and emission spectra do not provide any information on the path that each state traverses in the excited state, and it can be complicated to draw the connection between energy absorption and photoproducts formation. Topological descriptors can be very useful to characterize the nature of an excited state. In particular, they conveniently translate the information contained in mathematical objects, such as the 1DDM [115], into a more compact and readable representation of the electronic transition, and can, therefore, be useful to examine the nature of an excited state along a reaction coordinate. Still, fully understanding where among all vertical positions to find a state of interest, and mapping the position of one particular excited state at successive points of a reaction coordinate, remains a non-trivial task that is, nevertheless, indispensable to assemble a coherent description of a reaction pathway [151].

This problem forms the central task of this chapter. Here, we propose a new rigorous metric to track excited states along a reaction coordinate, based on the D_{CT} density-based descriptor. The D_{CT} translates the information contained in the densities of the initial and final states into a length and provides a simple measure of the spatial extent of an electronic transition. We have used this approach repeatedly in the previous chapters, where we have characterized the nature of excited states all along specific reaction coordinates through their D_{CT} values - calculated with respect to their corresponding ground state density distribution at same geometry. Although the D_{CT} is specific for a given transition, it is not sufficient to characterize a state uniquely among a set of vertical excited states. In fact, there may be several close-lying states with similar character, whose ambiguity may prevent the precise identification of a state of interest along a reaction coordinate.

We attempt to solve this indefiniteness with a new metric, which delivers a unique representation of the excited state. Instead of characterizing a vertical state in terms of a one-electron transition from the ground state, we use the collection of D_{CT} vectors calculated between that state and any other state, at same geometry. In other words, we characterize each state by encrypting its connotations in a state-specific "fingerprint." Then, we compare each pair of states using a purposely-defined geometrical distance between their corresponding fingerprints.

We have implemented such a metric in a simple algorithm to map the evolution of excited states along a reaction coordinate. The algorithm determines the relative arrangement of a set of vertical states by computing the distance between the fingerprints of each

pair of states at successive steps and selecting the one that minimizes all distances. We evaluate the performance of this reaction-map-search by comparing the results with a reference representation, where we estimate the similarity between all pairs of states by visually inspecting the main-contributing orbitals and the relevant density descriptors. Additionally, we discuss a possible alternative to the fingerprint-method, consisting in evaluating the distance between each pair of states through the overlap of the corresponding wavefunctions.

9.2 INTRODUCTION

From small compounds to transition metal complexes, the presence of electron donating and accepting groups gives rise to a rich variety of excited states, either localized or extended on more functional groups, which are responsible for the photophysical and photochemical properties of each system.

Tracking each excited state along a reaction coordinate is a crucial problem in photochemistry. Indeed, solving the "tracking problem" is the starting point to address detailed chemical questions, such as following excited state pathways and understanding how and where photoproducts are formed along the reaction path.

Not surprisingly, this problem has attracted a broad interest in the recent literature and several solutions have been proposed, for example, in the framework of vibrational quantum dynamics of molecules in different environments and in experimental and computational studies of organic and inorganic photochemistry [14, 274–278]. For what concerns theoretical approaches, a standard procedure is to identify the excited states by considering the most important excitation coefficients of the wave function and visually inspecting the corresponding orbitals [220, 231, 255, 278, 279], and more often natural transition orbitals [24, 92, 107, 202, 205, 206]. However, this procedure is often tedious and imprecise, as it relies on subjective inspection of the orbitals involved in the excitation. Therefore, it is desirable to devise more automatic and quantitative techniques for excited state characterization. Some attempts have been proposed in the recent literature, for example based on quantitative analysis of the wavefunction contributions through their overlaps [109, 280–282], but a general and standardized approach to this problem is, at the present day, still lacking.

In the previous chapter, we have shown that one can determine the relative importance of different decay pathways by using the Π index [7]. Such analysis was proven to be helpful to identify the pathway that interconnects excited states along a reaction coordinate. However, ambiguities might arise as it is not always easy to map the excited states in an unequivocal manner.

This chapter proposes a novel approach to the problem of following the evolution of different excited states along a reaction coordinate. Our aim is to establish a methodology to map the vertical position of any excited state along a reaction coordinate from the initial configuration - usually in the Franck-Condon region - up to a designated final conformation. In other words, we search for the position of each state, at different steps of reaction, relative to a reference distribution of vertical excited states at the initial step.

This question is unavoidably related to our capability of monitoring the character of the involved excited states, which, as pointed out throughout this thesis, collectively determine the photophysics and photo-chemistry of molecular systems.

In the previous chapters we have introduced and applied several descriptors for the characterization of excited states: The D_{CT} quantifies the global density redistribution upon excitation, and measures the charge-transfer character - i.e. the spacial amplitude of the charge separation produced by an electronic excitation. Another observable that we used is the q_{CT} i.e., the integrated charge transferred upon transition. Aside to these, the oscillator strength, denoted as f_{osc} is also significant, as it measures the efficiency with which a particular transition couples to the light at that frequency. Finally, a quantity that is clearly of primary importance is the energy of the excited state, it determines how states are distributed one respect to the other. In this regard, we remind that a small energy gap between two states increases the probability of transition [14, 151, 224]. Although all of these observables singularly account for a different aspect of an electronic transition, it is not always easy to combine them to achieve an unambiguous interpretation of the excitation process.

As we have previously shown, the D_{CT} vector to the ground state is a powerful descriptor for the state character. Moreover, it is easy to interpret this quantity as a displacement vector in the 3-dimensional space. Here, we extend this descriptor by considering, at the same time, the whole set of D_{CT} vectors from the state under consideration to all the other excited states at the same geometry. The idea is to use the geometrical properties of this collection of vectors as a "fingerprint" for the character of the excited state.

9.3 METHODS

9.3.1 *State tracking procedure*

We aim to track the reaction path of a set of vertically-excited states distributed along a reaction coordinate.

Definition 1 *We define* $\boldsymbol{S}$ *as the matrix of the excited states along the reaction coordinate, where* $S_{t,i}$ *is the excited state that has vertical index* i *at reaction coordinate* t*.*

Definition 2 *We define the "follow index"* $\boldsymbol{\mathcal{F}}$ *as the map of all state pathways along the reaction coordinate, where* $\mathcal{F}_{t,i}$ *is the vertical index, evolved at reaction coordinate* t*, of* $S(0,i)$*.*

In other words, $\mathcal{F}_{t,i}$ tells where, among the vertical positions, one can find the excited state that was at position i at the zero reaction coordinate. The latter implies that $\mathcal{F}(0,i) = i$. The goal of our computational protocol is to find the $\boldsymbol{\mathcal{F}}$ that better approximates the true matrix $\boldsymbol{\mathcal{F}}_T$, defined as the follow index as inferred by orbital and descriptors analysis by a human.

Each vertical state can be represented as a "star" of D_{CT} vectors, each vertex corresponding to a transitions with another vertical state at same geometry. This "star" constitutes a unique fingerprint, which can be used to track a specific state along the reaction.

Any excited state i is, at least formally, connected to all other vertical states by a one-electron transition and can, therefore, be collectively represented in terms of the vertical transitions to the other excited states, j, at the same geometry. Given a set of ni vertical states at one reaction step, one can construct $(ni-1)$ $S_i \rightarrow S_j$ transitions from each vertical excited state to the other states - these include both the transitions to the ground state and to the other vertical excited states at same geometry. Because a D_{CT} vector provides a compact description of a one-electron transition, such approach provides an all-embracing description of any state of interest. Thus, the D_{CT} values calculated between any vertical state and all others at same geometry can be thought as a "star of vectors" that constitutes a unique fingerprint for that state and through which a state can be tracked along a reaction coordinate.

Definition 3 *We define the fingerprint of the state $S_{t,i}$ as the collection of D_{CT} vectors computed between $S_{t,i}$ and $S_{t,j}$ for all $j \neq i$.*

$$\mathcal{V}(S_{t,i}) := \left\{ \overrightarrow{\mathrm{D_{CT}}} \begin{bmatrix} S_{t,j} \\ S_{t,i} \end{bmatrix} \right\}_{j \neq i} \tag{278}$$

The more similar the "stars" the more likely that two states at different reaction coordinates are the same diabatic state - i.e., they have the same character. Therefore, we need to define a measure of similarity - or, equivalently, distance - that estimates how close are the two fingerprints of any two states S_{i_1,t_1} and S_{t_2,i_2} that we want to compare. Since we don't know the follow index at reaction coordinate t_2, (that is precisely what we are trying to find!) we need a measure that is independent on the vertical index at $t = t_2$. One possibility is to sort the D_{CT} vectors in both $\mathcal{V}\left(S_{t_1,i_1}\right)$ and $\mathcal{V}\left(S_{t_2,i_2}\right)$, and compare their modules one by one. We therefore define the distance between two fingerprints as

Definition 4 *The distance between two states at different reaction coordinates S_{t_1,i_1} and S_{t_2,i_2} is defined as the cumulative difference of the D_{CT} modules of the corresponding fingerprints, compared one against the other in a sorted array*

$$\boldsymbol{D}\left(S_{t_1,i_1}, S_{t_2,i_2}\right) := \sum_{k=1}^{ni-1} \|\mathcal{V}_k^*\left(S_{t_1,i_1}\right)\| - \|\mathcal{V}_k^*\left(S_{t_2,i_2}\right)\| \tag{279}$$

where $\mathcal{V}^*$ is the sorted array of D_{CT} vectors according to their module.

If the character of state $S(t_1,i_1)$ and $S(t_2,i_2)$ is conserved, then this procedure will yield a low distance as the sum in Eq. 279 will likely run over similar vectors. On the contrary, if the fingerprints are different, i.e. the states do not share the same character,

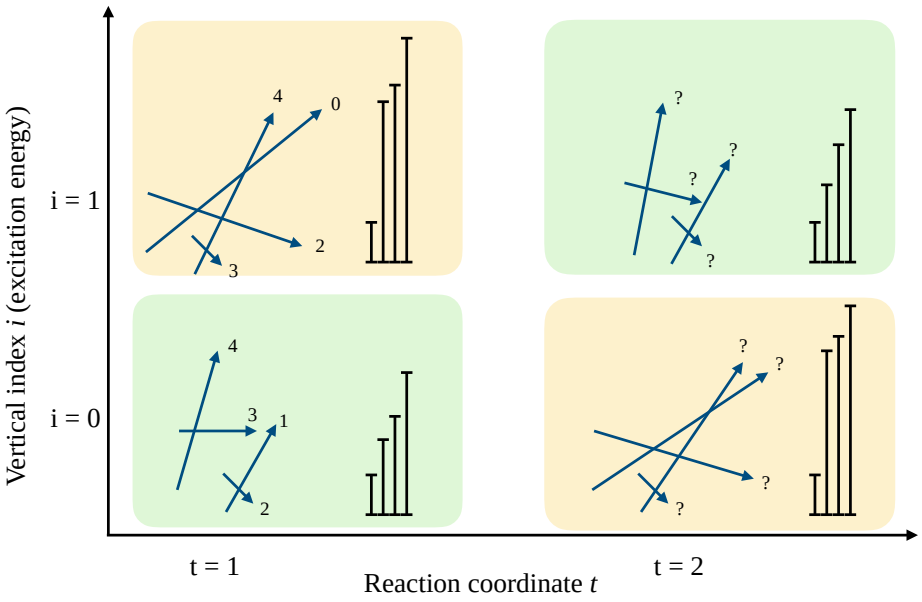

Figure 45

the sum will likely yield a higher value. A graphical illustration of this concept is shown in Fig. 45.

To reconstruct the full-reaction excited state map, we employ this state-distance definition and proceed step by step, iteratively. Starting from the first reaction coordinate $t = 0$ - typically in the Franck-Condon region - we compute the distance between all possible pairs of states at successive reaction steps t of and build the optimal *follow-index* vector $F_{t,i}$ $(i = 1,\dots,n)$ as the one that minimizes the cost function $\tilde{C}(t)$, defined as

$$\tilde{C}(t) := \sum_{i=1}^{n} \Big[(1-k)\mathbf{D}(S_{t-1,F_{t-1,i}},\, S_{t,F_{t,i}}) \;+\; k\mathbf{D}(S_{0,i},\, S_{t,F_{t,i}}) \Big] \tag{280}$$

$$\mathcal{F}_{t,i} := \min \tilde{C}(t) \tag{281}$$

$k \in [0,1]$ is a coupling parameter that modulates the cost contributions of the distances at step t computed at the previous reaction steps $(t-1)$ and at the initial reaction coordinate $(t = 0)$.

In the limit of $k = 0$, the cost function applies solely to adjacent positions, while for $k = 1$ the dependence to the previous step is ignored and the cost function is computed between

any state at reaction coordinate t and the initial step. The minimization procedure consists of trying all possible permutations of follow-index at each reaction step t and selecting, iteratively, the one that minimizes the cost function, $\tilde{C}(t)$, for all successive reaction steps $t \in (1,2,\ldots,nr)$.

In practice, each column of the follow-index matrix is occupied by a follow-index vector, $\boldsymbol{\mathcal{F}}_t = (\mathcal{F}(t,1),\mathcal{F}(t,2),\ldots,\mathcal{F}(t,ni)$, each of which contain the evolved vertical-states positions at step t. The algorithm computes the distance between two reaction coordinates according to Eq. 279, where the vector $\boldsymbol{\mathcal{F}}'_t$ is chosen among all possible permutations as the one that minimizes the state-distances. The complete procedure is represented graphically in Figure 46. Finally, the performance is computed as the fraction

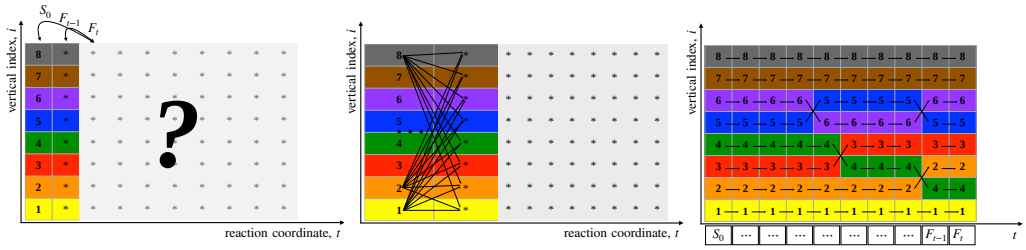

Figure 46: Illustration of the method

9.3.2 *Construction of the "true" matrix*

The present section involves a crucial aspect that we have only briefly mentioned until now: the construction of the true matrix $\mathcal{T}$. The construction of a "ground-truth" reference is essential to evaluate the performance of the methodology we have introduced.

If the size of the system allows for it, we may attempt to sort the puzzle "manually" and infer the reaction excited states' profile by combining the information delivered by different descriptors and orbitals. In general, one descriptor alone is not sufficient to characterize each state and define its path along the reaction coordinate. For example, two states may have similar D_{CT} values but be too separated in energy to affect one another. Therefore, in order to draw the reaction pathway of many different states along a reaction coordinate, one needs to combine several relevant state-observables such as energy, D_{CT}, q_{CT}, f_{osc}. Additionally, for a graphical and compact representation of a transition, it is informative to look at the natural transition orbitals - introduced in Chapter 3.

Therefore, constructing a reference true matrix manually can become a very cumbersome task, as it requires to inspect all orbital pairs for each state and as well as the nature of every excited state. Besides, this procedure is not devoid of arbitrariness. Still, we

τ	S	Hole	Particle	τ	State	Hole	Particle
40°	S_3	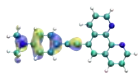	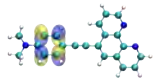	50°	S_3	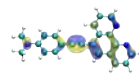	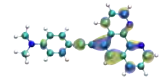
40°	S_4	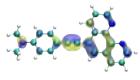	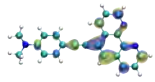	50°	S_4	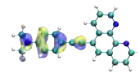	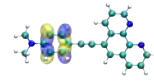
50°	S_5	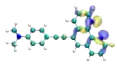	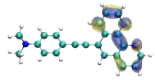	60°	S_5	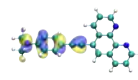	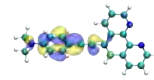
50°	S_6	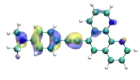	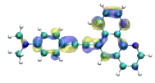	60°	S_6	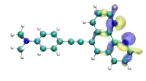	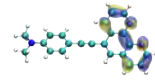
70°	S_2	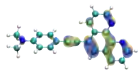	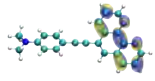	80°	S_2	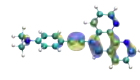	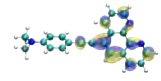
70°	S_3	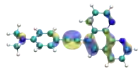	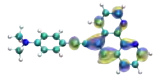	80°	S_3	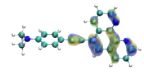	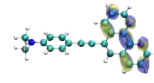

Table 7: Main contributing NTOs relative to the selected transitions.

argue that for model systems such as the one we consider in this work this approach is feasible and the outcome reliable. For the ease of reading, in the present we only discuss the construction of the reference for Phen-PENMe$_2$. For the other systems that we will later analyze, details on the construction of $\mathcal{T}$, as well as the computational details, can be found in the Appendix, Section 11.6 and 11.1, respectively.

Let us consider the intramolecular charge-transfer process in Phen-PENME$_2$. As discussed in Chapter 8, the reaction involves the formation of two emissive species trough an intramolecular twist. As discussed in the previous chapter, the reaction involves several crossing of states. We have previously attempted to draw a coherent picture of this reaction in terms of energy and density descriptors in Section 8.7.1. Here we review the basic outcomes of this procedure.

As shown in Figure 39, S_1 has a charge-transfer character throughout the PES. Conversely, S_2 changes its nature from a CT state at 0° to a LE at 90°. This change in character can be traced back to the stabilization of higher excited state, whose energy decreases as the torsion occurs. The third excited state S_3 approaches S_2 at around 80° (see Figure 39). The corresponding D_{CT} profiles cross in the same region. This occurrence implies that the difference between the positive and negative centroids cancels out in that precise position of the potential curve, and the two states interconvert. Accordingly, the NTOs of S_2 and S_3 at 70° and 80° (in Table 7) reveal that both are LE states, centered on the phenanthroline, and the D_{CT} profiles converge to a similar value. As a result, we hypothesize that S_2 at 90° originates from S_3. Analogously we can search backward the pathway of S_3. The

energy profile (in Figure 39) suggests that between 40° and 50° S_3 lies very close to S_4. Besides, the NTOs (in Table 7) indicate that S_3 is a $\pi\pi*$ state at 40° centered on the N-dimethylaminophenyl group. The same $\pi\pi*$ state shifts to S_4 at 50°; vice-versa, S_4 at 50° matches the character of S_3 at 60°. The f_{osc} curves (in Figure 39) cross in the same region. These pieces of evidence suggest that the S_3 and S_4 states intersect in the 40°-50° region. Altogether we may conclude that the LE state (S_2) at 90° originates from S_4. In addition, the S_5 ad S_6 curves in 39 hint to the presence of a crossing region between 50° and 60°. Analogously, the corresponding NTOs in Figure 7 point in the same direction. The considerations above allow us to construct a preliminary picture of the evolution of the first six excited states along the reaction coordinate. This brief description, although qualitative, is in agreement the analysis in Chapter 8 [7].

As previously alluded to, both the energy and the descriptors that we use to inspect the nature of the excited states are computed at a predefined level of theory (method and basis-set) at which the calculations are performed. Therefore, the resulting description may sensibly vary according to the applied methodology. The inclusion or not of solvent effects may also affect the outcome. As a consequence, the "fingerprint" strategy discussed here is as accurate as the method used to calculate the potential energy surfaces. In general, though, it is always advisable to choose a reliable method (as a start), such that the excited state densities are reliable.

Besides, one should be sure to take into account a sufficient number of excited states, and that the same states, in terms of character, can be found at each step of the reaction coordinate. Although it is not always possible to guesstimate the relative positioning of the vertical states, visually inspecting the lowest orbitals, for relatively small systems as the one discussed here, this procedure is generally accessible and simplifies this process.

Using the same strategy, we have constructed analogous excited state reference maps for the photo-induced proton-transfer reaction in CPDNO and for the charge transfer in DMABN. All the related data are collected in Section 11.6, in Appendix.

9.4 RESULTS

We have tested our tracking protocol on three different systems, namely CPDNO, Phen-PENMe$_2$ and DMABN. We refer to the discussion in Chapter 8 for the definition of the reaction coordinate, and description of the photoinduced reaction of each system. Just as discussed previously, we have sliced each reaction coordinate in a number of step - eight for CPDNO and ten for the other systems and calculated a number of vertical states at all the different steps of the reaction. In the present, we analyze the first five vertical states for CPDNO and the first 6 for Phen-PENMe$_2$ and DMABN.

We now examine the performance curves trends calculated on each different system using increasing values of k ranging from 0 to 1. We recall that k modulates the cost contributions of the distances at step t computed at the previous reaction steps $(t-1)$ and at the initial reaction coordinate $(t=0)$. Similar patterns can be observed in all system. In all cases, low values of k yield larger differences with respect to the ground truth reference state map in Table 8. Close to the Franck-Condon region the character of all states is close

to the one that each state has at the initial point of the reaction. Further on in the reaction, the nature of each vertical state evolves and can end changing significantly from the first assignment. Therefore, larger values of k reproduce more accurately the reference map, as the state-distance $\mathbf{D}$ is calculated with respect to the state vector at the previous step in the reaction, rather than with the initial step. Differently stated, as the excited states pathways gradually change along the reaction coordinate, it is more effective to compare vertical states at adjacent positions rather than including the contribution of the initial state-vector.

In Phen-PENMe$_2$ the performance values oscillates between two positions, with a maximum value of 0.89. The fingerprint method reveals correctly all the crossing of states. The only difference appears at step seven in the reaction coordinate, corresponding to $\tau = 60°$, were the state-fingerprint method individuates a crossing between states five and six, which is not present in the reference map. The paired distance values of the fifth and sixth vertical states at $\tau = 60°$ and $\tau = 70°$ is very little, ≈ 0.2 Å, which makes it difficult to unambiguously determine the relative position of these two states. The overall picture produced by the two methods remains very similar.

An analogous analysis can be done for the DMABN, with some additional complexity. For DMABN the construction of the reference matrix is not as straightforward as it is in the previous case, as the map is not fully consistent. At step seven of the reaction coordinate ($\tau = 60°$) a new vertical excited state appears, which cannot be "matched" with any of the states at the previous steps. The orbital shape of this state cannot be immediately recognized in the state-vectors at previous steps of the reaction. Besides, at successive steps of the reaction this same state descends to the fifth position. To restore the consistency one could simply add few more vertical state, however all vertical states are more and more mixed, making it difficult to assign the character unambiguously. We are left with some "intruder" states that will be certainly not correctly reproduced using our procedure. However, as these states appear quite high in energy, and they do not connect with the lower energy states, we can assume that their relevance in the photochemical process is negligible. Hence, we do not account for these "intruder" states in the performance measure. As shown in Table 8 (right panels), all state crossings that happen before the intruder state comes in are correctly retrieved by the method, therefore reaching an almost-optimal performance.

The third system we consider is CPDNO, shown in Table 8 (central panels). By visual inspecting the orbitals and descriptors we recognized only one state crossing, happening between states 1 and 2 at $t = 2$. Our method retrieves this transition correctly, leaving all other positions unchanged. Consequently, the computed performance is 1.0.

9.5 OVERLAP-BASED METHODS

One possible alternative to track the state evolution along a reaction coordinate is to define the state-distance as the overlap between the wave-functions of all pair of states at

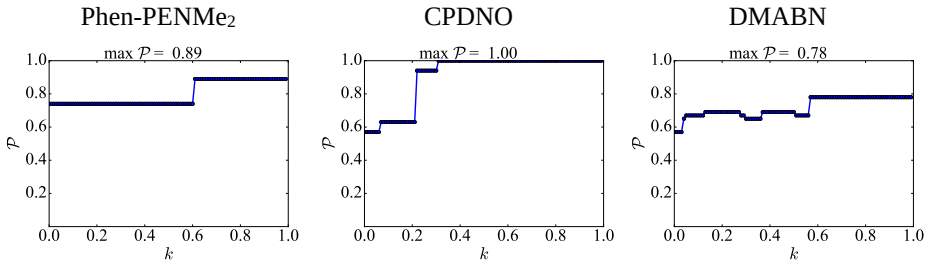

Figure 47: Computed performances relative to the visually-inferred reference map, as a function of the k parameter, for the three different systems.

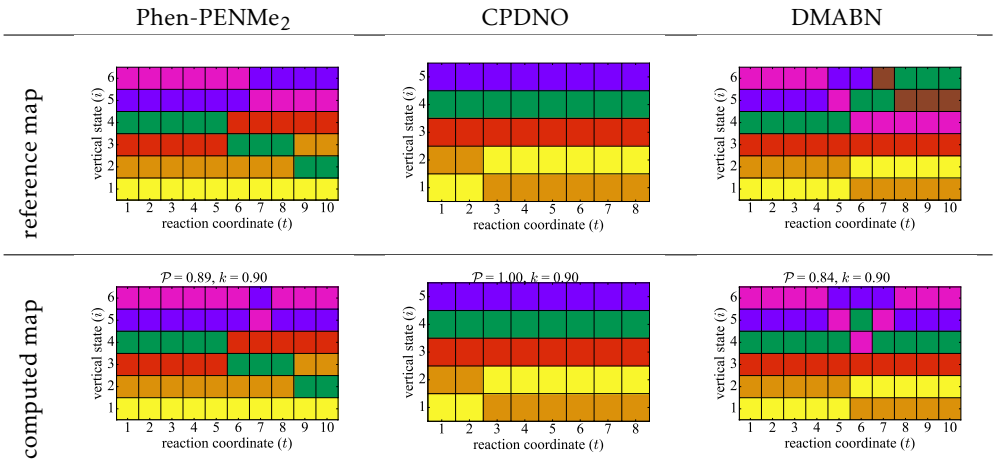

Table 8: Reference ground true matrices, obtained by inspection of the orbitals and density-descriptors and computed reaction maps, with associated performances w.r.t. to reference, for the three different systems

different geometries [280]. The usual concept holds: the higher the overlap, the smaller the state distance.

To better clarify, let us consider a pair of vertical states, corresponding to different nuclear configurations, described by their wavefunctions $\Psi_i^{(t)}$ and $\Psi_j^{(t')}$. The two configurations are chosen as to be relative to two different steps on a selected reaction coordinate.

As we consider these states to be derived in the framework of TDDFT, both are constructed as linear combination of singly-excited determinants. It is instructive to consider an underlying spin-orbital basis and express these last as

$$\Psi_i^{(t)}(\mathbf{x}_1,\mathbf{x}_2,\cdots,\mathbf{x}_N) = \sum_{\mu} C_{i\mu}\varphi_\mu, \tag{282}$$

$$\Psi_j^{(t')}(\mathbf{x'}_1,\mathbf{x'}_2,\cdots,\mathbf{x'}_N) = \sum_{\nu} C_{j\nu}\varphi_\nu. \tag{283}$$

The overlap between these two is defined as,

$$S_{ij} = \left\langle \Psi_i^{(t)} \middle| \Psi_j^{(t')} \right\rangle. \tag{284}$$

Such measure has a practical interest, very appealing for our purposes, in that it is related to the amplitude of the electronic transition [107]. In fact, it is reasonable to estimate that a transition between two states has a greater probability to occur the larger the overlap between the corresponding wavefunctions [219, 283]. Based on this consideration, we can use the overlap as a measure of the distance between a pair of states. As each excited configuration is constructed in a different basis - the atomic functions are centered on the same set of atoms with different coordinates - the elements of the overlap matrix couple each basis function of the initial state, $\Psi_i^{(t)}$, with each basis function of the final one, $\Psi_j^{(t')}$. The overlap matrix has, therefore, the following structure,

$$\mathbf{S}^{\mathrm{AO}} = \begin{pmatrix} S_{\mu\mu} & \boxed{S_{\mu\nu}} \\ \boxed{S_{\nu\mu}} & S_{\nu\nu} \end{pmatrix} \tag{285}$$

where the diagonal block-elements are normalized diagonal matrices, corresponding to the atomic orbital overlap matrices of state $\Psi_i^{(t)}$, and $\Psi_j^{(t')}$, respectively. The off diagonal terms, instead, map the transformation between the two bases, each being the transpose of the other. As we are usually interested in molecular properties, we can conveniently project the $S_{\nu\mu}$ - or, equivalently, $S_{\mu\nu}$ - into the molecular orbital basis by multiplying $S_{\nu\mu}$ on the left and on the right by the molecular orbital coefficients corresponding to the final and initial states. At this stage it is convenient to ponder on the meaning of the molecular coefficients. In the present we are interested in evaluating the overlap between two states, which possess different nuclear configurations, and use this measure to estimate the "distance" between these two states. Although the canonical molecular orbital coefficient could be used, these are are difficult to handle, as the information they encode is diluted in a huge matrix of $K \times K$ dimension - with K number of basis functions. More convenient is to use the natural transition orbital coefficients. As described in detail in Chapter 3, these are defined as the coefficients that diagonalize the $1TDM$, such that the transition is described by few orbital pairs. The AO to MO transformation then writes,

$$\mathbf{S}^{\mathrm{MO}} = C_i^{T,\mathrm{NTO}} S_{\nu\mu} C_j^{\mathrm{NTO}} \tag{286}$$

Since the C_i^{NTO} and C_j^{NTO} coefficients are not calculated in the same basis, it is convenient to normalize each column of the $\mathbf{S}^{\mathrm{MO}}$ matrix. We denote the normalized molecular orbital matrix as $\bar{\mathbf{S}}^{\mathrm{MO}}$. As we adopt the NTO formalism, $\bar{\mathbf{S}}^{\mathrm{MO}}$ has a compact form: the elements that actually describe the excitation are very little in number and can be easily isolated to obtain a clear and direct interpretation of the process. In particular, the *relevant* elements are those corresponding to the overlap between the atomic orbitals matrix columns associated with the highest NTO eigenvalues. By definition, these last are those corresponding to the HOMO and LUMO orbitals and, occasionally, to a few adjacent orbital pairs. In turn, the nonzero elements of the $\mathbf{S}^{\mathrm{MO}}$ matrix that we are interested to look at constitute a sub-square-matrix of reduced size. For example, if the nonzero NTO eigenvalues are only four, the sub-matrix will have dimensions of 2×2. Among these, the diagonal elements of the $\mathbf{S}^{\mathrm{NTO}}$ matrix are those that couple each relevant molecular orbital at one geometry with the same orbitals at a different geometry. A convenient way to translate this reduced-overlap-matrix into a quantitative measure of the overlap between the associated density distributions is to calculate its trace. Given N as the number of row (and columns) of $\mathbf{S}^{\mathrm{NTO}}$, we define the distance between any two states as the inverse of the trace of the normalized overlap matrix computed between the state $S_{t,i}$ and $S_{t,j}$, divided by N.

$$d = (Tr(\bar{\mathbf{S}}^{\mathrm{NTO}})/N)^{-1}. \tag{287}$$

By consequence, the distance between a pair of states will be large whenever the trace of the normalized overlap matrix is small, and small otherwise.

9.5.1 *Performance of the overlap method*

We have applied the overlap formalism to the same three systems described in the previous section, by plugging the state distance as defined in Eq. 279 in the cost function of Eq. 281 to find the follow index map $\mathcal{F}$ that minimizes it. The resulting state map is then compared to both the reference map computed by visual inspection and to the one found by the "fingerprint" protocol described in the previous section. For both these comparison we compute the performance (i.e., the similarity between matrices) as a function of $k \in [0,1]$. As shown in Figure 48, in the case of CPDNO and DMABN the three methods yield comparable results, as the values of similarity between maps (denoted as performance $\mathcal{P}$) ranges between $\mathcal{P} \sim 0.8$ and $\mathcal{P} \sim 0.94$ for $k > 0.5$. In the case of Phen-PENME2, on the contrary, performance values are very low (around $\mathcal{P} \sim 0.3/0.4$ for all values of k). This apparently high discrepancy, however, can be explained by visualizing the detailed maps given by the three protocols at a fixed value of k. The comparison, shown in Table 9, shows that the low performance is mostly due to a propagation of an initial error occurring at the first reaction steps ($t = 1,2$). In fact, important state crossing between low-energy states are indeed recognized by all methods (e.g. states $3,4$ at $t = 5,6$ and states $2,3$ at $t = 8,9$), even though the overlap method crosses the wrong indexes due to a series of false crossings happening at $t = 1,2$.

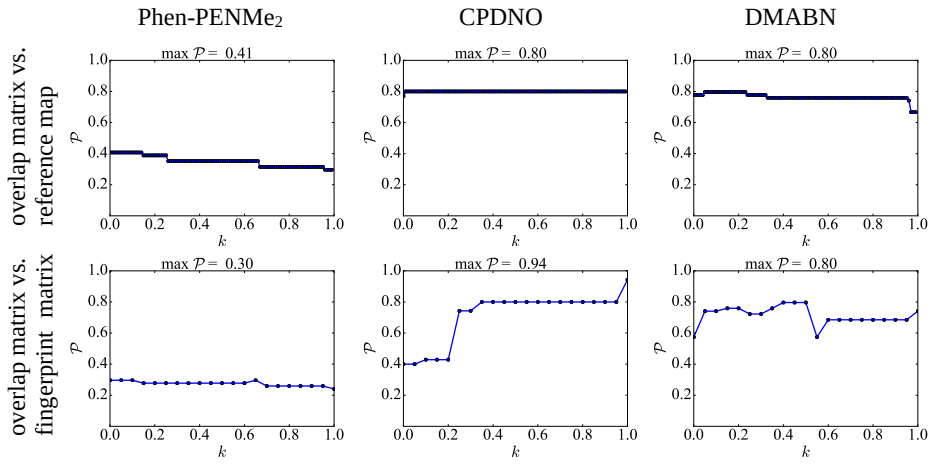

Figure 48: Computed performances of the overlap based method relative to the visually-inferred reference map (top) and to the reaction map obtained through the fingerprint method (bottom), as a function of the k parameter, for the three different systems.

9.6 DISCUSSION AND PERSPECTIVES

In the present section, we have outlined a computational protocol intended to determine the distribution of vertical excited state along a reaction coordinate and to construct a reaction map, based on a pairwise comparison of excited states at different geometries. At each reaction step, the algorithm selects the permutation of states that minimizes a cost function defined from the collection of state distances at a chosen reaction coordinate with the previous reaction step and with the arrangement of states at the initial reaction conditions ($t = 0$).

For each state and each reaction coordinate t we have introduced a fingerprint defined from the collection of D_{CT} vectors at the same geometry, and used the difference between fingerprints as a proxy for the state distance. The simplicity of this solution relies on the fact that we exploit entirely the information provided by an ensemble of vertical states to describe each state independently.

The map resulting from this protocol was compared to the one retrieved by detailed visual inspection of multiple descriptors and orbitals of the excited states, taken as a "ground truth" for the state map. Importantly, the only free parameter in our protocol is $k \in [0,1]$, which modulates the relative weight of the previous step and the initial step in the cost function. This comparison, applied to three evolving molecular systems, showed good performances ranging from a minimum value of 0.8 to a maximum value of 1.0 for any large enough value of k (> 0.6).

In order to get a distance value from an unordered collection of vectors (the D_{CT} fingerprint) we used the ranked comparison of their modules as an estimation of their distance.

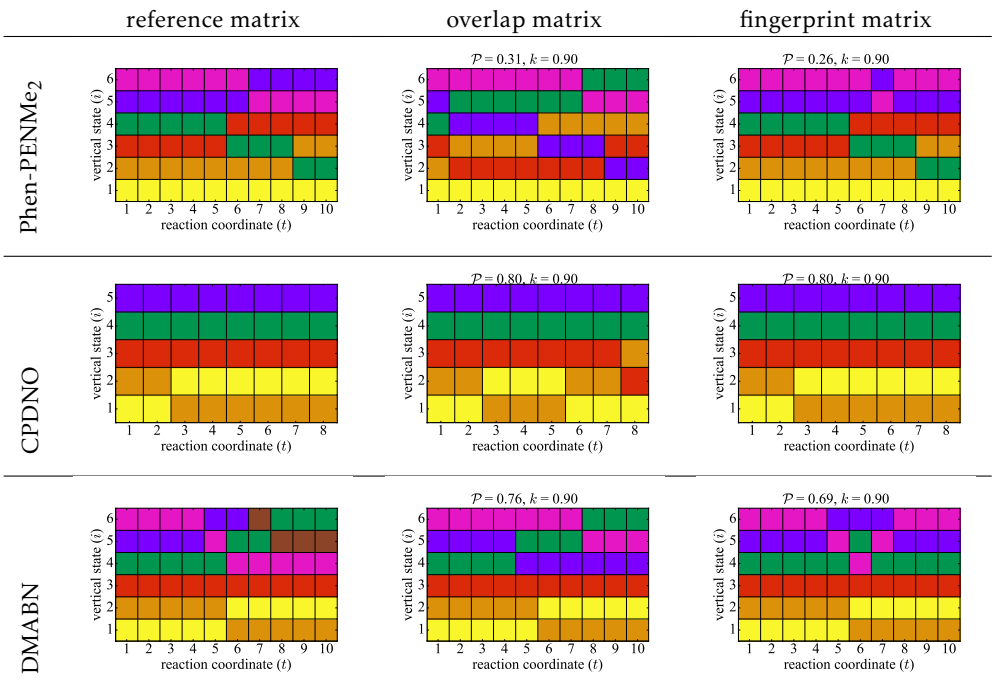

Table 9: Computed state maps for the three systems, using the three different tracking methods.

Essentially, for each vertical state we construct a "fingerprint" of D_{CT}-vectors, each of which represents the transition to another vertical state at the same geometry. Each fingerprint is translated into an ordered list of lengths, representing the individual modules of the D_{CT} vectors composing the fingerprint. For a couple of states at different geometries, these ordered lists are then compared by taking the cumulative difference between ordered pairs as an indicator of the states' distance. Besides the satisfying performances, this distance function is quite simple and could certainly be improved by considering more refined comparison between unordered ensembles of vectors in space, for example by computing their overlap up to solid transformations (stretch/rotation/translation) or other geometrical features.

The computational protocol that we use to find the best permutation is general, as any definition of state distance may be applied, provided that it yields a reliable estimate of the states' similarity. In fact, we used the same computational protocol for two different distance functions: the one defined from the comparison of D_{CT} fingerprints and the one, described in the last section, that uses the overlap between the NTO coefficients of a pair of excited states.

In conclusion, the overall advantage of the method proposed in this chapter lies in its simplicity. This methodology provides a simple and straightforward solution to track excited states along a reaction path, without the need for any parameter optimization, neither requiring the knowledge of the energy profiles.

10

CONCLUSION AND PERSPECTIVES

10.1 OUTLINE

The objective of this thesis was to devise, construct, and apply a cost-effective approach to calculate photophysical properties of molecular systems, based on ad-hoc density descriptors, to characterize the relevant photophysical pathways for the many processes taking place at the excited state. The result of our investigation is a collection of TDDFT-based protocols, which can be applied to characterize the excited-state potential energy surfaces of molecular systems, based on the knowledge of ground and excited state densities.

The inherent complexity in the modeling of excited-state processes is related to the fact that the molecular systems under study are typically out of equilibrium, perturbed upon the interaction with light. The computational setup that we have devised meets this context in that it allows us to monitor the evolution of excited states along a reaction coordinate.

The key observable and leitmotif of our investigations is the electronic density, which holds the response of the system to the light-induced perturbation. We have interpreted such observable through purposely defined descriptors, which we have used to track the changes in the electronic density distributions along photochemical pathways.

Besides defining an adapted metric for the excited state processes under analysis, the density descriptors that we have proposed and employed yield novel insights on relevant physical properties of the molecular systems, translating computational outcomes in simple chemical and physical concepts (such for instance the strength and spatial amplitude of the charge separation produced by an electronic excitation).

In Chapter 4, we have systematically analyzed the nature and impact of the density relaxation involved in the post-linear response treatment of time-dependent density functional theory on the measure of charge separation length that characterizes the hole/particle generation, i.e., the D_{CT} index. For this purpose, we have considered a family of push-pull dyes of increasing length, where the primary hole/particle charge-separation distance grows with the length of the molecular skeleton. Assessing the influence of the use of different density functional approximations on the topology of the density distribution generated upon transition allowed us to conclude that such response strongly depends on the kernel used for generating the exciton. Moreover, we showed that, qualitatively, both *unrelaxed* and *relaxed* densities deliver a consistent assessment of the nature of the excited states. From a quantitative standpoint, though, we observed significant discrepancies in the charge transfer distance for electronic transitions having substantial *charge transfer* (CT) character, independently of the nature of the exchange-correlation functional used.

Next, in Chapter 5 we tested the ability of the D_{CT} to reckon the nature of excited states along a full reaction. Using a prototype excited-state proton transfer reaction as a test case, we showed that density-based descriptors (such as the D_{CT} index) could be safely used to analyze excited states qualitatively and quantitatively. More precisely, the D_{CT} provided a good description of the electronic rearrangements occurring in the photochemical reaction studied, both using density functional and multiconfigurational methods - here CASSCF-CASPT. Our results suggest that the D_{CT} could be employed, just as the energy, to locate minima, on potential energy surfaces.

Our modeling of the excited-state energy profiles was complemented, in Chapter 6, with a diagnostic analysis to probe the accuracy of TDDFT methods. In this context, we proposed a new index, M_{AC}, for the detection of erratic TDDFT behavior, pointing out the region of excited-state potential energy curves claiming for a more in-depth description. The M_{AC} diagnostic analysis allows us to identify ghost- and spurious-low-lying excitations, that may result from a particular choice of approximated density functional. In Chapter 7 we used such index to characterize singlet and triplet excitations in metal-containing complexes. Overall, in Chapter 6 and 7 we have rationalized what the pitfalls of TDDFT are, what is the reason for their appearance and under what circumstances existing approximations work well or fail. By complementing the M_{AC} diagnostic analysis with experimental measurements, we were able to judge the reliability of a chosen methodology.

In Chapter 8, we extended our computational setup to characterize excited-state pathways in the case of reactions involving a profound structural change. This investigation fits in the broader context of the computer-assisted design of new molecular architectures with peculiar photochemical traits able, for instance, to store energy through reversible conformational changes induced by electronic excitations. In particular, we extended the definition of a previously-defined index,Π [2], to the case of the internal conversion between excited states, and applied it to investigate potential energy surfaces of low-lying excited states far Franck-Condon region, that is, in regions involved, for instance, in the radiative and non-radiative decay patterns.

Finally, in Chapter 9 we have introduced a new methodology to track the electronic states of interest along the nuclear trajectory, based on the definition of a state-specific fingerprint that leverages the full information contained in the transition vectors to characterize any excited state uniquely.

With the development of the state-tracking algorithm and the implementation of several density-descriptors outlined in this thesis, we have proposed a cost-effective way of addressing the challenge of disclosing excited state pathways in the modeling of photophysical processes. Indeed, we have shown how this is often crucial for the understanding and prediction of such phenomena. As for the results discussed in Chapter 9, further study into the behavior of the fingerprint-method is desirable - for instance by using different molecular architectures, by including metal complexes, or by considering a larger number of states. Nevertheless, the performance and versatility of this model looks, thus far, rather promising and should prompt further development in the direction of new-efficient excited-states optimization algorithms.

10.2 METHODOLOGY AND FUTURE RESEARCH

The application of TDDFT based modeling and density descriptors to the complex phenomenology of photochemical processes raises several methodological questions, which range from the large simplifications made in the theoretical models we apply to the constraints and lack of kinetic considerations in our approach. The possible strategies of the theoretical chemist' to investigate photochemical and photophysical issues are manifold, and it would be an utter simplification to attempt here a comprehensive outline of a discussion of such vast scope. At the same time, we believe that there are a few points that deserve mention, undoubtedly less general, and specifically related to the results that we have discussed in this work.

In the last two chapters, in particular, we have employed different metrics to recognize excited states of different nature along specific reaction coordinates to infer the excited state pathway of each state, first with the Π index, and secondly with the so-called fingerprint method. One of the most arguable features of these approaches is that the actual interpretation of the photophysical pathway depends on the accuracy of underlying densities, and thus on the quantum mechanical method used to generate these latter. Secondly, the overall picture that we obtain is qualitative, in the sense that what we obtain is a possible survey of accessible decay channels, rather than a precise characterization of funnel regions. However, in this somewhat simplistic view lies also the beauty of our approach, which is intended to provide a computationally inexpensive characterization of the excited state potential landscapes. As such, the indexes discussed herein are not intended to substitute the classical route of excited state exploration but more to provide easy-to-compute and easy-to-interpret descriptions of excited-state phenomena, which can be computed – on the fly- to allow both the identification of critical area for TDDFT approaches and the qualitative identification of possible reactions paths.

In a very general sense, the density descriptors that we have proposed and applied throughout this work condense the information contained in objects such as the difference density matrix in more compact and easy-to-interpret metrics, which provide an attractive alternative to more complex wavefunction analysis approaches. As such, they can aid in the rational design of molecular architectures for specific applications by, for example, serving as an optimization target. In fact, part of our current ongoing research focuses on the application of these tools to devise novel Ru(II) photosensitizers with exceptional characteristics for anti-cancer activity (intense absorption in the phototherapeutic window and stable, long-lived low-lying triplet states).

To conclude, the new "fingerprint" metric that we have proposed in Chapter 9 was proven to efficiently track the electronic states of interest along the nuclear trajectory. These preliminary results suggest that it might even be possible to employ the state-specific fingerprints in automatized diabatization schemes, by transforming the states such that the D_{CT} vectors change as little as possible. Further applications are also possible in theoretical chemistry method development, where D_{CT} fingerprints, that are based on results from less costly TDDFT computations, could be used to aid the design of sensible active spaces for multiconfigurational calculations.

Part IV

APPENDIX

11

SUPPLEMENTARY MATERIALS

11.1 COMPUTATIONAL DETAILS

Throughout this work we have chosen different organic chromophores, such as Phen-PENMe2, DMABN, CPDNO as test cases to exemplify the insights that density-based indexes may bring to the description excited state processes. All calculations - where not differently specified - were performed with a development version of the Gaussian program [145]. In general, the evaluation of all density-based indexes D_{CT}, M_{AC} and Π was done using self made freely distributed programs available at www.quanthic.fr, although the D_{CT} index can also be directly computed using the commercial release of the Gaussian software [145]. In general, for all systems we have have applied the same computational protocols, consisting of the following steps:

- preliminary geometry optimization using ground state DFT [32], to fully relax the structure. In "scan" calculation all degrees of freedom are relaxed except for that along which the reaction occurs;
- frequency calculation to characterize each structure as minimum or transition state;
- TDDFT calculation to obtain the excited state levels at each geometry (and calculation of density based indices, such as D_{CT}, M_{AC}, Π).

The details of the calculations reported in each chapter are summarized in Table 10. Natural transition orbitals [92] (NTO) relative to the ten lowest electronic transitions were also computed for a visual interpretation of the nature electronic transitions. All orbitals are collected in section 11.5.

Molecule	abbreviation	Chapter	Method(s)
α,ω-nitro-amino-oligo-phenylenes	O_N , with N spacers $\in [1,10]$	4	see Section 4.4
α,ω-nitro-amino-oligo-phenylenes	O_N , with N spacers $\in [1,4]$	6	Geometry optimizations were carried out using the PBE0 functional and the 6-31G(d,p) basis set. On top of each structure, TDDFT calculations were performed using the PBE [43], PBE0 [46], and LC-PBE [58] functionals and the 6-31G(d,p) basis set. Reference calculations were performed at CIS/6-31G(d,p) level.
(2-(2-hydroxyphenyl)thiazole	HT	5	see Section 5.3
2-(2′-hydroxyphenyl)benzothiazole	HBT	5	see Section 5.3
1-(cyclopropyl)diazo-2-naphthol	CPDNO	6, 8, 9	Using the optimized geometries reported in Ref. [163], single point calculations were performed at the TDDFT level of theory using the global hybrid PBE0 [46] functional supplied with the 6-31G(d) basis set.
N,N-dimethylaminobenzonitrile	DMABN	6	Geometry optimizations were carried out using the PBE0 functional and the 6-31+G(d,p) basis set. Vertical excitations were probed using TDDFT, combined with the same functional and basis set. Additionally, the same structures were optimized using a larger basis-set, 6-311+G(d,p), in in CH_3CN, to investigate the dependence of the M_{AC} diagnostics on the quality of the computed energies and densities.
N,N-dimethylaminobenzonitrile	DMABN	8 , 9	Geometry optimizations were carried out using the PBE0 functional and the 6-31+G(d,p) basis set. Vertical excitations were probed using TDDFT, combined with the same functional and basis set.
5-(4-dimethylaminophenylenylethylyn)-1,10-phenanthroline	Phen-PENMe$_2$	6	Geometry optimizations were carried out using the PBE0 functional and the 6-31+G(d,p) basis set. Vertical excitations were probed using TDDFT, combined with the same functional and basis set. With the aim of estimating the impact of the use of different methodologies on the calculation of the M_{AC}index, excited states were additionally computed using the following approaches: (a) PBE0/6-31+G(d,p), in gas phase (b) PBE0/6-31+G(d,p), in in CH_3CN (c) LC-PBE/6-31+G(d,p) [58], in CH_3CN (d) CAM-B3LYP/6-31+G(d,p) [56], in CH_3CN (e) CIS/6-31+G(d,p), in in CH_3CN.
5-(4-dimethylaminophenylenylethylyn)-1,10-phenanthroline	Phen-PENMe$_2$	8, 9	Geometry optimizations were carried out using the CAM-B3LYP functional and the 6-311+G(d,p) basis set. Vertical excitations were probed using TDDFT, combined with the same functional and basis set.

Table 10: Computational details

11.2 2D EXCITED STATE S_1 PES AND RELATED D_{CT} SURFACES COMPUTED FOR HBT AND HT

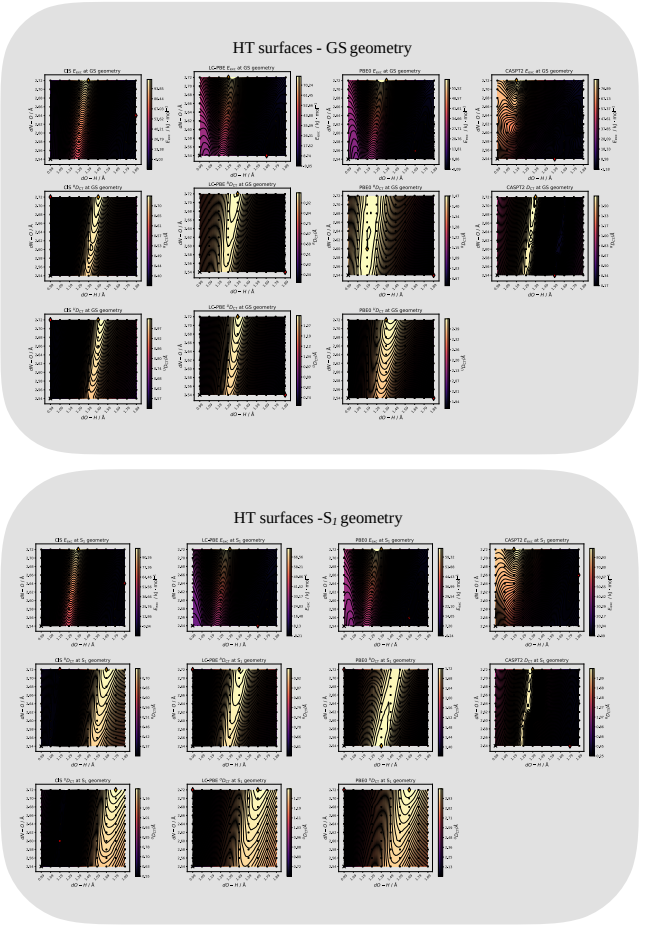

Figure 49: 2D excited state S_1 PES and related D_{CT} surfaces computed for HT at various levels of theory, using either the GS or the S_1 optimized PBE0/6- 31+G* geometry.

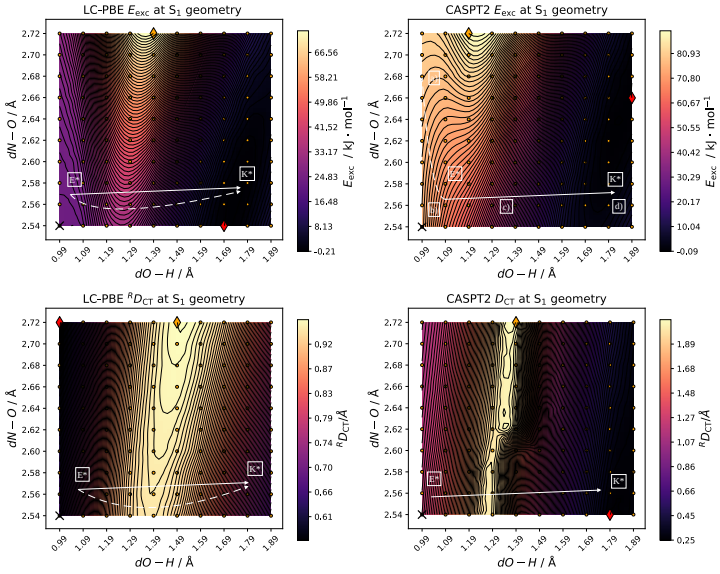

Figure 50: Relaxed S_1 LC-PBE energy - in the top left, and D_{CT} surface -in the bottom left; relaxed S_1 CASSCF-CASPT2 PES - in the top right, and the D_{CT} surface - in the bottom right corner. All geometries have been computed at the optimized S_1 PBE0/6- 31+G* level of theory. White arrow: ESIPT straight line pathway; dashed arrow: ESIPT minimum energy pathway; dashed white line: steepest decent pathway from Franck-Condon region to the minimum enol* tautomer.

11.3.1 *Raw data relative to Section 6.4.2*

Table 11: Transition energies (E), M_{AC} and D_{CT} index values, transition character (Char.) computed at different levels of theory on the push-pull system, for increasing number of spacers $N = 1$ to $N = 4$.

		PBE				PBE0				LC-PBE				CIS			
N	State Nr.	E_{exc} / eV	M_{AC} / eV	D_{CT} / Å	Char.	E_{exc} / eV	M_{AC} / eV	D_{CT} / Å	Char.	E_{exc} / eV	M_{AC} / eV	D_{CT} / Å	Char.	E_{exc} / eV	M_{AC} / eV	D_{CT} / Å	Char.
1	1	3.39	1.03	2.25	CT	3.97	1.58	2.25	CT	4.24	-16.88	0.53	$\pi\pi*$	5.22	-15.03	0.58	$\pi\pi*$
	2	3.64	-7.44	0.9	$\pi\pi*$	4.04	-11.89	0.68	$\pi\pi*$	4.71	1.71	2.04	CT	5.33	-2.75	1.47	$\pi\pi*$
	3	4.16	-3.17	1.32	$\pi\pi*$	4.58	-12.79	0.64	$\pi\pi*$	4.76	-20.65	0.46	$\pi\pi*$	5.55	-21.48	0.46	$\pi\pi*$
	4	4.23	-7.43	0.87	$\pi\pi*$	4.62	-3.64	1.26	$\pi\pi*$	5.04	-6.94	0.94	$\pi\pi*$	5.71	-9.07	0.94	$\pi\pi*$
	5	4.43	1.29	2.05	CT	5.18	1.47	2.05	CT	6.34	0.84	1.62	CT	7.14	-16.97	0.58	$\pi\pi*$
	6	4.62	-2.18	1.51	$\pi\pi*$	6.02	-2.87	1.76	$\pi\pi*$	6.83	1.19	1.95	CT	7.43	-8.56	1	$\pi\pi*$
	7	5.19	-1.36	1.55	$\pi\pi*$	6.19	-1.07	1.87	$\pi\pi*$	6.95	-6.84	0.84	$\pi\pi*$	7.59	-9.87	0.96	$\pi\pi*$
	8	5.29	-1.78	2.08	$\pi\pi*$	6.28	3.71	2.33	CT	7.17	-12.3	0.67	$\pi\pi*$	7.7	-51.89	0.24	$\pi\pi*$
	9	5.35	2.49	2.42	CT	6.41	-0.75	1.57	$\pi\pi*$	7.38	-4.87	1.29	$\pi\pi*$	8.03	-0.62	1.84	$\pi\pi*$
	10	5.59	-1.89	1.53	$\pi\pi*$	6.42	1.38	1.71	CT	7.9	-6.31	0.76	$\pi\pi*$	8.32	-22.03	0.54	$\pi\pi*$
2	1	2.31	4.08	3.99	ghost	3.17	4.24	3.95	ghost	4.19	-15.32	0.55	$\pi\pi*$	4.83	0.04	2.3	CT
	2	3.49	1.39	2.97	CT	3.98	-7.1	0.85	$\pi\pi*$	4.45	3.81	3.08	CT	5.16	-13.34	0.61	$\pi\pi*$
	3	3.5	-1.5	1.37	$\pi\pi*$	4.31	2.57	3	CT	4.68	-18.86	0.48	$\pi\pi*$	5.46	-20.4	0.47	$\pi\pi*$
	4	3.63	4.85	3.25	ghost	4.48	-30.66	0.36	$\pi\pi*$	4.88	-13.08	0.7	$\pi\pi*$	5.51	-16.06	0.66	$\pi\pi*$
	5	4.02	4.25	4.12	ghost	4.5	-5.01	1.05	$\pi\pi*$	5.18	0.17	1.67	CT	5.7	-5.17	1.24	$\pi\pi*$
	6	4.03	-6.27	1.1	$\pi\pi*$	4.72	4.55	3.29	CT	5.71	2.19	2.25	CT	6.13	-4.56	1.31	$\pi\pi*$
	7	4.07	-9.67	0.76	$\pi\pi*$	4.8	3.93	3.73	CT	6.23	4.27	3.05	CT	6.93	0.63	2.24	CT
	8	4.09	-8.85	0.81	$\pi\pi*$	4.82	4.54	3.76	CT	6.52	4.55	3.51	CT	6.99	1.8	3.07	CT
	9	4.15	4.02	4.02	CT	4.93	4.06	3.61	CT	6.64	3.79	2.62	CT	7.22	-9.39	1.07	$\pi\pi*$
	10	4.77	0.68	2.07	CT	5.74	-2.15	2.09	$\pi\pi*$	6.86	-31.89	0.34	$\pi\pi*$	7.39	-3.31	1.3	$\pi\pi*$
3	1	1.78	5.24	5.88	ghost	2.89	5.34	5.72	ghost	4.19	-14.06	0.57	$\pi\pi*$	4.72	0.23	2.3	CT
	2	3.15	3.32	4.95	ghost	3.97	-8.62	0.78	$\pi\pi*$	4.45	4.14	3.37	CT	5.15	-12.56	0.61	$\pi\pi*$
	3	3.22	5.75	5.32	ghost	4.1	5.2	5.37	ghost	4.67	-18.17	0.48	$\pi\pi*$	5.44	-19.73	0.47	$\pi\pi*$
	4	3.28	4.45	5.44	ghost	4.21	5.07	5.26	ghost	4.88	-19.04	0.56	$\pi\pi*$	5.48	-29.22	0.66	$\pi\pi*$
	5	3.29	6.53	5.21	ghost	4.27	3.57	4.47	CT	5.19	0.22	1.69	CT	5.62	-1.43	1.24	$\pi\pi*$
	6	3.47	4.79	4.75	ghost	4.39	4.03	4.82	CT	5.23	-1.61	1.36	$\pi\pi*$	5.67	-3.76	1.31	$\pi\pi*$
	7	3.48	0.62	1.65	CT	4.46	-7.47	0.86	$\pi\pi*$	5.26	3.67	2.87	CT	5.73	-5.21	2.24	$\pi\pi*$
	8	3.53	4.17	4.8	ghost	4.49	1.64	2	CT	6.08	4.46	3.54	CT	6.36	-6.8	3.07	$\pi\pi*$
	9	3.98	-17.69	0.61	$\pi\pi*$	4.6	5.98	5.14	ghost	6.3	5.74	5.14	CT	6.8	3.25	1.07	CT
	10	4.02	-110.42	0.12	$\pi\pi*$	4.65	5.56	4.79	ghost	6.32	5.06	3.72	CT	6.96	1.68	1.3	CT
4	1	1.53	5.84	7.82	ghost	2.81	5.93	7.55	ghost	4.19	-13.56	0.58	$\pi\pi*$	4.68	-0.61	2.11	$\pi\pi*$
	2	2.74	6.65	6.45	ghost	3.72	5.9	6.9	ghost	4.47	3.5	3.02	CT	5.15	-12.36	0.63	$\pi\pi*$
	3	2.8	4.24	6.65	ghost	3.84	5.5	6.74	ghost	4.67	-18.03	0.49	$\pi\pi*$	5.33	-0.89	1.98	$\pi\pi*$
	4	2.97	4.14	6.96	ghost	3.98	-9.37	0.73	$\pi\pi*$	4.88	-22.33	0.49	$\pi\pi*$	5.44	-19.5	0.48	$\pi\pi*$
	5	3.12	7.28	7.17	ghost	4.32	4.2	5.86	CT	5.02	3.87	2.92	CT	5.49	-50.45	0.26	$\pi\pi*$
	6	3.24	6.82	5.59	ghost	4.36	4.29	6.71	CT	5.2	-1.98	1.38	$\pi\pi*$	5.67	-5.54	1.23	$\pi\pi*$
	7	3.26	3.32	5.5	ghost	4.45	4.54	4.03	ghost	5.22	-3.86	1.1	$\pi\pi*$	5.72	-7.8	0.99	$\pi\pi*$
	8	3.46	0.52	1.6	CT	4.47	0.36	1.81	CT	5.27	-1.43	1.44	$\pi\pi*$	5.77	-4.63	1.33	$\pi\pi*$
	9	3.52	5.72	3.68	ghost	4.51	5.81	5.67	ghost	5.69	2.43	2.41	CT	5.99	-3.85	1.42	$\pi\pi*$
	10	3.56	1.77	3.67	CT	4.57	6.73	6.69	ghost	6.25	5.83	6.59	CT	6.46	-12.98	0.76	$\pi\pi*$

11.3.2 *Raw data relative to Section 6.5*

Excitation energies, computed prefactor - that is the weighted average of the orbital energies contributing to the transition, IP and EA, oscillator strength f_{osc} , ${}^{R}D_{\mathrm{CT}}$ and ${}^{U}D_{\mathrm{CT}}$, ${}^{R}\mathrm{M}_{\mathrm{AC}}$ and ${}^{U}\mathrm{M}_{\mathrm{AC}}$, and relative labels of the first 10 excited states for CPDNO,DMABN and Phen-PENMe$_2$, treated at different levels of theory, as discussed in section 6.5.
Note: if the M_{AC} value < $\mathrm{E}_{\mathrm{exc}}$ and then the electronic state is labeled as 'spurious' (S). If in addition the oscillator strength is lower that 0.001, the spurious state is then labeled as 'ghost' (G). Excited states having D_{CT} values > 2.0 Å are denoted as charge-transfer states (CT), otherwise they are demoted as local (L).

Table 12: M_{AC} **diagnostics along the proton-transfer coordinate in CPDNO calculated at the PBE0/6-31G(d) level of theory, in gas phase**

	vertical state	E_{exc} / eV	p / eV	IP / eV	EA / eV	f_{osc}	${}^{U}D_{\mathrm{DC}}$ /	${}^{R}D_{\mathrm{CT}}$ /	${}^{U}M_{\mathrm{CT}}$ / eV	${}^{R}M_{\mathrm{AC}}$ / eV	U	R
S001	1	2.9127	0.3578	7.9659	-1.7707	0.0000	1.1530	0.6040	-2.7523	-14.1039	L	L
S001	2	3.2796	0.3099	6.7933	-1.6384	0.2597	2.0410	1.3010	1.3765	-2.6364	CT	L
S001	3	3.8670	0.4074	9.1638	-1.9217	0.1002	2.8580	1.6590	6.0471	2.4058	S	L
S001	4	4.4204	0.3902	7.0061	-3.6117	0.0056	1.0950	0.7040	-2.5326	-9.8363	L	L
S001	5	4.7750	0.4319	9.2716	-2.4812	0.0876	0.7120	0.4280	-8.4715	-21.8913	L	L
S001	6	4.7909	0.4216	7.9659	-3.5060	0.0001	3.4760	1.6410	7.3293	2.6970	G	L
S001	7	5.0157	0.4229	8.6115	-2.8954	0.3438	1.2500	0.7290	-0.0129	-8.2458	L	L
S001	8	5.5076	0.4373	7.9659	-3.9349	0.0000	3.5120	1.7170	7.8007	3.5143	G	L
S001	9	5.7951	0.4850	11.5060	-1.6916	0.0034	3.9540	2.4430	9.5558	7.3033	S	S
S001	10	5.8117	0.4543	8.8192	-3.5417	0.5341	2.0200	1.2240	5.2323	0.5965	CT	L
S002	1	2.9255	0.3558	7.9814	-1.7002	0.0000	1.1450	0.5870	-2.8945	-14.8493	L	L
S002	2	3.2408	0.3069	6.7735	-1.5765	0.2619	1.9910	1.2680	1.1176	-3.0062	L	L
S002	3	3.8485	0.4055	9.1873	-1.8481	0.1030	2.8710	1.6490	6.0198	2.3030	S	L
S002	4	4.4005	0.3881	6.9832	-3.5785	0.0112	1.1820	0.8060	-1.6207	-7.3038	L	L
S002	5	4.7500	0.4304	9.3727	-2.3378	0.1004	0.8190	0.4690	-5.8715	-18.9924	L	L
S002	6	4.8229	0.4214	7.9814	-3.4862	0.0001	3.4560	1.6090	7.3011	2.5182	G	L
S002	7	4.9976	0.4229	8.5282	-2.9801	0.3212	1.1110	0.6470	-1.4526	-10.7477	L	L
S002	8	5.5588	0.4388	7.9814	-3.9589	0.0000	3.4810	1.6770	7.8037	3.3538	G	L
S002	9	5.7597	0.4831	11.5198	-1.6273	0.0033	3.9790	2.4480	9.5281	7.2648	S	S
S002	10	5.8014	0.4536	8.9414	-3.4010	0.4996	1.7020	1.0170	3.8819	-1.8166	L	L
S003	1	2.9876	0.2946	6.7277	-1.2893	0.2240	2.8200	1.6430	2.9108	-0.7472	CT	L
S003	2	3.0516	0.3925	9.3404	-1.3395	0.0000	0.7410	0.3350	-8.7528	-32.3041	L	L
S003	3	3.6604	0.3474	8.0488	-1.4031	0.1140	3.2700	1.7610	5.0484	1.2750	S	L
S003	4	4.3824	0.3809	6.8764	-3.4889	0.0413	2.1670	1.4030	3.7203	0.1018	CT	L
S003	5	4.4938	0.4278	10.2662	-1.3748	0.2647	1.5750	0.9770	2.4983	-3.0977	L	L
S003	6	4.8855	0.4057	7.3947	-3.6458	0.1385	0.9310	0.6130	-4.4264	-12.4500	L	L
S003	7	5.3288	0.4695	9.3404	-3.4367	0.0001	3.4080	1.5340	8.5518	3.3901	G	L
S003	8	5.4505	0.4726	11.5715	-1.2893	0.0036	3.5680	2.2430	8.8251	6.4410	S	S
S003	9	5.6494	0.4488	10.0632	-2.1485	0.0912	2.6560	1.4310	6.7902	2.1491	S	L
S003	10	5.8709	0.4392	9.4040	-2.5477	0.5743	1.2560	0.8130	0.4870	-5.7600	L	L
S004	1	2.9642	0.2967	6.7044	-1.3679	0.2092	2.9260	1.6980	3.1510	-0.4080	S	L
S004	2	3.0987	0.3950	9.3818	-1.3679	0.0000	0.5770	0.2560	-14.2064	-45.4990	L	L
S004	3	3.6545	0.3484	8.0252	-1.4550	0.1005	3.3910	1.8210	5.2338	1.5727	S	L
S004	4	4.3464	0.3789	6.7833	-3.5276	0.0582	1.9630	1.3250	2.9754	-0.5568	L	L
S004	5	4.5471	0.4299	10.2495	-1.4486	0.2509	1.5160	0.9390	2.1996	-3.6370	L	L
S004	6	4.8606	0.4046	7.3929	-3.6175	0.1344	0.9290	0.6060	-4.4897	-12.7514	L	L
S004	7	5.3452	0.4699	9.3818	-3.4038	0.0001	3.4180	1.5530	8.5727	3.5134	G	L
S004	8	5.4955	0.4758	11.5794	-1.3679	0.0034	3.4680	2.2210	8.7952	6.4639	S	S
S004	9	5.6505	0.4467	9.7865	-2.3693	0.1157	2.4690	1.4020	6.3235	1.8849	S	L
S004	10	5.8877	0.4392	9.2545	-2.6956	0.6064	0.5620	0.3580	-13.6721	-28.2725	L	L
S005	1	2.9395	0.2967	6.6921	-1.3821	0.2051	2.8450	1.6470	3.0128	-0.6688	S	L
S005	2	3.1132	0.3974	9.4305	-1.3821	0.0001	0.4420	0.1660	-21.7658	-75.9323	L	L
S005	3	3.6118	0.3468	7.9936	-1.4447	0.0973	3.4570	1.8440	5.2729	1.6293	S	L
S005	4	4.3241	0.3775	6.7484	-3.5249	0.0731	1.9730	1.3520	2.9749	-0.3773	L	L

S005	5	4.5735	0.4288	10.2080	-1.4591	0.2285	1.6350	1.0230	2.8601	-2.4087	L	L
S005	6	4.8705	0.4065	7.3718	-3.6891	0.1095	1.1380	0.7320	-1.5926	-8.6108	L	L
S005	7	5.3404	0.4730	9.4305	-3.4403	0.0002	3.3570	1.5180	8.5814	3.3849	G	L
S005	8	5.5415	0.4762	11.5749	-1.3821	0.0032	3.3580	2.1820	8.6688	6.3577	S	S
S005	9	5.6072	0.4448	9.7982	-2.3042	0.0994	2.6010	1.4920	6.5661	2.4511	S	L
S005	10	5.8856	0.4351	8.8943	-2.9443	0.6658	0.6910	0.2840	-9.0003	-38.8644	L	L
S006	1	2.7820	0.2934	6.6083	-1.3756	0.1769	2.9700	1.6620	3.1355	-0.6801	S	L
S006	2	3.1065	0.4003	9.5180	-1.3756	0.0001	0.5600	0.1210	-14.8200	-108.1117	L	L
S006	3	3.4595	0.3438	7.9377	-1.4173	0.0734	3.6350	1.9140	5.3936	1.8317	S	L
S006	4	4.2482	0.3738	6.6760	-3.4967	0.0861	1.9590	1.3290	2.8222	-0.6623	L	L
S006	5	4.5685	0.4291	10.2581	-1.4185	0.2302	1.8250	1.1520	3.7865	-0.8230	L	L
S006	6	4.8461	0.4038	7.2161	-3.7725	0.0735	1.5830	0.9750	1.8922	-3.7803	L	L
S006	7	5.3498	0.4806	9.9553	-3.1238	0.0004	3.1060	1.4280	8.4430	2.9953	G	L
S006	8	5.4404	0.4457	10.1430	-1.9840	0.0304	3.1470	1.8280	7.5514	4.2498	S	L
S006	9	5.5724	0.4766	11.4264	-1.5432	0.0027	2.7060	1.8590	7.6483	5.2237	S	L
S006	10	5.8397	0.4269	8.1753	-3.4417	0.6721	0.4700	0.3130	-19.0205	-34.3883	L	L
S007	1	2.6603	0.2853	6.5302	-1.2322	0.1580	2.8550	1.5280	2.7187	-1.6615	S	L
S007	2	2.9757	0.3983	9.6065	-1.2322	0.0002	1.2130	0.3390	-1.0324	-31.6382	L	L
S007	3	3.2906	0.3355	7.8431	-1.2854	0.0898	3.5840	1.8620	5.1108	1.3951	S	L
S007	4	4.2213	0.3722	6.6040	-3.5252	0.1115	2.0600	1.3520	3.1391	-0.5214	CT	L
S007	5	4.5203	0.4252	10.3377	-1.2322	0.2142	1.8640	1.1550	3.8447	-0.8974	L	L
S007	6	4.8702	0.4035	7.0621	-3.9171	0.0435	2.1550	1.2810	4.2972	-0.2618	CT	L
S007	7	5.1626	0.4887	10.9810	-2.3160	0.0008	1.7860	0.8690	5.2345	-3.2734	L	L
S007	8	5.2547	0.4392	10.2462	-1.7038	0.0080	3.2510	1.8430	7.5208	4.1369	S	L
S007	9	5.4412	0.4807	10.7148	-2.3663	0.0009	2.0810	1.0270	6.1615	-0.9400	G	L
S007	10	5.7803	0.4212	7.6754	-3.7866	0.5540	0.7540	0.4470	-7.6358	-20.7521	L	L
S008	1	2.6140	0.2820	6.5687	-1.1047	0.1297	2.8170	1.4650	2.5617	-2.1558	CT	L
S008	2	2.8186	0.3967	9.6895	-1.1047	0.0002	1.6110	0.4700	1.8559	-19.8434	L	L
S008	3	3.2012	0.3260	7.7009	-1.1709	0.1367	3.4680	1.7980	4.7197	0.8632	S	L
S008	4	4.2330	0.3722	6.6320	-3.4970	0.1396	2.1730	1.3940	3.5023	-0.2008	CT	L
S008	5	4.5199	0.4233	10.4142	-1.1047	0.2162	1.6550	1.0290	2.8182	-2.4750	L	L
S008	6	4.9092	0.4064	7.2227	-3.8349	0.0223	2.2630	1.3770	4.6946	0.6004	CT	L
S008	7	4.9587	0.4833	11.5334	-1.6186	0.0012	0.6680	0.3440	-8.4044	-28.7075	L	L
S008	8	5.1420	0.4320	10.1379	-1.6161	0.0103	3.2010	1.7450	7.2555	3.5021	S	L
S008	9	5.2767	0.4818	10.0735	-3.0359	0.0003	2.9850	1.2680	8.2854	1.7532	G	L
S008	10	5.7823	0.5146	9.8686	-4.1350	0.0002	3.1470	1.4080	9.4279	3.7765	G	L

Table 13: M_{AC} **diagnostics along the charge-transfer twisting coordinate of DMABN, calculated at the PBE0/6-31G(d) level of theory, in gas phase**

	vertical state	E_{exc}/eV	p / eV	IP / eV	EA / eV	f_{osc}	$^{U}D_{DC}/$	$^{R}D_{CT}/$	$^{U}M_{CT}/eV$	$^{R}M_{AC}/eV$	U	R
S001	1	4.5393	0.3543	7.8200	-1.8223	0.0347	1.3960	0.8710	-0.6727	-6.8901	L	L
S001	2	4.7481	0.3402	7.7178	-1.5406	0.5642	2.6990	1.8130	3.9232	1.3159	CT	L
S001	3	5.0122	0.3556	7.6573	-2.0186	0.0237	2.2370	1.9090	3.2388	2.1328	CT	L
S001	4	5.5931	0.3692	7.6573	-2.3879	0.0000	1.6800	1.4600	1.4739	0.1824	L	L
S001	5	5.6703	0.3743	7.6573	-2.5283	0.0000	0.8410	0.8550	-6.9365	-6.6561	L	L
S001	6	6.0311	0.4131	9.6348	-1.6059	0.1159	2.1920	1.5890	4.6716	2.1787	CT	L
S001	7	6.0544	0.3812	7.6573	-2.7147	0.0035	1.6850	1.4700	1.8262	0.5763	L	L
S001	8	6.0659	0.4001	7.8031	-3.0853	0.0000	3.4280	2.1110	6.6878	4.0671	G	CT
S001	9	6.1527	0.3775	7.6573	-2.6140	0.0255	2.0820	1.7110	3.3550	1.8553	CT	L
S001	10	6.1697	0.3785	7.6573	-2.6425	0.0085	0.2330	0.3520	-51.5013	-30.6083	L	L
S002	1	4.5205	0.3556	7.8184	-1.8586	0.0337	1.4230	0.8840	-0.4423	-6.6123	L	L
S002	2	4.7265	0.3407	7.7202	-1.5512	0.5594	2.7180	1.8170	3.9736	1.3465	CT	L
S002	3	5.0084	0.3558	7.6613	-2.0210	0.0236	2.2160	1.8970	3.1842	2.0915	CT	L
S002	4	5.5976	0.3690	7.6613	-2.3785	0.0000	1.6250	1.4230	1.1785	-0.0794	L	L
S002	5	5.6692	0.3746	7.6613	-2.5317	0.0000	0.7140	0.7620	-9.9745	-8.7041	L	L
S002	6	6.0091	0.4130	9.5704	-1.6684	0.1039	1.8470	1.2340	3.4425	-0.4303	L	L
S002	7	6.0612	0.3999	7.7988	-3.0832	0.0002	3.4440	2.1160	6.7009	4.0768	G	CT
S002	8	6.0613	0.3818	7.7257	-2.6648	0.0096	1.5270	1.3700	0.9604	-0.1203	L	L
S002	9	6.1324	0.3762	7.6613	-2.5767	0.0257	2.0300	1.6830	3.1446	1.6820	CT	L

S002	10	6.1858	0.3796	7.6613	-2.6688	0.0074	0.2120	0.3470	-57.5927	-31.1674	L	L
S003	1	4.4711	0.3583	7.8223	-1.9265	0.0303	1.5110	0.9320	0.2189	-5.7015	L	L
S003	2	4.6636	0.3425	7.7335	-1.5855	0.5489	2.7680	1.8220	4.1168	1.4158	CT	L
S003	3	5.0060	0.3567	7.6792	-2.0283	0.0234	2.1290	1.8480	2.9440	1.9155	CT	L
S003	4	5.6057	0.3688	7.6792	-2.3554	0.0000	1.4780	1.3310	0.2920	-0.7840	L	L
S003	5	5.6698	0.3750	7.6792	-2.5250	0.0003	0.3670	0.5140	-29.0319	-17.8107	L	L
S003	6	5.9539	0.4175	9.6900	-1.6709	0.0934	1.9680	1.3650	4.0440	0.8117	L	L
S003	7	6.0507	0.3951	7.8596	-2.8912	0.0031	3.2270	1.9450	6.2886	3.3474	S	L
S003	8	6.0783	0.3860	7.6792	-2.8256	0.0056	1.4640	1.3360	0.6690	-0.2733	L	L
S003	9	6.0859	0.3764	7.6792	-2.5622	0.0259	1.6620	1.4720	1.5774	0.4591	L	L
S003	10	6.2370	0.3859	7.6792	-2.8207	0.0040	0.0140	0.2240	-1018.0466	-53.7842	L	L
S004	1	4.4133	0.3619	7.8671	-1.9803	0.0244	1.6770	1.0290	1.2609	-4.1464	L	L
S004	2	4.5503	0.3462	7.7848	-1.6353	0.5251	2.8580	1.8290	4.3817	1.5471	CT	L
S004	3	5.0283	0.3593	7.7400	-2.0372	0.0232	1.9200	1.7180	2.2774	1.3956	L	L
S004	4	5.6343	0.3700	7.7400	-2.3275	0.0000	1.2080	1.1600	-1.8528	-2.3460	L	L
S004	5	5.6885	0.3740	7.7400	-2.4370	0.0014	0.0350	0.2360	-401.2417	-50.8385	L	L
S004	6	5.8593	0.4215	9.7386	-1.7303	0.0774	2.0120	1.4110	4.3119	1.2635	CT	L
S004	7	6.0356	0.3809	7.7400	-2.6252	0.0275	0.0030	0.4130	-4789.5188	-24.5008	L	L
S004	8	6.0706	0.3877	7.8128	-2.7363	0.0079	1.7740	0.8690	2.4320	-6.0213	L	L
S004	9	6.1228	0.3879	7.7400	-2.8149	0.0033	1.3380	1.2770	-0.2072	-0.7213	L	L
S004	10	6.3120	0.3902	7.7400	-2.8787	0.0014	0.4070	0.0620	-24.7613	-221.6338	L	L
S005	1	4.3654	0.3669	7.9703	-2.0132	0.0180	1.9320	1.1840	2.5303	-2.1784	L	L
S005	2	4.3879	0.3501	7.8613	-1.6652	0.4592	3.0560	1.9350	4.8145	2.0848	S	L
S005	3	5.0642	0.3640	7.8613	-2.0435	0.0227	1.6120	1.5290	0.9720	0.4871	L	L
S005	4	5.6818	0.3735	7.8613	-2.3033	0.0001	0.8570	0.9450	-6.6379	-5.0732	L	L
S005	5	5.7220	0.3970	8.7155	-2.0881	0.0185	0.8010	0.1900	-7.1734	-64.9840	L	L
S005	6	5.7317	0.4034	8.9562	-2.0221	0.0413	1.4290	0.6910	0.9016	-9.8605	L	L
S005	7	6.0249	0.3826	7.8613	-2.5502	0.0383	0.9050	1.0490	-5.4997	-3.3155	L	L
S005	8	6.0949	0.3941	7.9881	-2.7369	0.0017	3.2650	1.9130	6.3146	3.1977	S	L
S005	9	6.1909	0.4513	10.5710	-1.7096	0.0117	0.5350	0.4690	-14.6346	-18.4223	L	L
S005	10	6.1971	0.3966	7.8613	-2.9301	0.0033	1.0280	1.0970	-3.2161	-2.3351	L	L
S006	1	4.1791	0.3573	8.0354	-1.6867	0.3515	3.2700	2.0730	5.3185	2.7758	S	CT
S006	2	4.3194	0.3729	8.1189	-2.0275	0.0121	2.2580	1.3800	3.7691	-0.2882	CT	L
S006	3	5.0922	0.3707	8.0354	-2.0515	0.0220	1.2330	1.2920	-1.5917	-1.0584	L	L
S006	4	5.5737	0.4268	9.8029	-1.8110	0.0369	2.0780	1.3900	4.6843	1.2544	CT	L
S006	5	5.7264	0.3796	8.0354	-2.2933	0.0005	0.4780	0.7190	-19.7962	-9.6987	L	L
S006	6	5.7657	0.3770	8.0354	-2.2237	0.0042	0.8570	0.2750	-6.5433	-42.1033	L	L
S006	7	5.9630	0.4426	10.2817	-1.7619	0.0925	0.2030	0.2260	-58.8907	-51.6717	L	L
S006	8	6.0169	0.3909	8.1546	-2.4829	0.0152	0.8180	1.0040	-6.9660	-3.7048	L	L
S006	9	6.1370	0.4010	8.1901	-2.7208	0.0002	3.8420	2.2580	7.1629	4.5337	G	CT
S006	10	6.2655	0.4046	8.0354	-2.9745	0.0045	0.2730	0.5650	-41.7361	-14.4762	L	L
S007	1	3.9277	0.3656	8.2619	-1.6857	0.2217	3.3960	2.1720	5.7074	3.3179	S	CT
S007	2	4.2676	0.3813	8.3384	-2.0366	0.0071	2.5970	1.5840	4.8303	1.2843	S	L
S007	3	5.1004	0.3795	8.2619	-2.0638	0.0207	0.8140	1.0120	-7.3643	-3.9032	L	L
S007	4	5.4155	0.4327	9.9529	-1.8223	0.0225	1.9070	1.2410	4.2242	0.1719	L	L
S007	5	5.7573	0.3914	8.4531	-2.1975	0.0413	0.0600	0.4410	-229.3436	-22.0017	L	L
S007	6	5.7721	0.4124	9.4096	-1.8128	0.1349	0.0870	0.0450	-154.2909	-308.7699	L	L
S007	7	5.7966	0.3821	8.2619	-2.1366	0.0042	1.2970	0.5320	-0.7038	-16.6685	L	L
S007	8	5.9971	0.3953	8.2619	-2.4948	0.0189	0.5860	0.8660	-13.8161	-5.8711	L	L
S007	9	6.1898	0.4099	8.4842	-2.6705	0.0013	4.3340	2.4830	7.8321	5.3553	S	CT
S007	10	6.2800	0.4119	8.2619	-2.9470	0.0050	0.6550	0.1440	-10.7753	-88.7886	L	L
S008	1	3.6614	0.3749	8.5390	-1.6634	0.1044	3.4640	2.2370	6.0455	3.7654	S	S
S008	2	4.2072	0.3900	8.5666	-2.0457	0.0033	2.8780	1.7570	5.6089	2.4167	S	L
S008	3	5.0848	0.3900	8.5390	-2.0730	0.0183	0.4110	0.7190	-24.4236	-9.4153	L	L
S008	4	5.2777	0.4262	9.7862	-1.8125	0.0145	1.4030	0.8720	1.3352	-4.9146	L	L
S008	5	5.6295	0.4159	9.6177	-1.6987	0.2695	0.1370	0.3330	-93.7905	-31.9258	L	L
S008	6	5.7809	0.3980	8.5390	-2.2923	0.0012	0.3430	0.1800	-31.1501	-69.1667	L	L
S008	7	5.8123	0.3915	8.5390	-2.1151	0.0042	1.7090	0.7680	2.2283	-8.0954	L	L
S008	8	5.9714	0.4050	8.5390	-2.4823	0.0113	0.3200	0.6890	-33.9776	-9.8781	L	L
S008	9	6.2436	0.4204	8.5390	-2.8996	0.0028	0.9980	0.3930	-2.9899	-25.2018	L	L
S008	10	6.2506	0.4213	8.8326	-2.6328	0.0034	4.8520	2.6580	8.4977	6.0480	S	CT
S009	1	3.3870	0.3840	8.8418	-1.6083	0.0209	3.2960	2.1560	6.0812	3.7712	S	S
S009	2	4.1230	0.3996	8.8418	-2.0315	0.0007	2.9080	1.7760	5.9215	2.7654	G	L
S009	3	4.9780	0.3999	8.8418	-2.0402	0.0129	0.3290	0.6440	-32.8859	-11.4777	L	L

S009	4	5.1892	0.4165	9.5623	-1.7714	0.0101	0.7840	0.4110	-7.0333	-23.7020	L	L
S009	5	5.5450	0.4107	9.5314	-1.6442	0.3275	0.1690	0.2870	-74.0294	-38.9974	L	L
S009	6	5.7317	0.4105	8.8418	-2.3294	0.0012	0.6210	0.0310	-12.0166	-453.3337	L	L
S009	7	5.7545	0.4047	8.8418	-2.1698	0.0004	1.6760	0.7300	2.4199	-8.7140	L	L
S009	8	5.8647	0.4162	8.8418	-2.4838	0.0009	0.1550	0.5570	-81.5754	-14.5266	L	L
S009	9	6.2727	0.4295	8.8418	-2.8452	0.0048	0.6220	0.0260	-11.4636	-542.1458	L	L
S009	10	6.2787	0.4295	9.0258	-2.6620	0.0044	5.4180	2.7520	9.0300	6.4553	S	S
S010	1	3.3231	0.3942	9.1333	-1.5924	0.0000	3.3000	2.1660	6.3621	4.0776	G	G
S010	2	4.1123	0.4101	9.1333	-2.0265	0.0002	2.9490	1.8090	6.2769	3.1998	G	L
S010	3	4.9697	0.4105	9.1333	-2.0372	0.0122	0.2400	0.5660	-48.8280	-14.2706	L	L
S010	4	5.1614	0.4120	9.4485	-1.7612	0.0092	0.5630	0.2310	-14.3669	-51.1264	L	L
S010	5	5.5220	0.4002	9.2601	-1.6290	0.3469	0.2170	0.2950	-55.4687	-37.9233	L	L
S010	6	5.7496	0.4227	9.1333	-2.3684	0.0003	0.8860	0.2310	-4.7507	-50.8344	L	L
S010	7	5.7593	0.4160	9.1333	-2.1874	0.0003	1.7470	0.7810	3.0782	-7.1168	L	L
S010	8	5.8551	0.4268	9.1333	-2.4808	0.0000	0.2380	0.6130	-48.8886	-11.8763	L	L
S010	9	6.2634	0.4400	9.1333	-2.8396	0.0024	0.6150	0.0310	-11.4412	-452.5320	L	L
S010	10	6.3183	0.4350	9.1333	-2.7045	0.0054	5.6630	2.8020	9.2950	6.6987	S	S

Table 14: M_{AC} **diagnostics along the charge-transfer twisting coordinate of DMABN, calculated at the PBE0/6-311+G(d,p) level of theory, in CH_3CN**

	vertical state	E_{exc}/eV	p / eV	IP / eV	EA / eV	f_{osc}	$^{U}D_{DC}/$	$^{R}D_{CT}/$	$^{U}M_{CT}/eV$	$^{R}M_{AC}/eV$	U	R
S001	1	4.2746	0.3228	7.5730	-1.2113	0.9603	2.7550	2.3690	3.5576	2.7060	CT	CT
S001	2	4.3729	0.3414	7.6538	-1.6359	0.0760	1.4480	1.0850	-0.6548	-3.9819	L	L
S001	3	5.1914	0.3469	7.5730	-1.8664	0.0394	0.3610	0.6070	-30.4488	-14.2832	L	L
S001	4	5.6087	0.3696	7.6592	-2.3988	0.0000	3.7410	2.8790	6.2089	5.0565	G	CT
S001	5	5.7051	0.3556	7.5730	-2.1043	0.0101	1.6540	1.3430	0.9714	-1.0447	L	L
S001	6	5.7654	0.3984	9.5826	-1.2571	0.2163	1.4130	1.3570	0.6488	0.2283	L	L
S001	7	5.9016	0.3682	7.5730	-2.4464	0.0000	0.3770	0.6010	-28.1759	-13.9400	L	L
S001	8	6.1506	0.3798	7.5730	-2.7606	0.0008	0.6210	0.8250	-12.8542	-7.1205	L	L
S001	9	6.2346	0.3807	7.9118	-2.4475	0.1691	0.2800	0.5090	-41.0680	-17.9308	L	L
S001	10	6.3175	0.3741	7.5730	-2.6080	0.0046	1.4680	1.6040	0.3720	1.2037	L	L
S002	1	4.2708	0.3245	7.6062	-1.2241	0.9492	2.7340	2.3310	3.5635	2.6529	CT	CT
S002	2	4.3838	0.3430	7.6897	-1.6434	0.0737	1.4620	1.0970	-0.5161	-3.7933	L	L
S002	3	5.2225	0.3474	7.6062	-1.8479	0.0397	0.2890	0.5430	-40.3717	-17.0646	L	L
S002	4	5.6276	0.3711	7.7004	-2.3972	0.0000	3.7510	2.8880	6.2587	5.1115	G	CT
S002	5	5.7296	0.3570	7.6062	-2.1084	0.0105	1.6170	1.3050	0.8095	-1.3195	L	L
S002	6	5.7513	0.3990	9.5862	-1.2700	0.2168	1.4090	1.3540	0.6364	0.2213	L	L
S002	7	5.9280	0.3696	7.6062	-2.4509	0.0005	0.3680	0.5860	-29.0723	-14.5156	L	L
S002	8	6.1659	0.3772	7.6062	-2.6578	0.0089	0.7360	0.9330	-9.3007	-5.1697	L	L
S002	9	6.2489	0.3859	7.9797	-2.5218	0.1796	0.6750	0.7510	-10.8314	-8.6725	L	L
S002	10	6.3448	0.3742	7.6062	-2.5770	0.0046	1.3450	1.4890	-0.5228	0.5126	L	L
S003	1	4.2594	0.3278	7.6729	-1.2457	0.9112	2.7130	2.2770	3.6109	2.5946	CT	CT
S003	2	4.4047	0.3462	7.7617	-1.6599	0.0803	1.5240	1.1460	-0.0270	-3.1436	L	L
S003	3	5.2796	0.3501	7.6729	-1.8528	0.0396	0.1660	0.4350	-77.2192	-23.5769	L	L
S003	4	5.6642	0.3738	7.7806	-2.3914	0.0001	3.7670	2.9010	6.3494	5.2082	G	CT
S003	5	5.7220	0.4001	9.5950	-1.2930	0.2177	1.4190	1.3620	0.7403	0.3157	L	L
S003	6	5.7762	0.3597	7.6729	-2.1140	0.0101	1.5550	1.2410	0.5267	-1.8164	L	L
S003	7	5.9779	0.3719	7.6729	-2.4478	0.0013	0.3420	0.5550	-31.9835	-15.8246	L	L
S003	8	6.1968	0.3773	7.6729	-2.5943	0.0293	0.8670	1.0670	-6.3414	-3.2282	L	L
S003	9	6.2752	0.3901	8.1238	-2.4905	0.1971	0.9730	0.9740	-4.1849	-4.1697	L	L
S003	10	6.3937	0.3775	7.6729	-2.6004	0.0050	1.1390	1.3010	-2.3690	-0.7948	L	L
S004	1	4.2325	0.3326	7.7659	-1.2850	0.8424	2.7160	2.2320	3.7491	2.5995	CT	CT
S004	2	4.4338	0.3502	7.8601	-1.6692	0.1027	1.6570	1.2510	0.8392	-1.9812	L	L
S004	3	5.3523	0.3537	7.7659	-1.8589	0.0371	0.0420	0.3040	-333.2240	-37.7424	L	L
S004	4	5.6793	0.4018	9.6081	-1.3243	0.2194	1.4400	1.3750	0.9327	0.4599	L	L
S004	5	5.7129	0.3768	7.8872	-2.3666	0.0007	3.7960	2.9230	6.4604	5.3275	G	CT
S004	6	5.8372	0.3632	7.7659	-2.1159	0.0093	1.4730	1.1550	0.1061	-2.5854	L	L
S004	7	6.0417	0.3747	7.7659	-2.4294	0.0026	0.3020	0.5070	-37.4857	-18.2064	L	L
S004	8	6.2361	0.3788	7.7659	-2.5404	0.0657	0.9330	1.1420	-5.1274	-2.3028	L	L

S004	9	6.3050	0.3977	8.4705	-2.3503	0.2117	1.0460	1.0190	-2.9455	-3.3103	L	L
S004	10	6.4014	0.4369	10.2957	-1.5942	0.0072	1.5640	1.2210	2.6830	0.0967	L	L
S005	1	4.1812	0.3368	7.8404	-1.3252	0.7725	2.7570	2.2270	3.9427	2.6997	CT	CT
S005	2	4.4539	0.3533	7.9401	-1.6740	0.1275	1.8230	1.3820	1.7152	-0.8054	L	L
S005	3	5.4007	0.3570	7.8404	-1.8737	0.0335	0.1510	0.1890	-85.6478	-66.4745	L	L
S005	4	5.6358	0.4036	9.6223	-1.3593	0.2253	1.4400	1.3690	0.9819	0.4633	L	L
S005	5	5.7418	0.3779	7.9682	-2.3137	0.0005	3.8290	2.9460	6.5211	5.3940	G	CT
S005	6	5.8734	0.3655	7.8404	-2.1054	0.0097	1.3630	1.0360	-0.6188	-3.9534	L	L
S005	7	6.0810	0.3776	7.8404	-2.4336	0.0055	0.2320	0.4370	-51.7934	-22.6771	L	L
S005	8	6.2547	0.3870	8.1225	-2.4089	0.1016	0.9030	1.1350	-5.4150	-2.1555	L	L
S005	9	6.3030	0.4195	9.5331	-1.8824	0.1348	0.8200	0.6510	-6.1450	-10.7038	L	L
S005	10	6.3514	0.4177	9.2420	-2.1234	0.0422	0.9360	0.8020	-4.0189	-6.5893	L	L
S006	1	4.1455	0.3422	7.9601	-1.3509	0.7117	2.8870	2.3170	4.3232	3.0961	S	CT
S006	2	4.4820	0.3589	8.0672	-1.6987	0.1136	1.9300	1.4700	2.3049	-0.0298	L	L
S006	3	5.4637	0.3614	7.9601	-1.8752	0.0293	0.2170	0.1470	-56.5225	-88.1215	L	L
S006	4	5.5854	0.4058	9.6481	-1.3937	0.2279	1.5380	1.4570	1.6792	1.1587	L	L
S006	5	5.7969	0.3808	8.0971	-2.2649	0.0008	3.8680	2.9680	6.6393	5.5104	G	CT
S006	6	5.9289	0.3694	7.9601	-2.0928	0.0086	1.4150	1.0640	-0.1236	-3.4806	L	L
S006	7	6.1374	0.3826	7.9601	-2.4510	0.0099	0.3020	0.4310	-37.2699	-22.9988	L	L
S006	8	6.1973	0.4501	10.8404	-1.4072	0.0242	1.6120	1.3830	3.3148	1.8357	L	L
S006	9	6.2979	0.3905	8.2948	-2.3307	0.2132	0.7490	1.0030	-8.5997	-3.7311	L	L
S006	10	6.3923	0.3988	8.2504	-2.6008	0.1051	0.5730	0.6120	-14.2791	-12.6776	L	L
S007	1	4.1258	0.3488	8.1264	-1.3662	0.6384	3.0550	2.4500	4.7791	3.6152	S	CT
S007	2	4.5247	0.3666	8.2439	-1.7316	0.0843	2.0320	1.5610	2.8891	0.7509	CT	L
S007	3	5.5275	0.4069	9.6241	-1.4487	0.2012	1.6200	1.4820	2.1841	1.3564	L	L
S007	4	5.5550	0.3688	8.1820	-1.8547	0.0474	0.3070	0.1220	-36.8676	-107.9931	L	L
S007	5	5.8827	0.3856	8.2786	-2.2151	0.0014	3.9000	2.9840	6.8016	5.6681	S	CT
S007	6	6.0085	0.3873	8.5680	-1.9721	0.0150	1.6390	1.2780	1.7544	-0.7273	L	L
S007	7	6.0543	0.4399	10.4640	-1.5061	0.0643	1.8370	1.5850	4.1315	2.8852	L	L
S007	8	6.2180	0.3891	8.1264	-2.4629	0.0146	0.3790	0.4270	-27.4045	-23.1335	L	L
S007	9	6.3468	0.3982	8.5619	-2.2742	0.3155	0.6240	0.8790	-12.2402	-5.5457	L	L
S007	10	6.4791	0.4069	8.6443	-2.4278	0.2117	0.5430	0.7400	-15.4466	-8.3869	L	L
S008	1	4.1107	0.3568	8.3167	-1.3912	0.5451	3.2320	2.5940	5.2526	4.1568	S	S
S008	2	4.5684	0.3744	8.4340	-1.7533	0.0520	2.1610	1.6740	3.5239	1.5853	CT	L
S008	3	5.4654	0.4117	9.7323	-1.4701	0.2006	1.9130	1.7930	3.6751	3.1714	L	L
S008	4	5.6488	0.3744	8.3167	-1.8717	0.0246	0.2540	0.1410	-46.5031	-91.9367	L	L
S008	5	5.8761	0.4512	10.8691	-1.4100	0.1544	1.8470	1.6980	4.4829	3.7987	L	L
S008	6	5.9835	0.3915	8.4799	-2.1738	0.0023	3.9290	2.9980	6.9888	5.8507	S	CT
S008	7	6.1093	0.3816	8.3167	-2.0682	0.0071	1.7150	1.2840	1.9886	-0.8298	L	L
S008	8	6.3007	0.3960	8.3167	-2.4578	0.0217	0.4890	0.4490	-18.6726	-21.2960	L	L
S008	9	6.3931	0.4087	8.9585	-2.1627	0.4781	0.4640	0.6920	-19.9126	-9.6876	L	L
S008	10	6.5026	0.4409	10.1129	-1.8849	0.3189	0.3570	0.4080	-28.3374	-23.2955	L	L
S009	1	4.0902	0.3652	8.5266	-1.4110	0.4210	3.3900	2.7060	5.6899	4.6162	S	S
S009	2	4.6108	0.3824	8.6286	-1.7776	0.0258	2.3370	1.8190	4.2446	2.4900	CT	L
S009	3	5.3909	0.4151	9.7877	-1.5077	0.1613	2.1360	1.9790	4.5540	4.0192	CT	L
S009	4	5.6957	0.4452	10.6767	-1.4368	0.2679	1.7410	1.6270	3.8425	3.2630	L	L
S009	5	5.7425	0.3822	8.5266	-1.8729	0.0289	0.2220	0.1920	-54.4638	-64.5987	L	L
S009	6	6.0967	0.3982	8.6968	-2.1381	0.0035	3.9410	2.9930	7.1811	6.0238	S	CT
S009	7	6.2046	0.3907	8.5751	-2.0564	0.0065	2.0010	1.5120	3.4353	1.1079	CT	L
S009	8	6.3745	0.4155	9.0119	-2.2936	0.0265	0.6110	0.4590	-12.2619	-20.0663	L	L
S009	9	6.3989	0.4334	9.8854	-1.9079	0.5107	0.2830	0.2010	-39.0889	-59.8468	L	L
S009	10	6.4266	0.4272	9.5929	-2.0320	0.5685	0.1320	0.3130	-97.4633	-34.3803	L	L
S010	1	3.0698	0.3873	9.1434	-1.3966	0.0000	3.4040	2.7200	6.3098	5.2460	G	G
S010	2	3.9428	0.4054	9.1434	-1.8878	0.0001	2.9460	2.2040	6.1433	4.4977	G	G
S010	3	4.9877	0.4066	9.1434	-1.9199	0.0175	0.1380	0.2650	-93.2820	-43.2750	L	L
S010	4	5.0940	0.4092	9.6127	-1.5232	0.0491	0.9920	0.7870	-3.3799	-7.1610	L	L
S010	5	5.3136	0.3967	9.3846	-1.4103	0.6817	1.0410	1.1040	-3.0375	-2.2482	L	L
S010	6	5.6453	0.4097	9.1434	-2.0041	0.0004	3.6540	2.6970	7.2067	5.8084	G	G
S010	7	5.7457	0.4194	9.1434	-2.2695	0.0022	3.3100	2.1190	7.0626	4.6174	S	CT
S010	8	5.7959	0.4301	9.1434	-2.5609	0.0000	0.2210	0.1960	-53.4525	-61.7633	L	L
S010	9	5.9247	0.4223	9.1434	-2.3486	0.0105	3.9650	2.6090	7.8603	5.9728	S	S
S010	10	6.1698	0.4191	9.3580	-2.0468	0.3847	0.8910	0.7100	-4.7564	-8.8763	L	L

Table 15: M_{AC} **diagnostics along the charge-transfer twisting coordinate of Phen-PENME$_2$, calculated at the CAM-B3LYP/6-31+G(d) level of theory, in gas phase**

	vertical state	E_{exc}/eV	p / eV	IP / eV	EA / eV	f_{osc}	${}^{U}D_{CT}/$	${}^{R}D_{CT}/$	${}^{U}M_{CT}/eV$	${}^{R}M_{AC}/eV$	U	R
S001	1	3.6787	0.3072	6.7510	-1.6071	1.1488	4.1760	3.0310	4.9099	3.6073	S	CT
S001	2	4.0758	0.3289	7.3237	-1.6265	0.0068	3.7910	2.7710	5.1519	3.7537	S	CT
S001	3	4.4577	0.4050	9.3813	-1.6392	0.0000	1.3830	0.6350	0.6086	-11.6561	L	L
S001	4	4.5085	0.4081	9.4222	-1.6821	0.0031	1.9080	1.1060	3.5573	-1.9153	L	L
S001	5	4.5417	0.3325	7.0766	-1.9711	0.0319	0.1830	0.2900	-69.6390	-40.6063	L	L
S001	6	4.6553	0.3396	7.4950	-1.7453	0.2941	2.3910	1.8620	3.2178	1.5068	CT	L
S001	7	4.7884	0.3456	7.7718	-1.6312	0.1433	3.3580	2.5560	5.1148	3.7693	S	CT
S001	8	4.9224	0.3208	6.7951	-1.9354	0.0237	2.0600	2.0520	1.7404	1.7132	CT	CT
S001	9	4.9731	0.4272	9.9133	-1.7125	0.0009	1.9920	1.2790	4.3971	0.3673	L	L
S001	10	5.0258	0.3336	7.3506	-1.7272	0.1263	5.2270	3.3840	6.3229	4.8225	S	CT
S002	1	3.6852	0.3076	6.7596	-1.6116	1.1364	4.2060	3.0500	4.9476	3.6500	S	CT
S002	2	4.0799	0.3295	7.3366	-1.6308	0.0065	3.7710	2.7580	5.1489	3.7464	S	CT
S002	3	4.4577	0.4051	9.3790	-1.6433	0.0001	1.3820	0.6350	0.6029	-11.6543	L	L
S002	4	4.5085	0.4082	9.4206	-1.6859	0.0031	1.9030	1.1010	3.5397	-1.9721	L	L
S002	5	4.5434	0.3329	7.0857	-1.9738	0.0318	0.1650	0.2740	-78.2111	-43.4939	L	L
S002	6	4.6503	0.3418	7.5593	-1.7404	0.2795	2.3690	1.8720	3.2213	1.6076	CT	L
S002	7	4.7876	0.3445	7.7321	-1.6412	0.1382	3.4210	2.6150	5.1641	3.8667	S	CT
S002	8	4.9221	0.3211	6.8018	-1.9361	0.0210	1.8990	1.9420	1.1551	1.3230	L	L
S002	9	4.9714	0.4241	9.8445	-1.6953	0.0151	1.7760	1.1520	3.4319	-0.9599	L	L
S002	10	5.0045	0.3518	7.8482	-1.7235	0.1218	3.0910	2.1970	4.9131	3.0175	CT	CT
S003	1	3.7054	0.3090	6.7872	-1.6215	1.0976	4.2880	3.1030	5.0505	3.7681	S	S
S003	2	4.0922	0.3314	7.3772	-1.6396	0.0057	3.7020	2.7130	5.1271	3.7092	S	CT
S003	3	4.4575	0.4043	9.3549	-1.6468	0.0002	1.3790	0.6320	0.5596	-11.7825	L	L
S003	4	4.5086	0.4075	9.4152	-1.6722	0.0032	1.8880	1.0870	3.4605	-2.1598	L	L
S003	5	4.5493	0.3337	7.0955	-1.9839	0.0314	0.1260	0.2260	-105.2035	-54.6359	L	L
S003	6	4.6339	0.3479	7.7584	-1.7072	0.2303	2.3740	1.9170	3.4000	1.9540	CT	L
S003	7	4.7871	0.3410	7.6083	-1.6708	0.1413	3.5400	2.7170	5.2114	3.9793	S	CT
S003	8	4.9156	0.3337	7.2611	-1.8201	0.0591	0.4880	0.8750	-20.4262	-7.3755	L	L
S003	9	4.9629	0.3626	8.0712	-1.7952	0.1097	0.9610	0.9480	-5.1176	-5.3230	L	L
S003	10	4.9837	0.4049	9.2940	-1.7231	0.0557	1.1450	0.7690	-1.5590	-7.7081	L	L
S004	1	3.7385	0.3111	6.8316	-1.6340	1.0312	4.4150	3.1820	5.2041	3.9402	S	S
S004	2	4.1118	0.3342	7.4418	-1.6510	0.0045	3.5810	2.6320	5.0717	3.6218	S	CT
S004	3	4.4573	0.4045	9.3478	-1.6582	0.0006	1.3720	0.6270	0.5107	-11.9599	L	L
S004	4	4.5086	0.4064	9.3951	-1.6643	0.0034	1.8590	1.0600	3.3135	-2.5251	L	L
S004	5	4.5591	0.3350	7.1234	-1.9919	0.0302	0.1360	0.1430	-96.7645	-91.5815	L	L
S004	6	4.6030	0.3542	7.9519	-1.6874	0.1501	2.4730	1.9810	3.8165	2.3704	CT	L
S004	7	4.7892	0.3374	7.4621	-1.7198	0.1913	3.4630	2.6320	5.0237	3.7109	S	CT
S004	8	4.8892	0.3436	7.5669	-1.7835	0.1825	1.9470	1.1930	1.9545	-2.7198	L	L
S004	9	4.9635	0.3354	7.2054	-1.9223	0.0999	1.8270	1.8520	1.2461	1.3525	L	L
S004	10	4.9813	0.4181	9.6720	-1.7063	0.0217	1.8660	1.2800	3.6615	0.1286	L	L
S005	1	3.7839	0.3137	6.8909	-1.6461	0.9339	4.5750	3.2800	5.3896	4.1469	S	S
S005	2	4.1372	0.3378	7.5259	-1.6661	0.0033	3.3930	2.5020	4.9481	3.4368	S	CT
S005	3	4.4569	0.4046	9.3418	-1.6688	0.0014	1.3500	0.6120	0.3442	-12.5183	L	L
S005	4	4.5077	0.4043	9.3254	-1.6765	0.0043	1.7570	0.9750	2.8064	-3.7669	L	L
S005	5	4.5576	0.3583	8.0650	-1.6837	0.0573	2.2780	1.8510	3.4276	1.9694	CT	L
S005	6	4.5726	0.3370	7.1786	-1.9906	0.0456	0.2630	0.0360	-45.5822	-390.8210	L	L
S005	7	4.7888	0.3311	7.1996	-1.8100	0.3376	2.6000	1.9210	3.4713	1.5137	CT	L
S005	8	4.8687	0.3402	7.5334	-1.7249	0.2131	3.6050	2.5660	5.2640	3.6466	S	CT
S005	9	4.9726	0.3407	7.3400	-1.9305	0.0730	2.0230	1.9810	2.1525	2.0016	CT	L
S005	10	4.9822	0.4106	9.4349	-1.7392	0.0222	1.9580	1.4290	3.8198	1.0973	L	L
S006	1	3.8404	0.3196	7.0425	-1.6550	0.8038	4.7420	3.3790	5.6609	4.4361	S	S
S006	2	4.1663	0.3420	7.6216	-1.6842	0.0022	3.1220	2.3090	4.6934	3.0694	S	CT
S006	3	4.4543	0.4006	9.2090	-1.6931	0.0066	1.1750	0.4890	-1.3529	-18.5450	L	L
S006	4	4.4929	0.3780	8.6265	-1.6592	0.0195	0.9670	0.7910	-4.6054	-7.9187	L	L
S006	5	4.5196	0.3908	8.9517	-1.6828	0.0154	1.0260	0.4300	-3.4003	-22.8531	L	L
S006	6	4.5867	0.3390	7.2165	-2.0077	0.0366	0.3310	0.0710	-34.2793	-193.5878	L	L
S006	7	4.7766	0.3250	6.9340	-1.9085	0.5323	1.4230	1.0220	-1.2768	-5.2472	L	L
S006	8	4.8743	0.3428	7.6306	-1.6972	0.1684	4.8270	3.4450	6.3446	5.1479	S	S
S006	9	4.9808	0.4180	9.6344	-1.7397	0.0095	1.9640	1.3890	4.0422	1.0071	L	L

S006	10	4.9890	0.3361	7.1770	-1.9697	0.0746	1.9710	1.9650	1.8409	1.8186	L	L
S007	1	3.9055	0.3234	7.1394	-1.6608	0.6319	4.9020	3.4690	5.8627	4.6493	S	S
S007	2	4.1957	0.3460	7.7138	-1.7020	0.0013	2.7620	2.0410	4.2023	2.3606	S	CT
S007	3	4.4263	0.3604	8.1406	-1.6666	0.0659	1.9350	1.6740	2.3655	1.2052	L	L
S007	4	4.4646	0.4012	9.2025	-1.7155	0.0042	1.0420	0.3880	-2.9013	-26.1946	L	L
S007	5	4.5147	0.4073	9.3953	-1.6884	0.0050	1.7190	0.9460	2.7069	-4.1379	L	L
S007	6	4.6012	0.3401	7.2411	-2.0137	0.0370	0.4710	0.1880	-21.3178	-67.3392	L	L
S007	7	4.7587	0.3278	6.9907	-1.9303	0.6814	0.9920	0.7010	-5.5948	-11.6206	L	L
S007	8	4.9004	0.3445	7.6717	-1.7028	0.1494	5.5120	3.7800	6.7621	5.5651	S	S
S007	9	4.9830	0.4299	9.9664	-1.7304	0.0020	1.9090	1.2190	4.1538	-0.1158	L	L
S007	10	5.0010	0.3313	7.0156	-1.9988	0.0764	1.8810	1.9070	1.3590	1.4634	L	L
S008	1	3.9733	0.3306	7.3389	-1.6580	0.4158	5.0350	3.5440	6.1369	4.9337	S	S
S008	2	4.2208	0.3490	7.7809	-1.7161	0.0007	2.3560	1.7300	3.3850	1.1735	CT	L
S008	3	4.3681	0.3477	7.7963	-1.6659	0.1807	2.6240	2.0860	3.9746	2.5592	CT	CT
S008	4	4.4613	0.4089	9.3646	-1.7623	0.0003	1.2920	0.5620	-0.0184	-14.4953	L	L
S008	5	4.5144	0.4085	9.4231	-1.6924	0.0037	1.7510	0.9630	2.8918	-3.8375	L	L
S008	6	4.6136	0.3450	7.3319	-2.0559	0.0380	0.5920	0.2910	-14.9359	-40.0955	L	L
S008	7	4.7452	0.3309	7.0795	-1.9242	0.8000	0.9870	0.7180	-5.5856	-11.0515	L	L
S008	8	4.9374	0.3454	7.6782	-1.7217	0.1346	5.9880	3.9640	6.9952	5.7673	S	S
S008	9	4.9843	0.4310	9.9957	-1.7314	0.0015	1.8770	1.1740	4.0554	-0.5385	L	L
S008	10	5.0118	0.3348	7.0795	-2.0302	0.0764	1.7860	1.8280	1.0472	1.2325	L	L
S009	1	4.0337	0.3359	7.4814	-1.6593	0.1587	5.1370	3.6050	6.3375	5.1463	S	S
S009	2	4.2372	0.3504	7.8094	-1.7246	0.0058	2.0270	1.4760	2.4301	-0.2219	CT	L
S009	3	4.3149	0.3428	7.6591	-1.6688	0.3640	2.1240	1.7100	2.5484	0.9071	CT	L
S009	4	4.4606	0.4079	9.3439	-1.7556	0.0000	1.3130	0.5780	0.1325	-13.8134	L	L
S009	5	4.5146	0.4094	9.4238	-1.7172	0.0031	1.7490	0.9580	2.9080	-3.8899	L	L
S009	6	4.6217	0.3477	7.4114	-2.0505	0.0389	0.6760	0.3640	-11.8394	-30.0976	L	L
S009	7	4.7379	0.3336	7.1583	-1.9189	0.8922	1.1490	0.8740	-3.4551	-7.3984	L	L
S009	8	4.9796	0.3563	7.9533	-1.7418	0.0835	5.3310	3.6010	6.9940	5.6963	S	S
S009	9	4.9856	0.4251	9.8260	-1.7429	0.0096	1.3340	0.7420	0.7745	-7.8377	L	L
S009	10	5.0182	0.3381	7.1583	-2.0420	0.0792	1.6870	1.7470	0.6646	0.9578	L	L
S010	1	4.0617	0.3394	7.5528	-1.6827	0.0001	5.1690	3.6330	6.4497	5.2719	G	G
S010	2	4.2416	0.3502	7.8050	-1.7241	0.0324	1.8720	1.3510	1.8369	-1.1295	L	L
S010	3	4.2920	0.3416	7.6213	-1.6733	0.4728	1.5250	1.1690	-0.1477	-3.0232	L	L
S010	4	4.4604	0.4081	9.3434	-1.7604	0.0000	1.3150	0.5790	0.1535	-13.7660	L	L
S010	5	4.5147	0.4096	9.4260	-1.7186	0.0029	1.7460	0.9540	2.8974	-3.9493	L	L
S010	6	4.6251	0.3491	7.4491	-2.0497	0.0392	0.7040	0.3900	-10.9553	-27.4234	L	L
S010	7	4.7359	0.3372	7.2558	-1.9198	0.9273	1.2590	0.9760	-2.2617	-5.5781	L	L
S010	8	4.9852	0.4317	10.0052	-1.7429	0.0010	1.8210	1.1270	3.8405	-1.0289	L	L
S010	9	5.0083	0.3595	8.0192	-1.7631	0.0008	5.3140	3.6380	7.0725	5.8242	G	G
S010	10	5.0220	0.3398	7.1948	-2.0517	0.0880	1.6470	1.7140	0.5035	0.8453	L	L

Table 16: M_{AC} **diagnostics along the charge-transfer twisting coordinate of Phen-PENME$_2$, calculated at the CAM-B3LYP/6-311+G(d) level of theory, in CH_3CN**

	vertical state	E_{exc}/eV	p / eV	IP / eV	EA / eV	f_{osc}	${}^{U}D_{CT}/$	${}^{R}D_{CT}/$	${}^{U}M_{CT}/eV$	${}^{R}M_{AC}/eV$	U	R
S001	1	3.4441	0.2974	6.7138	-1.3776	1.6017	4.6650	4.0960	5.0046	4.5758	S	S
S001	2	4.0095	0.3228	7.1341	-1.6484	0.0391	4.4850	3.9130	5.5719	5.1026	S	S
S001	3	4.3958	0.3118	6.6530	-1.8319	0.0893	0.3890	0.0940	-28.5322	-144.7029	L	L
S001	4	4.4966	0.3248	7.2353	-1.6032	0.3092	2.6780	2.5810	3.4614	3.2593	CT	CT
S001	5	4.6012	0.4249	9.9267	-1.6366	0.0000	1.3140	0.8460	0.6047	-5.4575	L	L
S001	6	4.6484	0.3423	7.8610	-1.4546	0.4874	2.2920	2.2900	3.0330	3.0275	CT	CT
S001	7	4.7053	0.4202	9.9636	-1.4707	0.0079	1.7170	1.3370	3.0478	0.6642	L	L
S001	8	4.8655	0.3400	7.6268	-1.6248	0.1742	4.8380	4.0830	6.2752	5.7248	S	S
S001	9	5.0019	0.3179	6.6372	-2.0123	0.0377	0.8920	1.2570	-7.4937	-2.8061	L	L
S001	10	5.0117	0.3434	7.8094	-1.5347	0.6349	4.1740	3.6500	5.8943	5.3990	S	S
S002	1	3.4520	0.2977	6.7223	-1.3789	1.5870	4.6850	4.1080	5.0276	4.5959	S	S
S002	2	4.0146	0.3231	7.1461	-1.6457	0.0381	4.4730	3.9030	5.5726	5.1024	S	S

S002	3	4.3966	0.3122	6.6596	-1.8360	0.0898	0.4020	0.1010	-27.3244	-134.0752	L	L
S002	4	4.4942	0.3254	7.2597	-1.5952	0.3058	2.6340	2.5530	3.3880	3.2146	CT	CT
S002	5	4.6011	0.4247	9.9213	-1.6356	0.0024	1.2990	0.8330	0.4717	-5.7296	L	L
S002	6	4.6481	0.3419	7.8458	-1.4581	0.4796	2.3610	2.3600	3.2049	3.2023	CT	CT
S002	7	4.7055	0.4202	9.9599	-1.4737	0.0097	1.7100	1.3300	3.0128	0.6068	L	L
S002	8	4.8602	0.3381	7.5816	-1.6184	0.1623	5.0120	4.1880	6.3269	5.7617	S	S
S002	9	5.0006	0.3373	7.5367	-1.6429	0.5042	2.0390	1.6240	2.1175	0.3128	CT	L
S002	10	5.0027	0.3250	6.9588	-1.8844	0.2007	0.0900	0.4810	-151.1529	-21.0937	L	L
S003	1	3.4770	0.2988	6.7487	-1.3811	1.5409	4.7440	4.1420	5.0945	4.6533	S	S
S003	2	4.0305	0.3243	7.1836	-1.6407	0.0352	4.4300	3.8650	5.5738	5.0986	S	S
S003	3	4.3992	0.3135	6.6798	-1.8513	0.0917	0.4370	0.1260	-24.4200	-105.7518	L	L
S003	4	4.4864	0.3295	7.3918	-1.5731	0.2918	2.5080	2.4650	3.2234	3.1233	CT	CT
S003	5	4.6002	0.4240	9.9024	-1.6364	0.0098	1.2420	0.7800	-0.0551	-6.9223	L	L
S003	6	4.6478	0.3427	7.8519	-1.4746	0.4599	2.5570	2.5510	3.6951	3.6818	CT	CT
S003	7	4.7053	0.4196	9.9475	-1.4700	0.0154	1.6870	1.3050	2.8819	0.3833	L	L
S003	8	4.8416	0.3371	7.5816	-1.5917	0.1588	5.2180	4.2980	6.4137	5.8230	S	S
S003	9	4.9779	0.3546	8.0785	-1.5700	0.7344	2.9370	2.7460	4.7456	4.4046	CT	CT
S003	10	5.0058	0.3200	6.6680	-2.0395	0.0399	0.8520	1.2140	-8.1934	-3.1538	L	L
S004	1	3.5308	0.3021	6.8200	-1.4009	1.4693	4.7710	4.1510	5.2028	4.7520	S	S
S004	2	4.0650	0.3278	7.2798	-1.6404	0.0293	4.2620	3.7320	5.5416	5.0617	S	S
S004	3	4.4216	0.3140	6.7074	-1.8373	0.0896	0.4890	0.1870	-20.9024	-68.4587	L	L
S004	4	4.4724	0.3329	7.5126	-1.5466	0.2720	2.2950	2.2780	2.7848	2.7379	CT	CT
S004	5	4.5993	0.4243	9.9095	-1.6373	0.0172	1.1740	0.7160	-0.7187	-8.5645	L	L
S004	6	4.6552	0.3437	7.8414	-1.5104	0.4519	2.7810	2.7480	4.1739	4.1117	CT	CT
S004	7	4.7046	0.4176	9.9018	-1.4625	0.0306	1.6260	1.2450	2.5084	-0.2017	L	L
S004	8	4.8131	0.3354	7.5070	-1.6189	0.2238	4.8490	4.0360	6.1563	5.5581	S	S
S004	9	4.9603	0.3583	8.1489	-1.6019	0.7423	2.2990	2.2230	3.4873	3.2732	CT	CT
S004	10	5.0487	0.3246	6.7074	-2.1243	0.0402	0.7150	1.0690	-11.3076	-4.6385	L	L
S005	1	3.5884	0.3048	6.8757	-1.4173	1.3628	4.9050	4.2260	5.3573	4.8856	S	S
S005	2	4.0991	0.3309	7.3613	-1.6430	0.0237	4.1170	3.6090	5.5067	5.0143	S	S
S005	3	4.4277	0.3202	6.8499	-1.8637	0.0979	0.5710	0.2680	-16.5047	-45.0164	L	L
S005	4	4.4483	0.3359	7.6206	-1.5203	0.2183	2.2780	2.2620	2.8197	2.7749	CT	CT
S005	5	4.5974	0.4223	9.8280	-1.6624	0.0381	1.0130	0.5680	-2.7244	-13.8611	L	L
S005	6	4.6550	0.3446	7.8353	-1.5411	0.4444	3.1030	2.9830	4.7359	4.5492	S	CT
S005	7	4.7051	0.4139	9.7803	-1.4837	0.0585	1.4610	1.0910	1.4081	-1.9345	L	L
S005	8	4.7603	0.3344	7.4576	-1.6417	0.3576	4.2490	3.6640	5.7103	5.1693	S	S
S005	9	4.9461	0.3577	8.0943	-1.6393	0.7212	2.1790	2.1270	3.1252	2.9636	CT	CT
S005	10	5.0537	0.3270	6.7654	-2.1336	0.0390	0.6680	1.0150	-12.6574	-5.2879	L	L
S006	1	3.6618	0.3077	6.9474	-1.4263	1.2218	5.0560	4.3070	5.5256	5.0303	S	S
S006	2	4.1400	0.3344	7.4596	-1.6411	0.0172	3.8680	3.4000	5.3780	4.8656	S	S
S006	3	4.4146	0.3381	7.7129	-1.4869	0.1835	2.4510	2.3880	3.3247	3.1698	CT	CT
S006	4	4.4365	0.3253	6.9626	-1.8885	0.0862	0.6710	0.3740	-12.6088	-29.6506	L	L
S006	5	4.5935	0.4084	9.4599	-1.6527	0.1132	0.6000	0.2350	-12.8868	-50.1625	L	L
S006	6	4.6427	0.3435	7.6880	-1.6583	0.5081	2.8430	2.7450	4.2814	4.1006	CT	CT
S006	7	4.7070	0.4051	9.5250	-1.4993	0.1088	1.0380	0.6800	-2.8483	-10.1518	L	L
S006	8	4.7149	0.3473	7.8458	-1.6037	0.3846	3.3740	3.1160	5.1817	4.8283	S	S
S006	9	4.9361	0.3573	8.0631	-1.6599	0.6948	2.5750	2.4720	4.1309	3.8979	CT	CT
S006	10	5.0630	0.3304	6.8400	-2.1516	0.0393	0.6100	0.9480	-14.6144	-6.1979	L	L
S007	1	3.7492	0.3140	7.1119	-1.4320	1.0322	5.2230	4.3960	5.7869	5.2682	S	S
S007	2	4.1837	0.3379	7.5608	-1.6345	0.0107	3.4650	3.0600	5.0395	4.4895	S	S
S007	3	4.3689	0.3370	7.7254	-1.4442	0.1873	2.8250	2.6480	4.0724	3.7317	CT	CT
S007	4	4.4458	0.3289	7.0337	-1.9166	0.0926	0.7610	0.4710	-9.9717	-21.6222	L	L
S007	5	4.5767	0.3521	7.8463	-1.7337	0.6111	1.7360	1.8710	1.2853	1.8838	L	L
S007	6	4.6111	0.3943	9.0378	-1.6908	0.2598	0.4780	0.4440	-19.3962	-21.7031	L	L
S007	7	4.7015	0.3941	9.1935	-1.5298	0.1283	0.7200	0.6740	-9.2763	-10.6412	L	L
S007	8	4.7140	0.3645	8.3923	-1.5272	0.3097	2.4230	2.3940	3.9766	3.9046	CT	CT
S007	9	4.9226	0.3553	7.9813	-1.6860	0.6815	3.4940	3.1970	5.5460	5.1631	S	S
S007	10	5.0692	0.3430	7.6854	-1.6484	0.2502	4.3870	3.5860	6.0515	5.3183	S	S
S008	1	3.8444	0.3179	7.2237	-1.4258	0.7666	5.4060	4.4960	5.9858	5.4467	S	S
S008	2	4.2233	0.3405	7.6403	-1.6243	0.0052	2.8780	2.5510	4.2613	3.6199	S	CT
S008	3	4.3070	0.3340	7.6741	-1.4147	0.3615	3.1020	2.8060	4.4467	3.9571	S	CT
S008	4	4.4522	0.3333	7.1228	-1.9467	0.0962	0.8480	0.5650	-7.9112	-16.4166	L	L
S008	5	4.5339	0.3245	7.0144	-1.8170	0.9711	2.3810	2.3600	2.7837	2.7299	CT	CT
S008	6	4.6011	0.4250	9.8929	-1.6732	0.0267	1.0490	0.6020	-2.1610	-12.3537	L	L
S008	7	4.7002	0.4113	9.6570	-1.5362	0.0387	0.9130	0.5370	-4.5787	-15.6219	L	L
S008	8	4.7304	0.3462	7.8481	-1.5729	0.3458	4.9720	4.2160	6.5249	6.0055	S	S

S008	9	4.8962	0.3510	7.8645	-1.6871	0.6837	4.4370	3.8620	6.3062	5.8230	S	S
S008	10	5.0289	0.3492	7.9305	-1.5712	0.3500	3.5660	3.1230	5.4637	4.8909	S	CT
S009	1	3.9353	0.3215	7.3271	-1.4223	0.3779	5.5950	4.6110	6.1758	5.6266	S	S
S009	2	4.2349	0.3299	7.5593	-1.4167	0.7561	2.7050	2.4730	3.6526	3.1532	CT	CT
S009	3	4.2511	0.3415	7.6783	-1.6141	0.0051	2.2250	1.9640	2.8206	1.9606	CT	L
S009	4	4.4560	0.3376	7.1983	-1.9884	0.0980	0.9090	0.6320	-6.6546	-13.5976	L	L
S009	5	4.5025	0.3282	7.0908	-1.8408	1.0067	1.9620	1.9690	1.5924	1.6185	L	L
S009	6	4.5991	0.4219	9.8082	-1.6736	0.0039	1.0170	0.5690	-2.6771	-13.8251	L	L
S009	7	4.6998	0.4158	9.7753	-1.5401	0.0144	1.0980	0.7070	-1.7991	-9.0519	L	L
S009	8	4.7556	0.3383	7.5839	-1.6210	0.2499	6.6300	5.1330	7.0330	6.3996	S	S
S009	9	4.8567	0.3505	7.8836	-1.6551	0.7610	4.0220	3.5980	5.9585	5.5366	S	S
S009	10	5.0083	0.3538	8.0611	-1.5664	0.4086	1.8180	1.7270	1.7069	1.2896	L	L
S010	1	3.9889	0.3240	7.4029	-1.4135	0.0006	5.6960	4.6990	6.2884	5.7520	G	G
S010	2	4.1892	0.3276	7.4770	-1.4374	1.1481	1.3720	1.3550	-1.5810	-1.7127	L	L
S010	3	4.2609	0.3415	7.6842	-1.6092	0.0022	1.8790	1.6350	1.6300	0.4863	L	L
S010	4	4.4599	0.3411	7.2376	-2.0443	0.0973	0.9310	0.6560	-6.1850	-12.6688	L	L
S010	5	4.4916	0.3298	7.1452	-1.8298	1.0028	1.8000	1.8170	0.9752	1.0500	L	L
S010	6	4.5989	0.4221	9.8086	-1.6761	0.0002	1.0120	0.5640	-2.7443	-14.0467	L	L
S010	7	4.6993	0.4168	9.8037	-1.5390	0.0087	1.1740	0.7830	-0.9227	-7.0476	L	L
S010	8	4.7798	0.3326	7.3806	-1.6699	0.0004	7.4380	5.5580	7.1146	6.4597	G	G
S010	9	4.8288	0.3578	8.1282	-1.6083	1.0000	0.6670	0.7380	-11.8521	-9.7752	L	L
S010	10	5.0022	0.3547	8.0811	-1.5699	0.4307	1.4130	1.3660	-0.5399	-0.8905	L	L

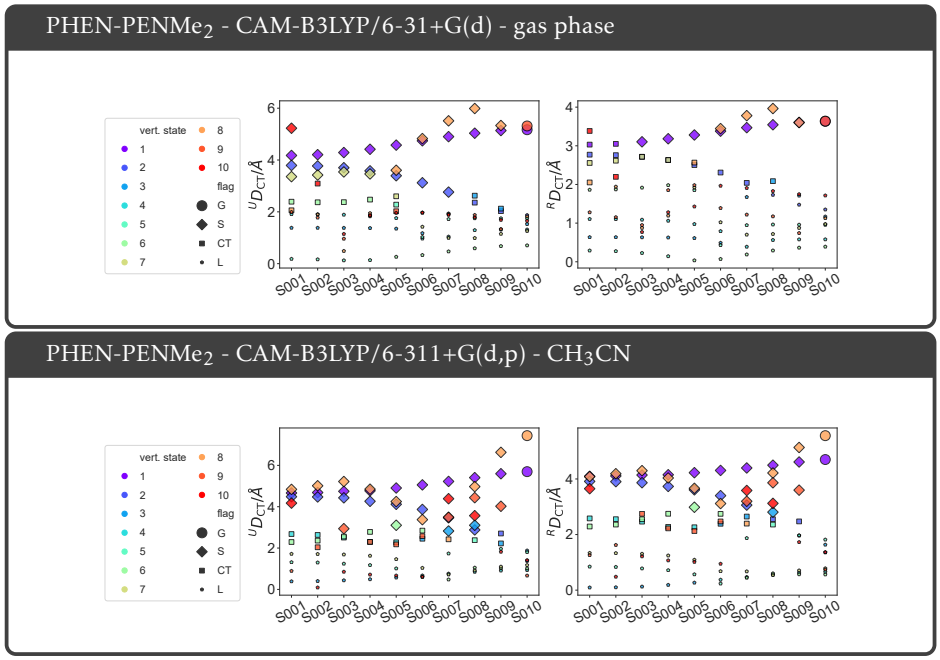

Figure 51: M_{AC} **diagnostics along the intramolecular charge-transfer coordinate in DMABN using different levels of theory**: ${}^{U}D_{CT}$ and ${}^{R}D_{CT}$ values for the first ten vertical states, along the intramolecular charge-transfer coordinate. The labels correspond to the following: G for ghost states, S for spurious states, CT for charge-transfer states - D_{CT}values $\geq$ 2.0 Å, L for local excitations. Each kind of excitation is represented with a circle of different dimensions.

11.4 RAW DATA RELATIVE TO CALCULATION OF Π VALUES IN SECTION 8.7

τ/ °	Transition S_4-S_3				Transition S_4-S_2			
	ΔE/a.u.	q_{CT} e^-	D_{CT}/Bohr	Π/a.u.	ΔE/a.u.	q_{CT}/ e^-	D_{CT}/ Bohr	Π
0	0.004	0.754	2.857	125.166	0.018	0.659	4.902	17.302
10	0.004	0.752	2.784	133.216	0.018	0.659	4.9	17.58
20	0.003	0.744	2.544	164.747	0.017	0.658	4.868	18.63
30	0.002	0.741	2.178	331.741	0.015	0.66	4.474	22.61
40	0.001	0.763	1.958	885.463	0.013	0.659	3.923	30.142
50	0.001	0.803	1.957	789.924	0.011	0.987	3.465	26.848
60	0.003	0.868	2.142	190.202	0.01	0.965	2.661	40.422
70	0.005	0.913	2.282	89.962	0.008	0.937	1.724	73.58
80	0.008	0.917	0.894	161.945	0.008	0.912	1.67	80.815
90	0.007	0.912	0.543	276.486	0.01	0.902	0.341	326.625
τ/ °	Transition S_3-S_2				Transition S_3-S_1			
	ΔE/a.u.	q_{CT} e^-	D_{CT}/Bohr	Π/a.u.	ΔE/a.u.	q_{CT}/ e^-	D_{CT}/ Bohr	Π
0	0.014	1.041	5.052	13.396	0.035	0.868	5.691	5.785
10	0.014	1.04	5.013	13.662	0.035	0.871	5.709	5.794
20	0.014	1.031	4.891	14.634	0.034	0.876	5.775	5.832
30	0.013	1.02	4.474	16.728	0.033	0.884	5.73	6.033
40	0.012	1.008	4.043	20.32	0.031	0.902	5.825	6.17
50	0.01	0.646	2.92	52.514	0.028	0.545	7.29	9.101
60	0.007	0.63	1.311	178.03	0.023	0.573	7.137	10.736
70	0.003	0.614	1.029	514.122	0.017	0.631	7.203	12.944
80	0.001	0.555	1.365	2213.65	0.012	1.079	6.57	12.15
90	0.003	0.438	0.432	2001.711	0.01	1.247	7.157	11.207
τ/ °	Transition S_3-S_0				Transition S_2-S_1			
	ΔE/a.u.	q_{CT} e^-	D_{CT}/Bohr	Π/a.u.	ΔE/a.u.	q_{CT}/ e^-	D_{CT}/ Bohr	Π
0	0.162	0.606	0.176	57.944	0.021	0.731	1.131	58.237
10	0.162	0.607	0.189	53.933	0.021	0.732	1.091	60.583
20	0.162	0.603	0.238	43.112	0.02	0.734	1.028	65.137
30	0.162	0.602	0.348	29.347	0.02	0.742	1.194	57.455
40	0.163	0.601	0.51	20.058	0.019	0.761	1.822	38.411
50	0.162	0.44	4.513	3.104	0.018	0.79	2.837	25.39
60	0.161	0.478	5.002	2.606	0.016	0.844	4.102	18.093
70	0.158	0.513	5.303	2.323	0.014	0.93	5.458	14.148
80	0.156	0.408	3.705	4.238	0.011	0.804	7.893	14.316
90	0.157	0.386	3.075	5.379	0.007	1.081	8.394	14.974
τ/ °	Transition S_2-S_0				Transition S_1-S_0			
	ΔE/a.u.	q_{CT} e^-	D_{CT}/Bohr	Π/a.u.	ΔE/a.u.	q_{CT}/ e^-	D_{CT}/ Bohr	Π
0	0.147	0.726	7.366	1.269	0.127	0.65	7.715	1.577
10	0.148	0.722	7.358	1.276	0.127	0.653	7.744	1.56
20	0.148	0.708	7.324	1.302	0.128	0.662	7.842	1.508
30	0.149	0.676	7.057	1.404	0.13	0.672	7.829	1.466
40	0.151	0.644	6.818	1.511	0.132	0.698	7.975	1.362
50	0.152	0.597	6.433	1.711	0.135	0.732	8.141	1.248
60	0.154	0.537	5.777	2.098	0.138	0.781	8.3	1.12
70	0.155	0.466	4.821	2.865	0.141	0.855	8.497	0.975
80	0.156	0.477	4.67	2.886	0.145	0.984	8.701	0.808
90	0.154	0.398	2.551	6.396	0.147	1.14	8.83	0.678

Table 17: ΔE (in a.u.), D_{CT}(in Bohr), q_{CT}(transferred electrons), Π computed for each excited state

Table 18: Vertical excitations energies (in eV), sorted by energy and by character, D_{CT}(in Å) oscillator strength (in a.u.), dipole moment (in Debye), computed for the lowest six vertical excited states.

τ/ °	Energy/eV w.r.t. minGS (Energy based)						
	GS	S_1	S_2	S_3	S_4	S_5	S_6
0	0	3.4442	4.0096	4.3959	4.4968	4.6013	4.6485
10	0.0005	3.4527	4.0152	4.3972	4.4948	4.6018	4.6488
20	0.004	3.481	4.0345	4.4033	4.4905	4.6043	4.6519
30	0.0086	3.5395	4.0737	4.4302	4.481	4.6079	4.6639
40	0.0145	3.603	4.1137	4.4423	4.4629	4.612	4.6696
50	0.0216	3.6834	4.1617	4.4362	4.4582	4.6152	4.6643
60	0.0283	3.7776	4.2121	4.3973	4.4743	4.6051	4.6396
70	0.034	3.8785	4.2574	4.3412	4.4863	4.5681	4.6353
80	0.0374	3.9728	4.2724	4.2886	4.4935	4.54	4.6366
90	0.0388	4.0278	4.2282	4.2999	4.4988	4.5306	4.6379
τ/ °	Energy/eV w.r.t. minGS (Character based)						
	GS	S_1	S_2	S_3	S_4	S_5	S_6
0	0	3.4442	4.0096	4.3959	4.4968	4.6013	4.6485
10	0.0005	3.4527	4.0152	4.3972	4.4948	4.6018	4.6488
20	0.004	3.481	4.0345	4.4033	4.4905	4.6043	4.6519
30	0.0086	3.5395	4.0737	4.4302	4.481	4.6079	4.6639
40	0.0145	3.603	4.1137	4.4423	4.4629	4.612	4.6696
50	0.0216	3.6834	4.1617	4.4582	4.4362	4.6152	4.6643
60	0.0283	3.7776	4.2121	4.4743	4.3973	4.6396	4.6051
70	0.034	3.8785	4.2574	4.4863	4.3412	4.6353	4.5681
80	0.0374	3.9728	4.2886	4.4935	4.2724	4.6366	4.54
90	0.0388	4.0278	4.2999	4.4988	4.2282	4.6379	4.5306
τ/ °	D_{CT}/Å						
		S_1	S_2	S_3	S_3	S_4	S_5
0		4.096	3.913	0.094	2.581	0.846	2.29
10		4.108	3.903	0.101	2.553	0.833	2.36
20		4.142	3.865	0.126	2.465	0.78	2.551
30		4.151	3.732	0.187	2.278	0.716	2.748
40		4.226	3.609	0.268	2.262	0.568	2.983
50		4.307	3.4	2.388	0.374	0.235	2.745
60		4.396	3.06	2.648	0.471	1.871	0.444
70		4.496	2.551	2.806	0.565	2.36	0.602
80		4.611	2.473	1.964	0.632	1.969	0.569
90		4.699	1.355	1.635	0.656	1.817	0.564
τ/ °	f_{osc}/a.u.						
		S_1	S_2	S_3	S_4	S_5	S_6
0		1.6017	0.0391	0.0893	0.3092	0	0.4874
10		1.587	0.0381	0.0898	0.3058	0.0024	0.4796
20		1.5409	0.0352	0.0917	0.2918	0.0098	0.4599
30		1.4693	0.0293	0.0896	0.272	0.0172	0.4519
40		1.3628	0.0237	0.0979	0.2183	0.0381	0.4444
50		1.2218	0.0172	0.1835	0.0862	0.1132	0.5081
60		1.0322	0.0107	0.1873	0.0926	0.6111	0.2598
70		0.7666	0.0052	0.3615	0.0962	0.9711	0.0267
80		0.3779	0.7561	0.0051	0.098	1.0067	0.0039
90		0.0006	1.1481	0.0022	0.0973	1.0028	0.0002
τ/ °	Dipole moment/Debye						
	GS	S_1	S_2	S_3	S_4	S_5	S_6
0		22.5202	23.5272	10.1365	15.6349	7.1779	15.561
10		22.6172	23.4199	10.1686	15.4865	7.2279	15.72
20		22.8891	23.0307	10.2364	15.0659	7.394	16.157
30		22.8481	21.769	10.2175	14.3255	7.407	16.506
40		23.5273	20.7365	10.3791	14.1615	7.8565	17.259
50		24.3885	19.222	14.4397	10.566	9.0604	16.872
60		25.5857	17.2321	15.3068	10.7129	14.5213	10.21
70		27.4669	14.9946	16.0584	10.8732	15.2363	7.5213
80		30.7316	14.8227	13.0864	11.007	13.8257	7.5517
90		34.547	11.8128	12.2619	11.0653	13.2866	7.5287

11.5 NATURAL TRANSITION ORBITALS OF CPDNO, DMABN AND PHEN-PENME$_2$

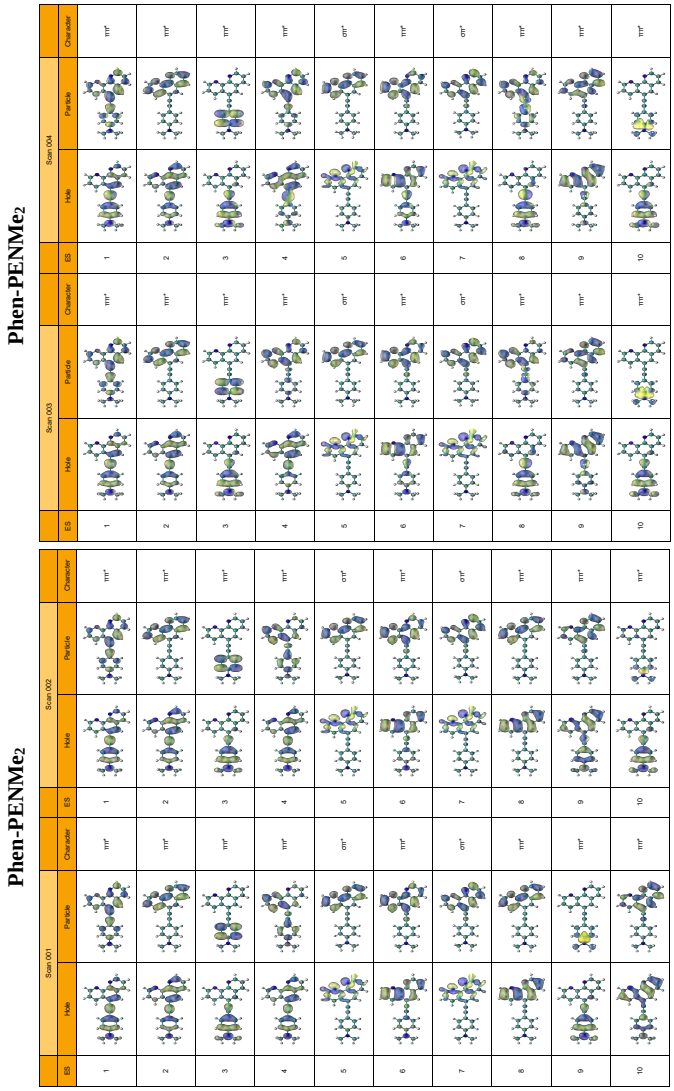

Figure 52: (a) Main contributing orbitals relative to electronic transitions 1 to 10 of Phen-PENMe$_2$, along the reaction coordinate and associated character of each transition.

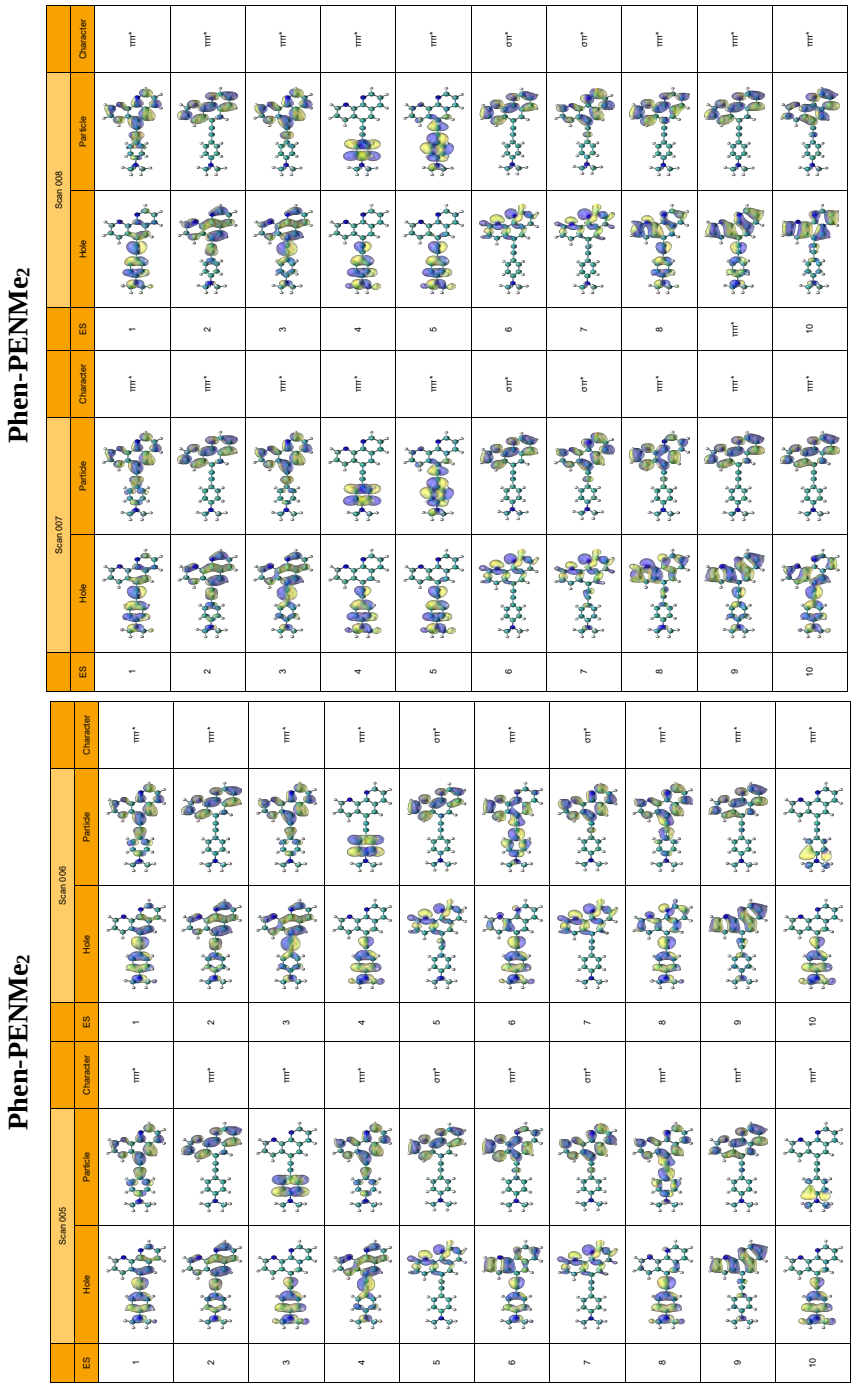

Figure 52: (b) Main contributing orbitals relative to electronic transitions 1 to 10 of Phen-PENMe$_2$, along the reaction coordinate and associated character of each transition.

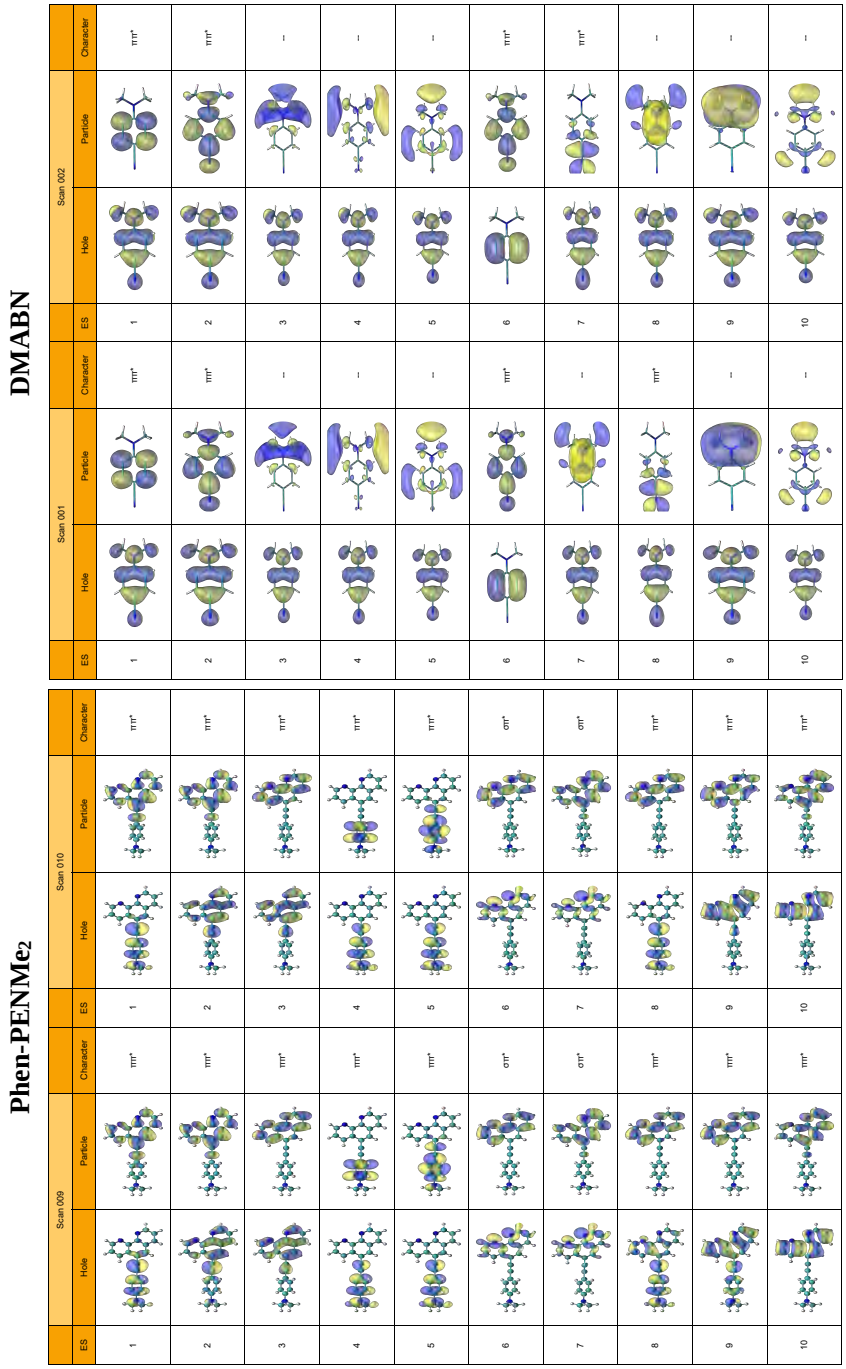

Figure 52: (c) Main contributing orbitals relative to electronic transitions 1 to 10 of Phen-PENMe$_2$(top) and DMABN (bottom), along the reaction coordinate and associated character of each transition.

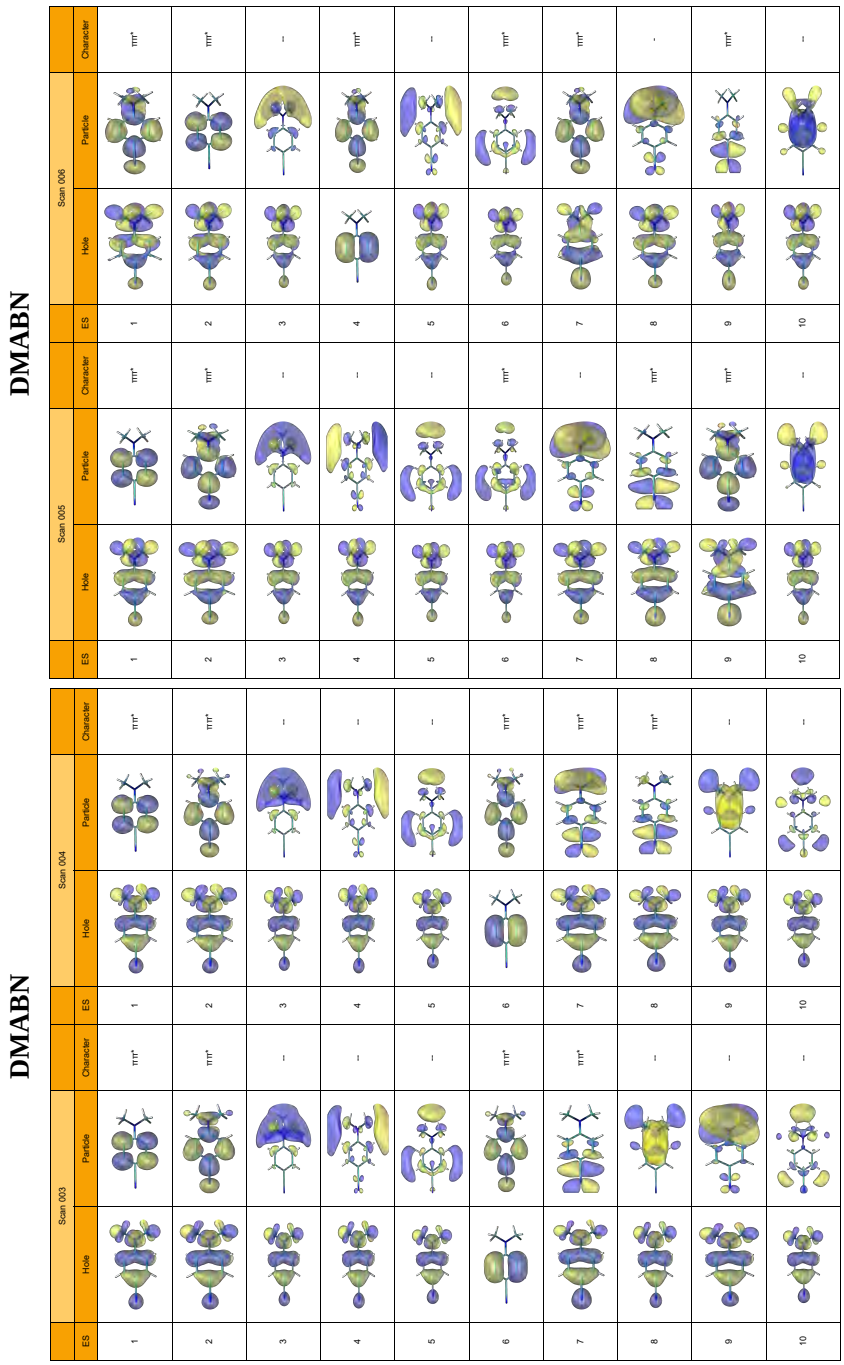

Figure 52: (d) Main contributing orbitals relative to electronic transitions 1 to 10 of DMABN, along the reaction coordinate and associated character of each transition.

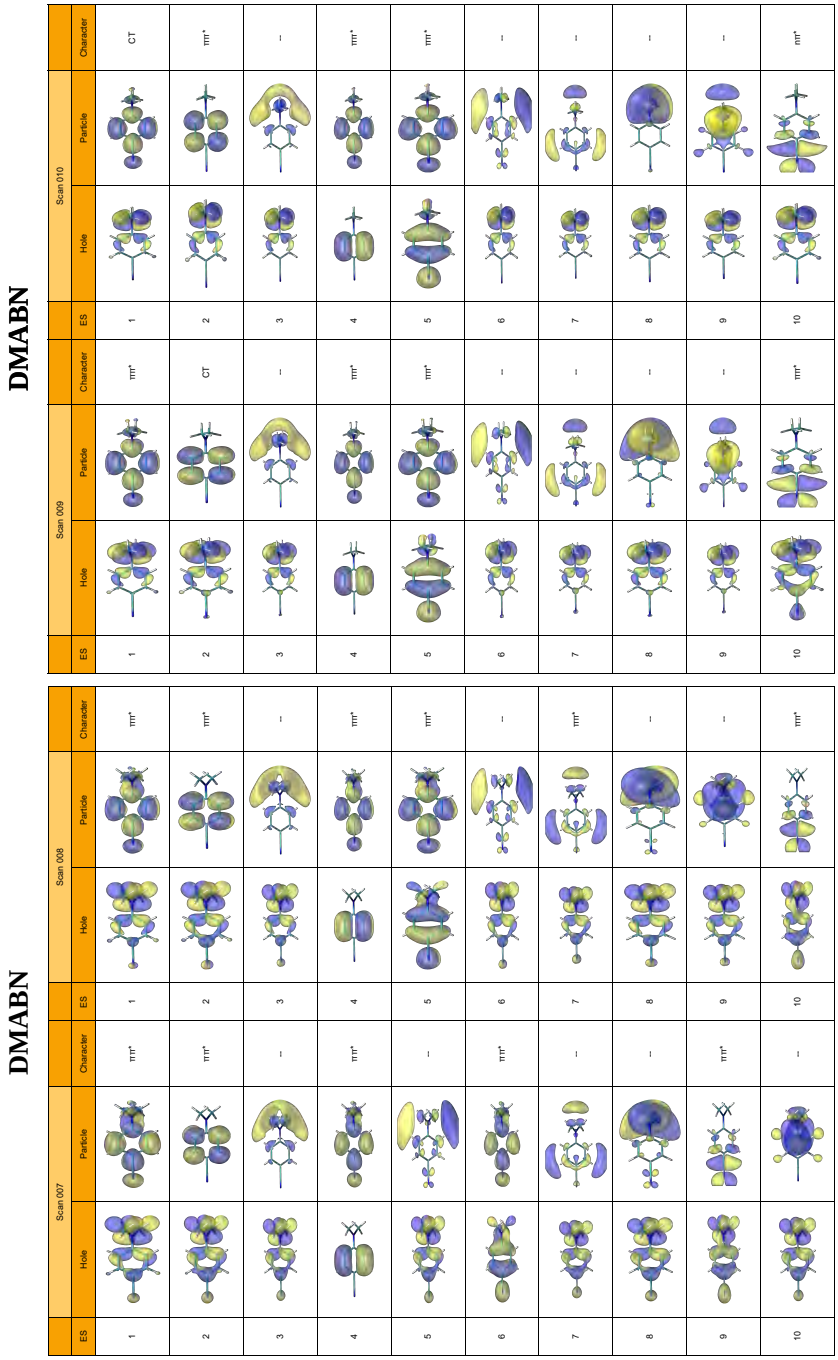

Figure 52: (e) Main contributing orbitals relative to electronic transitions 1 to 10 of DMABN, along the reaction coordinate and associated character of each transition.

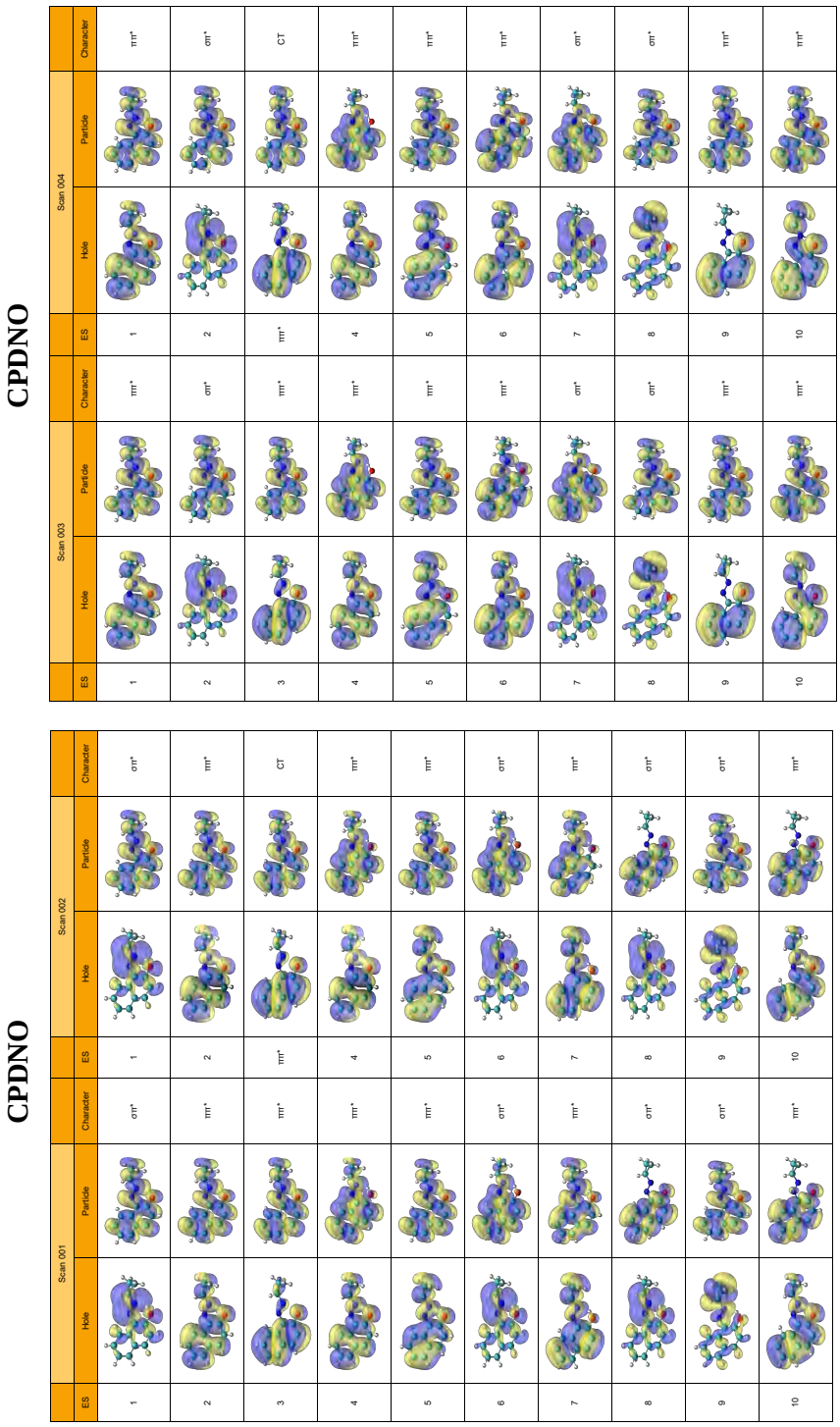

Figure 52: (f) Main contributing orbitals relative to electronic transitions 1 to 10 of CPDNO, along the reaction coordinate and associated character of each transition.

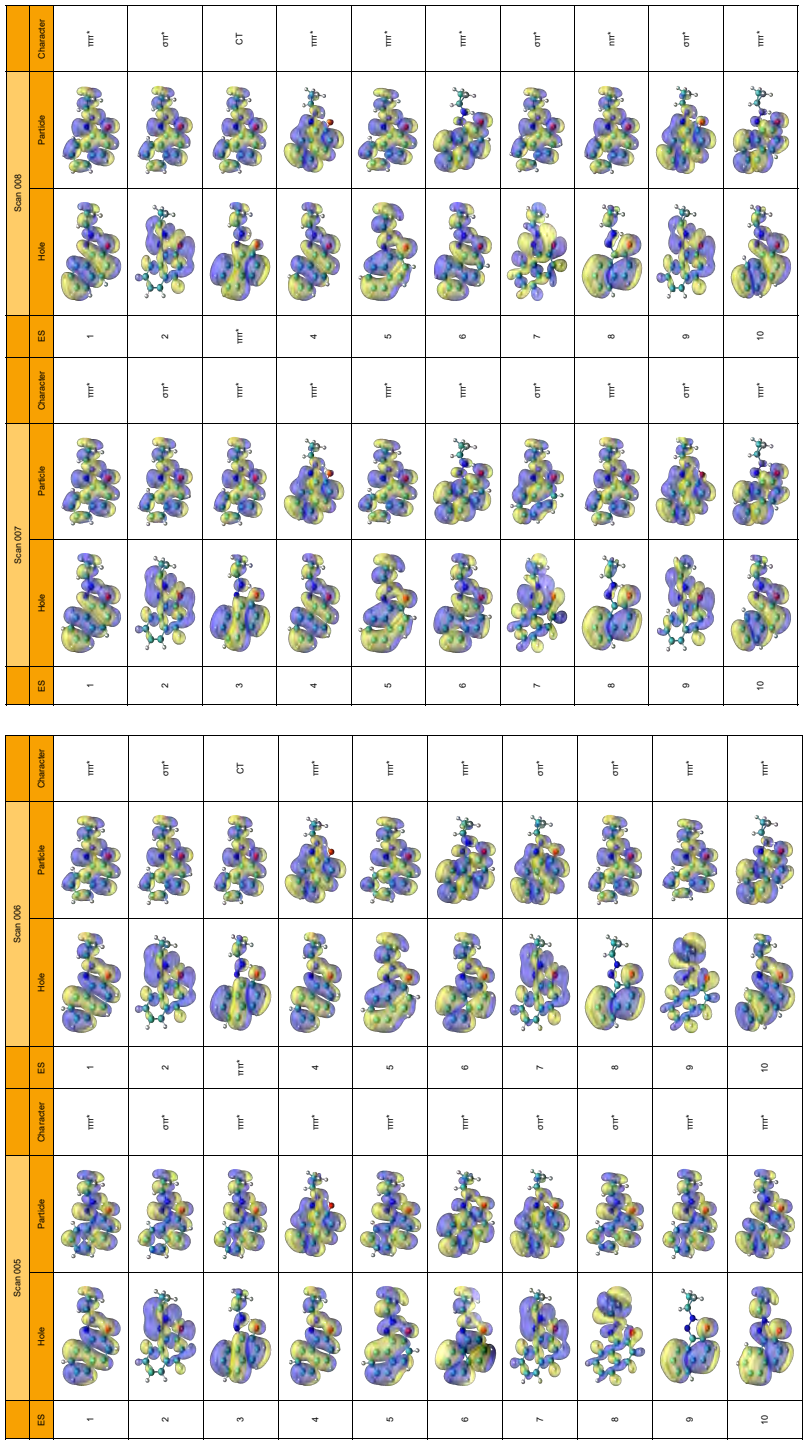

Figure 52: (g) Main contributing orbitals relative to electronic transitions 1 to 10 of CPDNO, along the reaction coordinate and associated character of each transition.

11.6 DATA FOR TO THE CONSTRUCTION OF THE REFERENCE MAP OF CPDNO AND DMABN

Just as we have illustrated in section 9.3.2 one may combine the information delivered by density descriptors, oscillator strength and energies together with the natural transition orbitals to infer a "reference map" describing the arrangement of vertical excited states at each reaction step. NTOs are collected in Section 11.5.

11.6.1 *DMABN*

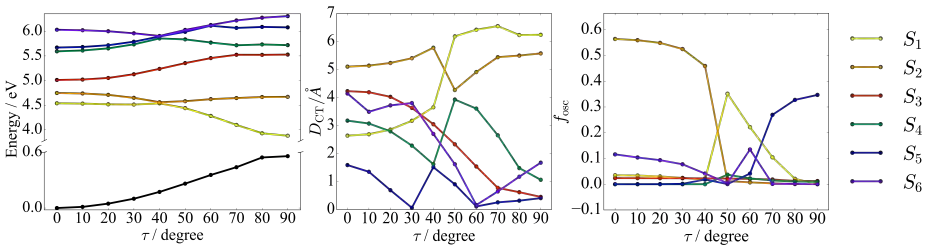

Figure 53: Ground (S_0) and first excited states (S_1-S_6) computed energy profiles (in eV) along the τ torsional degree of freedom. D_{CT} (in Å) and oscillator strength (f_{osc}, in a.u.) associated to each excited state.

11.6.2 *CPDNO*

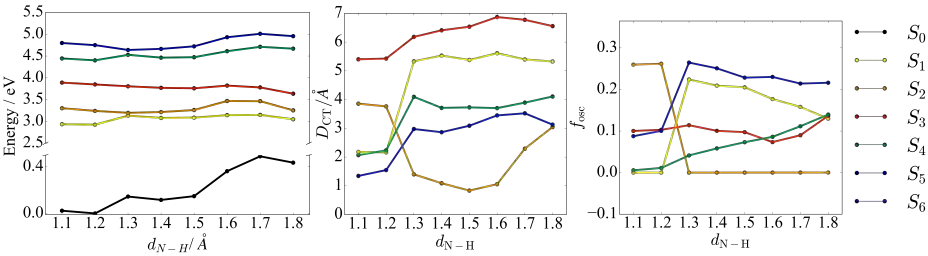

Figure 54: Ground (S_0) and first excited states (S_1-S_6) computed energy profiles (in eV) along the proton transfer coordinate. D_{CT} (in Å) and oscillator strength (f_{osc}, in a.u.) associated to each excited state.

11.7 COMPUTATIONAL DETAILS RELATIVE TO THE CALCULATIONS OF RU(II) COMPLEXES IN SECTION 7.4

All electronic structure calculations were performed with the Gaussian 16 quantum package [145]. Starting from the crystallographic X-ray structures, complexes 1 to 3 were optimized in acetonitrile using the Polarizable Continuum Model (PCM) [87] following the same protocol as described in Ref. [161]. Density Functional Theory (DFT) was employed using the standard hybrid functional B3LYP [45, 48] with the polarization valence-double-ζ (6-31G(d,p)) [172] basis set with one set of d polarization functions for the second-row elements and a set of p polarization functions for the hydrogen atoms. For the ruthenium atom, the uncontracted triple-ζ quality LANL08 [284] basis set with an effective core potential (including 28 core electrons) was used. This whole basis set will be denoted hereafter, and in Section 7.4 as BS1. Subsequently, vibrational frequency calculations were performed at the same level of theory in order to ensure that all structures correspond to minima. The UV-Vis absorption spectra of all complexes were computed employing the time-dependent version of the DFT (TDDFT) and the configuration interaction singles approach together with the BS1 basis set. For the TDDFT calculations, three different functionals were used: (i) the hybrid functional B3LYP [45, 48], (ii) the long-range corrected CAM-B3LYP [56] functional and (iii) the hybrid functional PBE0 [46]. The natural transition orbitals [92] (NTO) relative to the thirty lowest transitions were also computed to inspect the character of the transitions. These last are collected in section 11.9.

11.8 RAW DATA RELATIVE TO THE CALCULATIONS OF RU(II) COMPLEXES

Excitation energies, computed prefactor - that is the weighted average of the orbital energies contributing to the transition, IP and EA, oscillator strength f_{osc} , URD_{CT} and ${}^{R}D_{\text{CT}}$, ${}^{R}\text{M}_{\text{AC}}$ and ${}^{U}\text{M}_{\text{AC}}$, and relative labels of the first 30 excited states of $[\text{Ru(bpy)}_3]^{2+}$, $[\text{Ru(tpy)}_2]^{2+}$,$[\text{Ru(bpy)}_2\text{(dppz)}]^{2+}$,$[\text{Ru(bpy)}_2\text{(tpphz)}]^{2+}$calculated at the B3LYP/BS1, PBE0 /BS1, CAM-B3LYP/BS1 and CIS/BS1 level of theory, in acetonitrile.
Note: if the M_{AC} value < E_{exc} and then the electronic state is labeled as 'spurious' (S). If in addition the oscillator strength is lower that 0.001, the spurious state is then labeled as 'ghost' (G). Excited states having D_{CT} values > 2.0 Å are denoted as charge-transfer states (CT), otherwise they are demoted as local (L). Excitation with a D_{CT}value below $*10^{-5}$ are labeled as LL.

Table 19: M_{AC} diagnostics calculated for the first 30 vertical states of $[\text{Ru(tpy)}_2]^{2+}$using four different functionals, in acetonitrile

	B3LYP										
N	E_{exc}/eV	p / eV	IP / eV	EA / eV	f_{osc}	${}^{U}D_{\text{DC}}/$	${}^{R}D_{\text{CT}}/$	${}^{U}M_{\text{CT}}/eV$	${}^{R}M_{\text{AC}}/eV$	U	R
1	2.5875	0.3234	-6.1797	-2.6022	0.0237	1.5130	1.1680	-0.7180	-3.5291	L	L
2	2.5875	0.3234	-6.1796	-2.6022	0.0237	1.5130	1.1690	-0.7180	-3.5186	L	L
3	2.6070	0.3264	-6.2463	-2.6225	0.0000	0.0090	0.0080	-1591.0802	-1791.0754	L	L
4	2.6710	0.3255	-6.2458	-2.5982	0.0000	0.0080	0.0080	-1791.0997	-1791.0997	L	L
5	2.7790	0.3266	-6.2525	-2.6050	0.1783	0.0030	0.0030	-4790.9959	-4790.9959	L	L

6	2.8650	0.3212	-6.2200	-2.4962	0.0000	0.0030	0.0030	-4791.1448	-4791.1448	L	L
7	2.9565	0.3193	-6.1830	-2.4916	0.1742	0.0020	0.0010	-7191.1374	-14390.9632	L	L
8	2.9752	0.3209	-6.2527	-2.4669	0.0686	1.5880	1.2480	-0.3364	-2.8068	L	L
9	2.9754	0.3209	-6.2529	-2.4670	0.0685	1.5840	1.2460	-0.3590	-2.8250	L	L
10	2.9925	0.3184	-6.2450	-2.4126	0.0086	2.6310	1.6900	3.1916	0.1441	S	L
11	2.9926	0.3184	-6.2452	-2.4125	0.0087	2.6280	1.6880	3.1855	0.1342	S	L
12	3.2728	0.3158	-6.2824	-2.2367	0.0000	0.0020	0.0020	-7191.2336	-7191.2336	L	L
13	3.2795	0.2621	-6.2383	-0.8277	0.0000	0.0010	0.0010	-14392.5188	-14392.5188	L	L
14	3.6763	0.2582	-6.2922	-0.6501	0.0011	0.7350	0.5160	-12.5655	-20.8805	L	L
15	3.6768	0.2582	-6.2925	-0.6501	0.0011	0.7350	0.5160	-12.5653	-20.8802	L	L
16	3.8486	0.2870	-6.2008	-1.5894	0.0506	0.0050	0.0040	-2872.1196	-3592.1022	L	L
17	3.8671	0.3289	-6.8063	-2.1184	0.0825	0.3470	0.3900	-32.5469	-27.9716	L	L
18	3.8672	0.3289	-6.8063	-2.1184	0.0824	0.3480	0.3910	-32.4278	-27.8772	L	L
19	3.8787	0.2881	-6.2512	-1.5777	0.0038	0.7060	0.4180	-12.5570	-26.6098	L	L
20	3.8789	0.2881	-6.2514	-1.5777	0.0038	0.7060	0.4180	-12.5569	-26.6098	L	L
21	3.9625	0.2843	-6.2450	-1.4836	0.0000	1.6030	1.0810	-1.2465	-5.5842	L	L
22	3.9627	0.2843	-6.2452	-1.4836	0.0000	1.6030	1.0810	-1.2462	-5.5839	L	L
23	3.9917	0.2863	-6.2723	-1.5021	0.0002	0.0670	0.0880	-207.1303	-155.8426	L	L
24	3.9937	0.2859	-6.2661	-1.4978	0.0262	0.0670	0.0870	-207.1416	-157.7347	L	L
25	4.0055	0.3202	-6.6894	-1.9841	0.6349	1.3120	1.1290	-2.2609	-4.0399	L	L
26	4.0055	0.3203	-6.6896	-1.9844	0.6345	1.3140	1.1310	-2.2437	-4.0169	L	L
27	4.0529	0.2810	-6.3767	-1.2331	0.0065	0.3560	0.4020	-32.8032	-28.1748	L	L
28	4.0531	0.2812	-6.3796	-1.2373	0.0069	0.3740	0.4160	-30.8495	-26.9623	L	L
29	4.0671	0.3489	-7.0807	-2.4006	0.1355	3.1210	2.2290	4.8794	3.0331	S	CT
30	4.0671	0.3491	-7.0831	-2.4039	0.1357	3.1320	2.2310	4.9013	3.0445	S	CT

CAM-B3LYP

N	E_{exc}/eV	p / eV	IP / eV	EA / eV	f_{osc}	${}^{U}D_{DC}/$	${}^{R}D_{CT}/$	${}^{U}M_{CT}/eV$	${}^{R}M_{AC}/eV$	U	R
1	3.1055	0.3328	-7.5850	-1.2990	0.0241	1.8670	1.3690	1.3426	-1.4630	L	L
2	3.1056	0.3328	-7.5850	-1.2990	0.0241	1.8680	1.3690	1.3467	-1.4630	L	L
3	3.1827	0.3314	-7.6983	-0.3082	0.0000	0.0050	0.0050	-2870.9120	-2870.9120	L	L
4	3.2408	0.3296	-7.7017	0.0207	0.0000	0.0020	0.0020	-7190.8572	-7190.8572	L	L
5	3.2454	0.3371	-7.6819	-1.3786	0.2541	0.0020	0.0020	-7190.6539	-7190.6539	L	L
6	3.2548	0.3372	-7.6895	-1.3288	0.0001	0.0050	0.0050	-2870.7536	-2870.7536	L	L
7	3.4468	0.3342	-7.6835	-1.2718	0.0000	0.0030	0.0040	-4790.7902	-3590.8192	L	L
8	3.6457	0.3296	-7.7557	0.5157	0.0352	0.8300	0.7520	-8.3790	-10.1785	L	L
9	3.6459	0.3296	-7.7553	0.5032	0.0358	0.8380	0.7610	-8.2140	-9.9526	L	L
10	3.6995	0.3305	-7.7047	-0.5775	0.0742	1.8310	1.5250	1.1298	-0.4483	L	L
11	3.6996	0.3305	-7.7044	-0.5901	0.0749	1.8350	1.5270	1.1462	-0.4366	L	L
12	3.7647	0.3261	-7.5714	-1.2499	0.1874	0.0020	0.0020	-7190.9515	-7190.9515	L	L
13	3.8588	0.3299	-7.6893	-1.0349	0.0039	2.1600	1.4950	2.3096	-0.6558	CT	L
14	3.8590	0.3299	-7.6896	-1.0349	0.0039	2.1600	1.4950	2.3098	-0.6555	CT	L
15	3.9786	0.3294	-7.6680	-1.1481	0.0000	0.0010	0.0010	-14390.6874	-14390.6874	L	L
16	4.2372	0.3452	-7.8360	1.2134	0.0373	0.1020	0.0700	-131.7789	-196.3151	L	L
17	4.2375	0.3452	-7.8361	1.2127	0.0375	0.1020	0.0700	-131.7787	-196.3149	L	L
18	4.3252	0.3699	-8.6143	-1.0706	0.6287	0.3370	0.3900	-32.6643	-26.8576	L	L
19	4.3253	0.3699	-8.6140	-1.0698	0.6285	0.3360	0.3890	-32.7917	-26.9527	L	L
20	4.6202	0.3451	-7.6676	1.6572	0.0002	0.0000	0.0000	-2721130.2216	-2721130.2216	LL	LL
21	4.6740	0.3321	-8.2387	-0.6507	0.5156	0.0070	0.0060	-2048.0562	-2390.9050	L	L
22	4.7464	0.3689	-8.7406	-1.0665	0.0000	0.0020	0.0020	-7189.7869	-7189.7869	L	L
23	4.8299	0.2907	-7.6688	-0.1414	0.3550	0.6890	0.6910	-12.9885	-12.9280	L	L
24	4.8301	0.2907	-7.6691	-0.1417	0.3553	0.6940	0.6930	-12.8374	-12.8673	L	L
25	4.8364	0.3290	-8.1343	-0.6356	0.4071	0.1380	0.1160	-95.3918	-115.1815	L	L
26	4.8846	0.2935	-7.6996	-0.2029	0.0871	0.4650	0.2050	-22.9818	-62.2570	L	L
27	4.8848	0.2935	-7.6998	-0.2029	0.0866	0.4660	0.2060	-22.9150	-61.9157	L	L
28	4.9423	0.2904	-7.7109	-0.1148	0.0000	0.2200	0.1750	-57.5497	-74.3804	L	L
29	4.9435	0.2904	-7.7086	-0.1130	0.0001	0.2200	0.1740	-57.5518	-74.8555	L	L
30	4.9733	0.2942	-7.7482	-0.1473	0.0012	0.0770	0.1100	-179.0036	-122.9010	L	L

CIS

N	E_{exc}/eV	p / eV	IP / eV	EA / eV	f_{osc}	${}^{U}D_{DC}/$	${}^{R}D_{CT}/$	${}^{U}M_{CT}/eV$	${}^{R}M_{AC}/eV$	U	R
1	2.7282	0.6037	-10.1492	6.2776	0.0000	0.0000	0.0000	-2721123.1863	-2721123.1863	LL	LL
2	3.3099	0.6180	-10.2286	6.5869	0.0008	0.3370	0.3860	-25.9134	-20.4893	L	L
3	3.3104	0.6180	-10.2288	6.5874	0.0008	0.3370	0.3860	-25.9127	-20.4885	L	L
4	4.4280	0.6094	-10.1697	6.4131	0.0000	0.1220	0.0390	-101.4472	-352.6391	L	L
5	4.4284	0.6094	-10.1694	6.4135	0.0000	0.1220	0.0390	-101.4470	-352.6389	L	L
6	4.7612	0.3907	-9.3746	1.2560	0.6526	0.1740	0.2450	-72.1260	-48.1435	L	L

7	4.7614	0.3907	-9.3746	1.2560	0.6527	0.1740	0.2450	-72.1260	-48.1434	L	L
8	4.8408	0.6104	-10.0794	6.5298	0.0001	0.0010	0.0010	-14383.0425	-14383.0425	L	L
9	4.9444	0.4063	-9.5937	1.4621	0.3703	0.0080	0.0080	-1788.9006	-1788.9006	L	L
10	4.9684	0.4073	-9.5714	1.5107	0.0000	0.0080	0.0080	-1788.8744	-1788.8744	L	L
11	5.5829	0.4101	-9.7841	1.3764	0.3971	1.7440	1.2270	2.9037	-0.5752	L	L
12	5.5830	0.4101	-9.7841	1.3765	0.3969	1.7440	1.2280	2.9040	-0.5654	L	L
13	5.6271	0.4069	-9.6986	1.3725	1.4847	0.0080	0.0070	-1788.8854	-2046.0220	L	L
14	5.7144	0.4056	-9.9332	1.1037	0.0000	0.0040	0.0030	-3588.8760	-4788.8470	L	L
15	5.8182	0.4148	-9.9078	1.3796	0.0001	0.0040	0.0030	-3588.6256	-4788.5966	L	L
16	5.8605	0.4249	-9.9811	1.5802	0.0519	1.6430	1.3500	2.7971	0.8949	L	L
17	5.8608	0.4249	-9.9815	1.5804	0.0519	1.6430	1.3500	2.7976	0.8955	L	L
18	5.9265	0.4476	-10.1138	2.0661	0.0000	0.0010	0.0000	-14387.4718	-2721127.4333	L	LL
19	5.9364	0.4445	-10.1718	1.9225	0.4987	0.0020	0.0020	-7187.7316	-7187.7316	L	L
20	6.0305	0.4096	-9.7934	1.3522	0.0000	0.0030	0.0030	-4788.7382	-4788.7382	L	L
21	6.3721	0.4542	-10.0694	2.2901	0.5373	0.9230	0.7510	-3.2415	-6.8146	L	L
22	6.3721	0.4542	-10.0694	2.2901	0.5372	0.9240	0.7520	-3.2246	-6.7890	L	L
23	6.5383	0.4376	-10.3079	1.5996	0.1230	2.1570	1.3710	5.2317	1.4044	CT	L
24	6.5386	0.4376	-10.3082	1.5994	0.1229	2.1570	1.3710	5.2318	1.4045	CT	L
25	6.6471	0.4586	-10.4257	2.0546	0.0035	0.0120	0.0100	-1187.4906	-1427.4848	L	L
26	6.6622	0.4591	-10.5133	1.9801	0.0000	0.0130	0.0110	-1095.1721	-1296.5658	L	L
27	6.8053	0.4562	-10.3997	2.0134	0.6558	1.0720	0.9860	-1.0194	-2.1910	L	L
28	6.8055	0.4562	-10.3998	2.0133	0.6561	1.0720	0.9850	-1.0195	-2.2059	L	L
29	6.8544	0.4391	-9.9321	2.0167	0.9776	0.0060	0.0040	-2387.9932	-3587.9641	L	L
30	6.9191	0.4382	-9.9966	1.9275	0.0000	0.0010	0.0010	-14387.7277	-14387.7277	L	L

PBE0

N	E_{exc}/eV	p / eV	IP / eV	EA / eV	f_{osc}	${}^{U}D_{\text{DC}}/$	${}^{R}D_{\text{CT}}/$	${}^{U}M_{\text{CT}}/eV$	${}^{R}M_{\text{AC}}/eV$	U	R
1	2.6956	0.3329	-6.4891	-2.5456	0.0243	1.6390	1.2510	0.2729	-2.4519	L	L
2	2.6957	0.3329	-6.4891	-2.5455	0.0243	1.6400	1.2510	0.2783	-2.4520	L	L
3	2.7286	0.3365	-6.5714	-2.5657	0.0000	0.0070	0.0070	-2047.9366	-2047.9366	L	L
4	2.7997	0.3356	-6.5704	-2.5437	0.0000	0.0070	0.0070	-2047.9604	-2047.9604	L	L
5	2.8933	0.3371	-6.5775	-2.5574	0.2100	0.0030	0.0030	-4790.7114	-4790.7114	L	L
6	2.9983	0.3314	-6.5414	-2.4463	0.0000	0.0030	0.0030	-4790.8658	-4790.8658	L	L
7	3.1141	0.3285	-6.4875	-2.4366	0.1614	0.0010	0.0010	-14390.7126	-14390.7126	L	L
8	3.1311	0.3295	-6.5767	-2.3724	0.0823	2.0560	1.5030	1.9625	-0.6144	CT	L
9	3.1313	0.3295	-6.5770	-2.3724	0.0823	2.0550	1.5030	1.9593	-0.6142	CT	L
10	3.1627	0.3293	-6.5673	-2.3861	0.0002	2.8700	1.8250	3.9441	1.0712	G	L
11	3.1629	0.3293	-6.5675	-2.3862	0.0002	2.8690	1.8250	3.9427	1.0715	G	L
12	3.2272	0.2658	-6.5624	-0.5746	0.0000	0.0010	0.0010	-14392.4191	-14392.4191	L	L
13	3.4126	0.3300	-6.5983	-2.3042	0.0000	0.0010	0.0010	-14390.6710	-14390.6710	L	L
14	3.6429	0.2660	-6.6287	-0.4909	0.0014	0.7240	0.5380	-12.6507	-19.5268	L	L
15	3.6434	0.2660	-6.6289	-0.4908	0.0014	0.7240	0.5380	-12.6506	-19.5267	L	L
16	4.0030	0.3585	-7.3917	-2.3195	0.2867	0.2530	0.1650	-47.1591	-77.5140	L	L
17	4.0031	0.3586	-7.3917	-2.3195	0.2867	0.2520	0.1650	-47.3848	-77.5139	L	L
18	4.0459	0.2954	-6.5190	-1.4947	0.0570	0.0010	0.0010	-14391.6127	-14391.6127	L	L
19	4.0971	0.2949	-6.5726	-1.4328	0.0085	0.8180	0.5050	-9.5800	-20.4907	L	L
20	4.0973	0.2949	-6.5728	-1.4328	0.0085	0.8170	0.5050	-9.6014	-20.4905	L	L
21	4.1520	0.2658	-6.5979	-0.5287	0.0637	0.4920	0.5160	-22.0359	-20.6746	L	L
22	4.1522	0.2658	-6.5978	-0.5300	0.0644	0.4930	0.5170	-21.9755	-20.6196	L	L
23	4.1835	0.2927	-6.5708	-1.3806	0.0006	1.5420	1.0390	-1.3745	-5.8954	L	L
24	4.1837	0.2927	-6.5716	-1.3808	0.0019	1.5410	1.0390	-1.3796	-5.8944	L	L
25	4.1866	0.3048	-6.7340	-1.5131	0.5090	1.2120	1.0450	-3.5867	-5.4854	L	L
26	4.1866	0.3048	-6.7346	-1.5121	0.5091	1.2110	1.0460	-3.5967	-5.4724	L	L
27	4.2111	0.2960	-6.6141	-1.4192	0.0000	0.0380	0.0520	-370.8832	-268.8614	L	L
28	4.2152	0.2950	-6.5998	-1.4085	0.0185	0.0420	0.0540	-334.8208	-258.6322	L	L
29	4.2689	0.3680	-7.4935	-2.5141	0.0586	3.6300	2.3670	6.0469	3.9303	S	CT
30	4.2689	0.3680	-7.4936	-2.5142	0.0585	3.6300	2.3670	6.0471	3.9305	S	CT

Table 20: M_{AC} diagnostics calculated for the first 30 vertical states of $[Ru(bpy)_3]^{2+}$ using four different functionals, in acetonitrile

B3LYP

N	E_{exc}/eV	p / eV	IP / eV	EA / eV	f_{osc}	${}^{U}D_{DC}/$	${}^{R}D_{CT}/$	${}^{U}M_{CT}/eV$	${}^{R}M_{AC}/eV$	U	R
1	2.6404	0.3175	-6.0721	-2.5567	0.0030	1.2490	1.0280	-2.8891	-5.3676	L	L
2	2.6437	0.3135	-6.0748	-2.4416	0.0001	1.4650	1.1770	-1.2978	-3.7028	L	L
3	2.6443	0.3141	-6.0744	-2.4574	0.0005	2.6750	1.8510	3.1631	0.7668	G	L
4	2.8238	0.3201	-6.2398	-2.4578	0.0005	0.2300	0.2400	-53.8970	-51.2883	L	L
5	2.8405	0.3237	-6.2395	-2.5582	0.0413	1.2390	1.0560	-2.8135	-4.8275	L	L
6	2.8420	0.3237	-6.2395	-2.5577	0.0448	1.3860	1.1930	-1.5811	-3.2619	L	L
7	2.9280	0.3199	-6.2426	-2.4416	0.1786	0.9840	0.9420	-5.9283	-6.5807	L	L
8	2.9293	0.3199	-6.2428	-2.4411	0.1837	1.0310	1.0010	-5.2613	-5.6798	L	L
9	3.1783	0.3170	-6.2730	-2.2963	0.0000	0.0090	0.0110	-1591.3354	-1300.4334	L	L
10	3.5100	0.2898	-6.0838	-1.7948	0.0193	0.0250	0.0200	-568.1010	-712.0975	L	L
11	3.6704	0.2409	-6.1599	-0.3136	0.0001	0.2680	0.2180	-47.1736	-59.4970	L	L
12	3.6718	0.2414	-6.1592	-0.3263	0.0001	0.2790	0.2280	-45.0439	-56.5886	L	L
13	3.7012	0.2956	-6.2463	-1.7875	0.0178	0.4220	0.3120	-26.0791	-38.1094	L	L
14	3.7013	0.2956	-6.2462	-1.7874	0.0180	0.3710	0.2790	-30.7699	-43.5685	L	L
15	3.7902	0.2758	-6.1055	-1.3831	0.0027	0.5820	0.5170	-17.2367	-20.3473	L	L
16	3.7910	0.2753	-6.1064	-1.3675	0.0027	0.5760	0.5130	-17.5082	-20.5783	L	L
17	3.8137	0.2412	-6.2788	-0.1965	0.0021	0.0120	0.0120	-1193.4082	-1193.4082	L	L
18	3.8695	0.2778	-6.1337	-1.4056	0.0001	0.2170	0.2150	-58.7994	-59.4167	L	L
19	3.8975	0.2740	-6.0834	-1.3590	0.0543	0.6760	0.6020	-13.8448	-16.4632	L	L
20	3.8977	0.2740	-6.0833	-1.3592	0.0551	0.8710	0.7340	-9.0758	-12.1615	L	L
21	3.9611	0.2896	-6.3314	-1.5342	0.0010	0.0170	0.0160	-839.1577	-892.0976	L	L
22	3.9824	0.2845	-6.2886	-1.4325	0.0205	0.3250	0.2040	-36.5657	-62.8456	L	L
23	3.9832	0.2844	-6.2874	-1.4316	0.0216	0.4400	0.3030	-24.9877	-39.7848	L	L
24	3.9927	0.2837	-6.2466	-1.4568	0.0816	0.2010	0.2330	-63.9196	-54.0806	L	L
25	3.9929	0.2837	-6.2470	-1.4568	0.0826	0.2000	0.2370	-64.2772	-53.0370	L	L
26	4.0123	0.2827	-6.2378	-1.4431	0.0000	0.0180	0.0230	-792.2879	-618.3790	L	L
27	4.0561	0.2865	-6.3746	-1.3974	0.0038	0.0570	0.0830	-244.8281	-165.6925	L	L
28	4.0563	0.2868	-6.3771	-1.4017	0.0037	0.0400	0.0220	-352.1871	-646.7254	L	L
29	4.0735	0.2882	-6.3575	-1.4636	0.0012	0.0350	0.0420	-403.5760	-335.0062	L	L
30	4.2539	0.3576	-7.2645	-2.4288	0.1408	2.4170	2.1000	3.7743	2.8750	CT	CT

CAM-B3LYP

N	E_{exc}/eV	p / eV	IP / eV	EA / eV	f_{osc}	${}^{U}D_{DC}/$	${}^{R}D_{CT}/$	${}^{U}M_{CT}/eV$	${}^{R}M_{AC}/eV$	U	R
1	3.3340	0.3286	-7.6102	-0.8748	0.0017	1.3200	1.1200	-1.9673	-3.9153	L	L
2	3.3346	0.3285	-7.6100	-0.8810	0.0016	1.3330	1.0930	-1.8622	-4.2342	L	L
3	3.4306	0.3305	-7.5960	-1.3159	0.0013	0.0140	0.0150	-1019.5534	-950.9836	L	L
4	3.5193	0.3310	-7.7037	-1.0866	0.0005	0.0230	0.0240	-617.0661	-590.9797	L	L
5	3.5319	0.3334	-7.6879	-0.5687	0.1452	0.4390	0.4280	-23.7293	-24.5723	L	L
6	3.5331	0.3333	-7.6878	-0.6240	0.1547	0.6240	0.6060	-14.0079	-14.6934	L	L
7	3.5740	0.3345	-7.6939	-1.1392	0.0936	0.6270	0.5190	-13.8628	-18.6418	L	L
8	3.5741	0.3345	-7.6946	-1.1779	0.1027	0.5280	0.4160	-18.1700	-25.5125	L	L
9	3.6866	0.3400	-7.7153	0.6472	0.0250	0.4940	0.4500	-19.8986	-22.7487	L	L
10	3.6889	0.3400	-7.7155	0.6605	0.0225	0.5160	0.4760	-18.6531	-20.9982	L	L
11	3.7591	0.3465	-7.7856	1.5381	0.0001	0.0470	0.0470	-296.9473	-296.9473	L	L
12	3.8310	0.3326	-7.7527	-0.9798	0.0000	0.0090	0.0110	-1590.9107	-1300.0087	L	L
13	4.3077	0.3428	-7.7208	1.5127	0.0007	0.0550	0.0600	-252.4836	-230.6659	L	L
14	4.3098	0.3429	-7.7206	1.5130	0.0007	0.0480	0.0520	-290.6632	-267.5869	L	L
15	4.4485	0.3467	-8.4050	-0.9047	0.4077	0.0210	0.0200	-676.2625	-710.5474	L	L
16	4.4565	0.3425	-7.7650	1.4049	0.0000	0.0020	0.0030	-7190.5056	-4790.5637	L	L
17	4.4824	0.3662	-8.7213	-1.0740	0.2803	0.0990	0.1000	-135.4865	-134.0320	L	L
18	4.4830	0.3661	-8.7199	-1.0720	0.2828	0.0970	0.0960	-138.4890	-140.0354	L	L
19	4.6322	0.3232	-7.9861	-0.6970	0.7878	0.0290	0.0240	-487.7447	-591.1905	L	L
20	4.6838	0.3050	-7.7694	-0.4574	0.0034	0.4670	0.5020	-22.5343	-20.3844	L	L
21	4.6849	0.3050	-7.7694	-0.4571	0.0036	0.4310	0.4670	-25.1103	-22.5348	L	L
22	4.8722	0.2894	-7.6344	-0.1342	0.0019	0.5280	0.4250	-19.3967	-26.0062	L	L
23	4.8724	0.2893	-7.6344	-0.1350	0.0025	0.5090	0.4090	-20.4165	-27.3334	L	L
24	4.9193	0.2893	-7.6549	0.0004	0.0490	0.4950	0.4530	-21.2174	-23.9145	L	L
25	4.9211	0.2930	-7.7455	-0.0871	0.3983	0.4420	0.4580	-24.6068	-23.4687	L	L
26	4.9220	0.2934	-7.7565	-0.0994	0.4498	0.6690	0.6300	-13.5415	-14.8739	L	L
27	4.9352	0.2875	-7.6851	-0.0358	0.0127	0.2340	0.2600	-53.7130	-47.5593	L	L
28	4.9355	0.2875	-7.6851	-0.0352	0.0119	0.4390	0.4560	-24.9778	-23.7550	L	L
29	4.9943	0.2935	-7.7434	-0.1310	0.6188	0.0610	0.0690	-228.0725	-200.7032	L	L
30	4.9983	0.2897	-7.7071	-0.0852	0.0155	0.3880	0.4360	-29.2303	-25.1445	L	L

CIS

N	E_{exc}/eV	p / eV	IP / eV	EA / eV	f_{osc}	${}^{U}D_{DC}/$	${}^{R}D_{CT}/$	${}^{U}M_{CT}/eV$	${}^{R}M_{AC}/eV$	U	R

1	3.1660	0.6256	-10.2936	6.7286	0.0000	0.0710	0.0930	-185.7899	-137.8128	L	L
2	3.1678	0.6256	-10.2935	6.7296	0.0000	0.0690	0.0900	-191.6674	-142.9730	L	L
3	3.2298	0.6280	-10.3451	6.7444	0.0000	0.0050	0.0070	-2862.8409	-2040.0037	L	L
4	4.5348	0.6204	-10.2645	6.6185	0.0015	0.0160	0.0350	-883.0952	-394.5356	L	L
5	4.5361	0.6204	-10.2645	6.6180	0.0016	0.0140	0.0350	-1011.6640	-394.5361	L	L
6	4.7137	0.6215	-10.2991	6.6119	0.0000	0.0020	0.0010	-7182.9149	-14382.7407	L	L
7	4.9226	0.4043	-9.5410	1.4594	0.4049	0.0700	0.0930	-194.7089	-143.8345	L	L
8	4.9233	0.4043	-9.5405	1.4613	0.4169	0.0540	0.0740	-255.6584	-183.5881	L	L
9	4.9289	0.4044	-9.5442	1.4600	1.3866	0.0170	0.0240	-836.0341	-588.9812	L	L
10	5.8364	0.4377	-10.0669	1.8443	0.0914	0.4970	0.4510	-17.0620	-20.0171	L	L
11	5.8366	0.4376	-10.0672	1.8402	0.0907	0.5420	0.4930	-14.6603	-17.3009	L	L
12	5.8552	0.4426	-10.0759	1.9670	0.0002	0.4030	0.3250	-23.6883	-32.2637	L	L
13	5.8553	0.4427	-10.0757	1.9718	0.0008	0.2890	0.2190	-37.7783	-53.7044	L	L
14	5.8617	0.4457	-10.1116	2.0173	0.0456	0.1610	0.1590	-77.3099	-78.4350	L	L
15	5.9556	0.4497	-10.1081	2.1299	0.0000	0.0020	0.0030	-7187.5878	-4787.6459	L	L
16	6.3660	0.4166	-10.0038	1.3311	0.0041	0.1090	0.0890	-120.7719	-150.4589	L	L
17	6.3757	0.4591	-10.3205	2.1729	0.7762	0.3910	0.3410	-24.3343	-29.7343	L	L
18	6.3760	0.4592	-10.3272	2.1688	0.7666	0.3820	0.3320	-25.1994	-30.8764	L	L
19	6.3880	0.4206	-9.9223	1.5230	0.0017	1.5530	1.1620	2.1732	-0.9467	L	L
20	6.3900	0.4205	-9.9166	1.5262	0.0065	1.6930	1.2700	2.9374	0.1045	L	L
21	6.5222	0.4306	-9.9809	1.7359	0.0004	1.3100	1.0060	0.7247	-2.5970	L	L
22	6.5228	0.4306	-9.9788	1.7386	0.0005	1.3190	1.0340	0.8003	-2.2088	L	L
23	6.5486	0.4263	-9.7863	1.8128	0.2817	0.0290	0.0270	-484.9406	-521.7214	L	L
24	6.6118	0.4747	-10.7297	2.1882	0.0000	0.0030	0.0020	-4786.9661	-7186.9080	L	L
25	6.9027	0.4757	-10.5101	2.4348	0.7929	0.8930	0.8060	-3.1801	-4.9207	L	L
26	6.9042	0.4758	-10.5093	2.4373	0.7990	0.8680	0.8210	-3.6428	-4.5925	L	L
27	7.0045	0.4640	-10.4670	2.1592	0.0001	0.0240	0.0250	-587.3593	-563.3599	L	L
28	7.2379	0.4795	-10.5614	2.4853	2.3696	0.0100	0.0090	-1426.9185	-1586.9146	L	L
29	7.3226	0.5034	-11.1764	2.5210	0.2616	0.3190	0.3620	-31.4425	-26.0806	L	L
30	7.3233	0.5026	-11.1481	2.5286	0.2781	0.3290	0.3730	-30.0913	-24.9283	L	L

PBE0

N	E_{exc}/eV	p / eV	IP / eV	EA / eV	f_{osc}	${}^{U}D_{DC}/$	${}^{R}D_{CT}/$	${}^{U}M_{CT}/eV$	${}^{R}M_{AC}/eV$	U	R
1	2.7943	0.3234	-6.4126	-2.3643	0.0000	1.2490	1.0730	-2.7296	-4.6207	L	L
2	2.7943	0.3234	-6.4126	-2.3641	0.0000	1.4600	1.1840	-1.0637	-3.3628	L	L
3	2.8156	0.3283	-6.4086	-2.5117	0.0033	0.2420	0.2290	-50.5679	-53.9458	L	L
4	2.9655	0.3297	-6.5611	-2.3924	0.0003	0.1120	0.1150	-119.5956	-116.2417	L	L
5	3.0003	0.3333	-6.5596	-2.4962	0.0435	1.2190	1.0250	-2.7418	-4.9775	L	L
6	3.0015	0.3334	-6.5596	-2.4967	0.0485	1.2470	1.0730	-2.4759	-4.3485	L	L
7	3.0659	0.3292	-6.5620	-2.3689	0.1865	0.9510	0.9100	-6.1837	-6.8659	L	L
8	3.0671	0.3292	-6.5622	-2.3687	0.1929	1.0120	0.9810	-5.2708	-5.7204	L	L
9	3.3240	0.3273	-6.6000	-2.2413	0.0000	0.0090	0.0110	-1591.0547	-1300.1526	L	L
10	3.6323	0.2465	-6.5098	-0.0753	0.0007	0.2020	0.1670	-64.5788	-79.5188	L	L
11	3.6345	0.2465	-6.5100	-0.0749	0.0007	0.2070	0.1710	-62.8569	-77.5019	L	L
12	3.7342	0.2992	-6.4287	-1.7046	0.0161	0.0250	0.0200	-567.8436	-711.8401	L	L
13	3.7642	0.2483	-6.6129	-0.0221	0.0010	0.0070	0.0070	-2050.3362	-2050.3362	L	L
14	3.9106	0.3044	-6.5709	-1.6997	0.0233	0.2810	0.1860	-42.9609	-69.1341	L	L
15	3.9108	0.3044	-6.5712	-1.6999	0.0231	0.3300	0.2200	-35.3515	-57.1691	L	L
16	4.0069	0.2883	-6.4628	-1.3653	0.0036	0.6930	0.5990	-12.9326	-16.1934	L	L
17	4.0071	0.2885	-6.4632	-1.3687	0.0036	0.7000	0.6020	-12.7213	-16.0700	L	L
18	4.0801	0.2843	-6.4750	-1.2301	0.0000	0.1320	0.1320	-101.3528	-101.3528	L	L
19	4.1270	0.2828	-6.4228	-1.2520	0.0534	0.8070	0.7010	-10.1478	-12.8460	L	L
20	4.1272	0.2828	-6.4226	-1.2519	0.0546	0.9190	0.7730	-7.9735	-10.9330	L	L
21	4.1604	0.3072	-6.7680	-1.5682	0.0150	0.0260	0.0230	-545.4727	-617.7118	L	L
22	4.1711	0.2828	-6.5832	-1.0693	0.0208	0.8480	0.7070	-9.2840	-12.6705	L	L
23	4.1733	0.2836	-6.5858	-1.0876	0.0216	0.9010	0.7690	-8.2653	-11.0086	L	L
24	4.1963	0.2941	-6.6939	-1.2699	0.0175	0.2120	0.1660	-59.9198	-78.7418	L	L
25	4.1964	0.2938	-6.6899	-1.2643	0.0174	0.2410	0.2020	-51.7562	-63.2921	L	L
26	4.2150	0.2959	-6.7039	-1.3079	0.0508	0.5630	0.5940	-17.5250	-16.1902	L	L
27	4.2153	0.2958	-6.7058	-1.3033	0.0507	0.4640	0.5040	-22.9841	-20.5212	L	L
28	4.2338	0.2905	-6.5584	-1.3281	0.0000	0.1010	0.1070	-134.6662	-126.6715	L	L
29	4.2763	0.3031	-6.7552	-1.4613	0.0686	0.0200	0.0260	-711.7337	-545.5839	L	L
30	4.3664	0.2953	-6.8605	-1.0990	0.1810	0.8110	0.7840	-9.7194	-10.3309	L	L

Table 21: M_{AC} diagnostics calculated for the first 30 vertical states of $[Ru(bpy)_2(dppz)]^{2+}$ using four different functionals, in acetonitrile

B3LYP

N	E_{exc}/eV	p / eV	IP / eV	EA / eV	f_{osc}	${}^{U}D_{DC}/$	${}^{R}D_{CT}/$	${}^{U}M_{CT}/eV$	${}^{R}M_{AC}/eV$	U	R
1	2.5638	0.3284	-6.1220	-2.8081	0.0001	4.4190	3.0860	5.6783	4.2707	G	G
2	2.6791	0.3183	-6.1247	-2.5244	0.0016	1.8880	1.5620	1.0347	-0.5571	L	L
3	2.6792	0.3163	-6.1277	-2.4652	0.0003	1.8600	1.5450	0.8658	-0.7126	L	L
4	2.7266	0.3365	-6.2616	-2.8869	0.1557	4.7510	3.4270	6.1258	4.9549	S	S
5	2.7474	0.3340	-6.2735	-2.8105	0.0054	4.7280	3.4210	6.0435	4.8799	S	S
6	2.7725	0.3233	-6.1323	-2.6581	0.0048	4.7600	3.3270	5.7727	4.4697	S	S
7	2.8508	0.3229	-6.2730	-2.5024	0.0033	1.4690	1.5310	-1.0154	-0.6184	L	L
8	2.8734	0.3246	-6.2657	-2.5560	0.0033	1.2250	1.2100	-2.9231	-3.0688	L	L
9	2.9324	0.3268	-6.2841	-2.5938	0.1513	0.9830	0.9410	-5.7547	-6.4086	L	L
10	2.9677	0.3240	-6.2812	-2.5235	0.0709	2.9920	2.5810	4.0047	3.2383	S	S
11	2.9859	0.3239	-6.2775	-2.5147	0.1964	2.0630	2.0920	1.8330	1.9298	CT	CT
12	3.1285	0.3122	-6.1892	-2.2870	0.0157	2.7790	2.5390	3.3128	2.8230	S	CT
13	3.2929	0.3143	-6.2545	-2.2577	0.0087	2.6310	2.5360	3.0787	2.8737	CT	CT
14	3.2988	0.3795	-7.3943	-2.9025	0.0027	0.2630	0.2540	-44.4262	-46.3662	L	L
15	3.3260	0.3481	-6.7185	-2.6896	0.0051	0.5280	0.2420	-17.7995	-50.0301	L	L
16	3.3640	0.3278	-6.4696	-2.4175	0.0866	2.5390	2.1380	3.2482	2.1844	CT	CT
17	3.3692	0.3136	-6.2858	-2.2265	0.0656	3.8550	2.9530	4.7969	3.6559	S	S
18	3.6243	0.2773	-6.1567	-1.3626	0.0078	1.3720	1.1970	-2.9504	-4.4848	L	L
19	3.6355	0.3678	-7.1927	-2.7652	0.3708	0.8340	0.7090	-7.2572	-10.3012	L	L
20	3.6719	0.2529	-6.1995	-0.6196	0.0021	0.3660	0.3860	-32.4608	-30.4223	L	L
21	3.6743	0.2432	-6.2200	-0.3160	0.0003	0.2980	0.2820	-41.7030	-44.4446	L	L
22	3.7855	0.3289	-6.7740	-2.1416	0.0783	5.1200	3.9570	6.1378	5.3112	S	S
23	3.7985	0.2643	-6.4091	-0.7159	0.0074	1.5290	1.3750	-2.2247	-3.2795	L	L
24	3.8142	0.2897	-6.2558	-1.6156	0.0007	1.7470	1.5620	-0.3604	-1.3366	L	L
25	3.8314	0.2904	-6.2992	-1.5841	0.0333	1.3580	1.2540	-2.7022	-3.5816	L	L
26	3.8398	0.2823	-6.1749	-1.4943	0.0011	1.1370	1.0820	-4.9832	-5.6270	L	L
27	3.9195	0.2771	-6.1337	-1.3912	0.0667	1.3520	1.2550	-3.1111	-3.9343	L	L
28	3.9278	0.2803	-6.1881	-1.4207	0.0327	2.1080	1.8940	0.7968	0.0250	CT	L
29	3.9531	0.3452	-6.8614	-2.5300	0.0092	8.1670	5.8370	7.6300	6.9262	S	S
30	3.9964	0.2890	-6.3288	-1.5151	0.0695	0.7120	0.7600	-12.3611	-11.0838	L	L

CAM-B3LYP

N	E_{exc}/eV	p / eV	IP / eV	EA / eV	f_{osc}	${}^{U}D_{DC}/$	${}^{R}D_{CT}/$	${}^{U}M_{CT}/eV$	${}^{R}M_{AC}/eV$	U	R
1	3.3371	0.3341	-7.6667	-0.9786	0.0021	2.1140	1.7600	2.2809	0.9108	CT	L
2	3.3684	0.3320	-7.6749	-0.8053	0.0122	1.1890	1.0990	-3.0771	-4.0689	L	L
3	3.4515	0.3348	-7.6606	-1.2439	0.0031	0.1190	0.1430	-111.8952	-91.5866	L	L
4	3.4849	0.3409	-7.7433	-1.3951	0.5311	1.9510	1.8280	1.8970	1.4004	L	L
5	3.5240	0.3367	-7.7506	-1.1602	0.0005	1.9790	1.7790	1.8858	1.0678	L	L
6	3.5401	0.3356	-7.7292	-0.4484	0.0689	1.0900	1.0850	-4.0774	-4.1382	L	L
7	3.5741	0.3377	-7.7365	-0.4064	0.0173	1.1520	1.1610	-3.3112	-3.2143	L	L
8	3.5939	0.3375	-7.7539	-1.2881	0.1400	0.4710	0.5690	-21.3874	-16.1219	L	L
9	3.6643	0.3843	-8.7377	-1.0488	0.0362	0.1460	0.1210	-88.1713	-108.5490	L	L
10	3.6733	0.3569	-8.1339	-0.1339	0.0298	0.1170	0.1350	-113.3631	-96.9532	L	L
11	3.6881	0.3407	-7.7691	0.2435	0.0157	0.9120	0.8870	-6.5190	-6.9641	L	L
12	3.7439	0.3458	-7.8287	1.3913	0.0002	0.2420	0.2570	-50.0936	-46.6207	L	L
13	3.7883	0.3429	-7.8730	-1.1622	0.0090	0.2910	0.2820	-40.1520	-41.7312	L	L
14	3.8082	0.3695	-8.2223	-1.6511	0.0605	2.5210	2.2000	4.3427	3.5092	S	CT
15	3.8880	0.3598	-8.1962	-1.3345	0.2815	0.7680	0.8990	-8.9598	-6.2277	L	L
16	4.0810	0.3423	-7.7074	-1.4772	0.0113	5.0740	3.4720	6.4758	5.1663	S	S
17	4.2284	0.3444	-7.7740	-1.1227	0.0015	5.0500	3.5620	6.5213	5.3302	S	S
18	4.2485	0.3496	-7.9236	-1.2194	0.0774	4.5870	3.3390	6.3740	5.2007	S	S
19	4.2789	0.3319	-7.7357	0.1111	0.0513	2.3780	2.0750	2.9767	2.0925	CT	CT
20	4.3063	0.3338	-7.7704	0.0398	0.1962	2.4480	2.2000	3.2014	2.5383	CT	CT
21	4.3087	0.3403	-7.7810	0.8475	0.0029	1.0600	1.0640	-4.3253	-4.2742	L	L
22	4.3241	0.3357	-7.8559	-0.9068	0.0076	3.4580	2.7380	4.9711	3.8760	S	CT
23	4.4114	0.3287	-7.8090	-0.6940	0.0741	3.4180	2.5420	4.7314	3.2796	S	CT
24	4.4539	0.3430	-7.8371	1.1464	0.0105	0.1460	0.1290	-89.2944	-102.2918	L	L
25	4.4768	0.3643	-8.6783	-1.0665	0.4791	0.0790	0.1170	-172.3618	-113.1616	L	L
26	4.4886	0.3687	-8.7401	-1.0863	0.3221	0.3170	0.3510	-35.3915	-30.9914	L	L
27	4.5145	0.3583	-8.3870	-1.1854	0.6648	0.6030	0.5260	-14.1295	-17.6253	L	L
28	4.6348	0.3500	-8.3438	-0.9042	1.0506	0.8830	0.7440	-6.7842	-9.8309	L	L

29	4.7505	0.3086	-7.8105	-0.4684	0.3527	1.5600	1.3380	-0.8329	-2.3644	L	L
30	4.7931	0.3155	-7.9906	-0.4971	0.0815	1.0190	1.0340	-5.5459	-5.3409	L	L

CIS

N	E_{exc}/eV	p / eV	IP / eV	EA / eV	f_{osc}	${}^{U}D_{DC}/$	${}^{R}D_{CT}/$	${}^{U}M_{CT}/eV$	${}^{R}M_{AC}/eV$	U	R
1	3.1440	0.6252	-10.3672	6.6460	0.0000	0.0940	0.1480	-136.1746	-80.2818	L	L
2	3.1571	0.6260	-10.3752	6.6587	0.0000	0.0710	0.0930	-185.7782	-137.8012	L	L
3	3.2132	0.6278	-10.4145	6.6679	0.0000	0.0320	0.0370	-432.9068	-372.0974	L	L
4	4.4173	0.3603	-9.0521	0.7515	1.2037	0.2630	0.1180	-44.9480	-112.2274	L	L
5	4.4177	0.3729	-9.0621	1.0862	0.1131	1.7270	1.3920	1.8104	-0.1962	L	L
6	4.5256	0.6203	-10.3344	6.5454	0.0002	0.0060	0.0540	-2383.0622	-249.7804	L	L
7	4.5259	0.6205	-10.3444	6.5404	0.0009	0.0230	0.0580	-609.1870	-231.3851	L	L
8	4.6963	0.6214	-10.3691	6.5393	0.0000	0.0200	0.0080	-703.0741	-1783.0480	L	L
9	4.8569	0.4891	-11.8365	1.4724	0.0074	0.1570	0.0640	-78.4087	-211.6857	L	L
10	4.9213	0.4042	-9.5554	1.4430	0.3987	0.0740	0.1130	-183.5915	-116.4321	L	L
11	4.9255	0.4043	-9.5579	1.4440	1.0544	0.0670	0.1040	-203.9183	-127.4563	L	L
12	5.0371	0.3966	-9.4983	1.2924	0.3419	1.1870	1.2110	-1.3405	-1.1000	L	L
13	5.3275	0.4006	-9.3991	1.5012	0.4084	1.0920	0.9560	-2.2862	-4.1621	L	L
14	5.6165	0.4114	-9.8477	1.3484	0.3710	0.0440	0.0980	-316.0687	-135.7391	L	L
15	5.7683	0.4064	-9.2620	1.7954	1.8433	1.6410	1.2860	2.2825	-0.1398	L	L
16	5.8539	0.4386	-10.1082	1.8270	0.0615	0.8960	0.8500	-4.1359	-5.0056	L	L
17	5.8606	0.4448	-10.0934	2.0093	0.0008	0.8890	0.8250	-4.0949	-5.3514	L	L
18	5.8676	0.4461	-10.1276	2.0122	0.0248	0.7580	0.7280	-6.8571	-7.6400	L	L
19	5.9295	0.4459	-10.1106	2.0240	0.0089	0.6860	0.7050	-8.8561	-8.2904	L	L
20	6.0604	0.3978	-9.3768	1.4491	1.1400	0.3890	0.3700	-26.1912	-28.0920	L	L
21	6.2582	0.4473	-10.2561	1.9152	1.0870	1.1440	1.0660	-0.4158	-1.3368	L	L
22	6.2590	0.4093	-9.8940	1.2433	0.3152	2.9250	2.1080	6.2143	4.3063	CT	CT
23	6.3496	0.5719	-13.4523	2.1089	0.0000	0.6010	0.5020	-8.3983	-13.1234	L	L
24	6.3794	0.4141	-10.0326	1.2365	0.0212	2.2280	1.6190	4.8061	2.3750	CT	L
25	6.3905	0.4519	-10.3103	1.9856	0.5312	1.0530	0.9150	-1.3789	-3.4414	L	L
26	6.4388	0.4210	-9.9678	1.4889	0.0214	1.5530	1.2560	2.1846	-0.0079	L	L
27	6.4723	0.4262	-10.1664	1.4316	0.0932	0.3680	0.3600	-27.5316	-28.4011	L	L
28	6.4388	0.4210	-9.9678	1.4889	0.0214	1.5530	1.2560	2.1846	-0.0079	L	L
29	6.5262	0.4241	-9.8915	1.6485	0.0026	1.5900	1.3380	2.4836	0.7780	L	L
30	6.6107	0.4725	-10.7105	2.1470	0.0329	0.5710	0.5460	-12.3608	-13.5155	L	L

PBE0

N	E_{exc}/eV	p / eV	IP / eV	EA / eV	f_{osc}	${}^{U}D_{DC}/$	${}^{R}D_{CT}/$	${}^{U}M_{CT}/eV$	${}^{R}M_{AC}/eV$	U	R
1	2.7353	0.3371	-6.4672	-2.6919	0.0000	3.8670	2.7860	5.4483	4.0034	G	G
2	2.8347	0.3263	-6.4732	-2.3840	0.0006	1.3670	1.2600	-1.6542	-2.5487	L	L
3	2.8489	0.3293	-6.4689	-2.4744	0.0013	1.3330	1.2180	-1.8417	-2.8616	L	L
4	2.8959	0.3462	-6.5893	-2.8200	0.2253	4.2160	3.1470	6.0063	4.8461	S	S
5	2.9121	0.3429	-6.6088	-2.7124	0.0040	4.1250	3.0270	5.8407	4.5745	S	S
6	2.9864	0.3357	-6.4703	-2.6562	0.0063	5.0740	3.4450	6.2972	4.9553	S	S
7	3.0050	0.3335	-6.6004	-2.4589	0.0028	1.2790	1.3760	-2.1826	-1.3889	L	L
8	3.0389	0.3337	-6.5934	-2.4735	0.0001	1.3990	1.3750	-1.2113	-1.3910	L	L
9	3.0886	0.3337	-6.6093	-2.4448	0.2304	1.2360	1.3110	-2.5697	-1.9032	L	L
10	3.1513	0.3353	-6.6021	-2.4970	0.1537	2.4400	2.3800	3.2229	3.0741	S	CT
11	3.1561	0.3395	-6.6155	-2.6144	0.0051	5.0660	3.5340	6.3963	5.1641	S	S
12	3.3135	0.3250	-6.5563	-2.2551	0.0096	2.4260	2.4190	2.9070	2.8899	CT	CT
13	3.3580	0.3909	-7.7440	-2.8560	0.0026	0.1500	0.1470	-85.3612	-87.3204	L	L
14	3.4361	0.3707	-7.1794	-2.8181	0.0326	2.6880	2.2910	4.7290	3.8007	S	S
15	3.4759	0.3231	-6.5637	-2.1861	0.0122	2.9520	2.6660	3.9153	3.3920	S	CT
16	3.5462	0.3256	-6.6402	-2.2005	0.0654	3.6310	2.7300	4.8952	3.5864	S	S
17	3.5596	0.3211	-6.6143	-2.1014	0.0464	3.9160	2.9040	5.0591	3.7777	S	S
18	3.6122	0.2508	-6.5633	-0.1510	0.0011	0.1820	0.1890	-72.2937	-69.3634	L	L
19	3.6356	0.2532	-6.5708	-0.2078	0.0121	0.0300	0.0250	-473.0981	-569.0958	L	L
20	3.7295	0.3798	-7.5180	-2.7585	0.4487	0.4270	0.2750	-23.3871	-42.0266	L	L
21	3.7469	0.2522	-6.6624	-0.0889	0.0001	0.0460	0.0420	-306.1720	-335.9850	L	L
22	3.8681	0.2987	-6.5005	-1.6151	0.0056	1.5360	1.3260	-1.2475	-2.7322	L	L
23	3.9715	0.3558	-7.1894	-2.4573	0.1329	5.1830	3.9190	6.9041	6.0080	S	S
24	4.0310	0.3002	-6.5973	-1.5585	0.0000	1.7390	1.5280	-0.1111	-1.2545	L	L
25	4.0430	0.3036	-6.6308	-1.6127	0.0432	1.4850	1.3500	-1.4364	-2.4061	L	L
26	4.0600	0.2937	-6.5647	-1.4073	0.0007	1.0790	1.0330	-5.3538	-5.9481	L	L
27	4.1444	0.2871	-6.5554	-1.2243	0.0834	1.9400	1.8330	0.3910	-0.0423	L	L
28	4.1544	0.2855	-6.4848	-1.2613	0.0544	1.3480	1.2740	-2.9144	-3.5348	L	L
29	4.1861	0.2693	-6.5946	-0.6640	0.0290	1.5220	1.4610	-2.1341	-2.5291	L	L

30	4.1971	0.3085	-6.8043	-1.5598	0.0515	0.6560	0.7190	-13.5557	-11.6323	L	L

Table 22: M_{AC} diagnostics calculated for the first 30 vertical states of $[Ru(bpy)_2(tpphz)]^{2+}$ using four different functionals, in acetonitrile

B3LYP

N	E_{exc}/eV	p / eV	IP / eV	EA / eV	f_{osc}	${}^{U}D_{DC}/$	${}^{R}D_{CT}/$	${}^{U}M_{CT}/eV$	${}^{R}M_{AC}/eV$	U	R
1	2.5898	0.3255	-6.1328	-2.7163	0.0001	3.8110	2.8050	5.0795	3.7244	G	G
2	2.6836	0.3167	-6.1372	-2.4656	0.0000	1.3810	1.2830	-1.8094	-2.6059	L	L
3	2.6840	0.3191	-6.1343	-2.5364	0.0017	1.4480	1.3180	-1.2614	-2.2423	L	L
4	2.7640	0.3343	-6.2708	-2.8152	0.2601	4.0500	3.1510	5.5403	4.5259	S	S
5	2.7764	0.3313	-6.2845	-2.7243	0.0061	4.1390	3.1510	5.5368	4.4459	S	S
6	2.8040	0.3253	-6.1411	-2.7065	0.0045	5.4060	3.7800	6.1893	5.0435	S	S
7	2.8565	0.3238	-6.2824	-2.5174	0.0037	1.4290	1.5290	-1.2657	-0.6066	L	L
8	2.8821	0.3249	-6.2743	-2.5570	0.0009	1.0520	1.0790	-4.8466	-4.5041	L	L
9	2.9461	0.3254	-6.2923	-2.5421	0.2030	0.5780	0.6790	-16.0586	-12.3529	L	L
10	2.9874	0.3285	-6.2917	-2.6404	0.0192	5.1050	3.7180	6.1181	5.0658	S	S
11	2.9948	0.3254	-6.2754	-2.5614	0.1146	3.2310	3.0820	4.3968	4.1813	S	S
12	3.0074	0.3165	-6.1578	-2.4449	0.0631	4.0260	3.1010	5.0348	3.9679	S	S
13	3.1877	0.3212	-6.2938	-2.4404	0.0301	4.5130	3.3320	5.5509	4.4200	S	S
14	3.1887	0.3219	-6.2891	-2.4568	0.0495	4.6230	3.3630	5.6455	4.4785	S	S
15	3.2678	0.3205	-6.3140	-2.3469	0.0173	1.6480	1.8310	-0.0159	0.8574	L	L
16	3.4048	0.3610	-6.9441	-2.8299	0.6599	1.4680	1.3550	0.0151	-0.8029	L	L
17	3.4091	0.3607	-6.9263	-2.8480	0.0091	4.1560	3.4650	6.3497	5.6588	S	S
18	3.5003	0.3826	-7.5373	-2.8446	0.0032	0.2020	0.2480	-60.8731	-47.6508	L	L
19	3.5680	0.3676	-7.1478	-2.8491	0.0000	4.8580	3.5190	7.0376	5.9097	G	G
20	3.6273	0.2754	-6.1705	-1.2938	0.0068	1.2910	1.1550	-3.6601	-4.9735	L	L
21	3.6728	0.2560	-6.2048	-0.7015	0.0029	0.4590	0.4860	-24.4061	-22.6633	L	L
22	3.6735	0.2436	-6.2286	-0.3187	0.0008	0.3080	0.2950	-40.1233	-42.1836	L	L
23	3.7958	0.2473	-6.3297	-0.3227	0.0011	0.2440	0.2410	-52.2843	-53.0189	L	L
24	3.8077	0.3399	-6.8279	-2.3984	0.0313	5.0720	4.4190	6.4088	5.9893	S	S
25	3.2678	0.3205	-6.3140	-2.3469	0.0173	1.6480	1.8310	-0.0158	0.8574	L	L
26	3.8365	0.2920	-6.3091	-1.6198	0.0311	1.3550	1.2670	-2.6817	-3.4198	L	L
27	3.8434	0.2836	-6.1922	-1.5116	0.0007	1.1140	1.0860	-5.2102	-5.5435	L	L
28	3.8644	0.3437	-6.9025	-2.4110	1.0270	4.4290	3.8280	6.1001	5.5897	S	S
29	3.8754	0.3513	-6.9966	-2.5255	0.0086	6.7740	5.0580	7.4327	6.7115	S	S
30	3.9220	0.3363	-6.8142	-2.3041	0.2402	5.5390	4.7130	6.5519	6.0963	S	S

CAM-B3LYP

N	E_{exc}/eV	p / eV	IP / eV	EA / eV	f_{osc}	${}^{U}D_{DC}/$	${}^{R}D_{CT}/$	${}^{U}M_{CT}/eV$	${}^{R}M_{AC}/eV$	U	R
1	3.3362	0.3345	-7.6757	-0.9695	0.0017	2.0950	1.7590	2.2292	0.9163	CT	L
2	3.3715	0.3326	-7.6852	-0.8000	0.0218	1.1570	1.0850	-3.3951	-4.2210	L	L
3	3.4560	0.3351	-7.6699	-1.2332	0.0043	0.1300	0.1540	-101.6473	-84.3850	L	L
4	3.4714	0.3422	-7.7583	-1.4414	0.7626	1.5880	1.5730	0.2442	0.1578	L	L
5	3.5254	0.3371	-7.7582	-1.1418	0.0005	2.0070	1.8030	1.9974	1.1856	CT	L
6	3.5429	0.3359	-7.7369	-0.4513	0.0690	1.1590	1.1510	-3.2846	-3.3710	L	L
7	3.5757	0.3382	-7.7472	-0.3340	0.0239	1.1690	1.2000	-3.1163	-2.7981	L	L
8	3.5997	0.3378	-7.7603	-1.2819	0.1381	0.4850	0.5860	-20.4988	-15.3816	L	L
9	3.6725	0.3403	-7.7708	0.3811	0.0655	0.0620	0.0580	-222.9912	-239.0086	L	L
10	3.6838	0.3427	-7.8083	-0.1397	0.0682	1.0550	1.0330	-4.3237	-4.6143	L	L
11	3.7366	0.3517	-7.9810	-1.0832	0.1718	0.2640	0.2670	-44.9732	-44.3603	L	L
12	3.7438	0.3457	-7.8376	1.3689	0.0004	0.2460	0.2640	-49.1270	-45.1360	L	L
13	3.8285	0.3400	-7.8542	-1.1012	0.1689	0.1490	0.1870	-87.3896	-67.7511	L	L
14	3.8863	0.4038	-9.2642	-1.5121	0.0045	0.0130	0.0510	-1096.6777	-271.3583	L	L
15	4.0098	0.3591	-8.1635	-1.4627	0.0170	1.7270	1.5200	1.4345	0.2990	L	L
16	4.1538	0.3413	-7.7634	-1.3705	0.0353	4.7710	3.4820	6.2692	5.1519	S	S
17	4.1642	0.3295	-7.7136	-1.1317	0.1014	3.5820	2.7120	4.9472	3.6576	S	CT
18	4.2275	0.3394	-7.8218	-1.2219	0.0611	3.0790	2.5240	4.5594	3.5310	S	CT
19	4.2495	0.3340	-7.7859	-0.4846	0.1174	3.3480	2.6490	4.7889	3.6540	S	CT
20	4.2873	0.3449	-7.8432	-0.6186	0.1416	4.0720	3.2480	5.8479	4.9508	S	S

21	4.2902	0.3432	-7.7832	0.6621	0.0072	1.9000	1.7660	1.7591	1.1840	L	L
22	4.3351	0.3411	-7.8060	0.1417	0.0011	2.6720	2.4130	3.8919	3.3134	CT	CT
23	4.3451	0.3415	-7.7628	-0.8590	0.0042	4.8140	3.5200	6.3014	5.2018	S	S
24	4.4268	0.3482	-8.1515	-0.2468	0.5572	0.8050	0.7840	-8.4127	-8.8919	L	L
25	4.4706	0.3475	-8.1046	0.0963	0.6192	0.1530	0.1170	-84.6606	-113.6192	L	L
26	4.4791	0.3652	-8.6931	-1.0736	0.5639	0.1030	0.0870	-129.8653	-155.5761	L	L
27	4.4901	0.3664	-8.6498	-0.9137	0.0553	0.3620	0.4020	-29.8074	-25.8494	L	L
28	4.5478	0.3640	-8.4281	-1.3281	0.0222	1.8750	1.5660	2.2245	0.7091	L	L
29	4.5598	0.3685	-8.8808	-0.9243	0.0000	2.5290	1.9650	4.3332	2.6989	CT	L
30	4.6119	0.3564	-8.4136	-1.0962	0.0261	3.2800	2.9440	5.3079	4.8068	S	S

CIS

N	E_{exc}/eV	p / eV	IP / eV	EA / eV	f_{osc}	${}^{U}D_{DC}/$	${}^{R}D_{CT}/$	${}^{U}M_{CT}/eV$	${}^{R}M_{AC}/eV$	U	R
1	3.1432	0.6252	-10.3700	6.6421	0.0000	0.0930	0.1500	-137.8229	-78.9856	L	L
2	3.1563	0.6260	-10.3791	6.6546	0.0000	0.0710	0.0930	-185.7783	-137.8013	L	L
3	3.2128	0.6278	-10.4184	6.6640	0.0000	0.0320	0.0370	-432.9067	-372.0974	L	L
4	4.2729	0.3493	-8.7014	0.8033	1.5452	0.4300	0.3930	-23.9829	-27.1357	L	L
5	4.5242	0.5789	-10.1317	5.6208	0.0008	0.1110	0.0440	-113.9741	-311.5123	L	L
6	4.5243	0.6204	-10.3378	6.5446	0.0007	0.0050	0.0540	-2863.0479	-249.7778	L	L
7	4.5337	0.4238	-9.3059	2.2268	0.0053	0.8560	0.8330	-5.2893	-5.7537	L	L
8	4.6958	0.6213	-10.3727	6.5344	0.0000	0.0190	0.0080	-740.9693	-1783.0494	L	L
9	4.9214	0.4042	-9.5578	1.4408	0.3980	0.0750	0.1150	-180.9968	-114.2158	L	L
10	4.9257	0.4043	-9.5603	1.4419	1.0542	0.0680	0.1060	-200.7574	-124.8435	L	L
11	5.0571	0.4995	-11.9950	1.5961	0.0103	0.0300	0.0360	-466.3973	-386.3992	L	L
12	5.0751	0.4017	-9.5402	1.3909	0.3422	0.7860	0.8950	-7.3891	-5.1579	L	L
13	5.2039	0.3901	-9.2585	1.3576	0.3007	1.5760	1.4030	1.4792	0.3526	L	L
14	5.4344	0.4020	-9.1269	1.8133	0.4783	0.8830	0.6440	-5.3674	-11.4195	L	L
15	5.4545	0.4094	-9.2687	1.8727	1.9891	0.0360	0.0020	-388.8489	-7188.6845	L	L
16	5.6501	0.4018	-9.3142	1.6200	0.0638	2.2710	1.9670	4.5935	3.6136	CT	L
17	5.8464	0.3987	-9.4786	1.3699	0.6901	1.8900	1.6070	3.2296	1.8879	L	L
18	5.8545	0.4373	-10.0898	1.8098	0.1063	0.8160	0.7920	-5.7470	-6.2818	L	L
19	5.8573	0.4439	-10.0901	1.9886	0.1148	0.7680	0.7410	-6.6709	-7.3541	L	L
20	5.8677	0.4461	-10.1299	2.0103	0.0250	0.7630	0.7350	-6.7322	-7.4512	L	L
21	5.9092	0.4396	-10.0453	1.9172	0.2613	0.3460	0.3770	-29.6550	-26.2328	L	L
22	5.9686	0.5454	-11.8024	3.0384	0.0000	1.0360	0.5600	0.9415	-10.8729	L	L
23	6.0484	0.4102	-9.4014	1.7616	1.6652	0.5610	0.5790	-14.5048	-13.7068	L	L
24	6.1783	0.5551	-11.9519	3.1521	0.0201	0.9950	0.5520	0.6319	-10.9824	L	L
25	6.2543	0.4120	-9.8974	1.3150	0.3079	2.7440	2.0100	5.9647	4.0483	CT	CT
26	6.2772	0.4503	-10.2965	1.9581	0.0751	0.8060	0.8160	-5.6110	-5.3921	L	L
27	6.3814	0.4169	-10.0072	1.3376	0.0652	0.6260	0.5420	-11.6578	-15.2228	L	L
28	6.3895	0.4473	-10.2922	1.8785	0.4744	0.8980	0.8100	-3.8645	-5.6066	L	L
29	6.4377	0.4198	-9.9669	1.4575	0.0152	1.5770	1.2820	2.2934	0.1922	L	L
30	6.4449	0.4271	-9.8999	1.7231	0.0996	0.0900	0.0480	-148.3731	-288.3697	L	L

PBE0

N	E_{exc}/eV	p / eV	IP / eV	EA / eV	f_{osc}	${}^{U}D_{DC}/$	${}^{R}D_{CT}/$	${}^{U}M_{CT}/eV$	${}^{R}M_{AC}/eV$	U	R
1	2.7488	0.3350	-6.4788	-2.6215	0.0001	3.4520	2.5850	4.9441	3.5450	G	G
2	2.8396	0.3269	-6.4836	-2.3892	0.0004	1.3650	1.2750	-1.6541	-2.3988	L	L
3	2.8554	0.3301	-6.4794	-2.4867	0.0016	1.3470	1.2490	-1.7070	-2.5458	L	L
4	2.9207	0.3444	-6.5999	-2.7568	0.3504	3.5820	2.8660	5.3512	4.3469	S	S
5	2.9287	0.3408	-6.6210	-2.6389	0.0038	3.6290	2.7790	5.3046	4.0910	S	S
6	3.0120	0.3342	-6.6077	-2.4688	0.0029	1.1610	1.2940	-3.3100	-2.0353	L	L
7	3.0260	0.3375	-6.4823	-2.6964	0.0057	5.5620	3.8270	6.5960	5.4223	S	S
8	3.0461	0.3340	-6.6033	-2.4692	0.0063	1.3910	1.3970	-1.2645	-1.2200	L	L
9	3.0952	0.3338	-6.6185	-2.4367	0.2344	1.3050	1.3820	-1.9522	-1.3374	L	L
10	3.1669	0.3367	-6.6084	-2.5280	0.0942	2.8990	2.8450	4.1943	4.1000	S	S
11	3.1926	0.3420	-6.6214	-2.6780	0.0022	5.7180	3.9860	6.7869	5.6927	S	S
12	3.2102	0.3280	-6.5003	-2.4172	0.0228	4.3450	3.2640	5.6125	4.5149	S	S
13	3.3736	0.3328	-6.6194	-2.4180	0.0549	4.4820	3.2600	5.8433	4.6390	S	S
14	3.3796	0.3317	-6.6249	-2.3844	0.0320	4.1630	3.1790	5.5667	4.4961	S	S
15	3.4275	0.3326	-6.6579	-2.3299	0.0015	2.4530	2.5280	3.1798	3.3539	CT	CT
16	3.5112	0.3705	-7.2327	-2.7961	0.7197	0.6580	0.5220	-11.8014	-17.5030	L	L
17	3.5487	0.3711	-7.2359	-2.8163	0.0120	3.8980	3.3120	6.4040	5.7504	S	S
18	3.5708	0.3950	-7.9098	-2.8005	0.0032	0.1380	0.1830	-93.5966	-67.9379	L	L
19	3.6112	0.2517	-6.5745	-0.1646	0.0013	0.1860	0.1950	-70.5684	-66.9953	L	L
20	3.6330	0.2516	-6.5818	-0.1507	0.0033	0.1720	0.1670	-76.8729	-79.3795	L	L
21	3.7461	0.2528	-6.6732	-0.0928	0.0001	0.0550	0.0520	-254.9336	-270.0382	L	L

22	3.7747	0.3799	-7.5322	-2.7958	0.0000	4.6600	3.4400	7.2470	6.1511	G	G
23	3.8734	0.2993	-6.5119	-1.6219	0.0055	1.5110	1.3230	-1.3845	-2.7387	L	L
24	3.9832	0.3583	-7.2615	-2.4534	0.2798	5.5050	4.3490	7.1348	6.4395	S	S
25	4.0145	0.3557	-7.2412	-2.4015	0.8311	5.0470	4.1910	6.8273	6.2445	S	S
26	4.0308	0.3649	-7.3793	-2.4899	0.0788	4.4710	3.7060	6.7094	6.0446	S	S
27	4.0308	0.3649	-7.3793	-2.4899	0.0788	4.4710	3.7060	6.7094	6.0446	S	S
28	4.0308	0.3649	-7.3793	-2.4899	0.0788	4.4710	3.7060	6.7094	6.0446	S	S
29	4.0645	0.2944	-6.5771	-1.4140	0.0002	1.0680	1.0440	-5.4723	-5.7823	L	L
30	4.0347	0.3012	-6.6125	-1.5692	0.0054	1.7860	1.5790	0.1331	-0.9239	L	L

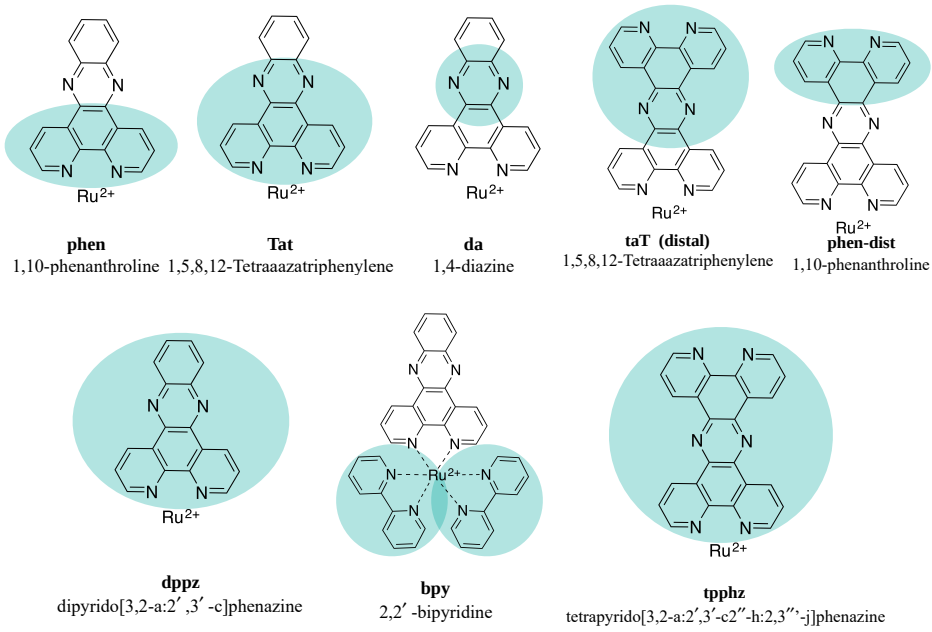

Figure 55: Nomenclature of the ligands and fragments present in the metal complexes.

11.9 NATURAL TRANSITION ORBITALS OF THE METAL COMPLEXES

N	B3LYP			PBE0			CAM-B3LYP		
	Hole	Particle	Character	Hole	Particle	Character	Hole	Particle	Character
1	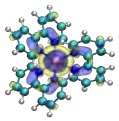	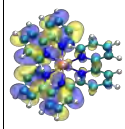	MLCT	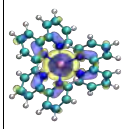	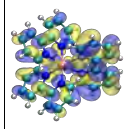	MLCT	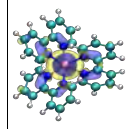	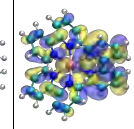	MLCT
2	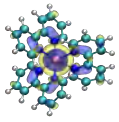	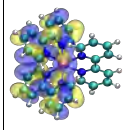	MLCT	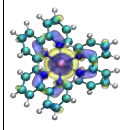	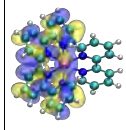	MLCT	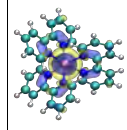	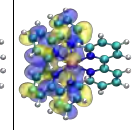	MLCT
3	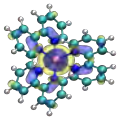	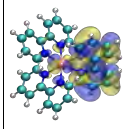	MLCT	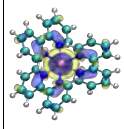	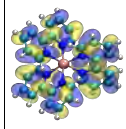	MLCT	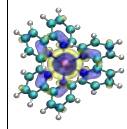	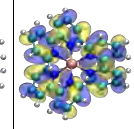	MLCT
4	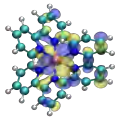	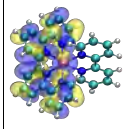	MLCT	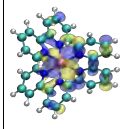	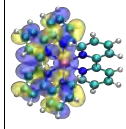	MLCT	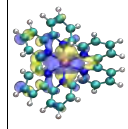	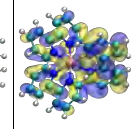	MLCT
5	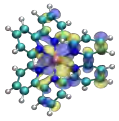	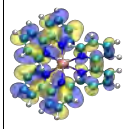	MLCT	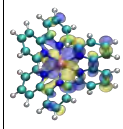	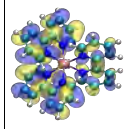	MLCT	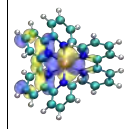	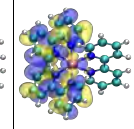	MLCT
6	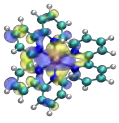	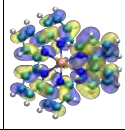	MLCT	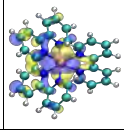	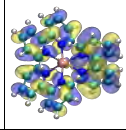	MLCT	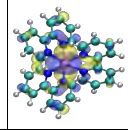	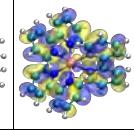	MLCT
7	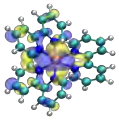	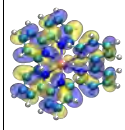	MLCT	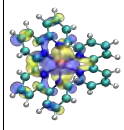	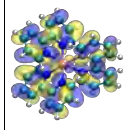	MLCT	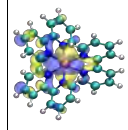	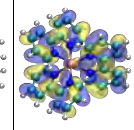	MLCT
8	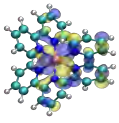	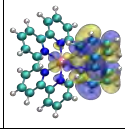	MLCT	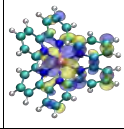	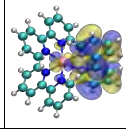	MLCT	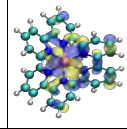	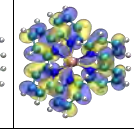	MLCT
9	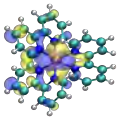	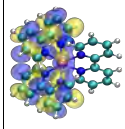	MLCT	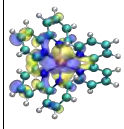	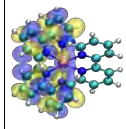	MLCT	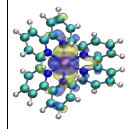	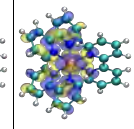	MC
10	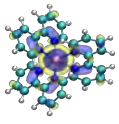	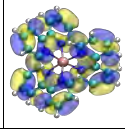	MLCT	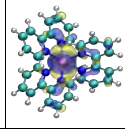	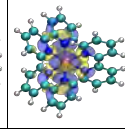	MC	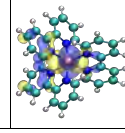	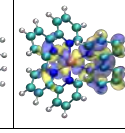	MLCT

Figure 56: (a) Main contributing orbitals relative to electronic transitions 1 to 10 of $[Ru(bpy)_3]^{2+}$ computed using three different functionals and associated character of each transition.

N	B3LYP			PBE0			CAM-B3LYP		
	Hole	Particle	Character	Hole	Particle	Character	Hole	Particle	Character
11	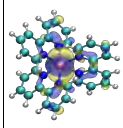	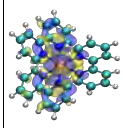	MLCT	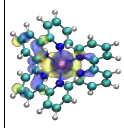	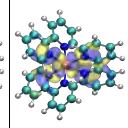	MLCT	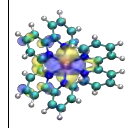	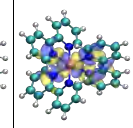	MLCT
12	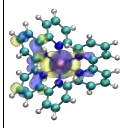	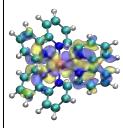	MLCT	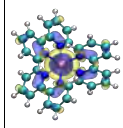	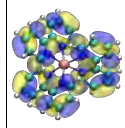	MLCT	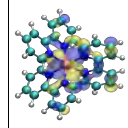	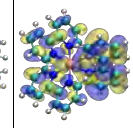	MLCT
13	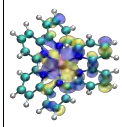	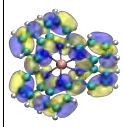	MLCT	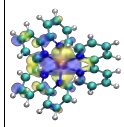	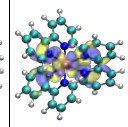	MC	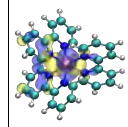	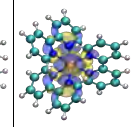	MC
14	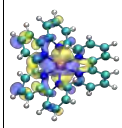	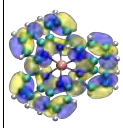	MLCT	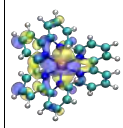	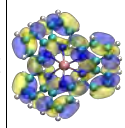	MLCT	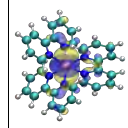	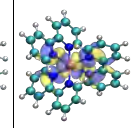	MC
15	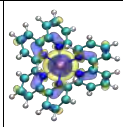	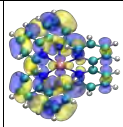	MLCT	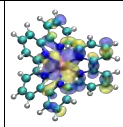	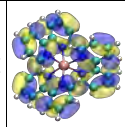	MLCT	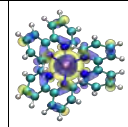	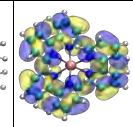	MLCT
16	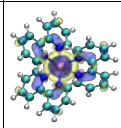	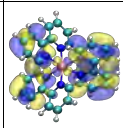	MLCT	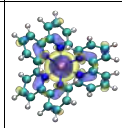	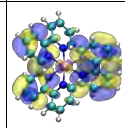	MLCT	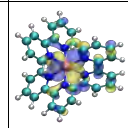	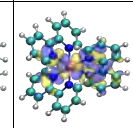	MC
17	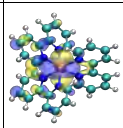	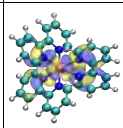	MC	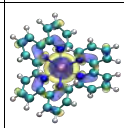	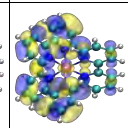	MLCT	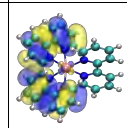	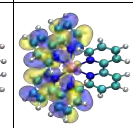	LC
18	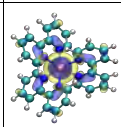	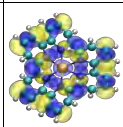	MLCT	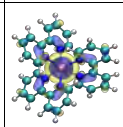	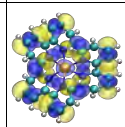	MLCT	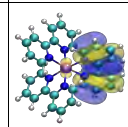	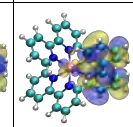	LC
19	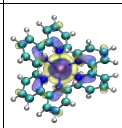	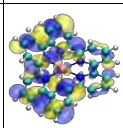	MLCT	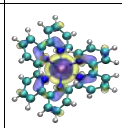	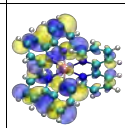	MLCT	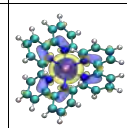	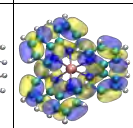	MLCT
20	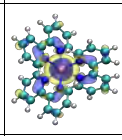	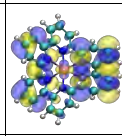	MLCT	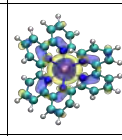	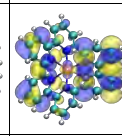	MLCT	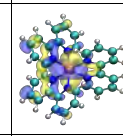	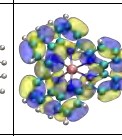	MLCT

Figure 56: (b) Main contributing orbitals relative to electronic transitions 11 to 20 of $[Ru(bpy)_3]^{2+}$ computed using three different functionals and associated character of each transition.

N	B3LYP			PBE0			CAM-B3LYP		
	Hole	Particle	Character	Hole	Particle	Character	Hole	Particle	Character
21	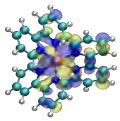	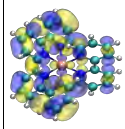	MLCT	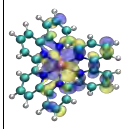	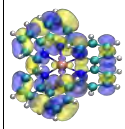	MLCT	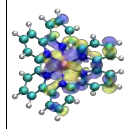	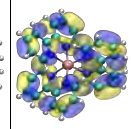	MLCT
22	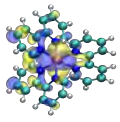	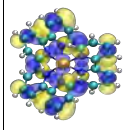	MLCT	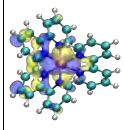	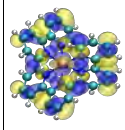	MLCT	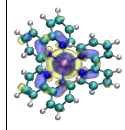	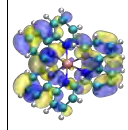	MLCT
23	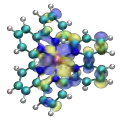	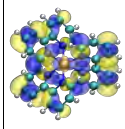	MLCT	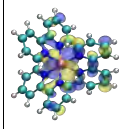	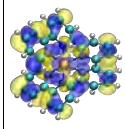	MLCT	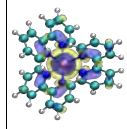	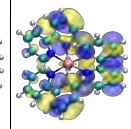	MLCT
24	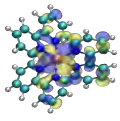	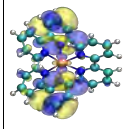	MLCT	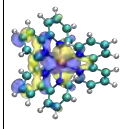	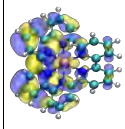	MLCT	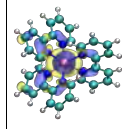	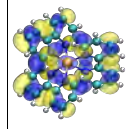	MLCT
25	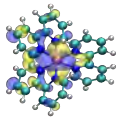	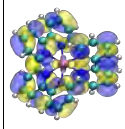	MLCT	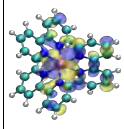	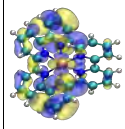	MLCT	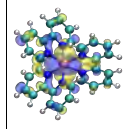	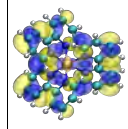	MLCT
26	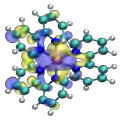	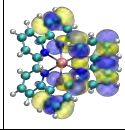	MLCT	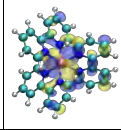	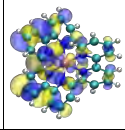	MLCT	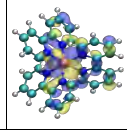	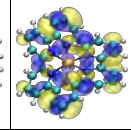	MLCT
27	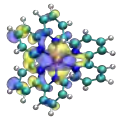	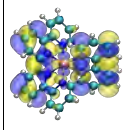	MLCT	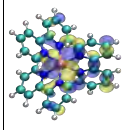	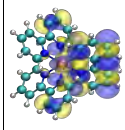	MLCT	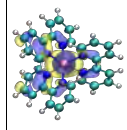	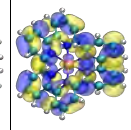	MLCT
28	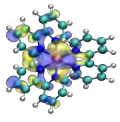	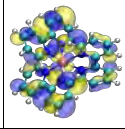	MLCT	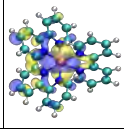	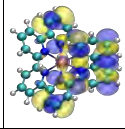	MLCT	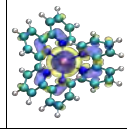	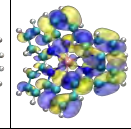	MLCT
29	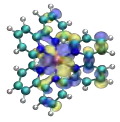	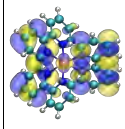	MLCT	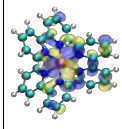	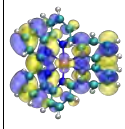	MLCT	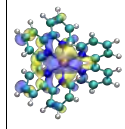	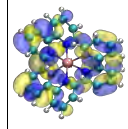	MLCT
30	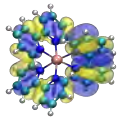	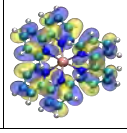	LC	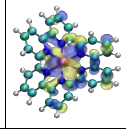	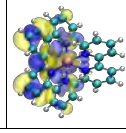	MLCT	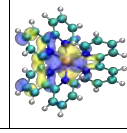	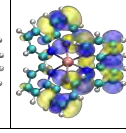	MLCT

Figure 56: (c) Main contributing orbitals relative to electronic transitions 21 to 30 of $[Ru(bpy)_3]^{2+}$ computed using three different functionals and associated character of each transition.

N	B3LYP			PBE0			CAM-B3LYP		
	Hole	Particle	Character	Hole	Particle	Character	Hole	Particle	Character
1	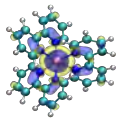	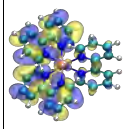	MLCT	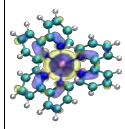	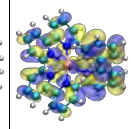	MLCT	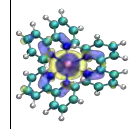	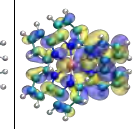	MLCT
2	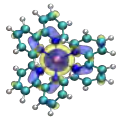	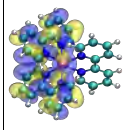	MLCT	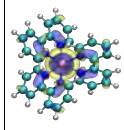	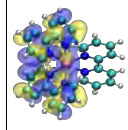	MLCT	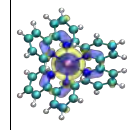	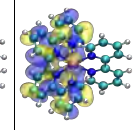	MLCT
3	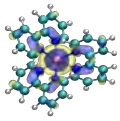	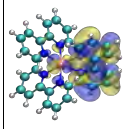	MLCT	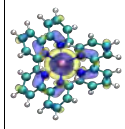	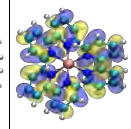	MLCT	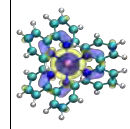	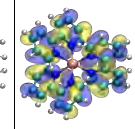	MLCT
4	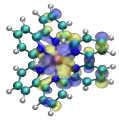	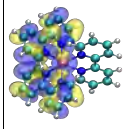	MLCT	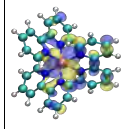	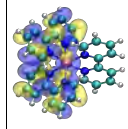	MLCT	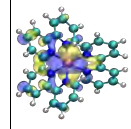	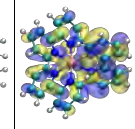	MLCT
5	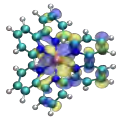	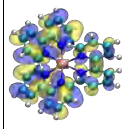	MLCT	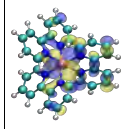	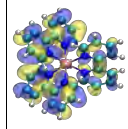	MLCT	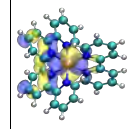	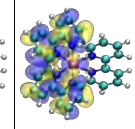	MLCT
6	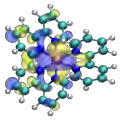	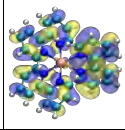	MLCT	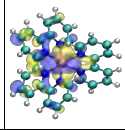	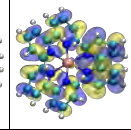	MLCT	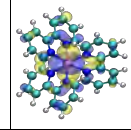	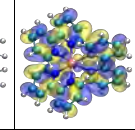	MLCT
7	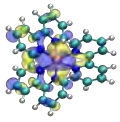	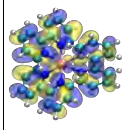	MLCT	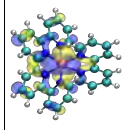	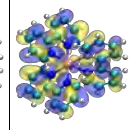	MLCT	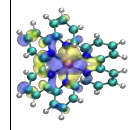	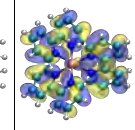	MLCT
8	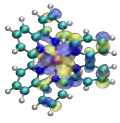	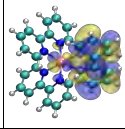	MLCT	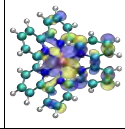	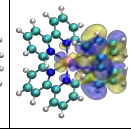	MLCT	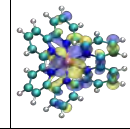	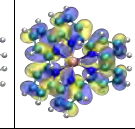	MLCT
9	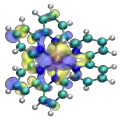	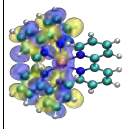	MLCT	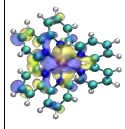	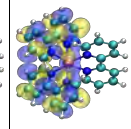	MLCT	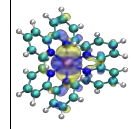	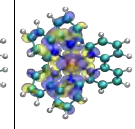	MC
10	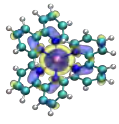	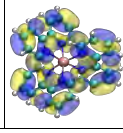	MLCT	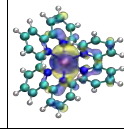	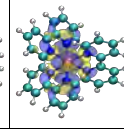	MC	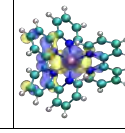	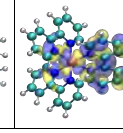	MLCT

Figure 57: (a) Main contributing orbitals relative to electronic transitions 1 to 10 of $[Ru(tpy)_2]^{2+}$ computed using three different functionals and associated character of each transition.

N	B3LYP			PBE0			CAM-B3LYP		
	Hole	Particle	Character	Hole	Particle	Character	Hole	Particle	Character
11	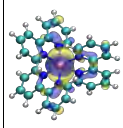	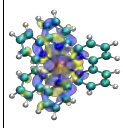	MLCT	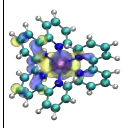	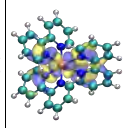	MLCT	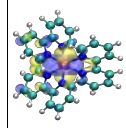	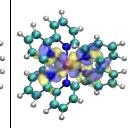	MLCT
12	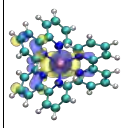	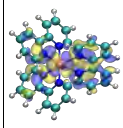	MLCT	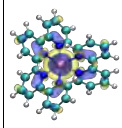	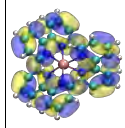	MLCT	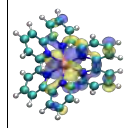	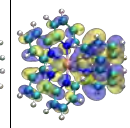	MLCT
13	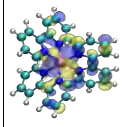	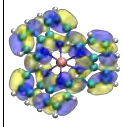	MLCT	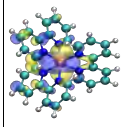	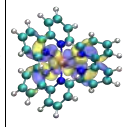	MC	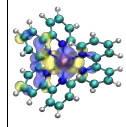	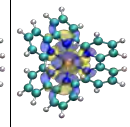	MC
14	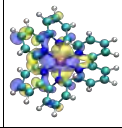	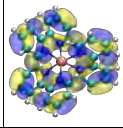	MLCT	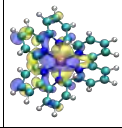	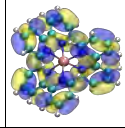	MLCT	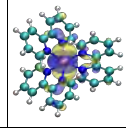	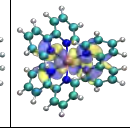	MC
15	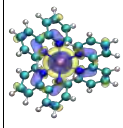	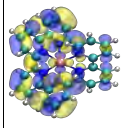	MLCT	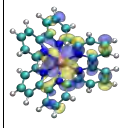	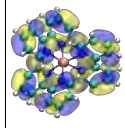	MLCT	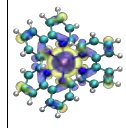	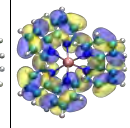	MLCT
16	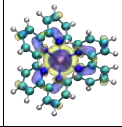	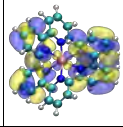	MLCT	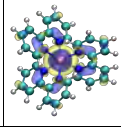	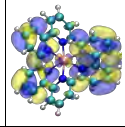	MLCT	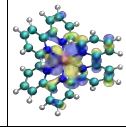	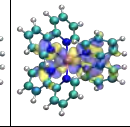	MC
17	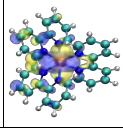	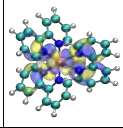	MC	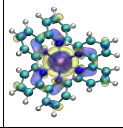	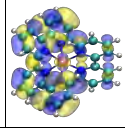	MLCT	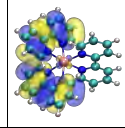	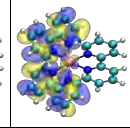	LC
18	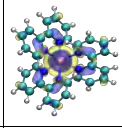	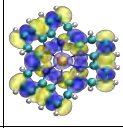	MLCT	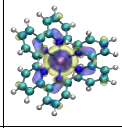	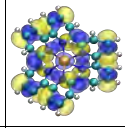	MLCT	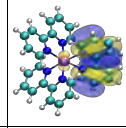	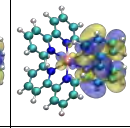	LC
19	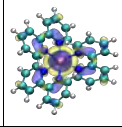	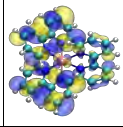	MLCT	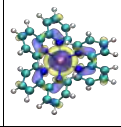	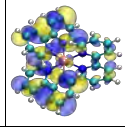	MLCT	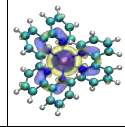	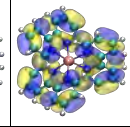	MLCT
20	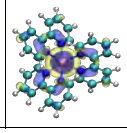	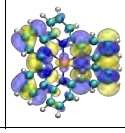	MLCT	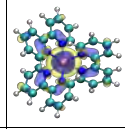	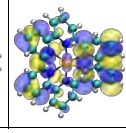	MLCT	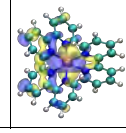	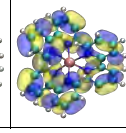	MLCT

Figure 57: (b) Main contributing orbitals relative to electronic transitions 11 to 20 of $[Ru(tpy)_2]^{2+}$ computed using three different functionals and associated character of each transition.

N	B3LYP			PBE0			CAM-B3LYP		
	Hole	Particle	Character	Hole	Particle	Character	Hole	Particle	Character
21	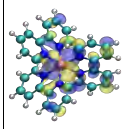	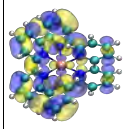	MLCT	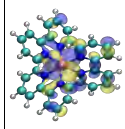	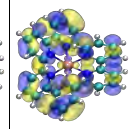	MLCT	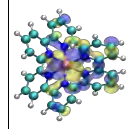	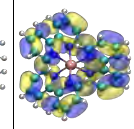	MLCT
22	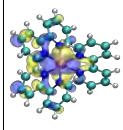	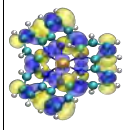	MLCT	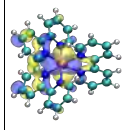	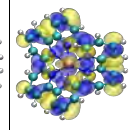	MLCT	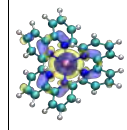	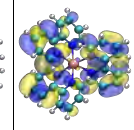	MLCT
23	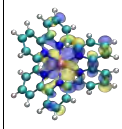	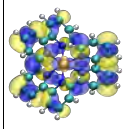	MLCT	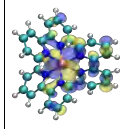	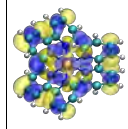	MLCT	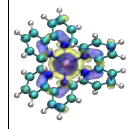	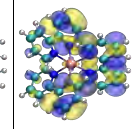	MLCT
24	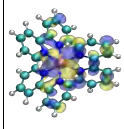	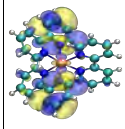	MLCT	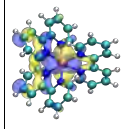	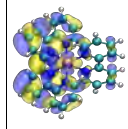	MLCT	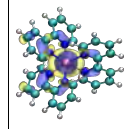	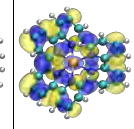	MLCT
25	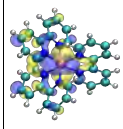	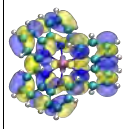	MLCT	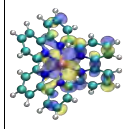	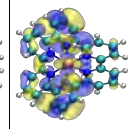	MLCT	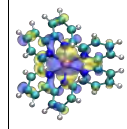	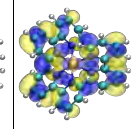	MLCT
26	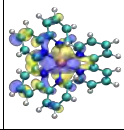	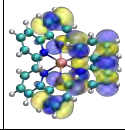	MLCT	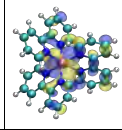	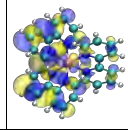	MLCT	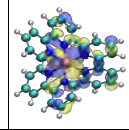	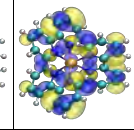	MLCT
27	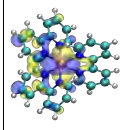	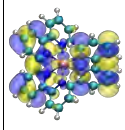	MLCT	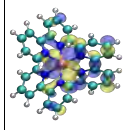	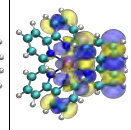	MLCT	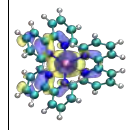	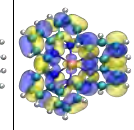	MLCT
28	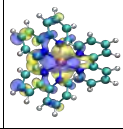	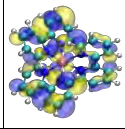	MLCT	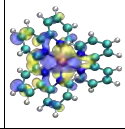	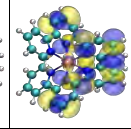	MLCT	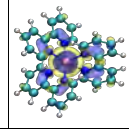	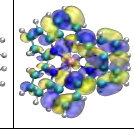	MLCT
29	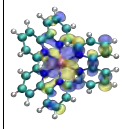	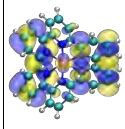	MLCT	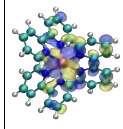	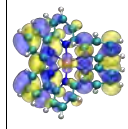	MLCT	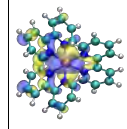	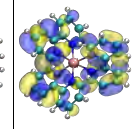	MLCT
30	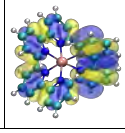	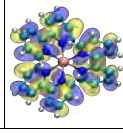	LC	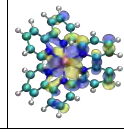	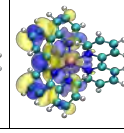	MLCT	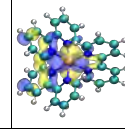	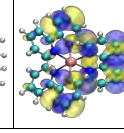	MLCT

Figure 57: (c) Main contributing orbitals relative to electronic transitions 21 to 30 of $[Ru(tpy)_2]^{2+}$ computed using three different functionals and associated character of each transition.

N	B3LYP			PBE0			CAM-B3LYP		
	Hole	Particle	Character	Hole	Particle	Character	Hole	Particle	Character
01	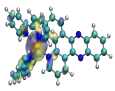	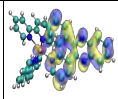	MLCT(dppz)	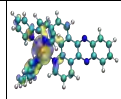	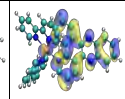	MLCT(dppz)	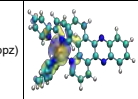	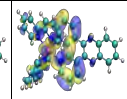	MLCT(phen)
02	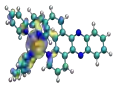	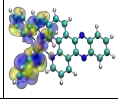	MLCT(bpy)	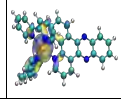	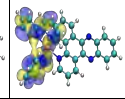	MLCT(bpy)	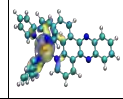	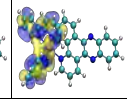	MLCT(bpy)
03	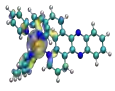	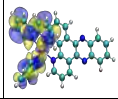	MLCT(bpy)	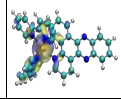	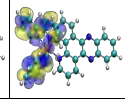	MLCT(dppz)	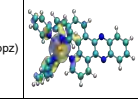	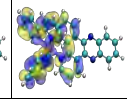	MLCT(bpy,phen)
04	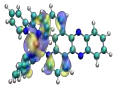	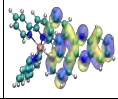	MLCT(dppz)	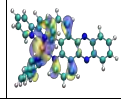	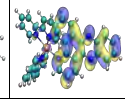	MLCT(dppz)	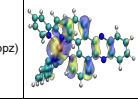	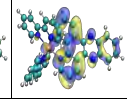	MLCT(dppz)
05	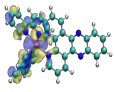	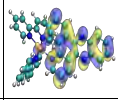	MLCT(dppz)	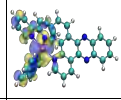	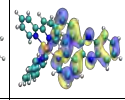	MLCT(dppz)	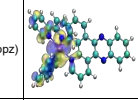	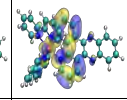	MLCT(phen)
06	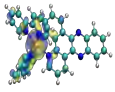	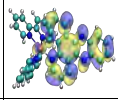	MLCT(dppz)	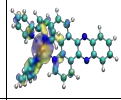	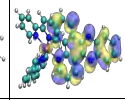	MLCT(dppz)	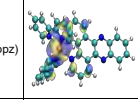	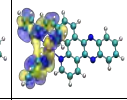	MLCT(bpy)
07	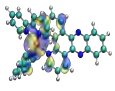	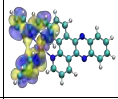	MLCT(bpy)	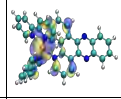	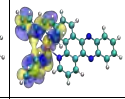	MLCT(bpy)	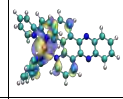	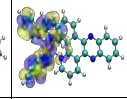	MLCT(bpy)
08	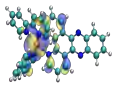	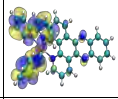	MLCT(bpy)	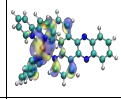	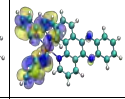	MLCT(bpy)	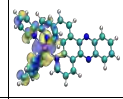	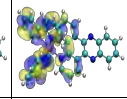	MLCT(bpy)
09	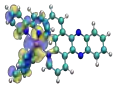	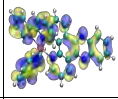	MLCT(dppz,bpy)	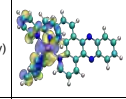	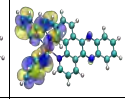	MLCT(bpy)	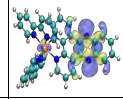	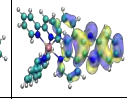	ILCT(da)(dppz)
10	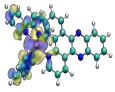	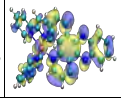	MLCT(dppz,bpy)	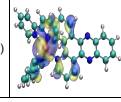	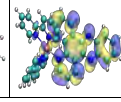	MLCT(dppz)	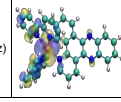	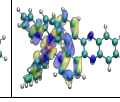	MC/MLCT(bpy,phen)

Figure 58: (a) Main contributing orbitals relative to electronic transitions 1 to 10 of $[Ru(bpy)_2(dppz)]^{2+}$ computed using three different functionals and associated character of each transition. A legend for the nomenclature of the fragments is given in Figure 55.

N	B3LYP			PBE0			CAM-B3LYP		
	Hole	Particle	Character	Hole	Particle	Character	Hole	Particle	Character
11	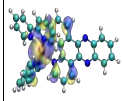	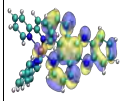	MLCT(dppz)	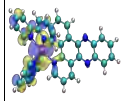	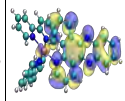	MLCT(dppz)	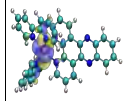	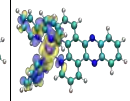	MC/MLCT(bpy)
12	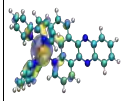	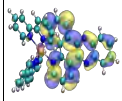	MLCT(dppz)	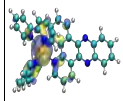	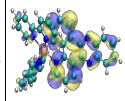	MLCT(dppz)	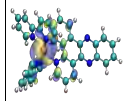	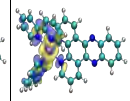	MC
13	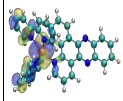	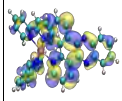	MLCT(dppz)	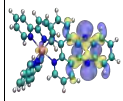	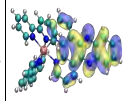	ILCT(da) (dppz)	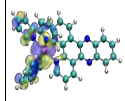	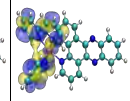	MLCT(bpy)
14	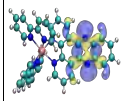	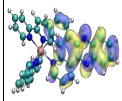	ILCT(da) (dppz)	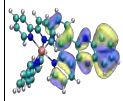	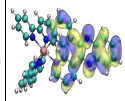	LC(dppz)	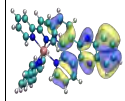	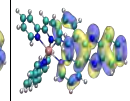	LC(dppz)
15	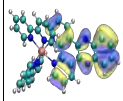	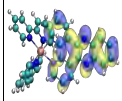	LC(dppz)	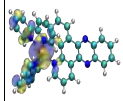	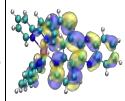	MLCT(dppz)	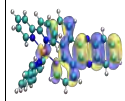	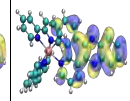	LC(dppz)
16	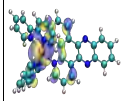	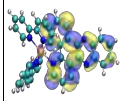	MLCT(dppz)	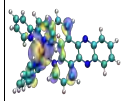	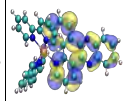	MLCT(dppz)	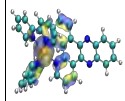	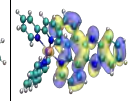	MLCT(dppz)
17	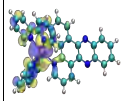	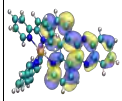	MLCT(dppz)	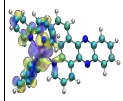	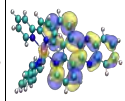	MLCT(dppz)	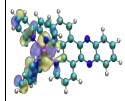	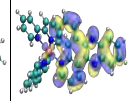	MLCT(dppz)
18	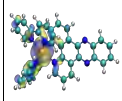	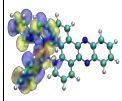	MLCT(bpy)	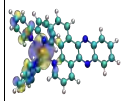	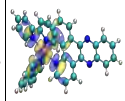	MLCT(MC)	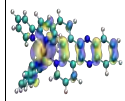	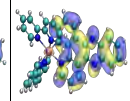	MLCT(dppz)
19	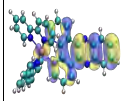	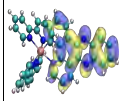	LC(dppz)	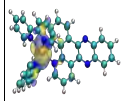	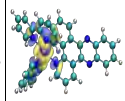	MLCT(MC)	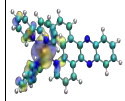	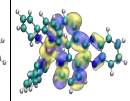	MLCT(Tat)
20	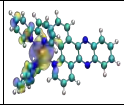	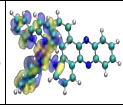	MLCT(bpy)	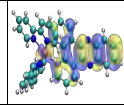	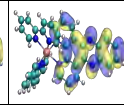	LC(dppz)	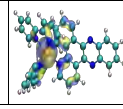	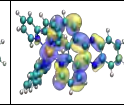	MLCT(Tat)

Figure 58: b) Main contributing orbitals relative to electronic transitions 11 to 20 of $[Ru(bpy)_2(dppz)]^{2+}$ computed using three different functionals and associated character of each transition. A legend for the nomenclature of the fragments is given in Figure 55.

N	B3LYP			PBE0			CAM-B3LYP		
	Hole	Particle	Character	Hole	Particle	Character	Hole	Particle	Character
21	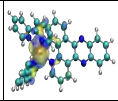	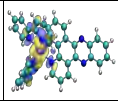	MC	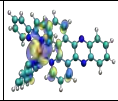	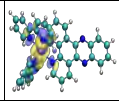	MC	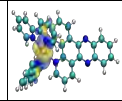	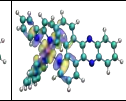	MC
22	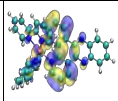	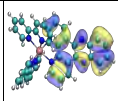	ILCT(Tat)(dppz)	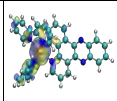	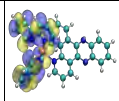	MLCT(bpy)	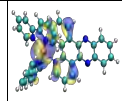	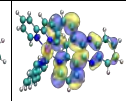	MLCT(dppz)
23	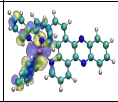	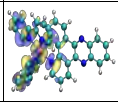	MC/MLCT(bpy)	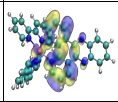	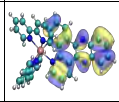	ILCT(dppz) (phen)	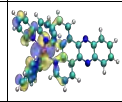	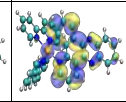	MLCT(dppz)
24	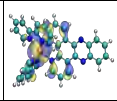	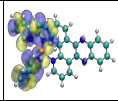	MLCT(bpy)	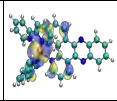	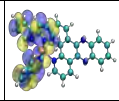	MLCT(bpy)	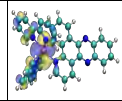	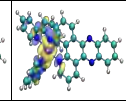	MC
25	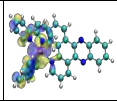	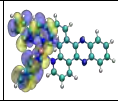	MLCT(bpy)	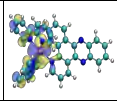	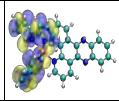	MLCT(bpy)	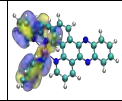	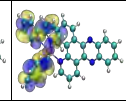	LC(bpy)
26	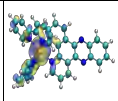	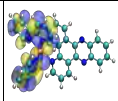	MLCT(bpy)	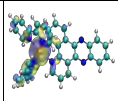	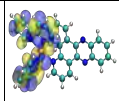	MLCT(bpy)	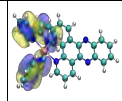	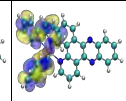	LC(bpy)
27	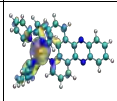	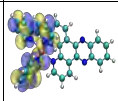	MLCT(bpy)	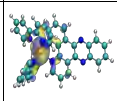	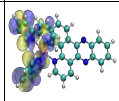	MLCT(bpy)	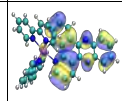	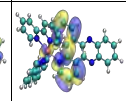	ILCT(dppz,phen)
28	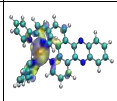	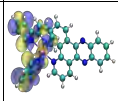	MLCT(bpy)	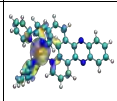	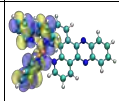	MLCT(bpy)	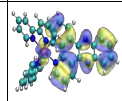	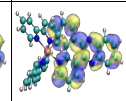	LC(dppz)
29	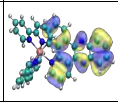	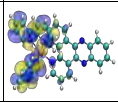	LLCT(dppz) (bpy)	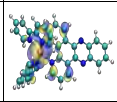	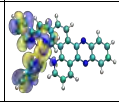	MLCT(bpy)	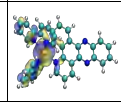	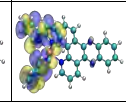	MLCT(bpy)
30	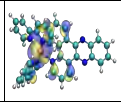	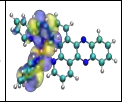	MC/MLCT(bpy)	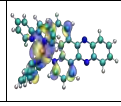	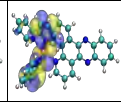	MLCT(bpy)	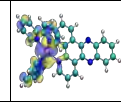	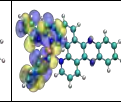	MLCT(bpy)

Figure 58: c) Main contributing orbitals relative to electronic transitions 21 to 30 of $[Ru(bpy)_2(dppz)]^{2+}$ computed using three different functionals and associated character of each transition. A legend for the nomenclature of the fragments is given in Figure 55.

N	B3LYP			PBE0			CAM-B3LYP		
	Hole	Particle	Character	Hole	Particle	Character	Hole	Particle	Character
01	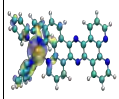	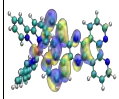	MLCT(Tat)	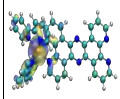	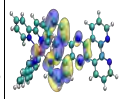	MLCT(Tat)	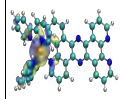	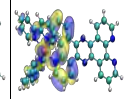	MLCT(phen)
02	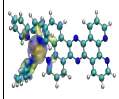	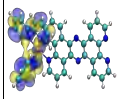	MLCT(bpy)	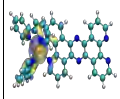	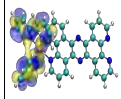	MLCT(bpy)	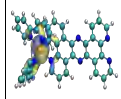	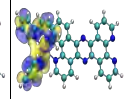	MLCT(bpy)
03	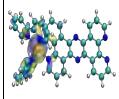	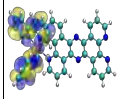	MLCT(bpy)	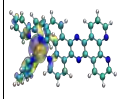	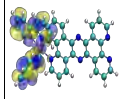	MLCT(bpy)	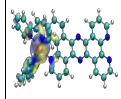	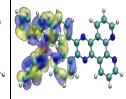	MLCT(bpy)
04	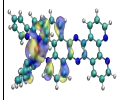	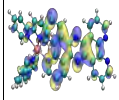	MLCT(tpphz)	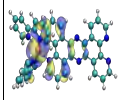	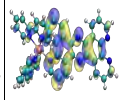	MLCT(tpphz)	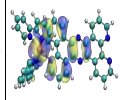	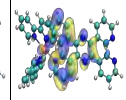	MLCT(Tat)
05	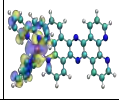	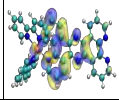	MLCT(Tat)	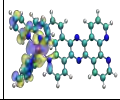	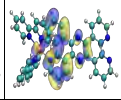	MLCT(Tat)	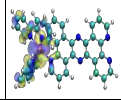	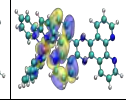	MLCT(phen-prox)
06	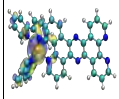	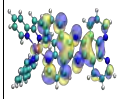	MLCT(tpphz)	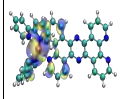	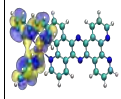	MLCT(bpy)	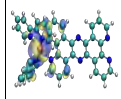	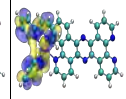	MLCT(bpy)
07	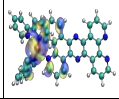	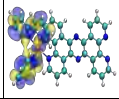	MLCT(bpy)	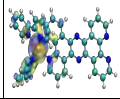	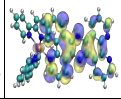	MLCT(Tat)	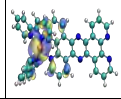	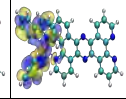	MLCT(bpy)
08	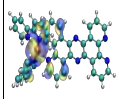	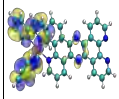	MLCT(bpy)	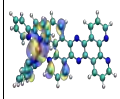	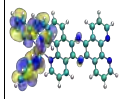	MLCT(bpy)	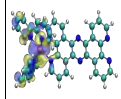	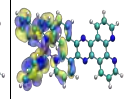	MLCT(bpy,phen-prox)
09	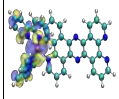	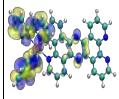	MLCT(bpy)	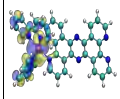	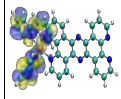	MLCT(bpy)	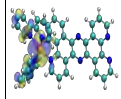	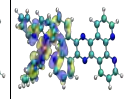	MC
10	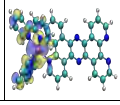	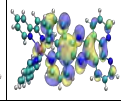	MLCT(tpphz)	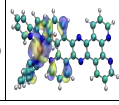	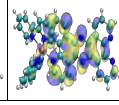	MLCT(tpphz)	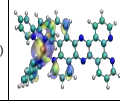	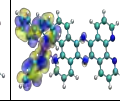	MLCT(bpy)

Figure 59: (a) Main contributing orbitals relative to electronic transitions 1 to 10 of $[Ru(bpy)_2(tpphz)]^{2+}$computed using three different functionals and associated character of each transition. A legend for the nomenclature of the fragments is given in Figure 55.

N	B3LYP			PBE0			CAM-B3LYP		
	Hole	Particle	Character	Hole	Particle	Character	Hole	Particle	Character
11	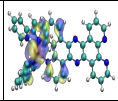	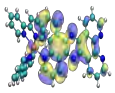	MLCT(tpphz)	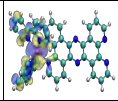	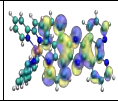	MLCT(tpphz)	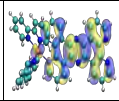	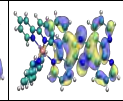	LC(tpphz)
12	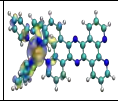	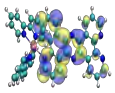	MLCT(tpphz)	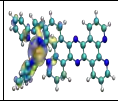	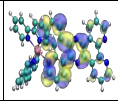	MLCT(tpphz)	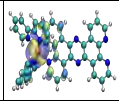	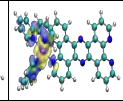	MC
13	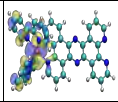	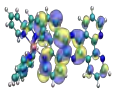	MLCT(tpphz)	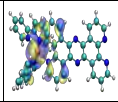	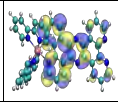	MLCT(tpphz)	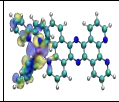	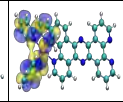	MLCT(bpy)
14	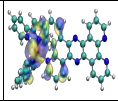	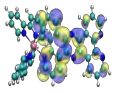	MLCT(tpphz)	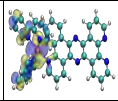	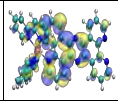	MLCT(tpphz)	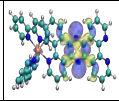	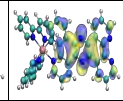	ILCT(da) (tpphz)
15	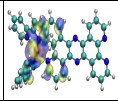	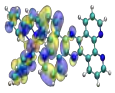	MLCT(Tat)	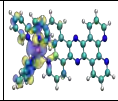	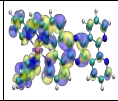	MLCT(bpy) (Tat)	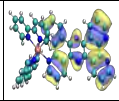	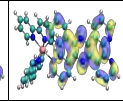	LC(tpphz)
16	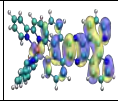	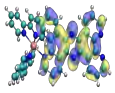	LC(tpphz)	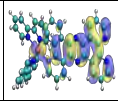	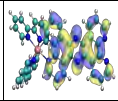	LC(tpphz)	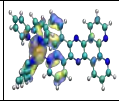	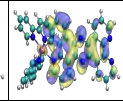	MLCT(tpphz)
17	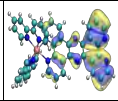	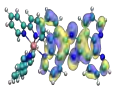	ILCT(tpphz)	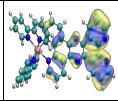	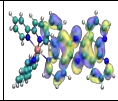	ILCT(tpphz)	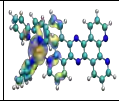	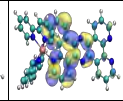	MLCT(Tat)
18	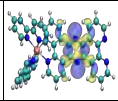	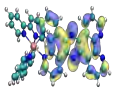	ILCT(da)(tpphz)	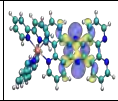	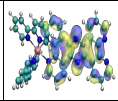	ILCT(da)(tppz)	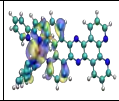	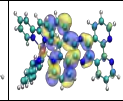	MLCT(Tat)
19	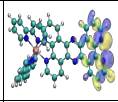	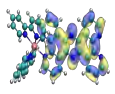	ILCT(phen-dist) (tpphz)	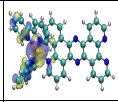	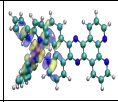	MC	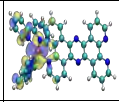	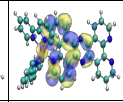	MLCT(Tat)
20	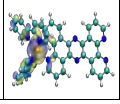	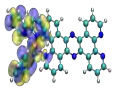	MLCT(bpy)	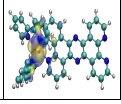	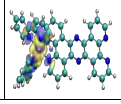	MC	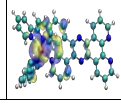	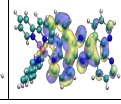	MLCT(tpphz)

Figure 59: (b) Main contributing orbitals relative to electronic transitions 11 to 20 of $[Ru(bpy)_2(tpphz)]^{2+}$ computed using three different functionals and associated character of each transition. A legend for the nomenclature of the fragments is given in Figure 55.

N	B3LYP			PBE0			CAM-B3LYP		
	Hole	Particle	Character	Hole	Particle	Character	Hole	Particle	Character
21	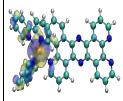	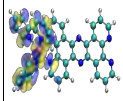	MC	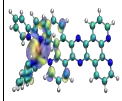	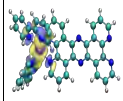	MC	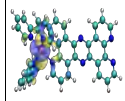	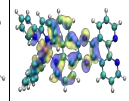	MLCT(Tat)
22	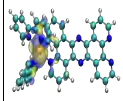	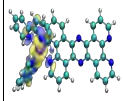	MC	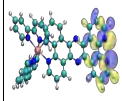	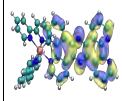	ILCT(phen-dist)(tpphz)	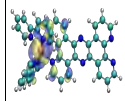	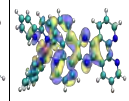	MLCT(Tat)
23	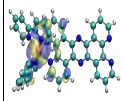	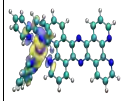	MC	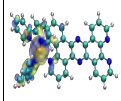	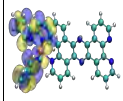	MLCT(Tat)	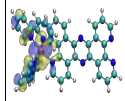	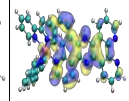	MLCT(tpphz)
24	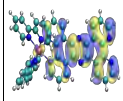	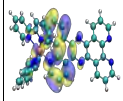	ILCT(tpphz) (phen-prox)	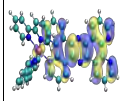	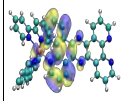	ILCT(tpphz) (phen-prox)	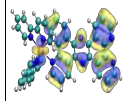	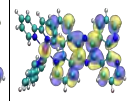	LC(tpphz)
25	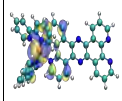	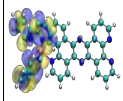	MLCT(bpy)	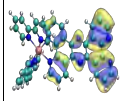	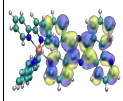	ILCT(tphhz)	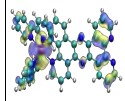	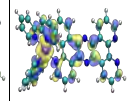	MC(partial LLCT)
26	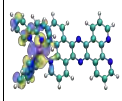	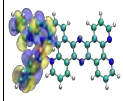	MLCT(bpy)	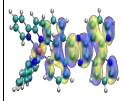	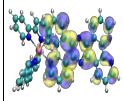	ILCT(tpphz)	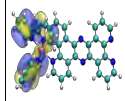	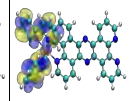	LC(bpy)
27	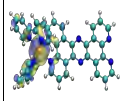	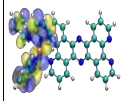	MLCT(bpy)	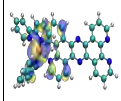	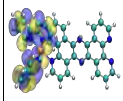	MLCT(bpy)	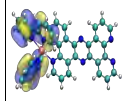	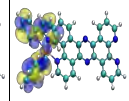	LC(bpy)
28	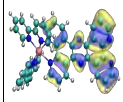	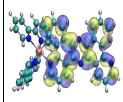	LC(tpphz)	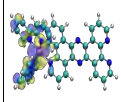	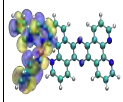	MLCT(bpy)	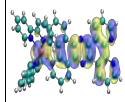	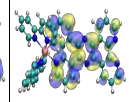	MLCT(tpphz)
29	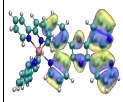	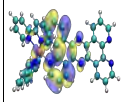	ILCT(tpphz) (phen-prox)	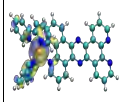	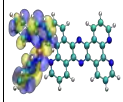	MLCT(bpy)	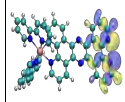	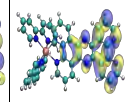	ILCT(phen-dist)(taT)
30	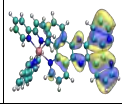	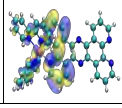	ILCT(taT) (phen-prox)	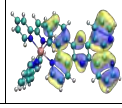	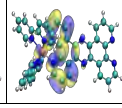	ILCT(tphhz) (phen-prox)	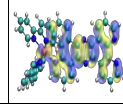	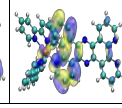	ILCT(tpphz) (phen-prox)

Figure 59: (c) Main contributing orbitals relative to electronic transitions 21 to 30 of $[Ru(bpy)_2(tpphz)]^{2+}$computed using three different functionals and associated character of each transition. A legend for the nomenclature of the fragments is given in Figure 55.

Part V

RÉSUMÉ EN FRANÇAIS

12

RESUMÉ EN FRANÇAIS

12.1 INTRODUCTION

12.1.1 *L'art de construire des modèles simples pour décrire des excitations électroniques complexes.*

Les molécules "photo-actives " sont celles dont la réponse observable peut être provoquée par une interaction avec la lumière [14]. La perturbation de la structure électronique peut être libérée par une réaction chimique induite, un changement de couleur ou de luminescence, une altération des propriétés magnétiques ou une combinaison des possibilités précédemment évoquées. Les molécules (et les matériaux) possédant de telles propriétés trouvent des applications dans un large éventail de domaines différents, et il est possible de fabriquer des dispositifs qui exploitent leurs propriétés intrinsèques à des fins particulières, du monde biologique et médical [15, 16] au stockage optoélectronique et énergétique [17, 18]. La recherche constante de nouvelles molécules photo-actives d'intérêt dans ces domaines est motivée par la nécessité d'une plus grande efficacité, d'une meilleure performance et de coûts réduits. L'innovation dans ce domaine ne peut qu'être liée à la connaissance précise des mécanismes a l'origine les phénomènes photo-induits, au niveau moléculaire, et encore plus profondément au niveau des structures électroniques. Les processus induits par la lumière peuvent être appréhendés en termes de réorganisation de la densité électronique, et la question de savoir comment la densité électronique se redistribue en réponse à une perturbation induite par la lumière peut être traitée. Il est évident que la capacité de moduler soigneusement l'ampleur d'une perturbation induite par la lumière est cruciale pour la conception rationnelle d'une telle classe de molécules.

La chimie théorique a maintenant atteint un niveau de spécificité et de diversification qui permet de caractériser l'ampleur d'une déformation ou la réactivité à l'état excité d'un chromophore donné en appliquant simplement différentes stratégies et outils informatiques, et il est possible d'obtenir une description complète d'un processus réactif - c'est-à-dire son évolution selon une coordonnée de réaction spécifique - de l'absorption d'énergie à la formation des photo-produits. Avec le ressources actuellement disponible et les développements récents dans les méthodes théoriques telles que la théorie fonctionnelle de la densité en fonction du temps (TDDFT), la chimie computationnelle a déjà démontré sa capacité à fournir des solutions pour une caractérisation en profondeur de ces processus et est bien placée pour mener les découvertes à travers la conception pré-synthétique rationnelle. Les nombreux travaux publiés au cours des dernières décennies sur les états excités témoignent de la pertinence de ce sujet dans la recherche actuelle.

Les approches possibles pour l'étude des processus photochimiques sont multiples. En général, deux grandes catégories peuvent être identifiées. La première consiste à étudier l'évolution temporelle d'un paquet d'ondes grâce à la résolution de l'équation de Schrödinger dépendante du temps. Une deuxième approche - celle que nous adoptons dans cette thèse - consiste à séquencer le cours d'une réaction induite par la lumière par la caractérisation de minima sur les surfaces d'énergie potentielle le long desquelles la réaction se déroule, identifiant ainsi les étapes pertinentes du trajet photochimique qui relie la région Franck-Condon, où le système absorbe, au retour à l'état fondamental, avec formation des photo-produits.

En plus de l'énergie de la réaction, une quantité essentielle que l'on peut examiner pour comprendre et moduler les propriétés d'état excité desdits systèmes moléculaires, est la densité électronique. Il est bien connu que les propriétés photo-physiques d'un système moléculaire donné peuvent être fortement influencées et sont généralement prédéterminées par la présence de caractéristiques structurales particulières, par exemple, des groupes très fortement électroattracteurs qui dirigent le transfert de charge à l'état excité. Dans ce contexte, au cours des dernières années, des ressources considérables ont été consacrées à l'élaboration de stratégies efficaces pour caractériser qualitativement et quantitativement ce transfert de charge photo-induit et pour contrôler différents processus à l'état excité qui peuvent donner lieu à des caractéristiques photo-physiques potentiellement utiles. C'est dans ce contexte général que se positionne cette thèse. Tout au long de ce travail, nous discuterons de la façon dont les informations combinées fournies par l'énergie et la densité peuvent fournir une vision complète des processus photo-induits, dans toute leur complexité, et avec la précision souhaitée. L'énergie permet de caractériser les propriétés locales des surfaces d'énergie potentielles, par exemple, les points de selle, les points maximum et minimum, les pentes et les barrières énergétiques, les intersections entre les états. L'analyse des distributions électroniques de densité ajoute les nuances souhaitées à cette description quelque peu discrète.

12.1.2 *Contexte générale de la thèse*

De nos jours, nous savons que la variation de densité d'électrons d'un chromophore résulte de la photogénération d'un exciton, c'est-à-dire de la génération d'une paire électron-trou. De nombreux travaux peuvent être trouvés dans la littérature traitant de la définition de méthodologies systématiques mais rentables et précises pour la description des états excités verticaux [19–21]. Au cours des dernières décennies, les progrès réalisés dans ce domaine ont prouvé la capacité de la TDDFT à fournir une description objective et complète des architectures moléculaires, du modèle aux systèmes complexes et pertinents sur le plan chimique Curutchet:2016fk,Hagfeldt:2010,Daniel:2015ew. Les approches fondées sur la TDDFT sont largement utilisées en raison de leur rapport coût-précision favorable et de leur capacité à intégrer les effets sur l'environnement, d'une manière peu coûteuse sur le plan informatique. De nombreux travaux [25, 26], évaluant et examinant la performance de la TDDFT par rapport aux méthodes basées sur la fonction d'onde et les méthodes expérimentales ont contribué à mettre en évidence les lacunes des approches

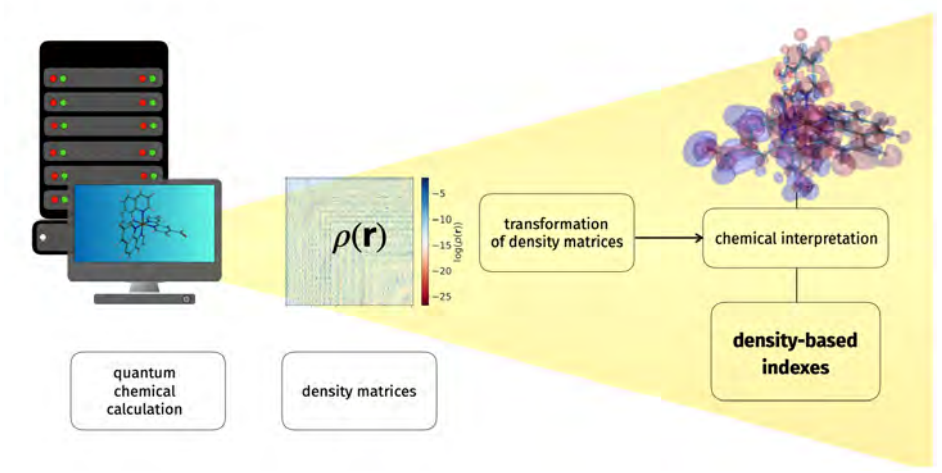

Figure 60: La densité électronique est une grandeur utile pour étudier les réactions photochimiques.
Le calcul de la chimie quantique donne accès à des quantités utiles telles que les matrices de densité.
Ces dernières sont des objets complexes, difficiles à interpréter, il est donc opportun de transformer ces dernières sous différentes formes.
Une stratégie consiste à segmenter les matrices de densité et à visualiser les différentes répartitions.
Une alternative consiste à définir des descripteurs ad hoc permettant une interprétation directe des processus photo-induits observés.
Tout au long de cette thèse, nous introduisons plusieurs descripteurs basés sur la densité. Ceux-ci sont tous basés sur la même métrique mais combinés, ils permettent d'acquérir une large compréhension des chemins photophysiques pour les nombreux processus se déroulant à l'état excité (réorganisation structurelle, décroissance radiative ou non radiative).
L'utilité de la stratégie que nous proposons est qu'elle permet une caractérisation cohérente des processus ES, avec l'avantage supplémentaire d'être abordable sur le plan informatique.

DFT, qui peuvent être principalement attribuées à l'utilisation d'approximation pour la définition de la fonction d'échange-corrélation [27–31]. Par exemple, il est maintenant bien connu que les approximations utilisées en (TD)DFT nécessitent des traitements uniques pour corriger la description erronée des transitions électroniques possédant un caractère de transfert de charge (TC) pertinent dans l'espace-temps [28, 29]. Bien que les limites des approximations en (TD)DFT aient été bien identifiées, la TDDFT demeure l'une des approches les plus utilisées dans le contexte de nos recherches, pour les raisons susmentionnées, ce qui en fait un choix optimal sur lequel construire une approche théorique permettant une exploration précise et efficace des états excités.

Il est donc essentiel de savoir comment faire face à ces limitations et trouver des solutions de contournement. Une partie des travaux présentés dans cette thèse vise cet

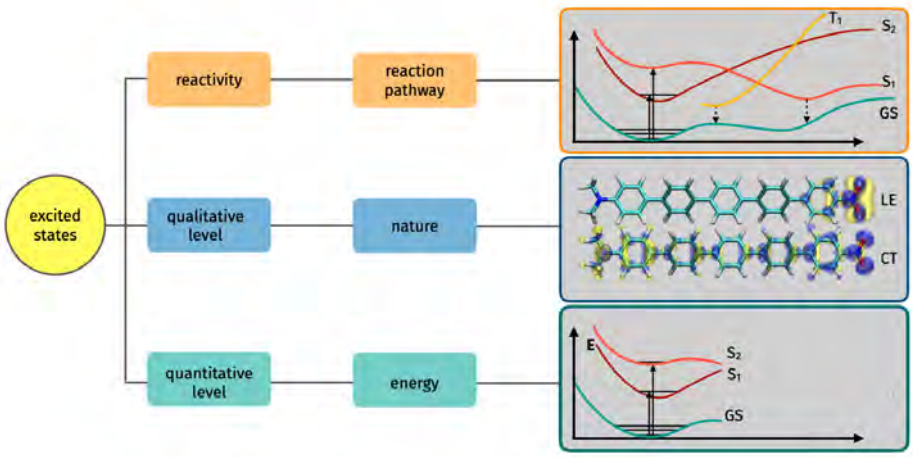

Figure 61: Un schéma illustrant la façon dont les calculs peuvent aider à acquérir une compréhension approfondie des processus photochimiques/photophysiques, à de nombreux niveaux différents.
Tout d'abord, on peut caractériser les minima sur la surface d'énergie potentielle, généralement le minimum de l'état du sol, où l'absorption a lieu.
Les processus à l'état excité sont inévitablement liés aux phénomènes de transfert de charge. Pendant une excitation, la charge est transférée d'un endroit à un autre. Il est très important de mesurer l'étendue spatiale de ce transfert de charge impliqué dans l'étape d'initiation, et de caractériser la nature de la transition (locale ou CT).
Il est également souhaitable de surveiller la réactivité, c'est-à-dire le changement de nature des états excités tout au long des PSE.
Une métrique adaptée aux processus des états excités est fonamentale pour traduire les résultats des calculs en concepts chimiques et physiques simples.

objectif. Comme la transition de l'état de base à l'état excité implique le transfert d'un électron d'une région à une autre - typiquement entre un donneur et un accepteur situés sur deux fragments différents de la même molécule - l'étape initiatrice d'un processus de réaction photochimique est inévitablement liée au phénomène du transfert de charge. Notre première préoccupation est donc d'introduire une mesure permettant de quantifier l'étendue spatiale du transfert de charge impliqué dans l'étape d'initiation d'une réaction photochimique. Cependant, comme nous visons à suivre les changements dans la nature et le caractère des états excités dans différentes régions des surfaces d'énergie potentielle, nous devons définir une mesure adaptée pour les processus impliquant des états excités. Dans ce contexte, nous cherchons à développer et à appliquer une stratégie relativement peu coûteuse pour caractériser les processus d'état excité et pour suivre l'évolution des états excités le long de coordonnées de réaction spécifiques. La stratégie que nous proposons est basée sur le développement de nouvelles procédures de calcul basées

sur la TDDFT et sur l'utilisation de descripteurs de densité spécialement développés. Ces derniers reposent tous sur la même métrique mais, lorsqu'ils sont combinés, ils permettent d'acquérir une image qualitative mais aussi une compréhension large des voies photophysiques des processus multiples et simultanés qui se déroulent à l'état excité (réorganisation structurelle, désintégration non radiative). Ces types d'indices traduisent les résultats de calcul en concepts chimiques et physiques simples, fournissant ainsi une interprétation qualitative des phénomènes observés expérimentalement.

12.2 CONTEXTE THÉORIQUE ET MÉTHODES

Ce travail s'intéresse principalement à la description théorique des processus d'excitation électronique et à l'évolution temporelle associée des photochromes impliqués. Les méthodes ab initio basées sur la structure électronique répondent à cette problématique en fournissant une voie d'investigation des propriétés électroniques via la résolution de l'équation de Schrödinger électronique - ici non relativiste - sans l'addition d'aucun paramètre réglable. Pour un système composé d'électrons et de noyaux, cela signifie que nous voulons tout d'abord déterminer des grandeurs telles que les énergies totales de l'état fondamental, les distributions électroniques de densité, les géométries d'équilibre, les longueurs et angles de liaison, les forces et constantes élastiques, les moments dipolaires et polarisabilités statiques, les moments magnétiques. Plus généralement, toutes les observables qui tombent dans le domaine d'applicabilité de la théorie fonctionnelle de la densité (DFT) de l'état fondamental [32].

Parmi les méthodologies ab initio, la DFT constitue une approche formellement exacte du problème à N corps. En outre, le DFT définit les prémices de base d'un autre cadre théorique et computationnel, la théorie de la fonctionnelle de la densité dépendante du temps (TDDFT) [32]. La TDDFT permet de décrire le comportement des systèmes quantiques hors de leur équilibre et s'applique donc à la description des processus d'excitation électronique qui sont décrits par l'équation de Schrödinger électronique (non relativiste) dépendante du temps. Bien que le concept de "hors d'équilibre" puisse délimiter toute une série de scénarios différents, l'image qui nous intéresse plus particulièrement concerne les systèmes qui sont initialement dans leur état fondamental et qui sont perturbés par un stimulus externe, généralement un rayonnement lumineux.

Ce phénomène est étroitement lié à diverses techniques spectroscopiques. En général, l'exécution d'une mesure spectroscopique signifie que le système en question est soumis à un certain stimulus externe - c'est-à-dire un champ électromagnétique - qui induit un changement dans l'échantillon, comme des transitions électroniques. Les effets de cette action sont ensuite mesurés et analysés par un détecteur, révélant les propriétés spectrales associées du système à l'étude. Il existe de nombreuses techniques spectroscopiques différentes. Dans ce travail, nous traiterons principalement la description des processus d'absorption et d'émission, qui sont généralement étudiés par spectroscopie d'absorption et de fluorescence UV-visible. Les deux techniques appartiennent à la classe des spectroscopies linéaires, ce qui signifie que le changement qu'elles mesurent est linéairement proportionnel à la force de la perturbation appliquée. Toutefois, il convient de mentionner

que les spectroscopies non linéaires peuvent également être étudiées par TDDFT. Dans le chapitre 2 du manuscript, nous passons d'abord en revue les bases de la DFT à l'état fondamental, puis nous explorons son extension aux états excités, en utilisant le cadre de la TDDFT. De plus, nous présentons un certain nombre de concepts et d'approximations utiles liés à l'étude des processus photochimiques.

12.3 MÉTHODES DE DESCRIPTION DES EXCITATIONS ÉLECTRONIQUES : UNE VUE D'ENSEMBLE

Dans le chapitre 2, nous avons présenté une description générale des processus photochimiques. Le chapitre 3, donne un aperçu des outils existants qui ont été développés pour analyser ces processus d'un point de vue théorique. En particulier, ces méthodes visent à quantifier la redistribution de la densité de charge impliquée dans l'excitation et permettent une description concise de la transition électronique.

Le but de ce chapitre est de donner un aperçu des méthodologies qui ont été conçues au cours des dernières décennies pour étudier la localisation des états excités, en soulignant les qualités et la nouveauté de chacun. Parmi les premières analyses détaillées des états excités figurent les contributions de Luzanov [93, 96–102], qui a d'abord introduit des "concepts explicites et des critères définis" impliquant l'estimation de la localisation des états excités et le transfert de charge pour interpréter les transitions électroniques. En particulier, il a d'abord suggéré de rejeter l'analyse orbitale en faveur de certaines entités non invariantes dérivées des matrices de densité de transition [96]. Les grandeurs essentielles de cette analyse, qu'il résumera plus tard sous le nom d'analyse structurale à l'état excité (ESSA) [102], sont les indices de localisation d'excitation pour l'évaluation quantitative du transfert de charge total entre fragments. Cette métrique de transfert de charge est basée sur la projection de la fonction de l'onde d'excitation dans la base atomique spin-orbitale et mesure la probabilité de transfert d'un électron d'un fragment moléculaire à un autre.

Une position pertinente dans cette aperçu des indices basés sur la densité est due à la métrique de transfert de charge (D_{CT}) [1], qui constitue le fondement théorique de l'analyse de l'état excité réalisée dans ce travail. La métrique DCT réside dans la partition du 1DDM et dans la définition correspondante des distributions de charges positives et négatives associées à la transition électronique. En s'appuyant sur une répartition similaire du 1DDM, Etienne [103–106] a dérivé plusieurs descripteurs additionnels et perspicaces dédiés à l'étude de la topologie des états excités basés sur les centroïdes de charge obtenus à partir des matrices de densité Attachment/Detachment (initialement présentées pour l'analyse des états excités par Head-Gordon [91]). Bien que cette approche consiste également en une analyse vectorielle de la distribution des différences de densité induites par la transition, il existe des différences substantielles par rapport à la métrique DCT, que nous illustrerons plus en détail plus loin dans cette discussion. De plus, le même auteur a largement contribué à former un formalisme cohérent et général pour l'analyse topologique des transitions électroniques à partir de calculs d'états excités à référence unique, faisant le pont entre l'approche 1DDM et l'approche 1TDM [94].

Le travail de Plasser et Drew mérite également d'être mentionné. Plasser [107–110] fournit une théorie générale et un formalisme complet pour l'évaluation correcte des propriétés d'exciton au niveau moléculaire et dans les systèmes étendus. Ceci est fait par la définition d'une fonction d'onde d'exciton à partir d'une fonction d'onde de beaucoup de corps obtenue par des calculs d'état excité quantum-chimique. Cette théorie de l'analyse de l'exciton repose sur l'hypothèse que le 1TDM peut être interprété comme une fonction d'onde d'exciton à deux corps décrivant le mouvement d'une entité électronique à trous corrélée. Dans la même veine que celle mentionnée ci-dessus pour le 1DDM, la fonction de l'onde d'exciton peut également être analysée à l'aide d'une série de descripteurs. Alors que le travail original proposait l'analyse de cette fonction d'onde d'excitation à travers une analyse de population[95], plus tard ce modèle a été généralisé [107, 110–112]. L'analyse d'exciton est réalisée par le calcul de la valeur attendue de tout opérateur agissant sur la même base orbitale du 1TDM. Cette stratégie s'avère alors indépendante des fonctions de base centrées sur l'atome et n'exige pas la partition de la fonction d'onde en contributions centrées sur l'atome ou le fragment [112].

Il existe plusieurs autres descripteurs alternatifs, dont certains ont été proposés comme une modification d'index existants, d'autres sont de toutes nouvelles définitions, visant à explorer davantage la métrique des états électroniques excités dans le cadre de la théorie fonctionnelle de la densité. Nous citons ici l'approche Δr de Guido et Adamo [113], qui repose sur le calcul des centroïdes de charge des paires orbitales naturelles de transition (pertinentes pour une transition donnée). Cet indice rend le concept de la distance moyenne entre les électrons et les trous lors de l'excitation. Les auteurs se penchent également sur les différences et les similitudes avec un autre indice bien connu (λ) de Tozer et Helgaker, qui mesure le recouvrement spatial dans une excitation donnée. Bien que λ puisse également fournir une estimation de l'étendue spatiale d'une transition électronique, il s'agit plutôt d'un outil de diagnostic des échecs méthodologiques de la TDDFT, et il a été conçu pour établir la fiabilité d'une transition électronique générale. Nous reviendrons plus en détail sur les indices de densité pour les diagnostics au chapitre 6.

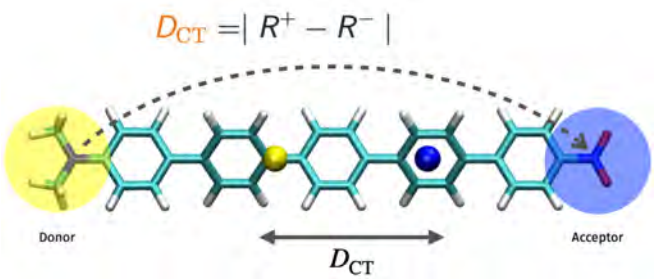

Figure 62: Representation de la distance du transfert de charge lors d'une éxcitation électronique

Une autre stratégie consiste à caractériser quantitativement le déplacement de charge occourant lors de l'excitation en intégrant la densité électronique selon un axe choisi (qui coïncide avec la coordonnée de transfert d'électrons) [114]. Dans l'ensemble, ces études ont contribué à l'évolution des modèles utilisés pour l'étude des états excités. Nous donnons ci-dessous une description plus détaillée de certains des descripteurs mentionnés ci-dessus. Ce résumé vise à donner une vue d'ensemble des méthodologies disponibles pour l'examen des excitations électroniques et à fournir un contexte pour les travaux présentés plus loin.

12.4 UNE MESURE DE TRANSFERT DE CHARGE DANS LES TRANSICTIONS ÉLECTRONIQUES

L'approche de la théorie de la réponse dépendant du temps décrite au chapitre 4 fournit une voie pour accéder aux énergies d'excitation et aux moments de transition. Les énergies totales de l'état excité (ES) sont alors accessibles en ajoutant l'énergie d'excitation à l'énergie correspondante de l'état fondamental (GS). Cette méthodologie donne accès à des objets utiles, tels que la matrice de différence de densité (1DDM), qui contiennent les informations relatives à la polarisation du nuage électronique se produisant dans l'excitation. Dans le cadre de la théorie de la fonctionnelle de la densité dépendante du temps (TDDFT), en outre, pour améliorer la description des matrices de densité, on peut aussi réaliser un traitement post linéaire aux calcul de l'état excité, par l'application de la méthode nommée "Z-Vector" [126]. Dans le schéma TDDFT, ce computation résulte en l'ajout d'une matrice (termes virtuels occupés) a la 1DDM pour tenir compte de l'assouplissement de la densité après la génération de trous/particules. La densité de l'état excité redistribuée qui en résulte est ce qu'on appelle la matrice de densité rélaxée.

Cette procédure soulève la question de savoir comment la qualité des densités calculées affecte les descripteurs qui en sont directement dérivés. Cette question fait l'objet d'une de nos publications récentes: "Comment les descripteurs de transfert de charge sont-ils affectés par la qualité de la densité électronique sous-jacente ? par Marco Campetella, Michael J. Frisch, Giovanni Scalmani, Carlo Adamo, Ilaria Ciofini et moi-même, publiés dans le Journal of Computational Chemistry. Le chapitre 4 de ce manuscrit constitue une adaptation de cette publication.

Dans le but d'étudier qualitativement et quantitativement l'impact de l'utilisation de la densité relaxée ou non relaxée pour l'estimation de la nature et des caractéristiques des états excités électroniques, nous avons analysé le l'effet de l'utilisation de 52 fonctionnelles de corrélation des échanges différents pour la prédiction de la distance de transfert de charge D_{CT} [1] pour une famille prototype composants de type push-pull.

Nos résultats montrent que bien qu'une évaluation qualitativement cohérente de la nature des états excités soit obtenue en utilisant la densité non relaxée ou relaxée, d'un point de vue quantitatif, nous observons de grandes différences dans la distance de transfert de charge pour les transitions électroniques ayant un caractère CT important. Ce comportement est indépendant de la nature de la fonction d'échange-corrélation utilisée.

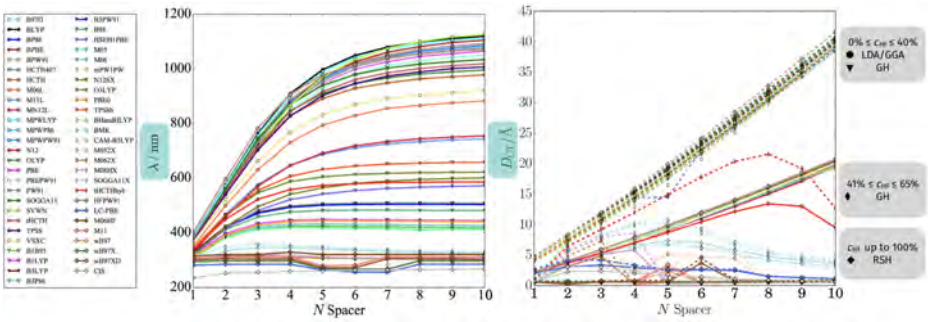

Figure 63: Sur la gauche, l'énergie d'excitation calculée avec 52 fonctions différentes est représentée sur la figure, il est clair que les valeurs d'énergie dépendent de manière cruciale du type de fonction utilisée. Nous pouvons distinguer trois plages - très faible, moyenne, haute énergie, qui correspondent à différentes classes de fonctions, y compris un pourcentage faible/intermédiaire et élevé d'échange HF exact.
NLes fonctions LDA et GGA donnent un profil linéaire.
Les fonctions, avec un pourcentage croissant d'échange HF exact et GH donnent des courbes en forme de cloche. Fonctionnel avec l'échange Exact jusqu'à 100 % de rendement d'un profil plat.
Les ${}^{R}D_{\mathrm{CT}}$ sont représentés par des lignes continues, tandis que les ${}^{U}D_{\mathrm{CT}}$ avec des lignes pointillées. Il est clair que, outre les différents comportements résultant des différents DFA, la relaxation a également un effet. En général, le ${}^{U}D_{\mathrm{CT}}$ a la même forme que le ${}^{R}D_{\mathrm{CT}}$, mais avec des valeurs plus importantes.

12.5 APPLICATION D'INDICES BASÉS SUR LA DENSITÉ POUR LA DESCRIPTION DES ÉTATS EXCITÉS

Dans le chapitre 5, nous examinons comment le D_{CT}peut être utilisé pour mesurer l'étendue spatiale d'un transfert de charge photo-induit, pour interpréter les réactions photochimiques et, plus généralement, tout processus de transfert de charge. Nous calculons le D_{CT} en utilisant des densités calculées à la fois à partir de méthodes de la fonctionnelle de la densité et post-HF. Les deux approches ont été largement appliquées pour caractériser les propriétés d'absorption/émission des systèmes ou pour étudier la surface d'énergie potentielle à l'état excité (PES) et pour obtenir des informations sur leur réactivité [14, 19, 115, 149–152]. Cependant, très peu de travaux comparatifs sont disponibles dans la littérature faisant état de l'utilisation d'indices basés sur la densité couplés à la fois à la TFD et aux méthodes de la fonction d'onde [153]. Dans les chapitres précédents, en effet, nous n'avons abordé les indices basés sur la densité que dans le contexte des méthodes de théorie fonctionnelle de la densité en fonction du temps [1, 4, 94, 95, 112]. Comme nous le montrons dans ce qui suit, la représentation compacte du processus d'état excité fournie par les descripteurs de densité peut être bénéfique également dans le cas de calculs multiconfiguration.

Dans ce qui suit, nous considérons le cas d'une simple réaction de transfert de protons à l'état excité intramoléculaire. Nous montrons l'application des index de la densité (D_{CT}) en utilisant à la fois fonctions d'ondes calculé par methodes du champ multi-configurationnel auto-cohérent (CASSCF-CASPT2) et derivé de méthodes de la fonctionnelle de la densité. Les résultats confirment que, même dans le cas de méthodes multiconfigurationnelles, la D_{CT} fournit des informations utiles concernant à la fois la charge et la réorganisation structurelle d'une molécule à l'état excité. Ce sujet fait l'objet d'une de nos récentes publications : "Using Density-Based Indexes and Wave Function Methods for the Description of Excited States : Excited State Proton-Transfer Reactions as a Test Case", publié par moi-même, Juan Sanz Garcia, Marco Campetella et Ilaria Ciofini dans le Journal of Physical Chemistry A. Le présent chapitre constitue une adaptation de cette dernière publication.

12.6 LA DESCRIPTION PROBLÉMATIQUE DES EXCITATIONS DE TRANSFERT DE CHARGES À L'AIDE DE LA DFT

Lorsque la TDDFT est utilisée, les états de transfert de charge (TC) a longue distance correspondent à des états excités dont le recouvrement entre les distributions des trous photo-excités et des charges électroniques est négligeable. Ce résultat, cependant, est typiquement un artefact de la méthode résultant de l'utilisation de potentiels xc approchés, dont les potentiels ont un tracé asymptotique incorrecte et sont erronément continus. Le potentiel exact d'échange-corrélation d'un état de transfert de charge saute de façon discontinue d'un montant de Δ_{xc} lorsque le nombre d'électrons croise l'entier. En conséquence, les énergies d'excitation de ces états sont généralement largement sous-estimées au point qu'elles peuvent apparaître énergie inférieure aux états optiques. Dans le chapitre 6, nous discutons d'une méthodologie permettant de repérer ces états non physiques erronés, grâce à un nouvel indice peu coûteux en termes de calcul - M_{AC}.

La formulation de l'indice M_{AC}est dérivée d'une modification de la relation de Mulliken de l'énergie de transition pour les excitations de TC.Elle repose sur deux ingrédients de base : une distance effective de CT, calculée à l'aide de notre indice basé sur la densité (D_{CT}), et une estimation pondérée du potentiel d'ionisation et de l'affinité des électrons. Pour vérifier la robustesse de notre approche, nous avons testé notre indice sur certains systèmes modèles, représentatifs des excitations de TC intermoléculaires et intramoléculaires, en utilisant des fonctionnelles appartenant à différentes classes (approximation de gradient généralisée, hybrides globaux et hybrides séparés en gamme). Ces résultats préliminaires confirment que les états fantômes sont correctement repérés, même dans le cas délicat d'excitations intramoléculaires présentant une délocalisation importante entre donneurs et accepteurs, régime dans lequel la formulation standard de Mulliken atteint ses limites. La première partie de cet chapitre est adaptée d'une publication précédente de moi-même, Marco Campetella, Mike J. Frisch, Giovanni Scalmani, Ilaria Ciofini et Carlo Adamo [5].

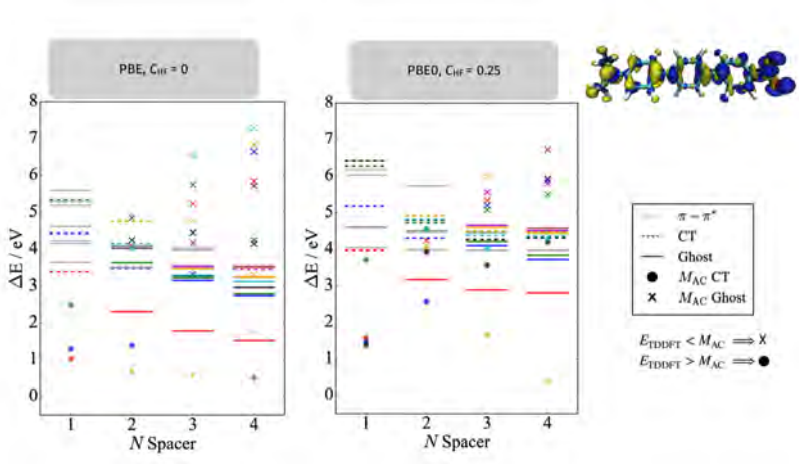

Figure 64

12.7 DIAGNOSTIC M_{AC} DANS LES COMPLEXES MÉTALLIQUES

Les nombreuses controverse concernant l'utilisation du TDDFT pour les états excités à transfert de charge à longue distance s'étendent également aux complexes métalliques.

Les complexes de métaux de transition cumulent la plupart des complexités inhérentes aux études théoriques : taille, délocalisation électronique, haute densité d'états électroniques de caractères divers, états multi-référence presque dégénérés, états de transfert de charge à longue distance et couplages vibronique. De plus, à mesure que les coquilles d an f se peuplent, les effets relativistes, le couplage spin-orbite, les états dissociatifs et le mélange des états deviennent importants.

Dans le but de mettre en place des protocoles de calcul permettant de prédire et de décrire avec précision la nature et l'énergie des états excités, des méthodes quantiques spécifiques ont été explicitement conçues et étalonnées sur les complexes contenant des métaux. Parmi celles-ci, les méthodes les plus populaires utilisées pour traiter ces systèmes sont les méthodes basées sur la densité mais aussi les approches variationnelles basées sur le formalisme du champ autoconsistant (SCF) et son extension multi-configuration le SCF espace actif complet (CASSCF) [168] ou les variantes du SCF espace actif restreint (RASSCF) [203]. Ces dernières ont été ultérieurement améliorées par l'ajout d'une correction perturbatrice (CASPT2) [169], qui permet d'inclure des effets de corrélation électronique non dynamiques. Si ces dernières approches se sont avérées très précises pour décrire l'absorption verticale et le comportement photochimique des complexes métalliques, elles imposent toutefois une lourde charge de calcul qui limite leur domaine d'application à des composés plutôt petits. En outre, elles nécessitent la sélection d'un espace actif spécifique au système, ce qui les rend peu pratiques et difficiles à utiliser pour des applications de routine.

Des méthodes hybrides ont également fait leur apparition [204], qui combinent la DFT à courte distance et la fonction d'onde ou les approches perturbatrices à longue distance. Ces dernières présentent toutefois les mêmes inconvénients.

Les approches TDDFT, au contraire, ont l'avantage d'une échelle favorable, qui a déterminé leur large diffusion dans le traitement des complexes à base de métaux. En outre, les approches fondées sur la densité limitent la dépendance de l'utilisateur au choix de la fonction de corrélation d'échange à utiliser, ce qui, en pratique, rend ces méthodes peu compliquées, bien qu'elles soient d'une précision impressionnante dans la description des propriétés structurelles et spectroscopiques des complexes de métaux de transition, du moins en ce qui concerne l'état électronique de base et les états excités les plus bas. Il n'est pas surprenant que les calculs de TDDFT et les spectres simulés obtenus à partir de ceux-ci soient de plus en plus utilisés pour étayer les résultats expérimentaux, où la caractérisation réelle de la nature de la transition observée par des calculs de structure électronique peut apporter un complément et un renforcement extrêmement précieux aux études expérimentales [24, 205, 206].

Pour ces études comparatives, le choix de la fonction de corrélation et d'échange est généralement basé sur des travaux préalables traitant de composés similaires, montrant un bon accord avec les résultats expérimentaux. Cependant, la correspondance entre les spectres expérimentaux et théoriques peut simplement survenir en raison d'une heureuse compensation des erreurs. Les limites de la DFT et de la TDDFT s'appliquent en effet également aux complexes contenant des métaux. Une fausse tracé asymptotique typique des fonctionnelles d'échange local a de fâcheuses conséquences sur les énergies d'excitation calculées de cette classe de composés, qui à leur tour, peuvent fortement affecter les propriétés photo-physiques et photochimiques prévues, et avec elles, l'interprétation du mécanisme des processus d'état excité correspondants. Une note de prudence est donc nécessaire. En particulier, les complexes de métaux de transition sont souvent conçus dans le but précis d'améliorer le caractère de la CT dans l'état électronique de base, ou dans l'état excité le plus bas, pour obtenir des composés possédant simultanément une faible longueur d'onde d'absorption et un coefficient d'extinction molaire élevé. Par exemple, les composés possédant de telles propriétés font l'objet de recherches approfondies dans le cadre de la thérapie photodynamique (TPD) [11, 207], des complexes de récolte de la lumière dans les plantes et les bactéries [22], ainsi que pour les applications des cellules solaires sensibilisées aux colorants [205]. Les états TC sont ensuite générés en fonctionnalisant les structures des complexes métalliques avec les groupes donneurs/accepteurs appropriés.

Naturellement, la description de ces transitions dans l'espace dépend fortement de l'approximation fonctionnelle de la densité choisie. Les complexes de métaux de transition présentant de telles caractéristiques sont en principe susceptibles de présenter des états de transfert de charge fantôme et ligand-à-ligand, en particulier dans le cas de systèmes avec des ligands étendus. Ces derniers, au contraire, sont généralement bien décrits car le degré de recouvrement entre les orbitales du métal d et l'orbitale d'acceptation sur le ligand est important. Il s'ensuit que pour caractériser ces composés avec la précision souhaitée, il est nécessaire d'utiliser la méthodologie appropriée et d'adopter une stratégie

adéquate pour diagnostiquer la fiabilité de l'approche TDDFT choisie. Comme nous demontrons dans le chapitre 7, l'indice Mac peut fournir des informations pertinentes pour détecter les états non physiques, qui sont calculés avec une précision insuffisante et apparaissent donc trop bas dans le spectre.

12.8 SUIVI DES ÉTATS EXCITÉS DANS LES SYSTÈMES MOLÉCULAIRES

Dans les chapitres précédents, nous avons longuement discuté du concept de transfert de charges, de la manière de mesurer l'étendue spatiale d'une transition donnée, des défis que pose une telle mesure et de la manière de les relever. Nous avons maintenant appliqué ces concepts dans le contexte des transitions verticales, qui se produisent entre l'état de base et tout état d'intérêt excité. L'étape logique consiste à étudier le processus de réorganisation de la charge qui en découle et qui conduit à la population de l'état émissif. Cette observation est cohérente avec l'image intuitive selon laquelle, après une excitation verticale, un système aura tendance à se détendre structurellement afin de minimiser la séparation et la réorganisation de la charge de l'état excité produit. Nous étendons ici les concepts introduits précédemment pour tenir compte des transitions d'état excité à état excité. Dans ce contexte, le D_{CT}n'est plus strictement lié à l'amplitude spatiale de la séparation de charge produite par l'excitation électronique d'état excité à état excité, mais à la distance entre deux états excités.

Le chapitre 8 s'inscrit dans ce contexte général. L'approche que nous exposons ici combine plusieurs descripteurs de densité, conçus à l'origine pour l'interprétation qualitative des phénomènes observés expérimentalement, et vise à fournir une image physique simple du mécanisme des processus d'état excité. Notre stratégie vise à permettre une caractérisation peu coûteuse des surfaces d'énergie potentielles à l'état excité, qui peuvent être calculées - à la volée - pour permettre à la fois l'identification des zones critiques pour les approches TDDFT et la reconnaissance qualitative - en conjonction avec des critères énergétiques - des chemins de réaction possibles.

Nous introduisons, dans ce qui suit, un nouvel indice basé sur la densité, Π, qui peut être utilisé pour obtenir une mesure qualitative du travail nécessaire pour redistribuer la densité d'électrons passant d'un état excité à un autre à une configuration électronique donnée. Auparavant appliqué pour révéler les canaux de désintégration non radiative du premier état excité à l'état de base [2], ce descripteur est simple, peu coûteux, et peut être couplé à toute méthode quantique capable de fournir une description des états excités électroniques. En effet, il repose uniquement sur la connaissance des densités énergétiques et électroniques des différents états électroniques impliqués dans une décroissance. Pour illustrer les connaissances que ces indices peuvent apporter à la description des processus d'états excités, nous examinons deux types distincts de réactions. Le premier est un transfert intramoléculaire de protons se produisant dans le CPDNO (1-(cyclopropyl)diazo-2-naphtol), un composé aromatique azoïque, suivi par les processus de transfert de charge photo-induit dans le DMABN (N,N-diméthylaminobenzonitrile) et le Phen-PENMe$_2$ (5-(4-diméthylaminophényléthylyn)-1,10-phénanthroline). Toutes ces molécules sont précédemment présentées dans le Chapitre 5, où nous vérifions la

fiabilité de la méthodologie TDDFT appliquée pour calculer leurs courbes d'énergie potentielle le long de coordonnées de réaction spécifiques. En outre, ces systèmes ont été largement étudiés et de nombreuses études existent dans la littérature, tant au niveau théorique [163, 216, 217] qu'expérimental [188, 193, 218]. L'accord avec ces études antérieures corrobore nos résultats.

Dans l'ensemble, l'indice Π s'est avéré capable d'identifier les régions où les états excités sont les plus susceptibles de s'echanger. Ce chapitre constitue une adaptation de deux travaux antérieurs de ma part, le premier publié dans le Journal of Computational Chemistry, en collaboration avec Juan Sanz-Garcia, Marco Campetella et Ilaria Ciofini [6], le second, présenté avec Anna Perfetto et Ilaria Ciofini et publié dans le Journal of Photochemistry and Photobiology A.

12.9 DETERMINER LA DISTRIBUTION RÉLATIVE DES ÉTATS EXCITÉS LE LONG D'UN CHEMIN RÉACTIONNEL

Le suivi de chaque état excité le long d'une coordonnée de réaction est un problème crucial en photochimie. Si le calcul des propriétés optiques est certainement un point de départ, les spectres d'absorption et d'émission ne fournissent aucune information sur le chemin parcouru par chaque état excité, et il peut être compliqué d'établir le lien entre l'absorption d'énergie et la formation de photoproduits. Les descripteurs topologiques peuvent être très utiles pour caractériser la nature d'un état excité. En particulier, ils traduisent de manière pratique les informations contenues dans les objets mathématiques, tels que la 1DDM [115], en une représentation plus compacte et plus lisible de la transition électronique, et peuvent donc être utiles pour examiner la nature d'un état excité le long d'une coordonnée de réaction. Néanmoins, comprendre pleinement où, parmi toutes les positions verticales, se trouve un état d'intérêt, et cartographier la position d'un état excité particulier en des points successifs d'une coordonnée de réaction, reste une tâche non triviale qui est néanmoins indispensable pour assembler une description cohérente d'un chemin de réaction [151]. Ce problème constitue le nucleus du chapitre 9. Nous proposons ici une nouvelle métrique rigoureuse pour suivre les états excités le long d'une coordonnée de réaction, basée sur le descripteur basé sur la densité D_{CT}. Le D_{CT} traduit les informations contenues dans les densités des états initiaux et finaux en une longueur et fournit une mesure simple de l'étendue spatiale d'une transition électronique. Nous avons utilisé cette approche à plusieurs reprises dans les chapitres précédents, où nous avons caractérisé la nature des états excités tout au long de coordonnées de réaction spécifiques par leurs valeurs D_{CT} - calculées par rapport à leur distribution de densité d'état de base correspondante à la même géométrie. Bien que la valeur D_{CT} soit spécifique pour une transition donnée, elle n'est pas suffisante pour caractériser un état de façon unique parmi un ensemble d'états excités verticaux. En fait, il peut y avoir plusieurs états proches ayant un caractère similaire, dont l'ambiguïté peut empêcher l'identification précise d'un état d'intérêt le long d'une coordonnée de réaction.

Nous tentons de résoudre cette indétermination avec une nouvelle métrique, qui fournit une représentation unique de l'état excité. Au lieu de caractériser un état vertical en termes

de transition d'un électron à partir de l'état fondamental, nous utilisons la collection de vecteurs calculés entre cet état et tout autre état, à la même géométrie. En d'autres termes, nous caractérisons chaque état en cryptant ses connotations dans une "empreinte" spécifique à l'état. Ensuite, nous comparons chaque paire d'états en utilisant une distance géométrique volontairement définie entre leurs empreintes correspondantes.

Nous avons implémenté une telle métrique dans un algorithme simple pour cartographier l'évolution des états excités le long d'une coordonnée de réaction. L'algorithme détermine la disposition relative d'un ensemble d'états verticaux en calculant la distance entre les empreintes de chaque paire d'états à des étapes successives et en sélectionnant celle qui minimise toutes les distances. Nous évaluons la performance de cette recherche de carte de réaction en comparant les résultats avec une représentation de référence, où nous estimons la similarité entre toutes les paires d'états en inspectant visuellement les orbitales principales et les descripteurs de densité pertinents. En outre, nous discutons d'une alternative possible à la méthode des empreintes, qui consiste à évaluer la distance entre chaque paire d'états en utilisant le recouvrement des fonctions d'onde correspondantes. Les résultats montrent que nous sommes capables de reconstruire les distributions et les croisements d'états excités tout au long de différentes coordonnées de réaction.

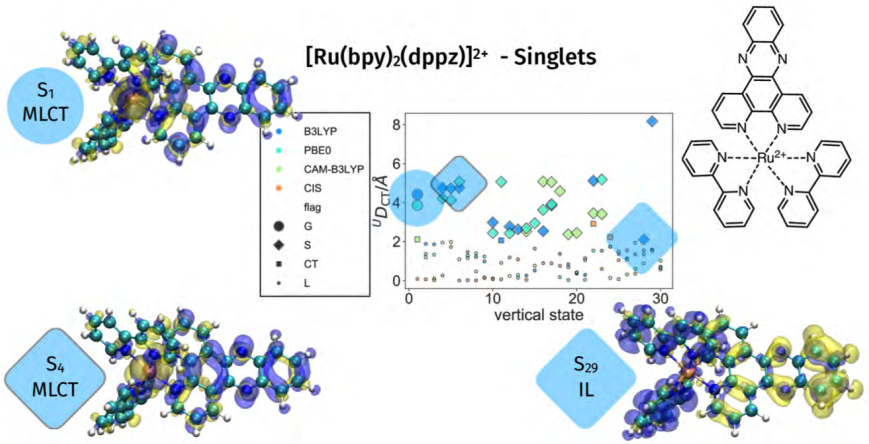

Figure 65: Dans la figure : Les couleurs représentent quatre différentes fonctionnelles - CIS, CAM-B3LYP, B3LYP, CIS. La figure montre les différences de densité pour différents états fantômes (points remplis) et parasites (carrés). Ces derniers ne sont que partiellement erronés, c'est-à-dire qu'ils semblent trop faibles en énergie mais leur valeur n'est que légèrement surestimée. Les états fantômes qui sont gravement affectés par l'erreur de CT ont une force d'oscillateur nulle, tandis que les états parasites ont une force d'oscillateur non négligeable et recouvrement significatif entre le trou et la particule.

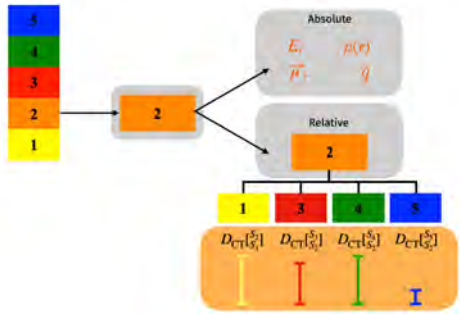

Figure 66: Représentation schematique de la classification d'un état éxcité basée a la fois sur des quantités absolutes propres à l'état, soit sur les distances de transfer de charge caclulés par rapport aux autres états éxcités à la mème geometrie.

[1] T. Le Bahers, C. Adamo, and I. Ciofini, "A Qualitative Index of Spatial Extent in Charge-Transfer Excitations.," Journal of Chemical Theory and Computation, vol. 7, pp. 2498–2506, Aug. 2011.

[2] M. Savarese, U. Raucci, P. A. Netti, C. Adamo, N. Rega, and I. Ciofini, "A qualitative model to identify non-radiative decay channels: the spiropyran as case study," Theoretical Chemistry Accounts, vol. 135, pp. 211–7, Aug. 2016.

[3] J. Sanz García, F. Maschietto, M. Campetella, and I. Ciofini, "Using Density Based Indexes and Wave Function Methods for the Description of Excited States: Excited State Proton Transfer Reactions as a Test Case," The Journal of Physical Chemistry A, vol. 122, pp. 375–382, Dec. 2017.

[4] F. Maschietto, M. Campetella, M. J. Frisch, G. Scalmani, C. Adamo, and I. Ciofini, "How are the charge transfer descriptors affected by the quality of the underpinning electronic density?," Journal of Computational Chemistry, vol. 39, pp. 735–742, Jan. 2018.

[5] M. Campetella, F. Maschietto, M. J. Frisch, G. Scalmani, I. Ciofini, and C. Adamo, "Charge transfer excitations in TDDFT: A ghost-hunter index," Journal of Computational Chemistry, vol. 38, pp. 2151–2156, Sept. 2017.

[6] F. Maschietto, J. Sanz García, M. Campetella, and I. Ciofini, "Using density based indexes to characterize excited states evolution.," Journal of Computational Chemistry, vol. 40, pp. 650–656, Feb. 2019.

[7] A. Perfetto, F. Maschietto, and I. Ciofini, "Following excited states in molecular systems using density-based indexes: A dual emissive system as a test case," "Journal of Photochemistry & Photobiology, A: Chemistry", vol. 383, p. 111978, Oct. 2019.

[8] F. Maschietto, J. S. Garcia, C. Adamo, and I. Ciofini, "Charge Transfer Metal Complexes using Time-Dependent Density Funcitional theory: hotw to spot ghost and spurious states?," In preparation, 2019.

[9] J. Karges, F. Heinemann, F. Maschietto, M. Patra, O. Blacque, I. Ciofini, B. Spingler, and G. Gasser, "A Ru(II) polypyridyl complex bearing aldehyde functions as a versatile synthetic precursor for long-wavelength absorbing photodynamic therapy photosensitizers," Bioorganic & Medicinal Chemistry, vol. 27, no. 12, pp. 2666–2675, 2019.

[10] F. Heinemann, M. Jakubaszek, J. Karges, C. Subecz, F. Maschietto, M. Dotou, J. Seguin, N. Mignet, E. V. Zahínos, M. Tharaud, O. Blacque, P. Goldner, B. Goud, B. Spingler, I. Ciofini, and G. Gasser, "Towards DFT-Rationally Designed Long-Wavelength Absorbing Ru(II) Polypyridyl Complexes as Photosensitizers for Photodynamic Therapy," In preparation, 2019.

[11] J. Karges, M. Jakubaszek, F. Maschietto, J. Seguin, N. Mignet, M. Tharaud, O. Blacque, P. Goldner, B. Goud, B. Spingler, I. Ciofini, and G. Gasser, "Evaluation of the Medicinal Potential of Ruthenium(II) Polypyridine based Complexes as One- and Two-Photon Photodynamic Therapy Photosensitizers," In preparation, 2019.

[12] T.-T. Bui, M. Ulfa, F. Maschietto, A. Ottochian, M.-P. Nghiêm, I. Ciofini, F. Goubard, and T. Pauporté, "Design of dendritic core carbazole-based hole transporting materials for efficient and stable hybrid perovskite solar cells," Organic Electronics, vol. 60, pp. 22–30, Sept. 2018.

[13] F. Maschietto, A. Ottochian, L. Posani, and I. Ciofini, "Mapping states along reaction coordinates: A state-specific fingerprint for efficient state tracking," In preparation, 2019.

[14] M. Garavelli, "Computational Organic Photochemistry: Strategy, Achievements and Perspectives," Theoretical Chemistry Accounts, vol. 116, pp. 87–105, Jan. 2006.

[15] A. Kamkaew, S. H. Lim, H. B. Lee, L. V. Kiew, L. Y. Chung, and K. Burgess, "BODIPY dyes in photodynamic therapy," Chemical Society Reviews, vol. 42, no. 1, pp. 77–88, 2013.

[16] M. E. Alberto, N. Russo, and C. Adamo, "The contribution of computational studies to photodynamic therapy: Challenges and opportunities for the future of computational prediction," Photodiagnosis and Photodynamic Therapy, vol. 17, p. A52, 2017.

[17] L. Ying, C.-L. Ho, H. Wu, Y. Cao, and W.-Y. Wong, "White Polymer Light-Emitting Devices for Solid-State Lighting: Materials, Devices, and Recent Progress," Advanced Materials, vol. 26, no. 16, pp. 2459–2473, 2014.

[18] H. Sasabe and J. Kido, "Recent Progress in Phosphorescent Organic Light-Emitting Devices," European Journal of Organic Chemistry, vol. 2013, no. 34, pp. 7653–7663, 2013.

[19] C. Adamo, T. Le Bahers, M. Savarese, L. Wilbraham, G. García, R. Fukuda, M. Ehara, N. Rega, and I. Ciofini, "Exploring excited states using Time Dependent Density Functional Theory and density-based indexes," Coordination Chemistry Reviews, vol. 304-305, pp. 166–178, Dec. 2015.

[20] A. Dreuw and M. Head-Gordon, "Single-reference ab initio methods for the calculation of excited states of large molecules," Chemical Reviews, vol. 105, pp. 4009–4037, Nov. 2005.

[21] D. P. Chong, Recent Advances in Density Functional Methods. World Scientific, 1995.

[22] C. Curutchet and B. Mennucci, "Quantum Chemical Studies of Light Harvesting," Chemical Reviews, vol. 117, pp. 294–343, Mar. 2016.

[23] A. Hagfeldt, G. Boschloo, L. Sun, L. Kloo, and H. Pettersson, "Dye-Sensitized Solar Cells," Chemical Reviews, vol. 110, no. 11, pp. 6595–6663, 2010.

[24] C. Daniel, "Photochemistry and photophysics of transition metal complexes: Quantum chemistry," Coordination Chemistry Reviews, vol. 282-283, pp. 19–32, Jan. 2015.

[25] R. Peverati and D. G. Truhlar, "Quest for a universal density functional: the accuracy of density functionals across a broad spectrum of databases in chemistry and physics.," Philosophical Transactions of the Royal Society a-Mathematical Physical and Engineering Sciences, vol. 372, p. 20120476, Mar. 2014.

[26] Y. Zhao and D. G. Truhlar, "Density functionals with broad applicability in chemistry.," Accounts of Chemical Research, vol. 41, pp. 157–167, Feb. 2008.

[27] C. A. Ullrich and Z.-h. Yang, "A Brief Compendium of Time-Dependent Density Functional Theory," Brazilian Journal of Physics, vol. 44, pp. 154–188, Feb. 2014.

[28] L. Kronik, T. Stein, S. Refaely-Abramson, and R. Baer, "Excitation Gaps of Finite-Sized Systems from Optimally Tuned Range-Separated Hybrid Functionals," Journal of Chemical Theory and Computation, vol. 8, pp. 1515–1531, Apr. 2012.

[29] T. Stein, L. Kronik, and R. Baer, "Reliable prediction of charge transfer excitations in molecular complexesusing time-dependent density functional theory," Journal of the American Chemical Society, vol. 131, pp. 2818–2820, Mar. 2009.

[30] D. J. Tozer, "Relationship between long-range charge-transfer excitation energy error and integer discontinuity in Kohn-Sham theory," Journal of Chemical Physics, vol. 119, pp. 12697–12699, Dec. 2003.

[31] S. Tretiak, K. Igumenshchev, and V. Chernyak, "Exciton sizes of conducting polymers predicted by time-dependent density functional theory," Physical Review B, vol. 71, p. 3171, Jan. 2005.

[32] C. A. Ullrich, Time-Dependent Density-Functional Theory: Concepts and Applications. Oxford Graduate Texts, Oxford: Oxford University Press, 2011.

[33] M. Born and R. Oppenheimer, "Zur Quantentheorie der Molekeln," Annalen der Physik, vol. 389, pp. 457–484, Jan. 1927.

[34] C. J. Cramer, Essentials of computational chemistry: theories and models. John Wiley & Sons, 2013.

[35] P. Hohenberg and W. Kohn, "Inhomogeneous Electron Gas," Physical Review, vol. 136, pp. 864–871, Nov. 1964.

[36] M. Levy, "Electron densities in search of Hamiltonians," Physical Review A, vol. 26, pp. 1200–1208, Jan. 1982.

[37] W. Kohn and L. J. Sham, "Self-consistent equations including exchange and correlation effects," Physical Review, vol. 140, pp. 1133–1138, Dec. 1965.

[38] A. Szabo and N. S. Ostlund, "Modern quantum chemistry : introduction to advanced electronic structure theory." Dover Publication Inc., NYC, 1982.

[39] C. C. J. Roothaan, "New developments in molecular orbital theory," Reviews of Modern Physics, vol. 23, pp. 69–89, Dec. 1951.

[40] T. Koopmans, "Über die Zuordnung von Wellenfunktionen und Eigenwerten zu den Einzelnen Elektronen Eines Atoms," Physica, vol. 1, pp. 104–113, Jan. 1934.

[41] T. Tsuneda, J. W. Song, S. Suzuki, and K. Hirao, "On Koopmans' theorem in density functional theory," The Journal of Chemical Physics, vol. 133, pp. 174101–10, Nov. 2010.

[42] P. A. Dirac, "Note on exchange phenomena in the Thomas atom," in Mathematical Proceedings of the Cambridge Philosophical Society, pp. 376–385, Cambridge Univ Press, 1930.

[43] J. P. Perdew, K. Burke, and M. Ernzerhof, "Generalized Gradient Approximation Made Simple ," Physical Review Letters, vol. 78, pp. 1396–, Feb. 1997.

[44] J. Tao, J. P. Perdew, V. N. Staroverov, and G. E. Scuseria, "Climbing the Density Functional Ladder: Non-Empirical Meta-Generalized Gradient Approximation Designed for Molecules and Solids," arXiv.org, p. 146401, June 2003.

[45] A. D. Becke, "Density-functional thermochemistry. III. The role of exact exchange," The Journal of Chemical Physics, vol. 98, pp. 5648–5652, Apr. 1993.

[46] C. Adamo and V. Barone, "Toward reliable density functional methods without adjustable parameters: The PBE0 model," The Journal of Chemical Physics, vol. 110, pp. 6158–6170, Apr. 1999.

[47] A. D. Becke, "Density-functional thermochemistry. IV. A new dynamical correlation functional and implications for exact-exchange mixing," Journal of Chemical Physics, vol. 104, no. 3, p. 1040, 1996.

[48] C. Lee, W. Yang, and R. G. Parr, "Development of the Colle-Salvetti correlation-energy formula into a functional of the electron density," Physical Review B, vol. 37, pp. 785–789, Jan. 1988.

[49] J. P. Perdew, "Density-functional approximation for the correlation energy of the inhomogeneous electron gas," Physical Review B, vol. 33, pp. 8822–8824, Jan. 1986.

[50] J. P. Perdew and K. Burke, "Generalized gradient approximation for the exchange-correlation hole of a many-electron system," Physical Review B - Condensed Matter and Materials Physics, vol. 54, pp. 16533–16539, Jan. 1996.

[51] R. Liljequist, M. Linnoila, M. J. Mattila, I. Saario, and T. Seppälä, "Effect of two weeks' treatment with thioridazine, chlorpromazine, sulpiride and bromazepam, alone or in combination with alcohol, on learning and memory in man.," Psychopharmacologia, vol. 44, pp. 205–208, Oct. 1975.

[52] S. Grimme, "Semiempirical ggc-type density functional constructed with a long-range dispersion contribution.," Journal of Computational Chemistry, vol. 27, pp. 1787–1799, 2006.

[53] A. D. Becke, "A new mixing of Hartree–Fock and local density-functional theories," Journal of Chemical Physics, vol. 98, no. 2, p. 1372, 1993.

[54] A. D. Boese and J. M. L. Martin, "Development of density functionals for thermochemical kinetics.," The Journal of Chemical Physics, vol. 121, pp. 3405–3416, Aug. 2004.

[55] A. D. Becke, "Density-functional exchange-energy approximation with correct asymptotic behavior," Physical Review A, vol. 38, pp. 3098–3100, Jan. 1988.

[56] T. Yanai, D. P. Tew, and N. C. Handy, "A new hybrid exchange-correlation functional using the Coulomb-attenuating method (CAM-B3LYP)," Chemical Physics Letters, vol. 393, pp. 51–57, July 2004.

[57] F. Hamprecht, A. Cohen, D. J. Tozer, and N. C. Handy, "Development and Assessment of new exchange-correlation Functionals," J. Chem. Phys., vol. 109, no. 15, pp. 6264–6272, 1998.

[58] Y. Tawada, T. Tsuneda, S. Yanagisawa, T. Yanai, and K. Hirao, "A long-range-corrected time-dependent density functional theory.," The Journal of Chemical Physics, vol. 120, pp. 8425–8433, May 2004.

[59] Y. Zhao, N. E. Schultz, and D. G. Truhlar, "Exchange-correlation functional with broad accuracy for metallic and nonmetallic compounds, kinetics, and noncovalent interactions.," The Journal of Chemical Physics, vol. 123, pp. 161103–161103, Oct. 2005.

[60] Y. Zhao, N. E. Schultz, and D. G. Truhlar, "Design of Density Functionals by Combining the Method of Constraint Satisfaction with Parametrization for Thermochemistry, Thermochemical Kinetics, and Noncovalent Interactions.," Journal of Chemical Theory and Computation, vol. 2, pp. 364–382, Mar. 2006.

[61] Y. Zhao and D. G. Truhlar, "A new local density functional for main-group thermochemistry, transition metal bonding, thermochemical kinetics, and noncovalent interactions.," The Journal of Chemical Physics, vol. 125, pp. 194101–1868, Nov. 2006.

[62] Y. Zhao and D. G. Truhlar, "A new local density functional for main-group thermochemistry, transition metal bonding, thermochemical kinetics, and noncovalent interactions," Journal of Chemical Physics, vol. 125, pp. 194101–194101, Dec. 2006.

[63] Y. Zhao and D. G. Truhlar, "Density functional for spectroscopy: No long-range self-interaction error, good performance for Rydberg and charge-transfer states, and better performance on average than B3LYP for ground states," Journal of Physical Chemistry A, vol. 110, no. 49, pp. 13126–13130, 2006.

[64] R. Peverati and D. G. Truhlar, "Improving the accuracy of hybrid meta-GGA density functionals by range separation," Journal of Physical Chemistry Letters, vol. 2, no. 21, pp. 2810–2817, 2011.

[65] R. Peverati and D. G. Truhlar, "M11-L: A Local Density Functional That Provides Improved Accuracy for Electronic Structure Calculations in Chemistry and Physics," The Journal of Physical Chemistry Letters, vol. 3, pp. 117–124, 2012.

[66] A. O. Bulanov, L. D. Popov, I. N. Shcherbakov, V. A. Kogan, V. A. Barachevsky, V. V. Lukov, S. N. Borisenko, and Y. N. Tkachenko, "Synthesis, IR, UV/vis-, (1)H NMR and DFT study of chelatophore functionalized 1,3-benzoxazinone spiropyrans.," Spectrochimica Acta Part A: Molecular and Biomolecular Spectroscopy, vol. 71, pp. 1146–1152, Dec. 2008.

[67] C. Adamo and V. Barone, "Exchange functionals with improved long-range behavior and adiabatic connection methods without adjustable parameters: The mPW and mPW1PW models," Journal of Chemical Physics, vol. 108, pp. 664–675, Jan. 1998.

[68] Y. Zhao, R. Peverati, K Yang... - University of Minnesota ..., and 2012, "MN-GFM, version 6.3: Minnesota Gaussian Functional Module."

[69] W. M. Hoe, A. J. Cohen, and N. C. Handy, "Assessment of a new local exchange functional OPTX," Chemical Physics Letters, vol. 341, no. 3-4, pp. 319–328, 2001.

[70] S. E. Miller, A. D. Roses, and S. H. Appel, "Scanning electron microscopy studies in muscular dystrophy.," Archives of neurology, vol. 33, pp. 172–174, Mar. 1976.

[71] É. Brémond and C. Adamo, "Seeking for parameter-free double-hybrid functionals: The PBE0-DH model," The Journal of Chemical Physics, vol. 135, pp. 024106–7, July 2011.

[72] R. Peverati, Y. Zhao, and D. G. Truhlar, "Generalized Gradient Approximation That Recovers the Second-Order," The Journal of Physical Chemistry Letters, pp. 1991–1997, 2011.

[73] R. Peverati and D. G. Truhlar, "Communication: A global hybrid generalized gradient approximation to the exchange-correlation functional that satisfies the second-order density-gradient constraint and has broad applicability in chemistry," Journal of Chemical Physics, vol. 135, pp. 191102–191102, Nov. 2011.

[74] S. H. Vosko, L. Wilk, and M. Nusair, "Accurate spin-dependent electron liquid correlation energies for local spin density calculations: a critical analysis," Canadian Journal of Physics. Vol. 59, vol. 58, pp. 1200–, Aug. 1980.

[75] A. D. Boese and N. C. Handy, "New exchange-correlation density functionals: The role of the kinetic-energy density," Journal of Chemical Physics, vol. 116, pp. 9559–9569, June 2002.

[76] J. Tao, J. P. Perdew, V. N. Staroverov, and G. E. Scuseria, "Climbing the Density Functional Ladder: Non-Empirical Meta-Generalized Gradient Approximation Designed for Molecules and Solids," arXiv.org, p. 146401, June 2003.

[77] J. C. Phys, T. V. Voorhis, and G. E. Scuseria, "Erratum : " A novel form for the exchange-correlation energy functional " [Erratum : " A novel form for the exchange-correlation energy functional ","The Journal of Chemical Physics, vol. 400, no. 1998, pp. 129–130, 2008.

[78] J.-D. Chai and M. Head-Gordon, "Systematic optimization of long-range corrected hybrid density functionals.," The Journal of Chemical Physics, vol. 128, pp. 084106–084106, Feb. 2008.

[79] J.-D. Chai and M. Head-Gordon, "Long-range corrected hybrid density functionals with damped atom–atom dispersion corrections," Physical Chemistry Chemical Physics, vol. 10, no. 44, p. 6615, 2008.

[80] M. Abramowitz, I. Stegun, and D. A. Mcquarrie, "Handbook of Mathematical Functions," American Journal of Physics, vol. 34, pp. 177–177, Jan. 1966.

[81] E. Runge and E. K. Gross, "Density-functional theory for time-dependent systems," Physical Review Letters, vol. 52, no. 12, p. 997, 1984.

[82] G. F. Giuliani, G. Vignale, and E. Tosatti, "Quantum Theory of the Electron Liquid," Physics Today, vol. 59, pp. 68–, 2006.

[83] K. L. Liu and S. H. Vosko, "A time-dependent spin density functional theory for the dynamical spin susceptibility," Canadian Journal of Physics. Vol. 67, vol. 67, pp. 1015–1021, 1989.

[84] M. C. T. Chemistry, Computational, and 1996, "Time-dependent density functional response theory of molecular systems: Theory, computational methods, and functionals."

[85] J. Hutter, "Excited state nuclear forces from the Tamm–Dancoff approximation to time-dependent density functional theory within the plane wave basis set framework," The Journal of Chemical Physics, vol. 118, pp. 3928–3934, Mar. 2003.

[86] R. S. Mulliken, "Molecular Compounds and their Spectra. II," Journal of the American Chemical Society, vol. 74, pp. 811–824, 1952.

[87] V. Barone and M. Cossi, "Quantum calculation of molecular energies and energy gradients in solution by a conductor solvent model," Journal of Physical Chemistry A, vol. 102, pp. 1995–2001, Mar. 1998.

[88] M. Cossi and V. Barone, "Time-dependent density functional theory for molecules in liquid solutions," The Journal of Chemical Physics, vol. 115, pp. 4708–4717, Sept. 2001.

[89] N. Minezawa, "State-specific solvation effect on the intramolecular charge transfer reaction in solution: A linear-response free energy TDDFT method," Chemical Physics Letters, vol. 608, pp. 140–144, 2014.

[90] S. Hirata and M. Head-Gordon, "Time-dependent density functional theory within the Tamm-Dancoff approximation," Chemical Physics Letters, vol. 314, pp. 291–299, Dec. 1999.

[91] M. Head-Gordon, A. M. Grana, D. Maurice, and C. A. White, "Analysis of Electronic Transitions as the Difference of Electron Attachment and Detachment Densities," The Journal of Physical Chemistry, vol. 99, pp. 14261–14270, Sept. 1995.

[92] R. L. Martin, "Natural transition orbitals," The Journal of Chemical Physics, vol. 118, pp. 4775–4777, Mar. 2003.

[93] A. V. Luzanov, "The excited state as the superposition of singly excited configurations in the density matrix formalism," Theoretical and Experimental Chemistry, vol. 9, pp. 567–574, Nov. 1975.

[94] T. Etienne, "Theoretical Insights into the Topology of Molecular Excitons from Single-Reference Excited States Calculation Methods," in Excitons, pp. 1–25, InTech, Mar. 2018.

[95] F. Plasser and H. Lischka, "Analysis of Excitonic and Charge Transfer Interactions from Quantum Chemical Calculations.," Journal of Chemical Theory and Computation, vol. 8, pp. 2777–2789, Aug. 2012.

[96] A. V. Luzanov, A. A. Sukhorukov, and V. E. Umanskii, "Application of transition density matrix for analysis of excited states," Theoretical and Experimental Chemistry, vol. 10, pp. 354–361, July 1976.

[97] A. V. Luzanov, "Many-particle correlations of fermion clusters in the method of transition density operators," Theoretical and Mathematical Physics, vol. 30, pp. 232–237, Mar. 1977.

[98] A. V. Luzanov, "Charge transfer and localization during electronic excitation of molecules," Theoretical and Experimental Chemistry, vol. 13, no. 5, pp. 433–440, 1978.

[99] A. V. Luzanov and M. M. Mestechkin, "On the population numbers of pair states in a system of excitons," Theoretical and Mathematical Physics, vol. 48, pp. 740–744, Aug. 1981.

[100] A. V. Luzanov and O. V. Prezhdo, "Analysis of multiconfigurational wave functions in terms of hole-particle distributions," The Journal of Chemical Physics, vol. 124, pp. 224109–17, June 2006.

[101] A. V. Luzanov, "The Structure of the Electronic Excitation of Molecules in Quantum-chemical Models," Russian Chemical Reviews, vol. 49, pp. 1033–1048, Oct. 2007.

[102] A. V. Luzanov and O. A. Zhikol, "Excited State Structural Analysis: TDDFT and Related Models," in Practical Aspects of Computational Chemistry II: An Overview of the Last Two Decades and Current Trends, pp. 415–449, Dordrecht: Springer Netherlands, Oct. 2011.

[103] T. Etienne, X. Assfeld, and A. Monari, "Toward a Quantitative Assessment of Electronic Transitions' Charge-Transfer Character," Journal of Chemical Theory and Computation, vol. 10, pp. 3896–3905, Aug. 2014.

[104] T. Etienne, X. Assfeld, and A. Monari, "New Insight into the Topology of Excited States through Detachment/Attachment Density Matrices-Based Centroids of Charge," Journal of Chemical Theory and Computation, vol. 10, pp. 3906–3914, Aug. 2014.

[105] T. Etienne, "Transition matrices and orbitals from reduced density matrix theory," The Journal of Chemical Physics, vol. 142, p. 244103, June 2015.

[106] T. Etienne, "Probing the Locality of Excited States with Linear Algebra," Journal of Chemical Theory and Computation, vol. 11, pp. 1692–1699, Mar. 2015.

[107] F. Plasser, M. Wormit, and A. Dreuw, "New tools for the systematic analysis and visualization of electronic excitations. I. Formalism," The Journal of Chemical Physics, vol. 141, pp. 024106–14, July 2014.

[108] F. Plasser, B. Thomitzni, S. A. Bäppler, J. Wenzel, D. R. Rehn, M. Wormit, and A. Dreuw, "Statistical analysis of electronic excitation processes: Spatial location, compactness, charge transfer, and electron-hole correlation.," Journal of Computational Chemistry, vol. 36, pp. 1609–1620, Aug. 2015.

[109] F. Plasser and L. González, "Communication: Unambiguous comparison of many-electron wavefunctions through their overlaps.," Journal of Chemical Physics, vol. 145, pp. 021103–6, July 2016.

[110] S. A. Mewes, F. Plasser, A. I. Krylov, and A. Dreuw, "Benchmarking Excited-State Calculations Using Exciton Properties," Journal of Chemical Theory and Computation, vol. 14, pp. 710–725, Jan. 2018.

[111] F. Plasser, S. A. Bäppler, M. Wormit, and A. Dreuw, "New tools for the systematic analysis and visualization of electronic excitations. II. Applications," The Journal of Chemical Physics, vol. 141, pp. 024107–13, July 2014.

[112] S. A. Bäppler, F. Plasser, M. Wormit, and A. Dreuw, "Exciton analysis of many-body wave functions: Bridging the gap between the quasiparticle and molecular orbital pictures," Physical Review A, vol. 90, pp. 1016–12, Nov. 2014.

[113] C. A. Guido, P. Cortona, and C. Adamo, "Effective electron displacements: A tool for time-dependent density functional theory computational spectroscopy," The Journal of Chemical Physics, vol. 140, pp. 104101–10, Mar. 2014.

[114] M. Pastore and F. De Angelis, "First-Principles Modeling of a Dye-Sensitized TiO 2/IrO 2Photoanode for Water Oxidation," Journal of the American Chemical Society, vol. 137, pp. 5798–5809, Apr. 2015.

[115] S. A. Mewes and A. Dreuw, "Density-based descriptors and exciton analyses for visualizing and understanding the electronic structure of excited states," Physical Chemistry Chemical Physics, vol. 21, no. 6, pp. 2843–2856, 2019.

[116] I. Mayer, "Using singular value decomposition for a compact presentation and improved interpretation of the CIS wave functions," Chemical Physics Letters, vol. 437, pp. 284–286, Apr. 2007.

[117] I. Ciofini, T. Le Bahers, C. Adamo, F. Odobel, and D. Jacquemin, "Through-space charge transfer in rod-like molecules: Lessons from theory," Journal of Physical Chemistry C, vol. 116, pp. 11946–11955, June 2012.

[118] M. Campetella, A. Perfetto, and I. Ciofini, "Quantifying partial hole-particle distance at the excited state: A revised version of the D_{CT} index," Chemical Physics Letters, vol. 714, pp. 81–86, Jan. 2019.

[119] T. Etienne, "Développement et application de stratégies d'étude théorique de propriétés remarquables relatives aux états excités moléculaires," Université de Lorraine, July 2015.

[120] C. A. Guido, P. Cortona, B. Mennucci, and C. Adamo, "On the metric of charge transfer molecular excitations: A simple chemical descriptor," Journal of Chemical Theory and Computation, vol. 9, pp. 3118–3126, July 2013.

[121] M. J. G. Peach, P. Benfield, T. Helgaker, and D. J. Tozer, "Excitation energies in density functional theory: An evaluation and a diagnostic test," Journal of Chemical Physics, vol. 128, pp. 044118–044118, Feb. 2008.

[122] Z.-L. Cai, K. Sendt, and J. R. Reimers, "Failure of density-functional theory and time-dependent density-functional theory for large extended π systems," The Journal of Chemical Physics, vol. 117, pp. 5543–5549, Sept. 2002.

[123] S. Grimme and M. Parac, "Substantial errors from time-dependent density functional theory for the calculation of excited states of large pi systems.," Chemphyschem : a European journal of chemical physics and physical chemistry, vol. 4, pp. 292–295, Mar. 2003.

[124] R. M. Richard and J. M. Herbert, "Time-Dependent Density-Functional Description of the 1L aState in Polycyclic Aromatic Hydrocarbons: Charge-Transfer Character in Disguise?," Journal of Chemical Theory and Computation, vol. 7, pp. 1296–1306, Apr. 2011.

[125] N. Kuritz, T. Stein, R. Baer, and L. Kronik, "Charge-Transfer-Like $\pi \rightarrow \pi^*$ Excitations in Time-Dependent Density Functional Theory: A Conundrum and Its Solution," Journal of Chemical Theory and Computation, vol. 7, pp. 2408–2415, July 2011.

[126] N. C. Handy and H. F. Schaefer, "On the evaluation of analytic energy derivatives for correlated wave functions," The Journal of Chemical Physics, vol. 81, pp. 5031–5033, Aug. 1998.

[127] C. Adamo and D. Jacquemin, "The calculations of excited-state properties with time-dependent density functional theory," Chemical Society Reviews, vol. 42, pp. 845–856, Feb. 2013.

[128] L. Wilbraham, M. Savarese, N. Rega, C. Adamo, and I. Ciofini, "Describing excited state intramolecular proton transfer in dual emissive systems: a density functional theory based analysis.," The Journal of Physical Chemistry B, vol. 119, pp. 2459–2466, Feb. 2015.

[129] W. Hieringer and A. Goerling, "Failure of time-dependent density functional methods for excitations in spatially separated systems," Chemical Physics Letters, vol. 419, pp. 557–562, Feb. 2006.

[130] M. R. Silva-Junior, M. Schreiber, S. P. A. Sauer, and W. Thiel, "Benchmarks for electronically excited states: Time-dependent density functional theory and density functional theory based multireference configuration interaction," Journal of Chemical Physics, vol. 129, pp. 104103–104103, Sept. 2008.

[131] A. Dreuw, J. L. Weisman, and M. Head-Gordon, "Long-range charge-transfer excited states in time-dependent density functional theory require non-local exchange," Journal of Chemical Physics, vol. 119, pp. 2943–2946, Aug. 2003.

[132] T. Ziegler, M. Seth, M. Krykunov, J. Autschbach, and F. Wang, "Is charge transfer transitions really too difficult for standard density functionals or are they just a problem for time-dependent density functional theory based on a linear response approach," Journal of Molecular Structure: THEOCHEM, vol. 914, pp. 106–109, Nov. 2009.

[133] B. Carlotti, E. Benassi, V. Barone, G. Consiglio, F. Elisei, A. Mazzoli, and A. Spalletti, "Effect of the π Bridge and Acceptor on Intramolecular Charge Transfer in Push-Pull Cationic Chromophores: An Ultrafast Spectroscopic and TD-DFT Computational Study.," Chemphyschem : a European journal of chemical physics and physical chemistry, vol. 16, pp. 1440–1450, May 2015.

[134] G. García, C. Adamo, and I. Ciofini, "Evaluating push–pull dye efficiency using TD-DFT and charge transfer indices," Physical chemistry chemical physics : PCCP, vol. 15, pp. 20210–20219, Nov. 2013.

[135] A. Dreuw and M. Head-Gordon, "Comment on: 'Failure of time-dependent density functional methods for excitations in spatially separated systems' by Wolfgang Hieringer and Andreas Görling," Chemical Physics Letters, vol. 426, pp. 231–233, July 2006.

[136] M. Ehara, R. Fukuda, C. Adamo, and I. Ciofini, "Chemically intuitive indices for charge-transfer excitation based on SAC-CI and TD-DFT calculations," Journal of Computational Chemistry, vol. 34, pp. 2498–2501, Nov. 2013.

[137] F. Cordova, L. J. Doriol, A. Ipatov, M. E. Casida, C. Filippi, and A. Vela, "Troubleshooting time-dependent density-functional theory for photochemical applications: Oxirane," The Journal of Chemical Physics, vol. 127, pp. 164111–19, Oct. 2007.

[138] F. Furche and R. Ahlrichs, "Adiabatic time-dependent density functional methods for excited state properties," Journal of Chemical Physics, vol. 117, pp. 7433–7447, Oct. 2002.

[139] F. Furche and D. Rappoport, "III. Density functional methods for excited states: Equilibrium structure and electronic spectra." Theoretical and Computational Chemistry, Karlsruhe Institute of Technology, Campus South, Karlsruhe, Germany, Jan. 2005.

[140] M. Pastore, X. Assfeld, E. Mosconi, A. Monari, and T. Etienne, "Unveiling the nature of post-linear response Z-vector method for time-dependent density functional theory.," The Journal of Chemical Physics, vol. 147, p. 024108, July 2017.

[141] E. Ronca, C. Angeli, L. Belpassi, F. De Angelis, F. Tarantelli, and M. Pastore, "Density Relaxation in Time-Dependent Density Functional Theory: Combining Relaxed Density Natural Orbitals and Multireference Perturbation Theories for an Improved Description of Excited States.," Journal of Chemical Theory and Computation, vol. 10, pp. 4014–4024, Sept. 2014.

[142] L. Belpassi, I. Infante, F. Tarantelli, and L. Visscher, "The chemical bond between Au(I) and the noble gases. Comparative study of NgAuF and NgAu+ (Ng = Ar, Kr, Xe) by density functional and coupled cluster methods.," Journal of the American Chemical Society, vol. 130, pp. 1048–1060, Jan. 2008.

[143] D. Cappelletti, E. Ronca, L. Belpassi, F. Tarantelli, and F. Pirani, "Revealing Charge-Transfer Effects in Gas-Phase Water Chemistry," Accounts of Chemical Research, vol. 45, pp. 1571–1580, July 2012.

[144] J. B. Foresman, M. Head-Gordon, J. A. Pople, and M. J. Frisch, "Toward a systematic molecular orbital theory for excited states," Journal of the American Chemical Society, vol. 96, pp. 135–149, Jan. 1992.

[145] M. J. Frisch, G. W. Trucks, H. B. Schlegel, G. E. Scuseria, M. A. Robb, J. R. Cheeseman, G. Scalmani, V. Barone, G. A. Petersson, H. Nakatsuji, X. Li, M. Caricato, A. V. Marenich, J. Bloino, B. G. Janesko, R. Gomperts, B. Mennucci, H. P. Hratchian, J. V. Ortiz, A. F. Izmaylov, J. L. Sonnenberg, D. Williams-Young, F. Ding, F. Lipparini, F. Egidi, J. Goings, B. Peng, A. Petrone, T. Henderson, D. Ranasinghe, V. G. Zakrzewski, J. Gao, N. Rega, G. Zheng, W. Liang, M. Hada, M. Ehara, K. Toyota, R. Fukuda, J. Hasegawa, M. Ishida, T. Nakajima, Y. Honda, O. Kitao, H. Nakai, T. Vreven, K. Throssell, J. J. A. Montgomery, J. E. Peralta, F. Ogliaro, M. J. Bearpark, J. J. Heyd, E. N. Brothers, K. N. Kudin, V. N. Staroverov, T. A. Keith, R. Kobayashi, J. Normand, K. Raghavachari, A. P. Rendell, J. C. Burant, S. S. Iyengar, J. Tomasi, M. Cossi, J. M. Millam, M. Klene, C. Adamo, R. Cammi, J. W. Ochterski, R. L. Martin, K. Morokuma, O. Farkas, J. B. Foresman, and D. J. Fox, "Gaussian 16 Revision B.01," tech. rep., 2016.

[146] T. M. Henderson, A. F. Izmaylov, G. Scalmani, and G. E. Scuseria, "Can short-range hybrids describe long-range-dependent properties?," Journal of Chemical Physics, vol. 131, pp. 044108–044108, Aug. 2009.

[147] R. W. H. Berry, P. Brocklehurst, and A. Burawoy, "The effect of terminal nitro and amino groups on the electronic spectra of conjugated hydrocarbon systems," Tetrahedron, vol. 10, pp. 109–117, Jan. 1960.

[148] A. Dreuw and M. Head-Gordon, "Failure of time-dependent density functional theory for long-range charge-transfer excited states: the zincbacteriochlorin-bacteriochlorin and bacteriochlorophyll-spheroidene complexes.," Journal of the American Chemical Society, vol. 126, pp. 4007–4016, Mar. 2004.

[149] Y.-J. Liu, D. Roca-Sanjuán, and R. Lindh, "Computational Photochemistry and Photophysics: the state of the art," in Photochemistry, pp. 42–72, Cambridge: Royal Society of Chemistry, 2012.

[150] M. A. Robb, M. Garavelli, M. Olivucci, and F. Bernardi, "A computational strategy for organic photochemistry," Reviews in Computational Chemistry, Vol 15, vol. 15, pp. 87–146, 2000.

[151] M. Olivucci, Computational Photochemistry. Elsevier, Oct. 2005.

[152] L. Serrano-Andrés, D. Roca-Sanjuán, and G. Olaso-González, "Recent trends in computational photochemistry," in Photochemistry, pp. 10–36, Cambridge: Royal Society of Chemistry, 2010.

[153] F. Plasser, S. A. Mewes, A. Dreuw, and L. González, "Detailed Wave Function Analysis for Multireference Methods: Implementation in the MolcasProgram Package and Applications to Tetracene," Journal of Chemical Theory and Computation, vol. 13, pp. 5343–5353, Oct. 2017.

[154] N. Tamai and H. Miyasaka, "Ultrafast Dynamics of Photochromic Systems," Chemical Reviews, vol. 100, pp. 1875–1890, May 2000.

[155] G. Berkovic, V. Krongauz, and V. Weiss, "Spiropyrans and Spirooxazines for Memories and Switches," Chemical Reviews, vol. 100, pp. 1741–1754, May 2000.

[156] V. Balzani, P. Ceroni, and A. Juris, Photochemistry and Photophysics. Concepts, Research, Applications, John Wiley & Sons, Mar. 2014.

[157] A. Zhugayevych and S. Tretiak, "Theoretical Description of Structural and Electronic Properties of Organic Photovoltaic Materials," dx.doi.org, vol. 66, pp. 305–330, Apr. 2015.

[158] S. Luber, K. Adamczyk, E. T. J. Nibbering, and V. S. Batista, "Photoinduced Proton Coupled Electron Transfer in 2-(2´-Hydroxyphenyl)-Benzothiazole," The Journal of Physical Chemistry A, vol. 117, pp. 5269–5279, June 2013.

[159] U. Raucci, M. Savarese, C. Adamo, I. Ciofini, and N. Rega, "Intrinsic and dynamical reaction pathways of an excited state proton transfer.," The Journal of Physical Chemistry B, vol. 119, pp. 2650–2657, Feb. 2015.

[160] M. Savarese, P. A. Netti, N. Rega, C. Adamo, and I. Ciofini, "Intermolecular proton shuttling in excited state proton transfer reactions: insights from theory," Physical Chemistry Chemical Physics, vol. 16, no. 18, pp. 8661–8666, 2014.

[161] H. C. Zhao, B.-L. Fu, D. Schweinfurth, J. P. Harney, B. Sarkar, M.-K. Tsai, and J. Rochford, "Tuning Oxyquinolate Non-Innocence at the Ruthenium Polypyridyl Core," European Journal of Inorganic Chemistry, vol. 2013, pp. 4410–4420, July 2013.

[162] B. An, H. Yuan, Q. Zhu, Y. Li, X. Guo, and J. Zhang, "Theoretical insight into the excited-state intramolecular proton transfer mechanisms of three amino-type hydrogen-bonding molecules," Spectrochimica Acta Part A: Molecular and Biomolecular Spectroscopy, vol. 175, pp. 36–42, Mar. 2017.

[163] G. Cui, P.-J. Guan, and W.-H. Fang, "Photoinduced Proton Transfer and Isomerization in a Hydrogen-Bonded Aromatic Azo Compound: A CASPT2//CASSCF Study," The Journal of Physical Chemistry A, vol. 118, pp. 4732–4739, June 2014.

[164] M. Savarese, P. A. Netti, C. Adamo, N. Rega, and I. Ciofini, "Exploring the metric of excited state proton transfer reactions," The Journal of Physical Chemistry B, vol. 117, pp. 16165–16173, Dec. 2013.

[165] M. Savarese, U. Raucci, P. A. Netti, C. Adamo, I. Ciofini, and N. Rega, "Modeling of charge transfer processes to understand photophysical signatures: The case of Rhodamine 110," Chemical Physics Letters, vol. 610-611, pp. 148–152, Aug. 2014.

[166] M. Savarese, U. Raucci, C. Adamo, P. A. Netti, I. Ciofini, and N. Rega, "Non-radiative decay paths in rhodamines: New theoretical insights," Physical Chemistry Chemical Physics, vol. 16, pp. 20681–20688, Sept. 2014.

[167] M. Ikegami and T. Arai, "Photoinduced intramolecular hydrogen atom transfer in 2-(2-hydroxyphenyl)benzoxazole and 2-(2-hydroxyphenyl)benzothiazole studied by laser flash photolysis," Journal of the Chemical Society, Perkin Transactions 2, pp. 1296–1301, May 2002.

[168] B. O. Roos, P. R. Taylor, and P. E. M. Si gbahn, "A complete active space SCF method (CASSCF) using a density matrix formulated super-CI approach," Chemical Physics, vol. 48, pp. 157–173, May 1980.

[169] K. Andersson, P. Å. Malmqvist, and B. O. Roos, "Second-order perturbation theory with a complete active space self-consistent field reference function," The Journal of Chemical Physics, vol. 96, pp. 1218–1226, Aug. 1998.

[170] N. Forsberg and P. Å. Malmqvist, "Multiconfiguration perturbation theory with imaginary level shift," Chemical Physics Letters, vol. 274, pp. 196–204, Aug. 1997.

[171] W. J. Hehre, R. Ditchfield, and J. A. Pople, "Self—Consistent Molecular Orbital Methods. XII. Further Extensions of Gaussian—Type Basis Sets for Use in Molecular Orbital Studies of Organic Molecules," The Journal of Chemical Physics, vol. 56, pp. 2257–2261, Mar. 1972.

[172] P. C. Hariharan and J. A. Pople, "The influence of polarization functions on molecular orbital hydrogenation energies," Theoretica Chimica Acta, vol. 28, no. 3, pp. 213–222, 1973.

[173] M. M. Francl, W. J. Pietro, W. J. Hehre, J. S. Binkley, M. S. Gordon, D. J. DeFrees, and J. A. Pople, "Self-consistent molecular orbital methods. XXIII. A polarization-type basis set for second-row elements," The Journal of Chemical Physics, vol. 77, pp. 3654–3665, Oct. 1982.

[174] T. Clark, J. Chandrasekhar, G. W. Spitznagel, and P. von Ragué Schleyer, "Efficient diffuse function-augmented basis sets for anion calculations. III. The 3-21+G basis set for first-row elements, Li–F," Journal of Computational Chemistry, vol. 4, pp. 294–301, Sept. 1983.

[175] G. W. Spitznagel, T. Clark, P. von Ragué Schleyer, and W. J. Hehre, "An evaluation of the performance of diffuse function-augmented basis sets for second row elements, Na-Cl," Journal of Computational Chemistry, vol. 8, pp. 1109–1116, Jan. 1987.

[176] F. Aquilante, J. Autschbach, R. K. Carlson, L. F. Chibotaru, M. G. Delcey, L. De Vico, I. Fdez Galván, N. Ferré, L. M. Frutos, L. Gagliardi, M. Garavelli, A. Giussani, C. E. Hoyer, G. Li Manni, H. Lischka, D. Ma, P. Å. Malmqvist, T. Müller, A. Nenov, M. Olivucci, T. B. Pedersen, D. Peng, F. Plasser, B. Pritchard, M. Reiher, I. Rivalta, I. Schapiro, J. Segarra-Martí, M. Stenrup, D. G. Truhlar, L. Ungur, A. Valentini, S. Vancoillie, V. Veryazov, V. P. Vysotskiy, O. Weingart, F. Zapata, and R. Lindh, "Molcas8: New capabilities for multiconfigurational quantum chemical calculations across the periodic table," Journal of Computational Chemistry, vol. 37, pp. 506–541, Nov. 2015.

[177] C. Group, "http://www.quanthic.fr. ."

[178] I. Ciofini, P. P. Lainé, F. Bedioui, and C. Adamo, "Photoinduced Intramolecular Electron Transfer in Ruthenium and Osmium Polyads: Insights from Theory," Journal of the American Chemical Society, vol. 126, pp. 10763–10777, 2004.

[179] M. E. Casida, C. Jamorski, K. C. Casida, and D. R. Salahub, "Molecular excitation energies to high-lying bound states from time-dependent density-functional response theory: Characterization and correction of the time-dependent local density approximation ionization threshold," Journal of Chemical Physics, vol. 108, pp. 4439–4449, Mar. 1998.

[180] D. Jacquemin, A. Planchat, C. Adamo, and B. Mennucci, "TD-DFT Assessment of Functionals for Optical 0–0 Transitions in Solvated Dyes," Journal of Chemical Theory and Computation, vol. 8, pp. 2359–2372, 2012.

[181] L. Cupellini, S. Jurinovich, M. Campetella, S. Caprasecca, C. A. Guido, S. M. Kelly, A. T. Gardiner, R. J. Cogdell, and B. Mennucci, "An Ab Initio Description of the Excitonic Properties of LH2 and Their Temperature Dependence," The Journal of Physical Chemistry B, 2016.

[182] V. Lemaur, M. Steel, D. Beljonne, J.-L. Brédas, and J. Cornil, "Photoinduced Charge Generation and Recombination Dynamics in Model Donor/Acceptor Pairs for Organic Solar Cell Applications: A Full Quantum-Chemical Treatment," Journal of the American Chemical Society, vol. 127, pp. 6077–6086, 2005.

[183] O. Gritsenko and E. J. Baerends, "Asymptotic correction of the exchange–correlation kernel of time-dependent density functional theory for long-range charge-transfer excitations," The Journal of Chemical Physics, vol. 121, pp. 655–660, 2004.

[184] D. J. Tozer, R. D. Amos, N. C. Handy, B. O. Roos, and L. Serrano-Andrés, "Does density functional theory contribute to the understanding of excited states of unsaturated organic compounds?," Molecular Physics, vol. 97, pp. 859–868, Jan. 1999.

[185] T. Risthaus, A. Hansen, and S. Grimme, "Excited states using the simplified Tamm–Dancoff-Approach for range-separated hybrid density functionals: development and application," Physical Chemistry Chemical Physics, vol. 16, no. 28, pp. 14408–14419, 2014.

[186] Y. Yamaguchi, "Effects of fluorination on electronic and excited states of fused zinc oligoporphyrins," The Journal of Chemical Physics, vol. 122, pp. 184702–11, May 2005.

[187] M.-C. Yoon, D. H. Jeong, S. Cho, D. Kim, H. Rhee, and T. Joo, "Ultrafast transient dynamics of Zn(II) porphyrins: Observation of vibrational coherence by controlling chirp of femtosecond pulses," The Journal of Chemical Physics, vol. 118, pp. 164–171, Jan. 2003.

[188] L. Duarte, B. M. Giuliano, I. Reva, and R. Fausto, "Tautomers and UV-Induced Photoisomerization of a Strongly Intramolecularly H-Bonded Aromatic Azo-Dye: 1-(Cyclopropyl)diazo-2-naphthol," The Journal of Physical Chemistry A, vol. 117, pp. 10671–10680, Oct. 2013.

[189] Z. R. Grabowski, K. Rotkiewicz, and W. Rettig, "Structural Changes Accompanying Intramolecular Electron Transfer: Focus on Twisted Intramolecular Charge-Transfer States and Structures," Chemical Reviews, vol. 103, pp. 3899–4032, Oct. 2003.

[190] S. I. Druzhinin, Y.-B. Jiang, A. Demeter, and K. A. Zachariasse, "Internal conversion with 4-(azetidinyl)benzonitriles in alkane solvents. Influence of fluoro substitution," Physical Chemistry Chemical Physics, vol. 3, pp. 5213–5221, Nov. 2001.

[191] I. Georgieva, A. J. A. Aquino, F. Plasser, N. Trendafilova, A. Köhn, and H. Lischka, "Intramolecular Charge-Transfer Excited-State Processes in 4-(N, N -Dimethylamino)benzonitrile: The Role of Twisting and the $\pi\sigma*$ State," Journal of Physical Chemistry A, vol. 119, pp. 6232–6243, June 2015.

[192] I. Gómez, P. J. Castro, and M. Reguero, "Insight into the mechanisms of luminescence of aminobenzonitrile and dimethylaminobenzonitrile in polar solvents. An ab initio study.," The Journal of Physical Chemistry A, vol. 119, pp. 1983–1995, Mar. 2015.

[193] S. Chevreux, R. Paulino Neto, C. Allain, K. Nakatani, P. Jacques, I. Ciofini, and G. Lemercier, "Solvent-tuned dual emission: a structural and electronic interplay highlighting a novel planar ICT (OPICT)," Physical chemistry chemical physics : PCCP, vol. 17, pp. 7639–7642, Mar. 2015.

[194] S. Mai, F. Plasser, J. Dorn, M. Fumanal, C. Daniel, and L. González, "Quantitative wave function analysis for excited states of transition metal complexes," Coordination Chemistry Reviews, vol. 361, pp. 74–97, Apr. 2018.

[195] A. Notaro and G. Gasser, "Monomeric and dimeric coordinatively saturated and substitutionally inert Ru(ii) polypyridyl complexes as anticancer drug candidates," Chemical Society Reviews, pp. 1–21, Oct. 2017.

[196] J. D. Knoll and C. Turro, "Control and utilization of ruthenium and rhodium metal complex excited states for photoactivated cancer therapy," Coordination Chemistry Reviews, vol. 282-283, pp. 110–126, Jan. 2015.

[197] R. E. Piau, T. Guillon, E. Lebon, N. Perrot, F. Alary, M. Boggio-Pasqua, J.-L. Heully, A. Juris, P. Sutra, and A. Igau, "Photophysical and electrochemical properties of polypyridine imine ruthenium(ii) complexes: a comparative experimental and theoretical study," New Journal of Chemistry, vol. 36, pp. 2484–2492, 2012.

[198] H. Huang, P. Zhang, B. Yu, Y. Chen, J. Wang, L. Ji, and H. Chao, "Targeting Nucleus DNA with a Cyclometalated Dipyridophenazineruthenium(II) Complex," Journal of Medicinal Chemistry, vol. 57, pp. 8971–8983, Oct. 2014.

[199] K. Kobayashi, H. Ohtsu, K. Nozaki, S. Kitagawa, and K. Tanaka, "Photochemical Properties and Reactivity of a Ru Compound Containing an NAD/NADH-Functionalized 1,10-Phenanthroline Ligand," Inorganic Chemistry, vol. 55, pp. 2076–2084, Feb. 2016.

[200] G. Li, L. Sun, L. Ji, and H. Chao, "Ruthenium(ii) complexes with dppz: from molecular photoswitch to biological applications," Dalton Transactions, vol. 45, no. 34, pp. 13261–13276, 2016.

[201] M. Schwalbe, M. Karnahl, S. Tschierlei, U. Uhlemann, M. Schmitt, B. Dietzek, J. Popp, R. Groake, J. G. Vos, and S. Rau, "The switch that wouldn't switch – unexpected luminescence from a ruthenium(II)-dppz-complex in water," Dalton Transactions, vol. 39, pp. 2768–2771, Mar. 2010.

[202] A. Chantzis, T. Very, A. Monari, and X. Assfeld, "Improved Treatment of Surrounding Effects: UV/vis Absorption Properties of a Solvated Ru(II) Complex," Journal of Chemical Theory and Computation, vol. 8, pp. 1536–1541, Apr. 2012.

[203] P. A. Malmqvist, A. Rendell, and B. O. Roos, "The restricted active space self-consistent-field method, implemented with a split graph unitary group approach," The Journal of Physical Chemistry, vol. 94, no. 14, pp. 5477–5482, 1990.

[204] E. D. Hedegård, S. Knecht, J. S. Kielberg, H. J. A. Jensen, and M. Reiher, "Density matrix renormalization group with efficient dynamical electron correlation through range separation," The Journal of Chemical Physics, vol. 142, pp. 224108–12, June 2015.

[205] M. Jäger, L. Freitag, and L. González, "Using computational chemistry to design Ru photosensitizers with directional charge transfer," Coordination Chemistry Reviews, vol. 304-305, pp. 146–165, Dec. 2015.

[206] A. Chantzis, T. Very, S. Despax, J.-T. Issenhuth, A. Boeglin, P. Hébraud, M. G. Pfeffer, A. Monari, and X. Assfeld, "UV–vis absorption spectrum of a novel Ru(II) complex intercalated in DNA: [Ru(2,2´-bipy)(dppz)(2,2´-ArPy)]+," Journal of Molecular Modeling, vol. 20, pp. 8120–10, Feb. 2014.

[207] F. Heinemann, J. Karges, and G. Gasser, "Critical Overview of the Use of Ru(II) Polypyridyl Complexes as Photosensitizers in One-Photon and Two-Photon Photodynamic Therapy," Accounts of Chemical Research, vol. 50, pp. 2727–2736, Oct. 2017.

[208] A. W. McKinley, P. Lincoln, and E. M. Tuite, "Environmental effects on the photophysics of transition metal complexes with dipyrido[2,3-a:3′,2′-c]phenazine (dppz) and related ligands," Coordination Chemistry Reviews, vol. 255, pp. 2676–2692, Nov. 2011.

[209] A. Yoshimura, M. Z. Hoffman, and H. Sun, "An evaluation of the excited state absorption spectrum of Ru(bpy)32+ in aqueous and acetonitrile solutions," "Journal of Photochemistry & Photobiology, A: Chemistry", vol. 70, pp. 29–33, Jan. 1993.

[210] S. Finck, J.-T. Issenhuth, S. Despax, C. Sirlin, M. G. Pfeffer, C. Poidevin, C. Gourlaouen, A. Boeglin, and C. Daniel, "Structural and optical properties of new cyclometalated Ru(II) derived compounds," Journal of Organometallic Chemistry, vol. 760, pp. 248–259, June 2014.

[211] T. Yoshihara, V. A. Galievsky, S. I. Druzhinin, S. Saha, and K. A. Zachariasse, "Singlet excited state dipole moments of dual fluorescent N-phenylpyrroles and 4-(dimethylamino)benzonitrile from solvatochromic and thermochromic spectral shifts," Photochemical & Photobiological Sciences, vol. 2, pp. 342–353, Mar. 2003.

[212] Y. Sun, S. N. Collins, L. E. Joyce, and C. Turro, "Unusual Photophysical Properties of a Ruthenium(II) Complex Related to [Ru(bpy) 2(dppz)] 2+," Inorganic Chemistry, vol. 49, pp. 4257–4262, May 2010.

[213] H. Torieda, K. Nozaki, A. Yoshimura, and T. Ohno, "Low quantum yields of relaxed electron transfer products of moderately coupled ruthenium(II)-cobalt(III) compounds on the subpicosecond laser excitation," Journal of Physical Chemistry A, vol. 108, pp. 4819–4829, June 2004.

[214] E. Jakubikova, W. Chen, D. M. Dattelbaum, F. N. Rein, R. C. Rocha, R. L. Martin, and E. R. Batista, "Electronic Structure and Spectroscopy of [Ru(tpy) 2] 2+, [Ru(tpy)(bpy)(H 2O)] 2+, and [Ru(tpy)(bpy)(Cl)] +," Inorganic Chemistry, vol. 48, pp. 10720–10725, Nov. 2009.

[215] Y. Sun and C. Turro, "Highly Solvent Dependent Luminescence from [Ru(bpy) n(dppp2) 3− n] 2+(n= 0−2)," Inorganic Chemistry, vol. 49, pp. 5025–5032, June 2010.

[216] S. Chevreux, C. Allain, L. Wilbraham, K. Nakatani, P. Jacques, I. Ciofini, and G. Lemercier, "Solvent tuned single molecule dual emission in protic solvents: effect of polarity and H-bonding," Faraday Discussions, vol. 185, pp. 285–297, 2015.

[217] D. Rappoport and F. Furche, "Photoinduced Intramolecular Charge Transfer in 4-(Dimethyl)aminobenzonitrile - A Theoretical Perspective," Journal of the American Chemical Society, vol. 126, pp. 1277–1284, Feb. 2004.

[218] J. Dreyer and A. Kummrow, "Shedding Light on Excited-State Structures by Theoretical Analysis of Femtosecond Transient Infrared Spectra: Intramolecular Charge Transfer in 4-(Dimethylamino)benzonitrile," Journal of the American Chemical Society, vol. 122, pp. 2577–2585, Mar. 2000.

[219] B. G. Levine, C. Ko, J. Quenneville, and T. J. Martínez, "Conical intersections and double excitations in time-dependent density functional theory," Molecular Physics, vol. 104, pp. 1039–1051, Mar. 2006.

[220] S. Prager, I. Burghardt, and A. Dreuw, "Ultrafast C_{spiro}-O dissociation via a conical intersection drives spiropyran to merocyanine photoswitching," Journal of Physical Chemistry A, vol. 118, pp. 1339–1349, Feb. 2014.

[221] L. Serrano-Andrés and M. Merchán, "Quantum chemistry of the excited state: 2005 Overview," in Journal of Molecular Structure: THEOCHEM, pp. 99–108, University of Valencia, Valencia, Spain, Sept. 2005.

[222] J. Calbo, C. E. Weston, A. J. P. White, H. S. Rzepa, J. Contreras-García, and M. J. Fuchter, "Tuning Azoheteroarene Photoswitch Performance through Heteroaryl Design," Journal of the American Chemical Society, vol. 139, pp. 1261–1274, Jan. 2017.

[223] M. C. Bacchus-Montabonel, K. Piechowska, Y. S. Tergiman, and J. E. Sienkiewicz, "Photodissociation of polyatomic systems: non-adiabatic effects and conical intersections," Journal of Molecular Structure: THEOCHEM, vol. 729, pp. 115–123, Sept. 2005.

[224] J. P. Malhado, "Non-adiabatic dynamics close to conical intersections and the surface hopping perspective," Frontiers in Chemistry, vol. 2, pp. 1–21, Nov. 2014.

[225] J. C. Germino, C. A. Barboza, F. J. Quites, P. A. M. Vazquez, and T. D. Z. Atvars, "Dual Emissions of Salicylidene-5-chloroaminepyridine Due to Excited State Intramolecular Proton Transfer: Dynamic Photophysical and Theoretical Studies," The Journal of Physical Chemistry C, vol. 119, pp. 27666–27675, Nov. 2015.

[226] B. F. E. Curchod, A. Sisto, and T. J. Martínez, "Ab Initio Multiple Spawning Photochemical Dynamics of DMABN Using GPUs," The Journal of Physical Chemistry A, vol. 121, pp. 265–276, Dec. 2016.

[227] E. Titov, A. Humeniuk, and R. Mitrić, "Exciton localization in excited-state dynamics of a tetracene trimer: a surface hopping LC-TDDFTB study," Physical Chemistry Chemical Physics, vol. 20, no. 40, pp. 25995–26007, 2018.

[228] P. Lutsyk, Y. Piryatinski, O. Kachkovsky, A. Verbitsky, and A. Rozhin, "Unsymmetrical Relaxation Paths of the Excited States in Cyanine Dyes Detected by Time-Resolved Fluorescence: Polymethinic and Polyenic Forms," The Journal of Physical Chemistry A, vol. 121, pp. 8236–8246, Oct. 2017.

[229] Z. He, X. Cai, Z. Wang, D. Chen, Y. Li, H. Zhao, K. Liu, Y. Cao, and S.-J. Su, "Reversible switching between normal and thermally activated delayed fluorescence towards "smart" and single compound white-light luminescence via controllable conformational distribution," Science China Chemistry, vol. 61, pp. 677–686, Apr. 2018.

[230] N. Nagarajan, G. Velmurugan, P. Venuvanalingam, and R. Renganathan, "Tunable single and dual emission behavior of imidazole fluorophores based on D-π-A architecture," "Journal of Photochemistry & Photobiology, A: Chemistry", vol. 284, pp. 36–48, June 2014.

[231] M. Segado, E. Benassi, and V. Barone, "A "Twist" on the Interpretation of the Multifluorescence Patterns of DASPMI," Journal of Chemical Theory and Computation, vol. 11, pp. 4803–4813, Sept. 2015.

[232] J. Catalán, "On the dual emission of p-dimethylaminobenzonitrile and its photophysical implications," Physical chemistry chemical physics : PCCP, vol. 15, pp. 8811–8820, May 2013.

[233] M. Barbatti, A. J. A. Aquino, H. Lischka, C. Schriever, S. Lochbrunner, and E. Riedle, "Ultrafast internal conversion pathway and mechanism in 2-(2´-hydroxyphenyl)benzothiazole : a case study for excited-state intramolecular proton transfer systems," Physical Chemistry Chemical Physics, vol. 11, no. 9, pp. 1406–1415, 2009.

[234] M. Savarese, É. Brémond, C. Adamo, N. Rega, and I. Ciofini, "Excited-State Proton Transfer and Intramolecular Charge Transfer in 1,3-Diketone Molecules," Chemphyschem : a European journal of chemical physics and physical chemistry, vol. 17, pp. 1530–1538, May 2016.

[235] J. Chen, T. Yu, E. Ubba, Z. Xie, Z. Yang, Y. Zhang, S. Liu, J. Xu, M. P. Aldred, and Z. Chi, "Achieving Dual-Emissive and Time-Dependent Evolutive Organic Afterglow by Bridging Molecules with Weak Intermolecular Hydrogen Bonding," Advanced Optical Materials, vol. 115, pp. 1801593–7, Jan. 2019.

[236] I. Marghad, F. Bencheikh, C. Wang, S. Manolikakes, A. Rérat, C. Gosmini, D. h. Kim, J.-C. Ribierre, and C. Adachi, "Control of the dual emission from a thermally activated delayed fluorescence emitter containing phenothiazine units in organic light-emitting diodes," RSC Advances, vol. 9, no. 8, pp. 4336–4343, 2019.

[237] Q. Huang, X. Mei, Z. Xie, D. Wu, S. Yang, W. Gong, Z. Chi, Z. Lin, and Q. Ling, "Photo-induced phosphorescence and mechanoluminescence switching in a simple purely organic molecule," Journal of Materials Chemistry C, vol. 7, no. 9, pp. 2530–2534, 2019.

[238] B. Huang, W.-C. Chen, Z. Li, J. Zhang, W. Zhao, Y. Feng, B. Z. Tang, and C.-S. Lee, "Manipulation of Molecular Aggregation States to Realize Polymorphism, AIE, MCL, and TADF in a Single Molecule," Angewandte Chemie (International ed. in English), vol. 57, pp. 12473–12477, Aug. 2018.

[239] Z. He, W. Zhao, J. W. Y. Lam, Q. Peng, H. Ma, G. Liang, Z. Shuai, and B. Z. Tang, "White light emission from a single organic molecule with dual phosphorescence at room temperature," Nature communications, pp. 1–7, Aug. 2017.

[240] U. Warde and S. Nagaiyan, "Comprehensive study on excited state intramolecular proton transfer in 2-(benzo[d]thiazol-2-yl)-3-methoxynaphthalen-1-ol and 2-(benzo[d]thiazol-2-yl)naphthalene-1,3-diol: Effect of solvent, aggregation, viscosity and TDDFT study," "Journal of Photochemistry & Photobiology, A: Chemistry", vol. 337, pp. 33–43, Mar. 2017.

[241] Y. Wu, X. Peng, J. Fan, S. Gao, M. Tian, J. Zhao, and S. Sun, "Fluorescence Sensing of Anions Based on Inhibition of Excited-State Intramolecular Proton Transfer," The Journal of Organic Chemistry, vol. 72, pp. 62–70, Dec. 2006.

[242] G. Ulrich, F. Nastasi, P. Retailleau, F. Puntoriero, R. Ziessel, and S. Campagna, "Luminescent Excited-State Intramolecular Proton-Transfer (ESIPT) Dyes Based on 4-Alkyne-Functionalized [2,2´-Bipyridine]-3,3´-diol Dyes," Chemistry - A European Journal, vol. 14, pp. 4381–4392, May 2008.

[243] U. Subuddhi, S. Haldar, S. Sankararaman, and A. K. Mishra, "Photophysical behaviour of 1-(4-N , N -dimethylaminophenylethynyl)pyrene (DMAPEPy) in homogeneous media," Photochemical & Photobiological Sciences, vol. 5, no. 5, pp. 459–466, 2006.

[244] H. Tanaka, K. Shizu, H. Nakanotani, and C. Adachi, "Dual Intramolecular Charge-Transfer Fluorescence Derived from a Phenothiazine-Triphenyltriazine Derivative," The Journal of Physical Chemistry C, vol. 118, pp. 15985–15994, July 2014.

[245] S. Jana, S. Dalapati, S. Ghosh, and N. Guchhait, "Excited state intramolecular charge transfer process in 5-(4-dimethylamino-phenyl)-penta-2,4-dienoic acid ethyl ester and effect of acceptor functional groups," "Journal of Photochemistry & Photobiology, A: Chemistry", vol. 261, pp. 31–40, June 2013.

[246] R. V. Pereira and M. H. Gehlen, "Photoinduced Intramolecular Charge Transfer in 9-Aminoacridinium Derivatives Assisted by Intramolecular H-Bond," The Journal of Physical Chemistry A, vol. 110, pp. 7539–7546, May 2006.

[247] R. V. Pereira and M. H. Gehlen, "Spectroscopy of auramine fluorescent probes free and bound to poly(methacrylic acid).," The Journal of Physical Chemistry B, vol. 110, pp. 6537–6542, Apr. 2006.

[248] M. K. Etherington, F. Franchello, J. Gibson, T. Northey, J. Santos, J. S. Ward, H. F. Higginbotham, P. Data, A. Kurowska, P. L. Dos Santos, D. R. Graves, A. S. Batsanov, F. B. Dias, M. R. Bryce, T. J. Penfold, and A. P. Monkman, "Regio- and conformational isomerization critical to design of efficient thermally-activated delayed fluorescence emitters," Nature communications, vol. 8, pp. 1–11, Apr. 2017.

[249] M. Okazaki, Y. Takeda, P. Data, P. Pander, H. Higginbotham, A. P. Monkman, and S. Minakata, "Thermally activated delayed fluorescent phenothiazine–dibenzo[a,j]phenazine–phenothiazine triads exhibiting tricolor-changing mechanochromic luminescence," Chemical Science, vol. 8, no. 4, pp. 2677–2686, 2017.

[250] K. Wang, C.-J. Zheng, W. Liu, K. Liang, Y.-Z. Shi, S.-L. Tao, C.-S. Lee, X.-M. Ou, and X.-H. Zhang, "Avoiding Energy Loss on TADF Emitters: Controlling the Dual Conformations of D-A Structure Molecules Based on the Pseudoplanar Segments," Advanced Materials, vol. 29, pp. 1701476–9, Nov. 2017.

[251] W.-H. Chen, Y. Xing, and Y. Pang, "A Highly Selective Pyrophosphate Sensor Based on ESIPT Turn-On in Water," Organic Letters, vol. 13, pp. 1362–1365, Feb. 2011.

[252] E. Lippert, W. Lüder, F. Moll, W. Nägele, H. Boos, H. Prigge, and I. Seibold-Blankenstein, "Umwandlung von Elektronenanregungsenergie," Angewandte Chemie, vol. 73, pp. 695–706, Nov. 1961.

[253] B. Mennucci, A. Toniolo, and J. Tomasi, "Ab initio study of the electronic excited states in 4-(N,N-dimethylamino)benzonitrile with inclusion of solvent effects: The internal charge transfer process," Journal of the American Chemical Society, vol. 122, pp. 10621–10630, Nov. 2000.

[254] S. Cogan, S. Zilberg, and Y. Haas, "The electronic origin of the dual fluorescence in donor-acceptor substituted benzene derivatives," Journal of the American Chemical Society, vol. 128, pp. 3335–3345, Mar. 2006.

[255] K. Suda and D. Yokogawa, "Theoretical Study on Nonradiative Decay of Dimethylaminobenzonitrile through Triplet State in Gas-Phase, Nonpolar, and Polar Solutions," The Journal of Physical Chemistry B, vol. 121, pp. 2164–2170, Mar. 2017.

[256] J. Catalán, "Can the dipolarity of the medium induce the formation of charge transfer structures? An unexpected finding in the photophysics of DMABN," Physical chemistry chemical physics : PCCP, vol. 16, pp. 7734–7740, Apr. 2014.

[257] Y. V. Il'ichev, W. Kühnle, and K. A. Zachariasse, "Intramolecular Charge Transfer in Dual Fluorescent 4-(Dialkylamino)benzonitriles. Reaction Efficiency Enhancement by Increasing the Size of the Amino and Benzonitrile Subunits by Alkyl Substituents," The Journal of Physical Chemistry A, vol. 102, pp. 5670–5680, July 1998.

[258] I. Gómez, M. Reguero, M. Boggio-Pasqua, and M. A. Robb, "Intramolecular charge transfer in 4-aminobenzonitriles does not necessarily need the twist," Journal of the American Chemical Society, vol. 127, pp. 7119–7129, May 2005.

[259] P. B. Coto, L. Serrano-Andrés, T. Gustavsson, T. Fujiwara, and E. C. Lim, "Intramolecular charge transfer and dual fluorescence of 4-(dimethylamino)benzonitrile: ultrafast branching followed by a two-fold decay mechanism," Physical chemistry chemical physics : PCCP, vol. 13, pp. 15182–15188, Sept. 2011.

[260] M. Segado, Y. Mercier, I. Gómez, and M. Reguero, "Intramolecular charge transfer in aminobenzonitriles and tetrafluoro counterparts: fluorescence explained by competition between low lying excited states and radiationless deactivation. Part II: influence of substitution on luminescence patterns," Physical Chemistry Chemical Physics, vol. 18, no. 9, pp. 6875–6884, 2016.

[261] Y. Dai, S. Zhang, H. Liu, K. Wang, F. Li, B. Han, B. Yang, and B. Zou, "Pressure Tuning Dual Fluorescence of 4-(N,N-Dimethylamino)benzonitrile," Journal of Physical Chemistry C, vol. 121, pp. 4909–4916, Mar. 2017.

[262] A. B. J. Parusel, W. Rettig, and W. Sudholt, "A comparative theoretical study on DMABN: Significance of excited state optimized geometries and direct comparison of methodologies," Journal of Physical Chemistry A, vol. 106, pp. 804–815, Feb. 2002.

[263] N. Minezawa and S. Kato, "Intramolecular charge-transfer state formation of 4-(N,N-dimethylamino) benzonitrile in acetonitrile solution: RISM-SCF study," Journal of Physical Chemistry A, vol. 109, pp. 5445–5453, June 2005.

[264] L. Serrano-Andrés, M. Merchán, B. O. Roos, and R. Lindh, "Theoretical Study of the Internal Charge Transfer in Aminobenzonitriles," Journal of the American Chemical Society, vol. 117, no. 11, pp. 3189–3204, 1995.

[265] A. Köhn and C. Hättig, "On the nature of the low-lying singlet states of 4-(Dimethyl-amino)benzonitrile," Journal of the American Chemical Society, vol. 126, pp. 7399–7410, June 2004.

[266] C. Hättig, A. Hellweg, and A. Köhn, "Intramolecular charge-transfer mechanism in quinolidines: The role of the amino twist angle," Journal of the American Chemical Society, vol. 128, pp. 15672–15682, Dec. 2006.

[267] S. Carlotto, A. Polimeno, C. Ferrante, C. Benzi, and V. Barone, "Integrated approach for modeling the emission fluorescence of 4-(N,N-Dimethylamino)benzonitrile-in polar environments," The Journal of Physical Chemistry B, vol. 112, pp. 8106–8113, July 2008.

[268] K. A. Zachariasse, M. Grobys, T. von der Haar, A. Hebecker, Y. V. Il'ichev, Y.-B. Jiang, O. Morawski, and W. Kühnle, "Erratum to "Intramolecular charge transfer in the excited state. Kinetics and configurational changes" [J. Photochem. Photobiol. A: Chem., 102 (1996) 59–70]," "Journal of Photochemistry & Photobiology, A: Chemistry", vol. 115, no. 3, p. 259, 1998.

[269] K. A. Zachariasse, S. I. Druzhinin, V. A. Galievsky, S. A. Kovalenko, T. A. Senyushkina, P. Mayer, M. Noltemeyer, M. Boggio-Pasqua, and M. A. Robb, "Counterintuitive absence of an excited-state intramolecular charge transfer reaction with 2,4,6-tricyanoanilines. experimental and computational results," Journal of Physical Chemistry A, vol. 113, pp. 2693–2710, Mar. 2009.

[270] W. Rettig, B. Bliss, and K. Dirnberger, "Pseudo-Jahn–Teller and TICT-models: a photophysical comparison of meta- and para-DMABN derivatives," Chemical Physics Letters, vol. 305, no. 1-2, pp. 8–14, 1999.

[271] P. J. Castro, A. Perveaux, D. Lauvergnat, M. Reguero, and B. Lasorne, "Ultrafast internal conversion in 4-aminobenzonitrile occurs sequentially along the seam," Chemical Physics, vol. 509, pp. 30–36, June 2018.

[272] J. C. Sancho-García and A. J. Pérez-Jiménez, "Nitrobenzene rotational energy barrier: A survey of several ab initiomethods," The Journal of Chemical Physics, vol. 119, pp. 5121–5127, Sept. 2003.

[273] A. P. Demchenko, V. I. Tomin, and P.-T. Chou, "Breaking the Kasha Rule for More Efficient Photochemistry," Chemical Reviews, vol. 117, pp. 13353–13381, Oct. 2017.

[274] J. Buback, M. Kullmann, F. Langhojer, P. Nuernberger, R. Schmidt, F. Würthner, and T. Brixner, "Ultrafast Bidirectional Photoswitching of a Spiropyran," Journal of the American Chemical Society, vol. 132, pp. 16510–16519, Nov. 2010.

[275] K. S. Conrad, C. C. Manahan, and B. R. Crane, "Photochemistry of flavoprotein light sensors," Nature Publishing Group, vol. 10, pp. 801–809, Oct. 2014.

[276] J. Fregoni, G. Granucci, E. Coccia, M. Persico, and S. Corni, "Manipulating azobenzene photoisomerization through strong lightâ€"molecule coupling," Nature communications, pp. 1–9, Nov. 2018.

[277] R. D. Levine, "Photochemistry of highly excited states," Proceedings of the National Academy of Sciences, vol. 114, pp. 13594–13596, Dec. 2017.

[278] S. Ruetzel, M. Kullmann, J. Buback, P. Nuernberger, and T. Brixner, "Tracing the Steps of Photoinduced Chemical Reactions in Organic Molecules by Coherent Two-Dimensional Electronic Spectroscopy Using Triggered Exchange," Physical Review Letters, vol. 110, pp. 148305–5, Apr. 2013.

[279] H. D. de Gier, R. Broer, and R. W. A. Havenith, "On the relation between local and charge-transfer exciton binding energies in organic photovoltaic materials," in SPIE Organic Photonics + Electronics (Z. H. Kafafi, P. A. Lane, and I. D. W. Samuel, eds.), pp. 95670N–26, SPIE, Sept. 2015.

[280] J. Sanz García, M. Boggio-Pasqua, I. Ciofini, and M. Campetella, "Excited State Tracking During the Relaxation of Coordination Compounds," arXiv.org, 2019.

[281] G. M. J. Barca, A. T. B. Gilbert, and P. M. W. Gill, "Simple Models for Difficult Electronic Excitations," Journal of Chemical Theory and Computation, vol. 14, pp. 1501–1509, Feb. 2018.

[282] A. T. B. Gilbert, N. A. Besley, and P. M. W. Gill, "Self-Consistent Field Calculations of Excited States Using the Maximum Overlap Method (MOM) †," The Journal of Physical Chemistry A, vol. 112, pp. 13164–13171, Dec. 2008.

[283] N. J. Turro, V. Ramamurthy, and J. C. Scaiano, Principles of Molecular Photochemistry: An Introduction. Raymond F. Boyer Library Collection, University Science Books, 2009.

[284] L. E. Roy, P. J. Hay, and R. L. Martin, "Revised Basis Sets for the LANL Effective Core Potentials," Journal of Chemical Theory and Computation, vol. 4, no. 7, pp. 1029–1031, 2008.

RÉSUMÉ

Cette thèse porte sur la conception, la construction et l'application d'une méthodologie de calcul qui vise à l'étude et à la rationalisation des propriétés photo-physiques de systèmes moléculaires dans le contexte de la théorie de la fonctionnelle de la densité dépendante du temps (TDDFT). L'objectif principal du travail décrit dans ce manuscrit est de définir un ensemble de descripteurs de la densité, déduits à dessein, qui peuvent être combinés pour fournir une interprétation simple des chemins photo-physiques d'intérêt, relatifs aux nombreux processus se déroulant à l'état excité. Plus spécifiquement, nous fournissons une collection de protocoles de calcul basés sur la TDDFT, construits à partir des distributions de densité électronique de l'état fondamental ainsi que des états excités, afin de caractériser les différentes surfaces d'énergie potentielle des systèmes moléculaires. Globalement, les descripteurs de densité ainsi que l'approche utilisée pour l'étude des états excités décrits dans cette thèse constituent un moyen fiable et peu coûteux de révéler les chemins de relaxation d'états excités dans la modélisation théorique des processus photo-physiques.

MOTS CLÉS

photochimie • index de la densité • calcul ab initio • états excités • spectroscopie • développements méthodologiques.

ABSTRACT

This thesis focuses on devising, constructing, and applying cost-effective approaches to calculate the photophysical properties of molecular systems in the context of time-dependent density functional theory (TDDFT). The objective of our work is to define a set of purposely-derived density descriptors that can be combined to provide a straightforward interpretation of the relevant photophysical pathways for the many processes taking place at the excited state. More specifically, we deliver a collection of TDDFT-based computational protocols, based on the knowledge of ground and excited state densities, to characterize the excited-state potential energy surfaces of molecular systems. Overall, the state-tracking algorithm and the density-descriptors outlined in this thesis collectively provide a reliable and cost-effective way of disclosing excited state pathways within the theoretical modeling of photophysical processes. The proposed approach can be computed "on the fly" to identify critical areas for TDDFT approaches while, contextually, providing a method for the qualitative identification - in conjunction with energy criteria - of possible reactions paths.

KEYWORDS

photochemistry • density-based indexes • ab initio calculations • spectroscopy • excited state tracking • modeling of excited states.